SCUOLA DI DOTTORATO
UNIVERSITÀ DEGLI STUDI DI MILANO-BICOCCA

Dipartimento di / Department of

Biotecnologie e bioscienze

Dottorato di Ricerca in / PhD program Scienze della Vita Ciclo / Cycle XXIX

Curriculum in (se presente / if it is) Biologia

Development of apoferritin nanoparticles for chemotherapeutic delivery and drug resistance overcoming in breast cancer models

Cognome / Surname Bellini Nome / Name Michela

Matricola / Registration number 787807

Tutore / Tutor: Prof. Paolo Tortora

Cotutore / Co-tutor:
(se presente / if there is one)

Supervisor:
(se presente / if there is one)

Coordinatore / Coordinator: Prof. Marco Vanoni

ANNO ACCADEMICO / ACADEMIC YEAR 2015/2016

Development of apoferritin nanoparticles for chemotherapeutic delivery and drug resistance overcoming in breast cancer models

Table of contents

Abstract

Cancer is a leading cause of disease worldwide and breast cancer, which exists in four major molecular subtypes, is the second most common cause of cancer mortality. Although there are many therapeutic options, chemotherapy is still subject to failures, due to (1) the low selectivity of drugs, which requires high doses with side effects and the risk of recurrence and (2) the development of resistance by different mechanisms that cells put in place to defend themselves from the action of drugs.

In my PhD project I exploited the unique features of a nanoparticle based on recombinant heavy-chain ferritin cages (HFn) for the targeted delivery of various active molecules to improve the treatment efficacy in breast cancer. My work is divided into three main subprojects, all sharing the use of HFn.

Initially, I exploited HFn nanocages for the encapsulation of a chemotherapeutic drug, doxorubicin (DOX). HFn-DOX acts as a "Trojan Horse": nanoparticles are internalized in cancer cells faster and more efficiently compared to free DOX, then promptly translocated into the nucleus with a self-triggered mechanism, thus promoting a fast and massive delivery of the drug inside the nuclear compartment, strongly affecting viability and circumventing MDR mechanisms. Then, I tested HFn-DOX on an aggressive breast cancer model, *in vitro* and *in vivo*, under a Low Dose Nanometronomic regimen (LDNM). Metronomic HFn-DOX strongly improved the antitumor potential of DOX chemotherapy arresting the tumor progression. Such effect is attributable to multiple nanodrug actions, including inhibition of tumor angiogenesis and avoidance of chemoresistance. Moreover, metronomic HFn-DOX drastically reduced cardiotoxicity.

In the second project, curcumin was encapsulated in HFn (CFn) and used to treat triple negative breast cancer (TNBC) cell lines. Curcumin is a natural anti tumor compound, but is rapidly degraded and scantily bioavailable. CFn had instead good stability and solubility and was able to enhance the sensitization of TNBC cells to DOX treatment.

Finally, HFn was used as a vehicle to transport anti-microRNAs, since miR21 plays a role in the development of resistance against Trastuzumab (TZ), the treatment of choice for HER2 positive breast cancer. The major limiting factor in gene therapy is the ability to specifically deliver nucleotide sequences: however, anti-miR21 cross-linked to HFn, was released into the cytoplasm.

Based on our results, ferritin is an effective system for the delivery of anti-tumor molecules, promoting their chemotherapic action and/or overcoming the problem of resistance that limits the effectiveness of many therapies.

CHAPTER 1

General introduction

1.1 Cancer

The term "cancer" refers to a group of diseases involving abnormal cell growth with the potential to invade or spread to other parts of the body. Normally, human cells grow and divide to form new cells as the organism needs them. When cancer develops, however, this orderly process breaks down: cells become more and more abnormal and survive when they should die. These extra cells can divide without stopping, forming growths called tumors. Cancerous tumors are malignant, which means they can spread into, or invade, nearby tissues. In addition, as these tumors grow, some cancer cells can break off and travel to distant places in the body through the blood or the lymph system and form metastasis.

The World Health Organization (WHO) attributed 8.2 million deaths to cancer in 2012, accounting for about 13% of all deaths. In the same year, 14.1 million new cases of cancer were diagnosed worldwide and the global cancer incidences are expected to increase to 23.6 millions in the next two decades. The good news is that about 32 million people diagnosed with cancer in the previous five years were alive at the end of 2012 and most of them were women after their breast cancer diagnosis (6.3 million)[1,2]. For sure, early detection, accurate diagnosis and effective treatment (thanks to a variety of therapeutic options), have helped to increase cancer survival rates. Despite all, cancer is still a leading cause of death worldwide and further improvements are needed.

We can identify two main reasons for treatment failure: the lack of selective delivery of anti-cancer compounds to neoplastic tissue and the development of resistance by the tumor tissue.

1.1.1 Challenges for chemotherapy (1): targeting

Several treatment options are available for cancer, including surgery, radiation therapy and chemotherapy. If surgery and radiation therapy remove, kill, or damage cancer cells in a specific area, on the other side chemotherapy can work throughout the whole body and kill cancer cells that have spread to parts of the body far away from the primary tumor. Conventional chemotherapy, which utilizes small molecular drugs, is the treatment of choice for many cancers but although these molecules are able to kill neoplastic cells with high efficacy, they lack precision and are systemically distributed without preferential localization to cancer tissue. This process results in drug-induced toxicity in healthy tissues, primarily affecting the fast-dividing cells of the body, but not only[3]. Furthermore, the poor selectivity also implies the necessity of using high doses of drugs and promotes a high risk of recurrence. Indeed, according to the “maximum tolerated dose” (MTD) paradigm, patients are administered with single or short courses of the highest tolerable dosage of a drug, in order to achieve the best therapeutic efficacy with minimal possible toxicity. These treatments cannot be protracted for a long time, just because of the low selectivity of the drugs, and prolonged breaks between different chemotherapy cycles are mandatory to allow recovery of healthy tissues and reduce myelosuppression[4,5]. The problem is that in fast-growing or metastatic tumors, during these therapeutic breaks a burst in cancer cell proliferation is likely, together with the manifestation of chemoresistance and accelerated angiogenesis[6].

Thus, there is an urgent need to develop drugs with high selectivity to target tumors, which may greatly reduce drug toxicity and enhance the therapeutic efficacy of chemotherapeutics. In this context, as we will see later, nanoparticles take on incredible importance[7].

1.1.2 Challenges for chemotherapy (2): Multidrug Resistance

Although chemotherapy drugs are an effective treatment for many types of tumors, not all patients can be cured by these approaches and some of them respond transiently or incompletely: the ability of cancer cells to become simultaneously resistant to different drugs remains a significant obstacle to therapeutic success[8]. "Multidrug resistance" (MDR) is the term used to describe this feature: patients may initially have a partial or complete response to the treatment, but eventually exhibit cancer progression or recurrence. With repeated treatment, tumors often become resistant not only to the specific chemotherapeutic agent being employed, but cross-resistant to both similar and structurally unrelated classes of cytotoxic drugs[9].

A first type of resistance is that which impairs the delivery of anticancer drugs to tumour cells: the presence of little amount of drug in the blood and hence into the tumor mass may be due to poor absorption, to an increased drug metabolism or to an elevated excretion. Otherwise, the resistance can arise also in the cancer cell itself, due to genetic and epigenetic alterations that affect drug sensitivity: cells can become resistant to a single drug or to a class with similar mechanism of action and if cells show cross-resistance to other structurally and mechanistically unrelated drugs, the phenomenon is called multidrug resistance[8].

Different mechanisms may be responsible for MDR: increased activity of efflux pump (ATP-dependent transporters), decreased drug influx, activation of DNA repair, activation of detoxifying systems (as cytochrome P450), altered expression of apoptosis-associated protein (like Bcl-2) and tumor suppressor protein (like p53)[8] (Fig. 1.1).

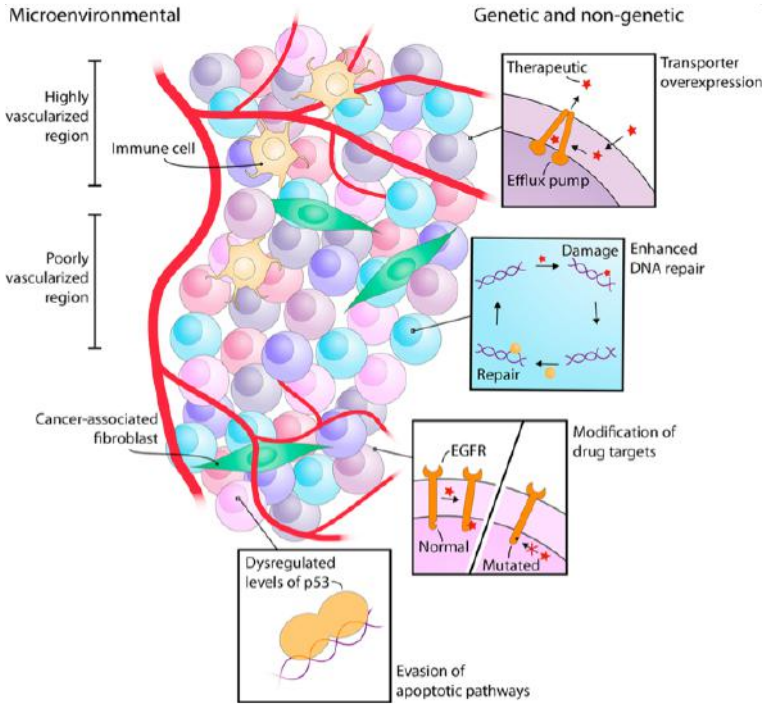

Fig 1.1 Factors influencing tumor heterogeneity and drug resistance. Genetic, nongenetic, and microenvironmental factors give rise to tumor heterogeneity, which significantly influences the drug sensitivity of cancer cells through an array of cellular mechanisms, such as transporter overexpression[10].

1.1.1.2 ATP-dependent transporters

The ATP-dependent transporters or ATP-binding cassette (ABC) are a superfamily of proteins, highly conserved, generally expressed on the membrane of cells and cellular vesicles (Fig. 1.2). The ATPase transporters utilize the energy of adenosine triphosphate (ATP) binding and hydrolysis to promote the translocation of various substrates across membranes; the export of these compounds can take place against considerable concentration gradients. There are 48 known transporters in the ABC family, which are classified into seven different subfamilies based on phylogenetic analysis[11]. ABC proteins in their functional form comprise a minimum of four core domains: two membrane-bound domains (or transmembrane domains, TMDs) and two nucleotide binding domains (NBDs). The role of the TMDs is to recognize and mediate the passage of substrate across the cell membrane, while the NBDs hydrolyze ATP to power this process. Only the subfamily ABCC possesses an extra N-terminal domain of unknown function[12]. There are currently no high resolution structures available for any eukaryotic ABC protein, but the nature and location of the drug-binding site have been extensively investigated, especially for P-gp and MRP1. The drug binding pocket within the protein is made up by the transmembrane regions, it is shaped like a funnel that is narrower at the cytoplasmic side, and it appears large and flexible, with a large number of amino acid side chains that could serve as hydrogen bond donors[13]. Two ATP hydrolysis events, which do not occur simultaneously, are needed to transport one drug molecule: the binding of substrate to the transmembrane regions stimulates the ATPase activity of transporter, causing a conformational change that releases substrate outside, while the hydrolysis of the second ATP seems to be required to 're-set' the transporter so that it can bind substrate again[8].

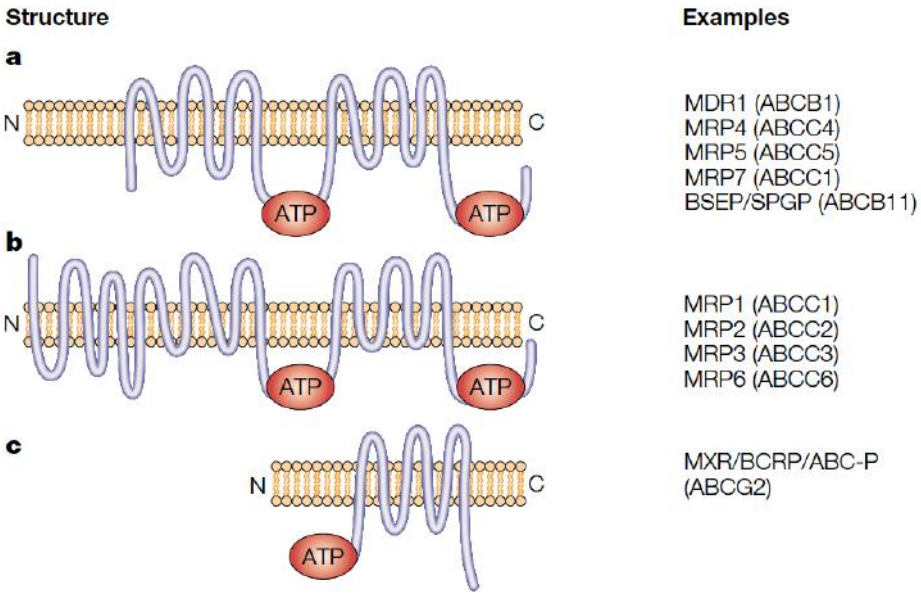

Fig. 1.2. Structures of ABC transporters known to confer drug resistance. The structures of three categories of ABC transporter. (a) ABC transporters such as multidrug resistance MDR1 have 12 transmembrane domains and two ATP binding sites. (b) The structure of MRP1 possesses two ATP binding regions and an additional domain that is composed of five transmembrane segments at the amino-terminal end. (c) The 'half-transporter' BCRP contains six transmembrane domains and one ATP-binding region on the amino-terminal side of the transmembrane domain. Half-transporters are thought to homodimerize or heterodimerize to function.

It is important to note that, even if many ABC transporters have been identified to play important roles in human diseases (cystic fibrosis, neurological disorders, tumors), they are all expressed in normal tissues and they transport a diverse array of substrates, including sugars, amino acids, drugs, antibiotics, nucleotides, endogenous metabolites and ions (Tab. 1.1). Anyway, several ABC transporters are efflux pumps that play an important role in the uptake and distribution of therapeutic drugs and therefore can affect the treatment of a pathology. Fifteen of the 49 known ABC transporters contribute to conferring resistance to chemotherapeutic agents, however three of them appear to account for most observed MDR in humans and have been demonstrated to have a well-defined role in the transport of clinically relevant drugs: P-glycoprotein (P-gp or ABCB1 or MDR1), MDR-associated protein (MRP1 or ABCC1) and breast cancer resistance protein (BCRP or ABCG2 or MXR). These proteins are all located in the plasma membrane; P-gp and MRP1 are 170-190 kDa single polypeptides while BCRP is a 72 kDa half-transporter and likely works as a homodimeric complex[13].

Table 1.1 Tissue localization, possible functions and substrates of ABC transporters[8].

Common name	Systematic name	Tissue	Non-chemotherapy substrates	Chemotherapy substrates
P-gp, MDR1	ABCB1	Intestine, liver, kidney, placenta, blood-brain barrier	Neutral and cationic organic compounds, many commonly used drugs	Doxorubicin, daunorubicin, vincristine, vinblastine, paclitaxel, docetaxel, etoposide
MDR2	ABCB4	Liver	Phosphatidylcholine, some hydrophobic drugs	Paclitaxel, vinblastine
MRP1	ABCC1	All tissues	Glutathione and other conjugates, organic anions, leukotriene C4	Doxorubicin, epirubicin, etoposide, vincristine, methotrexate
MRP3	ABCC3	Pancreas, kidney, intestine, liver, adrenal glands	Glucuronate and glutathione conjugates, bile acids	Etoposide, methotrexate, cisplatin, vincristine, doxorubicin
BCRP, MXR	ABCG2	Placenta, intestine, breast, liver	Prazosin	Doxorubicin, daunorubicin, mitoxantrone, topoteca, SN-38

P-glycoprotein (P-gp or MDR1)

The broad-spectrum multidrug efflux pump P-gp was discovered in 1976 and is possibly the best studied ABC transporter to date. It is the product of the *mdr1* gene and is a 170 kDa membrane-associated protein, containing 1280 amino acids with 12 transmembrane regions and 2

ATP-binding sites. P-gp is expressed at high levels in the apical membranes of epithelial cells in colon, small intestine, brain, testis, placenta and pregnant endometrium. These locations suggest that it has a physiological role in protecting sensitive organs and the fetus from toxic xenobiotics. For example, in the intestine P-gp extrudes many drugs into the lumen, reducing their absorption and oral bioavailability; in hematopoietic progenitor cells it protects the bone marrow from the toxicity of chemotherapeutic drugs[14]. Moreover, high expression of P-gp has been observed prior to chemotherapy treatment in many different tumor types, including kidney, colon, liver, breast and ovarian cancer. In other cancers, such as haematological malignancies, the low levels of this protein are increased after chemotherapy treatment[15].

P-gp is able to bind and efficiently remove a wide range of structurally dissimilar compounds, such as anticancer drugs (anthracyclines, vinca alkaloids, actinomycin-D and paclitaxel), HIV-protease inhibitor, analgesics, immunosuppressive agents, antibiotics. All are hydrophobic amphipathic molecules, with a molecular weight in the range of 300 to 1000 Da, often with aromatic rings and uncharged or positively charged at neutral pH[16]. Also some physiological substrates have been identified for P-gp, including steroid hormones, lipids, peptides and small cytokines. P-gp can also be easily inhibited by two drugs already in use for other disorders: the calcium channel blocker Verapamil and the immunosuppressant Cyclosporin A, now studied also to reverse drug resistance.

MRP1

P-gp is not the only ABC transporter implicated in drug resistance: the multidrug resistance associated protein 1 (MRP1 or ABCC1) is very similar in structure, with the exception of an amino-terminal extension. Differently to P-gp, it is expressed at the basolateral membrane of polarized epithelial cells: it protects bone marrow, kidney collecting tubules, oropharyngeal and intestinal mucosa from toxicants and it is also involved in drug clearance from the cerebrospinal fluid, testicular tubules and peritoneum. This protein is able to bind and transport a variety of endogenous molecules that are conjugated to the anionic tripeptide glutathione (GSH), to glucuronic acid or to sulphate. As regards anti-cancer agents, MRP1 prefers anionic substrates and conjugated drugs (or drugs co-transported with free glutathione) and it is expressed both in solid tumor and haematological malignancies[8,13].

BCRP

BCRP (breast cancer resistance protein) is a homodimer of two half-transporters, each containing an ATP binding domain and six transmembrane segments. As P-gp, it is expressed in a variety of normal tissues, like intestine, kidney, placenta, brain endothelial cells, hematopoietic stem cells and mammary gland during pregnancy and lactation; it exerts a role in intestinal absorption, brain penetration and transplacental passage of drugs. BCRP has been recently discovered in drug-resistant cell lines that did not express P-gp or MRP1; since then it has been reported in many solid tumors[8,13]. Initially it was discovered its ability to carry Mitoxantrone, but it has a broad specificity for both positively and negatively charged drugs, with the exception of taxols, cisplatin, verapamil or vinca alkaloids[17]. BCRP carries both imatinib and gefitinib, two recently introduced anticancer drugs that are tyrosine kinase inhibitors[13].

We can therefore consider that many drugs commonly used in clinical therapy are substrates of P-gp, MRP1 and BCRP. The ABC proteins play an important role in absorption and disposition

of these drugs *in vivo*, starting from the ability to limit their intestinal uptake. In cancer cells, P-gp and BCRP can export both unmodified and conjugates drugs, whereas MRP1 exports glutathione and other drug conjugates. All three transporters demonstrate an overlapping drug specificity: this redundancy indicates that a complex network of efflux pumps is involved in protecting the body from toxic xenobiotics[13]. The extent of involvement of ABC efflux pumps in multidrug resistance, and whether their modulation can result in increased patient survival, remains controversial. The first generation of P-gp modulators used clinically (verapamil and cyclosporine A) suffered from the dual problems of high toxicity and low efficacy at tolerable doses. Then, other generations of modulators have been developed and even if their clinically use appears to be a realistic goal, clinical trials have so far been disappointing[18].

1.1.2.2 Other MDR mechanisms

Cancer drug resistance is a complicated process that involves multiple mechanisms and even if the overexpression of ABC transporter is the most frequent, additional mechanisms include a decreased drug influx, activation of DNA repair, metabolic modification and detoxification, and altered expression of apoptosis-associated protein or tumor suppressors[10].

Normal cells have several repair mechanisms which are used to prevent the transmission of damaged DNA and to avoid malignant transformation. If any of these mechanisms fails, apoptosis is activated to eliminate the damaged cells. However, cell cycle arrest does not occur when mutations, chromosomal rearrangements, and epigenetic changes are present, even when induced by anticancer therapies that produce DNA damage to cause cytotoxicity. Further, the anti-apoptotic, prosurvival regulator Bcl-2 and the nuclear factor kappa B (NF-κB), a transcription factor that controls genes that suppress apoptotic responses, are frequently overexpressed in cancer cells and lead to increased survival[9].

In solid tumors also the microenvironment can have a role in MDR. The tumor stroma has an increased number of fibroblasts that synthesize growth factors, chemokines, and adhesion molecules (cell adhesion-mediated drug resistance, CAM-DR); the acidic pH of the microenvironment can influence the effectiveness of cytotoxic drugs and may inhibit the active transport of some therapeutics; hypoxia can lead to the activation of genes associated with angiogenesis and survival[19].

1.1.3 Breast cancer

Breast cancer (BC) is the most common cancer in women worldwide (Fig. 1.3), with nearly 1.7 million new cases diagnosed in 2012, and the second most common cancer overall, after lung cancer. It represents about 12% of all new cancer cases and 25% of all cancers in female. Although it is much more common in women, breast cancer does occur also in men (less than 1% of all cases)[2,20]. Focusing on Italy, breast cancer is the most frequent cancer in women and accounts for 29% of all tumors affecting them: every eight women, one will get sick in the course of her life. It is also the leading cause of cancer mortality, with a rate of 17% of all female deaths due to cancer[21].

BC is a very a heterogeneous group of diseases, with each tumour displaying unique characteristics in terms of pathogenesis and progression, response patterns to various treatment modalities and clinical outcomes[22]. Because of this heterogeneity both in morphological features and in clinical behaviour, different classification systems exist.

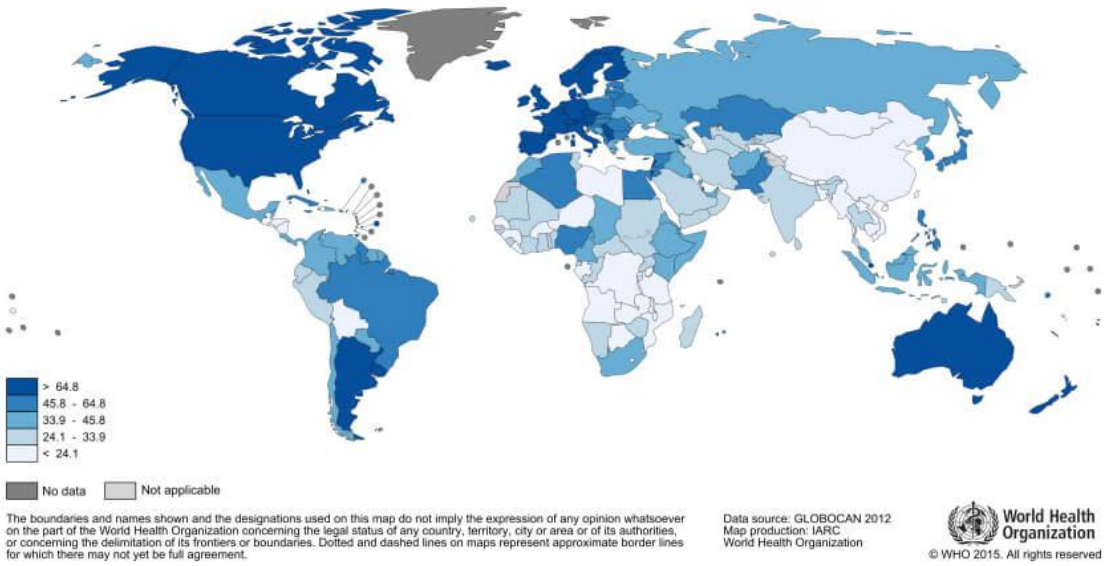

Fig. 1.3 Breast cancer incidence worldwide (WHO).

1.1.3.1 Histological classification of breast cancer

In females, breast serves as mammary gland and is made up of adipose tissue and a set of glandular structures, which are called lobules, joined together to form a lobe. In any breast there are 15 to 20 lobes. Milk comes from the lobules to the nipple through tiny tubes called milk ducts.

From an histological point of view, breast cancer can be categorized considering both the site of origin (ducts or lobules) and the invasiveness pattern (non-invasive/in situ or invasive/infiltrating) (Fig. 1.4). Between non-invasive carcinomas, ductal carcinoma in situ (DCIS) is considerably more common than its lobular counterpart and it has traditionally been further subclassified in five well recognized subtypes. Likewise, also invasive carcinomas, which spread outside the origin site, are a heterogeneous group of tumors differentiated into histological subtypes[23].

To simplify, the most common subtypes of breast cancer, based on their origin and invasiveness, are as follows:

Invasive ductal carcinoma (IDC): the most frequent type of breast cancer (~75% of invasive breast cancer cases). IDC originates in the epithelial lining of the milk duct and invades other breast tissues. Over time, it may metastasize to nearby lymph nodes and possibly to other areas of the body.

Invasive lobular carcinoma (ILC): it originates from the milk-producing glands of the breast and spreads to the lymph nodes and other tissues. ILCs are responsible for ~15% of invasive breast cancer diagnoses.

Ductal carcinoma *in situ* (DCIS): is the most common type of non-invasive breast cancer and it is found in the epithelial lining of milk ducts. It doesn't spread to other tissues and it isn't life-threatening, but may become invasive and be re-classified as IDC.

Lobular carcinoma *in situ* (LCIS): it is found in the milk-producing glands of the breast and it doesn't spread to other tissues in or outside the breast. People diagnosed with LCIS tend to have more than one lobule affected, but the tumor not causes symptoms and usually does not show up on a mammogram. LCIS may become invasive and be re-classified as ILC.

Inflammatory Breast Cancer (IBC): typically occurs without a defined tumour mass, and is identified by signs of inflammation in the breast tissue, like swelling and skin redness. IBC is rare (approximately 1% to 3% of BC cases) and aggressive.

Other rarer subtypes of breast cancer: *medullary carcinoma* (~5% of breast cancer cases; invasive carcinoma with unusually large cells), *tubular carcinoma* (~1% of breast cancer cases; invasive carcinoma with distinct tubular cells), *mucinous (colloid) carcinoma* (~2% of breast cancer cases; slower-growing, less invasive cancer characterized by cells producing large amounts of mucin).

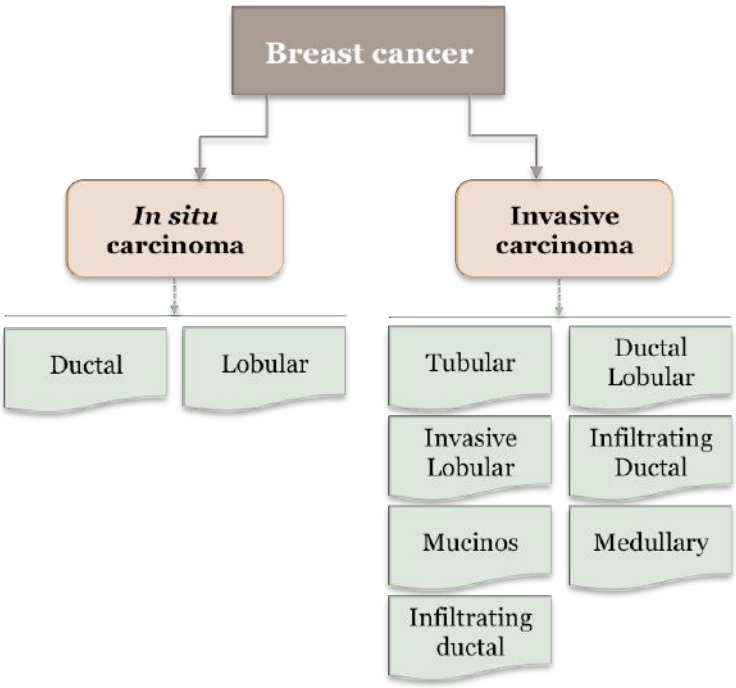

Fig. 1.4 Histological classification of breast cancer[23].

1.1.3.2 Molecular classification of breast cancer

The histological appearance of the tumors may not be sufficient to establish the underlying complex genetic alterations and the biological events involved in cancer development and progression. Therefore, recent studies have focused on defining more detailed biological characteristics to improve patient risk stratification and to ensure the highest chance of benefit and the least toxicity from a specific treatment modality. First the receptor status identified by immunohistochemistry and more recently the gene expression profiling have provided evidence for classifying breast cancer into distinct biological classes[22,23]. This important classification is mainly based on the expression of specific molecular markers, including estrogen receptor (ER), progesteron receptor (PR) and human epidermal growth factor receptor 2 (HER2), that can split breast cancer phenotype in different subtypes (Tab. 1.2).

Tab. 1.2 Molecular classification of breast cancer[22].

Subtypes	Specific markers	Percentage
Basal like (triple negative)	ER^- PR^- $HER2^-$ $EGFR^+$	15-20 %
HER2 positive	ER^- PR^- $HER2^+$	10-15%
Luminal A	ER^+ Pr^{low} $HER2^-$	40%
Luminal B	ER^+ Pr^{low} $HER2^+$	20%

Most studies divide breast cancer into four major molecular subtypes:

- **Basal like** cancers, which show high genome instability and do not express ER, PR and HER2 (hence referred to as triple-negative), but are epidermal growth factor receptor (EGFR) positive. These tumors tend to occur more often in young women and are often related to a mutation of the BRCA1 gene; they are often aggressive and have a poor prognosis.
- **HER2 type** cancers, which present an overexpression of HER2 but are hormone receptors negative. These tumors tend to grow faster and are more inclined to spread. However, therapies that specifically target HER2, such as Herceptin® (Trastuzumab), are very effective and able to reduced also the recurrence.
- **Luminal A**, when cancer starts in the inner cells lining the mammary ducts and is estrogen and progesterone receptors positive, but HER2 negative. Treatment of luminal A cancers often includes the hormone therapy. Among the four subtypes, these tumors tend to have the best prognosis, with fairly high survival rates and rather low recurrence rates.
- **Luminal B** cancers also develop from the luminal cells of mammary ducts and tend to be positive for all the three receptors. They present some factors that lead to a poorer prognosis than luminal A, including an high rate of proliferation, a large tumor size and the involvement of lymph nodes.

Minor subtypes of breast cancer, poorly described until now, are the “normal breast like” (less characterized, p53 positive) and the “claudin-low”. The latter is characterized by low expression of genes involved in tight junctions and cell-cell adhesions, including claudins and E-cadherin, showing high expression of epithelial to mesenchymal transition genes and stem cell features. Currently, it has been reported that patients with claudin-low tumors have poor clinical outcomes[22].

1.1.3.3 Breast cancer therapy

The biology and behaviour of a breast cancer affect the treatment plan: some tumors are small but grow fast, while others are large and grow slowly. So, treatment options depend on several factors, including the stage of the tumor, the receptor status (ER, PR and HER2), the presence of known mutations in inherited BC genes, such as *BRCA1*.

Often the first step is to surgically remove the tumor mass, even after treating large tumors with neoadjuvant therapy. Following surgery, the next step in managing early-stage breast cancer is to lower the risk of recurrence and to get rid of any remaining cancer cells which are undetectable but responsible for both local and distant recurrence of cancer. Treatment given after surgery is called adjuvant therapy and may include radiation therapy, chemotherapy, targeted therapy, and/or hormonal therapy. The same treatments may be given to shrink the tumors when surgery is not possible and cancer is called inoperable or if a patient has a metastatic breast cancer recurrence. A chemotherapy regimen consists of a specific treatment schedule of drugs given at repeating intervals for a set period of time, one drug at a time or combinations of different drugs. Common drugs for breast cancer include: carboplatin and cisplatin, docetaxel, paclitaxel and protein-bound paclitaxel (Abraxane), doxorubicin and pegylated liposomal doxorubicin (Doxil), 5-fluorouracil, gemcitabine, methotrexate[2,22,24].

The complex profile of each BC subtype, determined using molecular and genetic information from tumor cells, is critical as it defines the suitability of using targeted treatments as adjuvant for chemotherapy and so the appropriate treatment for a patient. Hormonal therapy is an effective treatment for most tumors that prove to be positive for either estrogen or progesterone receptors. For example, ER+ cancers can be treated with drugs able to reduce the effect of estrogen, such as tamoxifen, or to decrease its level, such as aromatase inhibitor. Indeed, targeted therapy is a treatment that hits cancer's specific genes, proteins, or the tissue environment that contributes to cancer growth and survival. These treatments are very focused, and work differently than chemotherapy because they block the growth and spread of cancer cells while limiting damage to healthy cells. As an example, HER2+ breast cancers respond very well to trastuzumab, a monoclonal antibody against the receptor, which in last years significantly improved the prognosis in combination with the conventional therapy.

1.2 Nanotechnology and nanomedicine

The concept of “nanotechnology” was introduced (not yet using this term) by the American physicist Richard Feynman during a lecture entitled “There's plenty of room at the bottom” at an American Physical Society meeting on December 29, 1959. Feynman was the first to assess the possibility of manipulate the matter on small-scale, interfering with the biological system at the atomic level. “A biological system - he said - can be exceedingly small. Many of the cells are very tiny, but they are very active; they manufacture various substances; they walk around; they wiggle; and they do all kinds of marvellous things - all on a very small scale. Also, they store information. Consider the possibility that we too can make a thing very small which does what we want - that we can manufacture an object that manoeuvres at that level!”. And he concluded as follows: “When we get to the very, very small world - say circuits of seven atoms - we have a lot of new things that would happen that represent completely new opportunities for design. Atoms on a small scale behave like *nothing* on a large scale, for they satisfy the laws of quantum mechanics. So, as we go down and fiddle around with the atoms down there, we are working with different laws, and we can expect to do different things. We can manufacture in different ways. […] At the atomic level, we have new kinds of forces and new kinds of possibilities, new kinds of effects. The problems of manufacture and reproduction of materials will be quite different. I am, as I said, inspired by the biological phenomena in which chemical forces are used in a repetitious fashion to produce all kinds of weird effects (one of which is the author). The principles of physics, as far as I can see, do not speak against the possibility of manoeuvring things atom by atom. It is not an attempt to violate any laws; it is something, in principle, that can be done; but in practice, it has not been done because we are too big”[25]. He concluded the speech proposing to reward those who would be able to fit the whole of the Encyclopaedia Britannica on the head of a pin, by writing the information from a book page on a surface 1/25,000 smaller in linear scale!

In 2004 the Royal Society and Royal Academy of Engineering (UK) defined nanoscience and nanotechnologies in this way: “Nanoscience is the study of phenomena and manipulation of materials at atomic, molecular and macromolecular scales, where properties differ significantly from those at a larger scale” and “Nanotechnologies are the design, characterisation, production and application of structures, devices and systems by controlling shape and size at nanometre scale”[26]. In the metric scale of linear measurements, a nanometer is one-billionth of a meter and the size range that holds the majority of interest is typically from 1 to 100 nm (Fig. 1.5), because in this range materials can have different or enhanced properties compared with the same materials at a larger size. Moreover, this is also the typical range size of biological molecules: atoms are below a nanometre in size, whereas many molecules, including some proteins, range from a nanometre upwards.

The concept of “nanotechnology” has gained significant boost in recent years and can be described as a multidisciplinary scientific approach for the design and fabrication of new materials with nanoscale dimensions[27]. Nanotechnologies involve many research fields, including: molecular biology, chemistry, materials science, physics, mechanical engineering, chemistry and electronics. In particular, areas that today are considered prominent and in which nanotechnologies can offer and already offer innovative solutions are nanomaterials, nanoelectronics and nanomedicine.

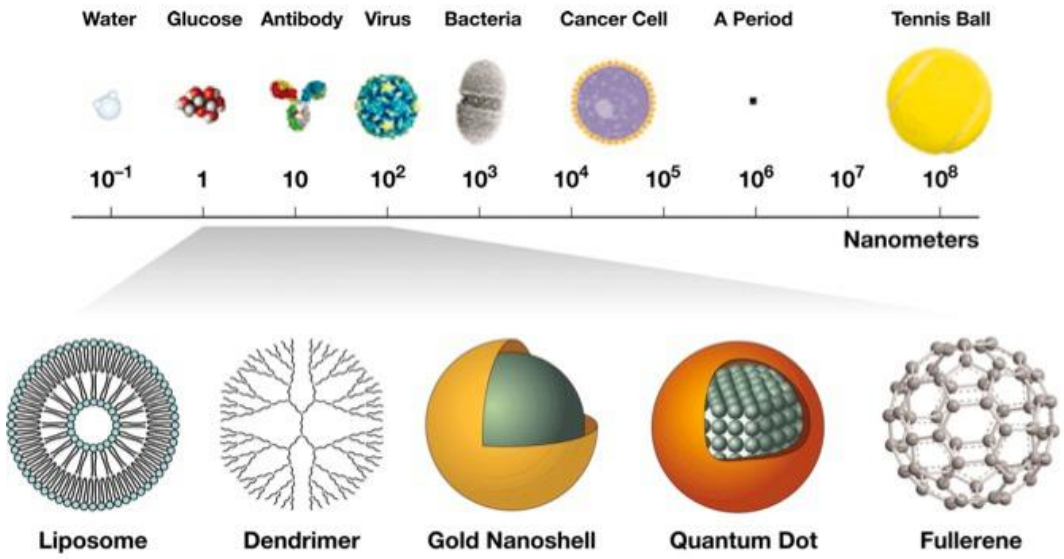

Fig. 1.5 Nanometer scale.

1.2.1 Nanomedicine

The application of nanotechnology to disease treatment and diagnosis has recently been referred to as “nanomedicine” by National Institutes of Health in USA. So, nanomedicine can be easily defined as the design and development of therapeutics and/or diagnostic agents in the nanoscale range, with the possibility, by moving within biological systems, to transport and deliver a variety of biomedical entities for treatment, prevention, and diagnosis of many diseases[28]. A great advantage is that many biological mechanisms in the human body occur at the nanoscale and nanoparticles (NPs), due to their small size, may potentially cross natural barriers and interact with biomolecules in the blood or within organs, tissues or cells. At the same time, these biological processes are affected by the physical features of nanocarriers, including their size, shape, surface charge and intrinsic chemical properties, as well as the incorporation of active ligands for recognition of biological receptors[29,30].

Nanomedicine applications range from cancer to inflammation and regenerative medicine and it is especially promising in area such as disease diagnosis and molecular imaging, targeted therapy, drug and gene delivery. In other words, the “find, fight and follow” concept is taking a new turn with developments in nanotechnology: early diagnosis and appropriate contrast agents for imaging on the level of a single cell (‘find’), delivery of therapeutic drugs (‘fight’) and monitoring of the therapeutic development (‘follow’) are key issues for future medical care[31]. With these purposes, potential advantages of engineered therapeutic NPs are the ability to: revert unfavorable physicochemical properties of bioactive molecules to desirable biopharmacologic profiles; improve the delivery of therapeutics across biological barriers and compartments; control the release of bioactive agents; enhance therapeutic efficacy by selective delivery of therapeutics to biological targets; and perform theranostic functions by combining multimodal imaging and simultaneous diagnosis and therapy into multifunctional nanoplatforms. In order to successfully translate nanomedicine into clinical practice several issues should be taken into consideration, including a favourable blood half-life, a physiologic behaviour with minimal off-target effects, effective

clearance from the human organism, and minimal or no toxicity to healthy tissues[28]. Nanotechnology currently affects three distinct areas of medicine: therapy, diagnosis and imaging; the potential in each of these areas is enormous.

Diagnosis and imaging

The term "imaging" is defined as the visualization of cellular functions and the follow up of molecular and biological processes in living organisms. For this purpose, magnetic NPs constituted by magnetic elements such as iron, cobalt and nickel are used. NPs can also be functionalized to allow a specific activity and are used as contrast agents to view, for example, a tumor tissue. Currently there are a large number of magnetic NPs undergoing clinical trial or already approved by FDA as contrast agents: Lumiren®, for bowel imaging, Federidex IV®, for imaging of liver and spleen and Combidex®, for lymph node metastases[32].

Other conventional approaches to making nano-imaging agents include high-density encapsulation of contrast agents such as gadolinium or manganese oxide into liposomes and PLGA, or loading the contrast agents onto the surface of NPs[33].

Drug delivery

The concept of "drug delivery" can be defined as the process of release of a bioactive agent to a specific site and with a specific rate[34]. A drug delivery system (DDS), favouring the release of the active substance exactly when and where it is necessary, circumscribes the biological effect of the molecule on a specific type of cells, thus improving the effectiveness and reducing the toxicity of the therapy.

Most of the drugs are limited by their low solubility, high toxicity, high-dose, non-specific delivery, degradation *in vivo* and short half-life. The development of DDSs for small molecules, proteins and DNA has been deeply influenced in the past decade by nanotechnologies and the interest has been directed to some particular diseases, including cancer. The advantages in the use of NPs as drug delivery systems are related to their size and to the possibility of using different materials and create unique architectures. Drugs can be encapsulated in a vesicle, entrapped in a matrix, or solubilized within a hydrophobic or hydrophilic component. Thanks to their small size, NPs can penetrate efficiently through the barriers and, through small capillaries, reach individual cells, allowing an effective drug accumulation in the target site. In this way, the side effects and the toxicity of the drug are reduced, the therapeutic efficacy is improved as well as increases the therapeutic index of biotechnological drugs, such as recombinant proteins and oligonucleotides[35].

1.2.2 Targeting

The potential impact of nanotechnology in medicine starts from the possibility to exploit targeting of NPs for an effective imaging and a controlled drug delivery. There are two main strategies by which targeting can be achieved, namely passive and active targeting. The first one allows for the efficient localization of NPs within the tumor microenvironment, while the second facilitates their active uptake by the tumor cells themselves[36] (Fig. 1.6).

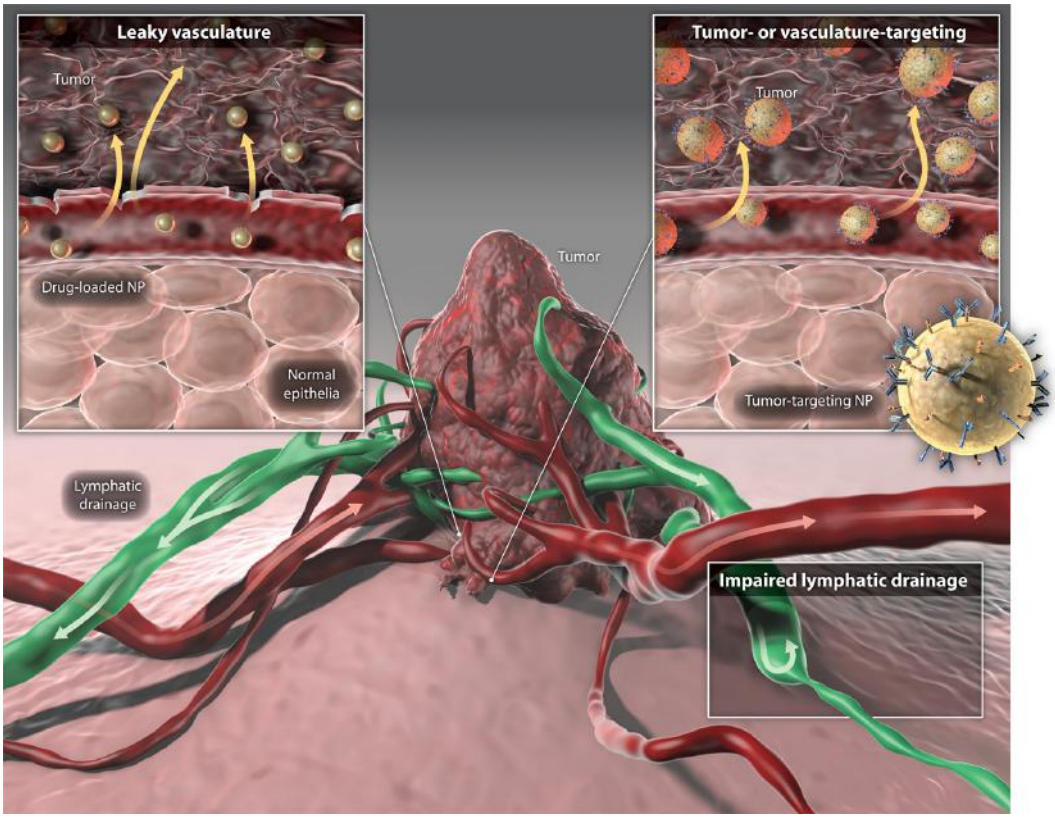

Fig. 1.6 **Passive and active targeted nanomedicine**. Nanoparticles larger than 8 nm in size can passively target tumors through preferential passage through larger interendothelial junctions (40 nm to 1 μm) compared to those of healthy tissue (≤8 nm). Large junctions are a key characteristic of the irregular tumor vasculature. Nanoparticles can also be conjugated with targeting agents, such as antibodies specific to proteins more highly expressed in tumors than healthy tissue, to actively target tumors. Once nanoparticles enter tumors, defective lymphatic drainage of nanoparticles results in enhanced retention[33].

1.2.2.1 Passive drug targeting

The majority of nanosystems show prolonged blood circulation times *in vivo* and accumulate at particular sites, simply due to the balance between vascular hemodynamic forces and diffusion mechanisms. Passive drug targeting is widely exploited in chemotherapy because nanoparticles circulating in the bloodstream can localize to neoplastic tissues through the well known “enhanced permeation and retention” (EPR) effect[28]. During tumor formation, rapid and imperfect angiogenesis occurs, creating leaky blood vessel, characterized by abnormal branching and enlarged inter-endothelial gaps, with associated breakdown of tight junctions between endothelial cells and a disrupted basement membrane. The endothelial lining of the blood vessel wall becomes more permeable than in the healty tissues, which ensure a sufficient supply of nutrients and oxygen to tumor tissues for rapid growth. At the same time, however, it allows large molecules and even particles ranging from 10 to 500 nm in size, to extravasate and accumulate inside the interstitial space via a passive targeting mechanism. Assuming these large molecules/particles are loaded with a pharmaceutical agent, they can bring it into the area with the increased vascular permeability, where the active drug can be eventually released. Such spontaneous accumulation works especially good with tumors because of the dysfunctional lymphatic drainage, which also results in drug accumulation[9,28,37]. Interestingly, it was recently shown that EPR effect can be modulated by the blood pressure, but also by the surrounding stroma,

the location and size of the tumor, the amount of infiltration by macrophages, patient characteristics such as age and gender, and additional medications. So, the EPR effect is a very heterogeneous phenomenon, varying dramatically within a tumor and between different tumor types and also patient to patient. This can lead to an unpredictable accumulation of the drug in the tumor, or possibly not at all[9].

In any case, compared with conventional anticancer drugs, most of which are small molecules, nanocarriers such as liposomes, micelles or polymeric nanoparticles have superior *in vivo* pharmacokinetic (e.g., a prolonged plasma half-life) and greater tumor selectivity via the EPR effect, so they produce improved antitumor effects. These nanoparticles demonstrate dose-independent, non-saturable, log-linear kinetics, and increased bioavailability and some of them are currently used in clinic. Doxorubicin in PEG-coated liposomes (Doxil® and Caelyx®) is successfully used for the treatment of solid tumors and many other polymeric or micellar drugs are in clinical stage development[7,37].

1.2.2.2 Active drug targeting

Passive targeting has shown several limitations and however it facilitates the efficient localization of nanoparticles in the tumor interstitium, but cannot further promote their uptake by cancer cells. This second step can be achieved by actively targeting nanoparticles to receptors or other surface membrane proteins overexpressed on target cells. In fact, nanoparticles allow for versatile modification possibilities and the functionalization with specific ligands promotes their delivery to uniquely identifiable cells and may facilitate their internalization by receptor-mediated endocytosis[36] (Fig. 1.6). Using different approaches, various types of targeting ligands have been employed to functionalize nanoparticles, including antibodies or their fragments, nucleic acid ligands (such as aptamers), peptides or whole proteins, and small molecules. Important factors that should be considered include expression level of the receptor, internalization capacity and rate, receptor binding affinity, ligand sizes, immunogenicity, as well as availability[38].

Antibody-based targeting

Antibodies were among the first agents used for targeting nanovehicles to specific cell types, based on surface antigens they presented. As targeting agents, they have extremely high selectivity and binding affinity by virtue of the presence of two epitope binding sites in a single molecule[36]. The ability of engineered monoclonal antibodies to target and interfere with cellular processes has been demonstrated by the success of several monoclonal antibody therapeutics. Some of these, including rituximab and trastuzumab, have been conjugated to nanoparticles, resulting in nanoconjugates that show a significant increase in the rate of particle uptake compared with their non-targeted counterparts[28]. Anyway, antibodies still have a number of limitations, including their large size and potentially immunogenic characteristics, resulting in rapid nanoparticle clearance. This has shifted the focus on using antibody fragments (Fab fragments, single chain variable fragments (scFv), ..) as targeting molecules able to retain the high antigen binding specificity of the parent antibodies, but with less immunogenicity and a smaller size[28].

Aptamer-based targeting

Aptamers are short single-stranded DNA or RNA sequences, that are folded into secondary and tertiary 3D structures rendering them capable of binding biological targets, most often proteins,

with high sensitivity and specificity. They are small in size (usually approximately 15 kDa), and have less immunogenicity with respect to monoclonal antibodies or other macromolecules, leading to better stability and biodistribution[28,36].

Proteins and peptide-based targeting molecules

Several endogenous proteins capable of selective binding to specific receptors on membrane cells can be used for targeting purposes via receptor-mediated endocytosis. For example, the upregulation of transferrin receptors on metastatic and drug-resistant malignant cells, the extracellular status of transferrin in the body and its internalization by cells make it suitable for delivery of cancer therapies[39,40]. However, the effectiveness of proteins for targeting purposes may be limited by their immunogenicity and susceptibility to early clearance or by the fact that the target receptors are also commonly expressed on various types of normal cells, which can lead to unwanted off-target effects.

Therefore, peptide-based ligands are emerging as an attractive alternative due to their small size, high stability, and relatively low immunogenicity as compared with many proteins. Like monoclonal antibodies and aptamers, peptides can bind to several molecular targets with a high degree of affinity and specificity, and are easy to manufacture by conjugation to nanoparticle surfaces[41,42].

Small molecules

Organic molecules with a molecular weight <500 Da constitute a promising class of targeting ligands because of their small size, high stability, chemical management, and low production cost. Furthermore, small molecules present other advantages: availability of coupling chemical methods for their conjugation; possibility to modulate ligand densities and charge on nanoparticle surfaces; availability of a wide range of targeting ligands with variable physicochemical properties and functional groups; fewer immunogenic effects *in vivo*; reproducible, scalable, and economical manufacturing[28].

Among the large number of small molecules identified as potential targeting ligands, one of the most extensively studied is folic acid, a vitamin that is required by eukaryotic cells for the biosynthesis of purines and pyrimidines. Folate receptors are overexpressed in many types of tumor cells and the folic acid has been used to deliver drug conjugates and many drug delivery systems[43].

1.2.3 Nanotechnologies and cancer

Currently the use of nanomaterials, and particularly nanoparticles, to treat and image cancer is probably the most active area of nanomedicine research and is also the one on which we will focus this work.

Cancer has a big impact on modern society, with high incidence and mortality rate, and early diagnosis and successful treatment of this disease are major challenges for the scientific community. As we have described previously, although there are many therapeutic possibilities for the treatment of cancer, the outcome is not always a success, mainly for two problems that concern the poor selectivity of the drugs and the development of resistance. In this scenario, nanobiotechnology developed very rapidly, opening a new avenue for cancer therapy and diagnosis[27]. The goal of nanomedicine is to develop safer and more effective drug carriers and imaging tools, improving the target and eluding resistance.

As we have already mentioned above, there are several convincing arguments in favour of developing nano-sized therapeutics. A nanocarrier may: 1) help to overcome problems about solubility and chemical stability of anti-cancer drugs and therefore also their bioavailability; 2) protect anti-cancer compounds from biodegradation or excretion, influencing their pharmacokinetic profile; 3) help to enhance the tumor accumulation of anticancer agents, by passive or active targeting strategies; 4) if properly designed, release its payload upon a trigger, such as pH, resulting in stimuli-sensitive nanomedicine therapeutics; 5) decrease resistance of tumors against anti-cancer drugs[44].

Most clinically available nanocarrier-based cancer therapeutics are passively targeted first-generation nanomedicine drugs, which rely on controlling the pharmacokinetics and biodistribution of a compound by modulating its physicochemical properties. Pathophysiological characteristics of cancers have been exploited for passive targeting: in particular, the EPR effect promotes the accumulation of nanoformulated drugs in the tumor tissue, but it is not sufficient to control the side effects of cytotoxic drugs and fully exploit the benefits of targeted delivery. Second-generation compounds are based on drug-delivery technologies with an active targeting vector or smart nanocarriers with stimuli-responsive properties. Thus, these nanodrugs hold the promise of improved targeting and increased efficacy[44].

Among a wide variety of nanosystems, only few nanomedicines are approved for use in the treatment of cancer. Among these, we can mention Doxil® (PEGylated liposomal doxorubicin), Myocet® (non-PEGylated liposomal doxorubicin), DaunoXome® (non-PEGylated liposomal daunorubicin), Depocyt® (non-PEGylated liposomal cytarabine), Abraxane® (albumin-based paclitaxel), Genexol-PM® (PEG-PLA paclitaxel).

1.3 Ferritin

Although Feynmann's lecture generally is accepted as a beginning of nanotechnology, the first pioneer in this field should be considered V. Laufberger (1890-1986), from Charles University in Prague. Laufberger in 1937 discovered and isolated from the horse spleen the protein ferritin, containing 4 nm large magnetic nanoparticles[45]. It was the first time that this iron-rich protein was observed and from that moment ferritin was found in many other organism, including humans and mammals, plants, fungi and bacteria.

Ferritin is a 24-subunits spherical protein encapsulating an iron oxide core. It is ubiquitously expressed in archaea, eubacteria, plants, invertebrates and mammals, with the only notable exception of yeasts, so it's probably the most common and ancient molecule of iron homeostasis; its 3D structure is highly conserved in eukaryotes and prokaryotes, even if big differences in amino acid sequence exist between the different species. Mammalian ferritin is mainly present intracellularly in the cytosol, as well as in the nucleus and mitochondria, while extracellular ferritin is found in serum, synovial and cerebrospinal fluids (CSF). It performs some basic functions of the cell, both storage and protection, primarily related to its ability to bind and sequester intracellular iron[46–48].

1.3.1 Ferritin structure

Members of the ferritin superfamily are proteins composed of 24 subunits, that combine to form an almost spherical cage arranged in octahedral (4,3,2) symmetry. The protein structure (Fig. 1.7) has an outer diameter of 12 nm and an inner cavity of 8 nm in which up to 4500 iron atoms can be accommodate as mineral core, traditionally named ferrihydrite[46].

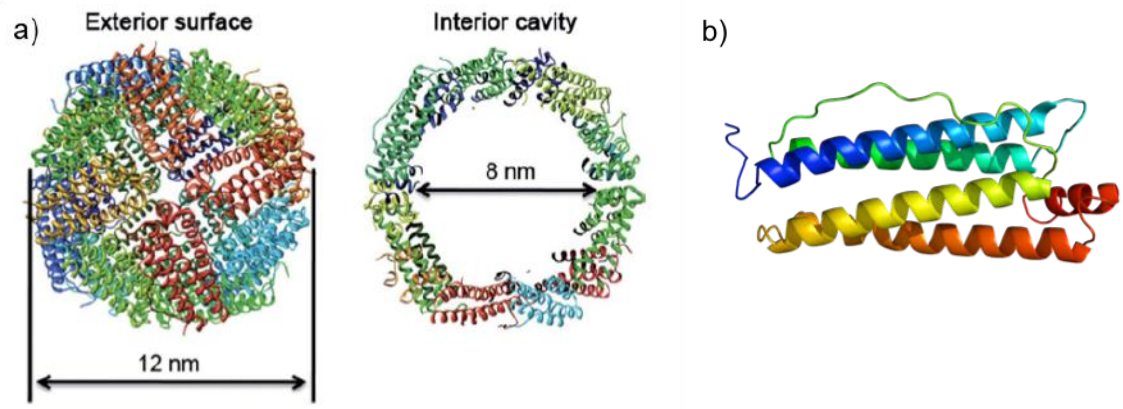

Fig. 1.7 Ribbon diagrams of exterior surface view and interior cavity of (A) Human heavy-chain ferritin and (B) one of its subunits[49].

Each ferritin subunit is folded into a four α-helix boundle of around 180 amino acids, with a long loop between helices B and C; a large number of salt bridges and hydrogen bonds are formed between subunits when they spontaneously self-assemble into the native protein cage. Once formed

the 24-mer structure, ferritin defines a hollow cavity for iron storage, which is separated from the solution by a 2-nm-thick protein shell. This is pierced by two type of channels: eight hydrophilic channels on the 3-fold symmetry axes, to allow the transport of metals in and out, and six hydrophobic channels along the 4-fold axes, that do not seem to be involved in ions exchange, although they might transport protons and probably oxygen[48,50].

Mammalians have two major ferritin genes that encode subunits with different properties, generally named H (heavy) and L (light), that usually co-assemble to form heteropolymers in different proportions, with a tissue-specific distribution. The terms "heavy" and "light" were assigned on the basis of their different electrophoretic mobility, in fact they have a molecular weight of 21 and 19 kDa, respectively. It is also true that the H subunit was discovered and is predominant in the heart, while the L in the liver. The main difference is that the H-subunit possesses a catalytic site, named ferroxidase center, able to promote the oxidation of Fe(II) to Fe(III) while the L-subunit lack this activity but has some acid residues (Asp and Glu) which facilitate the iron core formation[46].

1.3.2 Ferritin physiological role

In most tissues, ferritin is mainly present in cytosol, nucleus and mitochondria and plays a key role in iron storage and homeostasis. It is important to mention that iron is both potentially toxic and essential for life and the major and fundamental function of ferritin is to oxidize and incorporate iron, keeping it in a safe form. This task is biologically important for two reasons: first, the very high binding capacity (up to 4000 Fe atoms per molecule) concentrates iron in a compact and harmless form, making it readily available when needed but without risk of loss. Second, the reaction sequesters Fe(II) from Fenton-like reactions in which the spontaneous oxidation to Fe(III) donates single electrons to catalize the formation of reactive hydroxyl radicals leading to damage of DNA, lipids and protein[48] (Fig. 1.8).

Briefly, the entry of Fe(II) atoms via hydrophilic channels is facilitated by an electrostatic gradient and, once internalized, iron migrates to the ferroxidase center. Here, Fe(II) reacts with dioxygen to form a diferric complex, which rapidly decays leaving Fe(III). The oxidized iron then moves to the nucleation center where, in a slower reaction, it is hydrolysed with the release of protons and mineralized as ferrihydrite[48]. The reactions that lead to the formation of the iron oxide core can be summarized as follows (P is the protein):

$$P + 2Fe^{2+} \rightarrow P[Fe_2]^{4+} \quad (1)$$

$$P[Fe_2]^{4+} + O_2 \rightarrow P[Fe_2O_2]^{4+} \quad (2)$$

$$P[Fe_2O_2]^{4+} \rightarrow P[Fe_2{}^{6+}O_2{}^{2-}]^{4+} \quad (3)$$

$$P[Fe_2{}^{6+}O_2{}^{2-}]^{4+} + H_2O \rightarrow P[Fe_2O]^{4+} + H_2O_2 \quad (4)$$

$$P[Fe_2O]^{4+} + H_2O \rightarrow 2Fe(O)OH + 2H^{+} \quad (5)$$

Interestingly, the ferroxidase activity produces H_2O_2 as intermediate, which might react with Fe(II) to produce free radicals. But free radicals were not observed and the produced hydrogen peroxide is used in place of dioxygen as an oxidant in the reaction catalyzed at the ferroxidase center[48,51]. Since the ferroxidase activity can use both the Fenton reaction reagents, ferritin is

considered an important inhibitor of free radical production.

Though the reaction is catalyzed by the H-subunit, the presence of even small proportions of L-chains has been found to accelerate the transfer of iron from the ferroxidase center to the iron core and improve the overall iron sequestering process. It has also been observed that the shape of the mineralized iron core is affected by the presence and proportion of L-chains, consistent with the hypothesis that they facilitate iron nucleation[52]. Ferritins rich in the H subunit found in the heart and brain have a high ferroxidase activity, therefore they oxidize and sequester actively the iron and have a more pronounced anti-oxidant activity, while ferritins rich in the L subunits found in spleen and liver form molecules physically more stable which may contain a larger amount of iron in the cavity and have a more pronounced iron storage function[46].

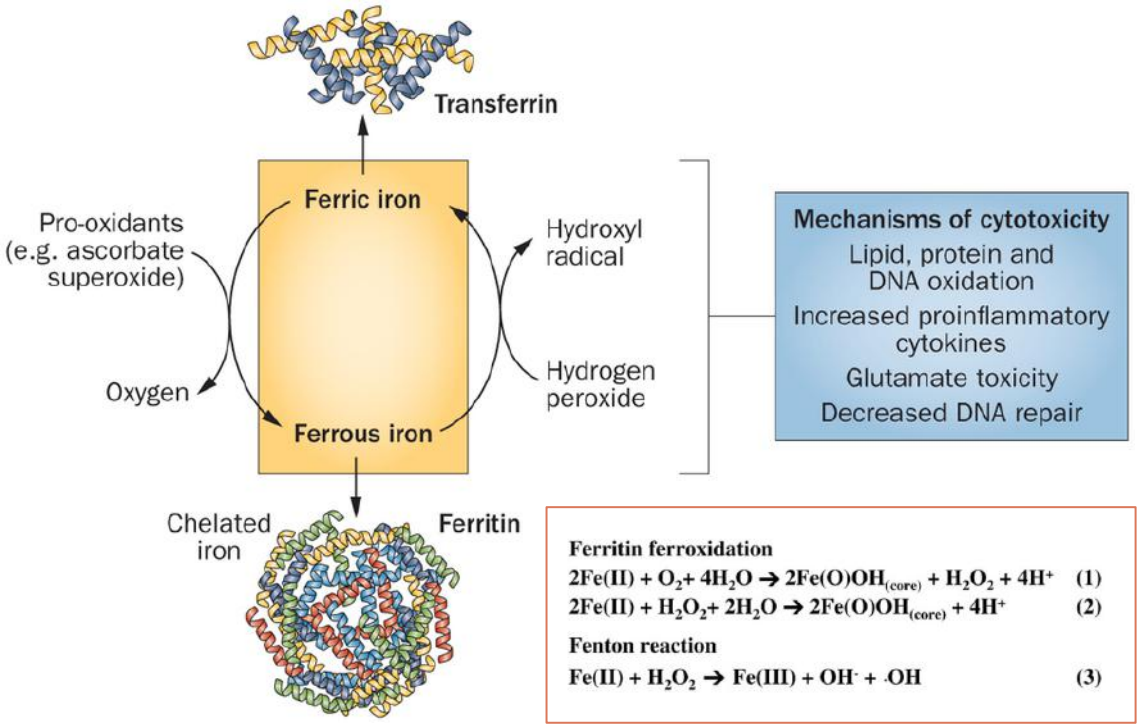

Fig. 1.8 Reaction of ferrous iron with hydrogen peroxide produces hydroxyl radicals via the Fenton reaction. Ferric iron can then be recycled back into ferrous iron by pro-oxidants, which enables iron to act as a catalyst for hydroxyl radical production. Iron accumulation promotes cytotoxicity through a variety of mechanisms, incuding oxidative stress, increased proinflammatory cytokines, glutamate toxicity and impaired DNA repair[53] .

1.3.3 Regulation of ferritin expression

Just as the ferritin structure is highly conserved in bacteria, plants and animals, so are the basic stimuli that regulate its expression: the iron availability and the response to oxidative stress. In mammals, most of the iron-dependent regulation occurs at a post-transcriptional level: the mRNAs of cytosolic ferritins contain a specific structure in the 5′UTR, named Iron Regulatory Element (IRE), which binds with high affinity the repressors Iron Responsive Proteins (IRP1 and IRP2). The formation of the IRE/IRP complex blocks ribosome binding and translation[48,54].

The transcriptional regulation of ferritin has been less extensively studied, but it is no less

important. It was found that the H-chain expression is induced by inflammatory cytokines activating NF-kB and downregulated by p53[55,56].

1.3.4 Mitochondrial ferritin

A new form of ferritin has been recently identified, encoded by an intronless gene and expressed as a 30 kDa precursor with high identity to the cytosolic H ferritin but characterized by a long N-terminal extension containing a mitochondrial localization sequence. Indeed, the product of this gene is specifically taken up by mitochondria and processed to form a stable ferritin shell with ferroxidase activity and functional in incorporating iron[57]. The presence of a mitochondrial ferritin (MtF) in mammalian is particularly interesting, because this organelle is tightly involved in iron trafficking and has a key role in important cellular activities, including respiration, production of ROS and regulation of apoptotic pathways. Mitochondrial ferritin lacks IREs and is expressed only in a few cell types with high metabolic activity. It was found primarily in the testis, heart, kidney and brain[58].

1.3.5 Nuclear ferritin

Over the last two decades, several studies have reported the presence of ferritin in cell nuclei, initially in cells under pathological conditions, such as hepatocytes of mice, rats and baboons following iron overload. Then, intranuclear ferritin was found in various cell types, which include hepatocytes, bone-marrow macrophages, muscle and nerve cells, some brain tumor cells and glial cell lines, and chicken corneal endothelial cells[48,59]. The latter cells have been studied in detail, showing that ferritin is inside the nucleus during the development, but no earlier than day 12. Ferritin was predominantly of the H-type, structurally analogous to the cytosolic ferritin and similarly inhibited by iron deprivation. The suppression of the nuclear protein made these cells more sensitive to DNA breaks caused by UV irradiations, and it was concluded that corneal cells developed nuclear ferritin as protectant against UV damage, to which they are easily exposed. The nuclear localization of ferritin did not involve a specific NLS signal, and seemed specific to the corneal cells that express a molecule, named ferritoid, containing an NLS and a ferritin-like domain [59,60]. The association of ferritoid with ferritin was shown to mediate the transfer to the nucleus, however ferritoid has not been found in species other than the chicken[61]. Various deletion constructs of H-ferritin were examined for their ability to translocate to the nucleus and it was found that 85% of the monomeric H-ferritin needs to be intact for nuclear translocation to occur efficiently. The deletion of the first 10 or the last 30 amino acids did not have a significant impact, while larger deletions in the C- and N-termini or within the protein body confined ferritin to the cytoplasm. These observations excluded the possibility of a role for a specific amino acid sequence in signalling nuclear translocation[62].

The mechanism of ferritin translocation in the nucleus was studied in human astrocytoma SW1088 cells. It was showed that H-ferritin is preferentially translocated over the L-ferritin, and that the mechanism does not require NLS-bearing cytosolic factors but seems to be energy-dependent and under the control of the nuclear pore complex[63]. The nuclear ferritin was found to be encoded by the same gene as the cytosolic H-ferritin, to accumulate preferentially in the heterochromatin, and to be present mainly in a O-glycosylated form. Since inhibitors of the O-

glycosylations prevent the translocation of ferritin in the nuclei, it was proposed that the process is post-translationally regulated and responds to environmental and nutritional stimuli[48].

About the functional significance of nuclear ferritin, studies demonstrated that it was associated with DNA, and in particular was able to bind the β-globin gene promoter[64], while *in vitro* experiments showed that it protects DNA from iron-induced oxidative damage[63]. Overall, it is clear that ferritin has the ability to bind DNA. This binding seems to be specific to H-ferritin and might require an intact ferroxidase site. The identification of a DNA binding motif for H-ferritin raises the novel possibility of a role for ferritin as a conventional transcription factor[64].

1.3.6 Serum ferritin

Mammalian ferritins are found in body fluids, such as serum, CSF and synovial fluids. The one in serum is predominantly composed of L-chains, which have a low iron content, and counts for a minor proportion of total body ferritin (normally 0.025% of the total body ferritin) but it is clinically important, since its level is a useful index of body iron status, and therefore largely used for the diagnosis of iron deficient anemias and iron overload[65,66]. It may originate from cell damage or from active and regulated ferritin secretion, but its source and its physiological functions are yet not clear and represent an interesting issue to be addressed.

Nevertheless, a significant increase in serum ferritin levels has confirmed to be related to pathological processes, such as inflammation, infection, liver diseases, cancer and in response to oxidative stress. In particular, it has attracted widespread attention that serum ferritin can be used as a tumor biomarker. For instance, serum ferritin is elevated in breast cancer patients, is markedly increased in all relapsed cases of acute leukemia and is secreted from melanoma cells, contributing to cancer progression[67–69]. Not only the amount, but also the H/L ratio of serum ferritin varies, increasing in pathological conditions; a number of studies have shown that H-ferritins are highly expressed in tumorigenic cell lines as well as in some malignant tissues from patients. Although mechanisms underlying these changes are still unclear, these studies reveal that H-ferritin may play an important role in malignancy, and could be a potential biomarker for many kinds of cancers[70,71].

1.3.7 Transferrin receptor

As far back as the 1960s, several research groups reported that human ferritin could be selectively taken up by tumor cells[72,73] but only in 2010 the Transferrin receptor 1 (TfR1) was identified as the human H-ferritin receptor by Seaman's group[74].

TfR1 (also named CD71) was originally identified as the receptor for transferrin (Tf) and it is required for iron delivery from Tf to cells, regulating the iron uptake. The TfR1 is a type II transmembrane glycoprotein found primarily as a homodimer (180 kDa) consisting of identical monomers joined by two disulfide bonds. Each monomer (760 amino acids, molecular weight 90-95 kDa) contains a large extracellular C-terminal domain (671 amino acids) that holds the Tf-binding site, a single-pass transmembrane domain (28 amino acids), and a short intracellular N-terminal domain (61 amino acids). TfR1 expression is primarily regulated at the post-transcriptional level in response to intracellular iron, in a similar way to ferritin[75]. Physiologically, delivery and uptake of iron from Tf into cells occur through the internalization of iron-loaded Tf, mediated by the TfR1 and this pathway has been studied extensively[76]. Briefly, diferric Tf binds the receptor and both are

internalized in clathrin-coated pits through receptor-mediated endocytosis. The decrease in pH in the endosome promotes a conformational change in Tf and the release of iron. Tf remains bound to the receptor and the apo-Tf/TfR1 complex is recycled back to the cell surface where apo-Tf is then released. The TfR1 is constitutively recycled independently from Tf binding[75] (Fig. 1.9).

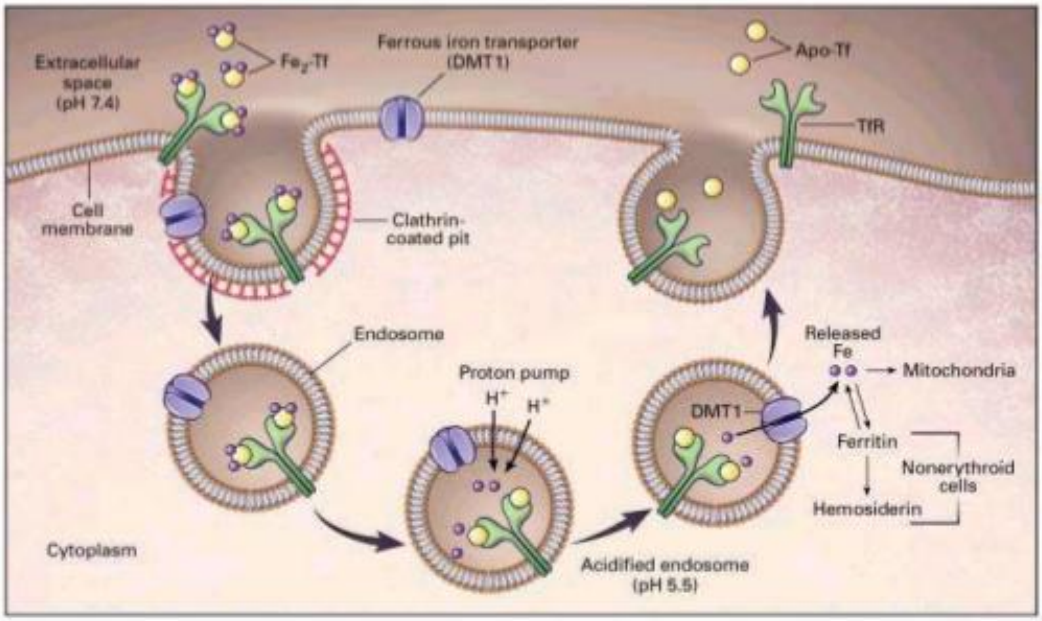

Fig. 1.9 Cellular iron uptake and release.

TfR1 is ubiquitously expressed at low levels on normal cells and at high levels in rapidly proliferating cells, such as those of the intestinal epithelium and the basal epidermis, and in cells that require large amounts of iron[77]. It is not expressed, however, by the mature erythrocytes. Several studies have shown elevated levels of the TfR expression on cancer cells compared to the healthy counterparts: in breast cancer, for example, the amount of TfR is 4-5 times greater[78,79], but in other cases can also be 100 times higher than the average expression on normal cells[80–83]. This overexpression is probably due to the increased need for iron by the enzymes involved in DNA synthesis, in rapidly proliferating cells. Moreover, it has also been shown that TfR1 can be used as a prognosis indicator in breast cancer, leukemia, lung cancer, and bladder cancer[84–87].

High levels of TfR1 in a variety of malignancies, its extracellular accessibility, its ability to be internalized, and its central role in the cellular pathology of human cancer, make this receptor an attractive target for tumor diagnosis and treatment. In fact, the TfR can be successfully used to deliver cytotoxic agents into malignant cells including chemotherapeutic drugs, cytotoxic proteins, or high molecular weight compounds including liposomes, viruses, or nanoparticles[88]. Several studies have shown that not only Tf binds TfR, but the receptor can interact with other proteins, among which ferritin, as demonstrated by Seamans's group. In particular they found that TfR1 binds specifically to H-ferritin with little or no binding to L-ferritin and after binding on the cell surface, the H-ferritin-TfR1 complex is internalized and can be found in early and recycling endosomes, just like transferrin[74]. Soon after the identification of the H-ferritin receptor, Fan *et al.* proved that ferritin can distinguish cancerous cells from normal cells via TFR1, with a sensitivity of

98% and specificity of 95%, in nine different type of cancers, on both tumor cells and tumor tissues from clinical samples[89].

A second transferrin receptor, called TfR2, was identified and characterized, but its expression is restricted to certain cell types and is unaffected by intracellular iron concentrations. Furthermore, it binds to transferrin with a 25-30 fold lower affinity than TfR1[75].

1.3.8 Ferritin as nanoparticle

Ferritin has a well-known physiological role, but over the years it has proven to have also a great potential in the field of nanomedicine, thanks to some features that make it unique in its kind. Not only it has nanometric dimensions and owns a natural iron core with paramagnetic properties, but even more it is stable, non-immunogenic and can be modified in different ways.

The protein structure contains large numbers of salt bridges and hydrogen bonds formed between subunits and for this reason it exhibits remarkable thermal and chemical stability. Unlike most other proteins, which are sensitive to temperature and pH outside of the physiological range, ferritin is able to bear high temperatures up to 70 °C and is stable to various denaturants such as urea or guanidinium chloride. An interesting recent finding is that the assembly of ferritin, despite its rigidness under physiological conditions, is pH-dependent: ferritin architecture can be broken down in an acidic environment and restored, almost completely, by returning the pH back to physiological conditions[49]. These features, together with the TfR1 binding capacity, have developed the interest of researchers to this protein and its potential use in nanomedicine.

From an application point of view, it is useful to keep in mind that recombinant ferritin nanocages are easily produced in *E. Coli*, at the milligram to gram scale. Purification is easy because it exploits the thermostability: established protocols separate recombinantly produced ferritin by heating E. coli cell to denature the native proteins and leave only the thermostable ferritin in solution. Further purification steps, such as chromatographic separations and differential centrifugation, may be performed to produce material with very high purity[90].

Once obtained, ferritin has many possibilities of use. First of all, recombinant ferritin provides a central cavity which can be efficiently loaded with transition metals, drugs, fluorescent molecules or contrast agents and since it has a uniform cage, ferritin allows the precise control of the amount of encapsulated molecules[91,92]. Non-metallic molecules, such as drugs, may enter into the cavity using the pH-dependent disassembly mechanism, described previously. If in the reaction environment a "foreign" molecule is present, this is trapped during the process of "unfolding-refolding" regulated by the pH, as demonstrated with cisplatin and doxorubicin[93,94].

The nanocage has also been extensively exploited as reaction chamber for the synthesis of highly crystalline and monodisperse nanoparticles, by biomimetic mineralization within the protein shell[89]. Indeed, ferritin represents a unique and simple biomineralization scaffold since the closed protein shell contains all the necessary element for biomineralization: an enzymatic catalyst for the molecular transformation of the precursor ions, a nucleation site and an architecture that defines and constrains the overall morphology of the biomineral. In addition, the colloidal nature of the protein cage makes the final biomineral soluble, yet biochemically inert[49]. In 1992, Mann *et al.* have demonstrated that ferromagnetic nanoparticles of iron oxide can be synthesized artificially in the internal cavity of apoferritin, with homogeneous size (7.3 ± 1.4 nm) and almost indistinguishable from naturally iron cores[95]. After that work, ferritin was used as a template to mineralise iron,

manganese, cobalt, chromium and nickel or as a synthesis chamber for semiconductor nanoparticles[96–98]. The plasticity of the *in vitro* mineralisation of ferritin makes it an ideal tool for cellular imaging; iron-loaded ferritin has been used as a contrast agent in both electron microscopy and MRI[99], while a gadolinium-loaded ferritin probe was useful to visualized tumor angiogenesis[100].

It is also possible to modify the surface of the ferritin cage, either genetically or chemically, through the addition of peptide, protein tags or other different functionalities. Despite the natural targeting of ferritin towards cancer cells, several research groups have modified the surface of ferritin nanocages by inserting a number of target motifs, such as antibodies, peptides and antibody fragments, in order to drive nanoparticles towards specific cells by selective recognition[101]. For example, the introduction of the RGD-4C peptide not significantly alters neither the assembly of the protein nor its mineralization capacity and ferritin shows affinity for the cells overexpressing αvβ3 integrin, linked by RGD4C[102].

All these characteristics have made ferritin an attractive vectors with potential application in nanomedicine.

1.4 Aim of the work

Cancer is a leading cause of disease worldwide, with 14 million of new cases and 8 million of deaths in one year and a trend which is expected to grow. Among all cancers, breast cancer is the most common cancer in women worldwide and even if progress in early detection and treatment have led to improve survival, it remains the second most common cause of cancer mortality (lung cancer is first) among women in developed countries. Breast cancer exists in four major molecular subtypes, that occur at different rates, respond to different kinds of treatment, are more or less aggressive and have varied long term survival rates.

Though there are many therapeutic options today for the treatment of cancer, there is still the risk that the chemotherapy fails, mainly for two aspects. On the one hand, the low selectivity of cytotoxic agents in killing cancer cells over normal cells, which requires high doses also affecting healthy tissues, causing serious side effects. Moreover, the traditional "maximum tolerated dose" (MTD) paradigm requires that patients be administered with single or short courses of the highest tolerable dosage of a drug in order to achieve the best therapeutic efficacy with minimal possible toxicity. This treatment need prolonged breaks between different chemotherapy cycles to allow recovery of healthy tissues, with the risk of recurrence. Second challenge is the development of resistance: the tumor cells put in place response mechanisms to defend themselves from the action of drugs. Different molecular mechanisms have been implicated in drug resistance (MDR) such as the local tumour microenvironment, the alterations in drug metabolism and the mutation of targets. But it has a very important role also the expression of membrane transporters, such as P-glycoprotein, which promote the efflux of drugs from the cell.

Many efforts have been made to face these limitations and nanothecnologies could offer groundbreaking solutions. In my case, I focused my PhD project on the development of protein nanosystems capable of promoting a targeted drug delivery to the tumor tissue, treat the disease and, together, overcome the MDR. The work presented in this PhD thesis has been divided in four chapters. In all individual projects, that are part of a single overall objective, ferritin was used as basic system.

Ferritins are a family of iron storage proteins composed of a regular assembly of 24 subunits to form a spherical cage architecture with an external size of ~12 nm and an internal cavity physiologically appointed to enclose a core of iron oxide. The protein plays a key role in the metabolism of iron as storage protein, protecting the cell from oxidative stress. This protective role is exerted both in the cytoplasm and in the nucleus and ferritin could be translocate into the nucleus in response to oxidative stimuli, in order to protect the DNA from potential damage caused by ROS production. An interesting recent finding is that the assembly of ferritin is pH-dependent and taking advantage of this feature, the protein can be loaded with different molecules. Moreover, the heavy chain subunits have also the ability to recognize with high specificity and high sensitivity cancer cell overexpressing the Transferrin receptor 1 (TfR1).

So, the general purpose of my work was to develop H-ferritin nanoparticles and investigated their potential as drug delivery systems in the field of cancer therapy, exploiting all the unique characteristics described above. In particular, I analysed the interaction of HFn with TfR1-positive cancer cell lines and tumor models, and I assessed its ability to selectively transport active molecules to the site of interest, increasing the cytotoxic action and eluding the resistance mechanisms put in place by the tumor.

HFn could be a good candidate nanocarrier specific for delivery of chemotherapeutics, as: 1) HFn could be easily loaded or functionalized with a broad range of molecules; 2) HFn was expected to sensitively and selectively recognize tumor cells exploiting the binding with TfR1; 3) the typical high level of ROS in cancer cells could promote the translocation and release of the drugs in the nucleus.

Initially, we studied and characterized the interaction of HFn with a model tumor cell lines and its ability to increase the targeted transport and the cytotoxic activity of a chemotherapy drug. We chose to use doxorubicin, one of the most widely used chemotherapeutics in the treatment of solid tumors, although the development of resistance and the occurrence of severe side effects limits its efficacy in the clinical practice. Then, starting from the increasing interest around “low dose metronomic” (LDM) approach in cancer therapy, we decide to test our doxorubicin nanocarrier on a breast cancer model, with the aim to evaluate the potential of combining a LDM treatment with the administration of the drug through H-ferritin nanoparticles.

In the last part of my PhD, I gradually broaden the outlook of my research exploiting ferritin for two specific issues related to breast cancer therapy. On the one hand, the treatment of triple negative breast cancers, more aggressive and difficult to treat, by analysing the ability of the ferritin to make usable a promising molecule of natural origin, curcumin. In fact, curcumin has anti-tumor properties and appears to modulate the resistance to chemotherapy drugs, but it is too little bioavailable to get the benefits.

Finally, we functionalized ferritin in order to make it a carrier also for gene therapy, with the purpose of treating those positive HER2 tumors that no longer respond to treatment with trastuzumab. In particular, we have developed a system for the transport of anti-miRNAs, conjugating nucleic acids on the outer protein surface of HFn.

1.5 References

1. Torre, L. A. *et al.* Global cancer statistics, 2012. *CA. Cancer J. Clin.* **65,** 87–108 (2015).
2. Stewart, B. & Wild, C. World Cancer Report 2014. (2014).
3. Greish, K. Enhanced permeability and retention (EPR) effect for anticancer nanomedicine drug targeting. *Methods Mol. Biol. Clifton NJ* **624,** 25–37 (2010).
4. Kaur, H. & Budd, G. T. Metronomic therapy for breast cancer. *Curr. Oncol. Rep.* **6,** 49–52 (2004).
5. Kareva, I., Waxman, D. J. & Lakka Klement, G. Metronomic chemotherapy: an attractive alternative to maximum tolerated dose therapy that can activate anti-tumor immunity and minimize therapeutic resistance. *Cancer Lett.* **358,** 100–106 (2015).
6. Cao, Y. & Langer, R. Optimizing the Delivery of Cancer Drugs That Block Angiogenesis. *Sci. Transl. Med.* **2,** 15ps3-15ps3 (2010).
7. Fang, J., Nakamura, H. & Maeda, H. The EPR effect: Unique features of tumor blood vessels for drug delivery, factors involved, and limitations and augmentation of the effect. *Adv. Drug Deliv. Rev.* **63,** 136–151 (2011).
8. Gottesman, M. M. Mechanisms of Cancer Drug Resistance. *Annu. Rev. Med.* **53,** 615–627 (2002).
9. Markman, J. L., Rekechenetskiy, A., Holler, E. & Ljubimova, J. Y. Nanomedicine therapeutic approaches to overcome cancer drug resistance. *Adv. Drug Deliv. Rev.* **65,** 1866–1879 (2013).
10. Yan, Y., Björnmalm, M. & Caruso, F. Particle carriers for combating multidrug-resistant cancer. *ACS Nano* **7,** 9512–9517 (2013).
11. Dean, M., Rzhetsky, A. & Allikmets, R. The human ATP-binding cassette (ABC) transporter superfamily. *Genome Res.* **11,** 1156–1166 (2001).
12. Chang, G. Multidrug resistance ABC transporters. *FEBS Lett.* **555,** 102–105 (2003).
13. Sharom, F. J. ABC multidrug transporters: structure, function and role in chemoresistance. *Pharmacogenomics* **9,** 105–127 (2008).
14. Fromm, M. F. Importance of P-glycoprotein at blood-tissue barriers. *Trends Pharmacol. Sci.* **25,** 423–429 (2004).
15. Polgar, O. & Bates, S. E. ABC transporters in the balance: is there a role in multidrug resistance?1. *Biochem. Soc. Trans.* **33,** 241–245 (2005).
16. Schinkel, A. H. & Jonker, J. W. Mammalian drug efflux transporters of the ATP binding cassette (ABC) family: an overview. *Adv. Drug Deliv. Rev.* **55,** 3–29 (2003).
17. Staud, F. & Pavek, P. Breast cancer resistance protein (BCRP/ABCG2). *Int. J. Biochem. Cell Biol.* **37,** 720–725 (2005).
18. Szakács, G., Paterson, J. K., Ludwig, J. A., Booth-Genthe, C. & Gottesman, M. M. Targeting multidrug resistance in cancer. *Nat. Rev. Drug Discov.* **5,** 219–234 (2006).
19. Trédan, O., Galmarini, C. M., Patel, K. & Tannock, I. F. Drug resistance and the solid tumor microenvironment. *J. Natl. Cancer Inst.* **99,** 1441–1454 (2007).
20. Globocan 2012 - Home. Available at: http://globocan.iarc.fr/Default.aspx. (Accessed: 20th December 2016)
21. AIRC-Associazione Italiana per la Ricerca sul cancro. Le statistiche dei tumori in Italia. *AIRC* Available at: http://www.airc.it/cancro/cos-e/statistiche-tumori-italia/. (Accessed: 20th

December 2016)
22. Yersal, O. & Barutca, S. Biological subtypes of breast cancer: Prognostic and therapeutic implications. *World J. Clin. Oncol.* **5,** 412–424 (2014).
23. Malhotra, G. K., Zhao, X., Band, H. & Band, V. Histological, molecular and functional subtypes of breast cancers. *Cancer Biol. Ther.* **10,** 955–960 (2010).
24. Figueroa-Magalhães, M. C., Jelovac, D., Connolly, R. M. & Wolff, A. C. Treatment of HER2-positive breast cancer. *Breast Edinb. Scotl.* **23,** 128–136 (2014).
25. Feynman, R. P. There's Plenty of Room at the Bottom. *Eng. Sci.* **23,** 22–36 (1960).
26. The Royal Society and Royal Academy. Nanoscience and nanotechnologies: opportunities and uncertainties. Available at: https://royalsociety.org/topics-policy/publications/2004/nanoscience-nanotechnologies/. (Accessed: 20th December 2016)
27. Liu, Y., Miyoshi, H. & Nakamura, M. Nanomedicine for drug delivery and imaging: A promising avenue for cancer therapy and diagnosis using targeted functional nanoparticles. *Int. J. Cancer* **120,** 2527–2537 (2007).
28. Sanna, V., Pala, N. & Sechi, M. Targeted therapy using nanotechnology: focus on cancer. *Int. J. Nanomedicine* **9,** 467–483 (2014).
29. Chang, E. H. *et al.* Nanomedicine: Past, present and future - A global perspective. *Biochem. Biophys. Res. Commun.* **468,** 511–517 (2015).
30. Verderio, P. *et al.* Delivering colloidal nanoparticles to mammalian cells: a nano-bio interface perspective. *Adv. Healthc. Mater.* **3,** 957–976 (2014).
31. Riehemann, K. *et al.* Nanomedicine--challenge and perspectives. *Angew. Chem. Int. Ed Engl.* **48,** 872–897 (2009).
32. Veiseh, O., Gunn, J. W. & Zhang, M. Design and fabrication of magnetic nanoparticles for targeted drug delivery and imaging. *Adv. Drug Deliv. Rev.* **62,** 284–304 (2010).
33. Chow, E. K.-H. & Ho, D. Cancer Nanomedicine: From Drug Delivery to Imaging. *Sci. Transl. Med.* **5,** 216rv4-216rv4 (2013).
34. Parveen, S., Misra, R. & Sahoo, S. K. Nanoparticles: a boon to drug delivery, therapeutics, diagnostics and imaging. *Nanomedicine Nanotechnol. Biol. Med.* **8,** 147–166 (2012).
35. Yih, T. c. & Al-Fandi, M. Engineered nanoparticles as precise drug delivery systems. *J. Cell. Biochem.* **97,** 1184–1190 (2006).
36. Bazak, R., Houri, M., El Achy, S., Kamel, S. & Refaat, T. Cancer active targeting by nanoparticles: a comprehensive review of literature. *J. Cancer Res. Clin. Oncol.* **141,** 769–784 (2015).
37. Torchilin, V. Tumor delivery of macromolecular drugs based on the EPR effect. *Adv. Drug Deliv. Rev.* **63,** 131–135 (2011).
38. Yu, B., Tai, H. C., Xue, W., Lee, L. J. & Lee, R. J. Receptor-targeted nanocarriers for therapeutic delivery to cancer. *Mol. Membr. Biol.* **27,** 286–298 (2010).
39. Byrne, J. D., Betancourt, T. & Brannon-Peppas, L. Active targeting schemes for nanoparticle systems in cancer therapeutics. *Adv. Drug Deliv. Rev.* **60,** 1615–1626 (2008).
40. Danhier, F., Feron, O. & Préat, V. To exploit the tumor microenvironment: Passive and active tumor targeting of nanocarriers for anti-cancer drug delivery. *J. Control. Release Off. J. Control. Release Soc.* **148,** 135–146 (2010).
41. Brissette, R., Prendergast, J. K. A. & Goldstein, N. I. Identification of cancer targets and therapeutics using phage display. *Curr. Opin. Drug Discov. Devel.* **9,** 363–369 (2006).
42. Sugahara, K. N. *et al.* Coadministration of a tumor-penetrating peptide enhances the efficacy

of cancer drugs. *Science* **328,** 1031–1035 (2010).
43. Lu, Y. & Low, P. S. Folate-mediated delivery of macromolecular anticancer therapeutic agents. *Adv. Drug Deliv. Rev.* **54,** 675–693 (2002).
44. Wicki, A., Witzigmann, D., Balasubramanian, V. & Huwyler, J. Nanomedicine in cancer therapy: Challenges, opportunities, and clinical applications. *J. Controlled Release* **200,** 138–157 (2015).
45. Laufberger, V. Sur la cristallisation de la ferritine. *Bull Soc Chem Biol* **19,** 1575–1582 (1937).
46. Harrison, P. M. & Arosio, P. The ferritins: molecular properties, iron storage function and cellular regulation. *Biochim. Biophys. Acta BBA - Bioenerg.* **1275,** 161–203 (1996).
47. Arosio, P. & Levi, S. Ferritin, iron homeostasis, and oxidative damage. *Free Radic. Biol. Med.* **33,** 457–463 (2002).
48. Arosio, P., Ingrassia, R. & Cavadini, P. Ferritins: a family of molecules for iron storage, antioxidation and more. *Biochim. Biophys. Acta* **1790,** 589–599 (2009).
49. Uchida, M., Kang, S., Reichhardt, C., Harlen, K. & Douglas, T. The Ferritin Superfamily: Supramolecular Templates for Materials Synthesis. *Biochim. Biophys. Acta* **1800,** 834–845 (2010).
50. Crichton, R. R. & Declercq, J.-P. X-ray structures of ferritins and related proteins. *Biochim. Biophys. Acta* **1800,** 706–718 (2010).
51. Arosio, P., Carmona, F., Gozzelino, R., Maccarinelli, F. & Poli, M. The importance of eukaryotic ferritins in iron handling and cytoprotection. *Biochem. J.* **472,** 1–15 (2015).
52. López-Castro, J. D. *et al.* A new approach to the ferritin iron core growth: influence of the H/L ratio on the core shape. *Dalton Trans. Camb. Engl. 2003* **41,** 1320–1324 (2012).
53. Stephenson, E., Nathoo, N., Mahjoub, Y., Dunn, J. F. & Yong, V. W. Iron in multiple sclerosis: roles in neurodegeneration and repair. *Nat. Rev. Neurol.* **10,** 459–468 (2014).
54. Walden, W. E. *et al.* Structure of Dual Function Iron Regulatory Protein 1 Complexed with Ferritin IRE-RNA. *Science* **314,** 1903–1908 (2006).
55. Kwak, E. L., Larochelle, D. A., Beaumont, C., Torti, S. V. & Torti, F. M. Role for NF-kappa B in the regulation of ferritin H by tumor necrosis factor-alpha. *J. Biol. Chem.* **270,** 15285–15293 (1995).
56. Faniello, M. C. *et al.* p53-mediated downregulation of H ferritin promoter transcriptional efficiency via NF-Y. *Int. J. Biochem. Cell Biol.* **40,** 2110–2119 (2008).
57. Drysdale, J. *et al.* Mitochondrial ferritin: a new player in iron metabolism. *Blood Cells. Mol. Dis.* **29,** 376–383 (2002).
58. Santambrogio, P. *et al.* Mitochondrial Ferritin Expression in Adult Mouse Tissues. *J. Histochem. Cytochem.* **55,** 1129–1137 (2007).
59. Cai, C. X., Birk, D. E. & Linsenmayer, T. F. Ferritin is a developmentally regulated nuclear protein of avian corneal epithelial cells. *J. Biol. Chem.* **272,** 12831–12839 (1997).
60. Cai, C. X., Birk, D. E. & Linsenmayer, T. F. Nuclear Ferritin Protects DNA From UV Damage in Corneal Epithelial Cells. *Mol. Biol. Cell* **9,** 1037–1051 (1998).
61. Millholland, J. M. *et al.* Ferritoid, a Tissue-specific Nuclear Transport Protein for Ferritin in Corneal Epithelial Cells. *J. Biol. Chem.* **278,** 23963–23970 (2003).
62. Cai, C. X. & Linsenmayer, T. F. Nuclear translocation of ferritin in corneal epithelial cells. *J. Cell Sci.* **114,** 2327–2334 (2001).
63. Thompson, K. J., Fried, M. G., Ye, Z., Boyer, P. & Connor, J. R. Regulation, mechanisms

and proposed function of ferritin translocation to cell nuclei. *J. Cell Sci.* **115,** 2165–2177 (2002).
64. Alkhateeb, A. A. & Connor, J. R. Nuclear ferritin: A new role for ferritin in cell biology. *Biochim. Biophys. Acta BBA - Gen. Subj.* **1800,** 793–797 (2010).
65. Fan, K., Gao, L. & Yan, X. Human ferritin for tumor detection and therapy. *Wiley Interdiscip. Rev. Nanomed. Nanobiotechnol.* **5,** 287–298 (2013).
66. Theil, E. C. Ferritin: the protein nanocage and iron biomineral in health and in disease. *Inorg. Chem.* **52,** 12223–12233 (2013).
67. Jézéquel, P. *et al.* Validation of tumor-associated macrophage ferritin light chain as a prognostic biomarker in node-negative breast cancer tumors: A multicentric 2004 national PHRC study. *Int. J. Cancer* **131,** 426–437 (2012).
68. Matzner, Y., Konijn, A. M. & Hershko, C. Serum ferritin in hematologic malignancies. *Am. J. Hematol.* **9,** 13–22 (1980).
69. Gray, C. P., Arosio, P. & Hersey, P. Association of increased levels of heavy-chain ferritin with increased CD4+ CD25+ regulatory T-cell levels in patients with melanoma. *Clin. Cancer Res. Off. J. Am. Assoc. Cancer Res.* **9,** 2551–2559 (2003).
70. Cazzola, M. *et al.* Immunological reactivity of serum ferritin in patients with malignancy. *Tumori* **71,** 547–554 (1985).
71. Wang, W., Knovich, M. A., Coffman, L. G., Torti, F. M. & Torti, S. V. Serum ferritin: Past, present and future. *Biochim. Biophys. Acta* **1800,** 760–769 (2010).
72. Caulfield, J. B. STUDIES ON FERRITIN UPTAKE BY ISOLATED TUMOR CELLS. *Lab. Investig. J. Tech. Methods Pathol.* **12,** 1018–1025 (1963).
73. Easty, G. C., Yarnell, M. M. & Andrews, R. D. The Uptake of Proteins by Normal and Tumour Cells In Vitro. *Br. J. Cancer* **18,** 354–367 (1964).
74. Li, L. *et al.* Binding and uptake of H-ferritin are mediated by human transferrin receptor-1. *Proc. Natl. Acad. Sci. U. S. A.* **107,** 3505–3510 (2010).
75. Daniels, T. R., Delgado, T., Rodriguez, J. A., Helguera, G. & Penichet, M. L. The transferrin receptor part I: Biology and targeting with cytotoxic antibodies for the treatment of cancer. *Clin. Immunol. Orlando Fla* **121,** 144–158 (2006).
76. Richardson, D. R. & Ponka, P. The molecular mechanisms of the metabolism and transport of iron in normal and neoplastic cells. *Biochim. Biophys. Acta* **1331,** 1–40 (1997).
77. Gatter, K. C., Brown, G., Trowbridge, I. S., Woolston, R. E. & Mason, D. Y. Transferrin receptors in human tissues: their distribution and possible clinical relevance. *J. Clin. Pathol.* **36,** 539–545 (1983).
78. Tonik, S. E., Shindelman, J. E. & Sussman, H. H. Transferrin receptor is inversely correlated with estrogen receptor in breast cancer. *Breast Cancer Res. Treat.* **7,** 71–76 (1986).
79. Walker, R. A. & Day, S. J. Transferrin receptor expression in non-malignant and malignant human breast tissue. *J. Pathol.* **148,** 217–224 (1986).
80. Soyer, H. P., Smolle, J., Torne, R. & Kerl, H. Transferrin receptor expression in normal skin and in various cutaneous tumors. *J. Cutan. Pathol.* **14,** 1–5 (1987).
81. Barnett, D., Wilson, G. A., Lawrence, A. C. & Buckley, G. A. Transferrin receptor expression in the leukaemias and lymphoproliferative disorders. *Clin. Lab. Haematol.* **9,** 361–370 (1987).
82. Prost, A. C. *et al.* Differential transferrin receptor density in human colorectal cancer: A

potential probe for diagnosis and therapy. *Int. J. Oncol.* **13,** 871–875 (1998).
83. Prutki, M. *et al.* Altered iron metabolism, transferrin receptor 1 and ferritin in patients with colon cancer. *Cancer Lett.* **238,** 188–196 (2006).
84. Yang, D. C., Wang, F., Elliott, R. L. & Head, J. F. Expression of transferrin receptor and ferritin H-chain mRNA are associated with clinical and histopathological prognostic indicators in breast cancer. *Anticancer Res.* **21,** 541–549 (2001).
85. Ja, H., Ta, L., Ag, S. & Mf, G. Correlation of transferrin receptor expression with histological class and outcome in non-Hodgkin lymphoma. *Lancet Lond. Engl.* **1,** 498–501 (1983).
86. Kondo, K. *et al.* Transferrin receptor expression in adenocarcinoma of the lung as a histopathologic indicator of prognosis. *Chest* **97,** 1367–1371 (1990).
87. Seymour, G. J., Walsh, M. D., Lavin, M. F., Strutton, G. & Gardiner, R. A. Transferrin receptor expression by human bladder transitional cell carcinomas. *Urol. Res.* **15,** 341–344 (1987).
88. Daniels, T. R., Delgado, T., Helguera, G. & Penichet, M. L. The transferrin receptor part II: targeted delivery of therapeutic agents into cancer cells. *Clin. Immunol. Orlando Fla* **121,** 159–176 (2006).
89. Fan, K. *et al.* Magnetoferritin nanoparticles for targeting and visualizing tumour tissues. *Nat. Nanotechnol.* **7,** 459–464 (2012).
90. He, D. & Marles-Wright, J. Ferritin family proteins and their use in bionanotechnology. *New Biotechnol.* **32,** 651–657 (2015).
91. Zhen, Z. *et al.* Ferritin nanocages to encapsulate and deliver photosensitizers for efficient photodynamic therapy against cancer. *ACS Nano* **7,** 6988–6996 (2013).
92. Sun, C. *et al.* Controlling Assembly of Paired Gold Clusters within Apoferritin Nanoreactor for in Vivo Kidney Targeting and Biomedical Imaging. *J. Am. Chem. Soc.* **133,** 8617–8624 (2011).
93. Yang, Z. *et al.* Encapsulation of platinum anticancer drugs by apoferritin. *Chem. Commun. Camb. Engl.* 3453–3455 (2007). doi:10.1039/b705326f
94. Bellini, M. *et al.* Protein nanocages for self-triggered nuclear delivery of DNA-targeted chemotherapeutics in Cancer Cells. *J. Controlled Release* **196,** 184–196 (2014).
95. Meldrum, F. C., Heywood, B. R. & Mann, S. Magnetoferritin: in vitro synthesis of a novel magnetic protein. *Science* **257,** 522–523 (1992).
96. Meldrum, F. C., Douglas, T., Levi, S., Arosio, P. & Mann, S. Reconstitution of manganese oxide cores in horse spleen and recombinant ferritins. *J. Inorg. Biochem.* **58,** 59–68 (1995).
97. Okuda, M., Iwahori, K., Yamashita, I. & Yoshimura, H. Fabrication of nickel and chromium nanoparticles using the protein cage of apoferritin. *Biotechnol. Bioeng.* **84,** 187–194 (2003).
98. Iwahori, K., Yoshizawa, K., Muraoka, M. & Yamashita, I. Fabrication of ZnSe Nanoparticles in the Apoferritin Cavity by Designing a Slow Chemical Reaction System. *Inorg. Chem.* **44,** 6393–6400 (2005).
99. Jin, R., Lin, B., Li, D. & Ai, H. Superparamagnetic iron oxide nanoparticles for MR imaging and therapy: design considerations and clinical applications. *Curr. Opin. Pharmacol.* **18,** 18–27 (2014).
100. Crich, S. G. *et al.* Magnetic Resonance Visualization of Tumor Angiogenesis by Targeting Neural Cell Adhesion Molecules with the Highly Sensitive Gadolinium-Loaded Apoferritin Probe. *Cancer Res.* **66,** 9196–9201 (2006).

101. Truffi, M. *et al.* Ferritin nanocages: A biological platform for drug delivery, imaging and theranostics in cancer. *Pharmacol. Res.* **107,** 57–65 (2016).
102. Uchida, M. *et al.* Targeting of cancer cells with ferrimagnetic ferritin cage nanoparticles. *J. Am. Chem. Soc.* **128,** 16626–16633 (2006).

CHAPTER 2

Protein nanocages for self-triggered nuclear delivery of DNA-targeted chemotherapeutics in cancer cells[1]

2.1 Doxorubicin

Doxorubicin (DOX) is an anthracycline antibiotic endowed with antitumor activity, originally isolated from *S. peucetius* var. *caesius*. It has always shown a great therapeutic potential, so as to be considered one of the most potent FDA-approved chemotherapeutic drugs; its ability to combat rapidly dividing cells and to slow disease progression has been widely acknowledged for several decades, limited only by its toxicity on noncancerous cells in the human body[2].

Doxorubicin belongs to the anthracycline family, a class of antineoplastic antibiotics, together with daunorubicin, epirubicin and others. In 1940 Waksman and Woodruff discovered the first antibiotic with antitumor activity: actinomycin A, produced by *Actinomyces antibioticus*[3]. From that moment, the attention to these compounds has grown and in 1957 Farmitalia Laboratories began an investigation in search for new biosynthetic antibiotics with antitumor activity obtained from a newly isolated *Streptomyces*. They isolated initially Daunorubicin and, after a mutagenic treatment of the bacterial strain, Doxorubicin[4].

The first commercially available formulation of DOX was Adriamycin®, approved by the FDA in 1974 and currently considered one of the most effective chemotherapeutic agents, commonly used as a first-line drug in numerous types of cancer. DOX is characterized by a wide antitumor spectrum and is indicated, alone or in combination with other molecules, for the treatment of solid tumors and haematological malignancies, including: leukemias, Hodgkin's disease, neuroblastoma, soft tissue and bone sarcomas, multiple myeloma and malignant neoplasms of the bladder, breast, stomach, lung, ovary and thyroid[5].

2.1.1 Chemical structure and properties

From a structural point of view, DOX as well as other anthracyclines is an amphiphilic molecule consisting of a water-insoluble organic portion (called aglycone) and a water-soluble, amino-sugar functional group (L-daunosamine) (Fig.2.1). The aglycone consists of a tetracyclic ring with adjacent quinine-hydroquinone groups, a methoxy substituent and a short side chain with a carbonyl group. The sugar component is attached to one of the rings by a glycosidic bond. The importance of the sugar is demonstrated by the fact that the aglycone alone has no anti-tumor activity[6,7].

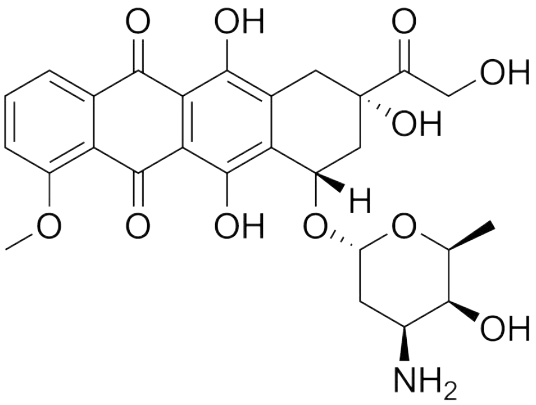

Fig. 2.1 Doxorubicin chemical structure.

The dihydroxyanthraquinone chromophore portion is responsible for the red color and the color shift in response to pH. The molecule exhibits three different pKa values. In particular, the amino group of the sugar is protonated, so the drug is available as doxorubicin hydrochloride salt (DOX HCl), which increases its solubility in aqueous environment. Doxorubicin is unstable at acidic pH and is not absorbed by the gastrointestinal tract, irritates tissues it comes in contact with, so it must necessarily be administered intravenously. When intravenously infused, DOX penetrates tissues rapidly and with high effectiveness: the distribution half-life is 3-5 min, pointing to the drug's rapid uptake by cells. Like most drugs, DOX enters the cell via passive diffusion and then moves to the nuclear compartments, where it can accumulate up to 50-fold compared to the cytoplasm. Terminal half-life of 24-48 h suggests that it takes far longer to be eliminated from the tissue than its uptake[6]. The drug is distributed widely in plasma (bonded to plasma proteins) and tissue and concentrates in liver, lymph nodes, muscles, bone marrow, fat and skin, while it does not cross the blood-brain barrier[8,9]. In liver, such as in other tissues, DOX is metabolised by the aldo-keto reductase enzyme system, forming doxorubicinol (active metabolite), doxorubicinone, aglycones and conjugates. It is primarily excreted by the hepatobiliary pathway (10-20% of a single dose within 24 hours after administration, 40-50% within 7 days) while only a small percentage of DOX appears in the urine, to which imparts a red color[8]. The substituent at C13 is the hydroxymethyl, which delays the action of cytosolic aldo-keto reductase and slows its conversion to doxorubicinol, as much active, contributing to a longer effect compared to analogues having a CH_3 at this location (for example, daunorubicin).

The metabolite, however, causes cardiotoxicity and although acute toxicity is transient and clinically manageable, the chronic one evolves into a progressive cardiomyopathy, limiting the use of DOX in cancer therapy[10,11]. Although the exact mechanism of cardiotoxicity is not clearly elucidated, it is assumed that it is related to the production of free radicals and DOX-iron complexes in mitochondrial membranes, which finally leads to mitochondrial dysfunction, loss of myocytes and cardiac failure[12]. Since DOX is not specifically targeted to tumors, it can affect the growth of many other cell types in the body, so cardiomyopathy is not the only adverse effect. DOX also manifested the most common side effects of chemotherapeutic agents, such as cutaneous injuries (reversible alopecia, rash, hyperpigmentation, photosensitivity), nausea, vomiting, mucositis (stomatitis and esophagitis), ulceration and necrosis of the colon, diarrhea, liver injury, nephropathy, myelosuppression with leukopenia. Extravasation of DOX can produce severe local tissue necrosis[5].

2.1.2 Mechanisms of action

DOX acts on nucleic acids of dividing cells by two main mechanisms: (1) intercalation between the base pairs of the DNA strands, thus blocking the replication and transcription processes in rapidly growing cells and (2) generation of iron-mediated free radicals, causing oxidative damage to cellular membranes, proteins and DNA[5,13]. In fact, the quinone structure of DOX participates in redox reactions as an electron acceptor, being turned into a semiquinone free radical; this unstable metabolite can provoke injury to the DNA itself or can be converted back to the quinone form, producing reactive oxygen species (ROS). ROS can cause oxidative stress, lipid peroxidation, membrane and DNA damage and trigger apoptosis[14,15].

Moreover, DOX binds covalently to proteins involved in DNA replication and transcription. So, it inhibits the enzyme topoisomerase II preventing DNA repair as the relaxing of supercoiled DNA is blocked. In fact, topoisomerase II catalyzes the unwinding of DNA, involving the process of cleavage of one strand and the formation of the "cleavable complex" intermediate. DOX inhibits the religation of the cleaved duplex, a lesion that results in a DNA double-strand break (DSB). The apoptosis pathway is triggered when the attempt to repair the DSBs fails and cellular growth is inhibited at phases G1 and G2[2,16].

It is noteworthy that DOX intercalates not only into nuclear but also mitochondrial DNA[17].

2.1.3 Resistance

Treatment with anthracyclines can lead to the development of the so-called Multidrug Resistance (MDR). The progression of this resistance can seriously compromise the success of chemotherapy and this is why the cytotoxic agents are often administered in combination. As regards DOX, the MDR derives primarily from the increased expression of ATP-binding proteins (also known as ABC-transporters), appointed to clear cells from harmful substances. DOX is surely a substrate of the P-glycoprotein (P-gp), a membrane protein that functions as a pump extruding from the cytoplasm amphipathic substances in an ATP-dependent manner[18,19]. The mechanism of resistance involves also MRP-1 and other transporters, but may also result from the amplification of topoisomerase II, which has been shown to affect the treatment response[20,21].

The administration of the drug using nanoparticles seems to escape these resistance mechanisms.

2.1.4 Nanotechnology-based doxorubicin formulations

DOX, as most anticancer drugs currently used in therapy, is nonspecific, thus also affecting normal cells. In recent times, many efforts have been made to develop drug delivery systems capable of targeting drugs directly at the tumor, as far as possible. Nanoparticles are very promising systems and several nanotechnology-based DOX preparations have been designed since the 1990s (Fig. 2.2). Some of them are FDA-approved, such as PEGylated liposomal Doxil® or liposomal Myocet® and others are in various phases of clinical trials[22]. Almost all of them are passively delivered to tumors via the so-called enhanced permeability and retention (EPR) effect, while only recently the attention has been focusing on active targeting of tumor cells[23].

Liposomes

Liposomes are vesicles formed by a lipid bilayer that entraps an aqueous core. The lipid membrane can be formed with phospholipids, lecithin and/or cholesterol and hydrophobic drugs can be incorporated in this bilayer, whereas hydrophilic drugs can be loaded in the aqueous core. The loading of hydrophobic molecules can occur during vesicle formation, attaining high entrapping effectiveness (≈100%), while water-soluble drugs with ionizable groups, such as DOX, are usually loaded employing active loading techniques, like pH gradients, where the drug is entrapped after the formation of the nanocarrier, obtaining equally high trapping effectiveness (≈100%)[5,24].

In 1995, FDA approved a liposomal formulation of DOX and one year later it was commercialized in the USA as **Doxil®** and in the European Union as Caelyx®. To date, this product

is marketed by Johnson & Johnson and indicated for the treatment of AIDS-related Kaposi's sarcoma (1995), recurrent ovarian cancer (1998), metastatic breast cancer (2003) and as monotherapy in patients with elevated cardiac risk and multiple myeloma (2007). It consists of a DOX-loaded PEGylated liposomal bilayer with a size of 80-90 nm, comprising three different lipids, in a precise molar ratio. The reason for the PEGylation is to be found in an attempt to avoid capture of liposomes by the reticuloendothelial system (RES), thereby increasing their circulation time in plasma (extended half-life up to 55 hours in humans)[25,26]. This nanoformulation, indeed, consistently improved the pharmacokinetics and biodistribution profile of DOX, inhibiting interaction with plasma proteins and mononuclear phagocytes and thus facilitating the longer circulation half-life and maximizing drug accumulation in tumor tissue[27]. However, as a result of the long-lasting circulation of the PEGylated liposomes to the skin capillaries, a desquamating dermatitis known as "foot-and-hand" syndrome appears as a dose-dependent adverse effect, characterized by redness, tenderness and peeling of the skin[5].

In February 2013, FDA approved a generic of this formulation, named Lipodox® (manufactured by Sun Pharma) as a result of a shortage of Doxil®. However, regulatory approval of generic liposomal formulations remains challenging and clearer guidelines are needed for characterization and quality control of nanosimilars (i.e. generic derivatives of nanomedicine products).

Five years after the approval of Doxil®/Caelyx®, the EMA approved **Myocet®**, a non-PEGylated alternative that, as with Doxil®, showed improvements in pharmacokinetic and toxicity profile when compared with conventional DOX. In addition, it decreases the appearance of the hand-foot symptom produced by the PEGylated formulations[24]. In this case, the liposomal membrane consists of two lipids (phosphatidylcholine and cholesterol) with a size of 190 nm, in which the drug is physically entrapped. Myocet® is currently commercialized by Teva Pharma and was approved in 2000 as the first-line treatment of metastatic breast cancer after three crucial Phase III clinical trials evaluated whether this liposomal formulation was superior to conventional DOX or other anthracyclines in terms of cardiotoxicity and efficacy[28].

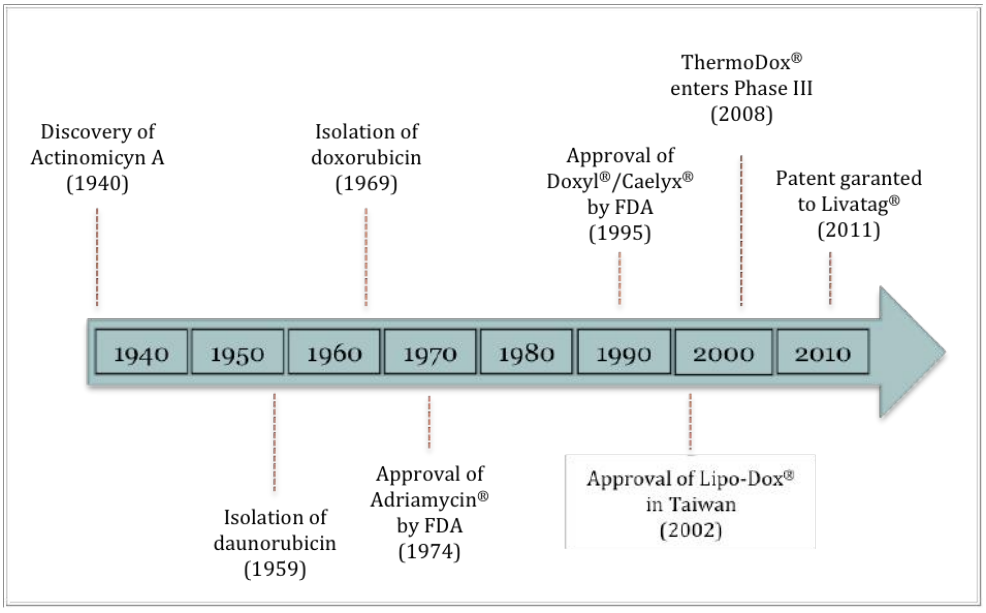

Fig. 2.2 Timeline based on the history and pharmaceutical research of DOX.

In 2002, the Department of Health of Taiwan approved **Lipo-Dox®**, the third DOX liposomal formulation that reached the market for the treatment of metastatic breast cancer, ovarian cancer and AIDS-related Kaposi's sarcoma[29]. Its lipid composition includes a saturated fatty acid that presents a relatively high phase-transition temperature, making the preparation less prone to drug leakage and enhancing its stability. This significantly prolonged the *in vivo* circulation time, while no other therapeutic improvement was achieved in comparison with Doxil®[28].

More recently, a thermosensitive liposomal DOX-based product called **ThermoDox®** has emerged as a promising formulation for liver cancer. These ≈100 nm liposomes comprise three synthetic phospholipids that confer sensitivity to temperature, thus rapidly releasing the active drug by mild thermal warming (≈40 °C) associated to thermal ablation techniques[30]. It is an interesting example of stimuli-responsive nanomedicine.

Polymeric nanoparticles

Polymeric nanoparticles are colloidal polymers whose size is in the range 100 to 1000 nm. These nanocarriers can be made of either natural or synthetic polymers, some of which are biocompatible and FDA-approved, such as poly(lactic acid) (PLA), poly(lactic-*co*-glycolic acid) (PLGA), and poly(methyl-methacrylate) (PMMA). They can be prepared by two methods: polymerization of the monomers and dispersion of preformed polymers, while drugs can be physically incorporated, chemically bound, adsorbed or absorbed[31]. Onxeo has been working since 2011 on Livatag®, a 100-300 nm DOX-loaded nanoparticles formed with polyisohexylcyanoacrylate (PIHCA). Currently, this preparation is in Phase III clinical studies with the main goal of treating patients suffering from hepatocellular carcinoma[32].

Polymer-drug conjugates

Polymer-drug conjugates are obtained by covalent linkage through conjugation of the antineoplastic drug to a hydrophilic or amphiphilic polymer. Usually, they present an adequate *in vivo* stability and prevent rapid drug release upon blood circulation dilution, in comparison with drug-loaded formulations[5]. In the past decade, three aqueous soluble polymer-drug conjugates transporting DOX have entered clinical trials: PK1 (Phase II), DOX-OXD (Phase I) and PK2 (Phase II). PK1 was developed by Pfizer and comprises N-(2-hydroxy-propyl)methacrylamide (HPMA) copolymer covalently bound to DOX by a peptidyl linker that is cleaved by lysosomal enzymes when taken up by malignant cells, promoting the release of the active drug[22].

Polymeric micelles

Polymeric micelles are probably one of the most studied delivery nanosystem in diagnosis and therapy. These nanocarriers comprise amphiphilic copolymers that self-assemble into spherical structures, with sizes in the range 20-200 nm. Poorly water-soluble drugs are loaded into the inner hydrophobic core, whereas the outer hydrophilic corona helps protect and stabilize the encapsulated molecules and can be functionalized with different moieties[33].

Among DOX micellar preparations, there are two formulations that have reached clinical trials. SP1049C was developed using Pluronics®, a ternary copolymers, and has proved to be effective against metastatic esophageal cancer refractory to standard chemotherapeutic protocols[27]. Instead, NK911 consists of a DOX-conjugated poly-aspartic acid/PEG nanocarrier with a particle size of ≈40 nm, currently in Phase II for various types of cancer[34].

Formulations for active targeting

The formulations above described are based on a passive drug targeting approach, exploiting only the EPR effect. However, in recent years many efforts have been made to actively target antineoplastic drugs to a certain cancer tissue or cell, by taking advantage of specific ligand-receptor interactions[35]. So far, the only DOX-active-targeting-based formulation that has reached clinical trials is a polymer-drug conjugate known as PK2. Unlike PK1, described previously, PK2 is a targeted DOX-polymer conjugate bound to galactosamine residues, which mediate active liver targeting through the asialoglycoprotein receptor (ASGPR) of hepatocytes. As the untargeted preparation, PK2 is a HPMA-based formulation, in which the drug is covalently bound to the copolymer by a peptidyl linker, also manufactured by Pfizer. PK2 is currently in Phase II clinical trials[22,36].

2.2 Aim of the work

In this work, we reasoned that a 24-heavy chain subunit variant of apoferritin (HFn) would facilitate the cumulative delivery of encapsulated DOX directly into the nucleus of cancer cells, potentially reducing DOX dosages and mitigating MDR effects. Therefore, we produced the monomeric H subunit by recombinant engineering, which proved valuable in self-assembling in apoferritin-like nanocages. We envisaged that HFn could be a good candidate nanocarrier, specific for nuclear delivery of chemotherapeutics, as: 1) HFn can be easily loaded with a broad range of drugs, including DOX; 2) HFn is expected to sensitively and selectively recognize tumor cells by exploiting its binding capability to TfR1; 3) heavy chain subunits are found in monomeric form in the nucleus[37], suggesting a disassembly mechanism inside or in close proximity of the nucleus, which would allow the drug to be intranuclearly released; 4) as cancer cells exhibit greater ROS stress than normal cells do[38,39], nuclear translocation of HFn should be also favored in cancer cells in response to oxidative stimuli; and 5) DOX could be passively released out of HFn shell inducing a DNA damage, which, in turn, could further trigger HFn nuclear translocation.

The aim of this work was to investigate the interaction of HFn using a model TfR1-positive cancer cell line, to assess possible increased cytotoxic efficacy of DOX incorporated in HFn, to study DOX release in cancer cells and to assess enhanced and self-triggered nuclear delivery.

2.3 Materials and methods

2.3.1 HFn nanocage design

The cDNA encoding for the heavy chain of human ferritin, modified by inserting the restriction sites for NdeI and NotI (respectively in 5′ and 3′), was synthesized by Eurofins MWG Operon and subcloned into the vector pET30b(+) from Eurofins MWG Operon to express the HFn under the control of a T7 promoter, as reported in Figure S1b (Supporting Information). The resulting plasmid pET30b/HFn was used to transform *Escherichia coli* expression strain BL21(DE3) by heat-shock method. The recombinant expression vector was confirmed by restriction endonuclease digestion and DNA sequencing.

2.3.2 HFn expression in *E. coli* and purification

BL21(DE3)/pET30b/HFn cells were grown at 37 °C in Luria Bertani kanamicin medium until OD_{600nm}=0.6 and induced with 0.5 mM isopropyl β-D-1-tiogalactopiranoside (IPTG) for 2 h and 30 min. Then, cells were collected, washed and resuspended in lysis buffer with lysozyme and DNase I. In order to prepare the crude extract, cellular suspension was sonicated six times for 10 s and centrifuged. After heat treatment at 70 °C for 15 min, the supernatant was loaded onto DEAE Sepharose anion exchange resin, pre-equilibrated with 20 mM K-MES, pH 6.0. The purified protein was eluted with a stepwise NaCl gradient, from 70 mM to 420 mM, in the same buffer. A yield of 56 mg L^{-1} of culture was obtained. Fractions were analyzed by SDS-PAGE using 12% (v/v) polyacrylamide gels[40] and the proteins detected by Coomassie Blue staining. Protein content was determined by both measuring absorbance at 280 nm and using the Coomassie Plus Protein Assay Reagent (Thermo Fisher Scientific) with IgG as standard protein. HFn for *in vitro* studies was labeled with fluorescein isothiocyanate (FITC) or with Alexa Fluor 546 according to the manufacturer's protocol (Sigma, Invitrogen).

2.3.3 HFn loading with DOX

HFn(DOX) was prepared using the disassembly/reassembly method. 200 μM doxorubicin hydrochloride was added to a HFn solution (0.5 mg mL^{-1} in 0.15 M NaCl) and adjusted to pH 2.0 by 0.1 M HCl. The pH was maintained for about 15 min and when the dissociation of HFn was completed, the pH value was increased up to 7.5 using 0.1 M NaOH. The resulting solution was stirred at room temperature for 2 h. In order to remove the excess doxorubicin and the adsorbed molecules, the solution was centrifuged through a 100 kDa Amicon filter (Millipore) and washed several times with PBS buffer. The amount of the encapsulated molecules was determined extracting DOX from HFn shell according to procedure previously described[41] and then measuring the fluorescence intensity at 555 nm of the DOX dispersion in chloroform by comparison with a predetermined DOX calibration curve. To evaluate the intracellular fate of encapsulated molecules HFn shell was also loaded with FITC using the same procedure described for DOX encapsulation.

2.3.4 Kinetics of DOX spontaneous release *in vitro*

HFn(DOX) was stored in a dialysis device and kept in a PBS bath at 37 °C for three days under shaking. At predetermined time points (30 min, 1 h, 2 h, 3 h, 4 h, 6 h, 24 h, 48 h, 72 h), the amount of drug released was quantified by fluorescence analysis and the buffer was replaced after each measurement.

2.3.5 Cell cultures

A HeLa cell line was used as a TfR1-positive model of tumor cells; human fibroblasts extracted from gut tunica submucosa of Crohn patients were used as healthy cell line, while MDA-MB-468 breast cancer cells were used as a MDR cells. HeLa, fibroblasts and MDAMB-468 were cultured in Dulbecco's Modified Eagle's Medium (DMEM) supplemented with 10% fetal bovine serum, 2mM L-glutamine, penicillin (50 UI mL^{-1}) and streptomycin (50 mg mL^{-1}) at 37 °C in humidified atmosphere containing 5% CO_2 and sub-cultured prior to confluence using trypsin/EDTA.

2.3.6 TfR1 expression

Cells (5×10^5) were treated for FACS analysis with standard methods. Briefly, cells were incubated for 30 min at 4 °C in blocking buffer (PBS, 2% BSA, 2% goat serum) and then with the anti-human TfR1 antibody (1 µg; Thermo Scientific). Cells were washed three times with PBS and incubated 30 min at 4 °C with the secondary antibody Alexa Fluor 488 (1 µL; Life Technologies) in blocking buffer used. Then, cells were washed and were analyzed on a FACS Calibur flow cytometer (Becton Dickinson). 10,000 events were acquired for each analysis, after gating on viable cells, and isotype-control antibodies were used to set the appropriate gates.

2.3.7 Cell binding assay

Cells (5×10^5) were incubated 2 h at 4 °C in flow cytometry tubes in the presence of 0.02 mg mL^{-1} of FITC-labeled HFn. After incubation, cells were washed three times with PBS. Labeled cells were resuspended with 0.5 mL of PBS and analyzed by a FACS Calibur flow cytometer (Becton Dickinson). 20,000 events were acquired for each analysis, after gating on viable cells, and a sample of untreated cells was used to set the appropriate gates.

2.3.8 HFn internalization

Cells were subjected to nanoparticle incubation with HFn labeled with FITC on the shell at the concentration of 0.1 mg mL^{-1} for 15 min, 1, 3, 24 and 48 h at 37 °C and then harvested for immunofluorescence analysis. To evaluate simultaneously the intracellular fate of HFn and encapsulated molecules, HeLa were incubated with 0.1 mg mL^{-1} of HFn labeled with Alexa Fluor 546 and loaded with FITC for 4 and 48 h at 37 °C and then treated for immunofluorescence.

2.3.9 Colocalization experiments

HFn labeled with FITC on the shell was used (0.1 mg mL^{-1}) and different organelles were stained with GM130 (at a 1:100 dilution; clone 35; BD Biosciences), CatD (1:50; clone BC011; Calbiochem), EEA1 (1:1000; clone 14; BD Biosciences), and Tf (1:100; clone 5G2; Abcam) antibodies by incubating 2 h at RT and revealed by a Alexa Fluor 546-conjugated antibody against murine IgGs (Invitrogen) at a 1:300 dilution by incubating for 2 h at RT in PBS, 2% BSA, 2% goat serum.

2.3.10 Confocal laser scanning microscopy

Cells were cultured on collagen pre-coated cover glass slides until sub-confluence and incubated with HFn nanoparticles, for different time periods. Cells were washed with phosphate-buffered saline (PBS, EuroClone), fixed for 5 min with 4% paraformaldehyde (Sigma) and then treated for 5 min with Triton X-100 0.1%. A blocking step was performed for 1 h at RT with a solution containing 2% bovine serum albumin (BSA, Sigma), 2% goat serum and 0.2 µg mL^{-1} DAPI (4′,6-diamino-2-phenylindole) in PBS. Microscopy analysis was performed with a Leica SPE microscope confocal system equipped with laser excitation lines 405 nm, 488 nm line, 514 nm and 633 nm. Images were acquired with 63× magnification oil immersion lenses at 1024 × 1024 pixel resolution. Image quantification was performed with Image J software. Pearson correlation coefficient was calculated using the Image J plugin JaCoP.

2.3.11 Cell proliferation assay

Cells were cultured on a 96 multiwell dish at a density of 5000 cells cm^{-1}. Then, cells were incubated with different amounts of the molecules to be tested. At the indicated time points (24, 48, 72 h), cells were washed with PBS and then incubated for 3 h at 37 °C with 0.1 mL of 3-(4,5-dimethyl-2-thiazolyl)-2,5-diphenyl-2H-tetrazolium bromide (MTT) stock solution previously diluted 1:10 in DMEM medium without phenol red. After incubation, MTT solubilizing solution (0.1 mL) was added to each well to solubilize the MTT formazan crystals (Promega). Absorbance was read immediately using a testing wavelength of 570 nm and a reference wavelength of 620 nm. The results are expressed as means ± standard error (s.e.) of six individual experiments.

2.3.12 Cell death assay

Cells were cultured on a 12 multiwell dish until sub-confluence. Then, cells were incubated 3 h and 24 h at 37 °C in the presence of different amounts of DOX or HFn(DOX). After incubation, cells were washed twice with PBS and treated for FACS analysis according to Annexin V-PE-Cy5 Apoptosis Detection Kit manufacturer's protocol (BioVision). Briefly, cells were resuspended in Binding Buffer and incubated for 5 min in the presence of 5 µL of Annexin V-PE-Cy5. Cells were analyzed within 1 h on a FACS Calibur flow cytometer (Becton Dickinson). 20,000 events were acquired for each analysis, after gating on viable cells. For evaluation of late apoptosis, the same protocol was used but incubation with 7-aminoactinomycin D (BD Biosciences; 51-68981E; 5 µL/sample) was accomplished.

2.3.13 DNA damage assay

Cells were subjected to nanoparticle incubation with DOX free or encapsulated in HFn cage at the concentrations of 0.1 or 1 μM for 24 h at 37 °C and then harvested for immunofluorescence analysis. Double strand breaks were stained with γH2A.X antibody (1:1000 dilution) by incubating 2 h at RT and revealed by an Alexa Fluor 546-conjugated antibody against rabbit IgGs (Invitrogen) at a 1:300 dilution by incubating for 2 h at RT in PBS, 2% BSA, 2% goat serum.

2.3.14 Doxorubicin release

Cells were subjected to nanoparticle incubation with DOX free or encapsulated in HFn cage at the concentrations of 0.1 or 1 μM for 3 and 24 h at 37 °C and then harvested for immunofluorescence analysis. DOX was revealed exciting the sample with 488 nm laser line and acquiring emitted signal from 550 nm to 600 nm (red). The signal represented in green color is the emission in the acquiring window between 520 to 545 nm, which corresponds to the fluorescence signal of a degradation product of DOX[42].

2.3.15 Nuclear translocation

In experiment of endogenous ferritin nuclear translocation, cells were incubated with 0.1 μM DOX for 15 min, 1, 3, 24 and 48 h at 37 °C and then treated for immunofluorescence. For image nuclear translocation of HFn nanoparticles, cells were incubated for 3 h at 37 °C with HFn (0.1mg mL^{-1}), treated with DOX 0.1 μM for 15 min, 1 and 3 h and then harvested for immunofluorescence analysis. Both endogenous and exogenous ferritin were stained with the anti-ferritin antibody (1:2000; ab7332; Abcam) and revealed by an Alexa Fluor 546-conjugated antibody against rabbit IgGs (Invitrogen) at a 1:300 dilution by incubating for 2 h at RT in PBS, 2% BSA, 2% goat serum. In order to assess self-triggered nuclear translocation cells were subjected to nanoparticles incubation with HFn(DOX) at DOX concentrations of 0.1 and 1 μM for 3 or 24 h and then harvested for immunofluorescence analysis. The corresponding amount of HFn void was used as control.

2.3.16 MDR protein inhibition

Percentage of MDR protein inhibition was determined using the Solvo MultiDrugQuant Assay Kit according to the manufacturer's protocols. Briefly 500,000 cells previously incubated with Cyclosporin-A 1 μM (CysA) were harvested by trypsinization and washed thrice with HBSS buffer (Sigma). Then, cells were incubated at 37 °C with calcein-AM solution (0.2 mL/tube) for 10 min. The reaction was stopped by rapid centrifugation of 1 min at 2000 ×g and cells were analyzed by flow cytometry. The percentage of inhibition was determined as follows:

$$\%\ MDR\ proteins\ inhibition\ = \frac{100 \times (Mean\ Fluorescence_{treated} - \ Mean\ Fluorescence_{control})}{Mean\ Fluorescence_{treated}}$$

2.4 Results and discussion

2.4.1 HFn nanoparticles: development, interaction with tumor cells and internalization

The H monomer of human ferritin was cloned and expressed in *E. coli* and purified as reported in the Methods section. A good degree of purity was observed in purified fractions showing a 21 kDa band in sodium docecyl sulfate-polyacrylamide gel electrophoresis (SDS-PAGE) corresponding to HFn monomer (Figure S1a). Moreover, PAGE performed under native conditions, using commercial Horse ferritin as reference standard, confirmed that our HFn was correctly folded and still able to spontaneously assemble in a 24-subunit nanosphere (Figure S1c). HFn nanoparticles were then labeled with FITC and used to evaluate tumor cell recognition. In a recent study, the interaction between apoferritin and tumor cells was reported to be mediated by transferrin receptor 1 (TfR1), which is overexpressed in most tumor cells and tissues[43]. In the present work, HeLa cancer cells derived from human cervical cancer were selected for the *in vitro* evaluation as a model tumor cell line with high TfR1 expression (Figure S2), while human fibroblasts, the most common type of cells found in connective tissue, were used as control healthy cells with low TfR1 expression (Figure S2). The binding assay, performed by flow cytometry after incubating the cells for 2 h at 4 °C with 0.02 mg mL^{-1} of HFn, demonstrated at least a fourfold increase in cell ratio in the region of positivity for HeLa cells compared to fibroblasts, confirming a remarkable HFn affinity and selectivity toward cancer cells (Figure S3a). Confocal laser scanning images of HeLa cells incubated with HFn nanoparticles demonstrated that a fast interaction with cellular membrane occurred, since HFn was almost completely attached to the cell surface after 15 min of incubation. In addition, HFn was already internalized after 1 h of incubation and, after 3 h, the internalization process was complete. After 24 h, the fluorescence signal of HFn dramatically decreased without, however, disappearing up to 48 h of incubation. This effect suggested that exogenous HFn was degraded or combined with the endogenous unlabeled one (Figure S3b).

Since natural apoferritin interacts with cell membrane through TfR1, we expected that HFn could be efficiently internalized into the cells using the same endocytic pathway of transferrin (Tf). Therefore, we characterized the endocytosis pathway of HFn by investigating its colocalization with specific endocytic compartments, using EEA1 marker for early endosomes, GM130 marker for the Golgi apparatus, CatD marker for lysosomes, and Tf as a marker for the recycling endosomes. We found that HFn uptake took place within 1 h and HFn basically localized at the early endosomes, corroborating our hypothesis that also HFn is internalized by a TfR1-mediated mechanism. Confocal images demonstrated that HFn did not localize at the Golgi and recycling endosomes even after 3 h of incubation with cells, suggesting that HFn neither is pushed out of the cells using recycling endosomes nor is sent to the Golgi by late endosomes. Amazingly, colocalization between HFn and lysosomes did not occur either after 1 or 3 h of incubation with HeLa cells, a time long enough to promote lysosome formation with this kind of bionanoconstructs[44]. This observation suggested that HFn was not recognized by the cell as something to degrade, thus remaining inside the cell for a long period of time (Figs. 2.3, S4, S5). This unexpected result let us postulate that HFn could be a good candidate as a drug bionanocarrier, since it did not prove liable to lysosomal degradation.

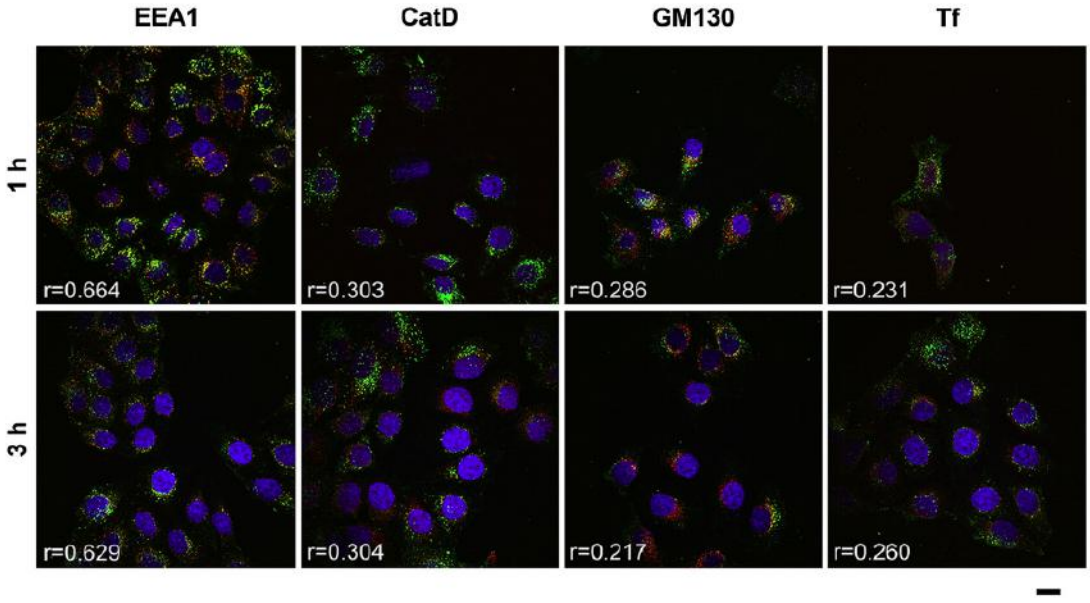

Fig. 2.3 Intracellular localization of HFn nanoparticles. Confocal microscopy merges images of HeLa cells, incubated for 1 h or 3 h at 37 °C with 0.1 mg mL^{-1} of HFn (green). Early endosomes, lysosomes, Golgi and recycling endosomes were recognized with early endosome marker EEA1, lysosomal protein CatD, Golgi marker GM130 and recycling endosome marker Tf antibodies, respectively, and labeled with an anti-mouse secondary antibody conjugated with Alexa Fluor 546 (red). Nuclei were stained with DAPI (blue). Scale bar: 10 μm.

2.4.2 HFn loading and release of chemotherapeutics

In order to set up the experimental conditions required for drug incorporation into the HFn shell, HFn was first loaded with fluorescent molecules using the disassembly/reassembly method already reported in the literature for native apoferritin[45]. This procedure exploited the ability of HFn to modify its quaternary structure in response to pH changes. In particular, in the absence of active disassembly mechanisms, HFn shell is unfolded into monomeric subunits at acidic pH around 2-3 and is refolded with perfect shape memory when the solution is brought to pH values around 7.5, as depicted in Figure S6a. Under the same conditions, DOX encapsulation was straightforward and highly reproducible and allowed us to load 28.3 molecules of DOX per HFn shell on average, in accordance with literature data[46].

Next, we evaluated the DOX release from HFn shell *in vitro*. Kinetics of release were performed dialyzing DOX-loaded nanoparticles (HFn(DOX)) at 37 °C in phosphate buffer saline (PBS), pH 7.4, and quantifying the leakage of drug from HFn by measuring the fluorescence emission in the supernatants. The amount of encapsulated DOX remained constant for the first 6 h of incubation, then decreased by 40% over 72 h of incubation in PBS (Figure S6b), confirming the presumed good stability of the HFn nanoformulation at physiological pH.

In order to study the cellular trafficking of encapsulated molecules after uptake, HFn was loaded under the above conditions with a more efficient dye, fluorescein isothiocyanate (FITC). HFn shell was concomitantly labeled with an orthogonal dye, Alexa Fluor 546. Our intent was to simultaneously follow the separate fate of the incorporated drug and of the protein cage by acquiring the fluorescence images at the relevant emission λ_{max} values. This doubly fluorescent nanoparticle was incubated with HeLa cells for 4 and 48 h. Confocal laser scanning microscopy

images demonstrated that, after 4 h of incubation at 37 °C, encapsulated FITC (green) and HFn shell (red) were still colocalized, as revealed by the predominant presence of yellow signals inside the cells. After 48 h of incubation at 37 °C, FITC signal was widespread inside the cells, while the signal attributable to HFn shell was almost completely disappeared, thus suggesting recombination of labeled monomers with endogenous unlabeled 24mers (Figure S7). These results corroborated our hypothesis about the potential use of HFn as nanovectors for the delivery of drugs in intracellular compartments.

2.4.3 Doxorubicin encapsulation in HFn improves the antitumor efficacy

Next, DOX efficacy was evaluated comparing the proliferation of cells treated with DOX or HFn(DOX). HeLa cells were treated with different amounts of DOX or HFn(DOX) in a DOX concentration range between 0.01 and 1 μM, for up to 72 h. Fibroblasts were also treated with DOX or HFn(DOX), as a healthy cell line control to assess the target selectivity. The percentage of cell viability over time was determined on samples treated with 0.01 μM, 0.1 μM and 1μM DOX or HFn(DOX) using the MTT assay and normalized on the cell proliferation of the respective untreated control at different time points. As reported in Figure S8a, samples treated with 0.01 μM DOX or HFn(DOX) did not show any meaningful decrease in cell proliferation, compared to untreated cells, both in normal and in tumor cells since cell survival remained higher than 60%. In contrast, 1 μM dosage resulted in detectable effects in cell proliferation with significant differences between groups treated with DOX or HFn(DOX). However, a significant reduction of cell survival was observed also on healthy fibroblasts, probably due to high DOX concentration (Figure S8b).

Interestingly, cells treated with 0.1 μM HFn(DOX) showed instead a substantial decrease in HeLa cell proliferation in comparison with samples treated with the same amount of free DOX, revealing remarkable differences in antiproliferative efficacy of DOX and HFn(DOX) (Fig. 2.4a). Indeed, HFn(DOX) exhibited a far higher efficiency in inhibiting the tumor cell proliferation in comparison to free DOX. Less significant differences between DOX and HFn(DOX) treatment were observed in fibroblasts suggesting that DOX cytotoxicity was basically low at this concentration against normal cells irrespective of the modality of DOX delivery (Fig. 2.4a). HeLa cells were also treated with relevant amounts of void HFn in order to assess the contribution of the void nanovector. Results reported in Figure S9 demonstrate that HFn does not affect cell viability.

Next, in order to determine if the arrest in proliferation was associated with an increase in cell death, the exposure to Annexin V was assayed, which provides a positive readout only in apoptotic cells. HeLa cells were incubated for 3 or 24 h with DOX or HFn(DOX) at decreasing concentrations, including 1 μM, 0.1 μM and 0.01 μM. Annexin V assay was measured by flow cytometry using untreated cells, to set the regions of positivity. The ratio of dead cells reported in Fig. 2.4b demonstrated that HFn(DOX) was much more effective than free DOX in inducing apoptosis at 0.1 μM after 3 h of incubation. However, at 24 h, the differences in apoptotic effect between DOX and HFn(DOX) in cancer cells were smoothed, suggesting a more efficient and rapid delivery of DOX when encapsulated in a HFn shell. Cells treated with 0.01 μM HFn(DOX) for 3 h basically did not show any increase in cell death in comparison with free drug, since the DOX dosage was probably too low to be effective. However, after 24 h of incubation, significant variations were observed, reflecting a DOX accumulation over time attributable to the effect of HFn

delivery. As expected, treatment of HeLa cells at the highest concentration (1 μM) induced rapid and complete cell death both with DOX and HFn(DOX). As Annexin V exposure is a characteristic feature of cells in early apoptosis, we decided to check if the reduced efficacy of free DOX after 3 h of treatment was rather an apparent event attributable to a fraction of cells that had already developed to a late apoptosis at the considered time points. To this aim, the 7-aminoactinomycin D (7-AAD) uptake was assessed, which occurs specifically in cells with a damaged plasma membrane. After flow cytometry analysis, we concluded that both DOX and HFn(DOX) treated cells were not in late apoptosis (Figure S10). The reduction of viability and the increase of apoptosis in cells treated with HFn(DOX) were further associated to a more substantial DNA damage compared with free DOX, as evidenced in Figs. 2.4c and S11. The amount of double strand break, visualized using γH2A.X antibody[47], is higher in cells treated with HFn(DOX) under the above experimental conditions, confirming that HFn(DOX) efficacy is incontrovertibly associated with a functional damage of nuclear DNA.

2.4.4 Nuclear delivery of doxorubicin

The fluorescence emission of DOX was exploited in this study to evaluate DOX cellular uptake and possible release from HFn. HeLa cells were treated with 0.1 μM DOX free or encapsulated in HFn for 3 or 24 h. Then, cells were washed, fixed and prepared for confocal microscopy analysis. When DOX is excited with an argon laser (488 nm), it exhibits a characteristic fluorescence spectra profile consisting in a double emission with relevant maximal peaks at 505 nm (green) and at 550 nm (red), respectively, which can be detected separately by setting the instrumentation appropriately[48]. Confocal images revealed that HFn(DOX) exhibits improved uptake in comparison with free DOX (Fig. 2.5). In particular, free DOX just entered the cells by diffusion and, as a result, was mainly localized in the cytoplasm (green) even after 24 h of incubation, as assessed by analysis of DOX fluorescence spatial distribution. In contrast, the uptake of HFn(DOX) was very fast, as it was mediated by TfR1 receptor endocytosis, and DOX was almost entirely released in the nucleus (red) ready after 3 h, as demonstrated by analysis of DOX fluorescence spatial distribution (Fig. 2.5). The significant difference in DOX uptake at 3 h observed with HFn(DOX) in comparison with free DOX could imply that nanoparticle formulation was capable of bypassing the well documented multi-drug resistance mechanism (MDR) activated by cancer cells to protect themselves from the cytotoxic effects of chemotherapeutics (Fig. 2.6). Noteworthy, the nuclear release of HFn(DOX) suggests that HFn shell mediates a nuclear translocation of DOX. This effect is likely correlated with the physiological function of ferritins. Indeed, as mentioned above, ferritin plays a key role in the metabolism of iron, protecting the cell from oxidative stress[49]. This protective role is exerted both in the cytoplasm and in the nucleus. Thus, ferritin is translocated into the nucleus in response to oxidative stimuli to protect the DNA from potential damage caused by anomalous ROS production[49].

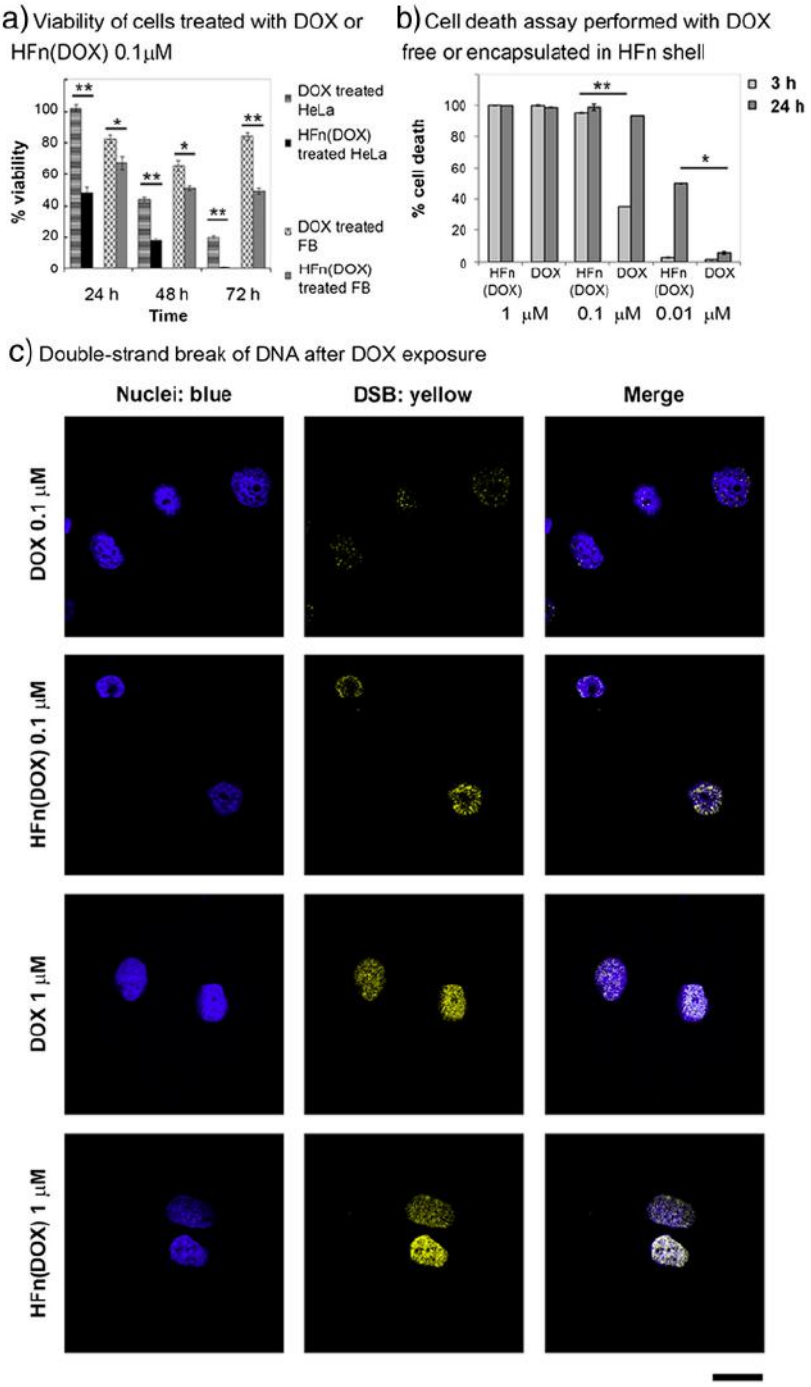

Fig. 2.4. a) Viability of cells treated with free DOX or HFn(DOX). Fibroblasts and HeLa cells were treated with 0.1 μM of DOX or HFn(DOX) for up to 72 h. Viability was assessed by measuring the conversion of MTT into formazan. Reported values are the mean of six replicates ± s.e., normalized on cell proliferation of untreated fibroblast or HeLa cells, respectively * $P<0.005$; **$P<0.0005$ (Student's t-test). b) Cell death assay with DOX free or encapsulated in HFn shell. HeLa cells were treated with 1, 0.1 and 0.01 μM of DOX or HFn(DOX) for 3 or 24 h. Cell death was assessed on the basis of the exposure to Annexin V, evaluated by flow cytometry. Untreated cells were used to set region of positivity. Reported values are the mean of three replicates ± s.e. * $P<0.01$; ** $P<0.005$ (Student's t-test). c) Double-strand break of DNA after DOX exposure. Confocal microscopy images of HeLa cells incubated with 1 μM or 0.1 μM DOX free or encapsulated in HFns. Anti γH2A.X antibodies were used to reveal the DNA double-strand breaks (DSB; yellow). Scale bar: 10 μm.

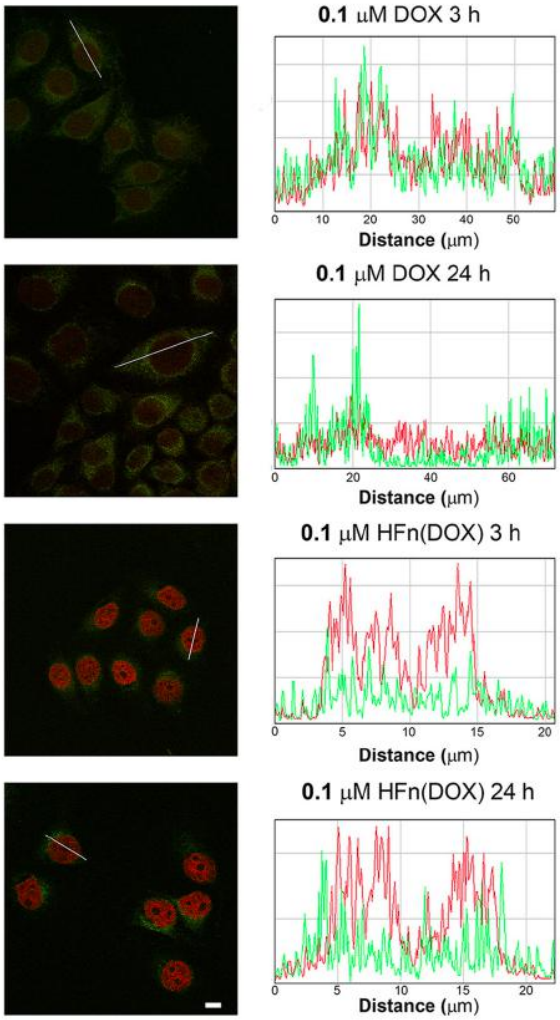

Fig. 2.5 Doxorubicin release inside the nuclear compartment. Confocal microscopy images of HeLa cells incubated with 0.1 μM DOX free or encapsulated in HFns and analysis of spatial distribution. Confocal laser scanning images of HeLa cells treated with 0.1 μM DOX (DOX degradation product in green) free or encapsulated in HFn shell for 3 h or 24 h at 37 °C. Scale bar: 10 μm. Spatial analysis was performed on merged images using Image J plugin RGB profile plot.

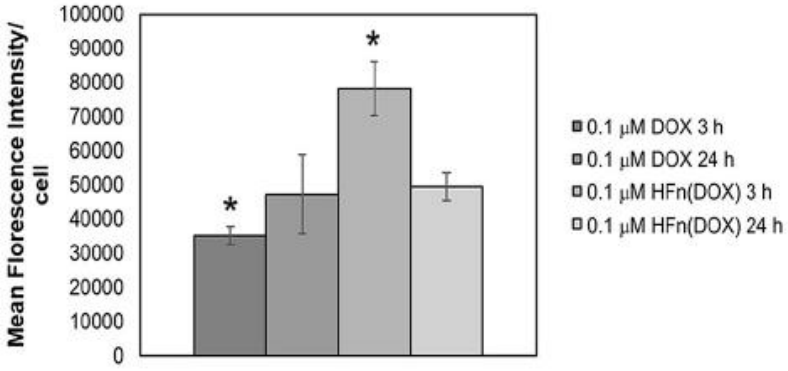

Fig. 2.6 Doxorubicin release inside the nuclear compartment. Quantification of total fluorescence intensity per cell. Reported values are a mean of measurements performed with Image J software on six different cells ± s.e. * P<0.01.

2.4.5 Doxorubicin cytoplasmatic release triggers HFn nuclear translocation

Our results let us speculate that HFn acts like a “Trojan horse”. Indeed, 1) HFn enters the cells as a result of the interaction with TfR1 and 2) partially releases DOX in the cytoplasm through hydrophobic channels of its architecture; 3) DOX diffuses in the nucleus where it causes the DNA damage, 4) which triggers the nuclear translocation of HFn(DOX), and 5) the release of DOX in the nuclear compartment. In order to verify this hypothesis, we studied the subcellular localization of endogenous ferritin upon DOX administration. Confocal microscopy images of HeLa cells, which were fixed 1, 3 and 24 h after administration of 0.1 μM DOX, clearly show that endogenous ferritin was localized in the nuclear compartment ready after 1 h, where it continued to accumulate over time (Fig. 2.7). In contrast, untreated HeLa cells (CTRL) displayed mainly a cytoplasmic confinement of ferritin, proving that the DOX administration triggered its nuclear translocation.

Next, we determined if the treatment with DOX could trigger also nuclear translocation of recombinant HFn. HeLa cells were incubated for 3 h with HFn labeled with FITC on the shell (HFn_FITC) in order to allow for a complete internalization of HFn (Figs. 2.8, 2.9). Then, 0.1 μM DOX was added to the culture medium and HFn nuclear translocation was recorded by confocal microscopy performed on cells fixed 15 min, 1 and 3 h after 0.1 μM DOX administration. Confocal microscopy images clearly show that HFn was still confined in the cytoplasm 15 min after DOX addition, even though it was apparent that HFn accumulated in the close proximity of the nucleus. However, after 1 h, the nuclear translocation was complete. These results confirm that the HFn nanoparticles were directly translocated into the nucleus, suggesting that they were recruited to carry out the physiological functions attributed to native ferritin. With the aim to assess if HFn acted by bringing the payload across the nuclear envelope or rather by releasing it in proximity of the nucleus, the same experiment was performed also with unlabeled HFn loaded with FITC (HFn(FITC)). Images of HeLa cells displayed in Figure S12 indicate that the payload was directly transported and released in the nucleus upon external cell stimulation with DOX. This result is particularly relevant considering that, different from DOX, FITC does not exhibit a natural propensity to penetrate the nucleus, thus such a massive nuclear translocation should necessarily imply an active transport. Finally, in order to evaluate if HFn(DOX) nuclear translocation could be self-triggered by DOX encapsulated in the HFn shell, 0.1 and 1 μM DOX were loaded inside HFn_FITC and then incubated with cells. DOX and FITC fluorescence signal were acquired simultaneously. Confocal microscopy images in Fig. 2.10 show that at a DOX concentration of 0.1 μM nuclear translocation of HFn was only marginally visible both after 3 and 24 h of incubation. However, at a HFn(DOX) concentration of 1 μM, HFn was clearly localized in the nuclear compartment even after 3 h of incubation, proving that HFn nuclear translocation was self-triggered by DOX release from the hydrophobic channels of HFn. Moreover, the correspondence between the signal of the nuclear HFn, here obtained with 1 μM HFn(DOX) and the signal detected in the previous experiment with 0.1 μM free DOX, provides an indirect confirmation that the amount of DOX released into the cytoplasm to cause self-triggered translocation was only a minor fraction of that encapsulated. Combining these results corroborate our hypothesis that the partial release of DOX in the cytoplasm and the likely consequent damage due to DOX intercalation in the DNA double-helix trigger the nuclear translocation of HFn(DOX), as depicted in Fig. 2.11. Therefore, we concluded that the DOX release was mainly accomplished upon entrance into the nucleus. Such

findings make HFn an ideal candidate for the development of nanodevices for the nuclear delivery of chemotherapeutics in cancer cells.

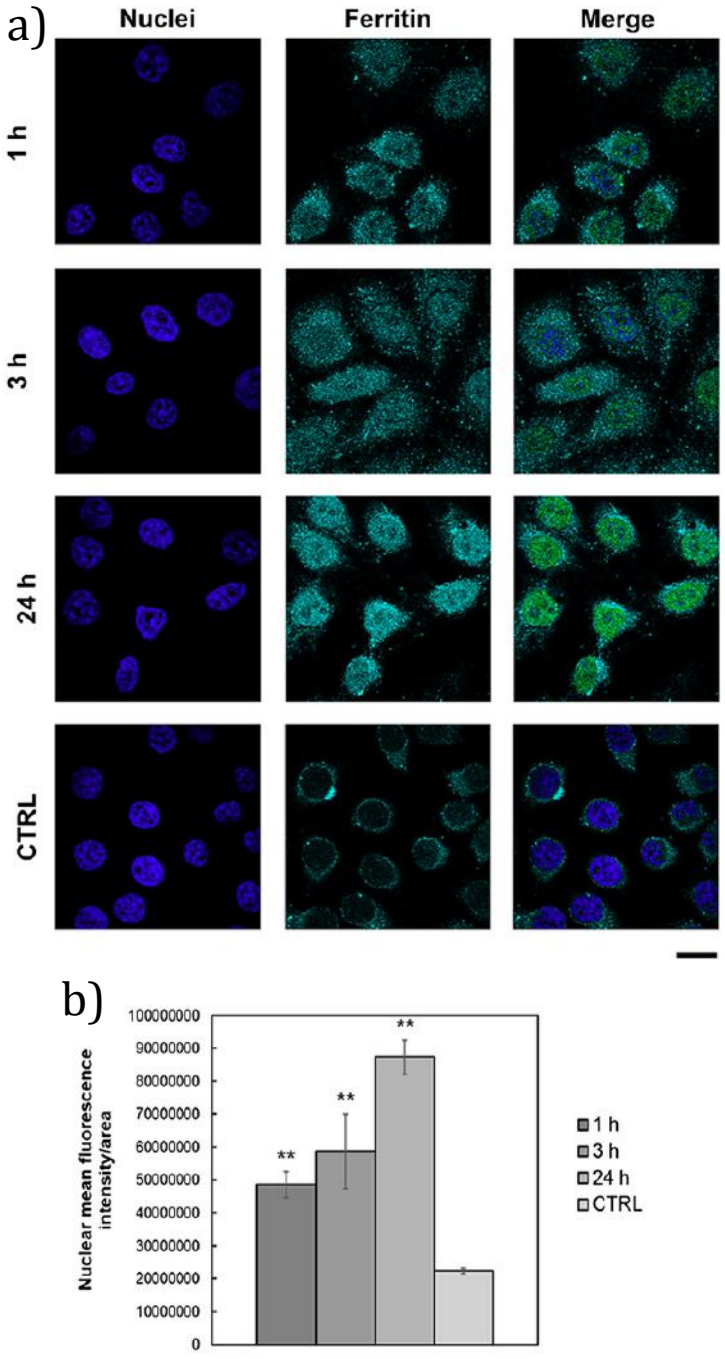

Fig. 2.7. a) Treatment with DOX triggers nuclear translocation of endogenous HFn. Confocal microscopy images of HeLa cells incubated for 1, 3 and 24 h at 37 °C with DOX 0.1 μM. Untreated cells are used as negative control (CTRL). Nuclei were stained with DAPI (blue). Endogenous ferritin were recognized with anti-ferritin antibody and labelled with an anti-rabbit secondary antibody conjugated with Alexa Fluor 546 (cyan; Invitrogen). Scale bar: 10 μm. b) Quantification of nuclear fluorescence intensity due to endogenous ferritin. Reported values are a mean of measurements performed with Image J software on nucleus five different cells normalized with respect to their area ± s.e. ** $P<0.0005$.

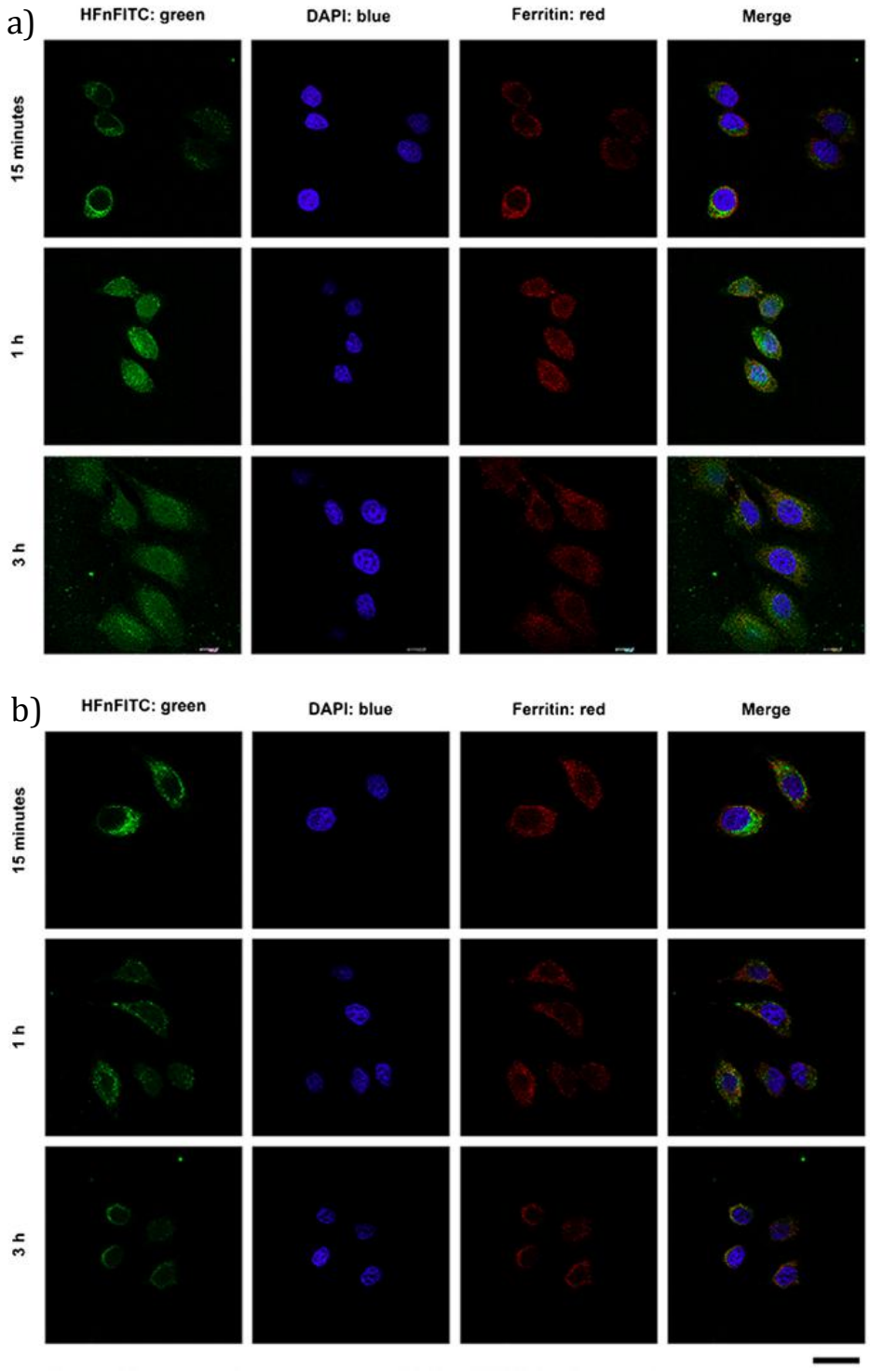

Fig. 2.8. Treatment with DOX trigger nuclear translocation of exogenous HFn. Confocal microscopy images of HeLa cells incubated for 3 h at 37 °C with 0.1 μg mL^{-1} of HFn labeled with FITC (HFn_FITC; green) and then treated (a) or not (b) with 0.1 μM DOX for 15 min, 1 or 3 h. Nuclei were stained with DAPI (blue). Ferritin were recognized with anti-ferritin antibody and labelled with an anti-rabbit secondary antibody conjugated with Alexa Fluor 546 (red; Invitrogen). Scale bar: 10 μm.

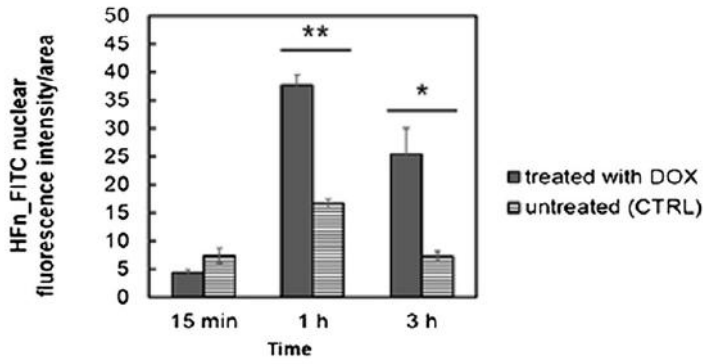

Fig. 2.9. Quantification of fluorescence signal of HFn_FITC in the nucleus. Reported values are a mean of 5 measurements performed with Image J software on the nucleus of different cells normalized with respect to their area ± s.e. * P<0.005; ** P<0.0005.

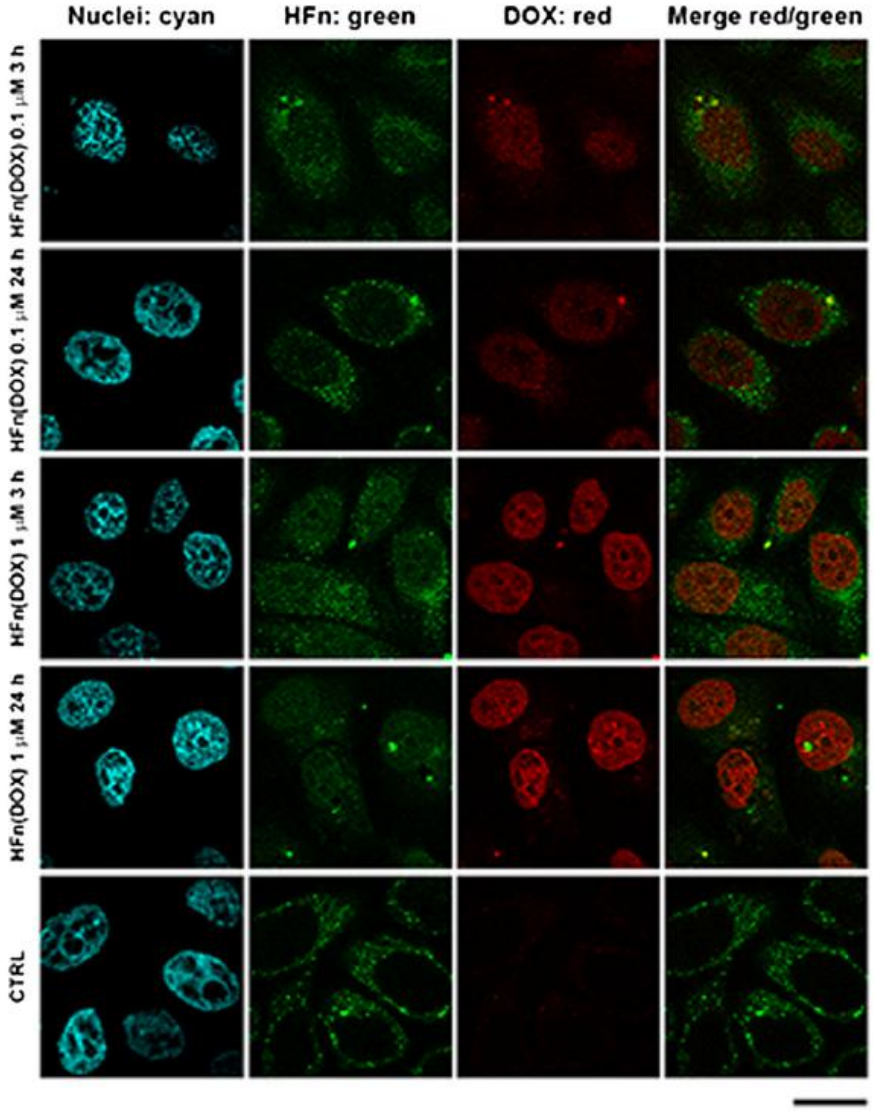

Fig. 2.10. Self-triggered nuclear delivery of DOX in HFn(DOX) nanoparticles. Confocal microscopy images of HeLa cells incubated for 3 and 24 h at 37 °C with 0.1 μM of HFn(DOX). HFn(DOX) was labeled with FITC (HFn; green) on the shell and then loaded with DOX (red). Nuclei were stained with DAPI (cyan). Scale bar: 10 μm.

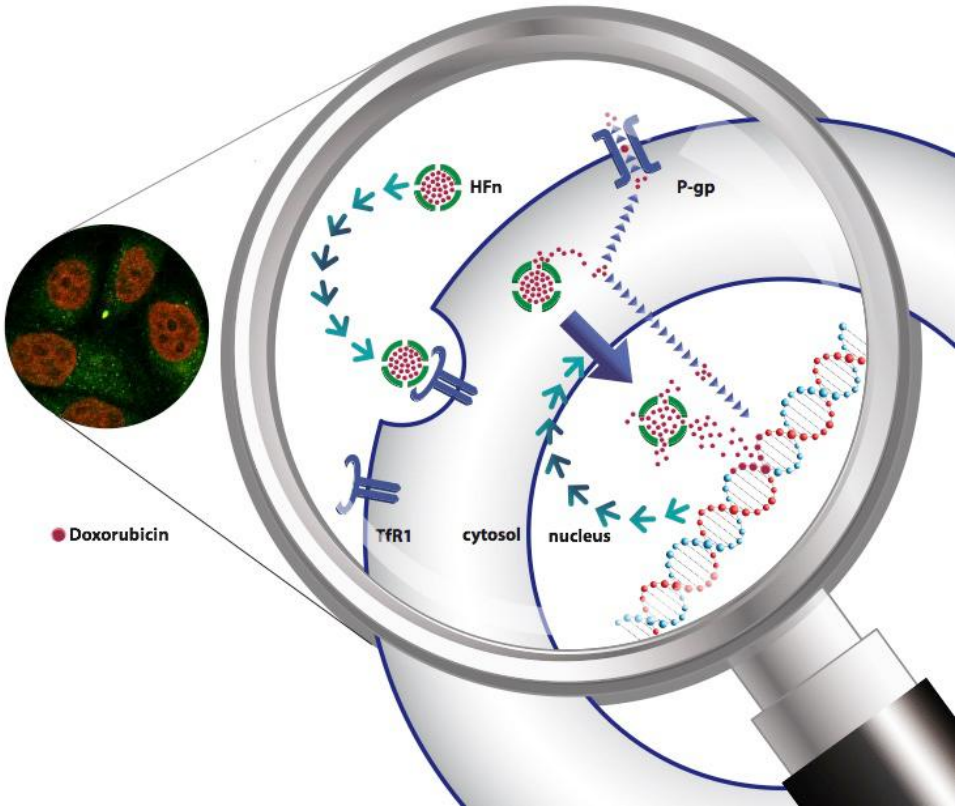

Fig. 2.11 Schematic representation of self-triggered nuclear delivery of HFn(DOX). HFn was internalized upon the interaction with TfR1 by receptor-mediated mechanism without incurring lysosomal degradation. Encapsulated DOX was partially released in the cytoplasm through hydrophobic channels of its architectucture. Then DOX is pumped out of the action of P-glycoprotein, or diffuses into the nucleus where it causes the DNA damage, which triggers the nuclear translocation of HFn(DOX) and the massive release of DOX in the nuclear compartment.

2.4.6 Enhanced DOX delivery by HFn in MDR cancer cells

To investigate the potential of HFn in the treatment of cancer cells affected by multidrug resistance mechanism, MDA-MB-468 breast cancer cells were used in the next experiment, as they have been demonstrated to exhibit P-gp-promoted MDR with DOX[18] and high TfR1 expression (Figure S2). MDA-MB-468 cells were incubated with 1 μM DOX or HFn(DOX) for 3 or 24 h in DMEM. After washing out the unreacted nanoparticles, cells were fixed and prepared for immunofluorescence. Fig. 2.12a shows the results of confocal images acquired on isolated MDR cells after treatment. As expected, in cells treated with free DOX, no traces of drug could be detected inside the cytoplasm both at 3 and 24 h. The nuclei appeared not to be affected by the drug at 3 h, while only a minimal amount of drug was revealed at 24 h. In contrast, HFn(DOX) efficiently delivered a detectable amount of drug into the nucleus ready after 3 h and a strong emission signal could be monitored after 24 h, in a similar behavior to what we observed with sensitive HeLa cells. The improved nuclear delivery of DOX due to HFn assistance was combined with an increased DOX efficacy, as assessed by viability assay (Fig. 2.12b). In order to evaluate if the increased DOX efficacy observed for HFn(DOX) formulation is mainly due to an escape from MDR efflux pump or to the HFn self-triggered drug release mechanism, MDA-MB-468 cells were treated with an inhibitor of MDR proteins. MDA-MB-468 cells were treated with 1 μM HFn(DOX)

and their viability was evaluated also in the presence of 1 µM Cyclosporin-A (CysA). The kind of inhibitor and their working concentration have been selected in order to obtain the maximal percentage of MDR inhibition (77%) without affecting cell viability. Results reported in Fig. 2.13 do not show statistically significant variations between samples incubated with HFn(DOX) or not with CysA at 72 h, which seems to corroborate the hypothesis of HFn contribution in escaping from MDR efflux pump. However, the decrease of percentage of viability observed at 24 and 48 h after treatment with CysA strongly supports the conclusion that the major efficacy of HFn(DOX) in comparison to free DOX is mainly due to the HFn self-triggered release mechanism, while the HFn escape from MDR efflux pump plays a marginal role.

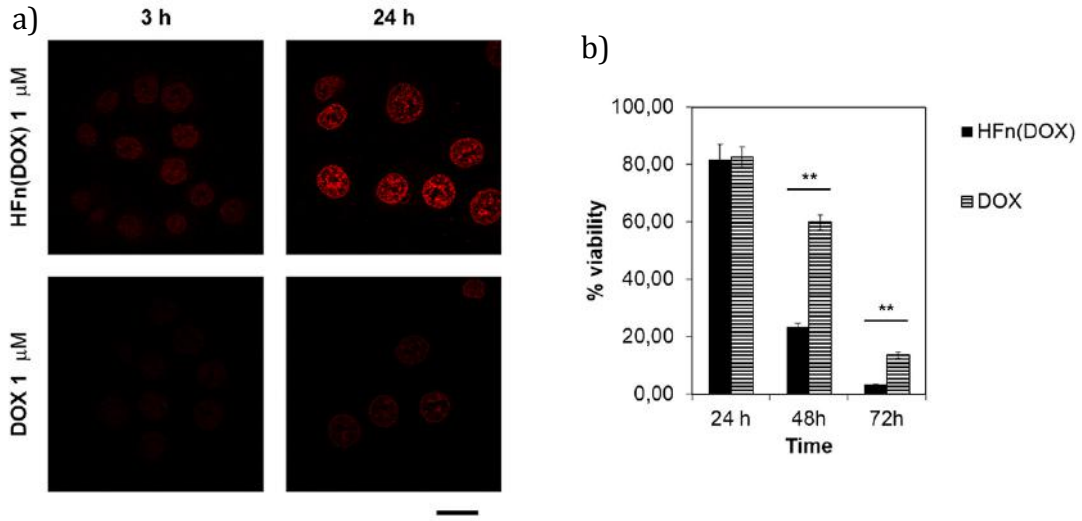

Fig. 2.12 a) Doxorubicin release inside the nuclear compartment of MDA-MB-468 cells. Confocal microscopy images of MDA-MB-468 cells incubated with 1 µM DOX free or encapsulated in HFn shell for 3 h or 24 h at 37 °C. Scale bar: 10 µm. b) Viability of cells treated with free DOX or HFn(DOX). MDA-MB-468 cells were treated with 1 µM of DOX or HFn(DOX) for up to 72 h. Viability was assessed by measuring the conversion of MTT into formazan. Reported values are the mean of six replicates ± s.e., normalized on cell proliferation of untreated cells, ** P<0.0005 (Student's t-test).

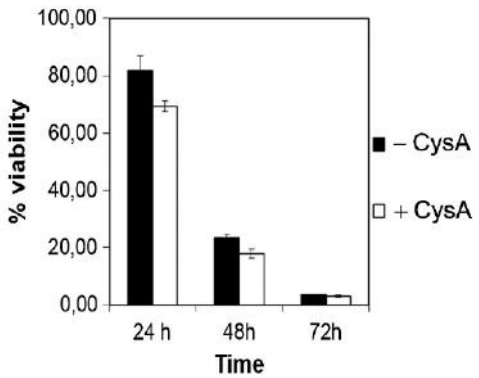

Fig. 2.13 Viability of cells treated with HFn(DOX) with or without MDR protein inhibition. MDA-MB-468 cells were treated with 1 µM of HFn(DOX) for up to 72 h with or without 1 µM Cyclosporin-A. Viability was assessed by measuring the conversion of MTT into formazan. Reported values are the mean of six replicates ± s.e., normalized on cell proliferation of untreated cells, respectively * P<0.05; ** P<0.01 (Student's t-test).

2.5 Conclusions

In summary, we have produced and purified a recombinant heavy-chain monomer of human apoferritin (HFn) in multimilligram amounts. HFn maintained the capability of self-assembling, disassembling and reassembling with shape memory into a 24-H subunit nanocage in dependence of the pH changes resembling native apoferritin. HFn was first labeled on the external surface with a fluorescent dye and filled in with an alternative dye to follow their internalization and fate in representative cancer (HeLa) drug-sensitive cells, suggesting a preferred receptor-mediated endocytosis pathway of entrance in cancer cells with remarkable selectivity in comparison with the uptake from healthy cells (fibroblasts). Next, HFn nanocage was efficiently loaded with doxorubicin (DOX) and used to treat HeLa cells in comparison with equal concentrations of free drug. Our results demonstrate that HFn(DOX) complex is engulfed by cancer cells more rapidly and efficiently than free DOX. Most important, confocal microscopy analysis combined with a DNA damage assay provided evidence that HFn allowed for fast and massive delivery of the antiproliferative chemotherapeutic agent inside the nuclear compartment, thus strongly enhancing the cytotoxic effect of DOX. Our interpretation of this effect is that an initial release of a small amount of DOX in the cytoplasm induces a DNA damage, triggering the recruitment of H-rich apoferritins into the nucleus. Indeed, under the same conditions, nontoxic dyes were principally released in the cytoplasm after prolonged incubation and not delivered to the nucleus. Hence, the point of strength of HFn nanoparticles is that they are activated to translocate into the nucleus upon noxious stimuli that the cell itself signals in the presence of a DNA damage.

HFn displays two important advantages over conventional nanocarriers of DNA-intercalating drugs: 1) the drug is principally released at its final destination with a subcellular precision through a self-triggered mechanism, thus optimizing the cytotoxic effect of the drug, and 2) the self-assembling recombinant nanocage exhibits a well documented target selectivity toward a broad selection of cancer cell types. However, HFn can be straightforwardly modified with specific targeting peptides by standard genetic engineering, which could further improve the nanocarrier selectivity toward specific cancer cell types. In our strategy, HFn nanocages loaded with DOX could behave like a “Trojan horse”: called back within the nucleus for the purpose of defense, HFn releases, instead, the cytotoxic anticancer drug directly into the most effective site of action. Eventually, HFn was shown to significantly improve the accumulation of DOX in drug-resistant cancer cells, enlarging the spectrum of possible cancer cell targets, allowing clinicians to reconsider the use of traditional chemotherapeutics, which have previously failed with several tumor types. We believe that this nanovector has great potential for the delivery of DNA-interacting molecules and anticancer drugs exerting a specific intranuclear action for both *in vitro* investigations and *in vivo* treatment of malignant tumors. We envisage that HFn may find application in the treatment of several solid tumors, as the targeted nuclear delivery would allow us to strongly reduce the dose of administered drug and to limit severe side effects due to chemotherapeutic exposure.

2.6 Supporting information

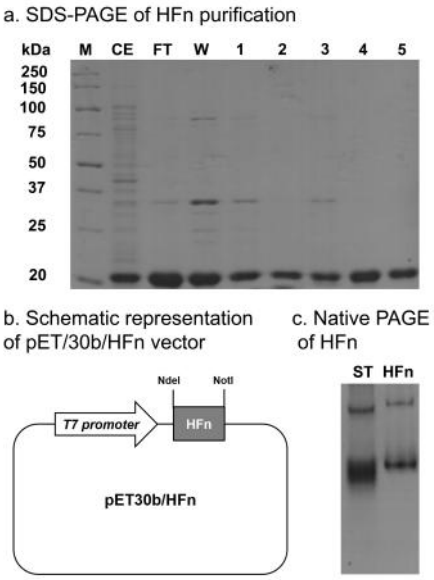

Figure S1. Production of HFn nanoparticles. a) Ion exchange purification of HFn. Proteins from crude extract (CE, 12 μg), flow through (FT, 12 μg), wash (W, 12 μg), fractions obtained by elution with a stepwise increasing gradient of NaCl (1-5; 2 μg) were separated by SDS-PAGE (12% acrylamide) and visualized by Coomassie staining. M = protein markers (kDa). b) Schematic representation of pET30b/HFn expression vector. The recombinant gene encoding the heavy chain of human ferritin was inserted into pET30b vector under the control of T7 promoter. c) Native PAGE of purified HFn: recombinant HFn (2 μg) were loaded onto PAGE (6% acrylamide) under native conditions to evaluate quaternary structure formation and visualized by Coomassie staining. Horse spleen ferritin was loaded as standard (2 μg; ST).

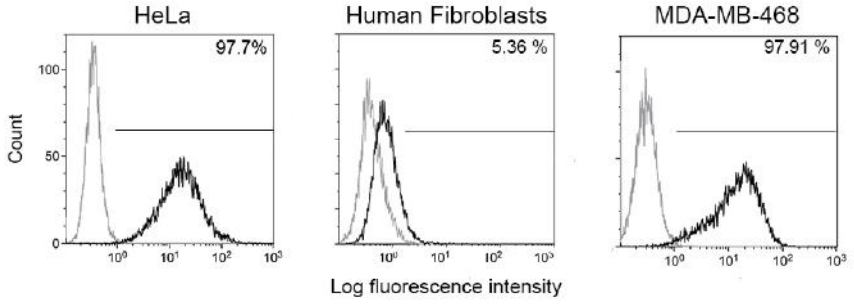

Figure S2. TfR1 expression of HeLa, human fibroblasts and MDA-MB-468 cells. TfR1 expression has been evaluated by flow cytometry. Untreated cells were used to set the positive region.

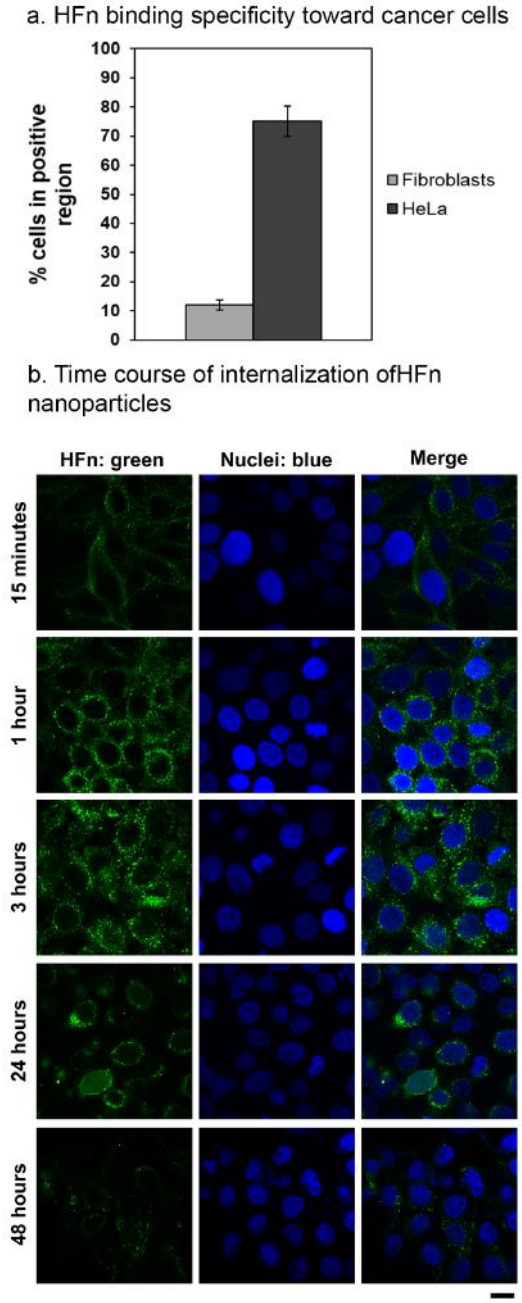

Figure S3. (a) HFn binding specificity toward cancer cells. HeLa and human fibroblast cells were incubated 2 h at 4 °C with FITC-labeled HFn (0.02 mg mL^{-1}) and then processed for flow cytometry. Untreated cells were used to set the positive region. (b) Time course of internalization of HFn nanoparticles. Confocal microscopy images of HeLa cells, incubated for 15 minutes, 1 h, 3 h, 24 h and 48 h at 37 °C with 0.1 μg mL^{-1} of HFn labelled with FITC (green). Nuclei were stained with DAPI (blue). Scale bar: 10 μm.

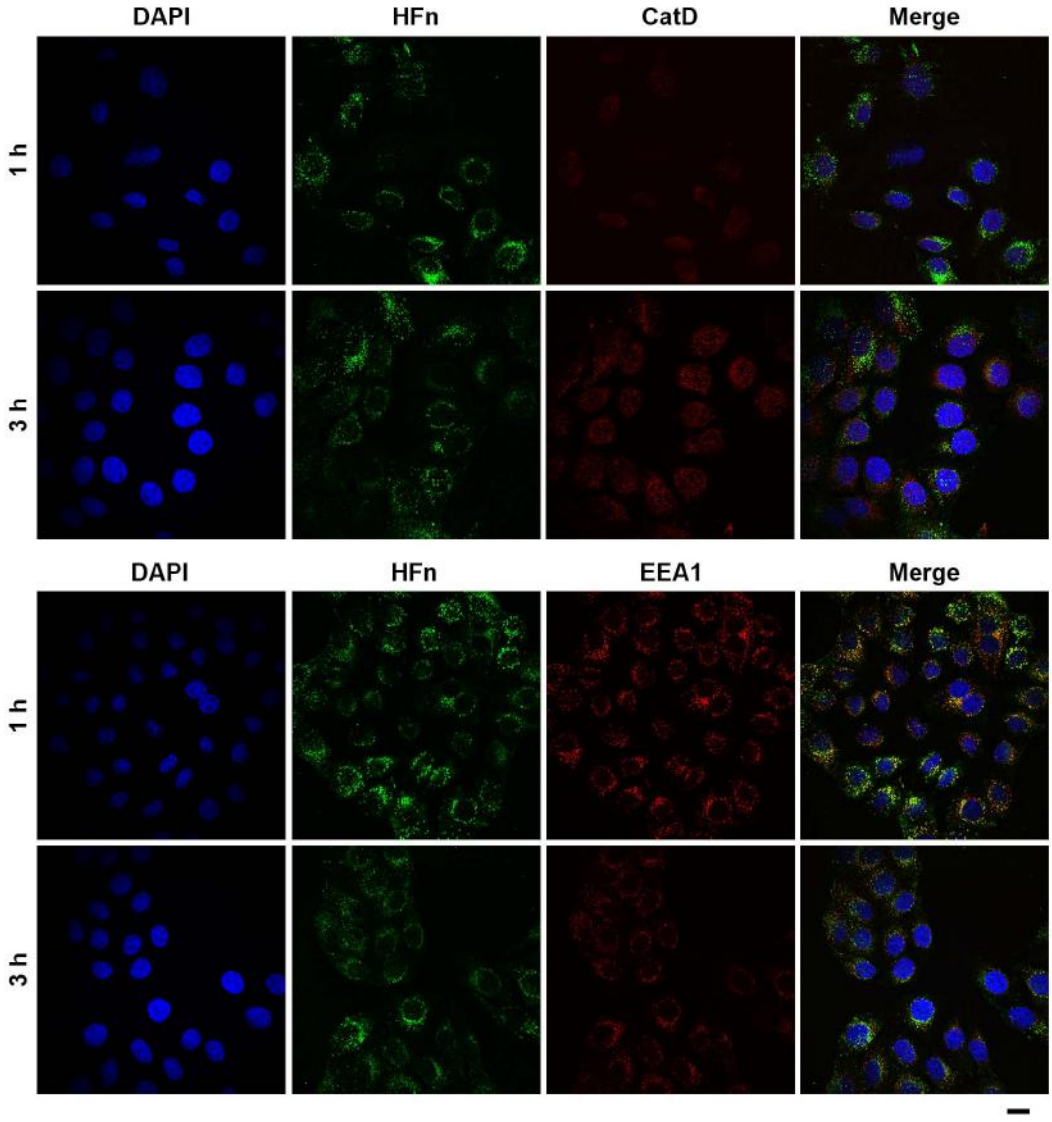

Figure S4. Intracellular localization of HFn nanoparticles. Confocal microscopy images of HeLa cells, incubated for 1 h or 3 h at 37 °C with 0.1 μg mL^{-1} of HFn (green). Early endosomes and lysosomes were recognized respectively with early endosome marker EEA1 and with the lysosomal protein CatD antibodies and labeled with an anti-mouse secondary antibody conjugated with Alexa Fluor 546 (red; Invitrogen). Nuclei were stained with DAPI (blue). Scale bar: 10 μm.

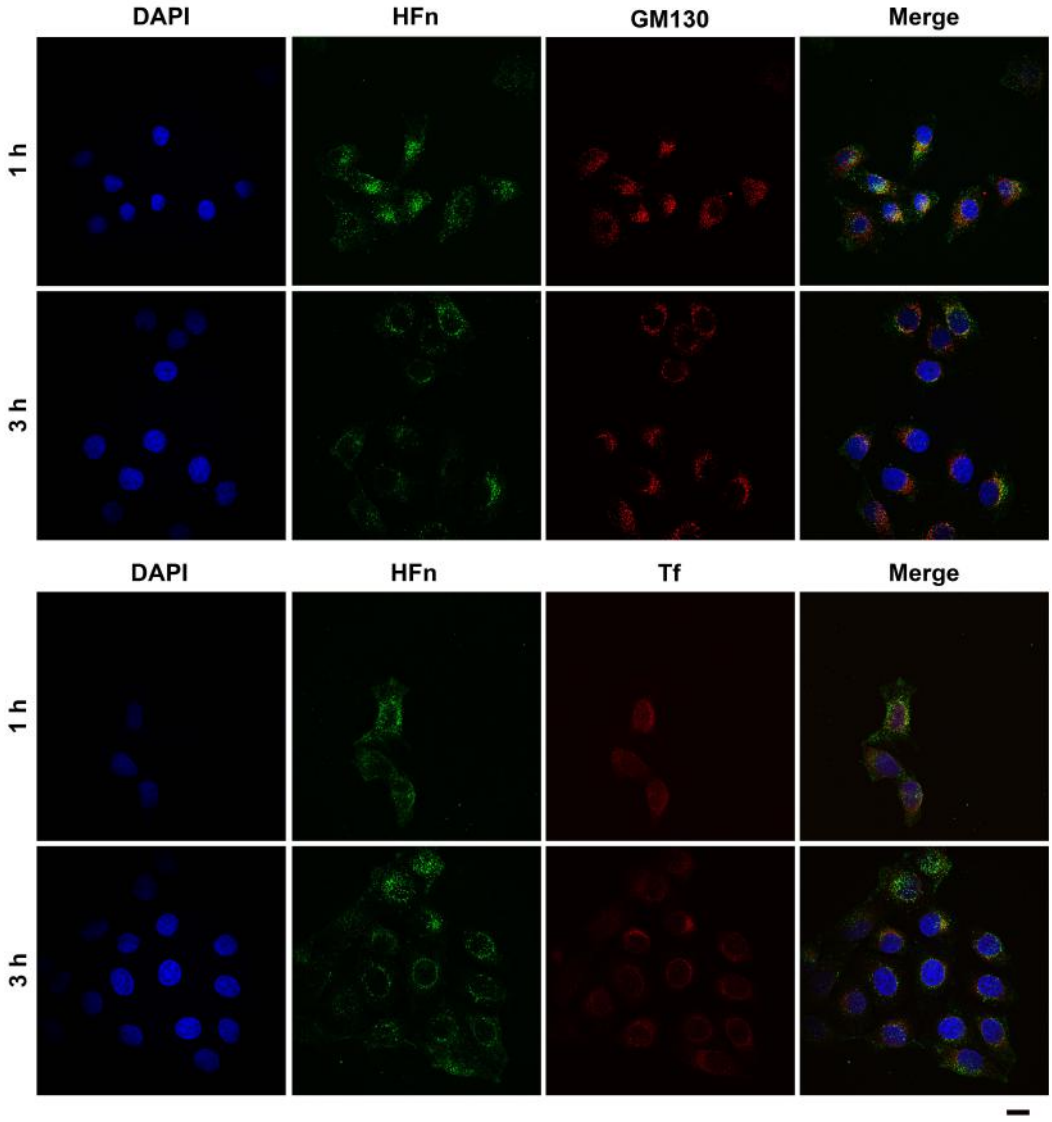

Figure S5. Intracellular localization of HFn nanoparticles. Confocal microscopy images of HeLa cells, incubated for 1 h or 3 h at 37 °C with 0.1 μg mL^{-1} of HFn (green). Golgi and recycling endosomes were recognized respectively with the Golgi marker GM130 and the recycling endosome marker Tf antibodies and labeled with an anti-mouse secondary antibody conjugated with Alexa Fluor 546 (red; Invitrogen). Nuclei were stained with DAPI (blue). Scale bar: 10 μm.

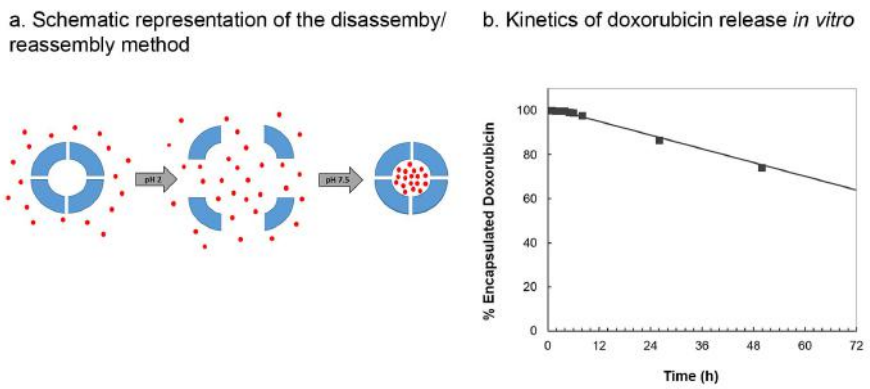

Figure S6. (a) Schematic representation of the disassemby/reassembly method used for HFn loading with fluorescent molecules or drugs. (b) Kinetics of doxorubicin release *in vitro*. HFn(DOX) is been incubated at 37 °C in PBS, pH 7.2, for 72 h. The percentage of encapsulated DOX is been calculated after measuring fluorescence emission of the sample.

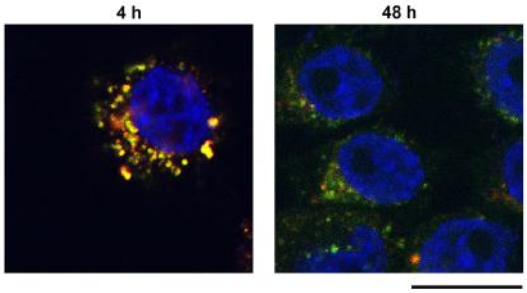

Figure S7 Evaluation of the fate of HFn shell and of relevant encapsulated molecules after internalization. Confocal microscopy merge images of HeLa cells, incubated for 4 h or 48 h at 37 °C with 0.1 mg mL^{-1} of HFn (red) loaded with FITC (green). Nuclei were stained with DAPI (blue). Scale bar: 10 μm.

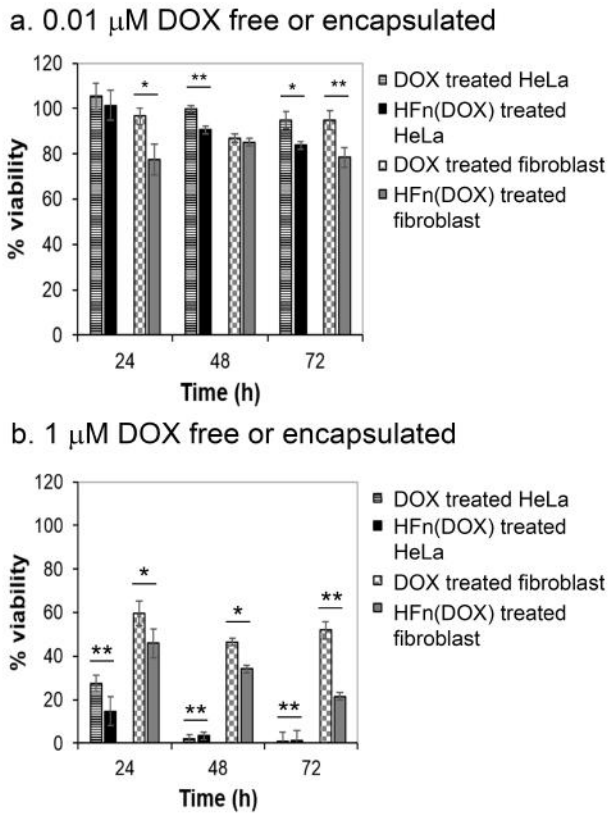

Figure S8. Viability of cells treated with DOX free or encapsulated in HFn shell. (a) Fibroblast (gray) and HeLa (black) cells were treated with 0.01 μM of DOX or HFn(DOX) for up to 72 h and tested by measuring the conversion of MTT into formazan. Reported values are the mean of six replicates ± s.e., normalized on cell proliferation of untreated fibroblast or HeLa cells, respectively * $P<0.005$; ** $P<0.0005$ (Student's t-test). (b) Fibroblast (gray) and HeLa (black) cells were treated with 1 μM of DOX or HFn(DOX) for up to 72 h and tested by measuring the conversion of MTT into formazan. Reported values are the mean of six replicates ± s.e., normalized on cell proliferation of untreated fibroblast or HeLa cells, respectively * $P<0.005$; ** $P<0.0005$ (Student's t-test).

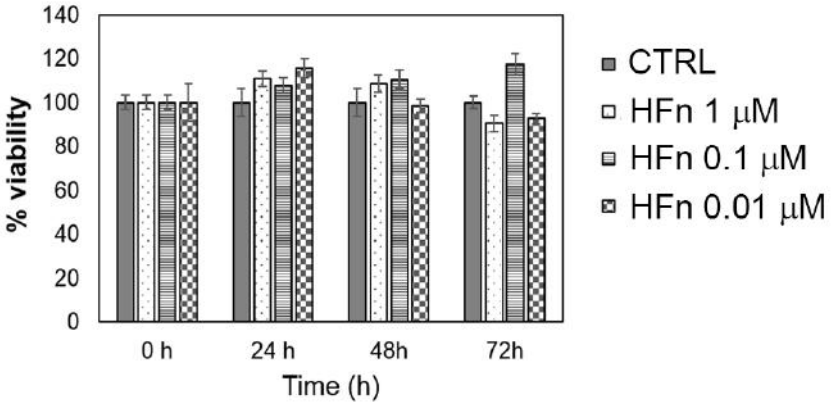

Figure S9 Viability of cells treated with void HFn shell. (a) HeLa cells were treated with amounts of HFn equal to that used in HFn(DOX) samples for up to 72 h and tested by measuring the conversion of MTT into formazan. Reported values are the mean of six replicates ± s.e.

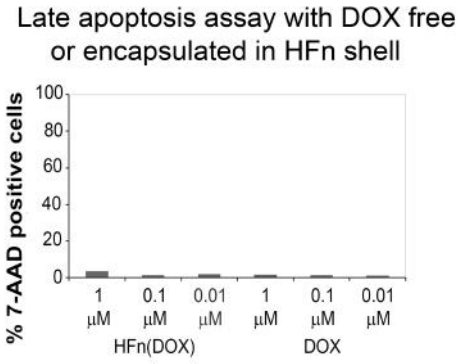

Figure S10 Late apoptosis assay with DOX free or encapsulated in HFn shell. HeLa cells were treated with 1 μM, 0.1 μM and 0.01 μM DOX or HFn(DOX) for 3 h. Late apoptosis was assessed measuring the uptake of 7-aminoactinomycin D, evaluated by flow cytometry. Untreated cells were used to set region of positivity. Reported values are the mean of three replicates ± s.e.

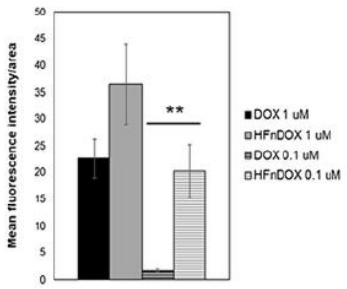

Figure S11 Quantification of fluorescence intensity due to DSB. Reported values obtainedwith Image J software represent the mean fluorescence intensity of six different cells normalizedwith respect to their area ± s.e. ** P<0.005.

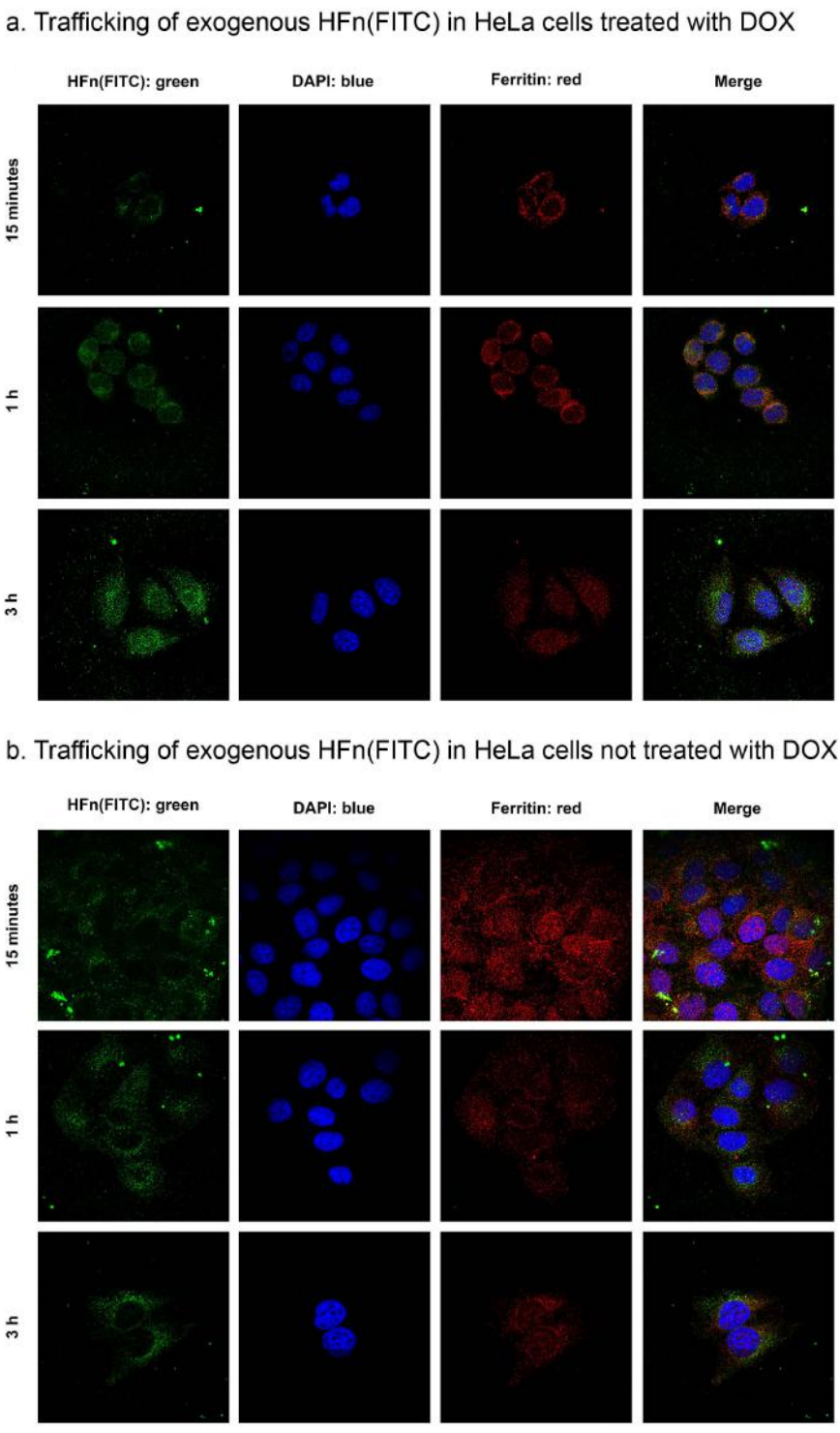

Figure S12. Treatment with DOX trigger nuclear translocation of exogenous HFn. Confocal microscopy images of HeLa cells incubated for 3 h at 37 °C with 0.1 mg mL^{-1} of HFn loaded with FITC (HFn(FITC); green) and then treated (a) or not (b) with DOX 0.1 μM for 15 minutes, 1 or 3 h. Nuclei were stained with DAPI (blue). Endogenous and exogenous ferritin were recognized with anti-ferritin antibody and labeled with an anti-rabbit secondary antibody conjugated with Alexa Fluor 546 (red; Invitrogen). Scale bar: 10 μm.

2.7 References

1. Bellini, M. *et al.* Protein nanocages for self-triggered nuclear delivery of DNA-targeted chemotherapeutics in Cancer Cells. *J. Controlled Release* **196,** 184–196 (2014).
2. Carvalho, C. *et al.* Doxorubicin: the good, the bad and the ugly effect. *Curr. Med. Chem.* **16,** 3267–3285 (2009).
3. Waksman, S. A. & Woodruff, H. B. Actinomyces antibioticus, a New Soil Organism Antagonistic to Pathogenic and Non-pathogenic Bacteria. *J. Bacteriol.* **42,** 231–249 (1941).
4. Arcamone, F. *et al.* Adriamycin, 14-hydroxydaunomycin, a new antitumor antibiotic from S. peucetius var. caesius. *Biotechnol. Bioeng.* **11,** 1101–1110 (1969).
5. Cagel, M., Grotz, E., Bernabeu, E., Moretton, M. A. & Chiappetta, D. A. Doxorubicin: nanotechnological overviews from bench to bedside. *Drug Discov. Today* (2016). doi:10.1016/j.drudis.2016.11.005
6. Tacar, O., Sriamornsak, P. & Dass, C. R. Doxorubicin: an update on anticancer molecular action, toxicity and novel drug delivery systems. *J. Pharm. Pharmacol.* **65,** 157–170 (2013).
7. Lemke, T. L. & Williams, D. A. *Foye's Principi di chimica farmaceutica*. (Piccin, 2011).
8. Arena, E. *et al.* Analysis of the pharmacokinetic characteristics, pharmacological and chemotherapeutic activity of 14-Hydroxy-daunomycin (Adriamycin), a new drug endowed with an antitumour activity. *Arzneimittelforschung.* **21,** 1258–1263 (1971).
9. Greene, R. F., Collins, J. M., Jenkins, J. F., Speyer, J. L. & Myers, C. E. Plasma pharmacokinetics of adriamycin and adriamycinol: implications for the design of in vitro experiments and treatment protocols. *Cancer Res.* **43,** 3417–3421 (1983).
10. Mordente, A. *et al.* Anthracycline secondary alcohol metabolite formation in human or rabbit heart: biochemical aspects and pharmacologic implications. *Biochem. Pharmacol.* **66,** 989–998 (2003).
11. Minotti, G., Ronchi, R., Salvatorelli, E., Menna, P. & Cairo, G. Doxorubicin irreversibly inactivates iron regulatory proteins 1 and 2 in cardiomyocytes: evidence for distinct metabolic pathways and implications for iron-mediated cardiotoxicity of antitumor therapy. *Cancer Res.* **61,** 8422–8428 (2001).
12. Rahman, A. M., Yusuf, S. W. & Ewer, M. S. Anthracycline-induced cardiotoxicity and the cardiac-sparing effect of liposomal formulation. *Int. J. Nanomedicine* **2,** 567–583 (2007).
13. Thorn, C. F. *et al.* Doxorubicin pathways: pharmacodynamics and adverse effects. *Pharmacogenet. Genomics* **21,** 440–446 (2011).
14. Gewirtz, D. A. A critical evaluation of the mechanisms of action proposed for the antitumor effects of the anthracycline antibiotics adriamycin and daunorubicin. *Biochem. Pharmacol.* **57,** 727–741 (1999).
15. Doroshow, J. H. Role of hydrogen peroxide and hydroxyl radical formation in the killing of Ehrlich tumor cells by anticancer quinones. *Proc. Natl. Acad. Sci. U. S. A.* **83,** 4514–4518 (1986).
16. Tewey, K. M., Rowe, T. C., Yang, L., Halligan, B. D. & Liu, L. F. Adriamycin-induced DNA damage mediated by mammalian DNA topoisomerase II. *Science* **226,** 466–468 (1984).
17. Ashley, N. & Poulton, J. Mitochondrial DNA is a direct target of anti-cancer anthracycline drugs. *Biochem. Biophys. Res. Commun.* **378,** 450–455 (2009).

18. Yan, Y., Björnmalm, M. & Caruso, F. Particle carriers for combating multidrug-resistant cancer. *ACS Nano* **7,** 9512–9517 (2013).
19. Germann, U. A. P-glycoprotein--a mediator of multidrug resistance in tumour cells. *Eur. J. Cancer Oxf. Engl. 1990* **32A,** 927–944 (1996).
20. Young, L. C., Campling, B. G., Cole, S. P., Deeley, R. G. & Gerlach, J. H. Multidrug resistance proteins MRP3, MRP1, and MRP2 in lung cancer: correlation of protein levels with drug response and messenger RNA levels. *Clin. Cancer Res. Off. J. Am. Assoc. Cancer Res.* **7,** 1798–1804 (2001).
21. Burgess, D. J. *et al.* Topoisomerase levels determine chemotherapy response in vitro and in vivo. *Proc. Natl. Acad. Sci.* **105,** 9053–9058 (2008).
22. Schütz, C. A. *et al.* Therapeutic nanoparticles in clinics and under clinical evaluation. *Nanomed.* **8,** 449–467 (2013).
23. Chang, E. H. *et al.* Nanomedicine: Past, present and future - A global perspective. *Biochem. Biophys. Res. Commun.* **468,** 511–517 (2015).
24. Banerjee, R. Liposomes: Applications in Medicine. *J. Biomater. Appl.* **16,** 3–21 (2001).
25. Leonard, R. C. F., Williams, S., Tulpule, A., Levine, A. M. & Oliveros, S. Improving the therapeutic index of anthracycline chemotherapy: focus on liposomal doxorubicin (Myocet). *Breast Edinb. Scotl.* **18,** 218–224 (2009).
26. Barenholz, Y. Doxil®--the first FDA-approved nano-drug: lessons learned. *J. Control. Release Off. J. Control. Release Soc.* **160,** 117–134 (2012).
27. Sanna, V., Pala, N. & Sechi, M. Targeted therapy using nanotechnology: focus on cancer. *Int. J. Nanomedicine* **9,** 467–483 (2014).
28. Fan, Y. & Zhang, Q. Development of liposomal formulations: From concept to clinical investigations. *Asian J. Pharm. Sci.* **8,** 81–87 (2013).
29. Marchal, S., El Hor, A., Millard, M., Gillon, V. & Bezdetnaya, L. Anticancer Drug Delivery: An Update on Clinically Applied Nanotherapeutics. *Drugs* **75,** 1601–1611 (2015).
30. Poon, R. T. & Borys, N. Lyso-thermosensitive liposomal doxorubicin: an adjuvant to increase the cure rate of radiofrequency ablation in liver cancer. *Future Oncol. Lond. Engl.* **7,** 937–945 (2011).
31. Koo, O. M., Rubinstein, I. & Onyuksel, H. Role of nanotechnology in targeted drug delivery and imaging: a concise review. *Nanomedicine Nanotechnol. Biol. Med.* **1,** 193–212 (2005).
32. Alphandéry, E., Grand-Dewyse, P., Lefèvre, R., Mandawala, C. & Durand-Dubief, M. Cancer therapy using nanoformulated substances: scientific, regulatory and financial aspects. *Expert Rev. Anticancer Ther.* **15,** 1233–1255 (2015).
33. Torchilin, V. P. Micellar nanocarriers: pharmaceutical perspectives. *Pharm. Res.* **24,** 1–16 (2007).
34. Matsumura, Y. *et al.* Phase I clinical trial and pharmacokinetic evaluation of NK911, a micelle-encapsulated doxorubicin. *Br. J. Cancer* **91,** 1775–1781 (2004).
35. Allen, T. M. Ligand-targeted therapeutics in anticancer therapy. *Nat. Rev. Cancer* **2,** 750–763 (2002).
36. Julyan, P. J. *et al.* Preliminary clinical study of the distribution of HPMA copolymers bearing doxorubicin and galactosamine. *J. Control. Release Off. J. Control. Release Soc.* **57,** 281–290 (1999).
37. Alkhateeb, A. A. & Connor, J. R. Nuclear ferritin: A new role for ferritin in cell biology. *Biochim. Biophys. Acta BBA - Gen. Subj.* **1800,** 793–797 (2010).

38. Behrend, L., Henderson, G. & Zwacka, R. M. Reactive oxygen species in oncogenic transformation. *Biochem. Soc. Trans.* **31,** 1441–1444 (2003).
39. Hileman, E. O., Liu, J., Albitar, M., Keating, M. J. & Huang, P. Intrinsic oxidative stress in cancer cells: a biochemical basis for therapeutic selectivity. *Cancer Chemother. Pharmacol.* **53,** 209–219 (2004).
40. Laemmli, U. K. Cleavage of structural proteins during the assembly of the head of bacteriophage T4. *Nature* **227,** 680–685 (1970).
41. Laginha, K. M., Verwoert, S., Charrois, G. J. R. & Allen, T. M. Determination of doxorubicin levels in whole tumor and tumor nuclei in murine breast cancer tumors. *Clin. Cancer Res. Off. J. Am. Assoc. Cancer Res.* **11,** 6944–6949 (2005).
42. Hovorka, O. *et al.* Spectral analysis of doxorubicin accumulation and the indirect quantification of its DNA intercalation. *Eur. J. Pharm. Biopharm.* **76,** 514–524 (2010).
43. Fan, K. *et al.* Magnetoferritin nanoparticles for targeting and visualizing tumour tissues. *Nat. Nanotechnol.* **7,** 459–464 (2012).
44. Li, L. *et al.* Binding and uptake of H-ferritin are mediated by human transferrin receptor-1. *Proc. Natl. Acad. Sci. U. S. A.* **107,** 3505–3510 (2010).
45. Maham, A., Tang, Z., Wu, H., Wang, J. & Lin, Y. Protein-based nanomedicine platforms for drug delivery. *Small Weinh. Bergstr. Ger.* **5,** 1706–1721 (2009).
46. Kilic, M. A., Ozlu, E. & Calis, S. A novel protein-based anticancer drug encapsulating nanosphere: apoferritin-doxorubicin complex. *J. Biomed. Nanotechnol.* **8,** 508–514 (2012).
47. Rogakou, E. P., Pilch, D. R., Orr, A. H., Ivanova, V. S. & Bonner, W. M. DNA double-stranded breaks induce histone H2AX phosphorylation on serine 139. *J. Biol. Chem.* **273,** 5858–5868 (1998).
48. Gigli, M., Doglia, S. M., Millot, J. M., Valentini, L. & Manfait, M. Quantitative study of doxorubicin in living cell nuclei by microspectrofluorometry. *Biochim. Biophys. Acta* **950,** 13–20 (1988).
49. Zhen, Z. *et al.* RGD-modified apoferritin nanoparticles for efficient drug delivery to tumors. *ACS Nano* **7,** 4830–4837 (2013).

CHAPTER 3

Nanometronomic treatment of 4T1 breast cancer with nanocaged doxorubicin prevents drug resistance and circumvents cardiotoxicity[1]

3.1 "Maximum tolerated dose" *vs* "Metronomic" treatment

Traditionally, cytotoxic chemotherapeutics have dominated the systemic management of cancer according to the "maximum tolerated dose" (MTD) paradigm[2,3]. Most of antitumor drugs are DNA-damaging agents or microtubule inhibitors that are designed to kill or inhibit rapidly dividing cells. Standard chemotherapy regimens require that patients be administered with single dose or short courses of the maximal drug dosage that can be tolerated, in order to achieve the best therapeutic efficacy, killing as many tumor cells as possible. However, due to low tumor selectivity, MTD treatments cannot be protracted in order to allow recovery of healthy tissues and reduce myelosuppression. So, these agents are administered in a pulsed manner, with prolonged time intervals (generally of 2-3 weeks in duration) between treatment cycles, to limit the toxicity and preserve other organs (Fig. 3.1)[4].

MTD chemotherapy has been established thanks to the success in treating acute lymphoblastic leukemia in children[5], whereas rarely the leukemic tumor clone can be completely eradicated. In the same way, MTD has proven to be successful on cancers lacking a complex network of activating mutations, such as testicular cancer, Hodgkin disease and B-cell non-Hodgkin lymphomas[2]. In contrast, complex cancers such as sarcomas, breast, prostate, pancreas and lung cancers, are less effectively treated using MTD doses, primarily because they engage extensively the host microenvironment[6]. In this kind of malignancies, standard chemotherapy may be initially effective with responses of tumor regression, disease stabilization and prolonged survival. However, these effects are often short lived, with relapses marked by aggressive cancers and resistance to cytotoxic agents. In fact, in fast-growing or metastatic tumors, a burst in cancer cell proliferation is likely during the necessary therapeutic breaks, together with the manifestation of chemoresistance and accelerated angiogenesis[7]. This is because MTD chemotherapy kills off chemotherapy-sensitive cancer cell populations, leaving chemoresistant cells behind to re-colonize the tumor bed, ultimately leading to disease relapse[2]. One strategy to prevent this event has been the development of increasing, and consequently more and more toxic drug regimens, including the combination of chemotherapeutic agents, in the expectation of achieving a complete eradication of all cancer cells[8].

Angiogenesis is a hallmark capability of cancer: tumor growth and metastasis strongly depends on continued angiogenesis[9], which thus takes on remarkable importance from also a therapeutic point of view. Therefore, antiangiogenic treatments for cancer have been developed, even though both intrinsic and acquired resistance to them are emerging as clinically relevant issues[10].

On the whole, based these considerations it is evident that a reappraisal of advanced-stage cancer management is necessary. In the last years a revaluation of the best ways to administer chemotherapy was made and there is now a shift towards the idea that more frequent administration schedules and smaller doses would be more effective, both in terms of reducing toxicity and even improving anticancer effects[11,12]. In 2000, Klement *et al.*[13] and Browder *et al.*[14] published two innovative articles showing that mice bearing subcutaneous tumors could respond to frequent repeated low doses of chemotherapy, even when they displayed acquired drug resistance to the

same agents administered in a conventional way. Hanahan *et al.*[15] coined the term "metronomic" to describe this type of treatment.

The refinement of this concept is called nowadays "low dose metronomic" chemotherapy (LDM). LDM regimens move from the "maximum tolerable" to the "minimum effective" dose paradigm and refer to the close, regular administration (daily, several times a week, or weekly) of chemotherapeutic drugs at doses significantly below the conventional MTD dosage, over prolonged period and with no extended drug-free breaks[16] (Fig. 3.1). Metronomic chemotherapy can thus be viewed as a form of "long term maintenance" chemotherapy that can be used on its own or combined with biological targeted therapies, especially antiangiogenic drugs[17]. Many different factors have contributed to expand the interest in LDM therapy. First, the MTD approach has not provided the expected survival benefits, besides being very expensive and toxic. Furthermore, genetically complex tumors grow and develop within the host's tissue, which implies that the survival of cancer cells is closely related to the state of the tumor microenvironment. So the main goal of LDM treatment is to kill the rapidly dividing endothelial cells, thus preventing angiogenesis, but also to hit the tumor microenvironment, making it less supportive for tumor growth. Therefore, metronomic chemotherapy has the potential to preserve efficacy while avoiding toxicity[2].

A growing appreciation of the LDM concept is witnessed today: this trend is confirmed by the fact that currently over 150 clinical trials of metronomic chemotherapy for various cancers are ongoing, with encouraging results. These include Phase III studies that combine metronomic chemotherapy regimens with other anticancer drugs such as antiangiogenic ones or anti-inflammatory agents[3].

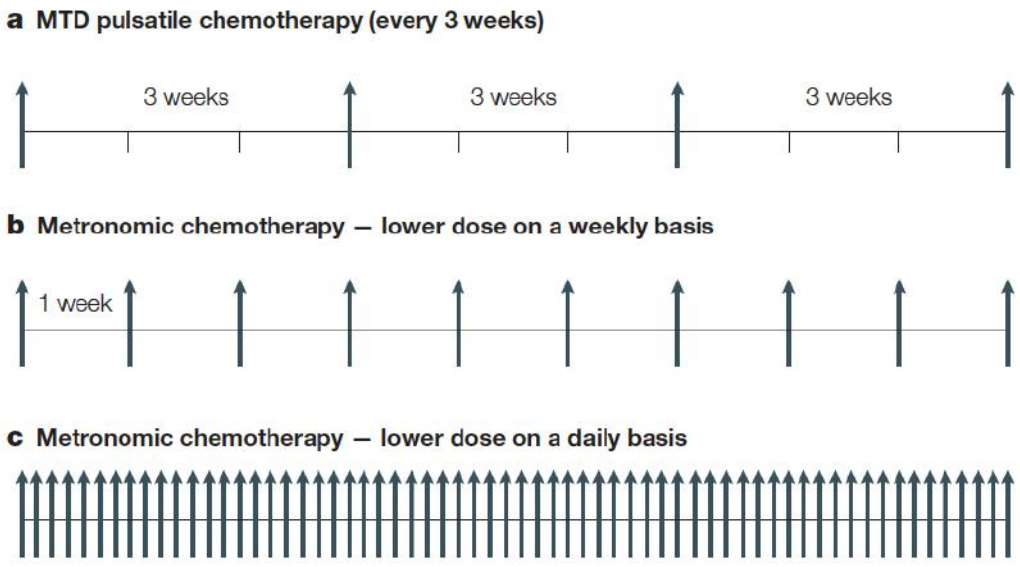

Fig. 3.1 Different therapeutic regimens. Metronomic chemotherapy regimens differ from the standard maximum tolerated dose (MTD) chemotherapy regimens that have been common practice in medical oncology for decades. In standard chemotherapy (a), a drug is typically given in a single bolus injection or infusion at the MTD, interspersed by a long break - for example, 3 weeks - before the next course of this therapy is administered. In metronomic chemotherapy regimens the chemotherapy drug is administered more frequently, such as weekly (b) or daily (c), with no prolonged drug-free interruptions. Drugs that can be administered orally would be ideal for prolonged daily administration schedules[16].

3.1.1 Rationales for LDM chemotherapy

While the conventional MTD chemotherapeutic setting is suggested to act by targeting the proliferating tumor cells, LDM is presumed to affect the vasculature growth and repair, reduce systemic toxicity and myelosuppression, improve the stimulation of the host immune system against the tumor, overcome drug resistance and damage cancer stem cells[1].

Antiangiogenic activity

The anticancer activity of LDM chemotherapy is mediated predominantly by inhibiting tumor angiogenesis[18]. Plenty of evidence, mostly in vitro, indicates that the activated endothelial cells of newly forming blood-vessel are highly sensitive to very low doses of some chemotherapeutic drugs, such as cyclophosphamide, vinblastine, doxorubicin, paclitaxel and docetaxel, which inhibit proliferation or migration of these cells, but not of other cell types[19,20]. Much higher doses of the same agents are required for tumor cell toxicity. Conversely, in standard MTD therapy the effect of chemotherapy on angiogenesis is negligible, perhaps because the endothelial cells might be protected by high local concentrations of endothelial-cell survival factors such as VEGF, basic fibroblast growth factor and angiopoietin-1[21]. More probably, this might be because the damage to the vasculature is largely repaired during the long recovery periods between successive cycles of therapy, perhaps by a massive hemopoiesis-like mobilization of circulation endothelial progenitor cells from the bone marrow[22].

It is important to emphasize that there is a clear distinction between the antiangiogenic effects of conventional antiangiogenic drugs, which target individual molecules or signaling pathways, and the antiangiogenic actions of LDM chemotherapy. Several mechanisms of action have been identified, including selective inhibition of proliferation and/or induction of apoptosis of activated endothelial cells, repression of endothelial cell migration, increase in the expression level of the endogenous angiogenesis inhibitor thrombospondin-1 and decrease in levels and viability of bone marrow-derived endothelial progenitor cells[16]. For instance, bevacizumab, an antiangiogenic monoclonal antibody, binds to extracellular vascular endothelial growth factor (VEGF), rendering it incapable of activating cell surface VEGF receptors[23]. In contrast, metronomic chemotherapy damages the source of this and other growth factors, namely fibroblasts and endothelial cells[13]. Therefore, the underlying mechanisms are different, with metronomic therapy potentially exerting longer lasting effects, due to its capability of targeting the source of vascular growth factors rather than the growth factors themselves.

Bypassing of resistance mechanisms

The use of lower dosages of cytotoxic drugs can imply the added benefit of minimizing the induction of acquired therapeutic resistance, particularly in the setting of combination therapy[24]. Cancer cells are characterized by genetic instability, resulting in high levels of both genotypic and phenotypic intratumoral heterogeneity, and as a consequence, most tumours are likely to contain one or even multiple cancer cell clones that are resistant to even the highest doses of cytotoxic drugs that can be given to a patient[2]. High doses of cytotoxic chemotherapy (*i.e.*, MTD chemotherapy) impose severe selective pressure on a heterogeneous tumor population, thereby killing drug-sensitive tumor cell clones and leading to the selection of the most drug-resistant ones[25]. In this context, it is also true that endothelial cells of the tumor neovasculature lack this genetic instability and are unable to acquire drug resistance, as shown by the unchanged maximum

level of myelosuppression observed in cancer patients after multiple cycles of chemotherapy, even when the tumor in these patients has become resistant[4]. But, at the same time, endothelial cells are not quiescent: fractions of proliferating endothelial cells can be detected during tumor angiogenesis and should therefore be vulnerable to the cytotoxic effect of antiproliferative chemotherapeutic drugs that target DNA or microtubules. As mentioned in the previous paragraph, if the pulsed MTD approach allows normal endothelial cells to repair cytotoxic damage during the periods of therapy suspension, on the other hand the minimal dose needed to inflict significant damage to these cells is so low that cancer cells are spared. In this way LDM, affecting primarily the stromal cells the malignant ones rely on for support and sustenance, ends up to injure the entire tumor cell population, both resistant and sensitive clones.

Cytotoxic activity against cancer stem cells (CSCs)

LDM could exert a major impact even in the subgroup of cells identified as cancer stem cells (CSCs). CSCs, also known as tumor-initiating cells, are a subpopulation of self-renewing cells that are more resistant to chemotherapy and radiation therapy than the surrounding cancer cells. CSCs are characterized by a self-renewal capacity and by the ability to differentiate into progenitor cells that can reconstitute and sustain tumor growth, as well as by a higher level of invasiveness and resistance to many anticancer agents[26]. Only antiangiogenic therapy offers promising prospects on these cells and since LDM has antiangiogenic properties, it may inhibit or reduce CSCs and therefore it can be used as a maintenance therapy to avoid the growth of relapsed tumours[3]. As an example, Folkins *et al*. have demonstrated that a treatment with LDM cyclophosphamide along with a direct antiangiogenic drug significantly reduced the number of CSCs in a rat glioma model[27].

Modulation of antitumor immunity

Emerging evidence suggests that some chemotherapeutic drugs commonly used in LDM protocols may act by also restoring anticancer immune response, which plays a crucial role in the control of the disease. Both innate and adaptive immune responses are involved in keeping cancer progression in check, but it is well known that these responses can be compromised by high dose chemotherapy, which has deleterious side effects, such as neutropenia and lymphopenia. Changes in dosage and time of chemotherapy, as in the case of LDM therapy, can instead lead to stimulation of antitumor immunity and suppression of pro-tumor immune response[6]. Low-dose cyclophosphamide or temozolomide can increase anti-tumor immune response through the selective depletion of T regulatory cells[28], whereas LDM administration of vinblastine, paclitaxel and etoposide could promote dendritic cell maturation and enhance their phagocytic ability, after the release of signals by killed tumor cells[29]. Studies have revealed that the timing of metronomic chemotherapy is crucial: specifically, it needs to be sufficiently frequent to activate a strong innate anti-tumor immune response, but also sufficiently spaced in time to minimize damage to the immune cells recruited to the tumor microenvironment[2].

Induction of tumor dormancy

Tumor dormancy plays a crucial role in both repression of cancer progression and cancer relapse, so it occurs during the very early phase of cancer growth (before the angiogenic switch) but also after treatments, when tumors can resume their development from remaining residual disease[30]. So, re-induction and maintenance of tumor dormancy is a desirable end point in cancer therapy[6].

Tumor dormancy, that can take place at primary sites but also in metastases, occurs as a result of cell cycle arrest or a dynamic equilibrium between cell proliferation and apoptosis[31]. Three different mechanisms are reported to participate in the induction of tumor dormancy: suppression of angiogenesis, induction of apoptosis in cancer cells, and tumor immune surveillance[18]. Thus, by inhibiting tumor angiogenesis and/or reinforcing anticancer immunity (mentioned above), metronomic chemotherapy may be able to induce and maintain angiogenic dormancy. However, thus far no clear evidence has shown that metronomic chemotherapy directly induces cellular dormancy in cancer cells[6,18].

3.1.2 Clinical trials

Multiple clinical trials have investigated the safety and efficacy of metronomic chemotherapy in a variety of human cancers; the earliest were conducted on breast, prostate, gastrointestinal, renal and pancreatic cancers, as well as refractory melanoma[1]. To date, the largest ones have been conducted in patients with advanced breast cancer: in eight of these (which included a total of almost 500 patients), metronomic chemotherapy alone[32,33] or in combination with letrozole[34], trastuzumab[35] or bevacizumab[36], was shown to be an effective approach and was associated with minimal toxic effects. Elsewhere, positive results were also reported with various LDM regimens for patients with recurrent ovarian cancer, hormone-resistant prostate cancer, advanced multiple myeloma, recurrent non-Hodgkin's lymphoma, recurrent malignant glioma and glioblastoma, metastatic or locally advanced neuroendocrine carcinoma and advanced cancer of various tumor types[6]. Overall, metronomic chemotherapy is associated with minimal toxicity and can provide significant clinical benefit and improve the quality of life in patients with advanced and/or relapsed cancer.

Unlike these encouraging results, at least four clinical trials have reported limited activity of metronomic chemotherapy. Importantly, these relatively disappointing results were exclusively reported in malignancies that are poorly responsive to conventional chemotherapy and with a dismal prognosis[6].

3.1.3 Limitations

Many aspects of LDM chemotherapy are empirical or unresolved, such as the choice of cytotoxic drug used for treatment, its optimal dose and dosing interval. On the average, single doses in LDM regimens tend to be in the range one tenth to one third of the MTD dose[16,37] and only drugs that could exert a remarkable antiangiogenic activity at relatively lower doses, rather than conventional MTD, are considered ideal candidates for the metronomic paradigm[18]. Future cancer research should be directed towards the identification of the best agents to use according to tumor type, to find the appropriate doses of each agent to be used alone or in combination and to define the timing of drug administration.

Moreover, several limiting factors remain for LDM before it can displace MTD treatments in clinical practice, including 1) low drug accumulation at tumor site, 2) controversial effectiveness against chemoresistance in advanced metastatic cancers, and 3) acquired resistance after prolonged treatment[1,38]. Recent advances in nanotechnology could offer groundbreaking solutions to improve the effectiveness of LDM chemotherapy, by taking advantage of the unique targeting efficiency of

engineered nanocarriers. For example, Yu *et al*. developed peptide-conjugated nanoparticles for docetaxel and demonstrated the superior antitumor efficacy of the targeted metronomic therapy in terms of prolonged survival and minimal toxicity[39].

3.2 Aim of the work

Over the past decades, cytotoxic chemotherapeutics have dominated the systemic management of cancer according to the "maximum tolerated dose" (MTD) paradigm[2,3]. MTD therapy requires that patients are administered with single dose or short courses of the highest tolerable dosage of a drug in order to achieve the best therapeutic efficacy. Due to low tumor selectivity, MTD treatments cannot be protracted in order to allow recovery of healthy tissues and to reduce myelosuppression associated with pulsed drug doses[4]. In fast-growing or metastatic tumors, during these therapeutic breaks, a burst in cancer cell proliferation accompanied by manifestation of chemoresistance and accelerated angiogenesis are likely[7,40]. Hence, a reappraisal of advanced-stage cancer management is ongoing, moving from the "maximum tolerable" to the "minimum effective" dose paradigm[41]. Indeed, cytotoxic agents administered at low dosages are expected to allow protracted treatments and have been suggested to up-regulate antiangiogenic factors such as thrombospondin-1 and to inhibit vascular endothelial growth factor and platelet-derived growth factor[3,6].

The first clinical trials using low-dose metronomic (LDM) chemotherapy were conducted for breast, prostate, gastrointestinal, renal and pancreatic cancers, as well as refractory melanoma[16,42,43]. This regimen is based on a lower dose of drugs administered more frequently, without the need of extensive interruptions[3,15]. While the conventional dose-dense chemotherapeutic setting is suggested to act by targeting the proliferating tumor cells[44], LDM is presumed to affect the vasculature growth and repair[16,45], to reduce systemic toxicity and myelosuppression, and to improve the stimulation of the host immune system against the tumor[2,7]. However, several limiting factors remain for LDM in order to displace MTD treatments in clinical practice, including 1) low drug accumulation at tumor site, 2) controversial effectiveness against chemoresistance in advanced metastatic cancers, and 3) acquired resistance after prolonged treatment[38].

Recent advances in nanotechnology could offer groundbreaking solutions to improve the effectiveness of LDM chemotherapy, by taking advantage of the unique targeting efficiency of engineered nanocarriers[46]. In the present work, we propose a new concept of low dose "nanometronomic" (LDNM) chemotherapy. In principle, it is possible to obtain a prolonged antitumor effect with LDNM by means of multitasking nanocarriers that deliver lower dose of drug selectively to the growing tumor, inhibit the neovascularization process and prevent chemoresistance. Doxorubicin (DOX) is an excellent pilot drug for use in a LDM regimen[47], as its great anticancer efficacy is notoriously dose-limited by severe systemic side effects above all long-term cardiotoxicity with different severity grades from reduction in left ventricular ejection fraction (LVEF) to severe congestive heart failure[48,49]. Liposomal anthracyclines, including pegylated liposomal doxorubicin (pl-DOX), have been introduced in clinical practice to enhance the therapeutic index and to avoid cardiotoxicity of these drugs thanks to higher accumulation of DOX in the tumor with reduced concentration in off-target organs[50]. However, meta-analyses of several clinical trials comparing pl-DOX to conventional DOX have demonstrated reduced (but not annulled) cardiotoxicity of pl-DOX, without improvement in progression-free or overall survival in advanced breast cancer (BC)[51]. Therefore, improving the therapeutic index of DOX remains an open challenge. As an ideal DOX nanocarrier for our LDNM study, we used H-Ferritin (HFn) nanocages, recently proposed as a promising bionanoparticle for cancer targeting[52] owing to its

affinity for transferrin receptor 1 (TfR-1), which is constitutively overexpressed in primary and metastatic cancer cells[53]. HFn-DOX complex was recently demonstrated to overcome chemoresistance by actively promoting DOX nuclear translocation *in vitro*[54,55] and was tested as a MTD treatment of a DOX-sensitive BC animal model with encouraging results[56].

3.3 Materials and methods

3.3.1 HFn production

HFn nanocages were produced in *E. coli* by DNA recombinant technology and purified as previously described[54]. HFn was labeled with fluorescein isothiocyanate (FITC) or with Alexa Fluor$_{660}$ for *in vitro* and *in vivo* studies, respectively. HFn was filled in with DOX with a loading efficiency of 29 drug molecules per HFn. Quantification of DOX payload was undertaken by fluorescence measurements[54].

3.3.2 Cell cultures

Murine Bioware-Ultra 4T1-Luc2 cell line (4T1-L), used as model of BC cells, have been purchased in 2011 from Perkin Elmer, confirmed by IMPACT I PCR profiling by the source, and have been passaged for fewer than 6 months. 4T1-L were cultured in RPMI 1640 medium supplemented with 10% fetal bovine serum, 2 mM l-glutamine, penicillin (50 UI mL^{-1}) and streptomycin (50 mg mL^{-1}) at 37 °C in humidified atmosphere containing 5% CO_2 and sub-cultured prior to confluence using trypsin/EDTA. 4T1 cells were used for *in vitro* tests and orthotopically implanted at passages lower than 4 in female Balb/C mice to obtain the BC animal model.

3.3.3 Cell binding assay

Cells (5×10^5) were incubated 2 h at 4 °C in flow cytometry tubes in the presence of 20 or 100 µg mL^{-1} of FITC-labeled HFn. After incubation, cells were washed three times with PBS. Labeled cells were resuspended with 0.5 mL of phosphate-buffered saline (PBS, EuroClone) and analyzed by a Gallios flow cytometer (Beckman Coulter). 20000 Events were acquired for each analysis, after gating on viable cells, and a sample of untreated cells was used to set the appropriate gates.

3.3.4 Cell proliferation assay

Cells were cultured on a 96 multiwell dish at a density of 5000 cells cm^{-1}. Then, cells were incubated with different amounts of the molecules to be tested. At the indicated time points (24, 48, 72 h), cells were washed with PBS and then incubated for 3 h at 37 °C with 0.1 mL of [3-(4,5-dimethylthiazol-2-yl)-5-(3- carboxymethoxyphenyl)-2-(4-sulfophenyl)-2H-tetrazolium salt (MTT) stock solution previously diluted 1:10 in DMEM medium without phenol red. After incubation, MTT solubilizing solution (0.1 mL) was added to each well to solubilize the MTT formazan crystals (Promega). Absorbance was read immediately using a testing wavelength of 570 nm and a reference wavelength of 620 nm. The results are expressed as means ± standard error (SE) of six individual experiments.

3.3.5 Cell death assay

Cells were cultured on a 12 multi-well dish until sub-confluence. Then, cells were incubated 3 h and 24 h at 37 °C in the presence of different amounts of DOX or HFn-DOX. After incubation, cells were washed twice with PBS and treated for FACs analysis according to Annexin V-PE-Cy5 Apoptosis Detection Kit manufacturer's protocol (BioVision). Cells were analyzed within 1 h on a Gallios flow cytometer (Beckman Coulter). 20000 Events were acquired for each analysis, after gating on cells.

3.3.6 Western blot

Briefly, 4T1-L cells were cultured in a 6-wells plate, lysed with 200 µL lysis buffer (20 mM Tris HCl pH 7.6, 150 mM NaCl, 1 mM EDTA, 1% Triton X-100, 1% glycerol, 1 mM Na_3VO_4, 10 mM NaF, Protease Inhibitor Cocktail, 1 mM PMSF). Total protein in lysate was quantified using the Coomassie Plus Protein Assay Reagent (Thermo Fisher Scientific) with Bovine Serum Albumin (BSA) as standard protein. Approximately 30 µg of protein from each sample were separated by SDS-PAGE using 12% (v/v) polyacrylamide gels and then transferred onto PVDF membrane. The membrane was blocked in 5% fat-free milk powder in PBS with 0.1 % Tween 20 for 1 h. The membrane was incubated overnight with mouse-monoclonal antibody against P-gp (cod. Ab170904; Abcam) at 1:1000 dilution or a mouse monoclonal antibody anti-α-tubulin (Sigma) at 1:1000 dilution in 5% fat-free milk powder in PBS with 0.1 % Tween 20 for 1 h. The membrane was washed three times with PBS with 0.1 % Tween 20 and reacted 1 h with the secondary antibody anti-mouse conjugated with horseradish peroxidase (1:5000; Abcam) for 1 h. The bound antibody was revealed using ECL star reagent (EuroClone) and the chemoluminescence signal was detected using the Chemidoc System (Biorad).

3.3.7 Confocal laser scanning microscopy

Cells were cultured on collagen pre-coated cover glass slides until sub-confluence and incubated with HFn for different time periods. To evaluate internalization, FITC labeled HFn (100 µg mL^{-1}) were incubated with cells for 15 min, 1, 3 and 48 h at 37 °C. DNA damage was assessed 24 h after incubation DOX free or encapsulated in HFn cage. To maintain a good degree of live cells we have worked with the DOX dosage of 0.01 µM. In order to evaluate nuclear DOX release cells were incubated for 3 h at 37 °C with DOX free or encapsulated in HFn at the concentrations of 0.1 or 1 µM. At the end of incubation with nanoparticles, cells were washed with PBS, fixed for 5 min with 4% paraformaldehyde (Sigma) and then treated for 5 min with 0.1% Triton X-100 (Sigma). A blocking step was performed for 1 h at room temperature with a solution containing 2% bovine serum albumin (BSA, Sigma), 2% goat serum (EuroClone) and 0.2 µg mL^{-1} DAPI (4',6-diamino-2-phenylindole; Invitrogen) in PBS. Golgi apparatus, lysosomes, early and recycling endosomes were stained respectively with Golgi marker 130 (GM-130; at a 1:100 dilution; clone 35; BD Biosciences), Cathepsin D (CatD; 1:50; clone BC011; Calbiochem), Early Endosomes Antigen-1 (EEA-1; 1:1000; clone 14; BD Biosciences), Transferrin (Tf; 1:100; clone 5G2; Abcam) antibodies by incubating 2 h at RT and revealed by a Alexa Fluor 546-conjugated antibody against murine IgGs (Invitrogen) at a 1:300 dilution by incubating for 2 h at RT in PBS, 2% BSA, 2% goat serum. Double strand break were stained with γH2A.X antibody (1:1000 dilution; Abcam) by

incubating 2 h at room temperature and revealed by Alexa Fluor 546-conjugated antibody against rabbit IgGs (Invitrogen) at a 1:300 dilution by incubating for 2 h at room temperature in PBS, 2% BSA, 2% goat serum. Microscopy analysis was performed with a Leica SPE microscope confocal system equipped with laser excitation lines 405 nm, 488 nm, 514 nm and 633 nm. Images were acquired with 63× magnification oil immersion lenses at 1024 × 1024 pixel resolution. DOX was revealed exciting the sample with 488 nm laser line and acquiring emitted signal from 550 nm to 600 nm (magenta). The signal represented in green color is the emission in the acquiring window between 520 to 545 nm, which correspond to the fluorescence signal of a degradation product of DOX, as previously reported[54].

3.3.8 Study design

The hypothesis was that HFn-DOX would exhibit higher antitumor efficacy and would induce minimal or negligible side effects compared to free drug and pl-DOX (Caelyx) in mice bearing strongly invasive and metastatic BC. HFn-DOX dose was set at 1.24 mg kg^{-1} DOX, about 1/7 of the average MTD dosage administered in 4T1 murine BC[55]. This tumor model was selected for its aggressiveness and spontaneous tendency to spread to multiple metastatic sites after orthotopic injection of luciferase-tagged cells. The endpoint of the *in vivo* experiments was defined at 21 days to appreciate the parametric differences in tumor growth, resistance onset and cardiotoxicity in living animals, while allowing us to operate in compliance with the National and European legislations that regulate animal experiments. The number of animals for each biodistribution, bioavailability, therapy and cardiotoxicity experiment was calculated with a power of at least 80 ± 5 %. Mice were randomized by primary tumor size before initiation of treatments. Dye-labeled HFn was first injected in tumor-bearing mice by tail vein, then targeting and biodistribution were assessed by live fluorescence imaging, while drug bioavailability was evaluated in healthy animals. Rodents were administered intravenously with placebo, DOX, pl-DOX or HFn-DOX at day 5, 9, 13 and 17, and monitored for 21 days during which tumor growth was followed by measurement of bioluminescence signal intensity (BLI) of 4T1-L cells after intraperitoneal injection of luciferin. BLI analyses were undertaken under standardized conditions to gain a quantitative estimation of live BC cells. Intermediate BLI values and mouse weights were determined before each administration. Collected BLI data were normalized to the mean tumor size calculated for all mice within each group at each time point. Animals were euthanized at day 21 to analyze resected tissues with the aim of determining the antitumor efficacy, antiangiogenic activity and cardiotoxicity of DOX, pl-DOX and or HFn-DOX. Histopathology and immunohistochemistry were analyzed from blinded samples. Outliers were not excluded. All experiments were conducted under an approved protocol of the Italian Ministry of Health. Animals were cared for according to the guidelines of the Italian Ministry of Health (see the Supplementary Materials and Methods).

3.3.9 Production of orthotopic 4T1-L tumor model

For the *in vivo* experiments, 8-week old female Balb/C mice purchased by Charles River Laboratories (Calco, Italy), were maintained in a fully equipped facility, housed in single cages, fed ad-libitum and observed daily. Animals were anesthetized by intraperitoneal injection of 250 mg kg^{-1} of avertin and were handled and euthanized according to ethical guidelines. Mice were used in

accordance with an experimental protocol subjected to the direct approval of the Italian Ministry of Health. 4T1-L cells, grown as described above, were injected in 8-week old female Balb/C mice. All tumor injections were done 2 days after abdominal trichotomy. 4T1-L (1×10^5 cells for each animal) were suspended in cold serum-free RPMI 1640 growth medium and injected into mammary fat pad. Animals were observed and tumor formation was recorded at least thrice per week. For biodistribution studies, the tumors were allowed to grow for 7 days, at which time they reached a size of 0.8 cm^3 approximately, while for efficacy studies, the tumors were allowed to grow only for 5 days.

3.3.10 Tumor targeting and biodistribution of AF660 labeled HFn nanovector

Balb/C mice bearing 4T1-L cells were immobilized in a restrainer (2 biological instrument) to be injected in the tail vein with AF660-labeled HFn void nanovectors (5 mg kg^{-1} body weight). Epifluorescence imaging was performed at 1, 2, 4, 24 and 48 h post-injection by placing the anesthetized animals in a IVIS Lumina II imaging system (Perkin Elmer) at 37 °C. Images were acquired with a 680 nm emission filter while excitation was scanned from 570 to 640 nm, and mice autofluorescence was removed by spectral unmixing. Bioluminescence (BLI) images were acquired 5 min after luciferin peritoneal injection (150 µg kg^{-1}, Perkin Elmer) with an exposure time of 5 s. The instrument setup for BLI acquisition is Fstop 4 and medium binning. After *in vivo* acquisitions, mice were sacrificed and urine were collected from the bladder. Dissected tumors and organs (liver, kidneys, spleen, heart, brain and lungs) were analyzed in IVIS system, as described above for the whole animals. Fluorescence intensity of equal amounts of urine was analyzed in a GloMax Multi Detection System (Promega), to evaluate the presence of HFn.

3.3.11 Plasma half-life

To determine plasma half-life of nanoformulated DOX in comparison to free drug, HFn-DOX or DOX (1.24 mg DOX kg^{-1} or 12.4 mg DOX kg^{-1}) were intravenously (i.v.) injected into healthy Balb/C mice. At selected time points blood was collected in EDTA coated tubes by collection from the retro-orbital plexus. Plasma was prepared by centrifugation at 1500 ×g for 15 min. DOX was extracted as reported[57] and the content was measured by a spectrofluorometer (Horiba; λ_{ex} = 500 nm; λ_{em} = 550 nm). The DOX amount in plasma was quantified using a standard curve previously obtained extracting known amounts of DOX from plasma. The data are the mean ± SE of samples collected from at least 3 different mice.

3.3.12 *In vivo* efficacy

Balb/C mice were orthotopically implanted with 4T1-L cells. Five days after implant, mice were randomly divided into three experimental groups and anesthetized. Five min after intraperitoneal injection of luciferin (150 µg kg^{-1}, Perkin Elmer) bioluminescence (BLI) images were acquired (IVIS Lumina II, Perkin Elmer, exposure time of 5 sec, Fstop 4 and medium binning). The region of interest (ROI) was drawn by fixing the lower value of the scale at 50. The number of photons emitted/sec in the ROI were used to measure tumor volume. Then, mice were

injected into the lateral tail vein with DOX, pl-DOX and HFn-DOX (1.24 mg kg^{-1}) or with sterile saline solution (placebo). Therapeutic treatment was repeated at day 9, 13 and 17 after 4T1-L cells implants and BLI signal of tumors were measured before every treatment. At day 21 tumor BLI were measured and mice were euthanized. Tumors were excised, weighed, fixed in 10% formalin and embedded in paraffin for immunohistochemistry. Liver, kidneys, lungs, spleen, gut and hearts (half) were excised (n = 3/group), fixed in 10% formalin and embedded in paraffin for histopathological analysis. Hearts (n = 9/ group) were excised, frozen in liquid nitrogen and stored at –80 °C for further evaluations.

3.3.13 Doxorubicin quantification in tumors

Balb/C mice orthotopically implanted with 4T1-L cells, as reported above, were anesthetized and injected into the lateral tail vein with DOX or HFn-DOX (1.24 mg kg^{-1}; n = 24 mice/group). 1, 2, 4 and 24 h after injection mice were euthanized (n = 3 mice/group) and tumors were collected. Tumor were weighted, homogenized in water (10% w/v) with potter (Glas-Col homogenizer) and DOX was extracted as reported[57]. The drug content was measured by a spectrofluorometer (Horiba; λ_{ex} = 500 nm; λ_{em} = 550 nm) and quantified using a standard curve previously obtained extracting known amounts of DOX from tumor homogenates. The data are the mean ± SE of samples collected from at least 3 different mice.

3.3.14 *Ex vivo* analyses

Excised tumors were analyzed by fluorescence imaging and by confocal microscopy of cryosections to establish the HFn cellular targeting *in vivo*, immunofluorescence of dissociated tumor to assess DOX accumulation, immunohistochemistry to determine the CD31 and MDR-1 expression in endothelial and tumor cells, respectively, and Tumor TACS In Situ Apoptosis Detection kit to determine cellular apoptosis. Excised organs were analyzed by fluorescence imaging to establish the HFn biodistribution in non-target organs. Histopathology was performed on samples from liver, kidneys, spleen, heart, brain, gut and lung tissues. Kidney and liver functionality was assessed before and after the treatment. The size of cardiomyocytes extracted from resected heart tissues was measured after wheat germ agglutinin (WGA) fluorescence labeling. Isolated mitochondria from heart tissue samples were investigated by membrane potential and ultrastructural analysis of transmission electron micrographs; the extent of ROS in heart was assessed by glutathione assay. Details are reported below.

3.3.15 *Ex vivo* analysis of tumor cryosections

4T1-L tumors were isolated and fixed in 4% paraformaldehyde solution for 3 h, washed in PBS and embedded in OCT for freezing in liquid nitrogen. 10 µm thick tumor cryosections were air dried at room temperature for 1 h, rinsed with PBS and, after 5 min of permeabilization at room temperature with 0.1% Triton X-100 in PBS, counterstained with DAPI (diluted 1:1500 in PBS) for 20 min at room temperature. Microscopy analysis of cryosections was performed with a Leica TCS SPE confocal microscope (Leica Microsystems). Images were acquired with 40× magnification oil immersion lenses at 1024 × 1024 pixel resolution.

3.3.16 Tumor dissociation

Balb/C mice orthotopically implanted with 4T1-L cells, as reported above, were anesthetized and injected into the lateral tail vein with DOX or HFn-DOX (1.24 mg kg^{-1}). Control mice were injected with sterile saline solution. Mice were euthanized (n = 2 mice/group); tumors were excised at 2 h after injection and dissociated using the Mouse Tumor Dissociation kit (Miltenyi Biotech). Dissociated cells were seeded on glass slide with the Cytospin Centrifuge (Thermo Scientific). The resulting samples were fixed with 4% paraformaldehyde and processed for immunofluorescence as described above.

3.3.17 Immunohistochemistry

Three micrometer thick paraffin-embedded tissues (n = 5/group) were cut, deparaffinized in xylene, and rehydrated in ethanol. Microwave oven pretreatment was performed (pH 8.0, EDTA buffer). Immunohistochemistry was performed using a polyclonal antibody anti-CD31 (1:200 dilution, DakoCytomation, 2 h incubation) and a rabbit monoclonal antibody anti-MDR-1 (1:100 dilution, Abcam, 2 h incubation). The reaction was revealed by means of supersensitive nonbiotin detection system (BioGenex) and diaminobenzidine as chromogen. The number of vessels was counted on 10 fields/sample, while quantification of MDR-1 expression was performed by ImagePro Plus software on 5 fields/sample. Magnification 40× (vessels number); magnification 20× (MDR-1 expression).

3.3.18 Apoptosis assay

Paraffin embedded tumor sections (n = 6/group) were treated with the Tumor TACS In Situ Apoptosis Detection kit (Trevigen) according to manufacturer’s protocols, which labels apoptotic nuclei in paraffin-embedded tissue sections. Apoptotic nuclei were counted on 10 squares/sample (n = 6/group). Magnification 20×.

3.3.19 Histopathological analysis

Liver, kidneys, spleen, heart, brain, gut and lung samples obtained from Balb/C mice (n = 3/group) were fixed in 10% buffered formalin for at least 48 h and embedded in paraffin. Three micrometer sections were cut, stained with hematoxylin and eosin, and examined in a blinded manner. For cardiomyocyte cross-dimensions analysis, heart sections were deparaffined by washing sections with xylene for 30 min at room temperature. Then, sections were washed with ethanol 100%, 95%, 90%, 85%, 80%, 70% and thrice with water, fixed with 4% paraformaldehyde in PBS for 1 h and stained 1 h with Wheat Germ Agglutinin coupled to Alexa Fluor 488 (1:200; Wheat Germ Agglutinin, Alexa Fluor488-conjugate, Invitrogen). Tissue were washed with PBS and mounted with Prolong Gold (Invitrogen). Slides stained with wheat germ agglutinin were acquired at using fluorescence microscope (Nikon Eclipse 80i) at magnification 40×. Image dimensions 2560 × 1920 pixels. Cardiomyocyte areas were quantified using ImageJ software.

3.3.20 Ultrastructural analysis (TEM)

Small portions of hearts (n = 3/group) samples were fixed in 2.5% glutaraldehyde in 0.1 M phosphate buffer, pH 7.2, for 2 h. After one rinsing with PBS, specimens were post-fixed in 1.5% osmium tetroxide for 2 h, dehydrated by 50, 70, 90, and 100% EtOH, and embedded in epoxy resin (PolyBed 812 Polysciences Inc.). Ultrathin sections were cut with an ultramicrotome (Ultracut E (Reichert-Jung)), stained with uranyl acetate and lead citrate and examined by means of a transmission electron microscope (TEM, Tecnai Spirit (FEI)). For mitochondria quantification at least 9 images/group were taken at 4200× magnification. Three mice were used for each experimental condition. Mitochondrial morphometric measurements were performed using ImageJ software on at least 10 images/group acquired at 11.500× magnification measuring the area of at least 100 mitochondria/sample. The percentage of area occupied by mitochondrial cristae was measured by ImageJ software imposing a threshold value of 118.

3.3.21 Mitochondria isolation and evaluation of membrane potential

Heart tissue (50 mg) were homogenized in a potter (Glas-Col) in 2 mL of Mitochondria Isolation Buffer supplemented with 1 mg mL^{-1} Bovine Serum Albumin (225 mM mannitol, 75 mM sucrose, 10 mM HEPES, 10 mM EDTA) and centrifuged for 10 min at 1000 ×g. Supernatants were centrifuged 10 min at 12000 ×g to harvest crude mitochondria pellet. Pellets were washed thrice in Mitochondria Isolation Buffer. Protein concentrations were determined using Bradford assay. Mitochondria membrane potential was determined in isolated mitochondria using JC-1 reagent (Life Technologies) according to the manufacturer's protocols. Briefly, mitochondria were labeled with 1.5 mg JC-1/mg protein and acquired in flow cytometry (Cytoflex, Beckman Coulter). Samples were excited using a 488 nm laser source. The signal of JC-1 monomers was captured by FL1, while the signal of JC-1 aggregates was collected by FL2. The mitochondrial membrane potential is represented by the ratio between the median fluorescence intensity of FL2 and FL1 normalized on protein concentration.

3.3.22 Glutathione assay

The measurement of reactive oxygen species (ROS) was performed by quantifying reduced glutathione (GSH) in hearts. 50 mg of heart tissue was washed in heparin (10000 U mL^{-1}), homogenized in PBS supplemented with 2 mM EDTA (1 mL) with a potter (Glas-Col) and centrifuged for 10 min at 10000 ×g. The GSH levels of the collected supernatants were assessed using a luminescence-based GSH-Glo Glutathione assay (Promega) according to the manufacturer's protocol.

3.3.23 Assessment of kidney and liver functionality

Kidney and liver functionality were assessed by measuring the amount of urea, creatinine, AST and ALT in plasma (n = 3/group) before (day 5) and after (day 21) the treatment with placebo, DOX (1.24 mg kg^{-1}), pl-DOX (1.24 mg kg^{-1} DOX) and HFn-DOX (1.24 mg kg^{-1} DOX).

Quantifications were performed according to the manufacturer's protocols using the following kits: QuantiChrom™ Urea Assay Kit, QuantiChrom™ Creatinine Assay Kit, EnzyChrom™ Aspartate Transaminase Assay Kit and EnzyChrom™ Alanine Transaminase Assay Kit (BioAssay Systems).

3.3.24 Statistical analyses

Statistical analyses were conducted using two-tailed Student's *t*-test. All plots show mean values ± SE. All tests assumed normal distribution and the statistical significance threshold was set at $P < 0.05$.

The *in vivo* experiments described hereinafter were performed by Dr. Serena Mazzucchelli, prof. Corsi's research group at the Department of Biomedical and Clinical Sciences "L. Sacco", University of Milan (Italy).

3.4 Results and discussion

3.4.1 *In vitro* uptake and cytotoxicity of HFn-DOX in 4T1 breast cancer cells

The 4T1 cell line (4T1-L) was selected as *in vitro* and *in vivo* BC model for three main reasons: 1) tumor aggressiveness due to 4T1 genetic patterning, which results in high level of proliferation, migration and invasiveness; 2) basal expression of MDR-1 transporter, which switches into overexpression upon treatment with DOX resulting in chemoresistance[58]; 3) stable luciferase expression, which allowed us to follow the tumor progression and metastases. 4T1-L cells were first treated with FITC-labeled HFn (FITC-HFn)[54] to investigate the nanoparticle-cell interaction. Cells were incubated with FITC-HFn for 15 min, 1, 3 and 48 h, and analyzed by confocal microscopy to evaluate the uptake and intracellular trafficking. HFn was quickly internalized, since it was recovered inside the cell cytoplasm after only 15 min of incubation, and it continued accumulating in the cytosol until 3 h (Fig. 3.2 A). The intracellular signal intensity decreased after 48 h probably due to ferritin disassembly, consistent with previous evidence[54]. HFn was found partly compartmentalized in early endosomes and partly free in the cytosol (Figure S1), while the absence of colocalization with lysosomes, Golgi and transferrin (Tf) marker suggested that HFn did not follow lysosomal degradation, elimination or recycling, respectively, in agreement of previous evidence[54]. Binding assays with HFn at 20 or 100 μg mL^{-1} confirmed a dose-dependent recognition of tumor cells (Fig. 3.2 B).

4T1-L cells were treated with DOX or HFn-DOX at increasing concentrations of DOX to assess cell proliferation, cell death, DNA damage and nuclear DOX accumulation. Proliferation was arrested for at least 72 h after treatment with 1 μM HFn-DOX, while DOX reduced cell proliferation for 24 h only, suggesting the onset of chemoresistance upon incubation with DOX (Fig. 3.2 C). Cell viability was evaluated by incubating the cells with 0.01, 0.1 and 1 μM DOX or HFn-DOX for up to 72 h. Results reported in Fig. 3.2 D show that inhibition of BC cell viability using HFn-DOX was significantly higher than that after treatment with DOX. Such a drop in viability was ascribed to a remarkable increase in cell death (Fig. 3.2 E). Treatment with 0.01 μM HFn-DOX caused pronounced apoptosis and necrosis induction and double strand breaks in contrast to DOX (Fig. 3.2 F). It can be assumed that the increase in cytotoxicity of HFn- DOX resides in the efficiency of HFn in promoting DOX nuclear translocation (Fig. 3.2 G), as already described for different tumor cell lines[54,55]. Quantitative fluorescence analysis of confocal images gave a nuclear DOX concentration of 15.2 and 9-fold higher than that detected in cultures treated with DOX at 0.1 and 1 μM, respectively (Figure S2).

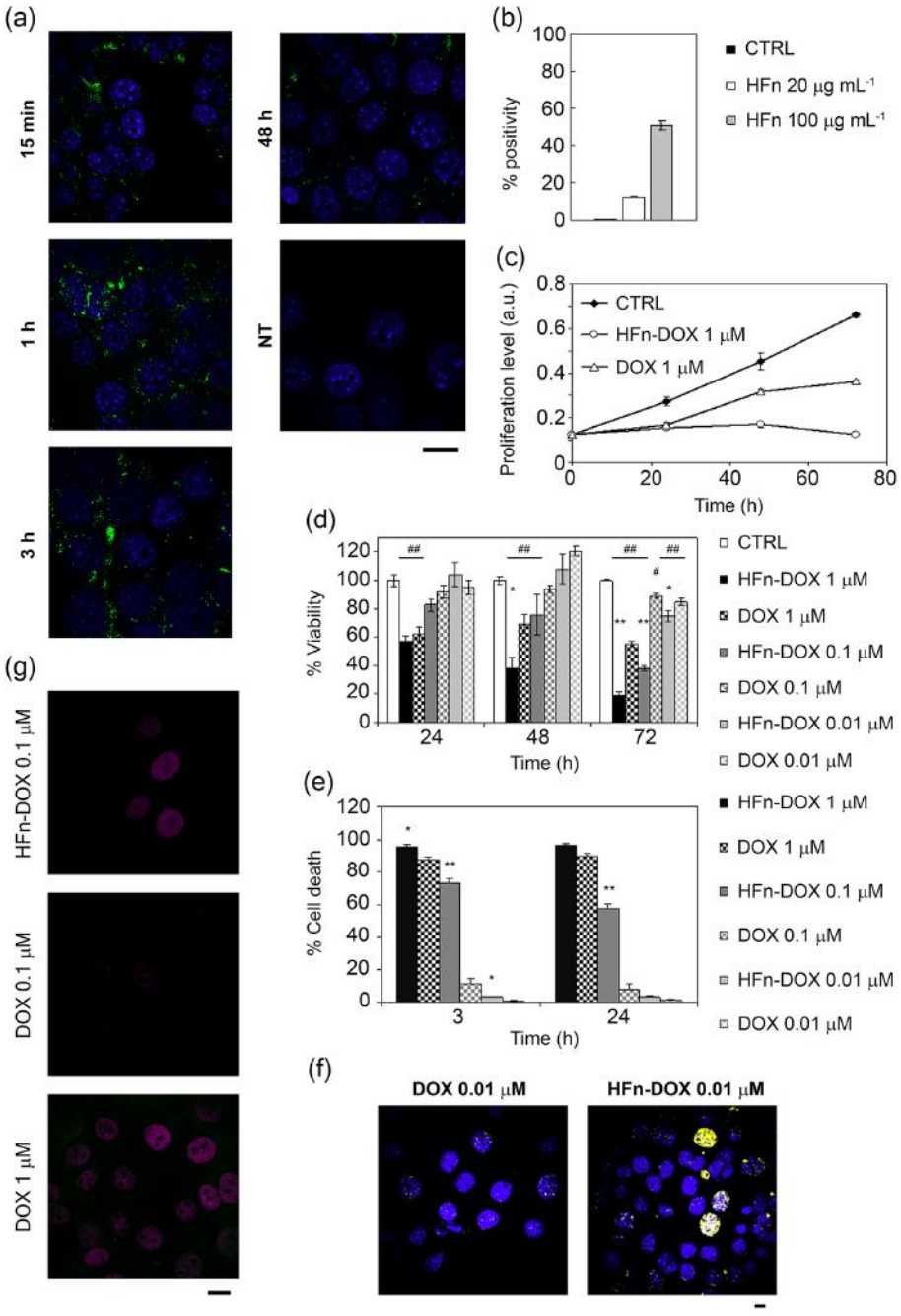

Fig. 3.2 *In vitro* activity of HFn-DOX nanocages toward tumor cells. a. Intracellular localization of HFn nanoparticles. Confocal microscopy merged images of 4T1-L cells, incubated with 100 μg mL^{-1} of FITC-HFn (green). Nuclei were stained with DAPI (blue). Scale bar: 10 μm. b. HFn binding. 4T1-L cells were incubated 2 h at 4 °C with FITC-HFn (20 and 100 μg mL^{-1}) and then processed for flow cytometry. Untreated cells were used as control to set the positive region. c. Proliferation profiles of cells treated with 1 μM DOX or HFn-DOX for up to 72 h. Untreated cells are used as control. Values are mean of six replicates ± SE. d. Viability of cells treated with free or nanoformulated DOX. 4T1-L cells were treated with 1, 0.1, and 0.01 μM DOX or HFn-DOX for up to 72 h. Viability was assessed by MTT assay, normalized on proliferation of untreated cells. Statistical significance *vs*. CTRL #P<0.05, ##P<0.005; Statistical significance *vs*. DOX *P<0.01; **P<0.005. e. Cell death assay using DOX or HFn-DOX. 4T1-L cells were treated with 1, 0.1, and 0.01 μM DOX or HFn-DOX for 3 or 24 h. Cell death was assessed on the basis of the exposure to Annexin V, evaluated by flow cytometry. Untreated cells were used to set region of positivity. Values are mean of three replicates ± SE. Statistical significance *vs*. DOX *P<0.005; **P<0.0005. f. Double-strand break of DNA after DOX exposure. Confocal microscopy images of 4T1-L cells incubated with 0.01 μM DOX or HFn-DOX. Anti-γH2A.X antibodies were used to reveal the DNA double-strand breaks (DSB; yellow). Nuclei were stained with DAPI (blue). Scale bar: 10 μm. g. Doxorubicin release inside the nuclear compartment. Confocal microscopy images of 4T1-L cells incubated with 0.1 μM DOX or HFn-DOX and with 1 μM DOX for 3 h at 37 °C. DOX signal is represented in magenta, while DOX degradation product in green. Scale bar: 10 μm.

3.4.2 *In vivo* targeting and biodistribution of HFn nanocarrier

An orthotopic 4T1 metastatic BC model was obtained by implanting 4T1-L cells (10^5 cells) subcutaneously in the mammary fat pad of female Balb/C mice[59]. This murine tumor was reported to metastasize primarily, yet not exclusively, by a hematogenous route leading to metastatic spread to lung, liver and lymph nodes[60]. The reliability of the model was confirmed by following tumor progression and early onset of metastases by bioluminescence intensity (BLI) imaging over 20 days (Figure S3A). Histopathological analysis performed on excised tumors confirmed that the primary mass was indeed derived from epithelial cancer cells without undesired morphological alterations (Figure S3B). 4T1 mice were injected into the tail vein with Alexa $Fluor_{660}$-labeled HFn (AF660-HFn) at 5 μg kg^{-1} [61] and monitored by live fluorescence imaging at 1, 2, 24 and 48 h. An intense epifluorescence signal (Epf) at the bladder was detected within the first 2 h, which however disappeared after 24 h (Fig. 3.3 A and B), suggesting renal excretion of HFn within 1 day. Epf of excised tumors 1, 2, 24 and 48 h after AF660-HFn injection displayed rapid tumor uptake, which progressively decreased in intensity over time (Fig. 3.3 C). Confocal images acquired on cryosections of excised tumors confirmed that HFn reached the 4T1 cell cytoplasm and thus were not confined to the tumor stroma or vessels, but actively entered into cancer cells (Figure S4). Combined data reported in Fig. 3.3 A-C suggested that a prevalent fraction of nanoparticles that were not captured by the tumor were rapidly sequestered by the kidneys, and presumably eliminated into the bladder. This hypothesis was confirmed by Epf analysis of excised kidneys that exhibited a detectable AF660-HFn fluorescence emission at 1 and 2 h (Fig. 3.3 D and E) and further evidence was provided by fluorescence measurement of collected urine (Fig. 3.3 F). Besides kidney filtration, our results suggested preferential distribution of HFn in the liver within the first 24 h and appreciable Epf was also detected in the spleen for up to 2 h. In contrast, HFn were not recovered in the lungs, heart and brain (Fig. 3.3 D and E).

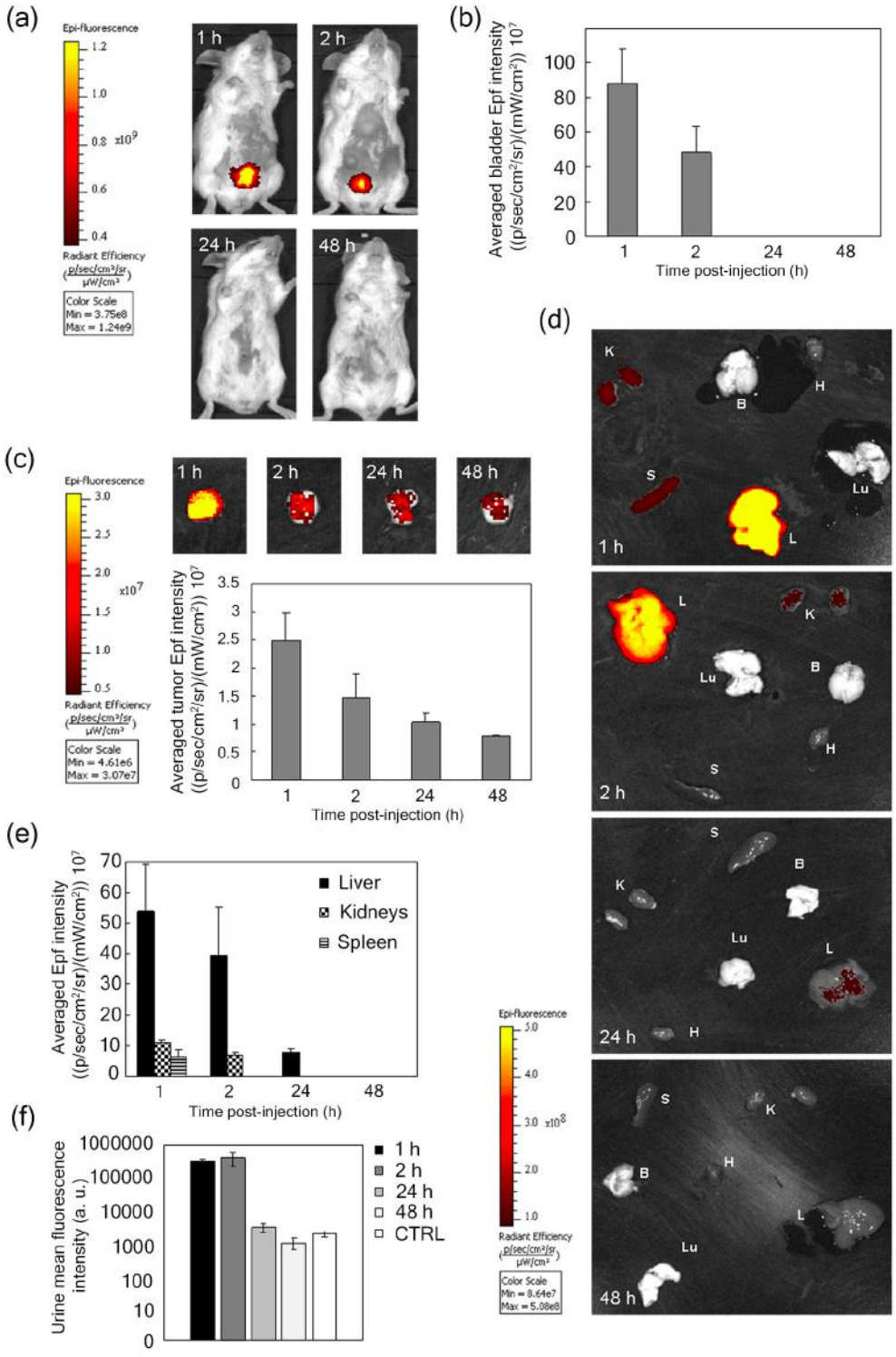

Fig. 3.3 *In vivo* targeting and distribution of void HFn nanocarrier. a. Epifluorescence (Epf) images of mice bearing 4T1-L tumors acquired 1, 2, 24 and 48 h after intravenous (i.v.) injection into the tail vein of 5 µg kg^{-1} AF660-HFn and b. averaged Epf intensity of the bladder region of interest (ROI). c. Epf of isolated 4T1 tumors and averaged Epf intensity of tumor ROI acquired 1, 2, 24 and 48 h after exposure to HFn. d. Epf of isolated spleen (S), kidneys (K), liver (L), brain (B), heart (H), lungs (Lu), and e. averaged Epf intensity of the ROI obtained after 1, 2, 24 and 48 h exposure to HFn. f. Fluorescence intensity of urine collected 1, 2, 24 and 48 h after i.v. injection of AF660-HFn. The color scale in panels a, c and d indicates the averaged epifluorescence expressed as radiant efficiency [(p/sec/cm_2/sr)/ (mW/cm_2)], where p/sec/cm_2/sr is the number of photons per second that leave a square centimeter of tissue and radiate into a solid angle of one steradian (sr). Values reported in panels b, c, e and f are mean ± SE of at least 4 different samples under each experimental condition.

3.4.3 Bioavailability of HFn-DOX and accumulation at the tumor

To evaluate the bioavailability of nanoformulated drug, 2 groups of healthy mice (5 mice/group) were treated with DOX or HFn-DOX at 1.24 mg kg^{-1}. Blood samples were collected from the retro-orbital plexus at 15, 30, 45 and 60 min. These tight time points were chosen to detect possible changes in blood bioavailability of DOX or HFn-DOX soon after administration, as in both cases the drug was injected intravenously. DOX was extracted from collected samples and quantified by fluorescence intensity analysis (FLI) at λ_{em} = 550 nm (λ_{ex} = 500 nm)[62]. Blood samples taken before drug administration were set as reference. Bioavailability of HFn-DOX was two-fold higher than DOX although the kinetic seems to maintain the same shape. To better discriminate kinetic's variations due to nanoformulation, a 10-fold higher dosage of DOX or HFn-DOX (*i.e.* 12.4 mg kg^{-1}) has been administered to healthy mice. Results reported in Fig. 3.4 A display different plasma distribution profiles and confirming that HFn-DOX increases drug bioavailability in comparison to DOX of at least four-fold at each time point.

Accumulation of DOX at primary tumors (Fig. 3.4 B) was determined by fluorescence after chemical extraction from homogenates of resected tumors at 1, 2, 24, and 48 h after single injection of HFn-DOX or DOX at 1.24 mg DOX kg^{-1} [57]. DOX was found in higher concentration in tumors of mice treated with HFn-DOX compared to DOX within 1 h. HFn-DOX displayed faster localization at the tumor compared to DOX, (Fig. 3.4 B), suggesting a crucial role for nanoparticle-mediated delivery in enhancing the tumor targeting, although after 2 h the DOX levels are equilibrated in both cases. Confocal images of 4T1-L dissociated from tumors excised at 2 h evoked higher tumor cell accumulation of DOX in samples treated with HFn-DOX compared to DOX (Fig. 3.4 C). Combining these results suggested that HFn-DOX were efficiently captured by tumor cells, while DOX was confined in blood vessels of the tumor to a much larger extent.

3.4.4 Impact of LDNM monotherapy on breast cancer management

Eight-week old Balb/C female mice were implanted with 4T1-L cells at day 0. Tumor-bearing mice were randomly divided into three experimental groups at day 5 and treated with placebo, DOX, pl-DOX or HFn-DOX under our LDNM setting: drug administration (1.24 mg DOX kg^{-1}) was performed at day 5, 9, 13 and 17. The progression of tumor volume was monitored *in vivo* before each individual drug injection by bioluminescence imaging. Images suggested that HFn-DOX could decrease tumor growth and metastatic spread (Fig. 3.5 A). Indeed, while DOX displayed a tumor progression similar to the control along the experimental window (Fig. 3.5 B), HFn-DOX could suppress the tumor growth as long as the drug was administered (day 17) and exhibited a prolonged effect up to the experimental endpoint (day 21). An even better effect was achieved with pl-DOX, which was indeed able to arrest the tumor development. Immunohistochemical analysis of tumor sections showed that the apoptotic effect of pl-DOX and HFn-DOX on BC cells was better than that of DOX (Fig. 3.5 C and Figure S5), presumably due to the improved tumor accumulation of the drug. However, the absence of statistical significance in apoptosis between HFn-DOX and DOX treated samples advocated alternative factors in the stronger antitumor efficacy of HFn-DOX beyond mere cytotoxicity.

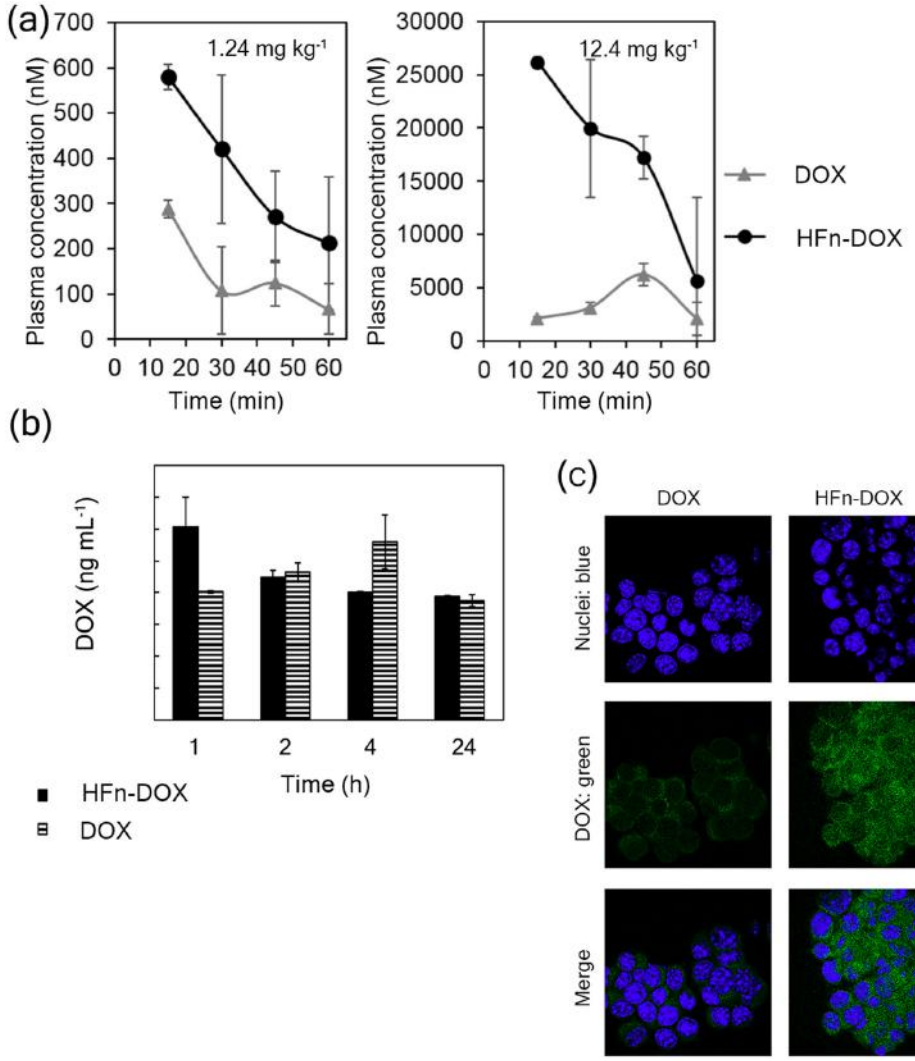

Fig. 3.4 Bioavailability and tumor accumulation of HFn-DOX in comparison with free DOX. a. Bioavailability of DOX and HFn-DOX at different time points. Plasma concentration of DOX after i.v. injection of HFn-DOX (black circles) or DOX (gray triangles) at 1.24 mg kg^{-1} and 12.4 mg kg^{-1} in healthy mice. **b.** DOX accumulation at 4T1-L tumor in mice at different time points after administration of 1.24 mg kg^{-1} DOX as free molecule or HFn-DOX. Female Balb/C mice orthotopically implanted with 4T1-L murine mammary carcinoma cells were injected 6 days after implantation (time 0) with DOX or HFn-DOX. DOX levels in tumor have been determined 1, 2, 4, and 24 h after i.v. injection following acidified isopropanol extraction from tumor homogenates. Aliquots from six mice per each time point concentration have been extracted and analyzed by spectrofluorimeter. Reported values are means of 3 samples/group ± SE. *P* values are summarized in Table S5. **c.** Confocal microscopy images of 4T1-L cells dissociated from tumor harvested 2 h after i.v. injection of DOX and HFn-DOX. DOX signal is represented in green, while nuclei were stained with DAPI (blue). Scale bar: 10 µm.

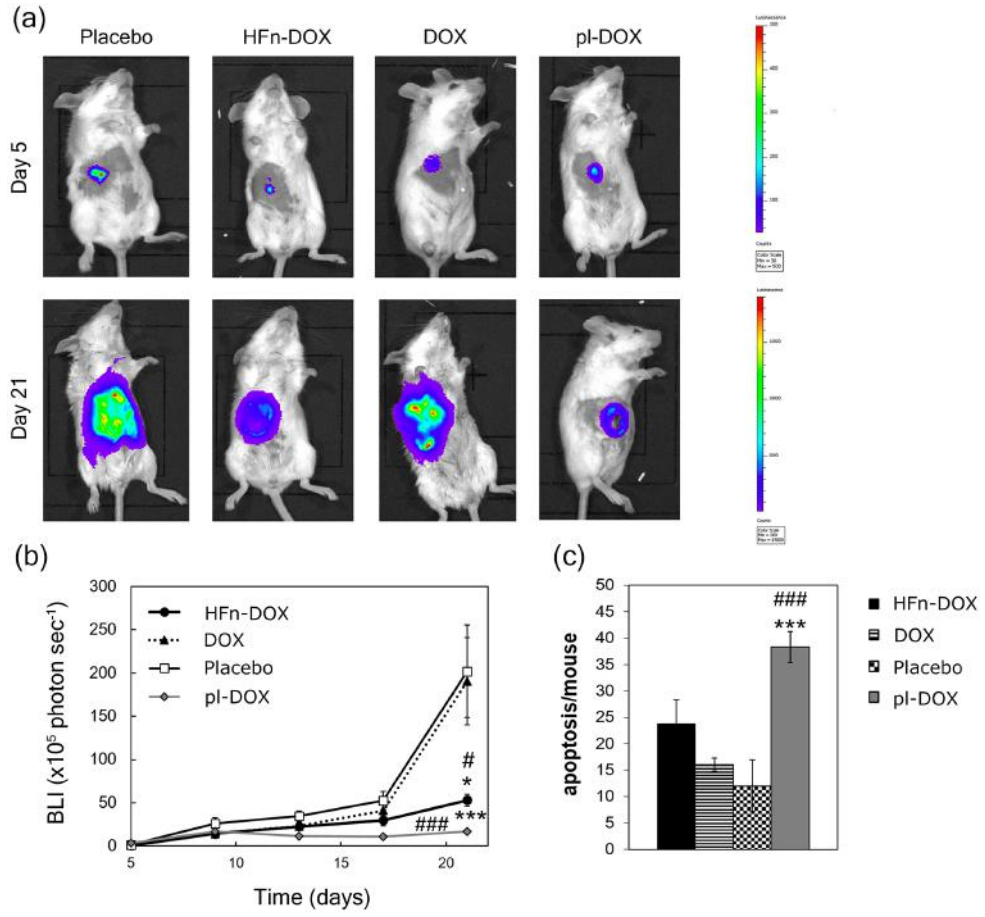

Fig. 3.5 Efficacy of LDNM treatment with HFn-DOX**.** a. DOX and HFn-DOX *in vivo* efficacy. Bioluminescence imaging of female Balb/C mice (n = 12/group) orthotopically implanted (day 0) with 4T1-L murine mammary carcinoma cells were treated with placebo or with 1.24 mg kg^{-1} of DOX, pl-DOX or HFn-DOX. Drug injections were performed into the tail vein at day 5, 9, 13 and 17. Mice were sacrificed at day 21. b. Quantification of tumor volume. Tumor volume was quantified by measuring the bioluminescence intensity signal of 4T1-L cells 5 min after intraperitoneal injection of luciferin. Dots represent the normalized mean value of BLI tumor signal ± SE. Statistical significance *vs*. placebo #*P*<0.05 ###*P*<0.005; *vs*. DOX **P*<0.05 ****P*<0.005. c. Quantification of apoptosis in tumor tissue upon treatment with HFn-DOX. Tumors excised at day 21 (n = 6/group) were fixed with formalin and embedded in paraffin. Histological slides were processed to label DNA fragments of apoptotic cells. Reported values are the mean of apoptotic cells number/field/sample ± SE. The count was performed on 10 fields/sample. Magnification 20×. Statistical significance *vs*. placebo ###*P*<0.005; *vs*. DOX ****P*<0.005.

3.4.5 Impact of LDNM regimen on tumor angiogenesis and chemoresistance

In line with the observed discrepancy in the results from the DNA fragmentation assay (Fig. 3.5 C), we investigated the possible involvement of antiangiogenic effect of HFn-DOX under the LDNM regimen. Vessel labeling with anti-CD31 antibody in BC histological slides revealed a remarkable decrease in the number of CD31-positive cells compared to DOX (Fig. 3.6 A and Figure S6), suggesting a role of the HFn-DOX-promoted antiangiogenic effect on the inhibition of tumor progression and diffusion. Analogously, it is likely that the strong inhibition in tumor growth observed with pl-DOX (Fig. 3.5 B) was primarily due to antiangiogenic activity (Fig. 3.6 A). 4T1-L BC cells have been described to develop drug resistance owing to induced overexpression of MDR-

1 protein upon standard treatment with DOX[58]. Western blot performed on 4T1 cells treated for 72 h with 0.1 μM DOX corroborated DOX induction of MDR-1 expression in vitro (Figure S7). We examined MDR-1 expression in tumor tissues dissected after LDNM treatment. Tumor sections from DOX and pl-DOX-treated mice displayed a three-fold and five-fold increase in MDR-1-positive cells, respectively, compared to animals treated with placebo and HFn-DOX treated animals (Fig. 3.6 B and Figure S8). As expected, both DOX and pl-DOX induced an obvious overexpression of MDR-1 in tumor cell membranes, which was particularly pronounced in the proximity of the tumor endothelium[63]. In contrast, MDR-1 expression was undetectable in tumor cell membranes after HFn-DOX treatment and was found only to a limited extent in tumor vessels after HFn-DOX treatment, at the same level of the placebo. This result is relevant in view of a protracted metronomic treatment preventing the onset of chemoresistance, and it is even more surprising considering that pl-DOX is commonly used in patients previously treated with anthracyclines and therefore affected by potentially chemoresistant cancers.

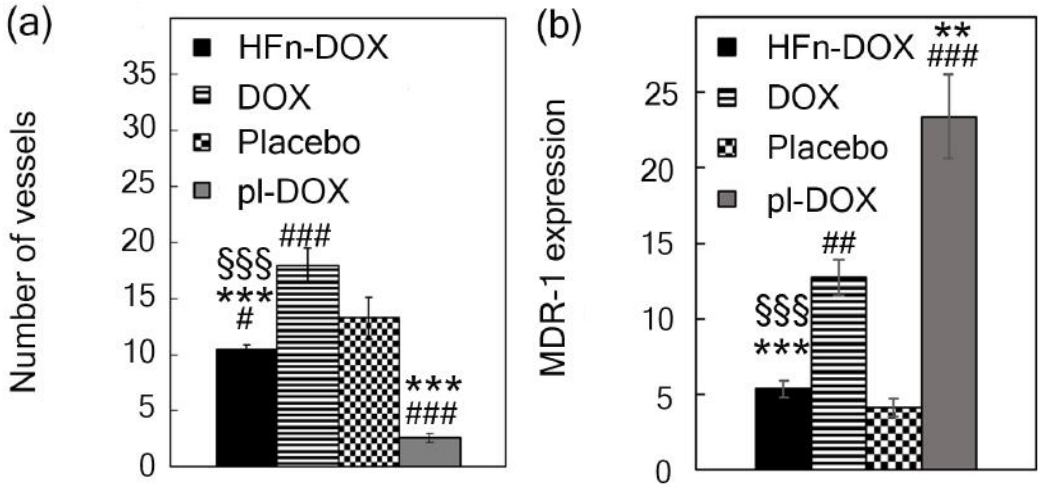

Fig. 3.6 Impact of LDNM regimen on tumor angiogenesis and chemoresistance. a. Quantification of angiogenesis in tumor tissue upon treatment with HFn-DOX. Tumors excised at day 21 (n = 5/group) were fixed with formalin and embedded in paraffin. Immunohistochemistry of histological slides were processed to label CD31+ cells. Reported values are mean of vessel number counted in 10 fields/sample ± SE. Magnification 40×. Statistical significance *vs.* placebo #*P*<0.005 ###*P*<0.00005; *vs.* DOX ***P<0.00005; *vs.* pl-DOX §§§*P*<0.0005. b. Quantification of MDR-1-expression. Excised tumors (n = 5/group) were processed for immunohistochemistry of MDR-1 antigen. The percentage of image area positive for MDR-1 expression was quantified using ImagePro Plus Software. Reported values are the mean of the percentage of MDR-1 positive signal counted in 5 fields/sample ± SE. Statistical significance *vs.* Placebo ##*P*<0.0005 ###*P*<0.00005; *vs.* DOX **P<0.005 ***P<0.0005; *vs.* pl-DOX §§§*P*<0.0005.

3.4.6 HFn-DOX suppresses DOX cardiotoxicity and systemic dysfunction under a LDNM therapeutic setting

Cardiotoxicity represents a life-threatening unresolved issue associated to DOX chemotherapy under clinically relevant settings[64]. To evaluate the incidence of LDNM monotherapy on cardiotoxicity, we followed a multiparametric approach[65]. First, histological slides of heart tissues were treated with FITC-conjugated wheat germ agglutinin (FITC-WGA), a cell

membrane label, and imaged by fluorescence microscopy (Figure S9). Cardiomyocyte cross-sections from mice treated with HFn-DOX, pl-DOX, DOX or non-treated were measured at day 21. Images showed a significant increase of cardiomyocyte area in DOX and pl-DOX samples suggesting a strong cellular damage response compared to HFn-DOX samples (Fig. 3.7 A). Detailed ultrastructural analysis of cardiac cells in DOX and pl-DOX treated samples revealed an increased number of mitochondria compared to HFn-DOX (Fig. 3.7 B and Figure S10). In addition, changes in mitochondria morphology, including larger surface area and cristae depletion, typical effects of DOX-induced cardiomyopathy[65], were clearly evident in DOX and pl-DOX treated samples but not in HFn-DOX samples (Fig. 3.7 C-E). Therefore, the absence of obvious alterations in mitochondria number and morphology in heart samples from mice treated with HFn-DOX strongly supports the lack of cardiotoxicity in LDNM HFn-DOX treatment, even compared to pl-DOX, which is currently considered the most safe anthracycline therapy in terms of cardiotoxicity.

To further investigate if the ultrastructural alterations were associated to mitochondrial dysfunction, mitochondria isolated from heart tissue of DOX, pl-DOX or HFn-DOX treated mice were analyzed in detail. The membrane potential decreased by 30% in DOX and pl-DOX samples compared to HFn-DOX (Fig. 3.7 F). As mitochondrial impairment was expected to generate reactive oxygen species (ROS)[66], we quantified the level of the ROS quencher glutathione (GSH) in heart tissue[67]. Fig. 3.7 G displays the lower amount of reduced GSH in DOX and pl-DOX-treated mice in comparison to HFn-DOX, confirming mitochondrial dysfunction induced by treatment with free and liposomal DOX only.

Finally, we assessed the systemic toxicity of HFn-DOX by histopathological examination of liver, kidneys, lung, spleen, heart, gut and brain isolated at day 21. No histological lesions were found in all organs (Figure S11). Liver and kidney functionalities were also determined to further evaluate the toxicity profile of HFn-DOX treatment. Serum levels of aspartate transaminase (AST) and alanine transaminase (ALT), and urea and creatinine, were monitored as markers of liver and kidney condition, respectively. Our results showed that AST/ALT and urea/creatinine ratios in HFn-DOX treated mice were comparable to the control and in the range of reference, confirming the overall nanodrug safety.

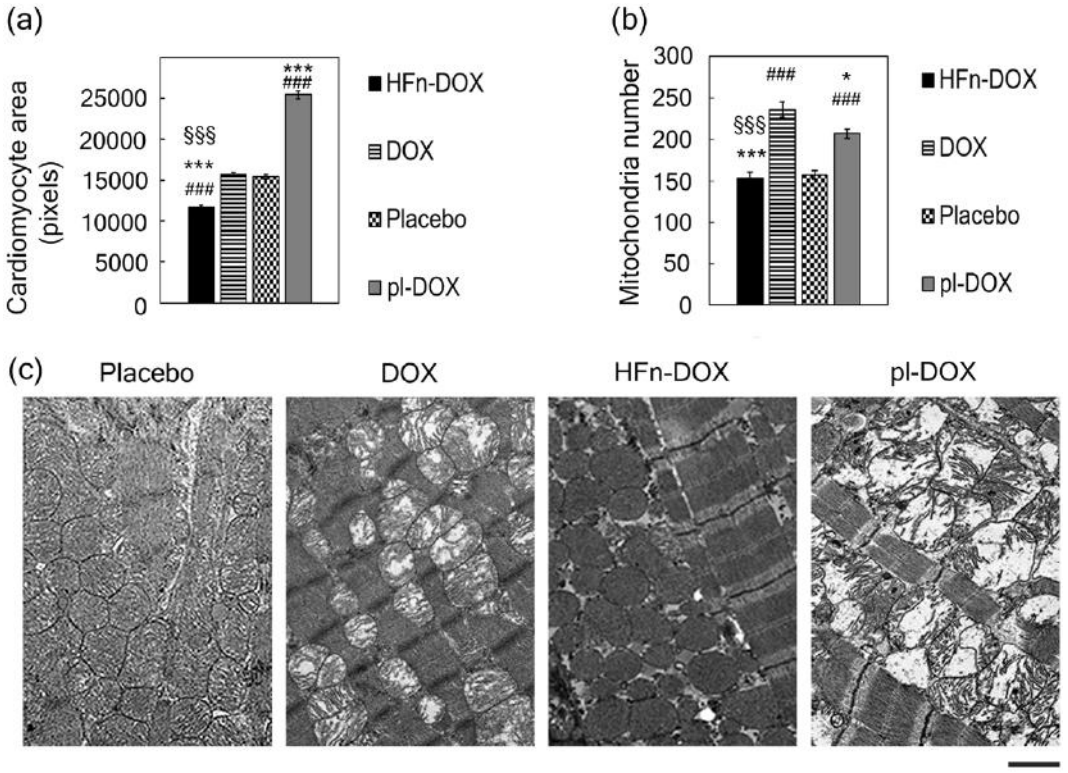

Fig. 3.7 (I) Examination of cardiotoxicity of HFn-DOX, pl-DOX and DOX. a. Nanodelivery protects cardiomyocytes from DOX-induced hypertrophy. Hearts excised at day 21 (n = 3/group) from mice treated with placebo or with 1.24 mg kg^{-1} of DOX, pl-DOX or HFn-DOX were fixed with formalin and embedded in paraffin. Histological slides of cardiac sections stained with FITC-WGA were analyzed with ImageJ software to measure cross-section area of cardiomyocytes. Quantification was performed on at least 5 images/group, reporting the mean value of cross-section area of 250 cells/group± SE. Statistical significance *vs.* Placebo ###*P*<0.00005; *vs.* DOX ***P<0.00005; *vs.* pl-DOX §§§P<0.00005. b. Nanodelivery protects against DOX-induced mitochondrial toxicity. Hearts excised at day 21 (n = 3/group) from mice treated with placebo or with 1.24 mg kg−1 of DOX, pl-DOX or HFn-DOX were fixed with glutaraldehyde and embedded in epoxy-resin. TEM images of ultrathin heart sections of cardiac tissues acquired at 4200 magnifications were analyzed with ImageJ to measure the number of mitochondria in heart tissue. Quantification was performed on at least 9 images/group, reporting the mean mitochondria number/image ± SE. Statistical significance *vs.* Placebo ###*P*<0.00005; *vs.* DOX ***P<0.00005 *P<0.005; *vs.* pl-DOX §§§P<0.00005. c. Representative images of hearts excised at day 21 (n = 3/group) from mice treated with placebo or with 1.24 mg kg−1 of DOX, pl-DOX or HFn-DOX. TEM images of ultrathin heart sections of cardiac tissues have been acquired at 11500 magnifications.

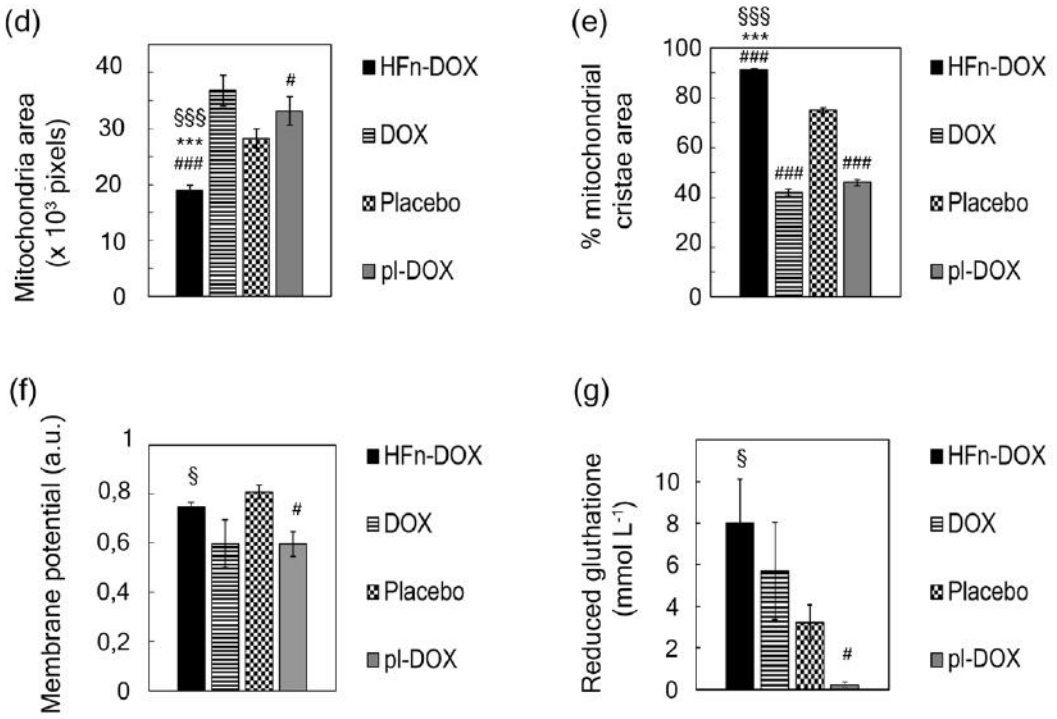

Fig. 3.7 (II) Examination of cardiotoxicity of HFn-DOX, pl-DOX and DOX d. Nanodelivery reduces the mitochondrial size growth due to DOX treatment. Quantification of TEM images (ImageJ) of ultrathin heart sections acquired at 11500 magnifications. Quantification was performed on at least 10 images/group, measuring at least 100 mitochondria/sample. Values represent the mean mitochondrial area ± SE. Statistical significance *vs.* Placebo ###*P*<0.00005 #*P*<0.05; *vs.* DOX ***P<0.00005; *vs.* pl-DOX §§§*P*<0.00005. e. Nano delivery limits the damage of mitochondrial cristae from DOX. Quantification of TEM images (Image J) of ultrathin heart sections acquired at 11500 magnifications. Quantification was performed on at least 10 images/group, measuring at least 100 mitochondria/sample. Values represent the percentage of mitochondrial area occupied by cristae ± SE. Statistical significance *vs.* Placebo ###*P*<0.00005; *vs.* DOX ***P<0.00005; *vs.* pl-DOX §§§*P*<0.00005 f. HFn-DOX does not affect mitochondrial membrane potential. Mitochondrial membrane potential was measured by staining-isolated mitochondria from mouse heart tissue dissected at day 21 (n = 3/group) from mice treated with placebo or with 1.24 mg kg−1 of DOX, pl-DOX or HFn-DOX. Statistical significance *vs.* Placebo #*P*<0.05; *vs*. pl-DOX §*P*<0.05. g. HFn-DOX does not decrease the concentration of reduced GSH. The extent of reduced GSH was measured in lysates of hearts excised at day 21 (n = 3/group) from mice treated with placebo or with 1.24 mg kg−1 of DOX, pl-DOX or HFn-DOX. Values represent the mean GSH concentration in heart extracts± SE. Statistical significance *vs.* Placebo #*P*<0.05; *vs.* pl-DOX §*P*<0.05.

3.5 Conclusions

In the present study a highly aggressive metastatic BC model based on murine 4T1 cells was established. This allowed us to simulate the dramatic clinical picture of advanced BC patients and to evaluate the impact of DOX nanoformulation under LDM monotherapy in compromised subjects, as DOX remains a mainstay therapy in various solid tumors. Our results suggest that DOX monotherapy does not affect tumor progression significantly: although the expected cytotoxicity was confirmed *in vitro*, this did not translate into substantial antitumor activity *in vivo* in an advanced-stage BC model, whereas off-target tissue accumulation and myocardial damage largely occurred. This result is reminiscent of the frustrating clinical condition in which chemotherapy fails to overcome BC progression and combination therapies become necessary to control the disease. Therefore, the potential of LDM DOX to overcome the limitations of dose-dense regimens in advanced-stage tumors remains questionable, since DOX requires high doses to gain a proper drug concentration at cancer deposits[68,69]. In contrast, the results of our study demonstrate that our LDNM strategy, which combines LDM administration of DOX with HFn-delivery resulted in a targeted effect of DOX on 4T1 cancer cells together with a sustained antiangiogenic activity in the tumor microenvironment. Indeed, HFn-DOX exhibited potent antitumor activity when administered at frequent doses as low as 1.24 mg kg^{-1} *in vivo* compared to free DOX and placebo. Such a strongly improved activity correlates with the pharmacokinetic profile of LDNM DOX, as emerged from a recent biodistribution study[70]. Indeed, while DOX displayed reduced bioavailability, high levels of HFn-DOX were recovered in plasma during the first few hours post-injection that were attributable to a lower sequestration by off-target organs[70]. HFn-DOX could accumulate in the tumor site exploiting the EPR effect[71] or by endothelial wall transcytosis promoted by TfR-1 recognition[72] and it is internalized in tumor cells by receptor-mediated endocytosis[73]. HFn-mediated target selectivity conferred earlier intra-tumor activity to the drug, lower off-target accumulation with fast liver metabolism and rapid clearance of circulating excess drug by renal excretion, suggesting optimal therapeutic index in future clinical translation[70,73]. Beyond its favorable bioavailability and target selectivity, a plausible explanation for enhanced antitumor activity of LDNM HFn-DOX resides in HFn propensity to behave like a Trojan horse, imparting DOX with drastically enhanced nuclear penetration even in resistant cancer cells[54,74]. Such HFn property can greatly improve current strategies of LDM chemotherapy, due to sustained nuclear release of a DNA-damaging drug. Indeed, our *in vitro* experiments showed that HFn-mediated delivery allowed a 15.2-fold increase of DOX nuclear concentration within 3 h as compared to the drug alone.

Even drug resistance significantly impacts on BC management, accounting for a relevant proportion of patients in which anthracycline therapy fails to persistently eradicate the tumor[75]. MDR-1 protein is one of the most active multidrug resistance mediators in BC and it is gradually overexpressed under DOX chemotherapy regimens[58]. Negligible MDR-1 induction in tumor cells *in vivo* after LDNM DOX administration suggested that the multidrug resistance machinery of BC cells did not “sense” the cytotoxic agent in HFn-DOX. Otherwise, the dramatic increase of MDR-1 expression observed in samples from mice treated with DOX and even with pl-DOX, suggested that LDNM administration associated with cell nuclear targeting could circumvent DOX resistance dependent by MDR-1.

The general assumption that LDM therapy is essentially due to inhibition of angiogenesis, rather than directly killing residual cancer cells[16], should be reconsidered in the framework of

LDNM regimen, in which a key role of targeted action could be reappraised. Combining our data from angiogenesis inhibition with the results from tumor progression (i.e BC growth curves and DNA fragmentation assay) we concluded that targeted action of HFn-DOX on BC cells and antiangiogenic effect of LDNM regimen could play a synergistic role in the increased antitumor efficacy of HFn-DOX compared to DOX alone.

Importantly, LDNM chemotherapy exhibited a safe toxicity profile, as proven by apparent lack of systemic side effects. This is expected to have great clinical impact because cardiotoxicity and general side effects lead to major restriction in the clinical use of anthracyclines. HFn-DOX was less cardiotoxic compared to DOX and even to pl-DOX, although the latter has been associated with improved cardiac safety in various clinical studies. Nevertheless, myocardial alterations provoked by pl-DOX (Fig. 3.7) are not surprising. Indeed, a certain degree of myocardial damage has been previously demonstrated in endomyocardial biopsies of patients treated with pl-DOX, and ultrastructural damage of pl-DOX has not been explored[67,76]. Moreover, although pl-DOX is less cardiotoxic, it does not significantly reduce relevant cardiac events, and a clinician's preference for pl-DOX over conventional DOX to avoid clinically significant cardiac events is not justified in patients without concurrent cardiac disorders that were not previously subjected to anthracycline exposure[77]. Therefore, the general confidence on low cardiotoxicity of pl-DOX should be reconsidered in the light of these considerations. Otherwise, LDNM treatment with HFn-DOX didn't display anthracycline-related cardiotoxicity, even in comparison with pl-DOX, and it is therefore a promising option for anthracycline therapeutic regimens in cardiosensitive subjects.

We acknowledge a potential limitation relating to immunogenicity in clinical translation of HFn-DOX[78]. Although it is difficult to predict the long-term effect of prolonged treatments in humans, we have collected preliminary data suggesting negligible immunogenicity of HFn in animals. Another limitation of the study is the experimental timespan limited to three weeks. However, based on our findings we could postulate that after 21 days the metronomic treatment by HFn-DOX would lead to further reduction of cancer deposits, as expected by the excellent cytotoxicity showed by HFn- DOX *in vitro*. Moreover, the fact that MDR-1 expression remained stable over time upon treatment with HFn-DOX suggests avoidance of chemoresistance, thus a sustained anticancer activity even after 21 days is expected. About cardiotoxicity, our findings suggest that substantially no myocardial damage is present after treatment with HFn-DOX, and we should expect the same lack in cardiotoxicity even after experimental timespan.

In summary, this study provides robust evidence that LDNM monotherapy with HFn-DOX is expected to remodel the therapeutic outcome of advanced metastatic BC compared to the drug alone and also to improve anthracycline therapies based on liposomal DOX, with a redefinition of the central role of DOX for solid malignancies under the new perspective of metronomic treatments. Further investigations are necessary to thoroughly elucidate the individual contributions of targeted therapy and neoangiogenesis inhibition in the strong enhancement of the antitumor efficacy of HFn- DOX. On the horizon after this study is the possibility of countless developments, one of which is a reappraisal of current clinical settings by combining low toxic LDNM regimens with administration of established antiangiogenic agents.

3.6 Supporting information

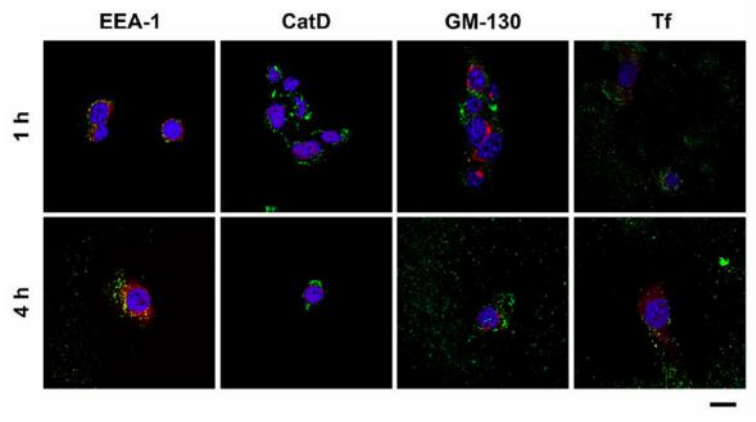

Supplementary Figure S1: Subcellular analysis of HFn interaction with 4T1 BC cells reveals early intracellular localization in endosomes: colocalization with markers of endocytic pathway. Confocal microscopy merged images of 4T1-L cells, incubated for 1, and 4 h at 37 °C with 100 μg mL^{-1} of HFn (green). Early endosomes, lysosomes, Golgi and recycling endosomes were recognized with primary antibodies against early endosome antigen-1 (EEA-1), lysosomal protein Cathepsin D (CatD), Golgi marker 130 (GM-130) and Transferrin (Tf) as recycling endosome marker, respectively, and labeled with an anti-mouse secondary antibody conjugated with Alexa Fluor 546 (red). Nuclei were stained with DAPI (blue). Scale bar: 10 μm.

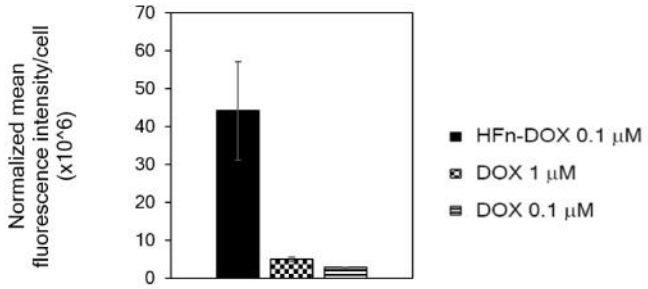

P-value	*vs* DOX 0.1 μM	*vs* DOX 1 μM
HFn-DOX 0.1 μM	0,005395653	0,008592103

Supplementary Figure S2: Quantification of DOX nuclear accumulation *in vitro* upon treatment with DOX or HFn-DOX. Quantification of the mean fluorescence signal of DOX in the nucleus. Reported values are mean of measurements performed with ImageJ software on nuclei of twenty different cells normalized with respect to their area.

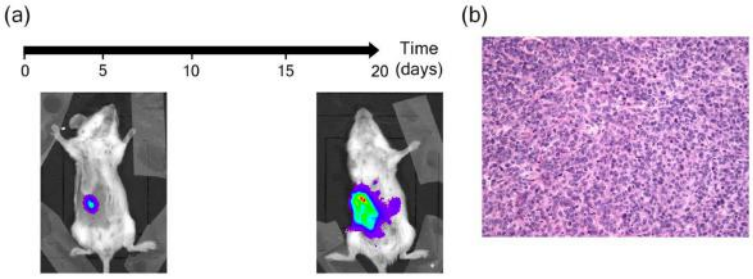

Supplementary Figure S3: Development of 4T1-L breast cancer model: tumor growth and metastasis. a. Balb/C female mice were injected in the mammary fat pad with 10^5 cells/mouse. Bioluminescence intensity emitted upon intraperitoneal injection of luciferin was acquired 5 and 20 days after tumor implantation. b. Hematoxylin-eosin staining of 4T1-L tumor section.

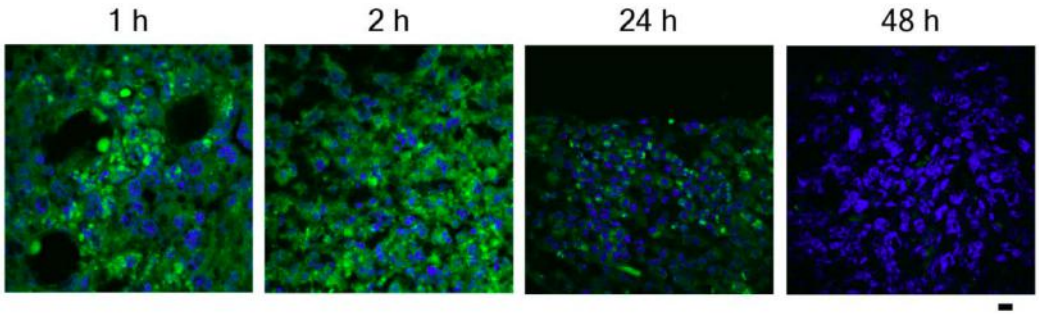

Supplementary Figure S4: HFn nanoparticle localization in tumor cryosections. Confocal microscopy merge images of cryosections obtained from 4T1-L tumors excised 1, 2, 24 and 48 h after HFn (green) intravenous injection. Nuclei were stained with DAPI (blue). Scale bar: 10 µm.

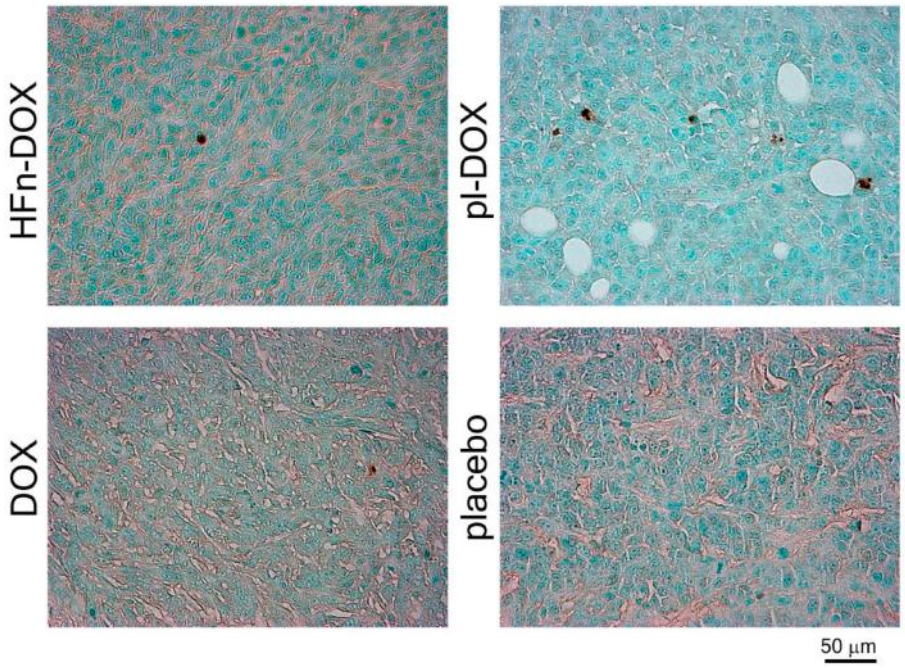

Supplementary Figure S5: Immunohistochemistry of Apoptosis assay in tumor. Representative images of tumors excised at day 21 (n = 6/group) from mice treated with placebo and 1.24 mg kg^{-1} of DOX, pl-DOX or HFn-DOX. Samples were fixed with formalin, embedded in paraffin and histological slides were stained with Tumor TACS In Situ Apoptosis Detection kit to reveal apoptosis.

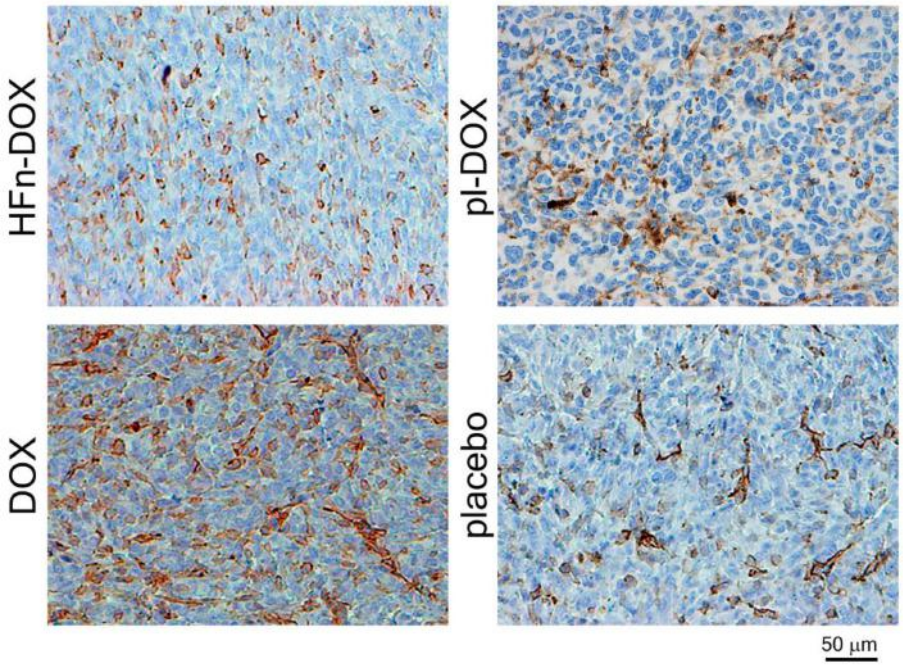

Supplementary Figure S6: Immunohistochemistry of CD31 expression in tumor. Representative images of tumors excised at day 21 (n = 5/group) from mice treated with placebo and 1.24 mg kg^{-1} of DOX, pl-DOX or HFn-DOX. Samples were fixed with formalin, embedded in paraffin and histological slides were subjected to immunohistochemistry staining with the CD-31 antibody to reveal tumor angiogenesis.

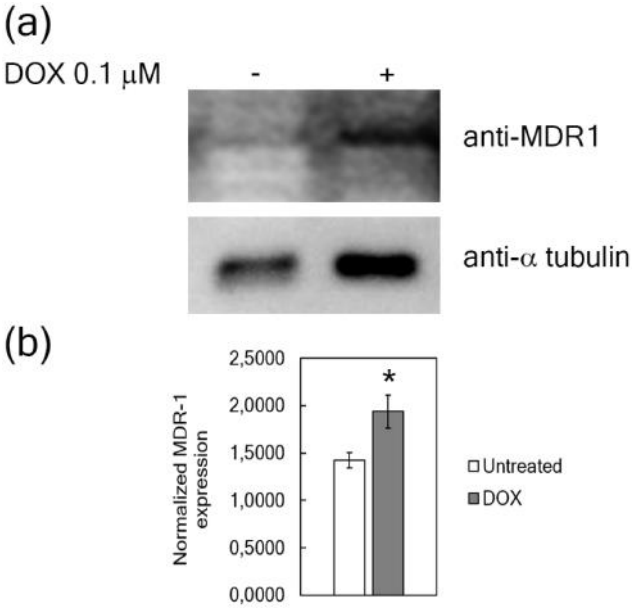

Supplementary Figure S7: Basal and DOX-induced expression of MDR-1 in 4T1-L cells. a. 4T1-L cells incubated for 72 h with or without DOX 0.1 μM were lysed. Whole cell extracts were loaded on SDS-PAGE application buffer, electrophoresed and immunoblotted using either anti-MDR-1 and anti-αtubulin antibodies. b. Quantification of the relative intensities of immunoblotted bands performed using ImageJ. Reported values represent the mean ± SE (n = 3). *$P<0.05(0.026)$.

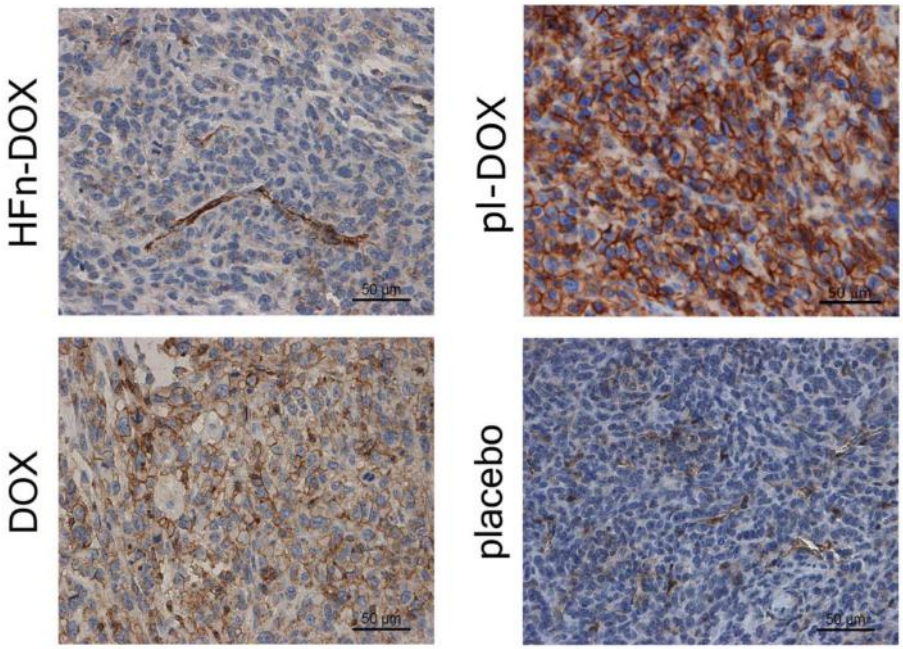

Supplementary Figure S8: Immunohistochemistry of MDR-1 expression in tumor. Representative images of tumors excised at day 21 (n = 5/group) from mice treated with placebo and 1.24 mg kg^{-1} of DOX, pl-DOX or HFn-DOX. Samples were fixed with formalin, embedded in paraffin and histological slides were subjected to immunohistochemistry staining with the rabbit monoclonal antibody anti- MDR-1 to reveal MDR-1 overexpression. Scale bar = 50 µm.

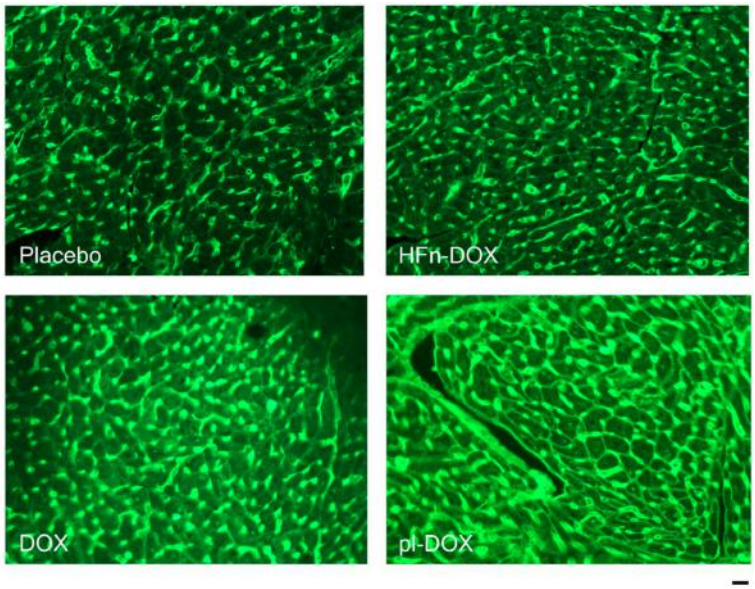

Supplementary Figure S9: Fluorescence images of WGA-labeled cardiomyocytes membrane. Representative fluorescence images of hearts excised at day 21 (n = 3/group) from mice treated with placebo or with 1.24 mg kg^{-1} of DOX, pl-DOX or HFn-DOX. Samples were fixed with formalin, embedded in paraffin and histological slides were stained with FITC-conjugated Wheat Germ Agglutinin.

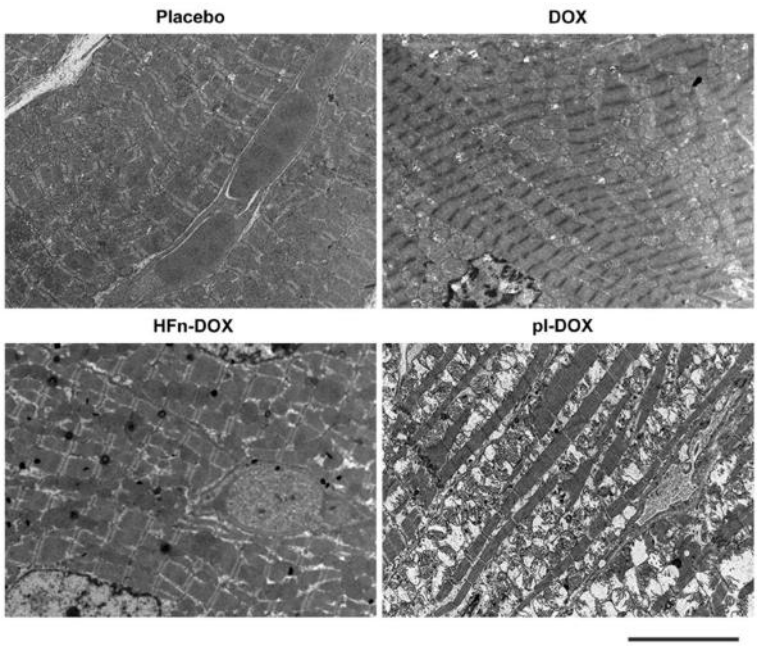

Supplementary Figure S10: Ultrastructural evaluation of heart tissue sections after LDNM chemotherapy cycle. Representative TEM images of hearts excised at day 21 (n = 3/group) from mice treated with placebo and with 1.24 mg kg^{-1} of DOX, pl-DOX or HFn-DOX. TEM images of ultrathin heart sections of cardiac tissues have been acquired at 4200× magnification. Scale bar: 5 µm.

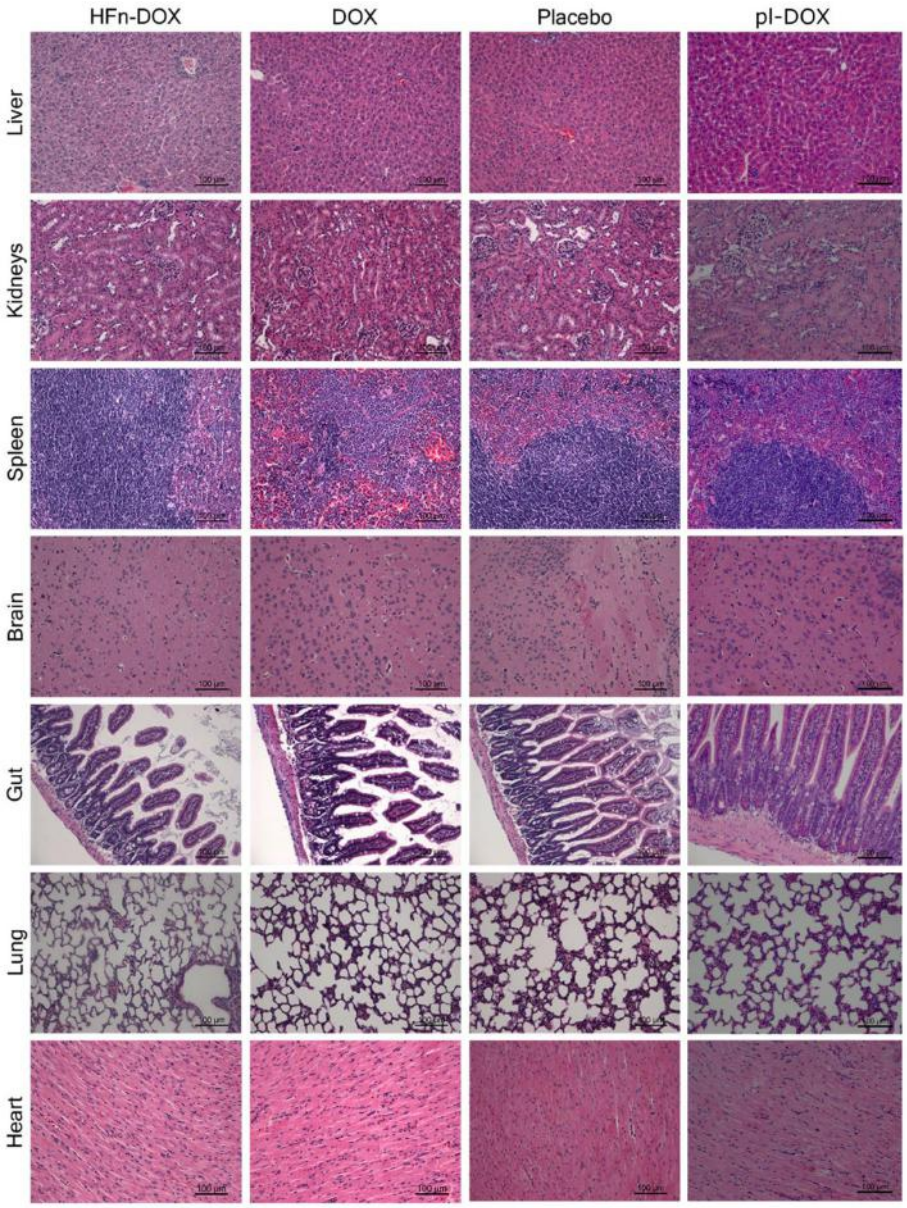

Supplementary Figure S11: Histopathology of liver, spleen, kidneys, lungs, heart, gut and brain after LDNM treatment. Histopathological analysis of tissue samples. No histological lesions were observed in liver, spleen, kidneys, lungs, heart, gut and brain. Hematoxylin-eosin staining. Magnification 20×.

3.7 References

1. Mazzucchelli, S. *et al.* Nanometronomic treatment of 4T1 breast cancer with nanocaged doxorubicin prevents drug resistance and circumvents cardiotoxicity. *Oncotarget* (2016). doi:10.18632/oncotarget.14204
2. Kareva, I., Waxman, D. J. & Lakka Klement, G. Metronomic chemotherapy: an attractive alternative to maximum tolerated dose therapy that can activate anti-tumor immunity and minimize therapeutic resistance. *Cancer Lett.* **358,** 100–106 (2015).
3. Loven, D., Hasnis, E., Bertolini, F. & Shaked, Y. Low-dose metronomic chemotherapy: from past experience to new paradigms in the treatment of cancer. *Drug Discov. Today* **18,** 193–201 (2013).
4. Kaur, H. & Budd, G. T. Metronomic therapy for breast cancer. *Curr. Oncol. Rep.* **6,** 49–52 (2004).
5. Skipper, H. E. *et al.* Implications of biochemical, cytokinetic, pharmacologic, and toxicologic relationships in the design of optimal therapeutic schedules. *Cancer Chemother. Rep.* **54,** 431–450 (1970).
6. Pasquier, E., Kavallaris, M. & André, N. Metronomic chemotherapy: new rationale for new directions. *Nat. Rev. Clin. Oncol.* **7,** 455–465 (2010).
7. Cao, Y. & Langer, R. Optimizing the Delivery of Cancer Drugs That Block Angiogenesis. *Sci. Transl. Med.* **2,** 15ps3-15ps3 (2010).
8. Savage, P., Stebbing, J., Bower, M. & Crook, T. Why does cytotoxic chemotherapy cure only some cancers? *Nat. Clin. Pract. Oncol.* **6,** 43–52 (2009).
9. Hanahan, D. & Weinberg, R. A. The hallmarks of cancer. *Cell* **100,** 57–70 (2000).
10. Bergers, G. & Hanahan, D. Modes of resistance to anti-angiogenic therapy. *Nat. Rev. Cancer* **8,** 592–603 (2008).
11. Gasparini, G. Metronomic scheduling: the future of chemotherapy? *Lancet Oncol.* **2,** 733–740 (2001).
12. Kerbel, R. S., Klement, G., Pritchard, K. I. & Kamen, B. Continuous low-dose anti-angiogenic/metronomic chemotherapy: from the research laboratory into the oncology clinic. *Ann. Oncol.* **13,** 12–15 (2002).
13. Klement, G. *et al.* Continuous low-dose therapy with vinblastine and VEGF receptor-2 antibody induces sustained tumor regression without overt toxicity. *J. Clin. Invest.* **105,** R15-24 (2000).
14. Browder, T. *et al.* Antiangiogenic scheduling of chemotherapy improves efficacy against experimental drug-resistant cancer. *Cancer Res.* **60,** 1878–1886 (2000).
15. Hanahan, D., Bergers, G. & Bergsland, E. Less is more, regularly: metronomic dosing of cytotoxic drugs can target tumor angiogenesis in mice. *J. Clin. Invest.* **105,** 1045–1047 (2000).
16. Kerbel, R. S. & Kamen, B. A. The anti-angiogenic basis of metronomic chemotherapy. *Nat. Rev. Cancer* **4,** 423–436 (2004).
17. Kerbel, R. S. Improving conventional or low dose metronomic chemotherapy with targeted antiangiogenic drugs. *Cancer Res. Treat. Off. J. Korean Cancer Assoc.* **39,** 150–159 (2007).
18. Abu Lila, A. S. & Ishida, T. Metronomic chemotherapy and nanocarrier platforms. *Cancer Lett.* (2016). doi:10.1016/j.canlet.2016.11.007

19. Bocci, G., Nicolaou, K. C. & Kerbel, R. S. Protracted low-dose effects on human endothelial cell proliferation and survival in vitro reveal a selective antiangiogenic window for various chemotherapeutic drugs. *Cancer Res.* **62,** 6938–6943 (2002).
20. Klement, G. *et al.* Differences in therapeutic indexes of combination metronomic chemotherapy and an anti-VEGFR-2 antibody in multidrug-resistant human breast cancer xenografts. *Clin. Cancer Res. Off. J. Am. Assoc. Cancer Res.* **8,** 221–232 (2002).
21. Tran, J. *et al.* A role for survivin in chemoresistance of endothelial cells mediated by VEGF. *Proc. Natl. Acad. Sci. U. S. A.* **99,** 4349–4354 (2002).
22. Bertolini, F. *et al.* Maximum tolerable dose and low-dose metronomic chemotherapy have opposite effects on the mobilization and viability of circulating endothelial progenitor cells. *Cancer Res.* **63,** 4342–4346 (2003).
23. Shih, T. & Lindley, C. Bevacizumab: an angiogenesis inhibitor for the treatment of solid malignancies. *Clin. Ther.* **28,** 1779–1802 (2006).
24. Kerbel, R. S. Inhibition of tumor angiogenesis as a strategy to circumvent acquired resistance to anti-cancer therapeutic agents. *BioEssays News Rev. Mol. Cell. Dev. Biol.* **13,** 31–36 (1991).
25. Greaves, M. & Maley, C. C. Clonal evolution in cancer. *Nature* **481,** 306–313 (2012).
26. Reya, T., Morrison, S. J., Clarke, M. F. & Weissman, I. L. Stem cells, cancer, and cancer stem cells. *Nature* **414,** 105–111 (2001).
27. Folkins, C. *et al.* Anticancer therapies combining antiangiogenic and tumor cell cytotoxic effects reduce the tumor stem-like cell fraction in glioma xenograft tumors. *Cancer Res.* **67,** 3560–3564 (2007).
28. Lutsiak, M. E. C. *et al.* Inhibition of CD4+25+ T regulatory cell function implicated in enhanced immune response by low-dose cyclophosphamide. *Blood* **105,** 2862–2868 (2005).
29. Tanaka, H., Matsushima, H., Mizumoto, N. & Takashima, A. Classification of chemotherapeutic agents based on their differential in vitro impacts on dendritic cells. *Cancer Res.* **69,** 6978–6986 (2009).
30. Aguirre-Ghiso, J. A. Models, mechanisms and clinical evidence for cancer dormancy. *Nat. Rev. Cancer* **7,** 834–846 (2007).
31. Sosa, M. S., Bragado, P. & Aguirre-Ghiso, J. A. Mechanisms of disseminated cancer cell dormancy: an awakening field. *Nat. Rev. Cancer* **14,** 611–622 (2014).
32. Colleoni, M. *et al.* Low-dose oral methotrexate and cyclophosphamide in metastatic breast cancer: antitumor activity and correlation with vascular endothelial growth factor levels. *Ann. Oncol.* **13,** 73–80 (2002).
33. González-Billalabeitia, E. *et al.* Long-Term Follow-Up of an Anthracycline-Containing Metronomic Chemotherapy Schedule in Advanced Breast Cancer. *Breast J.* **15,** 551–553 (2009).
34. Bottini, A. *et al.* Randomized Phase II Trial of Letrozole and Letrozole Plus Low-Dose Metronomic Oral Cyclophosphamide As Primary Systemic Treatment in Elderly Breast Cancer Patients. *J. Clin. Oncol.* **24,** 3623–3628 (2006).
35. Orlando, L. *et al.* Trastuzumab in combination with metronomic cyclophosphamide and methotrexate in patients with HER-2 positive metastatic breast cancer. *BMC Cancer* **6,** 225 (2006).
36. García-Sáenz, J. A. *et al.* Bevacizumab in combination with metronomic chemotherapy in patients with anthracycline- and taxane-refractory breast cancer. *J. Chemother. Florence*

Italy **20,** 632–639 (2008).
37. Maraveyas, A., Lam, T., Hetherington, J. W. & Greenman, J. Can a rational design for metronomic chemotherapy dosing be devised? *Br. J. Cancer* **92,** 1588–1590 (2005).
38. Cruz-Muñoz, W. *et al.* Analysis of acquired resistance to metronomic oral topotecan chemotherapy plus pazopanib after prolonged preclinical potent responsiveness in advanced ovarian cancer. *Angiogenesis* **17,** 661–673 (2014).
39. Yu, D.-H. *et al.* The use of nanoparticulate delivery systems in metronomic chemotherapy. *Biomaterials* **34,** 3925–3937 (2013).
40. Nars, M. S. & Kaneno, R. Immunomodulatory effects of low dose chemotherapy and perspectives of its combination with immunotherapy. *Int. J. Cancer* **132,** 2471–2478 (2013).
41. Veronesi, U., Stafyla, V., Luini, A. & Veronesi, P. Breast cancer: from 'maximum tolerable' to 'minimum effective' treatment. *Front. Oncol.* **2,** 125 (2012).
42. André, N., Carré, M. & Pasquier, E. Metronomics: towards personalized chemotherapy? *Nat. Rev. Clin. Oncol.* **11,** 413–431 (2014).
43. Kerbel, R. S. & Grothey, A. Gastrointestinal cancer: Rationale for metronomic chemotherapy in phase III trials. *Nat. Rev. Clin. Oncol.* **12,** 313–314 (2015).
44. Morris, P. G. & Hudis, C. A. Optimizing dose-dense regimens for early-stage breast cancer. *Nat. Rev. Clin. Oncol.* **7,** 678–679 (2010).
45. Kerbel, R. S. Antiangiogenic therapy: a universal chemosensitization strategy for cancer? *Science* **312,** 1171–1175 (2006).
46. Ng, S. S. W. *et al.* Influence of formulation vehicle on metronomic taxane chemotherapy: albumin-bound versus cremophor EL-based paclitaxel. *Clin. Cancer Res. Off. J. Am. Assoc. Cancer Res.* **12,** 4331–4338 (2006).
47. Riganti, C. *et al.* Two repeated low doses of doxorubicin are more effective than a single high dose against tumors overexpressing P-glycoprotein. *Cancer Lett.* **360,** 219–226 (2015).
48. Lotrionte, M. *et al.* Review and meta-analysis of incidence and clinical predictors of anthracycline cardiotoxicity. *Am. J. Cardiol.* **112,** 1980–1984 (2013).
49. Octavia, Y. *et al.* Doxorubicin-induced cardiomyopathy: from molecular mechanisms to therapeutic strategies. *J. Mol. Cell. Cardiol.* **52,** 1213–1225 (2012).
50. Rivera, E. Current Status of Liposomal Anthracycline Therapy in Metastatic Breast Cancer. *Clin. Breast Cancer* **4,** S76–S83 (2003).
51. Xing, M., Yan, F., Yu, S. & Shen, P. Efficacy and Cardiotoxicity of Liposomal Doxorubicin-Based Chemotherapy in Advanced Breast Cancer: A Meta-Analysis of Ten Randomized Controlled Trials. *PLOS ONE* **10,** e0133569 (2015).
52. Corsi, F. & Mazzucchelli, S. The potential of protein-based nanocages for imaging and drug delivery. *Ther. Deliv.* **7,** 149–151 (2016).
53. Fan, K. *et al.* Magnetoferritin nanoparticles for targeting and visualizing tumour tissues. *Nat. Nanotechnol.* **7,** 459–464 (2012).
54. Bellini, M. *et al.* Protein nanocages for self-triggered nuclear delivery of DNA-targeted chemotherapeutics in Cancer Cells. *J. Controlled Release* **196,** 184–196 (2014).
55. Zhang, L. *et al.* H-Chain Ferritin: A Natural Nuclei Targeting and Bioactive Delivery Nanovector. *Adv. Healthc. Mater.* **4,** 1305–1310 (2015).
56. Liang, M. *et al.* H-ferritin-nanocaged doxorubicin nanoparticles specifically target and kill tumors with a single-dose injection. *Proc. Natl. Acad. Sci. U. S. A.* **111,** 14900–14905 (2014).

57. Laginha, K. M., Verwoert, S., Charrois, G. J. R. & Allen, T. M. Determination of doxorubicin levels in whole tumor and tumor nuclei in murine breast cancer tumors. *Clin. Cancer Res. Off. J. Am. Assoc. Cancer Res.* **11,** 6944–6949 (2005).
58. Bao, L. *et al.* Increased expression of P-glycoprotein is associated with doxorubicin chemoresistance in the metastatic 4T1 breast cancer model. *Am. J. Pathol.* **178,** 838–852 (2011).
59. Pulaski, B. A. & Ostrand-Rosenberg, S. Mouse 4T1 breast tumor model. *Curr. Protoc. Immunol.* **Chapter 20,** Unit 20.2 (2001).
60. Aslakson, C. J. & Miller, F. R. Selective events in the metastatic process defined by analysis of the sequential dissemination of subpopulations of a mouse mammary tumor. *Cancer Res.* **52,** 1399–1405 (1992).
61. Fiandra, L. *et al.* Assessing the in vivo targeting efficiency of multifunctional nanoconstructs bearing antibody-derived ligands. *ACS Nano* **7,** 6092–6102 (2013).
62. Mayer, L. D., Dougherty, G., Harasym, T. O. & Bally, M. B. The role of tumor-associated macrophages in the delivery of liposomal doxorubicin to solid murine fibrosarcoma tumors. *J. Pharmacol. Exp. Ther.* **280,** 1406–1414 (1997).
63. Guo, Z., Zhu, J., Zhao, L., Luo, Q. & Jin, X. Expression and clinical significance of multidrug resistance proteins in brain tumors. *J. Exp. Clin. Cancer Res.* **29,** 122 (2010).
64. Khiati, S. *et al.* Mitochondrial topoisomerase I (top1mt) is a novel limiting factor of doxorubicin cardiotoxicity. *Clin. Cancer Res. Off. J. Am. Assoc. Cancer Res.* **20,** 4873–4881 (2014).
65. Tsutsui, H., Kinugawa, S. & Matsushima, S. Oxidative stress and heart failure. *Am. J. Physiol. Heart Circ. Physiol.* **301,** H2181-2190 (2011).
66. Marí, M., Morales, A., Colell, A., García-Ruiz, C. & Fernández-Checa, J. C. Mitochondrial Glutathione, a Key Survival Antioxidant. *Antioxid. Redox Signal.* **11,** 2685–2700 (2009).
67. Berry, G. *et al.* The use of cardiac biopsy to demonstrate reduced cardiotoxicity in AIDS Kaposi's sarcoma patients treated with pegylated liposomal doxorubicin. *Ann. Oncol. Off. J. Eur. Soc. Med. Oncol.* **9,** 711–716 (1998).
68. Todorova, V. K., Kaufmann, Y. & Klimberg, V. S. Increased efficacy and reduced cardiotoxicity of metronomic treatment with cyclophosphamide in rat breast cancer. *Anticancer Res.* **31,** 215–220 (2011).
69. Mainetti, L. E. *et al.* Therapeutic efficacy of metronomic chemotherapy with cyclophosphamide and doxorubicin on murine mammary adenocarcinomas. *Ann. Oncol. Off. J. Eur. Soc. Med. Oncol.* **24,** 2310–2316 (2013).
70. Mazzucchelli, S. *et al.* LC–MS/MS method development for quantification of doxorubicin and its metabolite 13-hydroxy doxorubicin in mice biological matrices: Application to a pharmaco-delivery study. *Biomed. Chromatogr.* n/a-n/a (2016). doi:10.1002/bmc.3863
71. Fisher, J. *et al.* Ferritin: a novel mechanism for delivery of iron to the brain and other organs. *Am. J. Physiol. Cell Physiol.* **293,** C641-649 (2007).
72. Li, L. *et al.* Binding and uptake of H-ferritin are mediated by human transferrin receptor-1. *Proc. Natl. Acad. Sci. U. S. A.* **107,** 3505–3510 (2010).
73. Sengupta, S. *et al.* Temporal targeting of tumour cells and neovasculature with a nanoscale delivery system. *Nature* **436,** 568–572 (2005).
74. Alkhateeb, A. A. & Connor, J. R. Nuclear ferritin: A new role for ferritin in cell biology. *Biochim. Biophys. Acta BBA - Gen. Subj.* **1800,** 793–797 (2010).

75. Wood, K. C. Mapping the Pathways of Resistance to Targeted Therapies. *Cancer Res.* **75,** 4247–4251 (2015).
76. Gabizon, A. A., Lyass, O., Berry, G. J. & Wildgust, M. Cardiac safety of pegylated liposomal doxorubicin (Doxil/Caelyx) demonstrated by endomyocardial biopsy in patients with advanced malignancies. *Cancer Invest.* **22,** 663–669 (2004).
77. Yamaguchi, N. *et al.* Comparison of cardiac events associated with liposomal doxorubicin, epirubicin and doxorubicin in breast cancer: a Bayesian network meta-analysis. *Eur. J. Cancer Oxf. Engl. 1990* **51,** 2314–2320 (2015).
78. Truffi, M. *et al.* Ferritin nanocages: A biological platform for drug delivery, imaging and theranostics in cancer. *Pharmacol. Res.* **107,** 57–65 (2016).

CHAPTER 4

Curcumin-encapsulated ferritin as chemosensitizer in triple negative breast cancer cell lines

4.1 Curcumin

4.1.1 A survey of history

Turmeric (*Curcuma longa*) is an herbaceous plant that belongs to the ginger family and is widely cultivated in southern and south-western regions of tropical Asia; India is currently the largest producing, consumer and exporter country. Turmeric was mentioned in the writings of the Italian explorer Marco Polo, concerning his voyage to China and India around 1280 ad., but it was first introduced in Europe only in the 13th century by Arabian traders. The Latin name *Curcuma* is derived from the Arabic word "Kourkoum" which was the original name for saffron, and as a consequence of its golden color, *Curcuma* became known as "Indian Saffron" in Europe. During the British rule of India, turmeric was combined with various other spices and renamed "curry powder" as it is currently known in the West[1,2].

For many centuries this golden spice has been used in the diet of several countries, including Iran, Malaysia, India, China, Polynesia and Thailand, not only as a component of food but also to treat a wide variety of ailments. In addition, the brilliant yellow color of turmeric, which persists even at very high dilutions, found its way to commercial use as a coloring agent for various items, including cotton, silk, paper, wood, foodstuffs (food additive E100), and cosmetics.

In Ayurveda (science of long life) turmeric has been used since the second millennium BC for many conditions, internally as a stomachic, tonic, and blood purifier and topically in the prevention and treatment of skin diseases. Interests in this plant have grown in recent years due to its vast array of beneficial pharmacological effects such as antioxidant, anti-inflammatory, anticarcinogenic, antibacterial, wound healing, antispasmodic and anticoagulant activities[4]. Extensive research within the last half century has proven that most of these activities, once associated with turmeric, are due to curcumin, a yellow-orange colored lipophilic polyphenol extract from dried rhizome of *Curcuma longa*. Although turmeric has been consumed as a dietary spice and a cure, the biological characteristics of curcumin were not scientifically identified until the mid-twentieth century. In a paper published in *Nature* in 1949, Scharaufstatter and colleagues reported that curcumin has anti-bacterial properties against strains of *Staphylococcus aureus*, *Salmonella paratyphi* and *Mycobacterium tuberculosis*[5]. Only in the 1970s curcumin became the subject of scientific investigation, which led to the discovery of its other pharmacological activities. Later, in the 1980s, Kuttan and colleagues demonstrated the anti-cancer activity of curcumin in both *in vitro* and *in vivo* models[6] and in 1995 Aggarwal's group demonstrated the anti-inflammatory activity by suppressing NF-kB[7]. Surprisingly, the first clinical trial was reported already in 1937, in *Lancet*, against biliary diseases[8]. Over the years, curcumin has been shown to exhibit a wide range of pharmacological activities, like antioxidant, anti-inflammatory, antiviral, antibacterial, antifungal, and anticancer and thus it has a potential against many malignant diseases, such as Alzheimer's disease, atherosclerosis, allergies, type II diabetes, rheumatoid arthritis, multiple sclerosis and other chronic illnesses. Evidence indicates that the divergent effects of curcumin are dependent on its pleiotropic molecular effects, which include the regulation of various transcription factors, growth factors, inflammatory cytokines, protein kinases, and other enzymes[2]. Moreover, curcumin is non-toxic even at high dose, so it could have multiple benefits associate with a safety profile: the U.S. Food and Drug Administration has approved curcumin as a "generally regarded as safe" compound[9,10]. Dose-escalating studies have demonstrated the safety of consuming up to 12 g

of curcumin per day, with no detrimental effects[11]. Considering the scientific concept that multitargeted therapy is better than monotargeted therapy for most diseases, curcumin can be considered an ideal “Spice for Life”. Anyway, most of the known activities of curcumin are based only on *in vitro* and *in vivo* studies and curcumin has yet not been approved for treatment of any human disease[10].

4.1.2 Structure and features

Curcuma spp. contains turmerin (a water soluble peptide), essential oils (such as turmerones and zingiberene) and curcuminoids, including curcumin. Curcumin is the phytochemical that gives a yellow color to turmeric and depending on origin and soil conditions, it is estimated that turmeric contains 2–10% of curcuminoids, among which curcumin is the major component[2].

Curcumin was first isolated from turmeric in 1815 by Vogel and Pelletier[12] and in 1910 Milobedzka and Lampe identified its chemical structure as diferuloylmethane[13]. In 1918 Lampe for the first time synthesized curcumin, in five steps, then a lot of methods to synthesize curcumin and its analogues were established[14].

Curcumin is a symmetrical molecule, the IUPAC name is [(E,E)-1,7-bis(4-hydroxy-3-methoxyphenyl)-1,6-heptadiene-3,5-ione], with molecular formula $C_{21}H_{20}O_6$ and molecular weight of 368.39 g mol^{-1} (Fig. 4.1). In its structure it presents three chemical entities: two aromatic ring systems, each of which carries two methoxy and two hydroxyl groups, connected by a seven carbons linker, which has an α,β-unsaturated β-diketone moiety. The diketonic group is subject to keto-enol tautomerism and exists in different conformers depending on the conditions, but the enol form is generally more stable[15]. Due to extended conjugation, the π electron cloud is all along the molecule. The two symmetrically arranged chromophores and the conjugated double bond give curcumin its yellow color[13]. The absorption spectrum of this molecule is characterized by the presence of two strong bands, one in the visible region, between 410 and 430 nm and another band in the UV region with a maximum at 265 nm. The absorption is highest in organic solvent and drastically reduced in aqueous solutions. Moreover, changing pH values the absorption spectra show different profiles and absorption intensity[3].

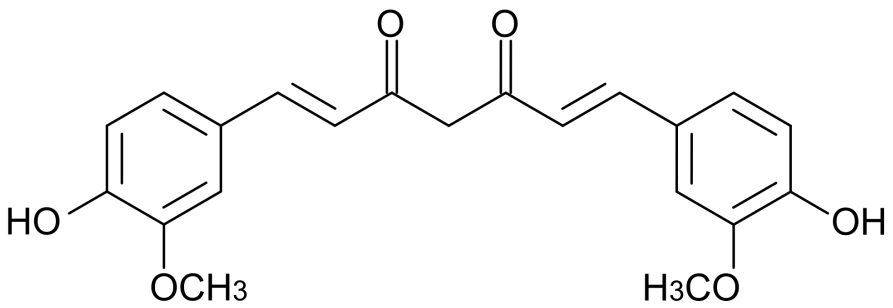

Fig. 4.1 Curcumin chemical structure.

Curcumin has a high hydrophobicity with a LogP value of about 3.0. It is very slightly soluble in water (about 0.0004 mg/ml at pH 7.3) and readily soluble in polar solvents such as DMSO, methanol, ethanol, acetonitrile, chloroform, ethyl acetate and in concentrated acetic acid. Curcumin is a weak Brönsted acid, with three labile protons, and accordingly three pK_a have been estimated (Fig. 4.2). The first pK_a in the pH range of 7.5 to 8.5 changes curcumin color from yellow to red. The solubility of the anionic curcumin increases at basic pH and this form of curcumin is more water soluble than the neutral one, while there is still a debate which one of the three -OH groups is the most acidic[16]. Aqueous curcumin solutions can be prepared also by adding surfactants, lipids or cyclodextrins.

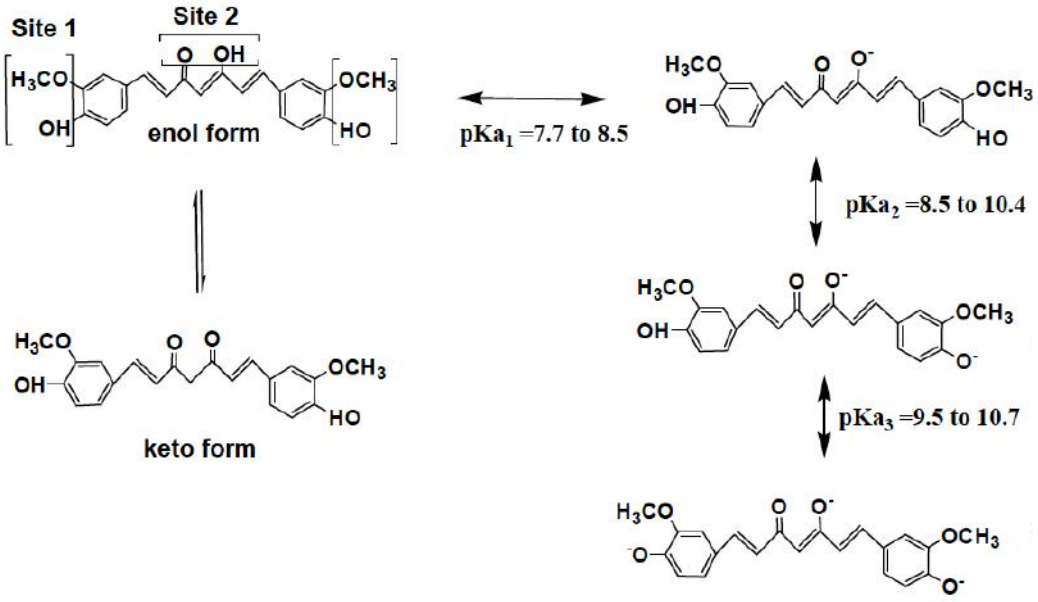

Fig. 4.2 Keto-enol tautomerism and prototropic equilibria of curcumin[16].

Curcumin reactivity

The three reactive sites of curcumin, the diketone and the two phenol groups, are responsible for the excellent properties scavenger of ROS, as all these groups can undergo oxidation by electron transfer (REV Molecules 2014). The α,β-unsaturated β-diketo moiety of curcumin participates also in nucleophilic addition reactions (also known as Michael addition) and these are extremely useful to explain the biological chemistry of curcumin in living cells, for example as regards the reaction of thiols like glutathione. Furthermore, the diketonic portion has excellent binding properties and makes the molecule a monobasic bidentate ligand capable of forming stable complexes with almost all metals and non-metals[16].

Curcumin stability

Curcumin is subjected to an easy degradation in aqueous solutions and its stability is pH dependent. Curcumin is most stable at pH 1-6 but becomes unstable at pH >7. In dilute solutions (micromolar) the 90% curcumin degrades in 30 minutes under physiological conditions (0.1 M

phosphate buffer, pH 7.2, 37 °C), but this percentage decreases at high concentrations or when curcumin is linked to lipids, liposomes, cyclodextrins or other macromolecular system[17]. Several degradation products have been identified, among them: trans-6(4'-hydroxy-3'-methoxyphenyl)-2,4-dioxo-5-hexanal, ferulic aldehyde, ferulic acid, vanillin and feruloylmethane[3,16] (Fig. 4.3). The degradation proceeds according to first-order kinetics[17] (Wang 1997). Furthermore, curcumin is light-sensitive so it will degrade much more quickly when exposed to sunlight: it is a common observation that curcumin stains can be removed by exposure to light, as the products generated by the photodegradation are vanillin, ferulic acid and other small phenols, all colorless[18].

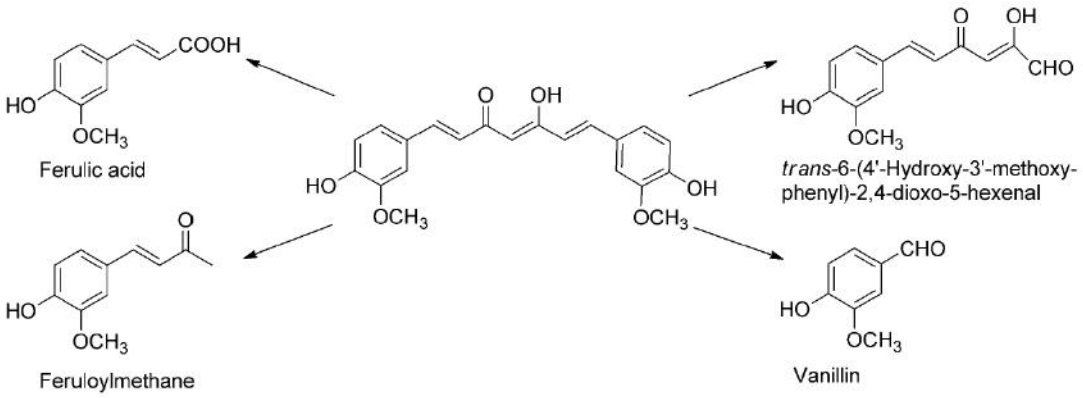

Fig. 4.3 Chemical structures of degradation products of curcumin (0.1 M phosphate buffer, pH 7.2, 37 °C)[3].

4.1.3 Bioavailability and metabolism

The bioavailability of curcumin has been studied in numerous investigations and even if what happens in rats and humans is only partially comparable, generally curcumin oral bioavailability is inadequate due to a relatively low intestinal absorption and a rapid metabolism in the liver, followed by elimination through the gall bladder[3]. The metabolites in rodents were characterized mainly as glucuronides of tetrahydrocurcumin and hexahydrocurcumin (Aggarwal book), but part of the curcumin is eliminated unchanged through the feces[19].

In human, plasma level of curcumin are often below 1 μmol L^{-1}, also after oral ingestion of high doses (in the gram range)[3]. Curcumin is metabolized by phase I and II enzymes and two major pathways have been identified: reduction and O-conjugation. The reduction products are tetrahydrocurcumin (THC), hexahydrocurcumin and other minor products including ferulic acid, while O-conjugation products are curcumin glucuronide and curcumin sulfate. The formation of such products was confirmed by HPLC and mass spectrometry while the enzymes involved in these reactions are still under investigation[16].

4.1.4 Biological activity and molecular target

At molecular level, curcumin has been shown to modulate a wide range of signaling molecules, that can be upregulate or downregulate. These include transcriptor factors, inflammatory

cytokines, enzymes, kinases, growth factors, receptors and various other proteins. Transcription factors are proteins that bind DNA at a specific promoter or enhancer region or site and act like "genetic switches" to regulate the expression of various genes. Curcumin targets transcription factors to prevent pathways that are harmful to cells' normal growth. Among the most important targets of curcumin, in fact, there are some pro-inflammatory transcriptor factors, such as the nuclear factor κB (NF-κB), the activator protein-1 (AP-1) and STAT proteins, which regulate the expression of genes involved in tumorigenesis, cell survival, cell proliferation, invasion and angiogenesis. Curcumin has been shown to negatively regulate this factors[10]. At cellular level, curcumin can reduce inflammatory response by modulating the production of pro-inflammatory molecules like cytokines. Its activity as an anti-oxidant and free-radical scavenger is related to the presence of both the β-diketone and the methoxy groups. But also, curcumin induces endogenous antioxidant defense mechanism and the redox-regulated transcriptor factor Nrf2 plays a key role in this process[3].

Another major target of curcumin is represented by protein kinases, like the epidermal growth factor receptor, protein kinase C, the mitogen-activated protein kinase (MAPK) and the PI3K/AKT pathway (Gupta 2012). All these protein are inhibited by curcumin in cancer cells[20,21]. Finally, curcumin mediated the expression of matrix metalloproteinase 9 (MMP-9), urokinase plasminogen activator (uPA) and its receptor (uPAR), intercellular adhesion molecule 1 (ICAM-1), and chemokine receptor 4[22].

By way of example and in order to better understand the vastness of action of curcumin, we go on to describe what can be considered one of his major target, NF-kB.

NF-κB

Nuclear factor κB (NF-κB) is a ubiquitously expressed eukaryotic transcription factor, responsible for the regulation of numerous genes involved in controlling cellular proliferation and growth, inflammatory responses, cell adhesion, and so forth. The functionally active NF-κB exists mainly as a heterodimer consisting of subunits of the Rel family which is normally sequestered in an inactive cytoplasmic complex by binding to an inhibitory protein, IκB. Exposure of cells to such external stimuli as bacterial lipopolysaccharides (LPS), ROS or pro-inflammatory cytokines, causes rapid phosphorylation of IκB and its dissociation from NF-κB which allows its translocation to the nucleus, where it induces the transcription of a large variety of target genes that normally encode cytokines, cell adhesion molecules and growth factors. Cell culture studies have reported the inhibition of the transcription factor NF-κB by curcumin in different cancer cell lines[7]. It has been reported that curcumin inhibited IκB kinase (IκK), suppressed both constitutive and inducible NF-κB activation and potentiated tumor necrosis factor (TNF)-induced apoptosis[23].

4.1.5 Curcumin in cancer therapy: targets and effects

Most of the drugs currently available for the treatment of cancer has a limited potential because of poor selectivity, toxicity and cost. In order to limit these disadvantages is desirable to find innovative therapeutic solutions and among these, the use of natural origin compounds are acquiring considerable interest.

Curcumin has been used for thousands of years in the East as healing agent and although it has been shown to exhibit beneficial effects in many diseases, its strong therapeutic potential on

cancer has been the most studied by researchers in the last decades. In fact, curcumin, alone or in combination with other agents, has already been studied for the prevention and treatment of various forms of cancer in humans, including colorectal cancer, pancreatic cancer, breast cancer, prostate cancer, multiple myeloma, lung cancer and oral cancer[24–26]. The explanation of this wide range of cancers can be found in the ability of curcumin to target multiple pathways, as described before. It has been proved, indeed, that curcumin is able to suppress the proliferation of cancer cells and the development of metastasis, and that these effects are exerted by influencing the cell cycle and the regulation of various transcription factors, growth factors, inflammatory cytokines, protein kinases and other enzymes. Moreover, it is also able to induce apoptosis[27,28]. Minor effects of curcumin in suppressing cancer oncogenesis are related to the modulation of microRNA, DNA, histone and mitochondria.

Going into detail, we can affirm that curcumin induce apoptosis by regulating the expression of apoptosis-related genes and by modulating the apoptosis-related proteins. For example, induced by curcumin, the antiapoptotic protein Bcl-2 increased, while the pro-apoptotic protein Bax decreased, leading to an elevated Bax/Bcl-2 ratio[29]. Often this effect is mediated by the tumor suppressor protein p53, as shown by Choudhuri *et al* in the human breast carcinoma cell line MCF-7[30]. It has been demonstrated that curcumin could also affect human breast cancer cells through inducing cell cycle arrest at the G2M phase and late S phase in MCF-7 cells. This arrest is due to a regulation of the spindle-related signaling pathways: chromosomes were not able to be segregated normally and cells were arrested in the M phase[31,32]. Even in this case, the mediator of the effect on the cell cycle can be p53[33]. Recently, it has been demonstrated that curcumin not only significantly inhibited growth of human breast cancer cells MDA-MB-231 and MCF-7 by inducing apoptosis in a dose- and time-dependent manner, accompanied by an increase in Bax/Bcl-2 ratios, *in vitro*, but also inhibited tumor growth in mouse model[34].

As regards the development of metastases, curcumin acts in two ways: first, it inhibits angiogenesis factors, such as vascular endothelial growth factor (VEGF)[31,35] and second, curcumin affects the function of molecules and receptors responsible for motility and invasion[36].

In addition to its role as a chemopreventive and chemotherapeutic agent, curcumin has been shown to act as chemosensitizer for other anticancer agents: it helps eliminate chemoresistant cells by sensitizing tumors to chemotherapy, in part by inhibiting pathways that lead to treatment resistance[22,37]. The assumption is that curcumin may modulate both the expression and function of multidrug resistance (MDR) proteins in tumor cells. In 2002, Anuchapreeda and his collaborators demonstrated that curcumin, interacting directly with P-gp, is able to down-regulate the expression and to reduce transporter-mediated efflux in drug resistant human cervical carcinoma cells (KB-V1), *in vitro*[38]. A study of Limtrakul *et al.* prove that also a metabolite form of curcuminoids, the tetrahydrocurcumin (THC), is able to modulate MDR in cancer cells, inhibiting the efflux function of P-gp, MXR and MRP1 in drug resistance cell lines[39]. Most of the studies about MDR proteins and curcumin utilized the commercial grade curcuminoids and were unable to identify the individual effect of the three major curcuminoids (curcumin, demethoxycurcumin, and bisdemethoxycurcumin) on P-gp. Teng *et al* studied individually the three curcuminoids, showing that DMC is the most potent P-gp inhibitor. DMC treatment inhibited human P-gp function through uncompetitive ATPase inhibition and also reversed the doxorubicin-resistant cells to doxorubicin-sensitive cells[40]. The consequence of these studies is also the development of nanoparticles functionalized with antibodies for a direct targeting of P-gp, which allows the transport of curcumin

to the resistant cells in order to overcome resistance and re-sensitize the cells to action of the drug (in this case, PLGA nanoparticles combined with paclitaxel)[41].

Encouraging results of preclinical findings led to a handful of clinical studies to evaluate the chemosensitizing effect of curcumin in cancer patients, in combination with docetaxel, quercetin, imatinib or gemcitabine. Although these studies have established a strong basis for future investigations into the high potential of curcumin in combination with standard chemotherapeutic agents, it remains essential to find solutions to increase the bioavailability of curcumin, reducing the oral dose and obtaining better efficacy[42].

4.1.6 Curcumin nanoformulations

As we said before, although curcumin has demonstrated therapeutic efficacy against many disease, it has limited bioavailability because it is poorly absorbed, rapidly metabolized and systemically eliminated. These characteristics are limiting factors which hamper its use as therapeutic agent. So, development of new formulations or analogues of curcumin with better bioavailability, as well as novel routes of administration, will be critical for future applications of curcumin. Some promising approaches include the use of adjuvants that can block the metabolic pathway (concomitant administration of piperine inhibits glucoronidation), the design of nano-sized delivery system such as liposomes, micelles and polymeric nanoparticles and synthesis of structural analogues[10].

There is a variety of nanoparticles available that could potentially improve delivery and bioavailability of curcumin and many studies have shown that nanocarriers are suitable for increasing curcumin's bioavailability and its targeted delivery to tumors and other sites of disease. Nanoparticles, which are between 10 and 100 nm, have the ability to take advantage of the enhanced permeability and retention (EPR) effect and can improve the circulation time of the loaded therapeutic agent. Best known and FDA approved nanoparticles are the liposomes, which are often the first choice because of their ease of formulation, possibility to vary the lipid composition and the extensive experience with the system[43]. Many liposomal curcumin formulations, PEGylated or not, have been developed in recent years and they were found to be useful, for example, in increasing bioavailability in rats[44] and to chemosensitize a mouse model of cervical cancer to the action of paclitaxel[45]. In 2014 the first liposomal formulations of curcumin have been patented[46,47].

In alternative, micelles could be an interesting system for lipophilic molecules, because of their hydrophobic core that can accommodate hydrophobic drugs. Curcumin-encapsulated polymeric micelles have been shown to suppress colon cancer, *in vitro* and *in vivo*[48]. Nanoencapsulation of curcumin using poly(latic-co-glycolic acid) (PLGA) can also lead to induce G2/M block in breast cancer cells, *in vitro*[49], and enhanced oral bioavailability in rats[50].

In some cases, also peptide or protein carriers were found to be useful for curcumin nanoformulation. Curcumin was loaded in the hydrophobic core of spontaneous casein micelles, with a solubility increased 2500 fold and application in food industry[51] while nanoparticles of cross-linked human serum albumin (HSA) have been used for drug delivery purposes[52]. Even ferritin has been exploited for this purpose, and recently some works have been published[4,53,54].

4.2 Triple negative breast cancer (TNBC)

Triple negative breast cancer (TNBC) is a discrete subset of breast cancer (BC) characterized by a lack of estrogen receptors (ER), progesterone receptors (PR) and HER2 expression and accounts for approximately 15-20% of BC patients[55]. Commonly, but not uniformly, the clinical classification of triple-negative breast cancer is synonymous with the basal-like subtype which, however, is determined via gene expression microarray analysis and approximately 80% of clinical TNBCs fall into the basal-subtype [56]. Indeed, using gene expression analyses, researchers were able to identify six distinct TNBC subtype, each displaying a unique biology[57].

TNBCs occur at higher rate in young and African-American or Hispanic women, are generally of a higher grade and poor prognosis, patients have an increased probability of distant recurrence and death compared with other types of BC[58]. Also, TNBCs exhibit a high proliferation index, an aggressive and early pattern of metastases (in particular visceral and CNS metastases) and a relative lack of therapeutic targets, which makes them insensitive to targeted anti-hormone and/or anti-HER2 therapies. So, improved approaches to treatment of these cancers are critical because the median survival of patients with metastatic TNBC is only 13 months, and virtually all women with metastatic TNBC ultimately die of their disease despite systemic therapy: it remains the hardest BC subtype to treat[58]. For all these reasons, TNBC is currently receiving a huge and appropriate amount of research attention and the identification of more affective and promising therapies remains an important clinical challenge[55,56].

4.2.1 Current and future treatments

The main treatment for TNBCs continues to be the conventional chemotherapy, with good initial response to anthracyclines and taxanes, but tumor is rarely eradicated. Therefore, new targeted therapies represent an urgent need and investigators have been fervently working in order to advance the development of novel therapeutic agents aimed at treating this clinically aggressive phenotype[56]. As we gain a deeper understanding of the biologic processes driving TNBC, the list of therapeutic agents will continue to evolve, including new strategies targeting enzymes, receptors, angiogenesis and beyond.

Currently, both preclinical and clinical studies indicate that tumors with BRCA1 dysfunction, the majority of which are triple negative, harbor deficient double-stranded DNA break repair mechanisms and are sensitive to DNA-damaging chemotherapeutic agents, such as platinum agents, including carboplatin and cisplatin[56,58]. Moreover, PARP1 chemical inhibitors, such as Olaparib, leads to a severe toxicity in BRCA1-defective cells, since PARP1 is a poly ADP-ribose polymerase with a key role in the repair of single-strand DNA breaks. If DNA breaks occur in the absence of PARP1, the replication fork stalls, resulting in accumulation of DNA lesions brings to chromosomal instability, cell cycle arrest and subsequent apoptosis[59].

Simultaneously, others groups focused their attention on EGFR/HER1, a cell surface transmembrane tyrosine kinase receptor and perhaps the most well-known protein overexpressed among triple-negative breast cancer. Anyway, the anti-EGFR Cetuximab has not given, up to now, the desired results[60]. Also the treatment with Bevacizumab, a mAb targeting vascular endothelial growth factor (VEGF) is controversial[61]. Numerous other experimental approaches are under way with the goal of identifying targets in TNBC, with mTOR inhibitors, MEK inhibitors and histone

deacetilase inhibitors under consideration, but keeping an eye also on other routes and signaling pathways[55]. Continued research aimed at more fully characterizing the molecular and epidemiologic factors, as well as patterns of metastases observed among TNBCs, will advance the development of prevention and treatment strategies aimed at improving outcomes for patients diagnosed with this aggressive disease[56].

4.2.2 Chemoresistance in TNBC

Standard chemotherapy remains the backbone of systemic TNBC treatment. At present, the cure for cancer continues to escape oncologists due in a large part to chemoresistance, which accounts for 90% of drug failures in metastatic cancers. Six different mechanisms of chemoresistance are described in TNBC: (1) ABC transporters efflux chemotherapeutics out of cancer cells, (2) β-tubulin III overexpression induces paclitaxel resistance, (3) mutations in DNA repair enzymes such as topoisomerase II and enzymes altering drug sensitivity, (4) alterations in genes involved in apoptosis prevent chemotherapy-induced apoptosis, (5) ALDH1 and GSH/GST overexpression mediate chemotherapeutic inactivation/detoxification, (6) NF-κB signaling aberrant regulation[61].

In particular, three ABC transporters have been extensively studied in TNBC:

a) multidrug resistant protein-1 (MRP1) which confers resistance to vinca alkaloids and anthracyclines;
b) breast cancer resistance protein (ABCG2) which is responsible for the efflux of drugs such as doxorubicin;
c) p-glycoprotein (MDR1) which pumps a wide array of chemotherapeutics, including paclitaxel.

For example, it has been demonstrated that a low cytotoxic Olaparib treatment clearly led to an increase expression of both BCRP an MDR1 in SUM1315 TNBC cells, *in vitro*[62].

Moreover, breast cancer cells are subjected to a high level of oxidative stress and it is known that TNBC is associated with a more hypoxic phenotype, possibly due to activation of the mTOR pathway. Importantly, hypoxia compromises chemotherapeutic efficacy due to the varying levels of oxygen present in the tumor and furthermore a hypoxic tumor environment results in an increase in cellular senescence and therefore potentially propagating a chemoresistance phenotype[63]. Other mechanisms, such as senescence and autophagy, are also related to chemoresistance in TNBCs[61].

4.3 Aim of the work

Under the definition of breast cancer a wide variety of clinical forms is included. About 15% of BCs are known as triple negative (TNBCs) that are characterized by the lack of three specific molecular markers: progesterone receptor (PR), estrogen receptor (ER) and human epidermal growth factor 2 (HER2). This means that a targeted therapy against PR, ER or HER2, currently used in clinic for breast cancer, is mostly ineffective. Patients have other treatment options: in fact, these tumors seem to be particularly chemosensitive to anthracyclines and taxanes, which are part of the standard therapy used for high risk patients. In spite of this, however, there is an overall poorer survival and the risk of relapse for TNBC patients in the first 3-5 years is significantly higher than for patients presenting hormone positive breast cancer. Moreover, these tumors are more prevalent in young women, display an higher prevalence of brain metastases and a rapid progression from the onset of metastasis to death[61,64]. This aggressive behavior pattern, a relative lack of effective therapies and a poor prognosis have encouraged to develop new therapies. Among these, the possibility to combine drugs that target different signalling pathways are currently a major trend in drug design and discovery[22].

Curcumin, a hydrophobic polyphenol extracted from *Curcuma Longa* has been recognized as an effective anticancer agent that negatively regulates various growth factors, protein kinases, transcription factors, inflammatory cytokines, cell receptors, and other oncogenic proteins. Induction of apoptosis and/or cell cycle arrest at different phases contribute to the antiproliferative effects of curcumin in cancer cells[65]. Even if various clinical trials and research articles had been demonstrated the great potential of curcumin, due to its influence of numerous biochemical and molecular pathways, this molecule has not yet been approved as a therapeutic agent because of its limitations. The flaws limiting the use of curcumin are multiple, in particular poor solubility and fast metabolism, which result in an insufficient bioavailability. To make this compound more attractive for medical applications is therefore necessary to find solutions to overcome these defects. In this project, we have encapsulated curcumin within ferritin protein shells, aiming at increasing its solubility and stability. To do this, we exploited the capability of HFn to assemble and disassemble its quaternary structure in a pH-dependent manner, opting for a loading in alkaline environment. Our goal is making curcumin available and effective on triple negative breast cancer cells through this nanoformulation.

4.4 Materials and methods

4.4.1 Curcumin purification

Commercially available curcumin from *Curcuma Longa* generally contains other curcuminoids as secondary products. The powder purchased by Sigma Aldrich was purified by column chromatography on silica gel (mobile phase Chloroform/Methanol 98:2) to get the desired product as a yellow solid. After elution, the purity of the fractions containing curcumin was evaluated with thin-layer chromathography (TLC), using the same mobile phase. Fractions containing the product of interest were collected and evaporated under reduced pressure.

4.4.2 HFn nanocage design, expression and purification

The cDNA encoding for the heavy chain of human ferritin, modified by inserting the restriction sites for NdeI and NotI (respectively in 5' and 3'), was synthesized and subcloned into the vector pET30b(+) by Eurofins MWG Operon, in order to express HFn under the control of a T7 promoter, as reported in Bellini *et al*[66]. The resulting plasmid pET30b/HFn was used to transform *Escherichia coli* expression strain BL21(DE3) by heat-shock method. The recombinant expression vector was confirmed by restriction endonuclease digestion and DNA sequencing.

H-ferritin (HFn) was expressed and purified following the protocol previously published[66]. Briefly, BL21(DE3)/pET30b/HFn cell were grown at 37 °C in Luria Bertani kanamicim medium until OD_{600}=0.6 and induced with 0.5 mM isopropyl β-D-1-tiogalactopiranoside (IPTG) for 2 h and 30 min. After growing, the cells were collected, washed and resuspended in lysis buffer with lysozyme and DNase I. In order to prepare the crude extract, cellular suspension was sonicated and centrifuged. After heat treatment, the supernatant was loaded onto DEAE Sepharose anion exchange resin and the purified protein was eluted with a stepwise NaCl gradient in 20 mM KMES, pH 6.0. Fractions were analyzed by SDS-PAGE using 12% (v/v) polyacrylamide gel and proteins detected with Imperial Protein Stain (ThermoFisher Scientific). Protein content was determined by both measuring absorbance at 280 nm and Coomassie Plus (Bradford) Assay with IgG as standard protein.

4.4.3 HFn loading with curcumin

Encapsulation of curcumin inside ferritin cavity was obtained exploiting the disassembly/reassembly method. The pH of a HFn solution (1 mg mL^{-1} in 0.15 M NaCl) was adjusted to 12.5 adding the appropriate volume of 1 M NaOH. After 15 min, a 400 μM solution of purified curcumin, freshly solubilized in 0.1 M NaOH, was added. Immediately, the pH value was reduced to 7.5 using 1 M HCl. The resulting solution was stirred at room temperature for 2 h to promote the assembly of the protein. Later, the solution was centrifuged through a 100 kDa Amicon filter (Millipore), washed several times with sterile PBS buffer and finally refine on Zeba™ Spin Desalting Columns (ThermoFisher Scientific), in order to remove the excess curcumin and the adsorbed molecules. The encapsulated curcumin will be retained inside the apoferritin shell because its size is larger than the pore size of the protein channels (3–4 Å)[67], while the excess molecules will

be removed in the washing steps. The final product, called CFn (curcumin-encapsulated ferritin), was subsequently characterized and used for *in vitro* experiments.

To evaluate the intracellular fate of CFn, the HFn shell was also labeled with fluorescein isothiocyanate (FITC) according to the manufacturer's protocol (Sigma, Invitrogen).

4.4.4 Loading efficiency

The amount of the encapsulated molecules was determined comparing the absorbance intensity at 423 nm of different CFn dilutions in acetic acid with a predetermined calibration curve, using EnSight™ Multimode Plate Reader (Perkin Elmer®) and 96-multiwell plates. Placing CFn in acetic acid the pH of the samples was reduced to 2.0, allowing the encapsulated curcumin to be released from ferritin. In order to construct the calibration curve, individual working standard solutions of purified curcumin (from 1 to 95 µM) were freshly prepared from curcumin stock standard solution by diluting in acetic acid.

4.4.5 CFn and curcumin stability

CFn was characterized analyzing its stability in physiologic and alkaline conditions, in comparison with a free curcumin solution. The nanocages and the free molecules were resuspended in phosphate buffer saline (PBS, pH 7.2) and sodium hydroxide (0.1 M NaOH, pH 13), at the same final concentrations. Since curcumin is soluble in alkaline environment but poorly soluble in water, for the stability in PBS a 50 mM solution of purified curcumin dissolved in DMSO was used as stock solution and then diluted in PBS buffer (final curcumin concentration = 50 µM or 100 µM). The concentration of DMSO in final aqueous solution was negligible.

At predetermined time points (30 min, 1 h, 2 h, 3 h, 4 h, 5 h, 6 h, 24 h, 48 h) an aliquot of the solutions was transferred into a cuvette and the absorption spectrum was analyzed by Nanodrop 2000c UV-Vis Spectrophotometer (Thermo Scientific), scanning UV/Vis spectra from 210 to 600 nm. The average absorbance of three different samples, at each time, was used to evaluate the stability of the solution over time.

4.4.6 TEM and DLS analyses

To check the morphology of CFn, the nanocages were analyzed by transmission electron microscopy (TEM). For the analysis, a sample of a CFn solution were dropped onto the surface of a copper net and stained with 2% phosphotungstic acid for 10 min. The molecular structure of the sample was directly observed using TEM at 60 K and 200 kV magnification after drying the samples at room temperature for 120 min.

For dynamic light scattering (DLS) experiments, CFn nanoparticles and free curcumin were suspended in PBS, pH 7.20 at a final concentration of 50 µM (of curcumin).

4.4.7 Cell cultures

MDA-MB-231 and MDA-MB-468 TNBC cell lines were cultured in Minimum Essential Media (MEM) and Dulbecco's Modified Eagle's Medium (DMEM), respectively, supplemented

with 10% fetal bovine serum (FBS), 2 mM L-glutamine, penicillin (50 UI mL^{-1}) and streptomycin (50 mg mL^{-1}) at 37 °C in humidified atmosphere containing 5% CO_2 and sub-cultured prior to confluence using trypsin/EDTA. Cell culture medium, supplements and antibiotics were purchased from EuroClone.

4.4.8 Interaction of CFn with TNBC cells

For uptake analysis, MDA-MB-231 and MDA-MB-468 were plate (3 x 10^5 cells) in 12-wells plate and incubated for 24 h at 37 °C. Then, cells were treated with 20 μM of free curcumin, 50 μg mL^{-1} of CFn and HFn, both labeled with FITC, for 15 minutes, 1, 4, 24, 48 and 72 h at 37 °C.

For the binding assay, MDA-MB-231 and MDA-MB-468 were harvested (3 x 10^5 cells) in FACS tubes. After centrifugation, cells were washed with PBS, 1% BSA solution and incubated for 2 h at 4 °C with 50 μg mL^{-1} of CFn labeled with FITC in PBS, 1% BSA.

For both experiments, after the incubation times cells were washed and analyzed by Gallios™ Flow Cytometer (Beckman Coulter Inc.). The mean fluorescence intensity of curcumin and FITC signals were analyzed acquiring 10000 events per samples. Results obtained are expressed as mean ± standard deviation of three independent biological replicates.

4.4.9 Viability assay

To test CFn and free curcumin toxicity, MTT assay (CellTiter 96 Non-Radioactive cell proliferation assay - Promega) was performed. MDA-MB-231 and MDA-MB-468 (10^3 cells cm^{-1}) were seeded in 96-well plate, five replicates per concentration. 24 h after plating, both cell lines were treated with 0.5, 1, 5, 10, 20, 35 and 50 μM of curcumin or CFn and incubated for 24, 48 and 72 h. Regarding the concentration of CFn, we referred to the concentration of curcumin encapsulated inside nanocages, in order to compare the effect with the free molecule.

According to the manufacturer's instructions, at the end of the exposure time 10 μL/well of 3-(4,5-dimethyl-2-thiazolyl)-2,5-diphenyl-2H-tetrazolium bromide (MTT) stock solution were added. After 4 h of incubation at 37 °C a solubilizing solution (0.1 mL per well) was added to solubilize the formazan crystals and the absorbance was read at 570 nm and at 620 nm, as background, with EnSight™ Multimode Plate Reader (Perkin Elmer®). Results were expressed as percentage ± standard deviation of three independent biological replicates, normalized with untreated cells as control.

4.4.10 Sensitization of cells to Doxorubicin treatment

Firstly, we assessed the activity of the three major ABC transporter proteins, responsible for chemoresistance, using a specific assay kit (EFFLUX-ID Gold multidrug resistance assay kit – Enzo Life Science Inc.). MDA-MB-231 and MDA-MB-468 cells (5 x 10^5) were collected inside FACS tubes, centrifuged and resuspended in DMEM without phenol red in the presence of P-gp and MRP1 inhibitors. After 5 minutes of incubation at 37 °C, a non-fluorescent compound (provided by the kit) was added to each samples: this compound readily penetrates the cell membrane and unless it is pumped out of the cells by MDR proteins, it is hydrolyzed to a hydrophilic fluorescent dye by intracellular esterases. After 30 minutes at 37 °C, cells where

analyzed by flow cytometry quantifying the fluorescence of the compound inside cells. The use of specific inhibitors for MDR proteins will give an higher fluorescence intensity and allows to measure the activity of each MDR protein.

To evaluate the effect of our nanoconstruct on sensitization of TNBC cells to doxorubicin treatment, we used MTT assay. 10^3 cells of MDA-MB-231 and MDA-MB-468 were seeded in 96-well plate and treated for 24, 48 and 72 h with 0.1, 0.5, 1, 2.5, 5, 7.5 μM of doxorubicin, five replicates per concentration, in order to evaluate the cytotoxicity of the anthracycline drug. To analyze if CFn and curcumin could enhance the sensitivity of the cells to doxorubicin treatments, we combine the range of doxorubicin tested with 5, 10 and 20 μM of free curcumin or CFn.

According to the manufacturer's instructions, at the end of the exposure time 10 μL/well of 3-(4,5-dimethyl-2-thiazolyl)-2,5-diphenyl-2H-tetrazolium bromide (MTT) stock solution were added. After 4 h of incubation at 37 °C a solubilizing solution (0.1 mL per well) was added to solubilize the formazan crystals and the absorbance was read at 570 nm and at 620 nm, as background, with EnSight™ Multimode Plate Reader (Perkin Elmer®). Results were expressed as percentage ± standard deviation of three independent biological replicates, normalized with untreated cells as control.

4.4.11 Cell cycle analysis

MDA-MB-231 and MDA-MB-468 cells were seeded in a 12-well plate (3×10^5 cells per well) and incubated for 24 h. Then, cells were treated with 5, 10 and 20 μM of free or encapsulated curcumin and incubated for 24 and 48 h at 37 °C. At the indicated time point, cells were collected and fixed (70% ethanol), then cellular DNA was stained with a mixture of propidium iodide (10 μg mL^{-1}) and RNase A (20 μg mL^{-1}). 10000 events were acquired for each sample, using flow cytometry equipped with a doublet discriminator module (Gallios™ Flow Cytometer - Beckman Coulter Inc.) and the DNA content was analyzed by FlowJo software (TreeStar Inc., OR, U.S.A.).

4.4.12 Quantification of NF-κB phosphorylation

To quantify the decrease of NF-κB phosphorylation we used the AlphaScreen® SureFire® NF-κB p65 p-Ser536 assay (Perkin Elmer), a sandwich immunoassay for quantitative detection of specific protein in cellular lysates using Alpha Technology.

MDA-MB-231 and MDA-MB-468 cells were seeded in a 96-well plate (35×10^3 cells per well) and after 24 h were treated with 20 μM free curcumin or CFn for 4 and 24 h at 37 °C. After incubations, the AlphaScreen® SureFire® were carried out according to manufacturer's instruction. Briefly, cells were lysed with lysis buffer provided by the assay kit, to which protease and phosphatase inhibitors mix were added. Then two-step assay procedures were used: the lysates (30 μl) were added to white 96-well half area plate and 15 μl mix of acceptor beads were added to the well. The plate was covered with a lid and incubated at room temperature for 1 hour. Subsequently, 15 μl of donor beads were added, the plate was covered again with a lid and incubated at room temperature for another 1 h in the dark. The AlphaLISA signal was measured with EnSight™ Multimode Plate Reader (Perkin Elmer®).

4.5 Results and discussion

4.5.1 Curcumin purification

Commercially available curcumin is generally composed of about 77% curcumin, 17% demethoxycurcumin and 3% bisdemethoxycurcumin[3] while commercially available curcumin in pure form is very expensive. However, it is possible to separate the three curcuminoids using crystallization and column chromatography[68]. This is why we purified the commercial product (Curcumin from *Curcuma longa*, powder, Sigma Aldrich) using silica column chromatography, choosing as a mobile phase a mixture of chloroform and methanol, 98:2. After elution, the purity of the curcumin-containing fractions was evaluated by thin-layer chromathography (TLC), using the same mobile phase. Then, all the fractions containing the product were collected and evaporated under reduced pressure. A TLC of the final product confirmed the purity of the compound (Fig. 4.4), TLC).

Fig. 4.4 Thin-layer chromatography (TLC) analysis of curcuminoids. Curcuminoids and pure curcumin were developed on a silica gel TLC plate with chloroform : methanol (98:2 v/v). (1) Curcumin from Sigma Aldrich, (2) standard of pure curcumin, (3) curcumin product after silica column chromatography.

4.5.2 Curcumin-encapsulated Ferritin (CFn) characterization

Although curcumin has a great potential for applications in cancer therapy and human health, it is unstable and easily degraded, resulting in loss of its biological properties. In contrast, the apoferritin shell is remarkably stable, so we assessed the ability of our nanoparticle formulation to improve its bioavailability and to prevent degradation, as compared with free drug stability.

The procedure for drug encapsulation into the ferritin shell exploits the ability of HFn to modify its quaternary structure in response to pH changes: HFn shell is unfolded into single subunits at acidic (around 2-3) and alkaline (around 11-12) pH and refolds with perfect shape memory when the pH of the solution is brought back to neutrality. Unlike our previous work[66] and other reports[4,53,54], in this work we took advantage of the alkaline pH disassembly of ferritin for curcumin incorporation. In this way, we could avoid the use of DMSO to solubilize this molecule, a procedure generally required, due to the poor curcumin solubility in aqueous solvents at neutral pH. Instead, curcumin is soluble at high pH values, although quite unstable. In particular, it is only

stable up to 2 h in 0.1 M sodium hydroxide, although its stability increases in aqueous solutions at pH>11.7[37,69]. For this reason we ran the reaction briefly (less than 30 min) at pH 12.5, then the pH was rapidly brought to neutrality allowing ferritin to enclose curcumin. NMR analysis confirmed that the molecule did not undergo a major degradation processes (data not shown).

The encapsulation procedure allows to improve some aspects related to curcumin employment as a drug. In particular, curcumin's pharmacological potential is limited because of its extremely poor water solubility. Data from literature indicate a solubility in aqueous solvents around 0.5 µg/mL[70,71]. After encapsulation we assessed by UV-vis measurements, that each ferritin shell can accomodate about 80-90 molecules of curcumin (Fig. 4.5), which implies that solutions at a final 350 µg mL^{-1} curcumin concentration can be easily obtained. This represent a 700-fold increase in solubility.

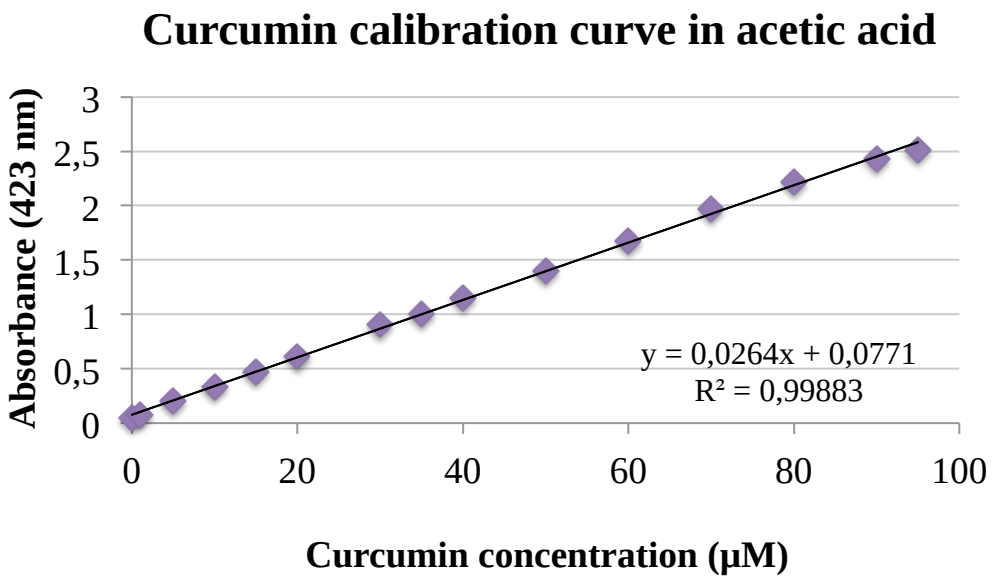

Fig. 4.5 Calibration curve obtained by measuring absorbance intensity of standard solutions of purified curcumin (from 1 to 95 µM) in acetic acid.

Molecules inside the HFn cavity are also more stable and protected from the external environment. Since curcumin possess a typical absorption peak, a set of absorption analyses were performed under both alkaline and physiological conditions, in order to confirm the stability enhancement for the nanoformulated curcumin. Free curcumin exhibits a maximal absorption at ~430 nm, while the HFn-loaded curcumin sample has a maximal absorption around 400 nm, suggesting a possible interaction with the protein shell. According to previous studies, the free curcumin decomposes rapidly at neutral pH[4,17]: as shown in Fig. 4.6, the intensity of the peak at 430 nm decreases over time, while a new peak appears at ~270 nm, probably due to degradation products, such as ferulic acid and vanillin. In contrast, the encapsulated molecules maintained their stability over time, and about the 70% was almost unchanged after 48 h (Fig. 4.7). In addition, it should be underlined that the yellow-orange color of CFn solutions at pH 7.2 was maintained, while the free curcumin, even if stored in the dark, gradually lose color confirming the photosensitivity of the molecule. Stability analysis performed at alkaline pH confirmed the rapid degradation even of

encapsulated curcumin: under these conditions the protein shell opens and ferritin no longer protects curcumin from degradation, then the two profiles are similar.

Transmission electron microscopy (TEM) analyses of CFn (Fig. 4.8) showed that the nanoparticles generated are spherical with a diameter of about 12 nm, as expected, very similar to the control sample of apoferritin. This result is confirmed by also the DLS, with a hydrodynamic diameter of 14,3 ± 0,18 nm (Fig. 4.9). Noteworthy, free curcumin dissolved in DMSO, then diluted in PBS displayed a large hydrodynamic diameter in DLS, suggesting that the lipophilic character of curcumin promotes the formation of aggregates, probably micellar.

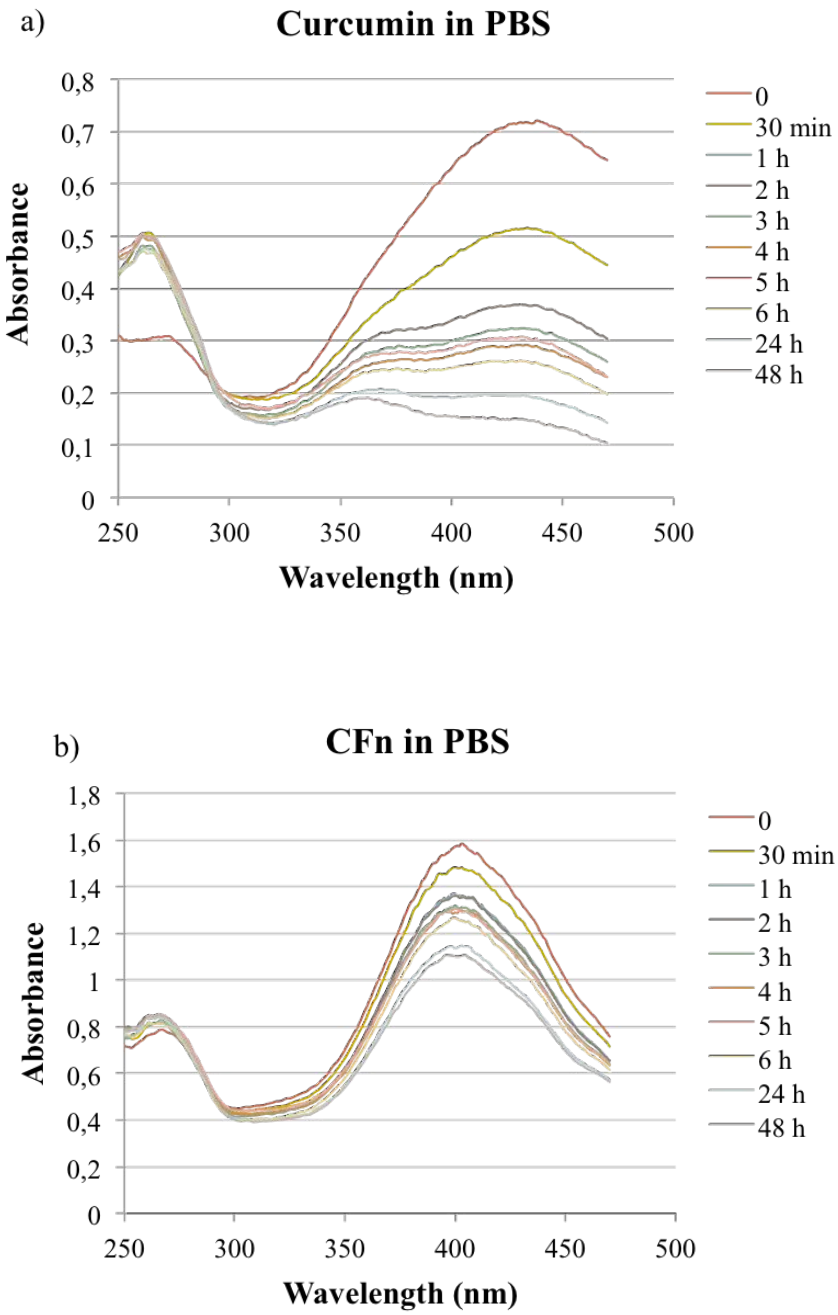

Fig. 4.6 UV spectra of (a) curcumin and (b) CFn in PBS pH 7.2, 25 °C, at different time points.

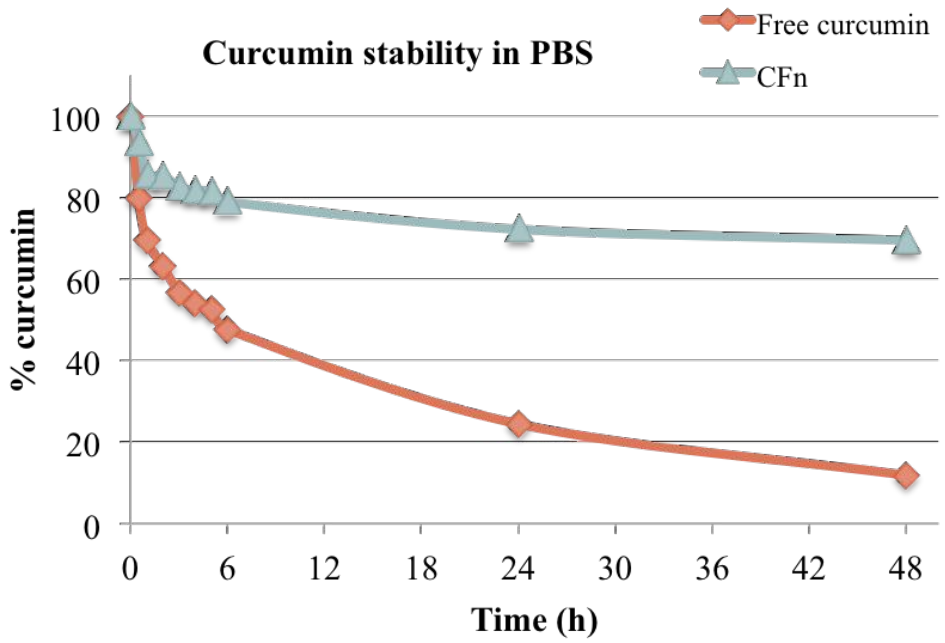

Fig. 4.7 Stability of free and encapsulated curcumin, in PBS pH 7.2 at 25 °C, obtained by analyzing the absorption intensity at λ = 434 nm and 403 nm, respectively.

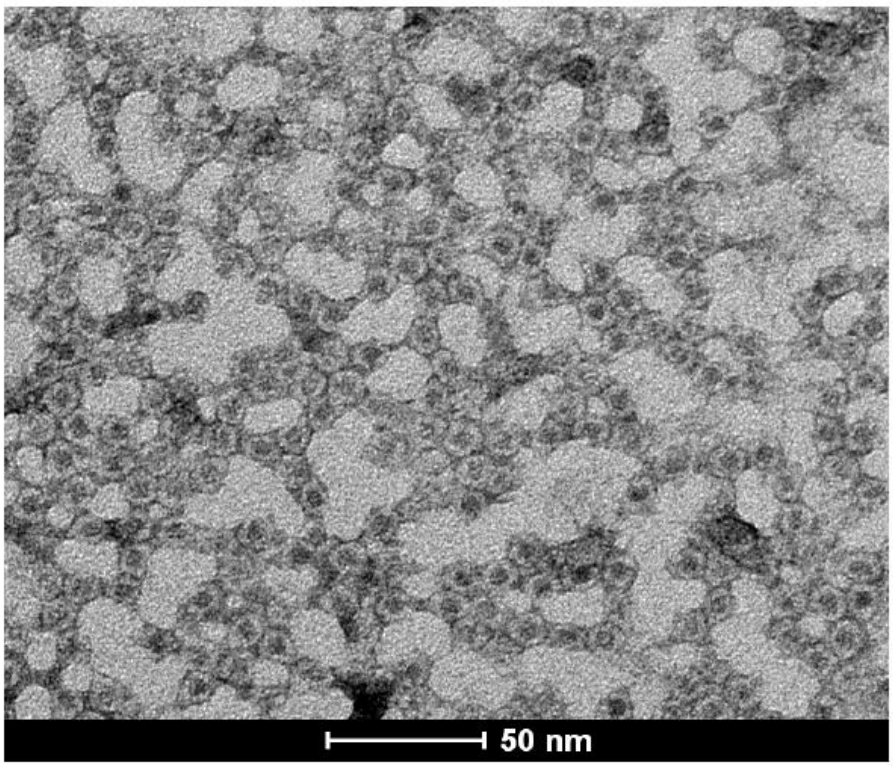

Fig. 4.8 Characterization of the nanocages. CFn morphology was evaluated with TEM analysis, obtaining a monodispersed solution of nanocages with spherical shape and a diameter of 12 nm, just like standard ferritin.

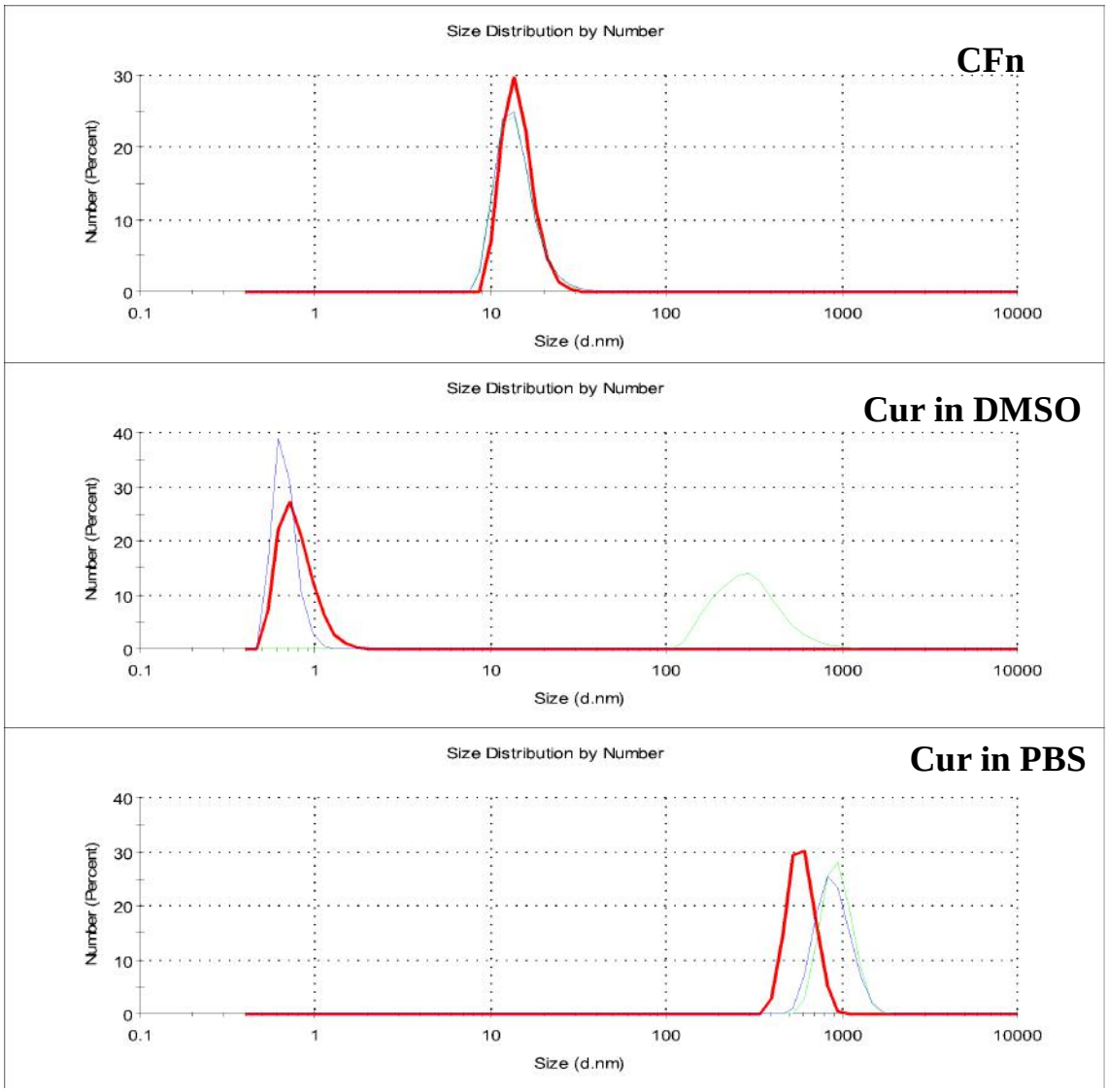

Fig. 4.9 Dynamic Light Scattering (DLS) analyses of (a) CFn in PBS buffer, (b) curcumin in DMSO and (c) curcumin solubilized in DMSO and then diluted in PBS buffer. The green, red and blue lines represent three different samples.

4.5.3 Interaction of CFn with TNBC cells

In the present work, MDA-MB-468 and MDA-MB-231 cancer cells derived from human breast adenocarcinoma were selected for the *in vitro* experiments as TNBC model cell lines. After the characterization of our nanocage, CFn nanoparticles were labeled with FITC (CFn-FITC) and used to evaluated tumor cell internalization. For this purpose, we treated MDA-MB-468 and MDA-MB-231 cells with 50 μg mL^{-1} of CFn-FITC and HFn-FITC, as a control, analyzing the fluorescence signal of FITC by flow cytometry at different time points. As shown in Fig. 4.10 CFn showed the same internalization kinetics observed for HFn in both cell lines, suggesting that our encapsulation does not affect the functionality and efficiency of nanocages. In addition, the data are consistent with our previous observations[66], whereby ferritin cages were internalized rapidly in the

first 4 h, while the fluorescence decreased after 24 h, suggesting that exogenous protein was degraded or combined with the endogenous unlabeled one.

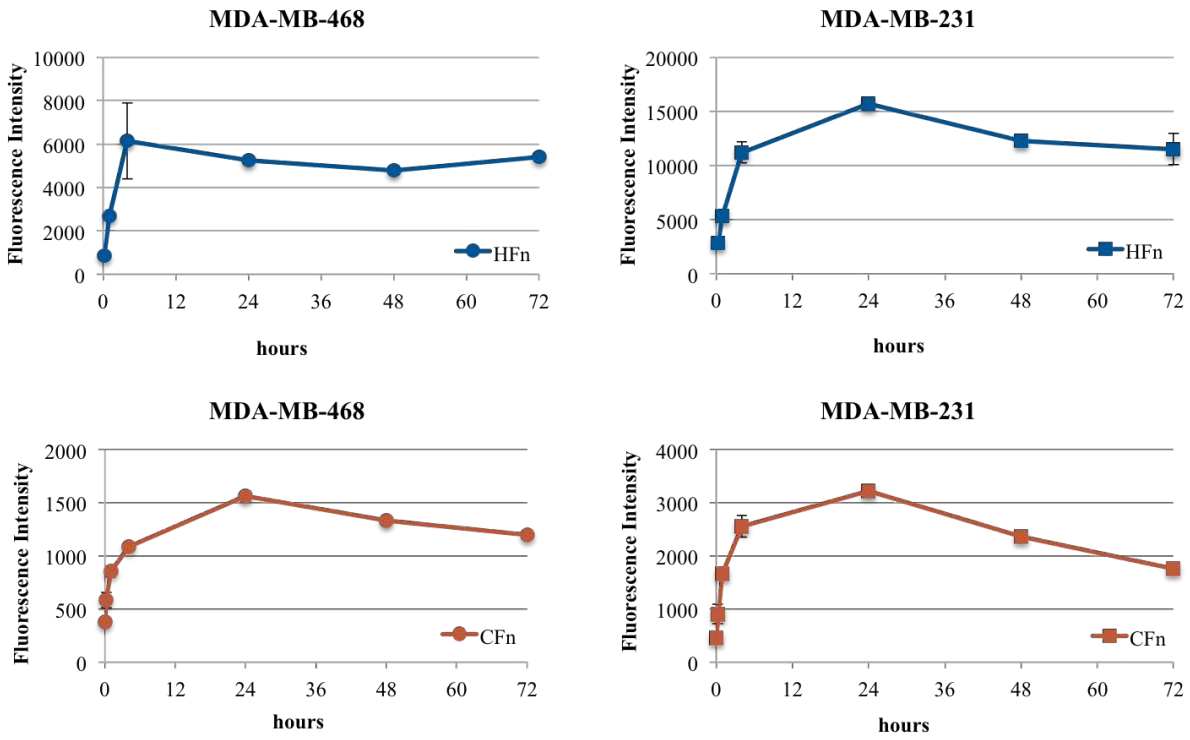

Fig. 4.10 Interaction of CFn with TNBC cells. For uptake analysis, MDA-MB-231 and MDA-MB-468 cells were treated with 50 μg mL^{-1} of CFn or HFn, both labeled with FITC, for 15 minutes, 1, 4, 24, 48 and 72 h at 37 °C. The mean fluorescence intensity of FITC was determined by flow cytometry.

To confirm that even after curcumin loading the internalization was mediated by TfR1 resulting in clathrin-dependent uptake, we inhibited active endocytosis by incubating CFn-FITC and maintaining cells at 4 °C for 2 h (Fig. 4.11). Results obtained by flow cytometry show that the inhibition of all active endocytosis pathways reduced the uptake of CFn up to 77% ± 0.70% and 68% ± 0.68% in MDA-MB-468 and MDA-MB-231 respectively, compared to the physiological condition at 37 °C, confirming that our nanovehicle exploits an active endocytosis pathway to enter the cells, presumably mediated by TfR1. Furthermore, the percentages that we have obtained also match the amount of internalized CFn by TNBC cells after 1 h of treatment[72].

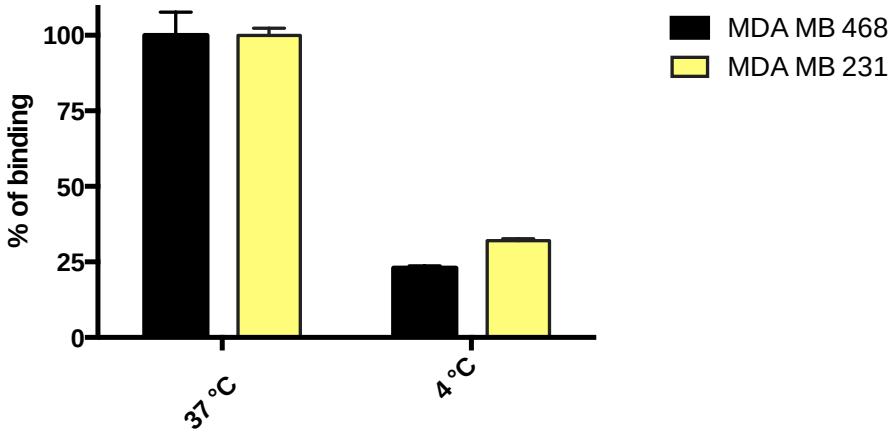

Fig 4.11 Effects of endocytosis inhibition on CFn internalization in MDA-MB-468 and MDA-MB-231. Histograms represent the percentage of CFn-FITC (50 µg mL^{-1}) internalized by cells without any endocytosis inhibition (at 37 °C) and cells maintained at 4 °C for 2 h. The percentage of uptake was calculated by fluorescence intensity, as measured by flow cytometry, setting at 100% the uptake of untreated cells. **, P<0.01 after one-way ANOVA.

4.5.4 Comparison of free curcumin and CFn cytotoxicity

One purpose of our work was to enhance the bioavailability of curcumin through its encapsulation inside the nanocages, thus increasing anticancer activity of the molecule against TNBC cells. We assessed preliminarily the cytotoxicity of free and nanoformulated curcumin (CFn) on MDA-MB-468 and MDA-MB-231 by the MTT viability assay, by treating both cell lines with the drug in a concentration range 0.5 to 50 µM. The range of concentration was established based on our previous work and on data from literature, without exceeding a 0.1% DMSO concentration[38,49,73].

The data presented in Fig. 4.12 show that free curcumin exerts a dose and time-dependent effect, which is not detected when the molecule is encapsulated inside HFn. This is more evident for MDA-MB-231 cells, where CFn shows the same effect at all concentrations, suggesting that the nanoformulation allows a stronger effect at minimal concentrations, compared to free drug. Furthermore, the action of CFn was faster on both cell lines: actually, after 24 h the percentage of viability was much lower in comparison to free curcumin, but the difference decreased at later times. Moreover, it is interesting to note that the treatment with CFn is more reproducible compared to free curcumin, probably due to the enhancement of the solubility of the molecule in aqueous solution.

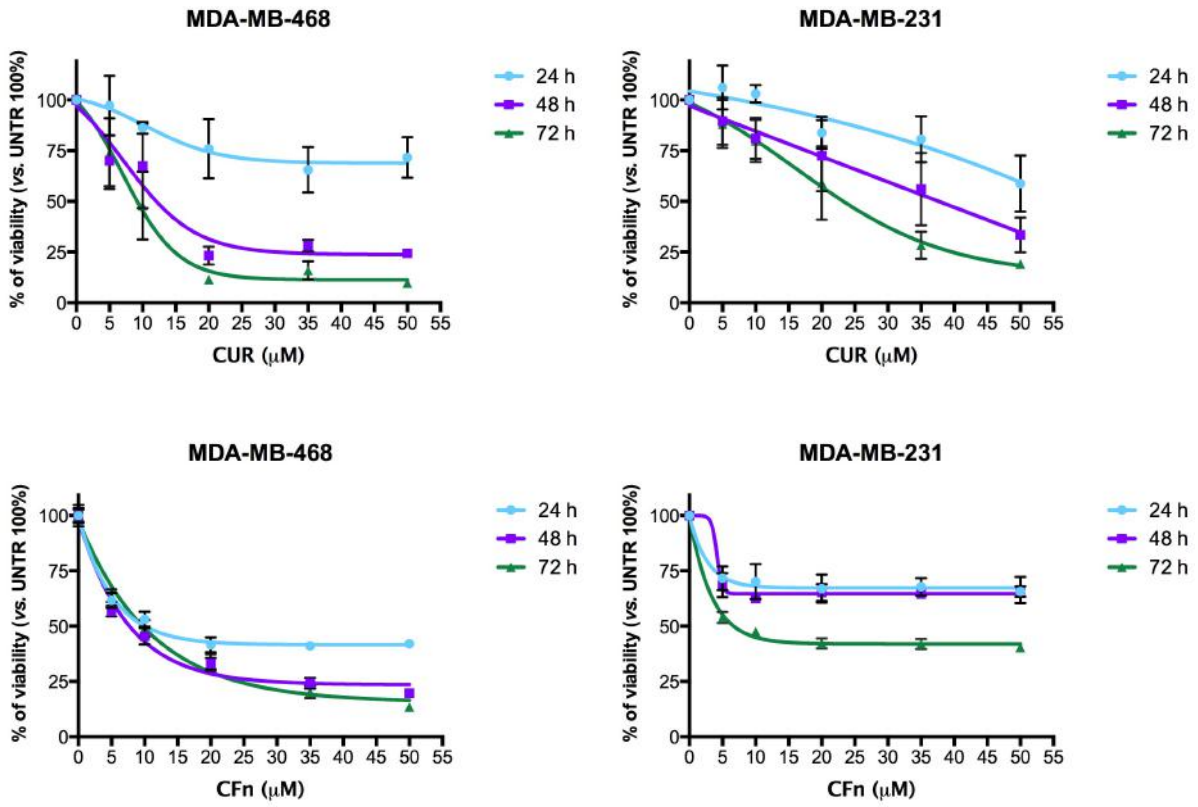

Figure 4.12 MTT-based cytotoxicity of free curcumin (A,B) and CFn (C,D) on TNBC cells. MDA-MB-468 (A,C) and MDA-MB-231 (B,D) were treated with different concentrations of free and nanoformulated curcumin for 24, 48 and 72 h. At the end of incubation time, MTT was added to cells and absorbance of formazan salt product was read at 570 nm. The profiles represent percentage of cell viability compared to untreated cells set at 100% ± standard deviation.

4.5.5 Sensitization of cells to doxorubicin treatment

As curcumin acts as a chemosensitizer, we evaluated the modulation of doxorubicin treatment by CFn, by incubating two cell lines with doxorubicin (0.1 to 7.5 µM), adding at the same time different concentrations of CFn or free curcumin (5, 10 and 20 µM equivalent to curcumin). At different time points (24, 48 and 72 h) we analyzed cell viability by the MTT assay (Fig. 4.13) observing that already after 24 h CFn enhanced the sensitization of MDA-MB-468 to doxorubicin much more than curcumin alone and also at the minimal concentration. In MDA-MB-231 CFn slightly enhanced the effect of doxorubicin only after 72 h of treatment, but also in this case as low as 5 µM of CFn is more effective than free curcumin.

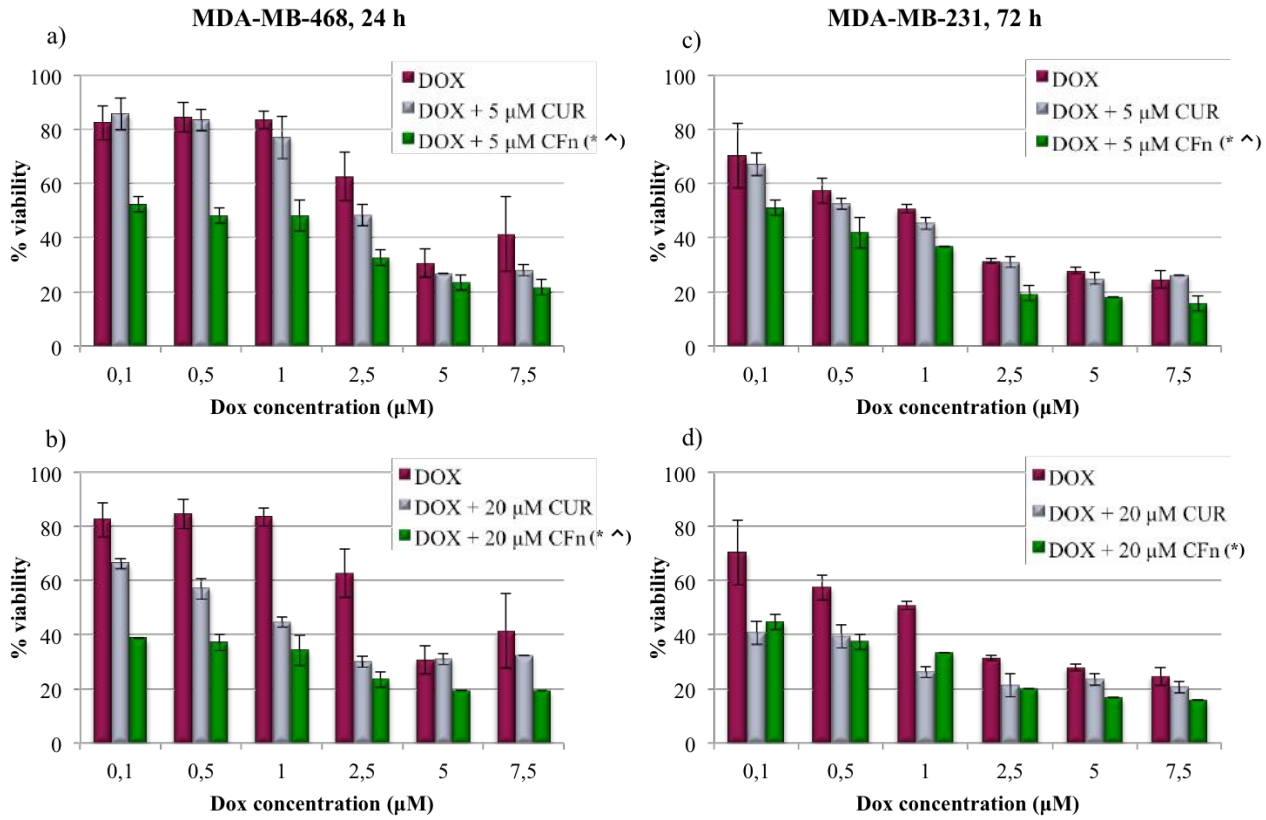

Figure 4.13 Cytotoxicity of free curcumin and CFn in combination with doxorubicin, on TNBC cells. MDA-MB-468 and MDA-MB-231 were treated with different concentrations of free and nanoformulated curcumin for 24, 48 and 72 h. At the end of the incubation time, MTT was added to cells and absorbance of formazan salt product was read at 570 nm. The profiles represent percentage of cell viability compared to untreated cells set at 100% ± standard deviation (* P<0.05 vs DOX, ^ P<0.05 vs DOX+CUR).

As mentioned above, curcumin has a "pleiotropic" effect, being able to act on multiple cellular targets related to cancer. One among its numerous activities is the capability of altering the functionality of MDR proteins through a direct inhibition of the efflux or the decrease in the genes expression[37–40], and MDR transporters are the main mechanism by which cells become resistant to doxorubicin. So we checked whether the observed effect in this type of cells could be mediated by an action of curcumin on these proteins. We assessed the presence of a basal MDR mechanism due to the presence of P-gp and MRP1 on our cell lines, using a specific assay (eFluxx-ID Gold multidrug resistance assay kit). The kit contains a hydrophobic non-fluorescent compound that penetrates the cell membrane and is subsequently hydrolyzed by intracellular esterases that cleave the compound, which becomes fluorescent. In this way, the dye is trapped inside the cells and could be effluxed only by MDR proteins. The addition of specific inhibitors of ABC transport allows us to analyze the activity of a particular ABC transporter quantifying the dye signal by flow cytometry. Our analysis demonstrated that in both cell lines the activity of P-gp (specific inhibitor: Verapamil) and MRP1 (specific inhibitor: MK571) is present, but in MDA-MB-231 MRP1 seems to be predominant (Fig. 4.14).

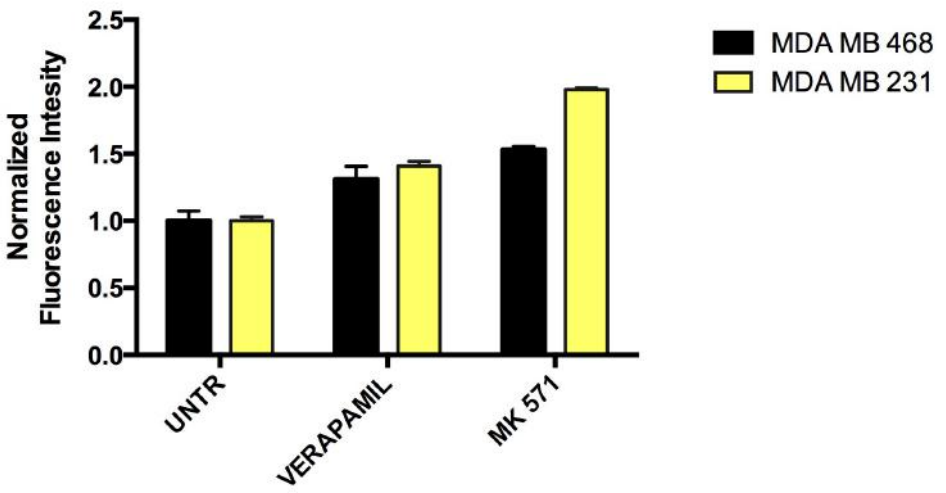

Fig. 4.14 The activity of ABC transporters was assessed using a specific assay kit in the presence and the absence of P-gp or MRP1 inhibitors. A non-fluorescent compound readily penetrates the cell membrane and unless it is pumped out of the cells by MDR proteins, it is hydrolyzed to a hydrophilic fluorescent dye by intracellular esterases. Cells where analyzed by flow cytometry by quantifying the fluorescence of the compound inside the cells.

4.5.6 Effect of CFn on cell cycle

Another important activity of curcumin is the ability to modulate the cell cycle causing the accumulation of cells in G2/M phase[31,32]. When treating the two TNBC cell lines with 5, 10 and 20 µM of curcumin up to 48 h we noticed the same effect reported in literature, in particular for MDA-MB-468 incubated with 20 µM of curcumin[49] (Fig. 4.15). As regards the treatment with CFn, all three concentrations assayed induced the accumulation of MDA-MB-468 in G2/M phase after 48 h of treatment. In the case of MDA-MB-231, we observed instead an increase in G0/G1 phase and a decrease in G2/M phase after 48 h of treatment. These data suggest that in this cell lines the nanoformulated curcumin could block the proliferation of cells, instead of inducing apoptosis.

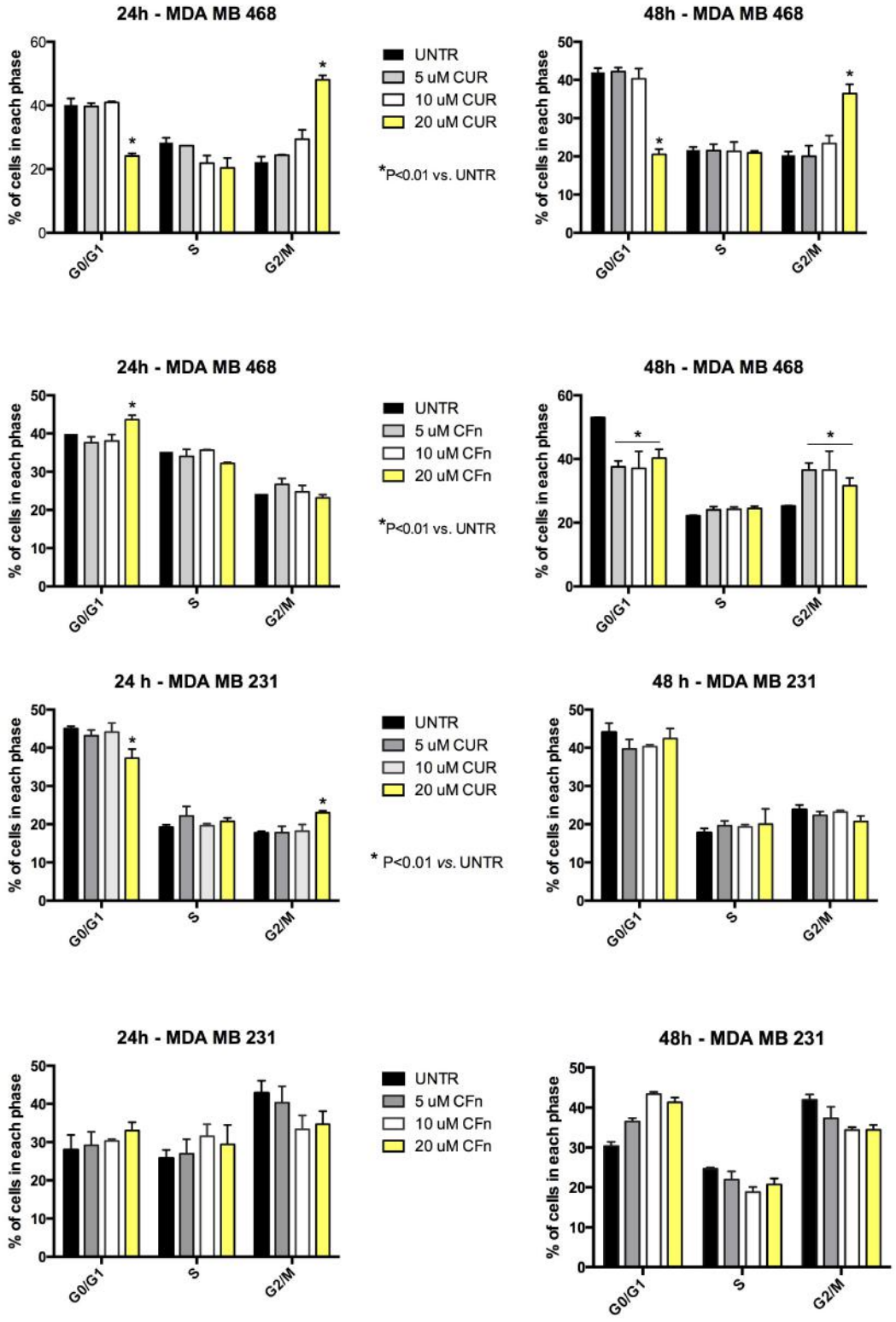

Fig. 4.15 Cell cycle analysis. Cell counts in each phase of cell cycle of MDA-MB-468 AND MDA-MB-231 treated with different concentrations of free or encapsulated curcumin.

4.5.7 Effect of CFn on the NF-κB pathway

It is well known that curcumin possesses anticancer properties also due to the inhibition of the NF-κB pathway, thus decreasing the proliferation of cancer cells[74,75]. NF-κB is a transcription factor existing in latent state in the cytoplasm through the binding with IκB protein. Under various stimuli, the IKK complex phosphorylates IκB proteins causing their degradation, while other protein kinases promote the translocation of NF-κB into the nucleus by phosphorylating p65, one of the NF-κB subunits[76]. Curcumin is able to interact with the IKK complex, thus inhibiting the degradation of IκB proteins and avoiding the activation of the transcription factor[7].

Using a novel technique called Alpha Technology (Perkin Elmer), we analyzed if curcumin encapsulated inside our nanoconstruct could induce a decrease in NF-κB activity in our TNBC cell line models. Alpha Technology is a bead-based proximity assay by which it is possible to quantitate complex cellular processes using simple no-wash microtiter plate based assays. Using beads specific for the phosphorylation of the p65 NF-κB subunit, we evaluated the Alpha signal of cell lysates after curcumin or CFn treatment. As expected, we observed that in both cell lines free curcumin induced a significant decrease in NF-κB phosphorylation after 4 and 24 h of treatment (Fig. 4.16). Surprisingly, the nanoformulation of curcumin was active only on MDA-MB-468 after 24 h of treatment, rather than in MDA-MB-231. We can therefore assume that NF-κB is no longer a preferred target for curcumin after its encapsulation: perhaps the cage, changing some of its features, directs curcumin primarily to other targets, which could still justify the observed effects. NF-κB does not seem any more to be a major mediator of curcumin action, while further experiments are required to identify what pathways modulate the action of CFn.

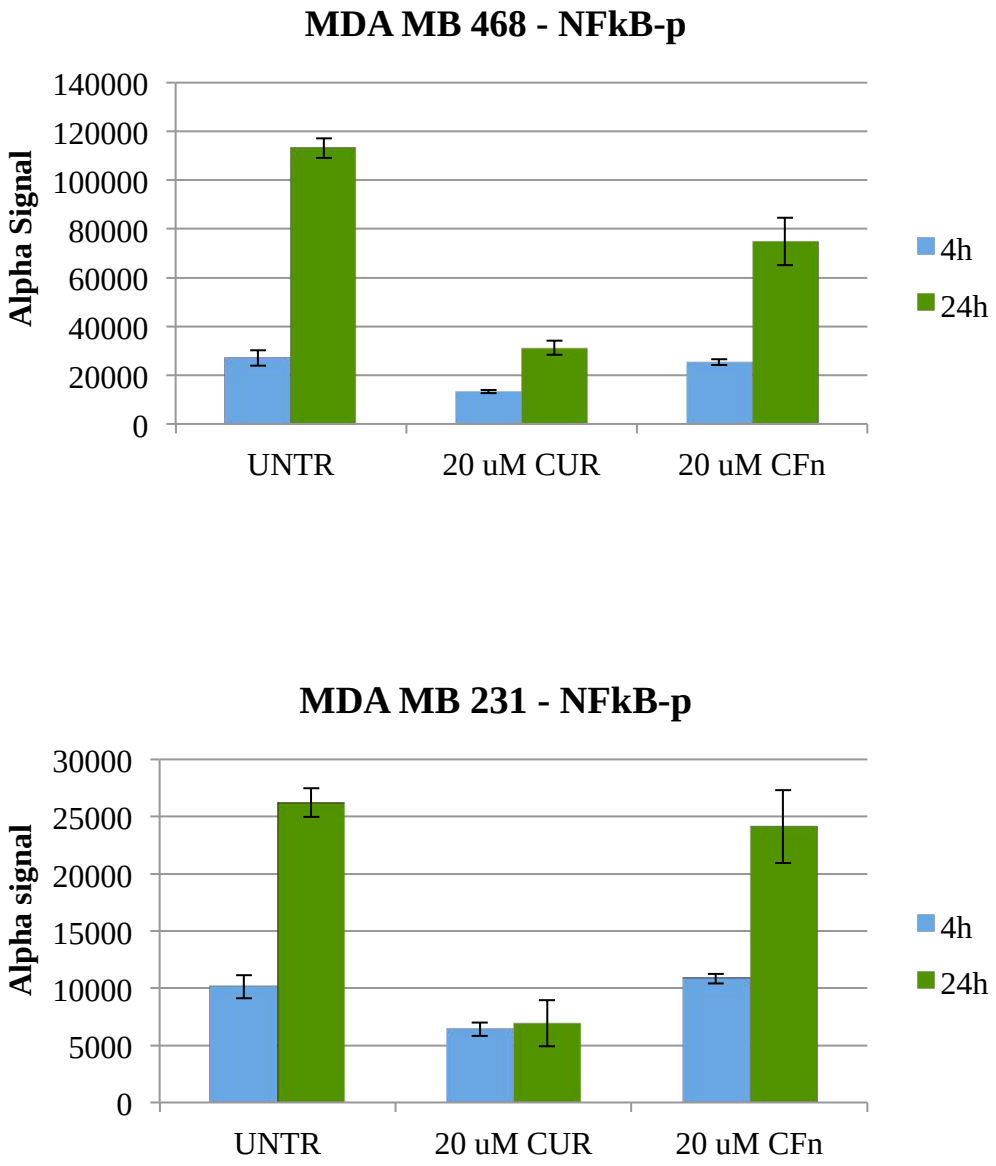

Fig. 4.16 Quantification of the decrease in NF-κB phosphorylation using a sandwich immunoassay for quantitative detection of specific protein in cellular lysates based on Alpha Technology. MDA-MB-231 and MDA-MB-468 cells were treated with 20 μM free curcumin or CFn for 4 and 24 h at 37 °C. The AlphaLISA signal was measured in an EnSight™ Multimode Plate Reader (Perkin Elmer®).

4.6 Conclusions

Turmeric offers a great potential as a source of a natural therapeutic such as curcumin, recognized as safe. Unfortunately, curcumin does not possess the characteristics that would make it a good drug candidate, and even though it is known since centuries and multiple therapeutic activities are ascribed to it, it still has dark sides, enough to be considered an "invalid metabolic panaceas". On one hand, it was used in Chinese medicine as early as the second millennium BC for the treatment of multiple diseases and it is considered to be active on many intracellular pathways. On the other hand, no double-blinded, placebo controlled clinical trial of curcumin has been successful[77].

In this work, by taking advantage of ferritin, we have developed a system that has enable us to overcome some of the most critical aspects related to curcumin administration: poor solubility, chemical instability, pharmacokinetic, pharmacodynamics and ADME problems. Nevertheless, other important issues have still to be addressed. HFn maintains the capability of self-assembling, disassembling and reassembling with shape memory into a 24-H subunit nanocage depending on pH changes: in particular, by exploiting basic pH, it was possible to load curcumin, in a simple and quite reproducible manner. Noteworthy, we worked on pure curcumin, purified from a commercial mixture by flash chromatographic on silica gel. In this way, we focused on a single active molecule, removing possible ambiguities that are often associated with the use of curcumin or more generally of turmeric extracts.

Once encapsulated, the protein shell protects the molecules from the external environment, increasing the stability of curcumin in aqueous solution under conditions that normally lead to a rapid degradation: actually, about 70% of curcumin was still stable after 48 h. Furthermore, the system allowed obtaining high concentrations of the drug in aqueous medium, thus overcoming the poor solubility of the molecule.

We then compared the effect of our curcumin nanoformulation with that of free curcumin, by assaying the effect of both on triple negative breast cancer cell lines, which are the most refractory to treatments, being resistant to common cytotoxic drugs and lacking receptors for a targeted therapy. We first verified that HFn was uptaken by the cells, as already seen in other cell lines[66,78]. As expected, ferritin cages were internalized rapidly and this process was still mediated by TfR1, resulting in clathrin-dependent uptake. Subsequently, we used CFn to treat MDA-MB-468 and MDA-MB-231 cells and comparing the effects with those exerted by equal concentrations of free molecule. The results obtained from viability assays revealed that encapsulated curcumin at minimal concentration was more effective compared to free drug. This is probably due to various factors, including the increase in solubility and chemical stability, but also because the free drug, in this concentration range, forms colloidal aggregates (as highlighted in DLS) which make its action more variable.

One of our goals was to verify the action of curcumin on resistance mechanisms that make this type of tumors scantily responsive to even the most effective drugs, such as doxorubicin. So, to evaluate the modulation of doxorubicin treatment by CFn, we treated both cell lines with a combination of doxorubicin and curcumin or CFn, then analyzed cell viability. CFn strongly enhanced the sensitization of MDA-MB-468 to doxorubicin, being much more effective than curcumin alone. In MDA-MB-231 cells this effect was weaker and appeared at longer times, but was still detectable. Unfortunately, it was not possible to clarify the mechanisms underlying CFn’s

activity. It is generally accepted that it has a pleiotropic effect[2], as it acts on multiple cellular pathways. We therefore analyzed three of them, *i.e.*, MDR proteins, cell cycle and NF-κB pathway. First, we sought to test whether CFn acts on proteins involved in MDR, namely the ABC transporters, that are primarily responsible for the resistance to treatments with doxorubicin. In both cell lines, the activity of P-gp and MRP1 was present, but in MDA-MB-231 the effect of latter was apparently stronger. It will be important to check whether the action and the expression of these proteins is modulated by curcumin, free or nanoformulated. Some previous reports have demonstrated this activity[38,39], but our preliminary experiments have yielded contradictory results: so this is an issue that should be definitely addressed and more thoroughly investigated. As regards the cell cycle, the accumulation observed in G0/G1 (in MDA-MB-231) or G2/M (in MDA-MB-468) phases after 48 h of treatment suggested that nanoformulated curcumin could block the proliferation of cells instead of inducing apoptosis. This result is only partially in agreement with previous works reporting on the effect of other types of nanoparticles, on breast cancer cells[49].

Finally, after encapsulation, NF-κB was no longer a preferred target for curcumin because the nanoformulation did not induce a significant decrease in NF-κB phosphorylation, unlike free curcumin. Perhaps the cage might primarly direct curcumin on other targets.

It can be concluded that ferritin overcomes some shortcomings in curcumin use, making it a promising molecule for cancer treatment. Further investigations are required to clarify the mechanisms underlying its action and of course, bioavailability studies will be also required. In any case HFn-encapsulated curcumin can be still regarded as an useful tool in the treatment of triple negative breast cancer.

4.7 References

1. LE Magazine, September 2001 - Cover Story: Unlocking the power of curcumin. *LifeExtension.com* Available at: http://www.lifeextension.com/magazine/2001/9/cover_curcumin/Page-01. (Accessed: 27th December 2016)
2. Aggarwal, B. B., Sundaram, C., Malani, N. & Ichikawa, H. in *The Molecular Targets and Therapeutic Uses of Curcumin in Health and Disease* (eds. Aggarwal, B. B., Surh, Y.-J. & Shishodia, S.) 1–75 (Springer US, 2007). doi:10.1007/978-0-387-46401-5_1
3. Esatbeyoglu, T. *et al.* Curcumin--from molecule to biological function. *Angew. Chem. Int. Ed Engl.* **51,** 5308–5332 (2012).
4. Chen, L. *et al.* Encapsulation of curcumin in recombinant human H-chain ferritin increases its water-solubility and stability. *ResearchGate* **62,** 1147–1153 (2014).
5. Schraufstatter, E. & Bernt, H. Antibacterial action of curcumin and related compounds. *Nature* **164,** 456 (1949).
6. Kuttan, R., Bhanumathy, P., Nirmala, K. & George, M. C. Potential anticancer activity of turmeric (Curcuma longa). *Cancer Lett.* **29,** 197–202 (1985).
7. Singh, S. & Aggarwal, B. B. Activation of transcription factor NF-kappa B is suppressed by curcumin (diferuloylmethane) [corrected]. *J. Biol. Chem.* **270,** 24995–25000 (1995).
8. Oppenheimer, A. TURMERIC (CURCUMIN) IN BILIARY DISEASES. *The Lancet* **229,** 619–621 (1937).
9. Strimpakos, A. S. & Sharma, R. A. Curcumin: preventive and therapeutic properties in laboratory studies and clinical trials. *Antioxid. Redox Signal.* **10,** 511–545 (2008).
10. Gupta, S. C., Patchva, S., Koh, W. & Aggarwal, B. B. Discovery of Curcumin, a Component of the Golden Spice, and Its Miraculous Biological Activities. *Clin. Exp. Pharmacol. Physiol.* **39,** 283–299 (2012).
11. Lao, C. D. *et al.* Dose escalation of a curcuminoid formulation. *BMC Complement. Altern. Med.* **6,** 10 (2006).
12. Vogel, H. & Pelletier, J. Curcumin-biological and medicinal properties. *Journal de Pharmacie* (1815).
13. Miłobędzka, J., v. Kostanecki, S. & Lampe, V. Zur Kenntnis des Curcumins. *Berichte Dtsch. Chem. Ges.* **43,** 2163–2170 (1910).
14. Lampe, V. Synthese von Curcumin. *Berichte Dtsch. Chem. Ges.* **51,** 1347–1355 (1918).
15. Priyadarsini, K. I. Photophysics, photochemistry and photobiology of curcumin: Studies from organic solutions, bio-mimetics and living cells. *J. Photochem. Photobiol. C Photochem. Rev.* **10,** 81–95 (2009).
16. Priyadarsini, K. I. The Chemistry of Curcumin: From Extraction to Therapeutic Agent. *Molecules* **19,** 20091–20112 (2014).
17. Wang, Y. J. *et al.* Stability of curcumin in buffer solutions and characterization of its degradation products. *J. Pharm. Biomed. Anal.* **15,** 1867–1876 (1997).
18. Khurana, A. & Ho, C.-T. High Performance Liquid Chromatographic Analysis of Curcuminoids and Their Photo-oxidative Decomposition Compounds in Curcuma Longa L. *J. Liq. Chromatogr.* **11,** 2295–2304 (1988).
19. Wahlström, B. & Blennow, G. A study on the fate of curcumin in the rat. *Acta Pharmacol.*

Toxicol. (Copenh.) **43,** 86–92 (1978).
20. Lev-Ari, S. *et al.* Inhibition of pancreatic and lung adenocarcinoma cell survival by curcumin is associated with increased apoptosis, down-regulation of COX-2 and EGFR and inhibition of Erk1/2 activity. *Anticancer Res.* **26,** 4423–4430 (2006).
21. Aoki, H. *et al.* Evidence that curcumin suppresses the growth of malignant gliomas in vitro and in vivo through induction of autophagy: role of Akt and extracellular signal-regulated kinase signaling pathways. *Mol. Pharmacol.* **72,** 29–39 (2007).
22. Wang, Y., Yu, J., Cui, R., Lin, J. & Ding, X. Curcumin in Treating Breast Cancer: A Review. *J. Lab. Autom.* **21,** 723–731 (2016).
23. Menon, V. P. & Sudheer, A. R. in *The Molecular Targets and Therapeutic Uses of Curcumin in Health and Disease* (eds. Aggarwal, B. B., Surh, Y.-J. & Shishodia, S.) 105–125 (Springer US, 2007). doi:10.1007/978-0-387-46401-5_3
24. He, Z.-Y. *et al.* Upregulation of p53 expression in patients with colorectal cancer by administration of curcumin. *Cancer Invest.* **29,** 208–213 (2011).
25. Kakarala, M. *et al.* Targeting breast stem cells with the cancer preventive compounds curcumin and piperine. *Breast Cancer Res. Treat.* **122,** 777–785 (2010).
26. Gupta, S. C., Kismali, G. & Aggarwal, B. B. Curcumin, a component of turmeric: from farm to pharmacy. *BioFactors Oxf. Engl.* **39,** 2–13 (2013).
27. Aggarwal, B. B., Kumar, A. & Bharti, A. C. Anticancer potential of curcumin: preclinical and clinical studies. *Anticancer Res.* **23,** 363–398 (2003).
28. Devassy, J. G., Nwachukwu, I. D. & Jones, P. J. H. Curcumin and cancer: barriers to obtaining a health claim. *Nutr. Rev.* **73,** 155–165 (2015).
29. Ramachandran, C. *et al.* Expression profiles of apoptotic genes induced by curcumin in human breast cancer and mammary epithelial cell lines. *Anticancer Res.* **25,** 3293–3302 (2005).
30. Choudhuri, T., Pal, S., Agwarwal, M. L., Das, T. & Sa, G. Curcumin induces apoptosis in human breast cancer cells through p53-dependent Bax induction. *FEBS Lett.* **512,** 334–340 (2002).
31. Shao, Z.-M. *et al.* Curcumin exerts multiple suppressive effects on human breast carcinoma cells. *Int. J. Cancer* **98,** 234–240 (2002).
32. Ke, C.-S. *et al.* Curcumin-induced Aurora-A suppression not only causes mitotic defect and cell cycle arrest but also alters chemosensitivity to anticancer drugs. *J. Nutr. Biochem.* **25,** 526–539 (2014).
33. Sa, G. & Das, T. Anti cancer effects of curcumin: cycle of life and death. *Cell Div.* **3,** 14 (2008).
34. Lv, Z.-D. *et al.* Curcumin induces apoptosis in breast cancer cells and inhibits tumor growth in vitro and in vivo. *Int. J. Clin. Exp. Pathol.* **7,** 2818–2824 (2014).
35. Gh, D., Hc, L., Zz, S. & Zm, S. [Analysis of anti-proliferation of curcumin on human breast cancer cells and its mechanism]. *Zhonghua Yi Xue Za Zhi* **83,** 1764–1768 (2003).
36. Kim, H. I., Huang, H., Cheepala, S., Huang, S. & Chung, J. Curcumin inhibition of integrin (alpha6beta4)-dependent breast cancer cell motility and invasion. *Cancer Prev. Res. Phila. Pa* **1,** 385–391 (2008).
37. Goel, A. & Aggarwal, B. B. Curcumin, the golden spice from Indian saffron, is a chemosensitizer and radiosensitizer for tumors and chemoprotector and radioprotector for normal organs. *Nutr. Cancer* **62,** 919–930 (2010).

38. Anuchapreeda, S., Leechanachai, P., Smith, M. M., Ambudkar, S. V. & Limtrakul, P. Modulation of P-glycoprotein expression and function by curcumin in multidrug-resistant human KB cells. *Biochem. Pharmacol.* **64,** 573–582 (2002).
39. Limtrakul, P., Chearwae, W., Shukla, S., Phisalphong, C. & Ambudkar, S. V. Modulation of function of three ABC drug transporters, P-glycoprotein (ABCB1), mitoxantrone resistance protein (ABCG2) and multidrug resistance protein 1 (ABCC1) by tetrahydrocurcumin, a major metabolite of curcumin. *Mol. Cell. Biochem.* **296,** 85–95 (2007).
40. Teng, Y.-N., Hsieh, Y.-W., Hung, C.-C. & Lin, H.-Y. Demethoxycurcumin modulates human P-glycoprotein function via uncompetitive inhibition of ATPase hydrolysis activity. *J. Agric. Food Chem.* **63,** 847–855 (2015).
41. Punfa, W. *et al.* Curcumin-loaded PLGA nanoparticles conjugated with anti- P-glycoprotein antibody to overcome multidrug resistance. *Asian Pac. J. Cancer Prev. APJCP* **15,** 9249–9258 (2014).
42. Bordoloi, D., Roy, N. K., Monisha, J., Padmavathi, G. & Kunnumakkara, A. B. Multi-Targeted Agents in Cancer Cell Chemosensitization: What We Learnt from Curcumin Thus Far. *Recent Patents Anticancer Drug Discov.* **11,** 67–97 (2016).
43. Allijn, I. E., Schiffelers, R. M. & Storm, G. Comparison of pharmaceutical nanoformulations for curcumin: Enhancement of aqueous solubility and carrier retention. *Int. J. Pharm.* **506,** 407–413 (2016).
44. Takahashi, M., Uechi, S., Takara, K., Asikin, Y. & Wada, K. Evaluation of an oral carrier system in rats: bioavailability and antioxidant properties of liposome-encapsulated curcumin. *J. Agric. Food Chem.* **57,** 9141–9146 (2009).
45. Sreekanth, C. N., Bava, S. V., Sreekumar, E. & Anto, R. J. Molecular evidences for the chemosensitizing efficacy of liposomal curcumin in paclitaxel chemotherapy in mouse models of cervical cancer. *Oncogene* **30,** 3139–3152 (2011).
46. Liposomal curcumin for treatment of diseases.
47. Ranjan, A. P., Mukerjee, A., Vishwanatha, J. K. & Helson, L. Curcumin-er, a liposomal-plga sustained release nanocurcumin for minimizing qt prolongation for cancer therapy. (2014).
48. Yang, X. *et al.* Curcumin-Encapsulated Polymeric Micelles Suppress the Development of Colon Cancer In Vitro and In Vivo. *Sci. Rep.* **5,** 10322 (2015).
49. Verderio, P., Bonetti, P., Colombo, M., Pandolfi, L. & Prosperi, D. Intracellular Drug Release from Curcumin-Loaded PLGA Nanoparticles Induces G2/M Block in Breast Cancer Cells. *Biomacromolecules* **14,** 672–682 (2013).
50. Xie, X. *et al.* PLGA nanoparticles improve the oral bioavailability of curcumin in rats: characterizations and mechanisms. *J. Agric. Food Chem.* **59,** 9280–9289 (2011).
51. Esmaili, M. *et al.* Beta casein-micelle as a nano vehicle for solubility enhancement of curcumin; food industry application. *LWT - Food Sci. Technol.* **44,** 2166–2172 (2011).
52. Elzoghby, A. O., Samy, W. M. & Elgindy, N. A. Albumin-based nanoparticles as potential controlled release drug delivery systems. *J. Control. Release Off. J. Control. Release Soc.* **157,** 168–182 (2012).
53. Cutrin, J. C., Crich, S. G., Burghelea, D., Dastrù, W. & Aime, S. Curcumin/Gd loaded apoferritin: a novel 'theranostic' agent to prevent hepatocellular damage in toxic induced acute hepatitis. *Mol. Pharm.* **10,** 2079–2085 (2013).
54. Geninatti Crich, S. *et al.* Targeting ferritin receptors for the selective delivery of imaging

and therapeutic agents to breast cancer cells. *Nanoscale* **7,** 6527–6533 (2015).
55. Jamdade, V. S. *et al.* Therapeutic targets of triple-negative breast cancer: a review. *Br. J. Pharmacol.* **172,** 4228–4237 (2015).
56. Anders, C. K. & Carey, L. A. Biology, Metastatic Patterns, and Treatment of Patients with Triple-Negative Breast Cancer. *Clin. Breast Cancer* **9,** S73–S81 (2009).
57. Lehmann, B. D. *et al.* Identification of human triple-negative breast cancer subtypes and preclinical models for selection of targeted therapies. *J. Clin. Invest.* **121,** 2750–2767 (2011).
58. Mayer, I. A., Abramson, V. G., Lehmann, B. D. & Pietenpol, J. A. New Strategies for Triple-Negative Breast Cancer—Deciphering the Heterogeneity. *Clin. Cancer Res.* **20,** 782–790 (2014).
59. Farmer, H. *et al.* Targeting the DNA repair defect in BRCA mutant cells as a therapeutic strategy. *Nature* **434,** 917–921 (2005).
60. Carey, L. A. *et al.* TBCRC 001: randomized phase II study of cetuximab in combination with carboplatin in stage IV triple-negative breast cancer. *J. Clin. Oncol. Off. J. Am. Soc. Clin. Oncol.* **30,** 2615–2623 (2012).
61. O'Reilly, E. A. *et al.* The fate of chemoresistance in triple negative breast cancer (TNBC). *BBA Clin.* **3,** 257–275 (2015).
62. Dufour, R. *et al.* BCRP and P-gp relay overexpression in triple negative basal-like breast cancer cell line: a prospective role in resistance to Olaparib. *Sci. Rep.* **5,** 12670 (2015).
63. Milane, L., Duan, Z. & Amiji, M. Role of hypoxia and glycolysis in the development of multi-drug resistance in human tumor cells and the establishment of an orthotopic multi-drug resistant tumor model in nude mice using hypoxic pre-conditioning. *Cancer Cell Int.* **11,** 3 (2011).
64. Chacón, R. D. & Costanzo, M. V. Triple-negative breast cancer. *Breast Cancer Res.* **12,** S3 (2010).
65. Shindikar, A., Singh, A., Nobre, M. & Kirolikar, S. Curcumin and Resveratrol as Promising Natural Remedies with Nanomedicine Approach for the Effective Treatment of Triple Negative Breast Cancer. *J. Oncol.* **2016,** 9750785 (2016).
66. Bellini, M. *et al.* Protein nanocages for self-triggered nuclear delivery of DNA-targeted chemotherapeutics in Cancer Cells. *J. Controlled Release* **196,** 184–196 (2014).
67. Masuda, T., Goto, F., Yoshihara, T. & Mikami, B. The universal mechanism for iron translocation to the ferroxidase site in ferritin, which is mediated by the well conserved transit site. *Biochem. Biophys. Res. Commun.* **400,** 94–99 (2010).
68. Péret-Almeida, L., Cherubino, A. P. F., Alves, R. J., Dufossé, L. & Glória, M. B. A. Separation and determination of the physico-chemical characteristics of curcumin, demethoxycurcumin and bisdemethoxycurcumin. *Food Res. Int.* **38,** 1039–1044 (2005).
69. Bernabé-Pineda, M., Ramírez-Silva, M. T., Romero-Romo, M., González-Vergara, E. & Rojas-Hernández, A. Determination of acidity constants of curcumin in aqueous solution and apparent rate constant of its decomposition. *Spectrochim. Acta. A. Mol. Biomol. Spectrosc.* **60,** 1091–1097 (2004).
70. Yallapu, M. M., Jaggi, M. & Chauhan, S. C. Curcumin nanoformulations: a future nanomedicine for cancer. *Drug Discov. Today* **17,** 71–80 (2012).
71. Naksuriya, O., Okonogi, S., Schiffelers, R. M. & Hennink, W. E. Curcumin nanoformulations: a review of pharmaceutical properties and preclinical studies and clinical

data related to cancer treatment. *Biomaterials* **35,** 3365–3383 (2014).
72. Illien, F. *et al.* Quantitative fluorescence spectroscopy and flow cytometry analyses of cell-penetrating peptides internalization pathways: optimization, pitfalls, comparison with mass spectrometry quantification. *Sci. Rep.* **6,** 36938 (2016).
73. Cridge, B. J., Larsen, L. & Rosengren, R. J. Curcumin and its derivatives in breast cancer: Current developments and potential for the treatment of drug-resistant cancers. *Oncol. Discov.* **1,** 6 (2013).
74. Zanotto-Filho, A. *et al.* The curry spice curcumin selectively inhibits cancer cells growth in vitro and in preclinical model of glioblastoma. *J. Nutr. Biochem.* **23,** 591–601 (2012).
75. NFκB Inhibitors Induce Cell Death in Glioblastomas. *PubMed Journals* Available at: https://ncbi.nlm.nih.gov/labs/articles/21040711/. (Accessed: 31st December 2016)
76. Viatour, P., Merville, M.-P., Bours, V. & Chariot, A. Phosphorylation of NF-kappaB and IkappaB proteins: implications in cancer and inflammation. *Trends Biochem. Sci.* **30,** 43–52 (2005).
77. Nelson, K. M. *et al.* The Essential Medicinal Chemistry of Curcumin. *J. Med. Chem.* (2017). doi:10.1021/acs.jmedchem.6b00975
78. Mazzucchelli, S. *et al.* Nanometronomic treatment of 4T1 breast cancer with nanocaged doxorubicin prevents drug resistance and circumvents cardiotoxicity. *Oncotarget* (2016). doi:10.18632/oncotarget.14204

CHAPTER 5

Apoferritin nanocages for targeted delivery of miRNA inhibitors to overcome Trastuzumab resistance in HER2+ breast cancer

5.1 HER2 positive breast cancer

Human epidermal growth factor receptor 2 (HER2) is overexpressed in about 20-30% of breast cancer tumors and it is associated with a more aggressive disease, higher recurrence rate and shortened survival[1,2]. It may be important to emphasize that although HER2 overexpression has been described in a variety of human malignant conditions, gene amplification is rare except in breast cancer where amplification of the gene occurs in approximately the same proportion of protein overexpression[3].

HER2, also referred to as HER2/neu or ErbB2, is a 185 kDa receptor first described more than three decades ago[4] and it is part of the epidermal growth factor (EGF) family, along with 3 other receptors: epidermal growth factor receptors HER1 (ErbB1), HER3 (ErbB3) and HER4 (ErbB4). These transmembrane tyrosine kinase receptors lie at the head of a complex signal transduction cascade that normally regulate cell growth and survival, adhesion, migration, differentiation and other cellular responses[5] (Fig. 5.1 A). The intracellular tyrosine kinase domains are activated by both homodimerization and heterodimerization, generally induced by ligand binding, but HER2 is able to adopt a fixed conformation resembling a ligand-activated state, permitting it to dimerize with one of the other EGF receptors in the absence of a ligand. Moreover, it is the only receptor in the EGF family without identified ligands[2].

While growth-factor-induced EGFR signaling is essential for many processes and involved in numerous additional cellular responses, the aberrant activity of members of this receptor family has been shown to play a key role in the development and growth of tumor cells. In particular, HER2 overexpression plays a crucial role in pathogenesis of many human cancer types[5,6]. Sure enough, HER2 signaling promotes cell proliferation through the Ras/MAPK pathway and inhibits cell death through the PI3K/Akt/mTOR cascade. MAPK is a protein kinase that regulates cell function including proliferation, gene expression, differentiation, mitosis, cell survival and apoptosis; AKT is a serine/threonine-specific protein kinase involved in cellular survival pathways, by inhibiting apoptotic processes (programmed cell death); mTOR regulates the cellular functions that integrate upstream signaling inputs and is a central regulator in mammalian metabolism and physiology[3].

Of our particular interest is a member of the PI3K/Akt pathway, the phosphatase and tensin homolog (PTEN). PTEN is a dual phosphatase that mainly dephosphorylates membrane phosphatidylinositol-(3,4,5)-triphosphate (PIP3) leading to the biphosphate product PIP2 and therefore resulting in inhibition of the AKT signaling pathway[7,8]. Loss of PTEN function have been reported in nearly 50% of breast cancers and in many other cancer types[9,10].

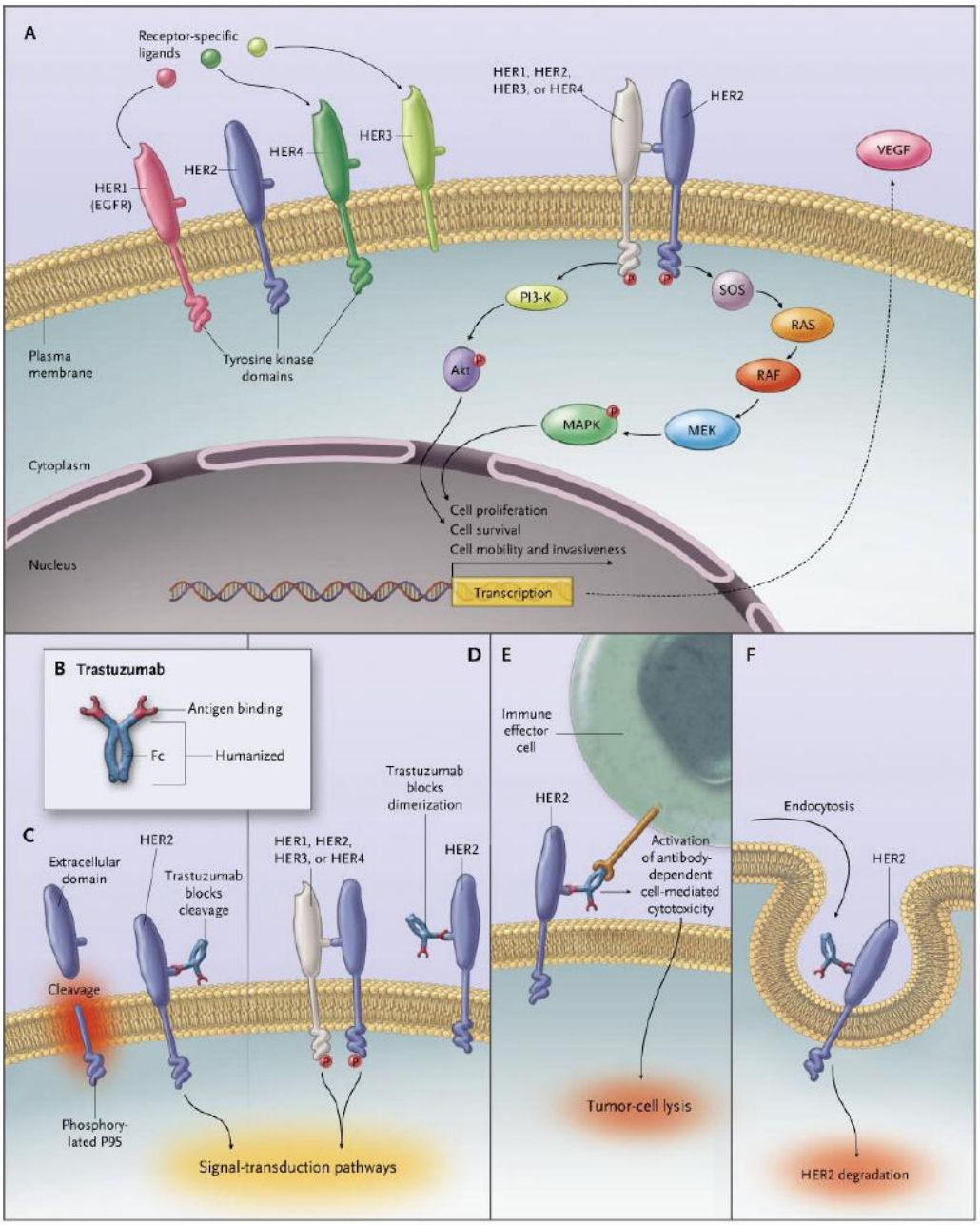

Fig. 5.1 Signal Transduction by the HER Family and Potential Mechanisms of Action of Trastuzumab. As shown in Panel A, the four members of the HER family are HER1, HER2, HER3, and HER4. There are receptor-specific ligands for HER1, HER3, and HER4. An intracellular tyrosine kinase domain exists for HER1, HER2, and HER4. Phosphorylation of the domain by means of homodimerization or heterodimerization induces both cell proliferation and survival signaling. HER2 is the preferred dimerization partner for the other HER family members. The phosphorylated (activated) tyrosine residues on the intracellular domain of HER2 activate the lipid kinase PI3K, which phosphorylates a phosphatidylinositol that in turn binds and phosphorylates the enzyme Akt, driving cell survival. In parallel, a guanine nucleotide exchange factor (SOS) activates RAS enzyme that, in turn, activates RAF and then the mitogen extracellular signal kinase (MEK). MEK phosphorylates, among others, the MAPK, driving cellular proliferation. One of many other downstream effects is the production of vascular endothelial growth factor (VEGF) supporting angiogenesis. The most well-documented potential mechanisms of action are shown in panels B-F. (B) Cleavage of the extracellular domain of HER2 leaves a membrane-bound phosphorylated p95, which can activate signal-transduction pathways. (C) Binding of trastuzumab to HER2 reduces shedding of the extracellular domain, thereby reducing p95. (D) Trastuzumab may reduce HER2 signaling by physically inhibiting either homodimerization or heterodimerization. (E) Trastuzumab may recruit Fc-competent immune effector cells and the other components of antibody-dependent cell-mediated cytotoxicity, leading to tumor-cell death. (F) Additional mechanisms such as receptor down-regulation through endocytosis have been postulated[3].

5.1.1 Trastuzumab treatment

Prior to the development of HER2-targeted therapy, HER2-positive BC was characterized by a very aggressive cancer phenotype and a poor prognosis, including higher mortality in early stage, reduced time to relapse and an increased incidence of metastasis[1,7,11]. Over the past decade, the management of these cancers has evolved considerably, thanks to advances in screening, genetic testing, imaging, surgical and radiation techniques, but also innovations in medical therapy including widespread use of HER2-directed therapy in early and advanced BC[12]. An ample numbers of agents that target the receptor have been introduced, including monoclonal antibodies, small molecule and antibody drug conjugates (Tab. 5.1). The prototype of this directed therapy is Trastuzumab, (TZ, Herceptin®) a humanized monoclonal antibody targeting the HER2 receptor, which was approved by the FDA in 1998[2]. It consists of two antigen specific sites that bind to the juxtamembrane portion of the extracellular domain of the receptor, preventing ligand-independent HER2 signaling and downregulating HER2 expression. The remainder of antibody is a human IgG with a conserved Fc portion[3].

Tab. 5.1 HER2 directed targeted therapy approved for the management of HER2-positive breast cancer[12].

Class	Comments
Monoclonal antibodies	
Trastuzumab	A humanized monoclonal antibody directed against the extracellular domain of the HER2 receptor that prevents ligand-independent HER2 signaling.
Pertuzumab	A humanized monoclonal antibody that binds to the extracellular domain II of HER2 and inhibits ligand-dependent HER2–HER3 dimerization.
Antibody drug conjugates	
Ado-trastuzumab emtansine	An antibody-drug conjugate consisting of the cytotoxic agent DM1 linked to trastuzumab.
Small molecules inhibitors	
Lapatinib	An oral dual EGFR/ErbB2 reversible tyrosine kinase inhibitor blocking both HER1 & HER2 that suppresses the downstream pathways.
Afatinib, neratinib	Irreversible tyrosine kinase inhibitor of EGFR/HER2/HER4

Trastuzumab: mechanism of action

The mechanism of action of TZ has not been clearly understood and it is likely multifaceted. Being an IgG1, its proposed functions may be divided into those mediated by Fab (fragment antigen binding) or Fc (fragment crystallisable) regions. The Fab contains the antigen-binding sites of the antibody, whereas the Fc contains the binding sites for Fc receptors present on immune cells, platelets, hepatocytes and endothelial cells[13].

Several possible mechanisms by which TZ might decrease intracellular signaling include prevention of HER2-receptor dimerization, increased endocytotic destruction of the receptor, inhibition of proteolytic cleavage that results in shedding of the extracellular domain and production of a truncated and phosphorylated (active) membrane-bound fragment, p95HER2[3,13] (Fig. 5.1 B-F). All these processes led to a cytostatic effect that is associated with G1 arrest, a noted increase in p27 levels and a decrease in cyclin D1 and cyclin-dependent kinase 2 activity[13–15].

TZ alone does not seem to promote a significant level of apoptosis, but it is synergistic with most chemotherapeutics, probably due to the inhibition of the PI3K/Akt signaling pathway, which normally promotes cell survival[16]. In 2004, Nagata *et al.* demonstrated that treatment with TZ quickly reduced the level of phosphorylated and activated Akt, in BT474 and SKBR3 breast cancer cells, and that this effect is mediated by PTEN, whose phosphatase activity dramatically increased. Moreover, TZ induces PTEN activation by increasing its translocation from the cytoplasm to the membrane, through reducing the inhibitory tyrosine phosphorylation of PTEN. TZ activates PTEN by inhibiting Src association with HER2 in HER2-overexpressing breast cancer cells[7]. Furthermore, normal PTEN levels are required for the antiproliferation function of TZ and consequently a PTEN reduction led to resistance to the antiproliferation effect of TZ in BC cells and in fact patients with PTEN-deficient breast cancers have a poor clinical response to trastuzumab[6] (as we will discuss later).

Nevertheless, the innate response alone does not fully explain the effect of TZ on tumor regression. Adaptive mechanisms are also present and involve antibody-dependent cell-mediated cytotoxicity (ADCC) and the need of an operational Fc receptor for trastuzumab antitumoral effect was shown in several xenograft models[17,18]. This is likely to be T-cell mediated, through activation of the Fc receptor, leading to increased cell death[19]. At the same time, the clinical importance of complement activation mediated by TZ Fc is less clear.

Apart from the Fc-mediated cytotoxicity, the Fc portion of human IgG1 such as trastuzumab is important also for maintaining the serum levels of the antibody: intact IgG has been long recognized as more stable in serum and having longer half-life than Fab fragments. Untouched human IgG1 Fc binds to FcRn (neonatal Fc receptors) on endothelial cells and on phagocytes, becomes internalized and recycled back to the blood stream to enhance its half-life within the body[13,20].

Therapeutic efficacy of Trastuzumab treatment

TZ has been shown to be effective and relatively safe in combination with most chemotherapeutic agents used in the treatment of breast cancer. In particular, it should be considered for the management of all **metastatic breast cancers with HER2 overexpression**: patients with moderate to high-risk, rapidly progressive cancer characterized by a negative hormone-receptor status and extensive visceral metastases are candidates for immediate treatment with chemotherapy and should receive the appropriate agent (or agents) with TZ. The benefit of TZ in the first-line treatment was demonstrated in a pivotal phase III trial in which women received standard chemotherapy (paclitaxel or anthracycline and cyclophosphamide) with or without trastuzumab[21]. Other trials showed similar findings and demonstrated the benefit of adding trastuzumab to taxanes-based chemotherapy[22,23], but also to other chemotherapeutic agents such as platinum compound and gemcitabine.

Indeed, it is not clear whether antibody therapy should precede, follow, or be added to hormone therapy for the subgroup of patients with **HER2-positive and hormone receptor positive** disease but surely the administration of HER2-targeted therapy plus an aromatase inhibitor is an effective treatment strategy for the subset of **postmenopausal women with HER2-positive metastatic breast cancer**[24,25].

However, since trastuzumab monotherapy appears to be effective for the treatment of advanced metastatic breast cancer, its use as a single agent for **newly discovered metastatic disease** can be considered and this strategy would delay the initiation of chemotherapy with its attendant side effects, possibly resulting in a better quality of life[3,26].

Lastly, the efficacy and adverse-event profile of trastuzumab for HER2-dependent metastatic breast cancer led to investigation of this antibody as **adjuvant treatment** for women with early-stage, HER2-positive breast cancer. Based on results from five randomized trials, one year of adjuvant TZ has become standard therapy for women with HER2-positive breast cancer[3,12].

Limitations in the use of trastuzumab

Despite the impact of TZ and improvement in outcomes for women with HER2-positive breast cancer, this drug present also some negative aspects. One important limitation is that it is a large molecule and does not efficiently cross the intact blood-brain barrier, to reach possible metastases in the brain. Thus, the central nervous system appears to serve as a sanctuary for the tumor, with disproportionate rates of relapse in the brain and baleful consequences[27,28]. New approaches to HER2-positive central nervous system disease are therefore needed.

Moreover, TZ therapy has been associated with an increased risk of cardiac toxicity, especially when used in combination with anthracyclines: Herceptin can damage the heart and its ability to pump blood effectively. This risk has ranged between 5% to 30%. In addition, it causes flu-like symptoms (fever, chills, muscle aches, nausea) in about 40% of the people who take it[2].

Resistance to trastuzumab therapy has also been documented: the response rate to TZ monotherapy is less than 35%, while the 60% of patients with HER2 positive cancers on regimens combining trastuzumab with microtubule stabilizing drugs do not respond to treatment[29]. Additionally, most patients who achieve an initial response develop resistance to trastuzumab within 1 year[30]. Resistance is a major clinical issue, occurring in both early and advanced breast cancer. For this reason, much effort has been spent on searching for biomarkers of trastuzumab sensitivity, other than HER2, and exploring the mechanisms underlying development of trastuzumab resistance. However, to date, there is still no convincing conclusion[6].

5.1.2 Trastuzumab resistance

Trastuzumab has become widely and successfully used for the treatment of HER2 positive breast cancer but as we touched on in the previous paragraph, resistance to this drug is an important issue which affects outcome for a subset of patients. Understanding the mechanisms of action and resistance to trastuzumab is therefore crucial for the development of new therapeutic strategies. Several models of resistance have been proposed; no clear etiology has been identified, but several hypotheses have emerged.

Generally, have been identified four mechanisms that can explain the development of resistance: (1) obstacles for trastuzumab binding to HER2, (2) upregulation of HER2 downstream

signaling pathways, (3) signaling through alternate pathways and (4) failure to trigger immune-mediated mechanisms to destroy tumor cells[13].

Obstacles for trastuzumab binding to HER2

It has been identified a constitutively active but amino terminal truncated form of HER2 receptor, called p95-HER2, which has kinase activity but lacks the extracellular domain and the binding site of trastuzumab (Fig. 5.2 A). A retrospective study revealed a strong association between the presence of p95-HER2 and clinical resistance to TZ treatment[31].

Not only the lack of TZ binding site, but also the epitope masking has been investigated as a mechanism of resistance to TZ: for example, mucin 4 (MUC4) is a large, highly O-glycosylated membrane-associated glycoprotein, which may interfere with trastuzumab binding to the HER2 receptor[32] (Fig. 5.2 B).

Up-regulation of HER2 downstream signaling pathways

As we know PTEN normally inhibits the activation of PI3K and therefore PTEN loss or decreased levels (caused by mutation of PTEN itself or by transcriptional regulation) results in increased PI3K/Akt phosphorylation and signaling, preventing TZ-mediated growth arrest of HER2-overexpressing breast cancer cells[6,7] (Fig. 5.3). Clearly even PI3K mutations and Akt changes have been implicated in trastuzumab resistance through PI3K/Akt/mTOR pathway activation: for example, TZ-resistant BT474 cells generated by continuous culture of previously sensitive cells in TZ-containing medium have elevated levels of phosphorylated Akt and Akt kinase activity as compared with BT474 parental cell line[33,34].

So, reduced PTEN expression has been identified as a strong indicator to predict TZ resistance in BC patients and members of the PI3K pathway, as well as PTEN, are molecular targets for overcoming trastuzumab resistance[7,35].

Signaling through alternate pathways

This mechanism has been linked to TZ resistance in various preclinical models, but more detailed studies are needed. Lu and colleagues showed that the trastuzumab-induced growth inhibition in HER2-overexpressing cells can be compensated for by increased IGF-IR (insulin-like growth factor receptor) signaling, resulting in resistance to trastuzumab[36,37]. As an alternative, overexpression of HER3, EGFR homodimers and EGFR/HER3 heterodimers, lacking HER2, could potentially bypass TZ blockade and contribute to resistance[38].

Failure to trigger immune-mediated mechanisms

Polymorphism influencing the affinity of IgG1 to the Fc receptor can lead to failed activation of immune-mediate mechanisms which should destroy tumor cells. And this is even more important taking in account that recent evidences has increasingly stressed the importance of ADCC as a major player in TZ antitumoral effect[13].

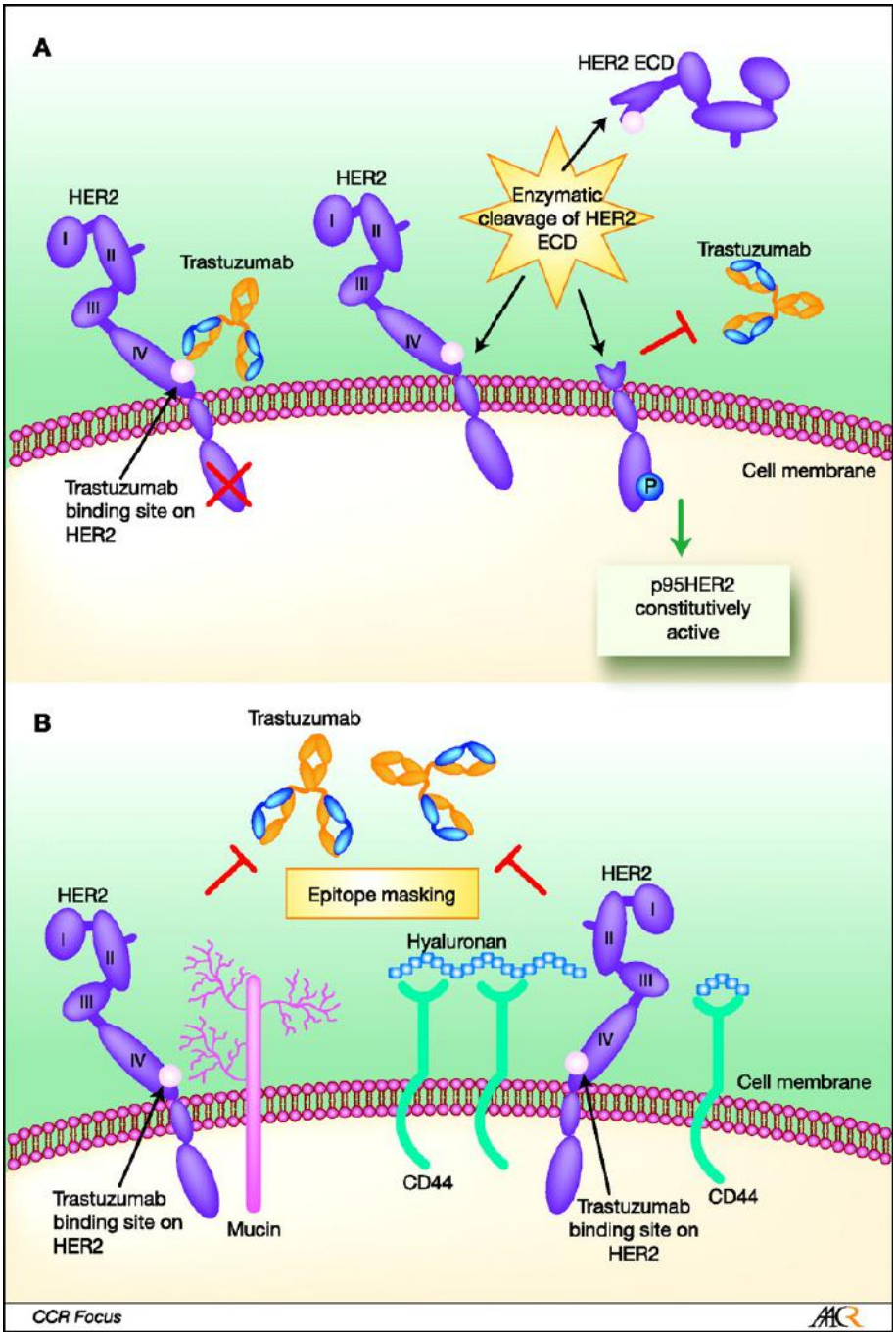

Fig. 5.2 General mechanisms of resistance to trastuzumab: obstacles for trastuzumab binding to HER2. (A) A constitutively active truncated form of HER2 receptor that has kinase activity but lacks the extracellular domain and the binding site of TZ is originated from cleavage of the full-length HER2 receptor. TZ does not bind to p95HER2 and therefore has no effect. The remaining intracellular domain of p95HER2 has operational kinase domains and can be targeted by the TK inhibitor lapatinib. (B) Epitope masking by mucin MUC4 or CD44/polymeric hyaluronan complex[13].

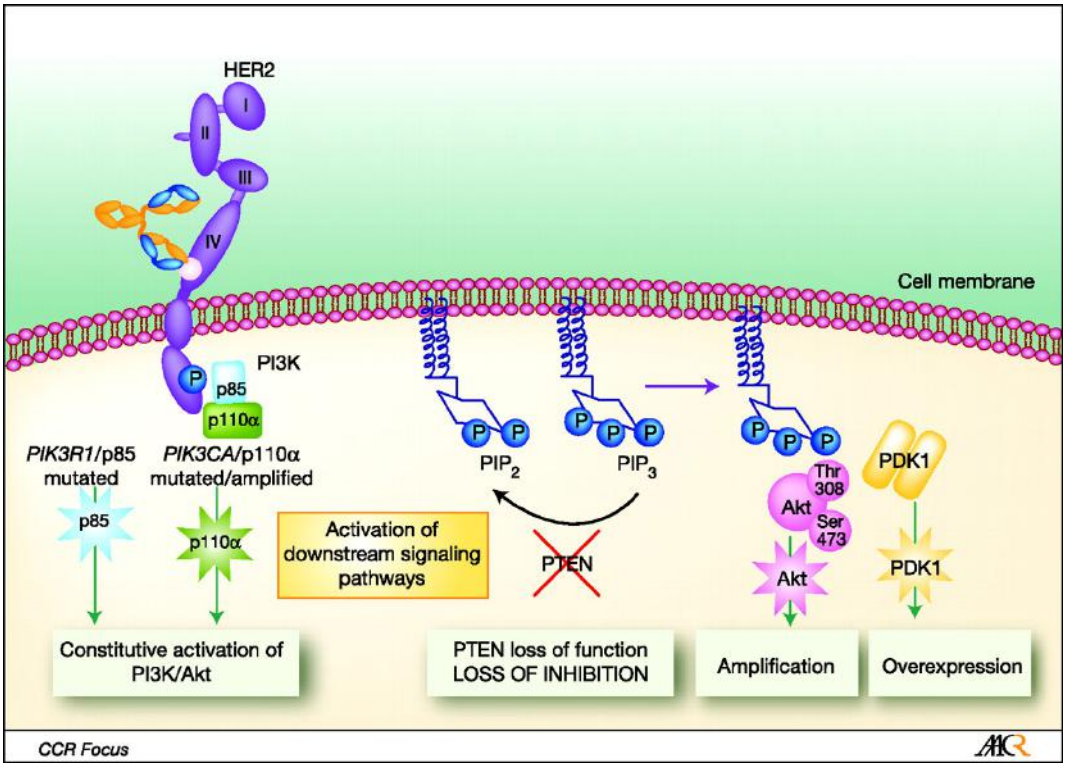

Fig. 5.3 General mechanisms of resistance to trastuzumab: presence of upregulation of HER2 downstream signaling pathways. PTEN is a tumor suppressor. TZ binding stabilizes and activates PTEN and consequently down-regulates the PI3K/Akt signaling pathway. When PTEN function is lost, PI3K remains constitutively active regardless of binding of TZ to HER2. Genomic aberrations in the PI3K pathway produce constitutive activation of the pathway, which will signal downstream to the nucleus regardless of TZ binding to HER2[13].

5.1.3 Other therapeutic options

The emergence of patterns of resistance to trastuzumab has led to the discovery of new monoclonal antibodies and other targeted agents aimed at overcoming TZ resistance and improving survival in patients diagnosed with HER2 positive breast cancers.

Lapatinib (Tykerb /Tyverb, GlaxoSmithKline) is a dual EGFR and HER2 reversible tyrosine kinase inhibitor (blocking both HER1 and HER2) that suppress the downstream signaling involving MAPK/Erk1/2 and PI3K/Akt pathways. Lapatinib has been shown to be effective in inhibiting growth of breast cancer cell lines known to be resistant to TZ[39]. Scaltriti and colleagues tested Lapatinib also in p95-HER2 preclinical models, as a strategy to prevent HER2 signaling despite loss of the TZ binding site[31].

Pertuzumab is a humanized monoclonal antibody that targets HER2 but attaches to a different site (domain II) on the receptor and, as such, inhibits heterodimerization between HER2 and other HER receptors[40]. So, its mechanism of action is complementary to TZ and in fact it has shown modest antitumor clinical activity alone, but appears to be a very good synergistic drug when combined with TZ[12].

Others HER2-directed therapies include Afatinib and Neratinib, irreversible binders of the HER receptors, as well as Hsp90 inhibitors and PI3K inhibitors.

Finally, active immunotherapy using therapeutic vaccine to activate patient's own immune system is a potential therapeutic option, based on the observation that some HER2 positive BC patients develop spontaneous anti-HER2-specific immunity with both cellular and humoral responses. HER2-directed vaccines which include peptide/protein-based, DNA-based, whole tumor cell-based, and dendritic cell-based vaccines are currently under various phases of investigation[41].

5.2 MicroRNAs

Micro-RNAs (miRNAs) are a class of non-coding and single-stranded small RNAs (20-24 nucleotides) that are endogenously expressed in mammalian cells. They modulate gene expression by negatively regulating the stability or translational efficiency of their target mRNAs, in one of two ways depending on the degree of complementarity between the miRNA and the target[30,42]. MiRNAs that bind with perfect or nearly perfect complementarity to protein-coding mRNA sequences induce the RNA-mediated interference (RNAi) pathway, resulting in the degradation of target mRNAs. However, most miRNAs are thought to use a second mechanism: they bind to imperfect complementary sites within the 3' untranslated regions (UTRs) of their mRNA targets and repress gene expression at the level of translation[43] (Fig. 5.4). The human genome may encode over than 1000 miRNAs.

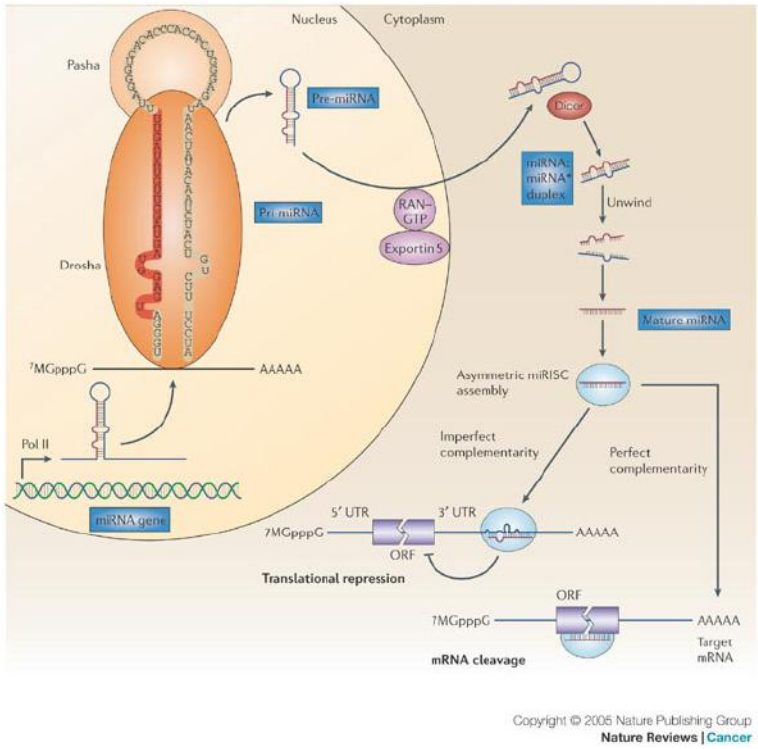

Fig. 5.4 The biogenesis of microRNAs. MicroRNA (miRNA) genes are generally transcribed by RNA Polymerase II (Pol II) in the nucleus to form large pri-miRNA transcripts, which are capped and polyadenylated. Pri-miRNA transcripts are processed by the RNase III enzyme Drosha and its co-factor, Pasha, to release the ~70-nucleotide pre-miRNA precursor product. RAN–GTP and exportin 5 transport the pre-miRNA into the cytoplasm. Subsequently, another RNase III enzyme, Dicer, processes the pre-miRNA to generate a transient ~22-nucleotide miRNA:miRNA* duplex. This duplex is then loaded into the miRNA-associated multiprotein RNA-induced silencing complex (miRISC), which includes the Argonaute proteins, and the mature single-stranded miRNA is preferentially retained in this complex. The mature miRNA then binds to complementary sites in the mRNA target to negatively regulate gene expression in one of two ways that depend on the degree of complementarity between the miRNA and its target. miRNAs that bind to mRNA targets with imperfect complementarity block target gene expression at the level of protein translation. Complementary sites for miRNAs using this mechanism are generally found in the 3′ untranslated regions (3' UTRs) of the target mRNA genes. miRNAs that bind to their mRNA targets with perfect (or nearly perfect) complementarity induce target-mRNA cleavage. miRNAs using this mechanism bind to miRNA complementary sites that are generally found in the coding sequence or open reading frame (ORF) of the mRNA target[43].

The current challenge is to accurately identify targets that are regulated by miRNAs. Because miRNAs usually bind to their targets with incomplete complementarity, the identification of gene targets with a simple BLAST (Basic Local Alignment Search Tool) is impossible. Moreover, a single miRNA might bind to as many as 200 gene targets, which can be diverse in their function. So, miRNAs potentially control the expression, at least, of about one-third of human mRNAs[44–46].

Out of hundreds of miRNAs that have been identified, a small number have been characterized and they have been shown to control cell growth, differentiation and apoptosis. Consequently, impaired miRNA expression has been implicated in tumorigenesis and may function as oncogenes or tumor suppressing genes[42,43,47]. Another evidence is that about 50% of human miRNAs are located in areas of the genome, known as “fragile sites”, that are associated with cancer. For example, mir-125b-1 is located in a fragile site on chromosome 11q24, which is deleted in a subset of patients with breast, lung, ovarian and cervical cancers[48].

For their role in cancer, miRNAs could potentially represent novel clinical and prognostic markers and they are likely to have a large effect on gene therapies that are designed to block tumor progression. Large-scale expression screens, that compare miRNA levels in tumors versus normal tissues, will be useful in identifying novel miRNAs that are involved in cancer while the administration of synthetic anti-sense oligonucleotides that encode sequences complementary to mature oncogenic miRNAs might effectively inactivate miRNAs in tumors and slow their growth. Conversely, techniques to overexpress miRNAs that function as tumor suppressors could be used to treat specific tumor types [43]. But development of all these methods is needed before miRNA treatments can move from the laboratory bench to the bedside.

As regards in particular breast cancers, miRNAs associated with HER2 status have been explored by miRNA expression profiling of breast cancer specimens. It was found that 5 miRNAs were significantly up-regulated as HER2 expression increased, while other 26 miRNAs were inversely correlates with HER2 expression[49]. In another study, a set of 69 miRNAs was found to distinguish tumor subtypes defined by immunohistochemical expression of ER, PR and HER2[50]. The identified miRNAs may not only be potential biomarkers of HER2 status but also be attractive candidates for further studies.

HER2 itself is a target for several miRNAs: transfection of these miRNAs alone or in combination successfully downregulates HER2 expression and inhibits HER2 signaling downstream, resulting in alteration of malignant cell behaviors such as proliferation, migration and invasiveness[6].

5.2.1 miR-21

Although most of the tumor-related miRNAs are down-regulated in cancer tissues as compared with their normal counterparts, miR-21 is one of the few miRNAs that are consistently up-regulated in malignancies of various tissue origins, including the breast[30]. Over the years, several studies have been published on miR-21 and cancer: miR-21 has been found to be up-regulated in glioblastoma[51], breast cancer[52], lung cancer[53] and chronic lymphocytic leukaemia[54]. As an example, it was found to be expressed at a 5-100-fold higher rate in gliomas than in normal tissue and antisense studies showed that it controls cell growth by inhibiting apoptosis but does not affect cell proliferation, which implies an oncogenic role for this miRNA[51].

Interestingly, miR-21 (as well as other) have been reported as direct regulators of the tumor suppressor PTEN in various type of carcinomas[43,55]. Kojiro *et al.* proved that miR-21 can bind directly to the 3' UTR of PTEN mRNA and decrease PTEN expression in HER2 positive gastric cancer cells, suppressing apoptosis induced by TZ[8]. However, as *mir-21* is not a tissue-specific gene and miR-21 expression is increased also in human breast cancer samples, this miRNA might have a wider function in tumor progression. In particular, it was demonstrated that miR-21 is significantly up-regulated in a subgroup of BCs and high miR-21 expression has been associated with unfavorable pathological and molecular features of the disease, including advanced tumor stage, high tumor grade, lymph node metastasis, negative hormone receptor status and poor patient survival[30]. Given that a single miRNA has multiple targets and different miRNAs might target the same gene, it has been speculated that increased miR-21 expression might block a panel of genes that regulate cell proliferation and apoptosis. In 2008 Yan *et al.*, in addition to evaluated that miR-21 expression level in BC was significantly higher (upregulated greater than twofold), suggested also that the up-regulation was acquired in the course of tumor progression and, in particular, during the acquisition of metastatic potential[42]. Furthermore, in breast cancer miR-21 expression was up-regulated also after trastuzumab therapy, in both the resistant and sensitive tumors and in line with miR-21 up-regulation, the protein expression of PTEN was significantly lower in trastuzumab-resistant tumors as compared with the sensitive ones[30].

Researchers have screened for trastuzumab-responsive miRNAs and available evidence suggests that the regulation of miRNAs on TZ is mainly associated with HER2 signaling pathway components and HER2 compensatory receptors (Fig. 5.5): PTEN is a target gene for both miR-21 and miR-221 in breast cancer[6,30,56]. Leticia De Mattos-Arruda *et al.* confirmed that miR-21 downregulating PTEN contributed to trastuzumab resistance. Besides, the expression level of miRNA-21 was lower in sensitive tumors than in resistant ones among patients with primary HER2-positive breast cancer who received trastuzumab as neoadjuvant therapy[57].

MiRNAs in tumors and plasma have been explored for new biomarkers for trastuzumab treatment but inconsistent results of miR-21 and miR-210, may be due to limited clinical samples, have obtained. So far, no robust miRNA biomarker for trastuzumab therapy has been demonstrated[6].

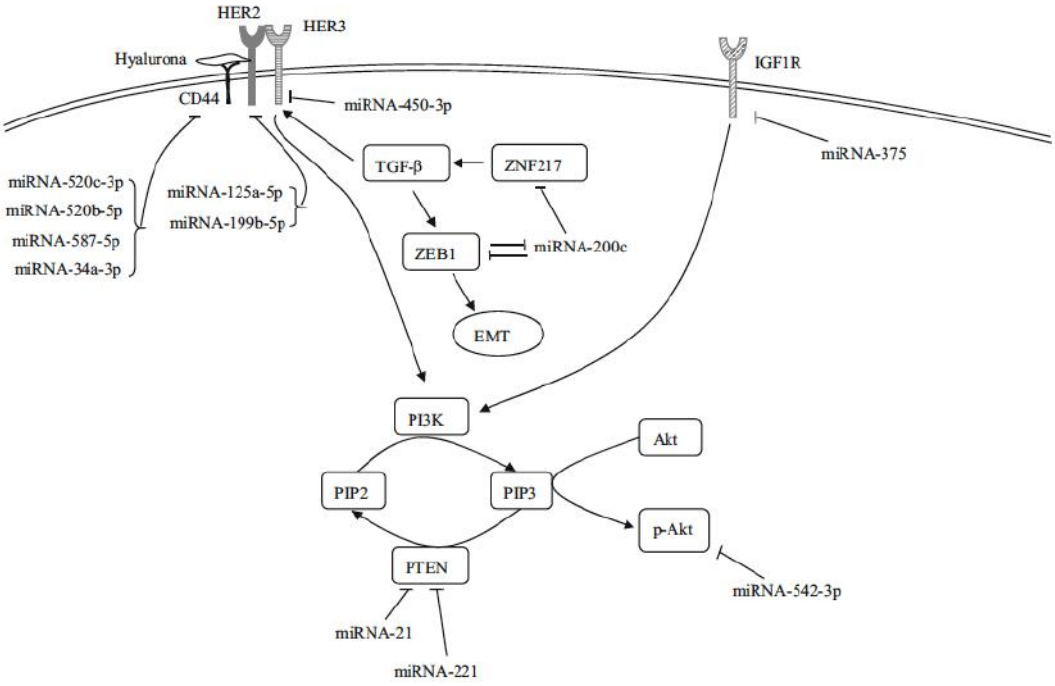

Fig. 5.5 Proposed mechanisms of miRNA regulation on TZ resistance. MiRNAs that regulate TZ resistance via HER2 signaling pathway components include miRNAs targeting HER2, reducing PTEN and inhibiting p-AKT. Other miRNAs enhance TZ sensitivity by targeting HER3 and IGF1R[6].

5.3 Aim of the work

Overexpression of HER2 in a large subgroup of mammary carcinomas circumscribes the disease and allows to define an appropriate treatment for the patients. The development of targeted therapies, has improved the outcome of the disease and mortality rates have been declining among women in many western countries (the 5-year survival trend increased from 75% in 1975 to 90% in 2008 and death rates have been falling on average 1.9% each year over 2004-2013, in USA)[58].

Trastuzumab is the first anti-HER2 monoclonal antibody that allows remarkably improved outcomes of patients with HER2-positive breast cancer, mostly in combination with traditional chemotherapy or as adjuvant therapy. Despite remarkable progress in treatment, patients frequently develop resistance to therapies through the alteration of different pathways that govern the survival of cancer, resulting in recurrences that exhibit increased aggressiveness and lower sensitivity to treatment. This problem also affects trastuzumab therapy and HER2 signaling network and mechanisms underlying the resistance have been broadly investigated in order to develop strategy to overcome the dilemma[6]. Several molecular mechanisms have been suggested for trastuzumab desensitization in breast cancer, including the dysregulation of HER2 downstream signaling pathways, alternative pathways and blocking of trastuzumab binding[13].

Furthermore, recent studies have demonstrated that miRNA expression patterns are altered in various human cancers, resulting in the dysregulation of numerous target genes, including oncogenes and tumor-suppressor genes[43,47]. Previous works identified sets of miRNAs reduced or up-regulated in resistant cell lines when compared with the parental ones[30]. Among them, miR-21 is consistently up-regulated in various types of malignant diseases, such as breast, prostate, esophagus, colon, and liver cancers and may be crucial not only for cancer progression, but also for resistance to anticancer agents[8,59]. Gong *et al.* established that miR-21 have been reported as direct regulator of tumor suppressing PTEN via targeting to its 3' UTR and by inhibiting the protein expression of PTEN, and as well as other miRNAs, promotes oncogenesis and progression of various carcinomas, contributing to chemotherapeutic resistance[30].

The discovery of miRNAs provides new hope for accomplishing novel therapeutics, attracting much attention of the researchers, so there are continuous advances in the development of a miRNA-based therapy[60]. Until now, successful suppression of breast cancer cells by miRNA-based drugs have been demonstrated in a number of cell experiments but despite these promising results, delivery of therapeutic miRNA-based drugs to the target tissue remains a problem[61]. Limitations of miRNAs include low cellular uptake, immunogenicity, renal clearance, degradation by nucleases, elimination by phagocytic immune cells, poor endosomal release and untoward side effects[6].

In this work, we developed a system that could permit a targeted delivery of an anti-miRNA to tumor cells, releasing it into the cytoplasm. We chose H-ferritin nanocage as vector for its well-known characteristics, which allow easy functionalization and promote a specific uptake through TfR1. We focused our attention on anti-miR21, choosing to treat HER2-positive breast cancer cell lines to evaluate the ability of our construct to overcome the resistance, re-sensitizing cells to the treatment with TZ.

5.4 Materials and methods

5.4.1 HFn nanocages design, expression and purification

The cDNA encoding for the heavy chain of human ferritin, modified by inserting the restriction sites for NdeI and NotI (respectively in 5' and 3'), was synthesized and subcloned into the vector pET30b(+) by Eurofins MWG Operon, in order to express HFn under the control of a T7 promoter, as reported in Bellini *et al.*[62]. The resulting plasmid pET30b/HFn was used to transform *Escherichia coli* expression strain BL21(DE3) by heat-shock method. The recombinant expression vector was confirmed by restriction endonuclease digestion and DNA sequencing.

H-ferritin (HFn) was expressed and purified following the protocol previously published[62]. Briefly, BL21(DE3)/pET30b/HFn cell were grown at 37 °C in Luria Bertani kanamicim medium until OD_{600}=0.6 and induced with 0.5 mM isopropyl β-D-1-tiogalactopiranoside (IPTG) for 2 h and 30 min. After growing, the cells were collected, washed and resuspended in lysis buffer with lysozyme and DNase I. In order to prepare the crude extract, cellular suspension was sonicated and centrifuged. After heat treatment, the supernatant was loaded onto DEAE Sepharose anion exchange resin and the purified protein was eluted with a stepwise NaCl gradient in 20 mM KMES, pH 6.0. Fractions were analyzed by SDS-PAGE using 12% (v/v) polyacrylamide gel and proteins detected with Imperial Protein Stain (ThermoFisher Scientific). Protein content was determined by both measuring absorbance at 280 nm and Coomassie Plus (Bradford) Assay with IgG as standard protein.

5.4.2 Locked nucleic acids (LNA™) and nuclease-free buffers

The Locked Nucleic Acid (LNA™) anti-miR21, directed against miRNA-21, and a negative control (cel-miR39, that is miR39 from *C. elegans*) were synthesized by Exiqon Inc. with the sequences and the desired modifications reported in table 5.2. A 3'-thiol modification (C3 S-S) was inserted into both sequences for conjugation to SPDP crosslinker and a 5'-TYE™ 705 dye (λ_{ecc}=686, λ_{em}=705) was attached for *in vitro* studies. The LNAs were resuspended in nuclease-free water, following the protocol from Exiqon miRCURY LNA™ instruction manual, aliquoted and stored at -20 °C.

Tab. 5.2 Custom LNA sequences and modifications.

	Sequence
Anti-miR21	/5TYE705/TCAGTCTGATAAGCT/3ThioMC3-D/
Cel-miR39	/5TYE705/TGATTTACACCCGGTG/3ThioMC3-D/

In preliminary experiments we also used random oligonucleotide sequences (hereafter called only "Oligo"), which allow us to mimic expensive miRNAs and set up the reactions protocol.

For all the reactions described below a PBS buffer (10 mM K_2HPO_4, 1,8 mM KH_2PO_4, 150 mM NaCl) added with 1mM EDTA and adjusted to a final pH 7.5 has been used (PBS-EDTA buffer). The buffer was prepared starting from UltraPure™ DNase/RNase-Free Distilled Water

(Invitrogen) and as last step treated overnight with 0,1 % diethyl pyrocarbonate (DEPC, Sigma Aldrich) and autoclaved.

Since LNA™ oligonucleotides are susceptible to degradation by exogenous nucleases introduced during handling, all operations were performed wearing powder-free gloves, using DNase-free reagents and filter pipette tips and working under a sterile hood. All non-sterile equipment (NAP-5 column, PD-10 column, Amicon Ultra filter device) was pretreated with 0,1 M NaOH and washed with UltraPure™ DNase/RNase-Free Distilled Water (Invitrogen) before use, as suggested by the manufacturers.

5.4.3 HFn-SPDP preparation

Recombinant HFn obtained as previously described was further conjugated to heterobifunctional linker N-succinimidyl 3-[2-pyridyldithio]-propionate (SPDP, Sigma Aldrich) in order to provide a thiol reactive terminus for miRNA conjugation. Briefly, 50 µL of a 20 mM SPDP solution in dimethyl sulfoxide (DMSO) were incubated with 5 mg of HFn in PBS-EDTA buffer, pH 7.5 for 1 h at 4 °C, stirring. The product was purified on PD-10 desalting column (contain Sephadex G-25 resin, GE Healthcare Life Science) in order to remove unreacted SPDP.

Later, the "Pyridine-2-Thione Assay" has been used to determine the level of SPDP-modification. Briefly, SPDP-modified HFn (HFn-SPDP) was diluted 1:10 in PBS-EDTA buffer and the absorbance at 343 nm was measured, in triplicate. Then, 10 µL of 15 mg mL^{-1} DTT solution were added to the protein samples and mixed to promote the reduction of the S-S bond, which releases the pyridine-2-thione group. After exactly 15 minutes the absorbance was read again and the difference between the absorbance values allows calculating the molar ratio of SPDP to HFn, using the following equation (were the value 8080 reflects the extinction coefficient for pyridine-2-thione at 343 nm, 8.08 x 10^3 M^{-1} cm^{-1}):

$$\frac{\Delta A}{8080} \times \frac{\text{MW of Protein}}{\text{mg/mL of Protein}} = \text{moles of SPDP per mole of Protein}$$

To perform some *in vitro* experiment, HFn-SPDP was labeled with fluorescein isothiocyanate (FITC), simply incubating HFn-SPDP with a molar excess of FITC, in PBS buffer overnight, at 4 °C. The final product was purified on PD-10 desalting column (GE Healthcare Life Science).

5.4.4 HFn-SPDP functionalization with anti-miRNA

The thiolate 3'-terminus of the LNA™ sequences was activated via 1,4-dithiothreitol treatment (DTT, 23 mg/mL), for 30 minutes at 4 °C, shaking, and then purified on Illustra NAP-5 Columns (GE Healthcare Life Science) to remove excess of DTT which would interfere with the upcoming formation of the disulfide bond. Activated LNA™ oligonucleotides were added to a HFn-SPDP solution in PBS-EDTA buffer, pH 7.5 and stirred for 18 h at 4 °C to allow the reaction between the –SH group of custom miRNA and the reactive terminus of SPDP. The resulting complex was purified on Amicon® Ultra 2 mL Centrifugal Filters (Millipore), washing with PBS-EDTA, pH 7.5.

Fluorescence spectroscopy was used to determine the amount of LNA™ sequences tied to HFn. The fluorescence signal intensity (λ_{ecc}=686, λ_{em}=705) of different dilutions of the final product was measured with a multi-plate reader (EnSight™ Multimode Plate Reader, PerkinElmer) and then compared with a calibration curve obtained from known samples of fluorescent miRNAs. For each of the two sequences has been built a different calibration line.

The product obtained by reaction with a random oligonucleotide sequence and used for preliminary experiments will be indicated as HFn-SPDP-Oligo.

5.4.5 Cell cultures

SKBR3 and BT474-TR human breast cancer cell lines were selected as HER2-positive breast cancer cell lines. SKBR-3 were purchased by LGC Standards S.r.l. and cultured in RPMI supplemented with 10% fetal bovine serum (FBS), 2 mM L-glutamine, penicillin (50 UI mL^{-1}) and streptomycin (50 mg mL^{-1}).

BT474-TR cells were generous gift from Dr. Santarpia (Humanitas Clinical and Research Center) who established TZ-resistant BT474 cell line by continuous treatment with low-dose trastuzumab. BT474-TR cells were cultured in Dulbecco's Modified Eagle's Medium (DMEM) high glucose, supplemented with 10% fetal bovine serum (FBS), 2 mM L-glutamine, penicillin (50 UI mL^{-1}) and streptomycin (50 mg mL^{-1}). Both cell lines were maintained at 37 °C in humidified atmosphere containing 5% CO_2 and sub-cultured prior to confluence using trypsin/EDTA. Cell culture medium, supplements and antibiotics were purchased from Euroclone.

5.4.6 Cell binding assay

Cells (3 x 10^5 cells/tube) were seeded onto 6-well tissue culture plates and incubated 1 h at 37 °C in the presence of 0.01 or 0.1 mg mL^{-1} of FITC-labeled HFn, FITC-labeled HFn-SPDP-Oligo and HFn-SPDP-cel-miR39. After incubation, cells were washed twice with PBS, detached from the plate with Trypsine/EDTA and processed for flow cytometry. Labeled cells were resuspended with 0.5 mL of PBS and analyzed by Gallios flow cytometer (Beckman Coulter) exploiting the fluorescence of FITC or Tye705. 10,000 events were acquired for each analysis, after gating on viable cells and on singlets; a sample of untreated cells was used to set the appropriate gates. The results are expressed as average percentage of positive cells ± standard error.

5.4.7 Confocal laser scanning microscopy

BT474-TR cells were cultured on collagen pre-coated cover glass slides until sub-confluence and incubated with 0.1 mg mL^{-1} FITC-labeled HFn-SPDP-anti-miR21 nanoparticles, for 15 min, 1, 4, 24 and 48 h at 37 °C and then harvested for immunofluorescence analysis. Briefly, cells were washed with phosphate-buffered saline, fixed for 5 min with 4% paraformaldehyde (Sigma Aldrich) and then treated for 10 min with 0.1 % Triton X-100 (Sigma Aldrich). A blocking step was performed for 2 h at RT with a solution containing 2% bovine serum albumin (BSA, Sigma), 2% goat serum and 0.1 µg mL^{-1} DAPI (4′ ,6-diamino-2-phenylindole) in PBS. Microscopy analysis was performed with a Leica SPE microscope confocal system equipped with

laser excitation lines 405 nm, 488 nm, 514 nm and 633 nm. Images were acquired with 63× magnification oil immersion lenses at 1024×1024 pixel resolution.

5.4.8 Viability assay

SKBR3 and BT474-TR cells were cultured on a 96 multiwell dish at a density of 3000 cells cm^{-1}. Then, cells were treated with the molecules to be tested (nanoparticles alone or in combination with TZ): 15 μg mL^{-1} HFn-SPSP-miRNAs and 10 μg mL^{-1} TZ by adding fresh components/drugs 3 times over 7 days of analysis. At the indicated time points (3, 5 and 7 days), cells were washed with PBS and incubated with 0.1 mL of MTS reagent solution, containing [3-(4,5-dimethylthiazol-2-yl)-5-(3-carboxymethoxyphenyl)-2-(4-sulfophenyl)-2H-tetrazolium inner salt and phenazine ethosulfate (PES) diluted in in DMEM without phenol red for 3 h at 37 °C (CellTiter 96® AQueous One Solution Reagent; Promega). Absorbance was recorded at 490 nm and a reference wavelength of 630 nm using a 96-well plate reader. The results are normalized on viability of untreated samples and expressed as means ± standard error (s.e.).

5.4.9 Western Blot

BT474-TR cells were cultured in a 6-wells plate and treated with HFn-SPDP-miRNAs (15 μg mL^{-1} HFn, which correspond to about 106 μg mL^{-1} miRNA) for 6, 12, 24 or 48 h in culture medium. Then cells were lysed with 300 μL lysis buffer (20 mM Tris HCl pH 7.6, 150 mM NaCl, 1 mM EDTA, 1% Triton X-100, 10% glycerol, 1 mM Na3VO4, 10 mM NaF, 4% Protease Inhibitor Cocktail, 1 mM PMSF). Proteins from each sample were separated by SDS-PAGE using 12% (v/v) polyacrylamide gels and then transferred onto PVDF membrane. The membrane was first blocked in 5% BSA in TBS with 0.1 % Tween 20 for 1 h and later incubated for 3h with rabbit mAb antibody against PTEN (138G6, Cell Signaling) at 1:1000 dilution or a rabbit antibody anti-GAPDH (Sigma Aldrich) at 1:5000 dilution in 5% BSA in TBS with 0.1 % Tween 20 for 1 h. The membrane was washed three times with TBS with 0.1 % Tween 20 and reacted 1 h with the secondary antibody anti-rabbit conjugated with horseradish peroxidase (1:10,000; Abcam) for 1 h. The bound antibody was revealed using ECL star reagent (Euroclone) and the chemoluminescence signal was detected using the Chemidoc System (Biorad).

5.5 Results

5.5.1 Nanoparticles synthesis

To carry on antisense inhibition experiments, we purchased oligonucleotides from Exiqon custom LNA™. LNA™ oligonucleotides are defined as DNA or RNA nucleotides containing one or more LNA™ nucleosides, a class of nucleic acid analogues in which the ribose moiety possesses an extra bridge connecting the 2'-O and 4'-C atoms and locking the carbohydrate in the 3'-endo conformation. LNA nucleotides can be mixed with DNA or RNA residues in the oligonucleotide whenever desired and the locking structure constrains LNA in the ideal conformation for Watson-Crick binding. Among the benefits of an anti-miRNA sequence containing these nucleosides we can list: (1) the high affinity binding to complementary RNA, resulting in superior potency when used for antisense inhibition, (2) the superior single nucleotide discrimination, (3) the resistance to exo- and endonucleases, resulting in high stability *in vivo* and *in vitro* applications, (4) the compatibility with standard enzymatic processes.

Two sequences were used for this study, one directed against miRNA-21 (anti-miR21) and one as a universal negative control (cel-miR39), have been modified by the insertion of a 3'-thiol modification, for conjugation to SPDP crosslinker, and of a 5'-TYE™ 705 dye (λ_{ecc}=686, λ_{em}=705) for *in vitro* studies. In some case, to set up the experiments, we used a HFn functionalized with a random oligonucleotide sequence, indicated as HFn-SPDP-Oligo.

The functionalization reaction of HFn was carried out following a scheme in two steps: (1) conjugation of N-succinimidyl 3-(2-pyridyldithio) propionate (SPDP) to the amino groups of H-ferritin; (2) activation of the anti-miRNA terminal thiol and conjugation to H-ferritin, through the cross-linker (Fig. 5.6). For each of these steps the best reaction conditions in terms of solvent, pH, reducing agent, and reaction time have been studied.

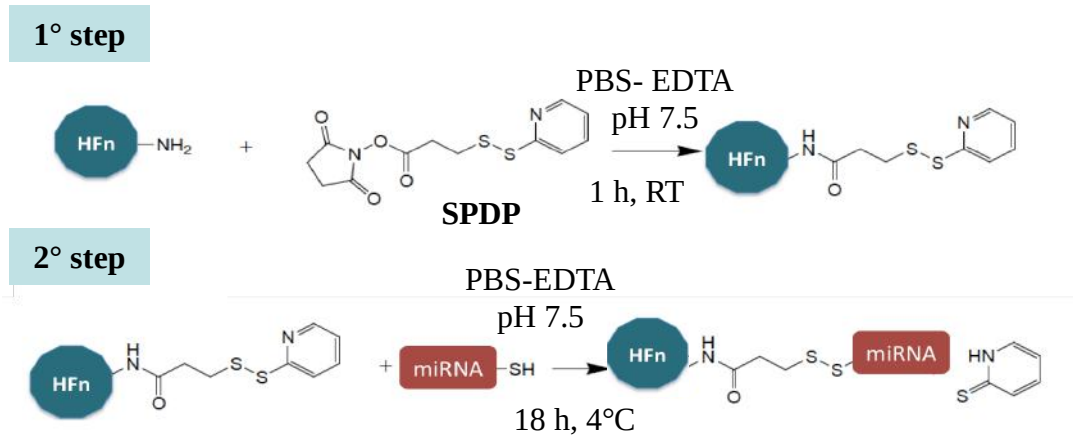

Fig. 5.6 Functionalization reaction scheme. In the first step, SPDP crosslinker was bound to amino groups exposed on the external surface of the protein shell; the reaction proceeds for 1 h in PBS-EDTA buffer, pH 7.5. In the second step the activated thiol group on the nucleotide sequences reacts with the pyridin-2-thione group of SPDP, with the formation of a disulfide bridge.

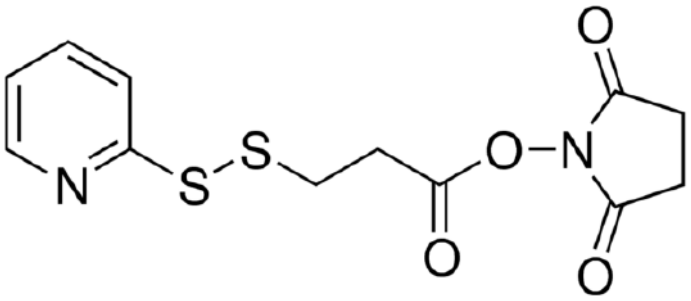

Fig. 5.7 The 3-(2-Pyridyldithio)propionic acid N-hydroxysuccinimide ester (SPDP) structure, with the two reactive groups.

The SPDP reagent (Fig. 5.7) is a heterobifunctional crosslinker, which produces disulfide-containing linkages that can be cleaved by reducing agents such as dithiothreitol (DTT) or, as in our interest, in a reducing environment such as cytoplasm. The amine-reactive portion of SPDP reagents is the N-hydroxysuccinimide (NHS) ester, which can easily react with the amino groups exposed on the protein surface. Instead, the sulfhydryl-reactive portion reacts optimally with thiols resulting in the displacement of a pyridine-2-thione group, whose concentration can be determined by measuring the absorbance at 343 nm. Both reactions may take place in buffers at pH 7-8, so we ran the reactions to occur in PBS-EDTA buffer, pH 7.5.

At the end of the first step, the extent of disulphide modification can be monitored by UV spectroscopy, using the pyridine-2-thione assay, i.e., by adding DTT and recording the absorbance of the released 2-thiopyridine. The extent of SPDP-modification was estimated between 20 and 25 nmol of crosslinker bound to each H-ferritin cage (roughly one for each subunit). When using reaction conditions different from those selected, namely changing SPDP concentrations or increasing the reaction time, the amount of SPDP bound to each ferritin molecule did not appreciably change.

We then functionalized the SPDP crosslinker with cel-miR39 or anti-miR21 molecules, choosing 1:1 or 1:3 molar ratios (SPDP:miRNA), with marginal changes in the outcome so we chose routinely the 1:3 molar ratio. We could quantify the fluorescent tag bound to the custom miRNAs by measuring the intensity of the fluorescence signal. The final products were compared each time with a calibration curve (Fig. 5.8), which showed that about 3 and 7 anti-miRNAs per HFn were bound in the case of anti-miR21 and cel-miR39, respectively (Tab. 5.3). It is not clear what factors may cause this difference. In any case, we judged that the number of miRNAs bound to the protein shell is sufficient for the following *in vitro* experimentations.

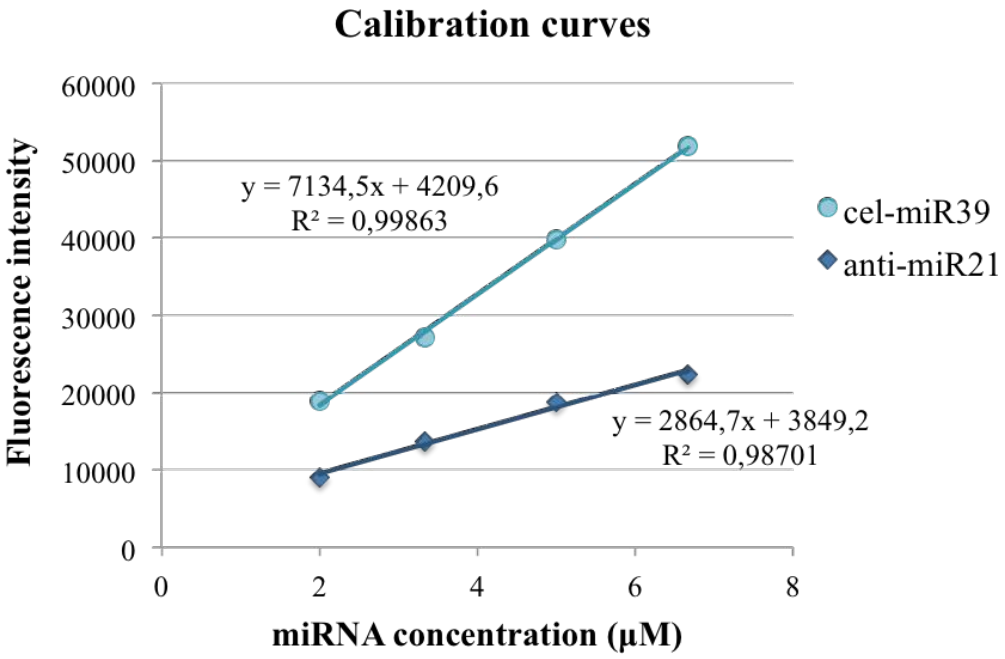

Fig. 5.8 Calibration curves for anti-miR21 and cel-miR39, obtained by measuring the fluorescence of several samples of known concentration.

Tab. 5.3 Degree of nanocages functionalization.

	SPDP per HFn	miRNAs per HFn
HFn-SPDP-anti-miR21	24.98 ± 3.11	3.06 ± 0.6
HFn-SPDP-cel-miR39	24.98 ± 3.11	6.85 ± 0.36

The *in vitro* tests described hereinafter were performed by Dr. Marta Truffi, prof. Corsi's research group at the Department of Biomedical and Clinical Sciences "L. Sacco", University of Milan (Italy).

5.5.2 Interaction with breast cancer cells

Binding assays were monitored by flow cytometry on SKBR3 and BT474-TR cell lines, after incubating the cells for 1 h at 37 °C with different concentrations of uncovered or functionalized HFn. Initially our aim was to compare the binding ability of HFn-SPDP-Oligo with that of uncovered HFn, to verify that the surface modification does not interfere with the specific recognition. As the two nanocages are labeled with the same fluorescent dye, the results obtained in either case are directly comparable. As shown in Fig. 5.9, they demonstrate a concentration-dependent trend without significant differences between the two types of nanoparticle. Ferritin functionalized with SPDP and oligonucleotide showed almost the same percentage of positive events of non-functionalized ferritin, used as a control, given its well-known binding capacity. This shows that lining the protein shell with the crosslinker does not alter its binding capacity to TfR1

receptors. Likewise, even HFn-SPDP-cel-miR39 maintained the binding capacity, confirming a remarkable HFn affinity toward cancer cells. So we can conclude that molecules bound at the surface of HFn do not compromise its ability to bind TfR1.

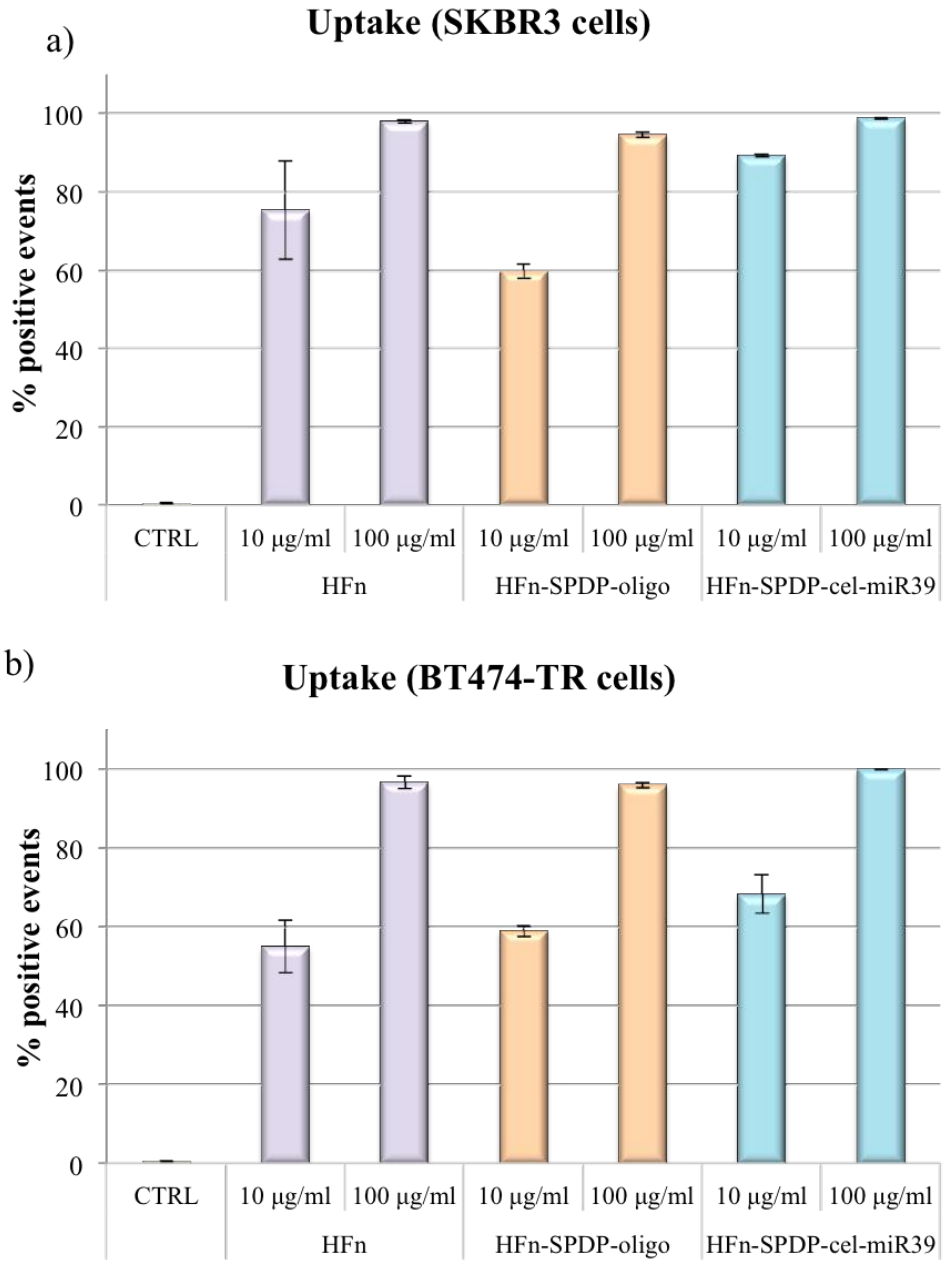

Fig. 5.9 Interaction of HFn nanoparticles with sensitive and resistant BC cells. For uptake analysis, SKBR3 (a) and BT474-TR (b) cells were treated with 0.01 or 0.1 mg mL^{-1} of FITC-labeled HFn, FITC-labeled HFn-SPDP-Oligo and HFn-SPDP-cel-miR39, 1 hour at 37°C. Histograms represent the percentage of positive cells. Fig. 4.10 Interaction of HFn nanoparticles with sensitive and resistant BC cells. For uptake analysis, SKBR3 (a) and BT474-TR (b) cells were treated with 0.01 or 0.1 mg mL^{-1} of FITC-labeled HFn, FITC-labeled HFn-SPDP-Oligo and HFn-SPDP-cel-miR39, 1 hour at 37°C. Histograms represent the percentage of positive cells.

Next, BT474-TR cells were incubated with HFn labeled with FITC and functionalized with the fluorescent anti-miR21 to evaluate the intracellular fate of both HFn and bound miRNA, which was monitored by immunofluorescence. As already observed in our previous works[62,63], HFn was quickly internalized: in fact, it localized to the membrane at 15 min and already after 1 h, a massive internalization took place, so that both components were found in the intracellular environment (Fig. 5.10). Over time, colocalization of the two fluorescent signals decreased, probably due to cleavage of the thiol bond between HFn-SPDP and anti-miR21 in the reducing intracellular environment. After 24 and 48 h, miRNA fluorescence was still strong and localized to the cytoplasm, while the green fluorescence of HFn disappeared, probably due to HFn disassembly and entry in the cellular ferritin pool with resulting fluorophore dilution, or to recycling to the receptor. We concluded that, as expected, the fates of the two components (protein and oligonucleotide) diverge as a result of the cleavage of the disulfide bridge in a reducing environment Note that the visible fluorescent spots at 24 and 48 h are probably caused by a partial loss of HFn stability.

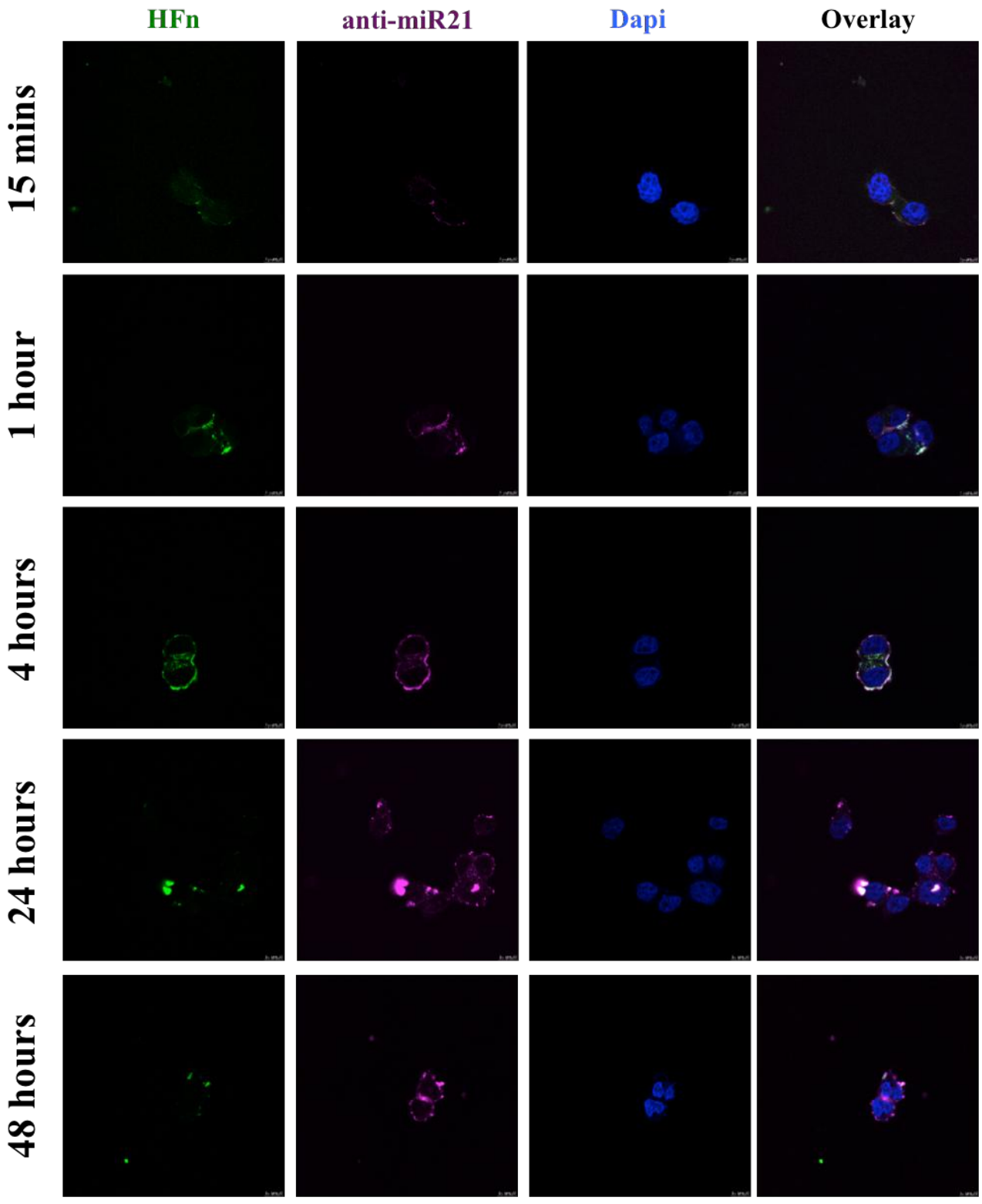

Fig. 5.10 Internalization of HFn-SPDP-anti-miR21 in BT474-TR cells. Confocal microscopy images of BT474-TR cells, incubated for 15 min, 1, 4, 24 and 48 h at 37 °C with 0.1 mg mL^{-1} FITC-labeled HFn-SPDP-anti-miR21 nanoparticles (HFn: green, mir21: violet). Nuclei were stained with DAPI (blue). Scale bar: 10 µm.

5.5.3 Cell viability

Cell viability on both cell lines was assayed to check the effectiveness of the nanoconstructs alone or in combination with TZ. As expected, treatment with the sole TZ did not interfere with the proliferation of BT474-TR resistant cells (Fig. 5.11b), nor did the incubation of functionalized nanocages negatively affect cell viability. Furthermore, the treatment with HFn lead to a slight increase in viability, as already observed in other works[64,65]. Instead, the combination of TZ and miRNAs-functionalized HFn nanoparticles decreased the viability, especially after 5 days, but not at the latest time. Surprisingly, no significant differences were observed between the two microRNAs: the protein modified with the control oligonucleotide (cel-anti-miR39) also exerted a synergistic effect with the monoclonal antibody. The effect, however, was transitory and disappeared after 7 days of treatment.

As regards the sensitive SKBR3 cells, the effect of the constructs HFn-SPDP-miRNAs administered along with TZ was indistinguishable from that of TZ alone, while HFn-SPDP-miRNAs were ineffective (Fig. 5.11a).

These results led us to speculate that, while the two microRNAs bound to ferritin exert the same effect, irrespective of their identity, ferritin causes cellular responses so far unknown, but capable of enhancing free TZ effect on cell viability. To confirm this hypothesis and rule out that this effect is due to the presence of SPDP on nanoparticle surface or to a reaction of the nanoparticles with TZ, we repeated the MTS assay with naked or SPDP-functionalized HFn (Fig. 5.12). The results reveal a trend similar to that previously observed, namely a tendency to reduction of proliferation after co-administration of nanocages and TZ. The same decline is not detected when the sole HFn or HFn-SPDP are administered, confirming these effects are not caused by SPDP, but it is required the co-presence of HFn and TZ.

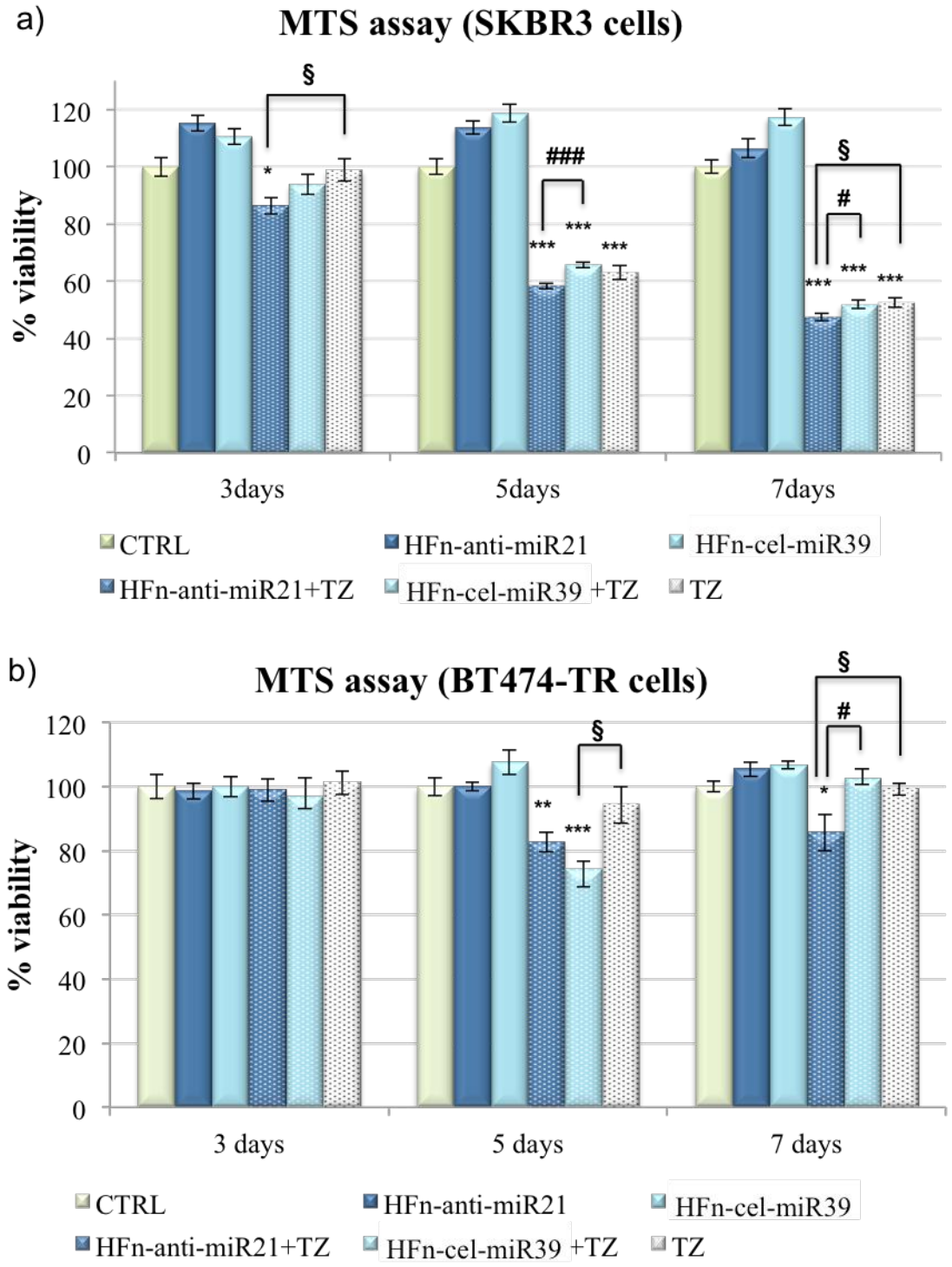

Fig. 5.11 Cytotoxicity of HFn-miRNAs nanoparticles. Sensitive SKBR3 (a) and resistant BT474-TR (b) cells were treated with HFn functionalized with anti-mir21 or cel-mir39, alone or in combination with trastuzumab. Histograms represent percentage of cell viability compared to untreated cells set at 100% ± standard deviation. * P<0.05; ** P<0.01; *** P<0.001 *vs* non treated-control (100% viability). # P<0.05; ## P<0.01; ### P<0.001 *vs* HFn-cel-miR39 + TZ treatment. § P<0.05 *vs* TZ treatment.

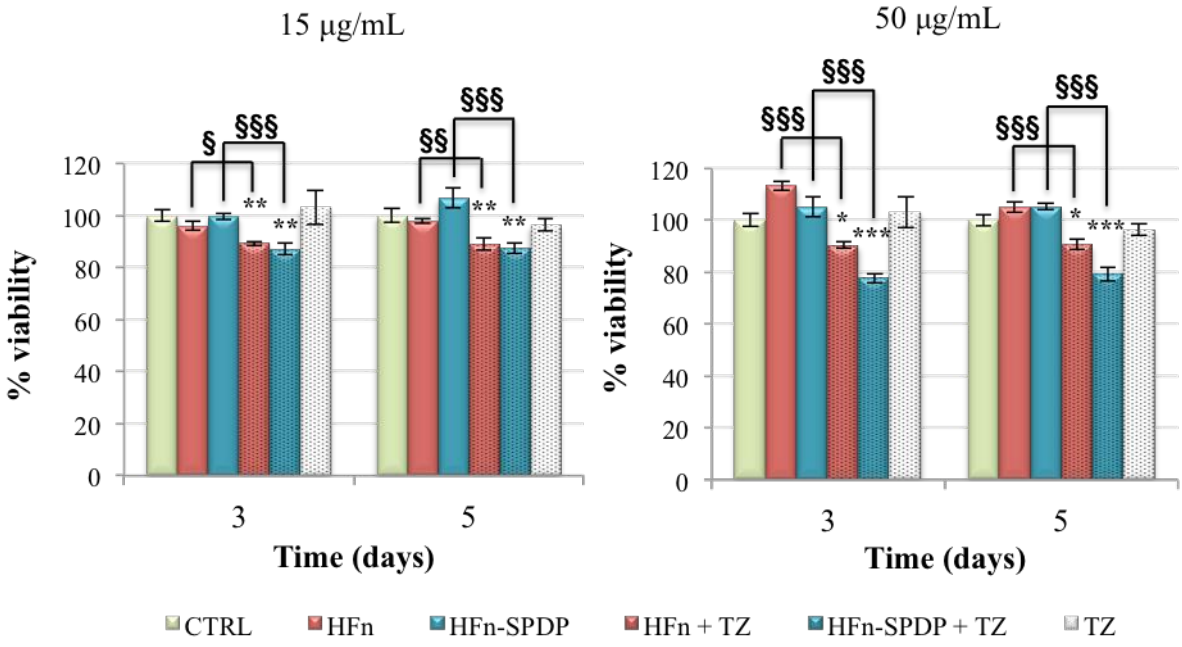

Fig. 4.12 Cytotoxicity of HFn nanoparticles. Sensitive BT474-TR cells were treated with 15 µg mL^{-1} or 50 µg mL^{-1} of HFn or HFn-SPDP, alone or in combination with TZ. Histograms represent percentage of cell viability compared to untreated cells set at 100% ± standard deviation. * P<0.05; ** P<0.01; *** P<0.001 *vs* non treated-control (100% viability). § P<0.05; §§ P<0.01; §§ P<0.001 *vs* HFn o HFn-SPDP.

5.5.4 PTEN expression

As mentioned above, miR-21 has been identified as a direct regulator of the tumor suppressor PTEN in various types of carcinomas[43,55]. As anti-miR21 could modulate PTEN expression, we analyzed the effect of HFn-SPDP-cel-miR39 or HFn-SPDP-anti-miR21 on BT474-TR cells. In keeping with the viability assays, the nanoparticles did not evoke significant effects. Indeed, PTEN expression did not vary significantly in response to the treatment with miRNAs at any time (Fig. 5.13).

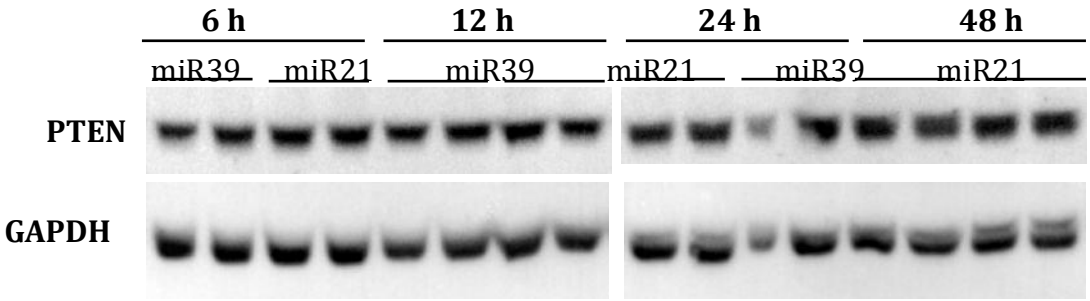

Fig. 5.13: PTEN expression in BT474-TR cells after treatment with HFn-miRNA.

5.6 Conclusions

Overexpression of HER2 occurs in a significant proportion of breast cancers and represents an ideal target for targeted therapy. Trastuzumab is a monoclonal antibody that targets the extracellular domain of HER2 and that is widely used in clinical treatments. However, primary and acquired resistance remains an obstacle and contributes to treatment failure: often the tumor, albeit initially responsive, elicits responses that make it refractory to the treatment, with resulting poor prognosis.

MiRNAs are a group of small non-coding RNAs, which modulate cellular processes by regulating target genes at the post-transcriptional level. Numerous miRNAs are implicated in malignant diseases, often as oncogenes or tumor suppressing genes. In particular, miR-21 regulates the effect of trastuzumab, altering HER2 downstream signaling pathways. This makes it an important target for overcoming TZ resistance, for example exploiting antisense oligonucleotides. Unfortunately, as regards gene therapy, there are some obvious issues, in particular those related to the delivery: it is required that oligonucleotides reach target cells intact and in suitable amounts, although this goal is not straightforward. For this purpose, we chose to use ferritin nanocages suitably functionalized, so as to target the molecules of interest to cancer cells. The protein surface is susceptible to a variety of functionalization reactions. In our case, a crosslinker has been usefully adopted, allowing, in turn, to make a thiol group available for binding to the anti-miRNA. The reaction was effective, though the amount of bound anti-miRNA was significantly dependent on the identity of the oligonucleotide used.

After confirming the unaltered efficient recognition of tumor cells, we observed a massive cellular uptake of miRNA molecules. This result is of great significance, because poor cellular uptake is a major issue as far as miRNA-based therapies are concerned. However, HFn allowed to efficiently transport these molecules into cancer cells.

We also analyzed the activity of HFn-SPDP-anti-miR21 on sensitive and resistant HER2+ breast cancer cells. The results did not match our expectations: although co-administration of nanoparticles and TZ could overcome the resistance towards the antibody, this effect was independent from the nucleotide sequence transported, as shown by the fact that even cel-miR39 reduced cell proliferation and restored a partial and transient responsiveness of BT474-TR cells to the drug. We can thus conclude, as also confirmed by the gene silencing experiment, that the effect observed is not due to an anti-miR21 action on the downstream pathway of HER2, which includes PTEN, but probably to an unknown response involving the effect of ferritin itself. Other assumptions that must definitely be taken into consideration are the loss of functionality of the miRNA following conjugation or even timing problems, as the effects the miRNAs are supposed to be exerting, may be faster or slower than the experimental time used to date.

5.7 References

1. Slamon, D. J. *et al.* Human breast cancer: correlation of relapse and survival with amplification of the HER-2/neu oncogene. *Science* **235,** 177–182 (1987).
2. Mitri, Z., Constantine, T. & O'Regan, R. The HER2 Receptor in Breast Cancer: Pathophysiology, Clinical Use, and New Advances in Therapy. *Chemother. Res. Pract.* **2012,** (2012).
3. Hudis, C. A. Trastuzumab — Mechanism of Action and Use in Clinical Practice. *N. Engl. J. Med.* **357,** 39–51 (2007).
4. Schechter, A. L. *et al.* The neu oncogene: an erb-B-related gene encoding a 185,000-Mr tumour antigen. *Nature* **312,** 513–516 (1984).
5. Yarden, Y. The EGFR family and its ligands in human cancer: signalling mechanisms and therapeutic opportunities. *Eur. J. Cancer* **37,** S3–S8 (2001).
6. Mao, L., Sun, A., Wu, J. & Tang, J. Involvement of microRNAs in HER2 signaling and trastuzumab treatment. *Tumor Biol.* 1–10 (2016). doi:10.1007/s13277-016-5405-3
7. Nagata, Y. *et al.* PTEN activation contributes to tumor inhibition by trastuzumab, and loss of PTEN predicts trastuzumab resistance in patients. *Cancer Cell* **6,** 117–127 (2004).
8. Eto, K. *et al.* The microRNA-21/PTEN pathway regulates the sensitivity of HER2-positive gastric cancer cells to trastuzumab. *Ann. Surg. Oncol.* **21,** 343–350 (2014).
9. Li, J. *et al.* PTEN, a putative protein tyrosine phosphatase gene mutated in human brain, breast, and prostate cancer. *Science* **275,** 1943–1947 (1997).
10. Parsons, R. & Simpson, L. in *Tumor Suppressor Genes* (eds. El-Deiry, W. & MD, W. S. E.-D.) 147–166 (Humana Press, 2003). doi:10.1385/1-59259-328-3:147
11. Gonzalez-Angulo, A. M. *et al.* High risk of recurrence for patients with breast cancer who have human epidermal growth factor receptor 2-positive, node-negative tumors 1 cm or smaller. *J. Clin. Oncol. Off. J. Am. Soc. Clin. Oncol.* **27,** 5700–5706 (2009).
12. Ahmed, S., Sami, A. & Xiang, J. HER2-directed therapy: current treatment options for HER2-positive breast cancer. *Breast Cancer* **22,** 101–116 (2015).
13. Pohlmann, P. R., Mayer, I. A. & Mernaugh, R. Resistance to Trastuzumab in Breast Cancer. *Clin. Cancer Res.* **15,** 7479–7491 (2009).
14. Mukohara, T. Mechanisms of resistance to anti-human epidermal growth factor receptor 2 agents in breast cancer. *Cancer Sci.* **102,** 1–8 (2011).
15. Yakes, F. M. *et al.* Herceptin-induced inhibition of phosphatidylinositol-3 kinase and Akt Is required for antibody-mediated effects on p27, cyclin D1, and antitumor action. *Cancer Res.* **62,** 4132–4141 (2002).
16. Pegram, M. D. *et al.* Rational Combinations of Trastuzumab With Chemotherapeutic Drugs Used in the Treatment of Breast Cancer. *J. Natl. Cancer Inst.* **96,** 739–749 (2004).
17. Clynes, R. A., Towers, T. L., Presta, L. G. & Ravetch, J. V. Inhibitory Fc receptors modulate in vivo cytotoxicity against tumor targets. *Nat. Med.* **6,** 443–446 (2000).
18. Spiridon, C. I., Guinn, S. & Vitetta, E. S. A comparison of the in vitro and in vivo activities of IgG and F(ab')2 fragments of a mixture of three monoclonal anti-Her-2 antibodies. *Clin. Cancer Res. Off. J. Am. Assoc. Cancer Res.* **10,** 3542–3551 (2004).
19. Park, S. *et al.* The Therapeutic Effect of Anti-HER2/neu Antibody Depends on Both Innate

and Adaptive Immunity. *Cancer Cell* **18,** 160–170 (2010).
20. Roopenian, D. C. & Akilesh, S. FcRn: the neonatal Fc receptor comes of age. *Nat. Rev. Immunol.* **7,** 715–725 (2007).
21. Slamon, D. J. *et al.* Use of Chemotherapy plus a Monoclonal Antibody against HER2 for Metastatic Breast Cancer That Overexpresses HER2. *N. Engl. J. Med.* **344,** 783–792 (2001).
22. Gasparini, G. *et al.* Randomized Phase II Trial of weekly paclitaxel alone versus trastuzumab plus weekly paclitaxel as first-line therapy of patients with Her-2 positive advanced breast cancer. *Breast Cancer Res. Treat.* **101,** 355–365 (2007).
23. Marty, M. *et al.* Randomized phase II trial of the efficacy and safety of trastuzumab combined with docetaxel in patients with human epidermal growth factor receptor 2-positive metastatic breast cancer administered as first-line treatment: the M77001 study group. *J. Clin. Oncol. Off. J. Am. Soc. Clin. Oncol.* **23,** 4265–4274 (2005).
24. Kaufman, B. *et al.* Trastuzumab plus anastrozole versus anastrozole alone for the treatment of postmenopausal women with human epidermal growth factor receptor 2-positive, hormone receptor-positive metastatic breast cancer: results from the randomized phase III TAnDEM study. *J. Clin. Oncol. Off. J. Am. Soc. Clin. Oncol.* **27,** 5529–5537 (2009).
25. Huober, J. *et al.* Higher efficacy of letrozole in combination with trastuzumab compared to letrozole monotherapy as first-line treatment in patients with HER2-positive, hormone-receptor-positive metastatic breast cancer - results of the eLEcTRA trial. *Breast Edinb. Scotl.* **21,** 27–33 (2012).
26. Piccart, M. J. Proposed treatment guidelines for HER2-positive metastatic breast cancer in Europe. *Ann. Oncol.* **12,** S89–S94 (2001).
27. Romond, E. H. *et al.* Trastuzumab plus Adjuvant Chemotherapy for Operable HER2-Positive Breast Cancer. *N. Engl. J. Med.* **353,** 1673–1684 (2005).
28. Smith, I. *et al.* 2-year follow-up of trastuzumab after adjuvant chemotherapy in HER2-positive breast cancer: a randomised controlled trial. *Lancet Lond. Engl.* **369,** 29–36 (2007).
29. Wolff, A. C. *et al.* American Society of Clinical Oncology/College of American Pathologists Guideline Recommendations for Human Epidermal Growth Factor Receptor 2 Testing in Breast Cancer. *J. Clin. Oncol.* **25,** 118–145 (2006).
30. Gong, C. *et al.* Up-regulation of miR-21 mediates resistance to trastuzumab therapy for breast cancer. *J. Biol. Chem.* **286,** 19127–19137 (2011).
31. Scaltriti, M. *et al.* Expression of p95HER2, a Truncated Form of the HER2 Receptor, and Response to Anti-HER2 Therapies in Breast Cancer. *JNCI J. Natl. Cancer Inst.* **99,** 628–638 (2007).
32. Carraway, K. L. *et al.* Muc4/sialomucin complex in the mammary gland and breast cancer. *J. Mammary Gland Biol. Neoplasia* **6,** 323–337 (2001).
33. Berns, K. *et al.* A functional genetic approach identifies the PI3K pathway as a major determinant of trastuzumab resistance in breast cancer. *Cancer Cell* **12,** 395–402 (2007).
34. Chan, C. T., Metz, M. Z. & Kane, S. E. Differential sensitivities of trastuzumab (Herceptin)-resistant human breast cancer cells to phosphoinositide-3 kinase (PI-3K) and epidermal growth factor receptor (EGFR) kinase inhibitors. *Breast Cancer Res. Treat.* **91,** 187–201 (2005).
35. Esteva, F. J. *et al.* PTEN, PIK3CA, p-AKT, and p-p70S6K status: association with trastuzumab response and survival in patients with HER2-positive metastatic breast cancer. *Am. J. Pathol.* **177,** 1647–1656 (2010).

36. Lu, Y., Zi, X., Zhao, Y., Mascarenhas, D. & Pollak, M. Insulin-like growth factor-I receptor signaling and resistance to trastuzumab (Herceptin). *J. Natl. Cancer Inst.* **93,** 1852–1857 (2001).
37. Lu, Y., Zi, X. & Pollak, M. Molecular mechanisms underlying IGF-I-induced attenuation of the growth-inhibitory activity of trastuzumab (Herceptin) on SKBR3 breast cancer cells. *Int. J. Cancer* **108,** 334–341 (2004).
38. Sergina, N. V. *et al.* Escape from HER-family tyrosine kinase inhibitor therapy by the kinase-inactive HER3. *Nature* **445,** 437–441 (2007).
39. Konecny, G. E. *et al.* Activity of the Dual Kinase Inhibitor Lapatinib (GW572016) against HER-2-Overexpressing and Trastuzumab-Treated Breast Cancer Cells. *Cancer Res.* **66,** 1630–1639 (2006).
40. Agus, D. B. *et al.* Targeting ligand-activated ErbB2 signaling inhibits breast and prostate tumor growth. *Cancer Cell* **2,** 127–137 (2002).
41. Milani, A., Sangiolo, D., Montemurro, F., Aglietta, M. & Valabrega, G. Active immunotherapy in HER2 overexpressing breast cancer: current status and future perspectives. *Ann. Oncol.* **24,** 1740–1748 (2013).
42. Yan, L.-X. *et al.* MicroRNA miR-21 overexpression in human breast cancer is associated with advanced clinical stage, lymph node metastasis and patient poor prognosis. *RNA* **14,** 2348–2360 (2008).
43. Esquela-Kerscher, A. & Slack, F. J. Oncomirs — microRNAs with a role in cancer. *Nat. Rev. Cancer* **6,** 259–269 (2006).
44. Lewis, B. P., Shih, I. -hun., Jones-Rhoades, M. W., Bartel, D. P. & Burge, C. B. Prediction of mammalian microRNA targets. *Cell* **115,** 787–798 (2003).
45. John, B. *et al.* Human MicroRNA Targets. *PLOS Biol.* **2,** e363 (2004).
46. Lim, L. P. *et al.* Microarray analysis shows that some microRNAs downregulate large numbers of target mRNAs. *Nature* **433,** 769–773 (2005).
47. Calin, G. A. & Croce, C. M. MicroRNA signatures in human cancers. *Nat. Rev. Cancer* **6,** 857–866 (2006).
48. Calin, G. A. *et al.* Human microRNA genes are frequently located at fragile sites and genomic regions involved in cancers. *Proc. Natl. Acad. Sci. U. S. A.* **101,** 2999–3004 (2004).
49. Sakurai, M. *et al.* Correlation of miRNA expression profiling in surgical pathology materials, with Ki-67, HER2, ER and PR in breast cancer patients. *Int. J. Biol. Markers* **30,** e190-199 (2015).
50. Dai, X., Chen, A. & Bai, Z. Integrative investigation on breast cancer in ER, PR and HER2-defined subgroups using mRNA and miRNA expression profiling. *Sci. Rep.* **4,** 6566 (2014).
51. Chan, J. A., Krichevsky, A. M. & Kosik, K. S. MicroRNA-21 is an antiapoptotic factor in human glioblastoma cells. *Cancer Res.* **65,** 6029–6033 (2005).
52. Iorio, M. V. *et al.* MicroRNA gene expression deregulation in human breast cancer. *Cancer Res.* **65,** 7065–7070 (2005).
53. Yanaihara, N. *et al.* Unique microRNA molecular profiles in lung cancer diagnosis and prognosis. *Cancer Cell* **9,** 189–198 (2006).
54. Fulci, V. *et al.* Quantitative technologies establish a novel microRNA profile of chronic lymphocytic leukemia. *Blood* **109,** 4944–4951 (2007).
55. Zhang, B. G. *et al.* microRNA-21 promotes tumor proliferation and invasion in gastric cancer by targeting PTEN. *Oncol. Rep.* **27,** 1019–1026 (2012).

56. Ye, X. *et al.* MiR-221 promotes trastuzumab-resistance and metastasis in HER2-positive breast cancers by targeting PTEN. *BMB Rep.* **47,** 268–273 (2014).
57. De Mattos-Arruda, L. *et al.* MicroRNA-21 links epithelial-to-mesenchymal transition and inflammatory signals to confer resistance to neoadjuvant trastuzumab and chemotherapy in HER2-positive breast cancer patients. *Oncotarget* **6,** 37269–37280 (2015).
58. Cancer of the Breast (Female) - Cancer Stat Facts. Available at: https://seer.cancer.gov/statfacts/html/breast.html. (Accessed: 18th January 2017)
59. Mei, M. *et al.* Downregulation of miR-21 enhances chemotherapeutic effect of taxol in breast carcinoma cells. *Technol. Cancer Res. Treat.* **9,** 77–86 (2010).
60. Bader, A. G., Brown, D., Stoudemire, J. & Lammers, P. Developing therapeutic microRNAs for cancer. *Gene Ther.* **18,** 1121–1126 (2011).
61. Kaboli, P. J., Rahmat, A., Ismail, P. & Ling, K.-H. MicroRNA-based therapy and breast cancer: A comprehensive review of novel therapeutic strategies from diagnosis to treatment. *Pharmacol. Res.* **97,** 104–121 (2015).
62. Bellini, M. *et al.* Protein nanocages for self-triggered nuclear delivery of DNA-targeted chemotherapeutics in Cancer Cells. *J. Controlled Release* **196,** 184–196 (2014).
63. Mazzucchelli, S. *et al.* Nanometronomic treatment of 4T1 breast cancer with nanocaged doxorubicin prevents drug resistance and circumvents cardiotoxicity. *Oncotarget* (2016). doi:10.18632/oncotarget.14204
64. Alkhateeb, A. A., Han, B. & Connor, J. R. Ferritin stimulates breast cancer cells through an iron-independent mechanism and is localized within tumor-associated macrophages. *Breast Cancer Res. Treat.* **137,** 733–744 (2013).
65. Alkhateeb, A. A. *et al.* Elevation in inflammatory serum biomarkers predicts response to trastuzumab-containing therapy. *PloS One* **7,** e51379 (2012).

List of publications

- S. Mazzucchelli, M. Bellini, L. Fiandra, M. Truffi M, M. A. Rizzuto, L. Sorrentino, E. Longhi, M. Nebuloni, D. Prosperi, F. Corsi. *"Nanometronomic treatment of 4T1 breast cancer with nanocaged doxorubicin prevents drug resistance and circumvents cardiotoxicity"*, Oncotarget, 2016, DOI: 10.18632/oncotarget.14204

- L. Fiandra, S. Mazzucchelli, M. Truffi, M. Bellini, L. Sorrentino, F. Corsi. *"In vitro permeation of FITC-loaded ferritins across a rat blood-brain barrier: a model to study the delivery of nanoformulated molecules"*; J Vis Exp, 2016, 114.

- E. Galbiati, L. Gambini, V. Civitarese, M. Bellini, D. Ambrosini, R. Allevi, S. Avvakumova, S. Romeo, D. Prosperi. *"'Blind" targeting in action: From phage display to breast cancer cell targeting with peptide-gold nanoconjugates"*. Pharmacol Res, 2016, 111, 155-162.

- M. Bellini, S. Mazzucchelli, E. Galbiati, S. Sommaruga, L. Fiandra, M. Truffi, M. A. Rizzuto, M. Colombo, P. Tortora, F. Corsi, D. Prosperi. *"Protein nanocages for self-triggered nuclear delivery of DNA-targeted chemotherapeutics in Cancer Cells"*; J Control Release, 2014, 28, 184-196.

- P. Verderio, S. Avvakumova, G. Alessio, M. Bellini, M. Colombo, E. Galbiati, S. Mazzucchelli, J. P. Avila, B. Santini, D. Prosperi. *"Delivering colloidal nanoparticles to mammalian cells: a nano-bio interface perspective"*; Adv Healthc Mater, 2014, 3, 957-976.

- L. Fiandra, S. Mazzucchelli, C. De Palma, M. Colombo, R. Allevi, S. Sommaruga, E. Clementi, M. Bellini, D. Prosperi, F. Corsi. *"Assessing the in vivo targeting efficiency of multifunctional nanoconstructs bearing antibody-derivatives ligands"*; ACS Nano, 2013, 7, 6092-6102.

Journal of Controlled Release 196 (2014) 184–196

Contents lists available at ScienceDirect

Journal of Controlled Release

journal homepage: www.elsevier.com/locate/jconrel

Protein nanocages for self-triggered nuclear delivery of DNA-targeted chemotherapeutics in Cancer Cells

Michela Bellini [a,1], Serena Mazzucchelli [b,1,*], Elisabetta Galbiati [a], Silvia Sommaruga [b], Luisa Fiandra [b], Marta Truffi [b], Maria A. Rizzuto [a], Miriam Colombo [a], Paolo Tortora [a], Fabio Corsi [b], Davide Prosperi [a,**]

[a] Dipartimento di Biotecnologie e Bioscienze, Università di Milano-Bicocca, Piazza della Scienza 2, 20126 Milano, Italy
[b] Dipartimento di Scienze Biomediche e Cliniche "Luigi Sacco", Università di Milano, Ospedale L. Sacco, Via G.B. Grassi 74, 20157 Milano, Italy

ARTICLE INFO

Article history:
Received 5 June 2014
Accepted 3 October 2014
Available online 13 October 2014

Keywords:
Bionanoparticles
Apoferritin
Drug delivery system
Anticancer drugs
Self-triggered translocation
Nuclear targeting

ABSTRACT

A genetically engineered apoferritin variant consisting of 24 heavy-chain subunits (HFn) was produced to achieve a cumulative delivery of an antitumor drug, which exerts its cytotoxic action by targeting the DNA at the nucleus of human cancer cells with subcellular precision. The rationale of our approach is based on exploiting the natural arsenal of defense of cancer cells to stimulate them to recruit large amounts of HFn nanoparticles loaded with doxorubicin inside their nucleus in response to a DNA damage, which leads to a programmed cell death. After demonstrating the selectivity of HFn for representative cancer cells compared to healthy fibroblasts, doxorubicin-loaded HFn was used to treat the cancer cells. The results from confocal microscopy and DNA damage assays proved that loading of doxorubicin in HFn nanoparticles increased the nuclear delivery of the drug, thus enhancing doxorubicin efficacy. Doxorubicin-loaded HFn acts as a "Trojan Horse": HFn was internalized in cancer cells faster and more efficiently compared to free doxorubicin, then promptly translocated into the nucleus following the DNA damage caused by the partial release in the cytoplasm of encapsulated doxorubicin. This self-triggered translocation mechanism allowed the drug to be directly released in the nuclear compartment, where it exerted its toxic action. This approach was reliable and straightforward providing an antiproliferative effect with high reproducibility. The particular self-assembling nature of HFn nanocage makes it a versatile and tunable nanovector for a broad range of molecules suitable both for detection and treatment of cancer cells.

1. Introduction

Cancer is the third cause of mortality in the world and the global burden of cancer continues to increase [1]. The primary option for the treatment of most solid tumors is surgery, followed by adjuvant chemotherapy to prevent the onset of metastasis. However, in recurrent cancer, the first clinical approach is chemotherapy [2–4]. The main advantage of chemotherapy resides in the systemic action towards both primary and metastatic tumors. However, non-selective activity causes severe side effects that strongly affect the therapeutic outcomes.

Doxorubicin (DOX) is one of the most widely used chemotherapeutics in the treatment of solid tumors, although the development of resistance and the occurrence of severe side effects, including cardiotoxicity and myelosuppression, caused by high dosages, limits its efficacy in the clinical practice [5]. DOX presents chemical suboptimal characteristics, including poor solubility and easy metabolism to doxorubicinol [6], while the entry of DOX into cancer cells basically occurs by diffusion. However, even at low concentrations, the process reaches saturation, which drastically limits the uptake of the compound [7]. In addition, DOX is subjected to the effect of multi-drug resistance mechanisms (MDR) that remove the drug from the cytoplasm, preventing it to exert its cytotoxic action [7]. Therefore, the increase of DOX therapeutic index is of utmost importance in cancer research. Recent effort has led to novel DOX delivery strategies, including the use of liposomes or inorganic nanoparticles with the aim to reduce the drug-related toxicity and to escape from MDR mechanisms [8–10].

Apoferritin nanoshells have been proposed to be a promising and versatile solution [11]. Ferritins are a family of iron storage proteins composed of a regular assembly of 24 subunits to form a spherical cage architecture with an external size of ~12 nm [12,13]. Mammalian ferritins consist of a mixture of two different types of self-assembling subunits known as H (heavy) and L (light) chain [14]. H chain includes a catalytic ferroxidase site, which catalyzes the oxidation of Fe(II) to Fe(III), while L chain plays a role in the iron nucleation process. Ferritin inner cavity has a diameter of 8 nm to enclose a core of hydrated iron oxide, which can contain up to 4000 iron atoms [12]. This cavity has been exploited

* Correspondence to: S. Mazzucchelli, Via G.B. Grassi 74, 20157 Milano, Italy.
** Correspondence to: D. Prosperi, Piazza della Scienza 2, 20126 Milano, Italy. Tel.: +39 026448 3302; fax: +39 026448 3565.
E-mail addresses: serena.mazzucchelli@gmail.com (S. Mazzucchelli), davide.prosperi@unimib.it (D. Prosperi).
[1] These authors made equal contributions.

http://dx.doi.org/10.1016/j.jconrel.2014.10.002
0168-3659/

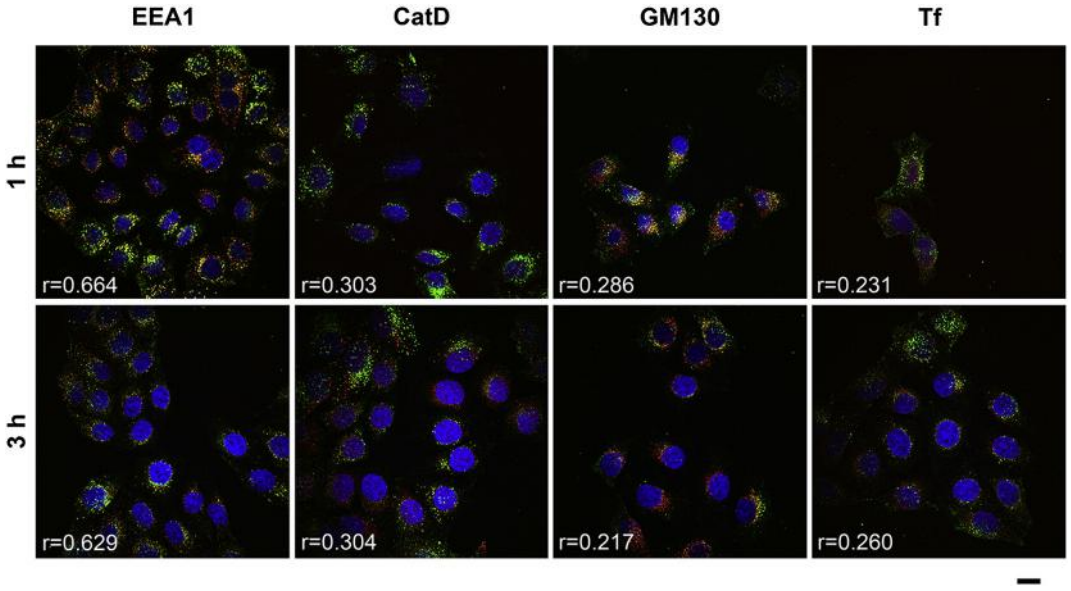

Fig. 1. Intracellular localization of HFn nanoparticles. Confocal microscopy merges images of HeLa cells, incubated for 1 h or 3 h at 37 °C with 0.1 mg mL^{-1} of HFn (green). Early endosomes, lysosomes, Golgi and recycling endosomes were recognized with early endosome marker EEA1, lysosomal protein CatD, Golgi marker GM130 and recycling endosome marker Tf antibodies, respectively, and labeled with an anti-mouse secondary antibody conjugated with Alexa Fluor 546 (red). Nuclei were stained with DAPI (blue). Scale bar: 10 μm. (For interpretation of the references to colour in this figure legend, the reader is referred to the web version of this article.)

in nanomaterial chemistry as a reaction chamber for the template synthesis of nanoparticles with a well-defined size and shape and a narrow size distribution [14–19]. Moreover, since the subunits can be disassembled at acidic pH and reassembled by bringing back the pH to neutrality in a shape-memory fashion, apoferritin can be exploited for the encapsulation of various organic molecules thus representing an interesting scaffold for the development of a biocompatible drug delivery system [20]. Ferritin is specifically cross-recognized in humans by the receptor of transferrin 1 (TfR1), which is found overexpressed in many types of tumor cells but not in normal cells and healthy tissues [21]. Recently, an RGD-modified apoferritin cage was demonstrated to improve the delivery of DOX in the cytoplasm of a glioblastoma cell line [11].

Ferritin plays a key role in the oxidative metabolism by converting Fe^{2+}, which is a source of toxic reactive oxygen species (ROS), into inoffensive Fe^{3+} [12]. This protective mechanism is particularly important in the nucleus, where it is needed to shield DNA from iron-induced oxidative damages [22]. In eukaryotic cells, the nuclear pore complex is responsible for translocation of molecules into the nucleus, partly by passive diffusion provided that the molecular size is small enough (≤40 kDa) [23]. However, larger molecules, including proteins, can be efficiently transported through the involvement of signal- and energy-dependent pathways, usually exploiting "nuclear localization signals" (NLS) [24]. These may include a peptide sequence that can bind to importin β, which in turn binds to the nuclear pore complex [25], or short consensus sequences not involving the interaction with importins [26]. Recent evidence has been provided that ferritin is translocated into the nucleus by an active transport mechanism [22,27]. Available data suggest that the H subunit is involved in nuclear translocation mechanisms, which, however, occurs without any NLS involvement [28]. It has been observed that if as low as 15% of the monomeric H-ferritin is deleted or replaced, nuclear translocation is inhibited and ferritin is confined in the cytoplasm [29]. Although the size of monomeric H-ferritin (21 kDa) allows passive diffusion into the nucleus [30], the efficiency of translocation suggests the involvement of an active mechanism, in which the import of an integral ferritin cage cannot be ruled out despite its molecular weight (~450 kDa). Indeed, macromolecules with a diameter of up to 39 nm are capable to penetrate the nucleus *via* an active signal-mediated transport [31].

Based on the above considerations, we reasoned that a 24-H subunit variant of apoferritin (HFn) would facilitate the cumulative delivery of encapsulated DOX directly inside the nucleus, potentially reducing DOX dosages and mitigating MDR effects. Therefore, we produced the monomeric H subunit by recombinant engineering, which proved valuable in self-assembling in apoferritin-like nanocages. We envisaged that HFn could be a good candidate nanocarrier specific for nuclear delivery of chemotherapeutics, as: 1) HFn could be easily loaded with a broad range of drugs, including DOX; 2) HFn was expected to sensitively and selectively recognize tumor cells exploiting the binding with TfR1; 3) H subunits were found in monomeric form in the nucleus [29], suggesting a disassembly mechanism inside or in close proximity of the nucleus, which would allow the drug to be intranuclearly released; 4) as cancer cells exhibit greater ROS stress than normal cells do [32–34], nuclear translocation of HFn should be also favored in cancer cells in response to oxidative stimuli; and 5) DOX could be passively released out of HFn shell inducing a DNA damage, which, in turn, could further trigger HFn nuclear translocation.

The intent of this work was to investigate the interaction of HFn with a model TfR1-positive cancer cell line, to assess the increased cytotoxic efficacy of DOX incorporated in HFn, to study DOX release in cancer cells and to demonstrate enhanced and self-triggered nuclear delivery.

2. Materials and methods

2.1. HFn nanocage design

The cDNA encoding for the heavy chain of human ferritin, modified by inserting the restriction sites for *NdeI* and *NotI* (respectively in 5′ and 3′), was synthesized by Eurofins MWG Operon and subcloned into the vector pET30b(+) from Eurofins MWG Operon to express the HFn under the control of a T7 promoter, as reported in Figure S1b (Supporting Information). The resulting plasmid pET30b/HFn was used to transform *Escherichia coli* expression strain BL21(DE3) by heat-shock method. The recombinant expression vector was confirmed by restriction endonuclease digestion and DNA sequencing.

2.2. HFn expression in E. coli and purification

BL21(DE3)/pET30b/HFn cells were grown at 37 °C in Luria Bertani kanamicin medium until OD_{600nm} = 0.6 and induced with 0.5 mM isopropyl β-D-1-tiogalactopiranoside (IPTG) for 2 h and 30 min. Then,

a) Viability of cells treated with DOX or HFn(DOX) 0.1μM

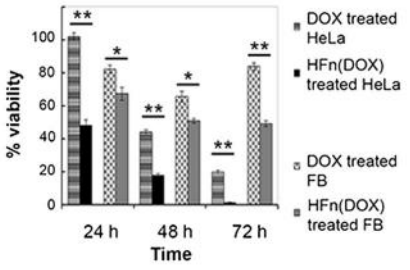

b) Cell death assay performed with DOX free or encapsulated in HFn shell

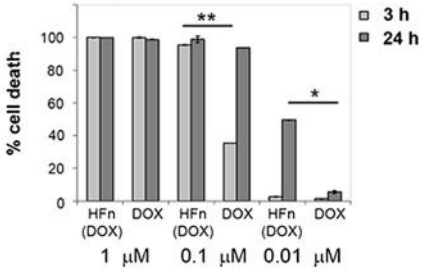

c) Double-strand break of DNA after DOX exposure

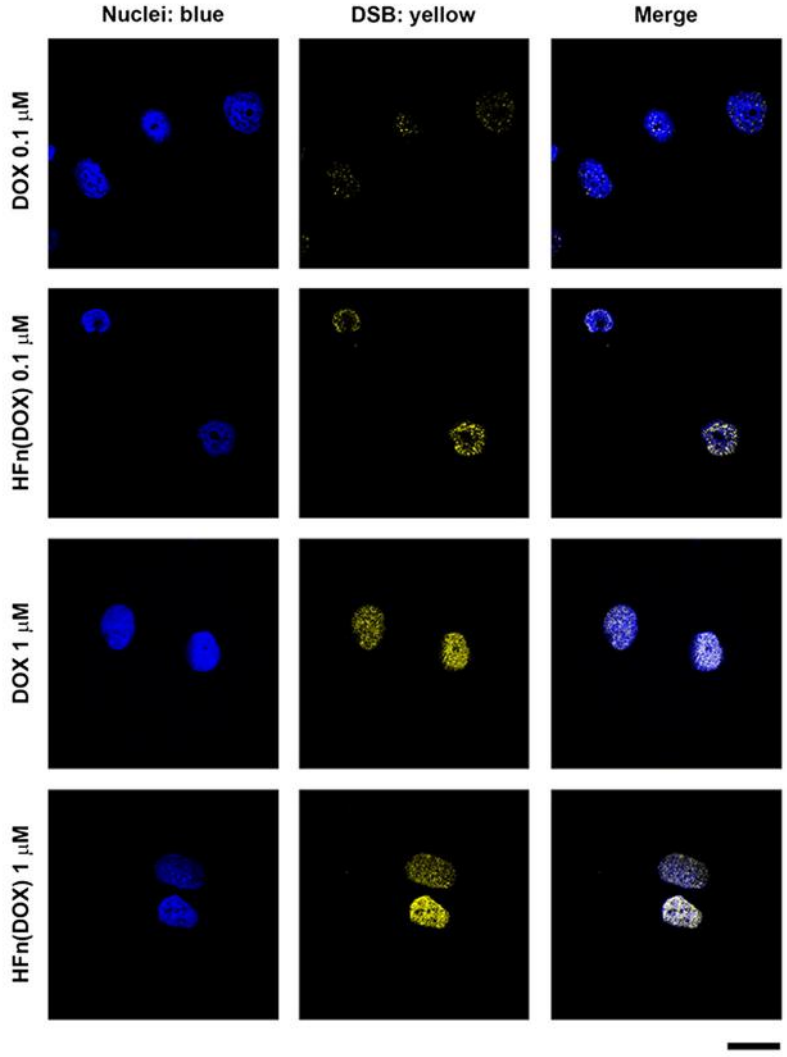

d) Quantification of DNA double-strand breaks after DOX or HFn(DOX) exposure

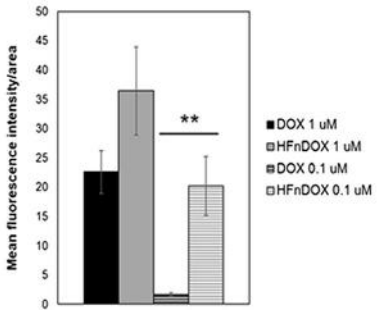

cells were collected, washed and resuspended in lysis buffer with lysozyme and DNase I. In order to prepare the crude extract, cellular suspension was sonicated six times for 10 s and centrifuged. After heat treatment at 70 °C for 15 min, the supernatant was loaded onto DEAE Sepharose anion exchange resin, pre-equilibrated with 20 mM K-MES, pH 6.0. The purified protein was eluted with a stepwise NaCl gradient, from 70 mM to 420 mM, in the same buffer. A yield of 56 mg L^{-1} of culture was obtained. Fractions were analyzed by SDS-PAGE using 12% (*v*/*v*) polyacrylamide gels [35] and the proteins detected by Coomassie Blue staining. Protein content was determined by both measuring absorbance at 280 nm and using the Coomassie Plus Protein Assay Reagent (Thermo Fisher Scientific) with IgG as standard protein. HFn for *in vitro* studies was labeled with fluorescein isothiocyanate (FITC) or with Alexa Fluor 546 according to the manufacturer's protocol (Sigma, Invitrogen).

2.3. HFn loading with DOX

HFn(DOX) was prepared using the disassembly/reassembly method. 200 μM doxorubicin hydrochloride was added to a HFn solution (0.5 mg mL^{-1} in 0.15 M NaCl) and adjusted to pH 2.0 by 0.1 M HCl. The pH was maintained for about 15 min and when the dissociation of HFn was completed, the pH value was increased up to 7.5 using 0.1 M NaOH. The resulting solution was stirred at room temperature for 2 h. In order to remove the excess doxorubicin and the adsorbed molecules, the solution was centrifuged through a 100 kDa Amicon filter (Millipore) and washed several times with PBS buffer. The amount of the encapsulated molecules was determined extracting DOX from HFn shell according to procedure previously described [36] and then measuring the fluorescence intensity at 555 nm of the DOX dispersion in chloroform by comparison with a predetermined DOX calibration curve. To evaluate the intracellular fate of encapsulated molecules HFn shell was also loaded with FITC using the same procedure described for DOX encapsulation.

2.4. Kinetics of DOX spontaneous release in vitro

HFn(DOX) was stored in a dialysis device and kept in a PBS bath at 37 °C for three days under shaking. At predetermined time points (30 min, 1 h, 2 h, 3 h, 4 h, 6 h, 24 h, 48 h, 72 h), the amount of drug released was quantified by fluorescence analysis and the buffer was replaced after each measurement.

2.5. Cell cultures

A HeLa cell line was used as a TfR1-positive model of tumor cells; human fibroblasts extracted from *gut tunica submucosa* of Crohn patients were used as healthy cell line, while MDA-MB-468 breast cancer cells were used as a MDR cells. HeLa, fibroblasts and MDA-MB-468 were cultured in Dulbecco's Modified Eagle's Medium (DMEM) supplemented with 10% fetal bovine serum, 2 mM L-glutamine, penicillin (50 UI mL^{-1}) and streptomycin (50 mg mL^{-1}) at 37 °C in humidified atmosphere containing 5% CO_2 and sub-cultured prior to confluence using trypsin/EDTA.

2.6. TfR1 expression

Cells (5×10^5) were treated for FACS analysis with standard methods. Briefly, cells were incubated for 30 min at 4 °C in blocking buffer (PBS, 2% BSA, 2% goat serum) and then with the anti-human TfR1 antibody (1 μg; Thermo Scientific). Cells were washed three times with PBS and incubated 30 min at 4 °C with the secondary antibody Alexa Fluor 488 (1 μL; Life Technologies) in blocking buffer used. Then, cells were washed and were analyzed on a FACS Calibur flow cytometer (Becton Dickinson). 10,000 events were acquired for each analysis, after gating on viable cells, and isotype-control antibodies were used to set the appropriate gates.

2.7. Cell binding assay

Cells (5×10^5) were incubated 2 h at 4 °C in flow cytometry tubes in the presence of 0.02 mg mL^{-1} of FITC-labeled HFn. After incubation, cells were washed three times with PBS. Labeled cells were resuspended with 0.5 mL of PBS and analyzed by a FACS Calibur flow cytometer (Becton Dickinson). 20,000 events were acquired for each analysis, after gating on viable cells, and a sample of untreated cells was used to set the appropriate gates.

2.8. HFn internalization

Cells were subjected to nanoparticle incubation with HFn labeled with FITC on the shell at the concentration of 0.1 mg mL^{-1} for 15 min, 1, 3, 24 and 48 h at 37 °C and then harvested for immunofluorescence analysis. To evaluate simultaneously the intracellular fate of HFn and encapsulated molecules, HeLa were incubated with 0.1 mg mL^{-1} of HFn labeled with Alexa Fluor 546 and loaded with FITC for 4 and 48 h at 37 °C and then treated for immunofluorescence.

2.9. Colocalization experiments

HFn labeled with FITC on the shell was used (0.1 mg mL^{-1}) and different organelles were stained with GM130 (at a 1:100 dilution; clone 35; BD Biosciences), CatD (1:50; clone BC011; Calbiochem), EEA1 (1:1000; clone 14; BD Biosciences), and Tf (1:100; clone 5G2; Abcam) antibodies by incubating 2 h at RT and revealed by a AlexaFluor 546-conjugated antibody against murine IgGs (Invitrogen) at a 1:300 dilution by incubating for 2 h at RT in PBS, 2% BSA, 2% goat serum.

2.10. Confocal laser scanning microscopy

Cells were cultured on collagen pre-coated cover glass slides until sub-confluence and incubated with HFn nanoparticles, for different time periods. Cells were washed with phosphate-buffered saline (PBS, EuroClone), fixed for 5 min with 4% paraformaldehyde (Sigma) and then treated for 5 min with Triton X-100 0.1%. A blocking step was performed for 1 h at RT with a solution containing 2% bovine serum albumin (BSA, Sigma), 2% goat serum and 0.2 μg mL^{-1} DAPI (4′,6-diamino-2-phenylindole) in PBS. Microscopy analysis was performed with a Leica SPE microscope confocal system equipped with laser excitation lines 405 nm, 488 nm line, 514 nm and 633 nm. Images were acquired with 63× magnification oil immersion lenses at

Fig. 2. a) Viability of cells treated with free DOX or HFn(DOX). Fibroblasts and HeLa cells were treated with 0.1 μM of DOX or HFn(DOX) for up to 72 h. Viability was assessed by measuring the conversion of MTT into formazan. Reported values are the mean of six replicates ± s.e., normalized on cell proliferation of untreated fibroblast or HeLa cells, respectively * $P < 0.005$; ** $P < 0.0005$ (Student's *t*-test). b) Cell death assay with DOX free or encapsulated in HFn shell. HeLa cells were treated with 1, 0.1 and 0.01 μM of DOX or HFn(DOX) for 3 or 24 h. Cell death was assessed on the basis of the exposure to Annexin V, evaluated by flow cytometry. Untreated cells were used to set region of positivity. Reported values are the mean of three replicates ± s.e. * $P < 0.01$; ** $P < 0.005$ (Student's *t*-test). c) Double-strand break of DNA after DOX exposure. Confocal microscopy images of HeLa cells incubated with 1 μM or 0.1 μM DOX free or encapsulated in HFns. Anti γH2A.X antibodies were used to reveal the DNA double-strand breaks (DSB; yellow). Scale bar: 10 μm. d) Quantification of fluorescence intensity due to DSB. Reported values obtained with Image J software represent the mean fluorescence intensity of six different cells normalized with respect to their area ± s.e. ** $P < 0.005$. (For interpretation of the references to colour in this figure legend, the reader is referred to the web version of this article.)

1024 × 1024 pixel resolution. Image quantification was performed with Image J software. Pearson correlation coefficient was calculated using the Image J plugin JaCoP.

2.11. Cell proliferation assay

Cells were cultured on a 96 multiwell dish at a density of 5000 cells cm^{-1}. Then, cells were incubated with different amounts of the molecules to be tested. At the indicated time points (24, 48, 72 h), cells were washed with PBS and then incubated for 3 h at 37 °C with 0.1 mL of 3-(4,5-dimethyl-2-thiazolyl)-2,5-diphenyl-2H-tetrazolium bromide (MTT) stock solution previously diluted 1:10 in DMEM medium without phenol red. After incubation, MTT solubilizing solution (0.1 mL) was added to each well to solubilize the MTT formazan crystals (Promega). Absorbance was read immediately using a testing wavelength of 570 nm and a reference wavelength of 620 nm. The results are expressed as means ± standard error (s.e.) of six individual experiments.

2.12. Cell death assay

Cells were cultured on a 12 multiwell dish until sub-confluence. Then, cells were incubated 3 h and 24 h at 37 °C in the presence of different amounts of DOX or HFn(DOX). After incubation, cells were washed twice with PBS and treated for FACS analysis according to Annexin V-PE-Cy5 Apoptosis Detection Kit manufacturer's protocol (BioVision). Briefly, cells were resuspended in Binding Buffer and incubated for 5 min in the presence of 5 μL of annexin V-PE-Cy5. Cells were analyzed within 1 h on a FACS Calibur flow cytometer (Becton Dickinson). 20,000 events were acquired for each analysis, after gating on viable cells. For evaluation of late apoptosis, the same protocol was used but incubation with 7-aminoactinomycin D (BD Biosciences; 51-68981E; 5 μL/sample) was accomplished.

2.13. DNA damage assay

Cells were subjected to nanoparticle incubation with DOX free or encapsulated in HFn cage at the concentrations of 0.1 or 1 μM for 24 h at 37 °C and then harvested for immunofluorescence analysis. Double strand breaks were stained with γH2A.X antibody (1:1000 dilution) by incubating 2 h at RT and revealed by an AlexaFluor 546-conjugated antibody against rabbit IgGs (Invitrogen) at a 1:300 dilution by incubating for 2 h at RT in PBS, 2% BSA, 2% goat serum.

2.14. DOX release

Cells were subjected to nanoparticle incubation with DOX free or encapsulated in HFn cage at the concentrations of 0.1 or 1 μM for 3 and 24 h at 37 °C and then harvested for immunofluorescence analysis. DOX was revealed exciting the sample with 488 nm laser line and acquiring emitted signal from 550 nm to 600 nm (red). The signal represented in green color is the emission in the acquiring window between 520 to 545 nm, which corresponds to the fluorescence signal of a degradation product of DOX [37].

2.15. Nuclear translocation

In experiment of endogenous ferritin nuclear translocation, cells were incubated with 0.1 μM DOX for 15 min, 1, 3, 24 and 48 h at 37 °C and then treated for immunofluorescence. For image nuclear translocation of HFn nanoparticles, cells were incubated for 3 h at 37 °C with HFn (0.1 mg mL^{-1}), treated with DOX 0.1 μM for 15 min, 1 and 3 h and then harvested for immunofluorescence analysis. Both endogenous and exogenous ferritin were stained with the anti-ferritin antibody (1:2000; ab7332; Abcam) and revealed by an AlexaFluor 546-conjugated antibody against rabbit IgGs (Invitrogen) at a 1:300 dilution by

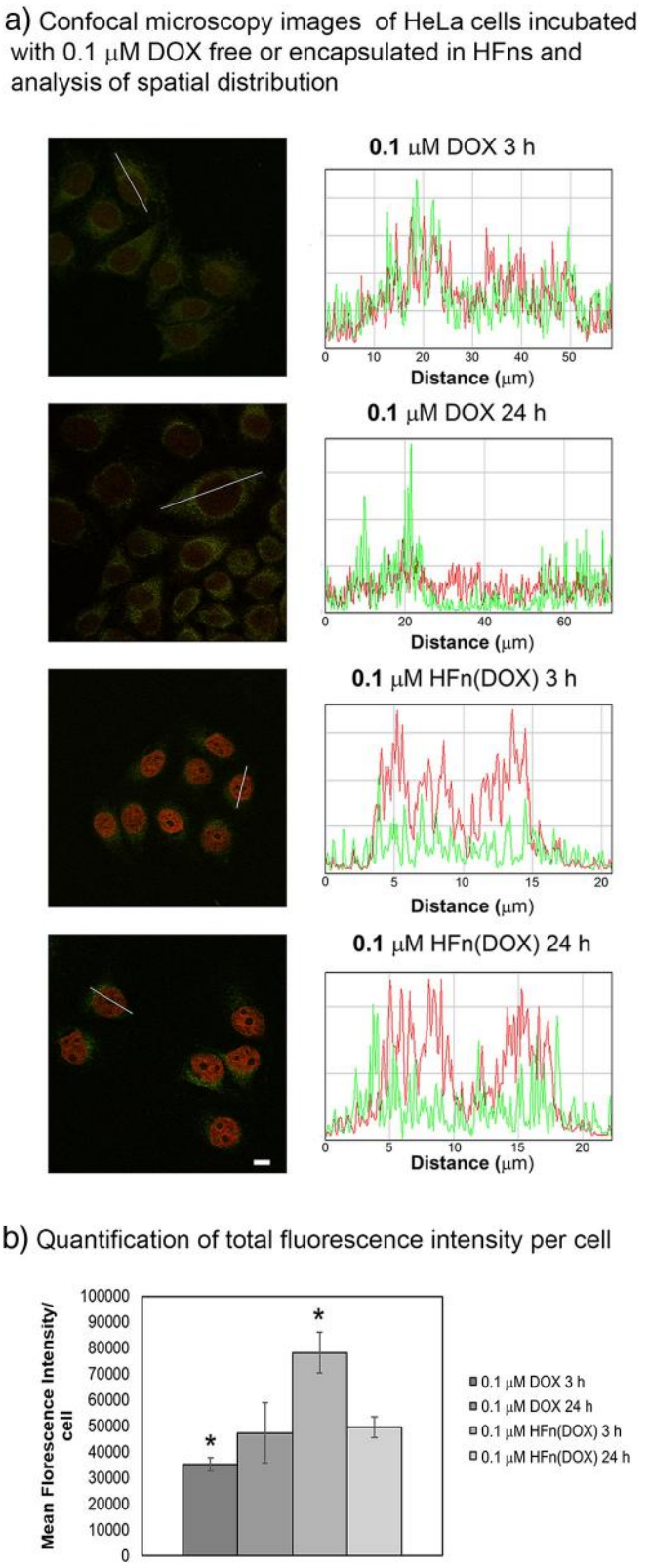

Fig. 3. Doxorubicin release inside the nuclear compartment. a) Confocal microscopy images of HeLa cells incubated with 0.1 μM DOX free or encapsulated in HFns and analysis of spatial distribution. Confocal laser scanning images of HeLa cells treated with 0.1 μM DOX (DOX degradation product in green) free or encapsulated in HFn shell for 3 h or 24 h at 37 °C. Scale bar: 10 μm. Spatial analysis was performed on merged images using Image J plugin RGB profile plot. b) Quantification of total fluorescence intensity per cell. Reported values are a mean of measurements performed with Image J software on six different cells ± s.e. * $P < 0.01$. (For interpretation of the references to colour in this figure legend, the reader is referred to the web version of this article.)

incubating for 2 h at RT in PBS, 2% BSA, 2% goat serum. In order to assess self-triggered nuclear translocation cells were subjected to nanoparticles incubation with HFn(DOX) at DOX concentrations of 0.1 and 1 μM for 3 or 24 h and then harvested for immunofluorescence analysis. The corresponding amount of HFn void was used as control.

2.16. MDR protein inhibition

Percentage of MDR protein inhibition was determined using the Solvo MultiDrugQuant Assay Kit according to the manufacturer's protocols. Briefly 500,000 cells previously incubated with Cyclosporin-A 1 μM (CysA) were harvested by trypsinization and washed thrice with HBSS buffer (Sigma). Then, cells were incubated at 37 °C with calcein-AM solution (0.2 mL/tube) for 10 min. Then reaction was stopped by rapid centrifugation of 1 min at 2000 ×*g* and cells were analyzed by flow cytometry. The percentage of inhibition was determined as follows:

$$\%\ \text{MDR proteins inhibition} = 100 \times (\text{Mean Fluorescence}_{\text{treated}} - \text{Mean fluorescence}_{\text{control}}) / \text{Mean Fluorescence}_{\text{treated}}$$

3. Results and discussion

3.1. HFn nanoparticles: development, interaction with tumor cells and internalization

The H monomer of human ferritin was cloned and expressed in *E. coli* and purified as reported in the Methods section. A good degree of purity was observed in purified fractions showing a 21 kDa band in sodium docecyl sulfate-polyacrylamide gel electrophoresis (SDS-PAGE) corresponding to HFn monomer (Figure S1a). Moreover, PAGE performed under native conditions, using commercial Horse ferritin as reference standard, confirmed that our HFn was correctly folded and still able to spontaneously assemble in a 24-subunit nanosphere (Figure S1c). HFn nanoparticles were then labeled with FITC and used to evaluate tumor cell recognition. In a recent study, the interaction between apoferritin and tumor cells was reported to be mediated by transferrin receptor 1 (TfR1), which is overexpressed in most tumor cells and tissues [20]. In the present work, HeLa cancer cells derived from human cervical cancer were selected for the *in vitro* evaluation as a model tumor cell line with high TfR1 expression (supplementary Figure S2), while human fibroblasts, the most common type of cells found in connective tissue, were used as control healthy cells with low TfR1 expression (Figure S2). The binding assay, performed by flow cytometry after incubating the cells for 2 h at 4 °C with 0.02 mg mL^{-1} of HFn, demonstrated at least a fourfold increase in cell ratio in the region of positivity for HeLa cells compared to fibroblasts, confirming a remarkable HFn affinity and selectivity toward cancer cells (Figure S3a). Confocal laser scanning images of HeLa cells incubated with HFn nanoparticles demonstrated that a fast interaction with cellular membrane occurred, since HFn was almost completely attached to the cell surface after 15 min of incubation. In addition, HFn was already internalized after 1 h of incubation and, after 3 h, the internalization process was complete. After 24 h, the fluorescence signal of HFn dramatically decreased without, however, disappearing up to 48 h of incubation. This effect suggested that exogenous HFn was degraded or combined with the endogenous unlabeled one (Figure S3b).

Since natural apoferritin interacts with cell membrane through TfR1, we expected that HFn could be efficiently internalized into the cells using the same endocytic pathway of transferrin (Tf). Therefore, we characterized the endocytosis pathway of HFn by investigating its colocalization with specific endocytic compartments, using EEA1 marker for early endosomes, GM130 marker for the Golgi apparatus, CatD marker for lysosomes, and Tf as a marker for the recycling endosomes. We found that HFn uptake took place within 1 h and HFn basically localized at the early endosomes, corroborating our hypothesis that also HFn is internalized by a TfR1-mediated mechanism. Confocal images demonstrated that HFn did not localize at the Golgi and recycling endosomes even after 3 h of incubation with cells, suggesting that HFn neither is pushed out of the cells using recycling endosomes nor is sent to the Golgi by late endosomes. Amazingly, colocalization between HFn and lysosomes did not occur either after 1 or 3 h of incubation with HeLa cells, a time long enough to promote lysosome formation with this kind of bionanoconstructs [21]. This observation suggested that HFn was not recognized by the cell as something to degrade, thus remaining inside the cell for a long period of time (Figs. 1, S4–6). This unexpected result let us postulate that HFn could be a good candidate as a drug bionanocarrier, since it did not prove liable to lysosomal degradation.

3.2. HFn loading and release of chemotherapeutics

In order to set up the experimental conditions required for drug incorporation into the HFn shell, HFn was first loaded with fluorescent molecules using the disassembly/reassembly method already reported in the literature for native apoferritin [38]. This procedure exploited the ability of HFn to modify its quaternary structure in response to pH changes. In particular, in the absence of active disassembly mechanisms, HFn shell is unfolded into monomeric subunits at acidic pH around 2–3 and is refolded with perfect shape memory when the solution is brought to pH values around 7.5, as depicted in Figure S7a. Under the same conditions, DOX encapsulation was straightforward and highly reproducible and allowed us to load 28.3 molecules of DOX per HFn shell on average, in accordance with literature data [39].

Next, we evaluated the DOX release from HFn shell *in vitro*. Kinetics of release were performed dialyzing DOX-loaded nanoparticles (HFn(DOX)) at 37 °C in phosphate buffer saline (PBS), pH 7.4, and quantifying the leakage of drug from HFn by measuring the fluorescence emission in the supernatants. The amount of encapsulated DOX remained constant for the first 6 h of incubation, then decreased by 40% over 72 h of incubation in PBS (Figure S7b), confirming the presumed good stability of the HFn nanoformulation at physiological pH.

In order to study the cellular trafficking of encapsulated molecules after uptake, HFn was loaded under the above conditions with a more efficient dye, fluorescein isothiocyanate (FITC). HFn shell was concomitantly labeled with an orthogonal dye, AlexaFluor 546. Our intent was to simultaneously follow the separate fate of the incorporated drug and of the protein cage by acquiring the fluorescence images at the relevant emission λ_{max} values. This doubly fluorescent nanoparticle was incubated with HeLa cells for 4 and 48 h. Confocal laser scanning microscopy images demonstrated that, after 4 h of incubation at 37 °C, encapsulated FITC (green) and HFn shell (red) were still colocalized, as revealed by the predominant presence of yellow signals inside the cells. After 48 h of incubation at 37 °C, FITC signal was widespread inside the cells, while the signal attributable to HFn shell was almost completely disappeared, thus suggesting recombination of labeled monomers with endogenous unlabeled 24mers (Figure S8). These results corroborated our hypothesis about the potential use of HFn as nanovectors for the delivery of drugs in intracellular compartments.

3.3. Doxorubicin encapsulation in HFn improves the antitumor efficacy

Next, DOX efficacy was evaluated comparing the proliferation of cells treated with DOX or HFn(DOX). HeLa cells were treated with different amounts of DOX or HFn(DOX) in a DOX concentration range between 0.01 and 1 μM, for up to 72 h. Fibroblasts were also treated with DOX or HFn(DOX), as a healthy cell line control to assess the target selectivity. The percentage of cell viability over time was determined on samples treated with 0.01 μM, 0.1 μM and 1 μM DOX or HFn(DOX) using the MTT assay and normalized on the cell proliferation of the respective untreated control at different time points. As reported in Figure S9a,

a) Nuclear translocation of endogenous ferritin

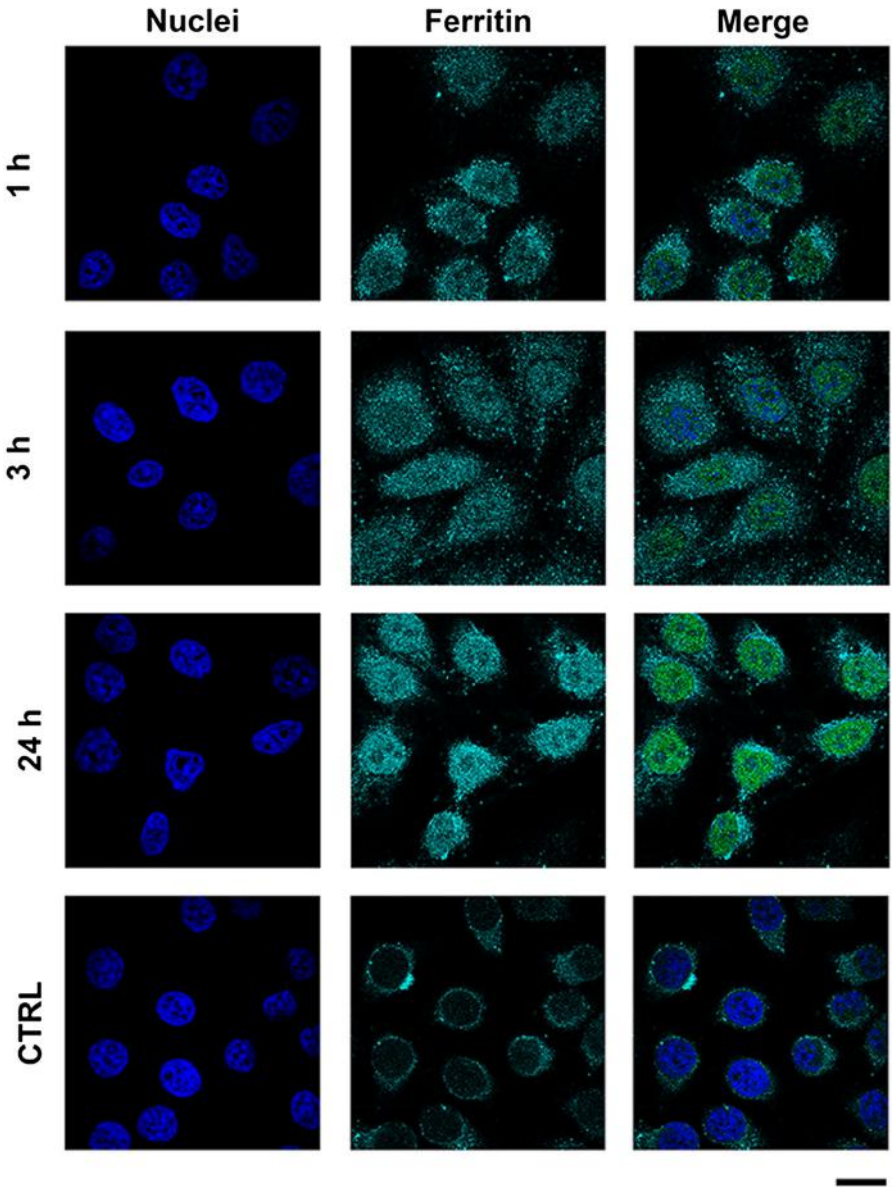

b) Quantification of ferritin in the nuclear compartment

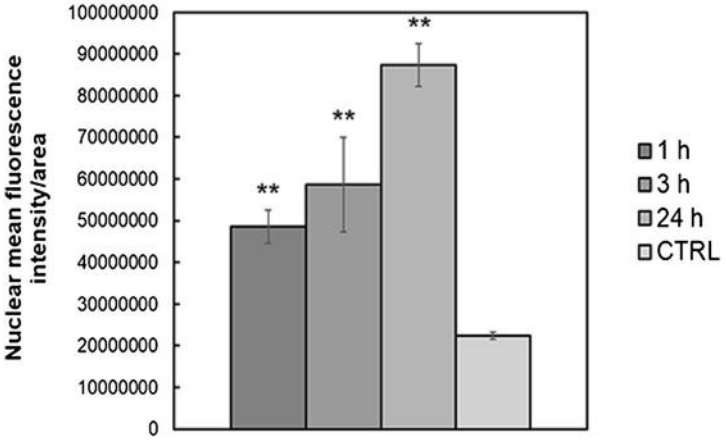

samples treated with 0.01 μM DOX or HFn(DOX) did not show any meaningful decrease in cell proliferation, compared to untreated cells, both in normal and in tumor cells since cell survival remained higher than 60%. In contrast, 1 μM dosage resulted in detectable effects in cell proliferation with significant differences between groups treated with DOX or HFn(DOX). However, a significant reduction of cell survival was observed also on healthy fibroblasts, probably due to high DOX concentration (Figure S9b).

Interestingly, cells treated with 0.1 μM HFn(DOX) showed instead a substantial decrease in HeLa cell proliferation in comparison with samples treated with the same amount of free DOX, revealing remarkable differences in antiproliferative efficacy of DOX and HFn(DOX) (Fig. 2a). Indeed, HFn(DOX) exhibited a far higher efficiency in inhibiting the tumor cell proliferation in comparison to free DOX. Less significant differences between DOX and HFn(DOX) treatment were observed in fibroblasts suggesting that DOX cytotoxicity was basically low at this concentration against normal cells irrespective of the modality of DOX delivery (Fig. 2a). Hela cells were also treated with relevant amounts of void HFn in order to assess the contribution of the void nanovector. Results reported in Figure S10 demonstrate that HFn does not affect cell viability.

Next, in order to determine if the arrest in proliferation was associated with an increase in cell death, the exposure to Annexin V was assayed, which provides a positive readout only in apoptotic cells. HeLa cells were incubated for 3 or 24 h with DOX or HFn(DOX) at decreasing concentrations, including 1 μM, 0.1 μM and 0.01 μM. Annexin V assay was measured by flow cytometry using untreated cells, to set the regions of positivity. The ratio of dead cells reported in Fig. 2b demonstrated that HFn(DOX) was much more effective than free DOX in inducing apoptosis at 0.1 μM after 3 h of incubation. However, at 24 h, the differences in apoptotic effect between DOX and HFn(DOX) in cancer cells were smoothed, suggesting a more efficient and rapid delivery of DOX when encapsulated in a HFn shell. Cells treated with 0.01 μM HFn(DOX) for 3 h basically did not show any increase in cell death in comparison with free drug, since the DOX dosage was probably too low to be effective. However, after 24 h of incubation, significant variations were observed, reflecting a DOX accumulation over time attributable to the effect of HFn delivery. As expected, treatment of HeLa cells at the highest concentration (1 μM) induced rapid and complete cell death both with DOX and HFn(DOX). As Annexin V exposure is a characteristic feature of cells in early apoptosis, we decided to check if the reduced efficacy of free DOX after 3 h of treatment was rather an apparent event attributable to a fraction of cells that had already developed to a late apoptosis at the considered time points. To this aim, the 7-aminoactinomycin D (7-AAD) uptake was assessed, which occurs specifically in cells with a damaged plasma membrane. After flow cytometry analysis, we concluded that both DOX and HFn(DOX) treated cells were not in late apoptosis (Figure S11). The reduction of viability and the increase of apoptosis in cells treated with HFn(DOX) were further associated to a more substantial DNA damage compared with free DOX, as evidenced in Fig. 2c and d. The amount of double strand break, visualized using γH2A.X antibody [40], is higher in cells treated with HFn(DOX) under the above experimental conditions, confirming that HFn(DOX) efficacy is incontrovertibly associated with a functional damage of nuclear DNA.

3.4. Nuclear delivery of doxorubicin

The fluorescence emission of DOX was exploited in this study to evaluate DOX cellular uptake and possible release from HFn. HeLa cells were treated with 0.1 μM DOX free or encapsulated in HFn for 3 or 24 h. Then, cells were washed, fixed and prepared for confocal microscopy analysis. When DOX is excited with an argon laser (488 nm), it exhibits a characteristic fluorescence spectra profile consisting in a double emission with relevant maximal peaks at 505 nm (green) and at 550 nm (red), respectively, which can be detected separately by setting the instrumentation appropriately [41]. Confocal images revealed that HFn(DOX) exhibits improved uptake in comparison with free DOX (Fig. 3). In particular, free DOX just entered the cells by diffusion and, as a result, was mainly localized in the cytoplasm (green) even after 24 h of incubation, as assessed by analysis of DOX fluorescence spatial distribution (Fig. 3a). In contrast, the uptake of HFn(DOX) was very fast, as it was mediated by TfR1 receptor endocytosis, and DOX was almost entirely released in the nucleus (red) ready after 3 h, as demonstrated by analysis of DOX fluorescence spatial distribution (Fig. 3a). The significant difference in DOX uptake at 3 h observed with HFn(DOX) in comparison with free DOX could imply that nanoparticle formulation was capable of bypassing the well documented multi-drug resistance mechanism (MDR) activated by cancer cells to protect themselves from the cytotoxic effects of chemotherapeutics (Fig. 3b). Noteworthy, the nuclear release of HFn(DOX) suggests that HFn shell mediates a nuclear translocation of DOX. This effect is likely correlated with the physiological function of ferritins. Indeed, as mentioned above, ferritin plays a key role in the metabolism of iron, protecting the cell from oxidative stress [11]. This protective role is exerted both in the cytoplasm and in the nucleus. Thus, ferritin is translocated into the nucleus in response to oxidative stimuli to protect the DNA from potential damage caused by anomalous ROS production [11].

3.5. DOX cytoplasmatic release triggers HFn nuclear translocation

Our results let us speculate that HFn acts like a “Trojan horse”. Indeed, 1) HFn enters the cells as a result of the interaction with TfR1 and 2) partially releases DOX in the cytoplasm through hydrophobic channels of its architecture; 3) DOX diffuses in the nucleus where it causes the DNA damage, 4) which triggers the nuclear translocation of HFn(DOX), and 5) the release of DOX in the nuclear compartment. In order to verify this hypothesis, we studied the subcellular localization of endogenous ferritin upon DOX administration. Confocal microscopy images of HeLa cells, which were fixed 1, 3 and 24 h after administration of 0.1 μM DOX, clearly show that endogenous ferritin was localized in the nuclear compartment ready after 1 h, where it continued to accumulate over time (Fig. 4a, b). In contrast, untreated HeLa cells (CTRL) displayed mainly a cytoplasmic confinement of ferritin, proving that the DOX administration triggered its nuclear translocation. Next, we determined if the treatment with DOX could trigger also nuclear translocation of recombinant HFn. HeLa cells were incubated for 3 h with HFn labeled with FITC on the shell (HFn_FITC) in order to allow for a complete internalization of HFn (Fig. 5). Then, 0.1 μM DOX was added to the culture medium and HFn nuclear translocation was recorded by confocal microscopy performed on cells fixed 15 min, 1 and 3 h after 0.1 μM DOX administration. Confocal microscopy images clearly show that HFn was still confined in the cytoplasm 15 min after DOX addition, even though it was apparent that HFn accumulated in the close proximity of the nucleus. However, after 1 h, the nuclear translocation was complete. These results confirm that the HFn nanoparticles were directly translocated into the nucleus, suggesting that they were recruited to carry out the physiological functions attributed to native ferritin. With the aim to assess if HFn acted by bringing the payload across the nuclear envelope or rather by releasing it in proximity of the nucleus, the same experiment was performed also

Fig. 4. a) Treatment with DOX triggers nuclear translocation of endogenous HFn. Confocal microscopy images of HeLa cells incubated for 1, 3 and 24 h at 37 °C with DOX 0.1 μM. Untreated cells are used as negative control (CTRL). Nuclei were stained with DAPI (blue). Endogenous ferritin were recognized with anti-ferritin antibody and labeled with an anti-rabbit secondary antibody conjugated with Alexa Fluor 546 (cyan; Invitrogen). Scale bar: 10 μm. b) Quantification of nuclear fluorescence intensity due to endogenous ferritin. Reported values are a mean of measurements performed with Image J software on nucleus five different cells normalized with respect to their area ± s.e. ** $P < 0.0005$. (For interpretation of the references to colour in this figure legend, the reader is referred to the web version of this article.)

with unlabeled HFn loaded with FITC (HFn(FITC)), Figure S12). Images of HeLa cells displayed in Figure S12 indicate that the payload was directly transported and released in the nucleus upon external cell stimulation with DOX. This result is particularly relevant considering that, different from DOX, FITC does not exhibit a natural propensity to penetrate the nucleus, thus such a massive nuclear translocation should necessarily imply an active transport. Finally, in order to evaluate if HFn(DOX) nuclear translocation could be self-triggered by DOX encapsulated in the HFn shell, 0.1 and 1 μM DOX were loaded inside HFn_FITC and then incubated with cells (Fig. 6a). DOX and FITC fluorescence signal were acquired simultaneously. Confocal microscopy images in Fig. 6a show that at a DOX concentration of 0.1 μM nuclear translocation of HFn was only marginally visible both after 3 and 24 h of incubation. However, at a HFn(DOX) concentration of 1 μM, HFn was clearly localized in the nuclear compartment even after 3 h of incubation, proving that HFn nuclear translocation was self-triggered by DOX release from the hydrophobic channels of HFn. Moreover, the correspondence between the signal of the nuclear HFn, here obtained with 1 μM HFn(DOX) and the signal detected in the previous experiment with 0.1 μM free DOX, provides an indirect confirmation that the amount of DOX released into the cytoplasm to cause self-triggered translocation was only a minor fraction of that encapsulated. Combining these results corroborate our hypothesis that the partial release of DOX in the cytoplasm and the likely consequent damage due to DOX intercalation in the DNA double-helix trigger the nuclear translocation of HFn(DOX), as depicted in Fig. 6c. Therefore, we concluded that the DOX release was mainly accomplished upon entrance into the nucleus. Such findings make HFn an ideal candidate for the development of nanodevices for the nuclear delivery of chemotherapeutics in cancer cells.

3.6. Enhanced DOX delivery by HFn in MDR cancer cells

To investigate the potential of HFn in the treatment of cancer cells affected by multidrug resistance mechanism, MDA-MB-468 breast cancer cells were used in the next experiment, as they have been demonstrated to exhibit P-gp-promoted MDR with DOX [42] and high TfR1 expression (Figure S2). MDA-MB-468 cells were incubated with 1 μM DOX or HFn(DOX) for 3 or 24 h in DMEM. After washing out the unreacted nanoparticles, cells were fixed and prepared for immunofluorescence. Fig. 7a shows the results of confocal images acquired on isolated MDR cells after treatment. As expected, in cells treated with free DOX, no traces of drug could be detected inside the cytoplasm both at 3 and 24 h. The nuclei appeared not to be affected by the drug at 3 h, while only a minimal amount of drug was revealed at 24 h. In contrast, HFn(DOX) efficiently delivered a detectable amount of drug into the nucleus ready after 3 h and a strong emission signal could be monitored after 24 h, in a similar behavior to what we observed with sensitive HeLa cells. The improved nuclear delivery of DOX due to HFn assistance was combined with an increased DOX efficacy, as assessed by viability assay (Fig. 7b). In order to evaluate if the increased DOX efficacy observed for HFn(DOX) formulation is mainly due to an escape from MDR efflux pump or to the HFn self-triggered drug release mechanism, MDA-MB-468 cells were treated with an inhibitor of MDR proteins.

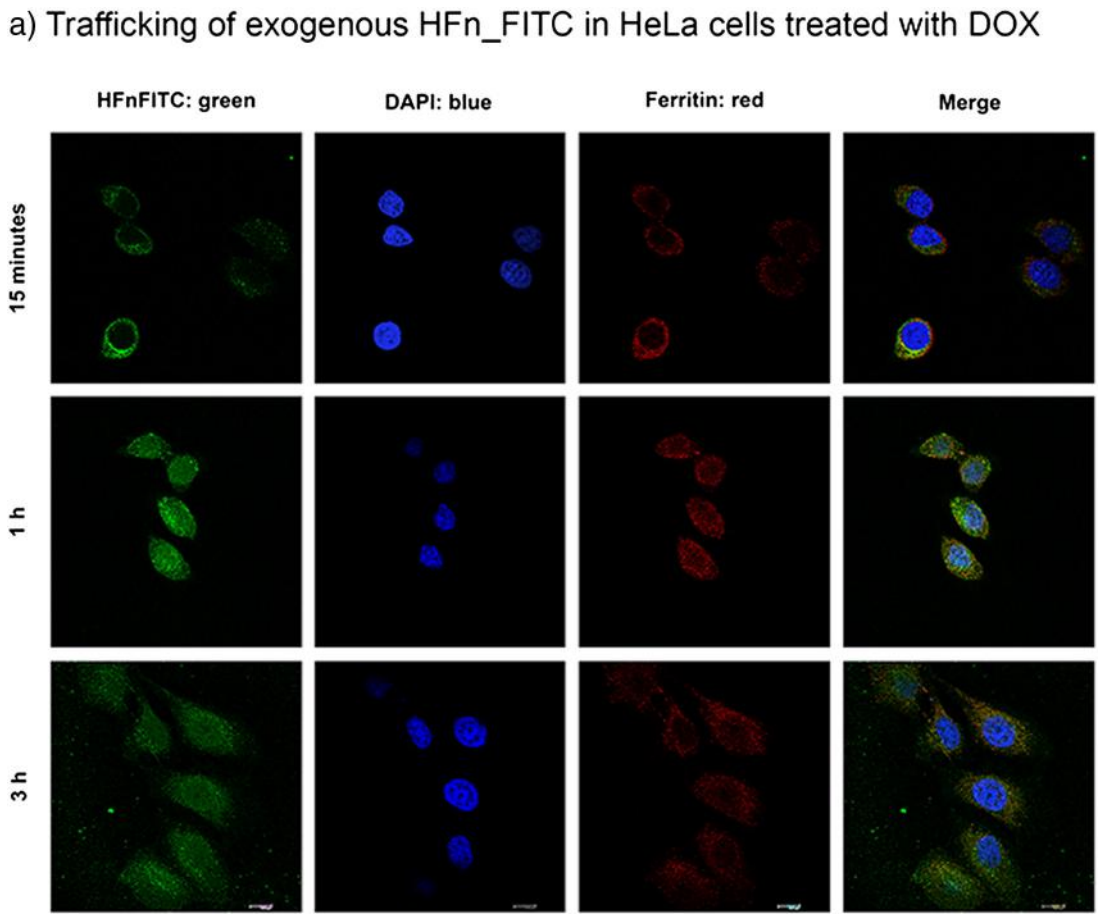

Fig. 5. Treatment with DOX trigger nuclear translocation of exogenous HFn. Confocal microscopy images of HeLa cells incubated for 3 h at 37 °C with 0.1 μg mL^{-1} of HFn labeled with FITC (HFn_FITC; green) and then treated (a) or not (b) with 0.1 μM DOX for 15 min, 1 or 3 h. Nuclei were stained with DAPI (blue). Ferritin were recognized with anti-ferritin antibody and labeled with an anti-rabbit secondary antibody conjugated with Alexa Fluor 546 (red; Invitrogen). Scale bar: 10 μm. c) Quantification of fluorescence signal of HFn_FITC in the nucleus. Reported values are a mean of 5 measurements performed with Image J software on the nucleus of different cells normalized with respect to their area ± s.e. * $P < 0.005$; ** $P < 0.0005$. (For interpretation of the references to colour in this figure legend, the reader is referred to the web version of this article.)

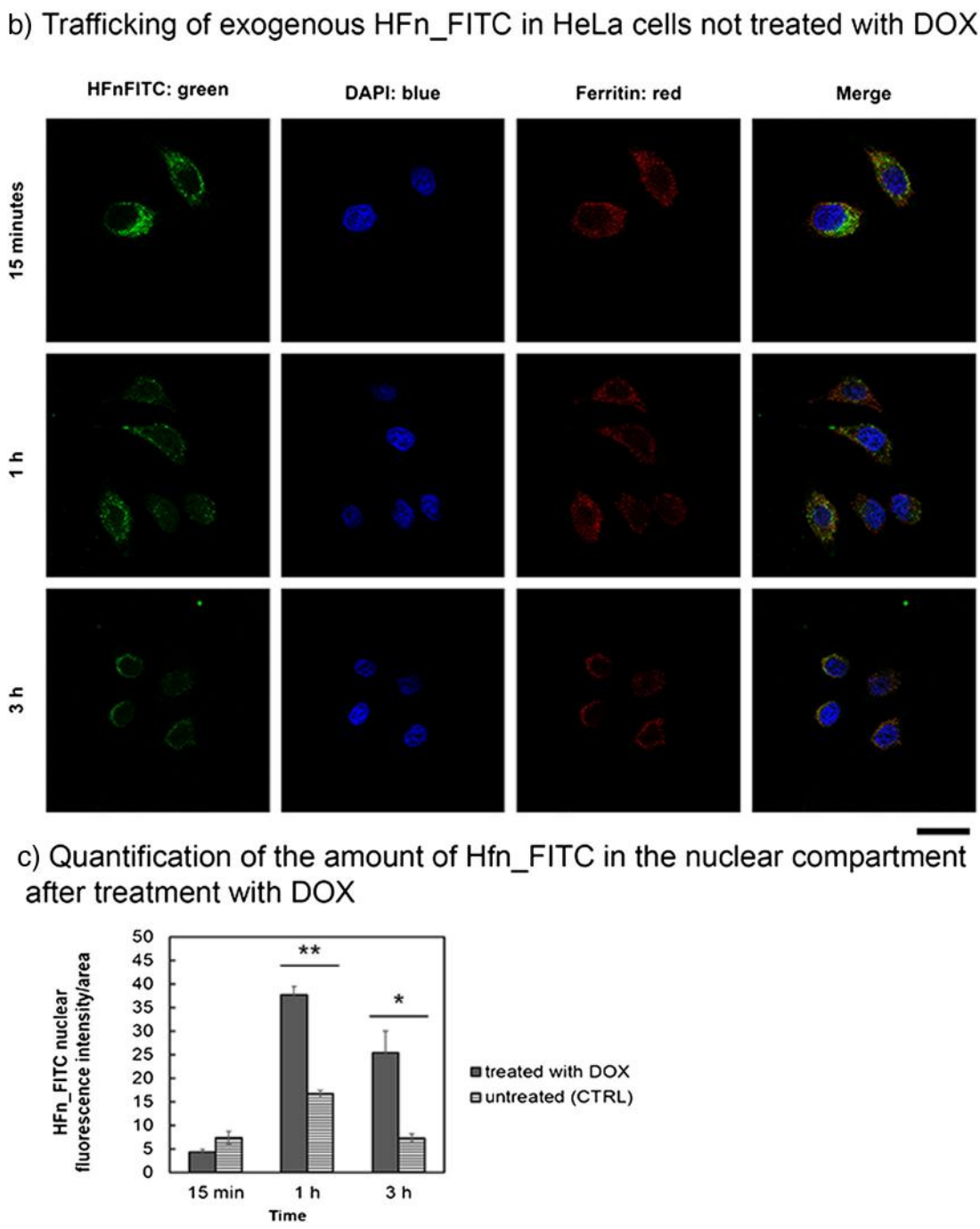

Fig. 5 (*continued*).

MDA-MB-468 cells were treated with 1 μM HFn(DOX) and their viability was evaluated also in the presence of 1 μM Cyclosporin-A (CysA). The kind of inhibitor and their working concentration have been selected in order to obtain the maximal percentage of MDR inhibition (77%) without affecting cell viability. Results reported in Fig. 8 do not show statistically significant variations between samples incubated with HFn(DOX) or not with CysA at 72 h, which seems to corroborate the hypothesis of HFn contribution in escaping from MDR efflux pump. However, the decrease of percentage of viability observed at 24 and 48 h after treatment with CysA strongly supports the conclusion that the major efficacy of HFn(DOX) in comparison to free DOX is mainly due to the HFn self-triggered release mechanism, while the HFn escape from MDR efflux pump plays a marginal role.

4. Conclusions

In summary, we have produced and purified a recombinant heavy-chain monomer of human apoferritin (HFn) in multimilligram amounts. HFn maintained the capability of self-assembling, disassembling and reassembling with shape memory into a 24-H subunit nanocage in dependence of the pH changes resembling native apoferritin. HFn was first labeled on the external surface with a fluorescent dye and filled in with an alternative dye to follow their internalization and fate in representative cancer (HeLa) drug-sensitive cells, suggesting a preferred receptor-mediated endocytosis pathway of entrance in cancer cells with remarkable selectivity in comparison with the uptake from healthy cells (fibroblasts). Next, HFn nanocage was efficiently loaded

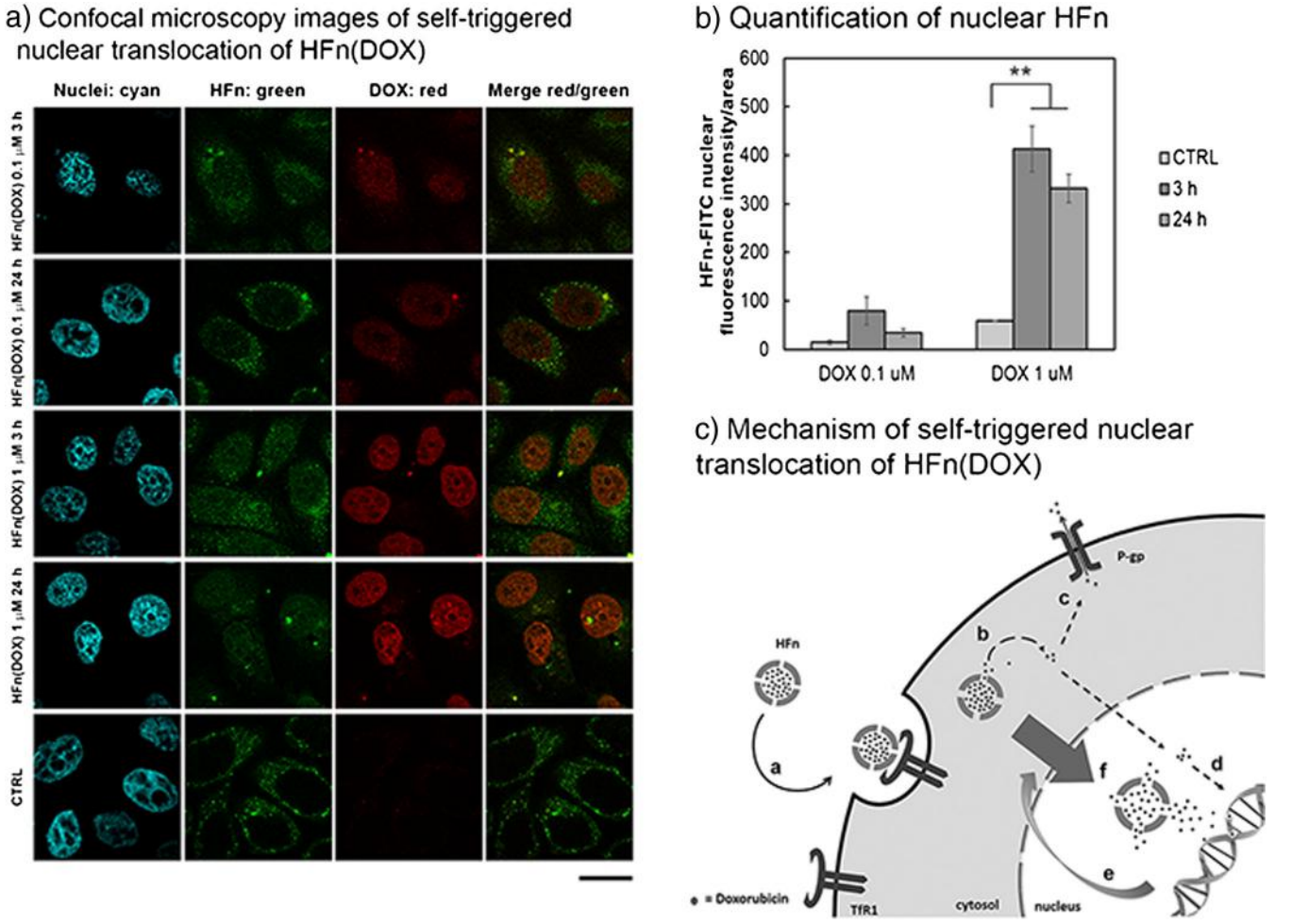

Fig. 6. a) Self-triggered nuclear delivery of DOX in HFn(DOX) nanoparticles. Confocal microscopy images of HeLa cells incubated for 3 and 24 h at 37 °C with 0.1 μM of HFn(DOX). HFn(DOX) was labeled with FITC (HFn; green) on the shell and then loaded with DOX (red). Nuclei were stained with DAPI (cyan). Scale bar: 10 μm. b) Quantification of fluorescence signal of HFn_FITC in the nucleus. Reported values are a mean of 5 measurements performed with Image J software on the nucleus of different cells normalized with respect to their area ± s.e. ** $P < 0.0005$. c) Schematic representation of self-triggered nuclear delivery of HFn(DOX). HFn was internalized upon the interaction with TfR1 by receptor-mediated mechanism without incurring lysosomal degradation (a). Encapsulated DOX was partially released in the cytoplasm through hydrophobic channels of its architectucture (b). Then DOX is pumped out of the action of P-glycoprotein (c), or diffuses into the nucleus where it causes the DNA damage (d), which triggers the nuclear translocation of HFn(DOX) (e), and the massive release of DOX in the nuclear compartment (f). (For interpretation of the references to colour in this figure legend, the reader is referred to the web version of this article.)

with doxorubicin (DOX) and used to treat HeLa cells in comparison with equal concentrations of free drug. Our results demonstrate that HFn(DOX) complex is engulfed by cancer cells more rapidly and efficiently than free DOX. Most important, confocal microscopy analysis combined with a DNA damage assay provided evidence that HFn allowed for fast and massive delivery of the antiproliferative chemotherapeutic agent inside the nuclear compartment, thus strongly enhancing the cytotoxic effect of DOX. Our interpretation of this effect is that an initial release of a small amount of DOX in the cytoplasm induces a DNA damage, triggering the recruitment of H-rich apoferritins into the nucleus. Indeed, under the same conditions, nontoxic dyes were principally released in the cytoplasm after prolonged incubation and not delivered to the nucleus. Hence, the point of strength of HFn nanoparticles is that they are activated to translocate into the nucleus upon noxious stimuli that the cell itself signals in the presence of a DNA damage.

HFn displays two important advantages over conventional nanocarriers of DNA-intercalating drugs: 1) the drug is principally released at its final destination with a subcellular precision through a self-triggered mechanism, thus optimizing the cytotoxic effect of the drug, and 2) the self-assembling recombinant nanocage exhibits a well documented target selectivity toward a broad selection of cancer cell types. However, HFn can be straightforwardly modified with specific targeting peptides by standard genetic engineering, which could further improve the nanocarrier selectivity toward specific cancer cell types. In our strategy, HFn nanocages loaded with DOX could behave like a "Trojan horse": called back within the nucleus for the purpose of defense, HFn releases, instead, the cytotoxic anticancer drug directly into the most effective site of action. Eventually, HFn was shown to significantly improve the accumulation of DOX in drug-resistant cancer cells, enlarging the spectrum of possible cancer cell targets, allowing clinicians to reconsider the use of traditional chemotherapeutics, which have previously failed with several tumor types. We believe that this nanovector has great potential for the delivery of DNA-interacting molecules and anticancer drugs exerting a specific intranuclear action for both *in vitro* investigations and *in vivo* treatment of malignant tumors. We envisage that HFn may find application in the treatment of several solid tumors, as the targeted nuclear delivery would allow us to strongly reduce the dose of administered drug and to limit severe side effects due to chemotherapeutic exposure.

Acknowledgment

This work was supported by Fondazione Regionale per la Ricerca Biomedica (FRRB), Nerviano Medical Sciences, NanoMeDia Project (L. Sacco Hospital and Regione Lombardia), Cariplo Foundation ("The MULAN program", Project N. 2011-2096) and "Centro di Microscopia

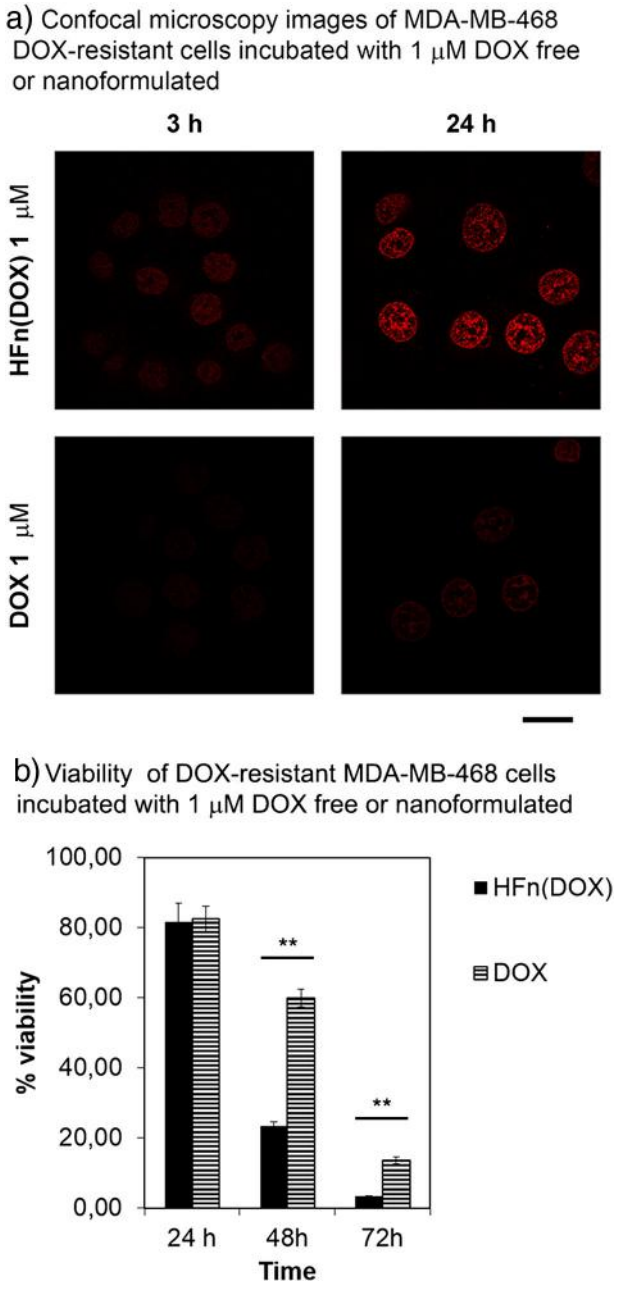

Fig. 7. a) Doxorubicin release inside the nuclear compartment of MDA-MB-468 cells. Confocal microscopy images of MDA-MB-468 cells incubated with 1 μM DOX free or encapsulated in HFn shell for 3 h or 24 h at 37 °C. Scale bar: 10 μm. b) Viability of cells treated with free DOX or HFn(DOX). MDA-MB-468 cells were treated with 1 μM of DOX or HFn(DOX) for up to 72 h. Viability was assessed by measuring the conversion of MTT into formazan. Reported values are the mean of six replicates ± s.e., normalized on cell proliferation of untreated cells, ** $P < 0.0005$ (Student's *t*-test).

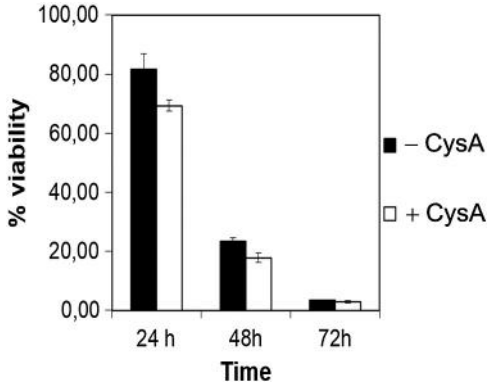

Fig. 8. Viability of cells treated with HFn(DOX) with or without MDR protein inhibition. MDA-MB-468 cells were treated with 1 μM of HFn(DOX) for up to 72 h with or without 1 μM Cyclosporin-A. Viability was assessed by measuring the conversion of MTT into formazan. Reported values are the mean of six replicates ± s.e., normalized on cell proliferation of untreated cells, respectively * $P < 0.05$; ** $P < 0.01$ (Student's *t*-test).

Elettronica per lo sviluppo delle Nanotecnologie applicate alla medicina" (CMENA, University of Milan).

Appendix A. Supplementary data

Supplementary data to this article can be found online at http://dx.doi.org/10.1016/j.jconrel.2014.10.002.

References

[1] A. Jemal, F. Bray, M.M. Center, J. Ferlay, E. Ward, D. Forman, CA Cancer J. Clin. 61 (2011) 69–90.
[2] L. Hutchinson, Nat. Rev. Clin. Oncol. 7 (2010) 669–670.
[3] F.B. Zimmermann, M. Molls, B. Jeremic, Semin. Surg. Oncol. 21 (2003) 122–127.
[4] W. ten Bokkel Huinink, M. Gore, J. Carmichael, A. Gordon, J. Malfetano, I. Hudson, C. Broom, C. Scarabelli, N. Davidson, M. Spanczynski, G. Bolis, H. Malmström, R. Coleman, S.C. Fields, J.F. Heron, J. Clin. Oncol. 15 (1997) 2183–2193.
[5] P.K. Singaland, N. Iliskovic, N. Engl. J. Med. 339 (1998) 900–905.
[6] A. Mordente, G. Minotti, G.E. Martorana, A. Silvestrini, B. Giardina, E. Meucci, Biochem. Pharmacol. 66 (2003) 989–998.
[7] R. Misra, S.K. Sahoo, Eur. J. Pharm. Sci. 39 (2010) 152–163.
[8] L. Harris, G. Batist, R. Belt, D. Rovira, R. Navari, N. Azarnia, L. Welles, E. Winer, Cancer 94 (2002) 25–36.
[9] J. Panyam, V. Labhasetwar, Mol. Pharm. 1 (2004) 77–84.
[10] L. Pan, Q. He, J. Liu, Y. Chen, M. Ma, L. Zhang, J. Shi, J. Am. Chem. Soc. 134 (2012) 5722–5725.
[11] Z. Zhen, W. Tang, H. Chen, X. Lin, T. Todd, G. Wang, T. Cowger, X. Chen, J. Xie, ACS Nano 7 (2013) 4830–4837.
[12] P. Arosio, R. Ingrassia, P. Cavadini, Biochim. Biophys. Acta 1790 (2009) 589–599.
[13] G.C. Ford, P.M. Harrison, D.W. Rice, J.M.A. Smith, A. Treffry, J.L. White, J. Yariv, Philos. Trans. R. Soc. Lond. B 304 (1984) 551–565.
[14] D.M. Lawson, P.J. Artymiuk, S.J. Yewdall, J.M.A. Smith, J.C. Livingstone, A. Treffry, A. Luzzago, S. Levi, P. Arosio, G. Cesareni, C.D. Thomas, W.V. Shaw, P.M. Harrison, Nature 349 (1991) 541–544.
[15] C. Cao, X. Wang, Y. cai, L. Sun, L. Tian, H. Wu, X. He, H. Lei, W. Liu, G. Chen, R. Zhu, Y. Pan, Adv. Mater. 26 (2014) 2566.
[16] M. Uchida, D.A. Willits, K. Muller, A.F. Willis, L. Jackiw, M. Jutila, M.J. Young, A.E. Porter, T. Douglas, Adv. Mater. 21 (2009) 458–462.
[17] E. Fantechi, C. Innocenti, M. Zanardelli, M. Fittipaldi, E. Falvo, M. Carbo, V. Shullani, L. Di Cesare Mannelli, C. Ghelardini, A.M. Ferretti, A. Ponti, C. Sangregorio, P. Ceci, ACS Nano 8 (2014) 4705–4719, http://dx.doi.org/10.1021/nn500454n.
[18] X. Lin, J. Xie, L. Zhu, S. Lee, G. Niu, Y. Ma, K. Kim, X. Chen, Angew. Chem. Int. Ed. 50 (2011) 1569–1572.
[19] E. Falvo, E. Tremante, R. Fraioli, C. Leonetti, C. Zamparelli, A. Boffi, V. Morea, P. Ceci, P. Giacomini, Nanoscale 5 (2013) 12278.
[20] K. Fan, C. Cao, Y. Pan, D. Lu, D. Yang, J. Feng, L. Song, M. Liang, X. Yan, Nat. Nanotechnol. 7 (2012) 459–464.
[21] L. Li, C.J. Fang, J.C. Ryan, E.C. Niemil, J.A. Lebrón, P.J. Björkman, H. Arase, F.M. Torti, S.V. Torti, M.C. Nakamura, W.E. Seaman, Proc. Natl. Acad. Sci. U. S. A. 107 (2010) 3505–3510.
[22] K.J. Thompson, M.G. Fried, Z. Ye, P. Boyer, J.R. Connor, J. Cell Sci. 115 (2002) 2165–2177.
[23] R. Peters, Biochim. Biophys. Acta 864 (1986) 305–359.
[24] C. Dingwall, R.A. Laskey, Trends Biochem. Sci. 16 (1991) 475–481.
[25] F. Melchior, L. Gerace, Curr. Opin. Cell Biol. 7 (1995) 310–318.
[26] V.W. Pollard, W.M. Michael, S. Nakielney, M.C. Siomi, F. Wang, G. Dreyfuss, Cell 86 (1996) 985–994.
[27] N. Surguladze, S. Patton, A. Cozzi, M.G. Fried, J.R. Connor, Biochem. J. 388 (2005) 731–740.
[28] C.X. Cai, T.F. Linsenmayer, J. Cell Sci. 114 (2001) 2327–2334.
[29] A.A. Alkhateeb, J.R. Connor, Biochim. Biophys. Acta 1800 (2010) 793–797.
[30] P.L. Paine, L.C. Moore, S.B. Horowitz, Nature 254 (1975) 109–114.
[31] N. Pentè, M. Kanns, Mol. Biol. Cell 13 (2002) 425–434.
[32] L. Behrend, G. Henderson, R.M. Zwacka, Biochem. Soc. Trans. 31 (2003) 1441–1444.
[33] E.O. Hileman, J. Liu, M. Albitar, M.J. Keating, P. Huang, Cancer Chemother. Pharmacol. 53 (2004) 209–219.

[34] S. Toyokuni, K. Okamoto, J. Yodoi, H. Hiai, FEBS Lett. 358 (1995) 1–3.
[35] U.K. Laemmli, Nature 227 (1970) 680–685.
[36] K.M. Laginha, S. Verwoert, G.J.R. Charrois, Clin. Cancer Res. 11 (2005) 6944–6949.
[37] O. Hovorka, V. Subr, D. Větvička, L. Kovář, J. Strohalm, M. Strohalm, A. Benda, M. Hof, K. Ulbrich, B. Říhová, Eur. J. Pharm. Biopharm. 76 (2010) 514–524.
[38] A. Ma-Ham, Z. Tang, H. Wu, J. Wang, Y. Lin, Small 5 (2009) 1706–1721.
[39] M.A. Kilic, E. Ozlu, S. Calis, J. Biomed. Nanotechnol. 8 (2012) 508–514.
[40] E.P. Rogakou, D.R. Pilch, A.H. Orr, V.S. Ivanova, W.M. Bonner, J. Biol. Chem. 273 (1998) 5858–5868.
[41] M. Gigli, S.M. Doglia, J.M. Millot, L. Valentini, M. Manfait, Biochim. Biophys. Acta 950 (1988) 13–20.
[42] Y. Yan, M. Björnmalm, F. Caruso, ACS Nano 7 (2013) 9512.

Nanometronomic treatment of 4T1 breast cancer with nanocaged doxorubicin prevents drug resistance and circumvents cardiotoxicity

Serena Mazzucchelli[1], Michela Bellini[2], Luisa Fiandra[1], Marta Truffi[1], Maria A. Rizzuto[2], Luca Sorrentino[1], Erika Longhi[1], Manuela Nebuloni[1], Davide Prosperi[2], Fabio Corsi[1,3]

[1]Department of Biomedical and Clinical Sciences "Luigi Sacco", University of Milan, Milan, Italy

[2]Department of Biotechnology and Biosciences, University of Milan-Bicocca, Milano, Italy

[3]Surgery Department, Breast Unit, ICS Maugeri S. p. A. SB, Pavia, Italy

Correspondence to: *Fabio Corsi,* ***email:*** *fabio.corsi@unimi.it*
Davide Prosperi, ***email:*** *davide.prosperi@unimib.it*

Keywords: *metronomic chemotherapy, breast cancer, doxorubicin, drug resistance, tumor targeting*

Received: *October 07, 2016* ***Accepted:*** *November 24, 2016* ***Published:*** *December 25, 2016*

ABSTRACT

Chemotherapeutic treatment of breast cancer is based on maximum tolerated dose (MTD) approach. However, advanced stage tumors are not effectively eradicated by MTD owing to suboptimal drug targeting, onset of therapeutic resistance and neoangiogenesis. In contrast, "metronomic" chemotherapy is based on frequent drug administrations at lower doses, resulting in neovascularization inhibition and induction of tumor dormancy. Here we show the potential of H-ferritin (HFn)-mediated targeted nanodelivery of metronomic doxorubicin (DOX) in the setting of a highly aggressive and metastatic 4T1 breast cancer mouse model with DOX-inducible expression of chemoresistance. We find that HFn-DOX administered at repeated doses of 1.24 mg kg^{-1} strongly improves the antitumor potential of DOX chemotherapy arresting the tumor progression. We find that such a potent antitumor effect is attributable to multiple nanodrug actions beyond cell killing, including inhibition of tumor angiogenesis and avoidance of chemoresistance. Multiparametric assessment of heart tissues, including histology, ultrastructural analysis of tissue morphology, and measurement of markers of reactive oxygen species and hepatic/renal conditions, provided evidence that metronomic HFn-DOX allowed us to overcome cardiotoxicity. Our results suggest that HFn-DOX has tremendous potential for the development of "nanometronomic" chemotherapy toward safe and tailored oncological treatments.

INTRODUCTION

Over the past decades, cytotoxic chemotherapeutics have dominated the systemic management of cancer according to the "maximum tolerated dose" (MTD) paradigm [1, 2]. MTD therapy requires that patients are administered with single dose or short courses of the highest tolerable dosage of a drug in order to achieve the best therapeutic efficacy. Due to low tumor selectivity, MTD treatments cannot be protracted in order to allow recovery of healthy tissues and to reduce myelosuppression associated with pulsed drug doses [3]. In fast-growing or metastatic tumors, during these therapeutic breaks, a burst in cancer cell proliferation accompanied by manifestation of chemoresistance and accelerated angiogenesis are likely [4, 5]. Hence, a reappraisal of advanced-stage cancer management is ongoing, moving from the "maximum tolerable" to the "minimum effective" dose paradigm [6]. Indeed, cytotoxic agents administered at low dosages are expected to allow protracted treatments and have been suggested to up-regulate antiangiogenic factors such as thrombospondin-1 and to inhibit vascular endothelial growth factor and platelet-derived growth factor [2, 7].

The first clinical trials using low-dose metronomic (LDM) chemotherapy were conducted for breast, prostate, gastrointestinal, renal and pancreatic cancers,

as well as refractory melanoma [8–10]. This regimen is based on a lower dose of drugs administered more frequently, without the need of extensive interruptions [2, 11]. While the conventional dose-dense chemotherapeutic setting is suggested to act by targeting the proliferating tumor cells [12], LDM is presumed to affect the vasculature growth and repair [8, 13], to reduce systemic toxicity and myelosuppression, and to improve the stimulation of the host immune system against the tumor [1, 4]. However, several limiting factors remain for LDM in order to displace MTD treatments in clinical practice, including 1) low drug accumulation at tumor site [14], 2) controversial effectiveness against chemoresistance in advanced metastatic cancers [15], and 3) acquired resistance after prolonged treatment [16].

Recent advances in nanotechnology could offer groundbreaking solutions to improve the effectiveness of LDM chemotherapy, by taking advantage of the unique targeting efficiency of engineered nanocarriers [17]. In the present work, we propose a new concept of low dose "nanometronomic" (LDNM) chemotherapy. In principle, it is possible to obtain a prolonged antitumor effect with LDNM by means of multitasking nanocarriers that deliver lower dose of drug selectively to the growing tumor, inhibit the neovascularization process and prevent chemoresistance. Doxorubicin (DOX) is an excellent pilot drug for use in a LDM regimen [18], as its great anticancer efficacy is notoriously dose-limited by severe systemic side effects above all long-term cardiotoxicity with different severity grades from reduction in left ventricular ejection fraction (LVEF) to severe congestive heart failure [19, 20]. Liposomal anthracyclines, including pegylated liposomal doxorubicin (pl-DOX), have been introduced in clinical practice to enhance the therapeutic index and to avoid cardiotoxicity of these drugs thanks to higher accumulation of DOX in the tumor with reduced concentration in off-target organs [21]. However, meta-analyses of several clinical trials comparing pl-DOX to conventional DOX have demonstrated reduced (but not annulled) cardiotoxicity of pl-DOX, without improvement in progression-free or overall survival in advanced breast cancer (BC) [22]. Therefore, improving the therapeutic index of DOX remains an open challenge. As an ideal DOX nanocarrier for our LDNM study, we used H-Ferritin (HFn) nanocages, recently proposed as a promising bionanoparticle for cancer targeting [23] owing to its affinity for transferrin receptor 1 (TfR-1), which is constitutively overexpressed in primary and metastatic cancer cells [24]. HFn-DOX complex was recently demonstrated to overcome chemoresistance by actively promoting DOX nuclear translocation *in vitro* [25, 26] and was tested as a MTD treatment of a DOX-sensitive BC animal model with encouraging results [27].

RESULTS

In vitro uptake and cytotoxicity of HFn-DOX in 4T1 breast cancer cells

The 4T1 cell line (4T1-L) was selected as *in vitro* and *in vivo* BC model for three main reasons: 1) tumor aggressiveness due to 4T1 genetic patterning, which results in high level of proliferation, migration and invasiveness; 2) basal expression of MDR-1 transporter, which switches into overexpression upon treatment with DOX resulting in chemoresistance [28]; 3) stable luciferase expression, which allowed us to follow the tumor progression and metastases. 4T1-L cells were first treated with FITC-labeled HFn (FITC-HFn) [25] to investigate the nanoparticle-cell interaction. Cells were incubated with FITC-HFn for 15 min, 1, 3 and 48 h, and analyzed by confocal microscopy to evaluate the uptake and intracellular trafficking. HFn was quickly internalized, since it was recovered inside the cell cytoplasm after only 15 min of incubation, and it continued accumulating in the cytosol until 3 h (Figure 1A). The intracellular signal intensity decreased after 48 h probably due to ferritin disassembly, consistent with previous evidence [25]. HFn was found partly compartmentalized in early endosomes and partly free in the cytosol (Supplementary Figure S1), while the absence of colocalization with lysosomes, Golgi and transferrin (Tf) marker suggested that HFn did not follow lysosomal degradation, elimination or recycling, respectively, in agreement of previous evidence [25]. Binding assays with HFn at 20 or 100 μg mL^{-1} confirmed a dose-dependent recognition of tumor cells (Figure 1B).

4T1-L cells were treated with DOX or HFn-DOX at increasing concentrations of DOX to assess cell proliferation, cell death, DNA damage and nuclear DOX accumulation. Proliferation was arrested for at least 72 h after treatment with 1 μM HFn-DOX, while DOX reduced cell proliferation for 24 h only, suggesting the onset of chemoresistance upon incubation with DOX (Figure 1C). Cell viability was evaluated by incubating the cells with 0.01, 0.1 and 1 μM DOX or HFn-DOX for up to 72 h. Results reported in Figure 1D show that inhibition of BC cell viability using HFn-DOX was significantly higher than that after treatment with DOX. Such a drop in viability was ascribed to a remarkable increase in cell death (Figure 1E). Treatment with 0.01 μM HFn-DOX caused pronounced apoptosis and necrosis induction and double strand breaks in contrast to DOX (Figure 1F). It can be assumed that the increase in cytotoxicity of HFn-DOX resides in the efficiency of HFn in promoting DOX nuclear translocation (Figure 1G), as already described for different tumor cell lines [25, 26]. Quantitative fluorescence analysis of confocal images gave a nuclear DOX concentration of 15.2 and 9-fold higher than that detected in cultures treated with DOX at 0.1 and 1 μM, respectively (Supplementary Figure S2).

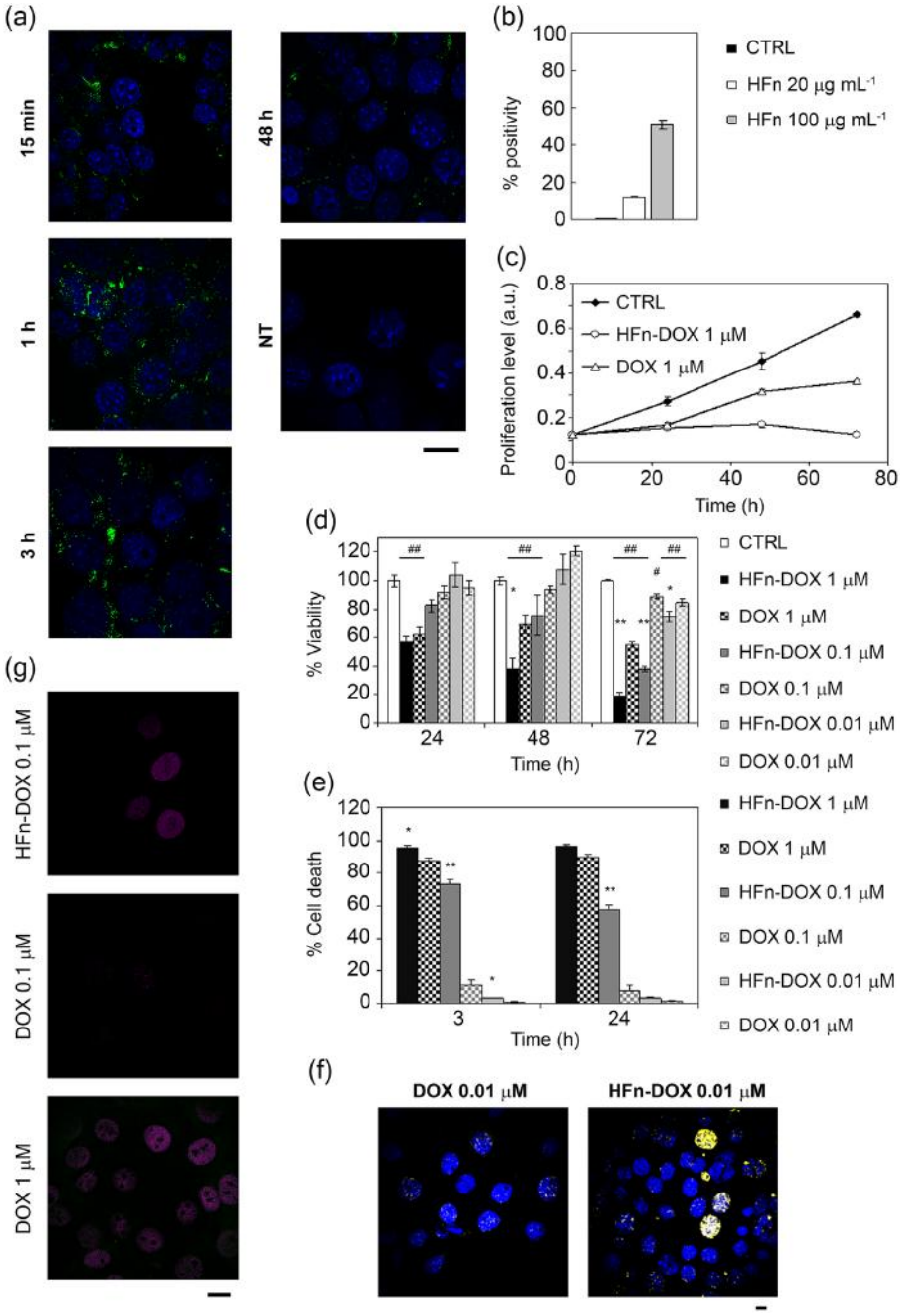

Figure 1: *In vitro* activity of HFn-DOX nanocages toward tumor cells. a. Intracellular localization of HFn nanoparticles. Confocal microscopy merged images of 4T1-L cells, incubated for 15 min, 1, 3 and 48 h at 37 °C with 100 μg mL^{-1} of FITC-labeled HFn (green). Nuclei were stained with DAPI (blue). Scale bar: 10 μm. **b.** HFn binding toward 4T1-L breast cancer cells. 4T1-L cells were incubated 2 h at 4 °C with FITC-labeled HFn (20 and 100 μg mL^{-1}) and then processed for flow cytometry. Untreated cells were used as control to set the positive region. **c.** Proliferation profiles of cells treated with 1 μM DOX or HFn-DOX for up to 72 h. Untreated cells are used as control. Values are mean of six replicates ± SE. **d.** Viability of cells treated with free or nanoformulated DOX. 4T1-L cells were treated with 1, 0.1, and 0.01 μM DOX or HFn-DOX for up to 72 h. Viability was assessed by measuring the conversion of MTT into formazan, normalized on cell proliferation of untreated cells. Statistical significance *vs*. CTRL #P<0.05, ##P<0.005; Statistical significance *vs*. DOX *P<0.01; **P<0.005. **e.** Cell death assay using DOX or HFn-DOX. 4T1-L cells were treated with 1, 0.1, and 0.01 μM DOX or HFn-DOX for 3 or 24 h. Cell death was assessed on the basis of the exposure to Annexin V, evaluated by flow cytometry. Untreated cells were used to set region of positivity. Values are mean of three replicates ± SE. Statistical significance *vs*. DOX *P<0.005; **P<0.0005. **f.** Double-strand break of DNA after DOX exposure. Confocal microscopy images of 4T1-L cells incubated with 0.01 μM DOX or HFn-DOX. Anti-γH2A.X antibodies were used to reveal the DNA double-strand breaks (DSB; yellow). Nuclei were stained with DAPI (blue). Scale bar: 10 μm. **g.** Doxorubicin release inside the nuclear compartment. Confocal microscopy images of 4T1-L cells incubated with 0.1 μM DOX or HFn-DOX and with 1 μM DOX for 3 h at 37 °C. DOX signal is represented in magenta, while DOX degradation product in green. Scale bar: 10 μm.

In vivo targeting and biodistribution of HFn nanocarrier

An orthotopic 4T1 metastatic BC model was obtained by implanting 4T1-L cells (10^5 cells) subcutaneously in the mammary fat pad of female Balb/C mice [29]. This murine tumor was reported to metastasize primarily, yet not exclusively, by a hematogenous route leading to metastatic spread to lung, liver and lymph nodes [30]. The reliability of the model was confirmed by following tumor progression and early onset of metastases by bioluminescence intensity (BLI) imaging over 20 days (Supplementary Figure S3A). Histopathological analysis performed on excised tumors confirmed that the primary mass was indeed derived from epithelial cancer cells without undesired morphological alterations (Supplementary Figure S3B). 4T1 mice were injected into the tail vein with Alexa $Fluor_{660}$-labeled HFn (AF660-HFn) at 5 μg kg^{-1} [31] and monitored by live fluorescence imaging at 1, 2, 24 and 48 h. An intense epifluorescence signal (Epf) at the bladder was detected within the first 2 h, which however disappeared after 24 h (Figure 2A and 2B), suggesting renal excretion of HFn within 1 day. Epf of excised tumors 1, 2, 24 and 48 h after AF660-HFn injection displayed rapid tumor uptake, which progressively decreased in intensity over time (Figure 2C). Confocal images acquired on cryosections of excised tumors confirmed that HFn reached the 4T1 cell cytoplasm and thus were not confined to the tumor stroma or vessels, but actively entered into cancer cells (Supplementary Figure S4). Combined data reported in Figure 2A-2C suggested that a prevalent fraction of nanoparticles that were not captured by the tumor were rapidly sequestered by the kidneys, and presumably eliminated into the bladder. This hypothesis was confirmed by Epf analysis of excised kidneys that exhibited a detectable AF660-HFn fluorescence emission at 1 and 2 h (Figure 2D and 2E) and further evidence was provided by fluorescence measurement of collected urine (Figure 2F). Besides kidney filtration, our results suggested preferential distribution of HFn in the liver within the first 24 h and appreciable Epf was also detected in the spleen for up to 2 h. In contrast, HFn were not recovered in the lungs, heart and brain (Figure 2D and 2E).

Bioavailability of HFn-DOX and accumulation at the tumor

To evaluate the bioavailability of nanoformulated drug, 2 groups of healthy mice (5 mice/group) were treated with DOX or HFn-DOX at 1.24 mg kg^{-1}. Blood samples were collected from the retro-orbital plexus at 15, 30, 45 and 60 min. These tight time points were chosen to detect possible changes in blood bioavailability of DOX or HFn-DOX soon after administration, as in both cases the drug was injected intravenously. DOX was extracted from collected samples and quantified by fluorescence intensity analysis (FLI) at λ_{em} = 550 nm (λ_{ex} = 500 nm) [32]. Blood samples taken before drug administration were set as reference. Bioavailability of HFn-DOX was two-fold higher than DOX although the kinetic seems to maintain the same shape. To better discriminate kinetic's variations due to nanoformulation, a 10-fold higher dosage of DOX or HFn-DOX (i.e. 12.4 mg kg^{-1}) has been administered to healthy mice. Results reported in Figure 3A display different plasma distribution profiles and confirming that HFn-DOX increases drug bioavailability in comparison to DOX of at least four-fold at each time point

Accumulation of DOX at primary tumors (Figure 3B) was determined by fluorescence after chemical extraction from homogenates of resected tumors at 1, 2, 24, and 48 h after single injection of HFn-DOX or DOX at 1.24 mg DOX kg^{-1} [33]. DOX was found in higher concentration in tumors of mice treated with HFn-DOX compared to DOX within 1 h. HFn-DOX displayed faster localization at the tumor compared to DOX, (Figure 3B), suggesting a crucial role for nanoparticle-mediated delivery in enhancing the tumor targeting, although after 2 h the DOX levels are equilibrated in both cases. Confocal images of 4T1-L dissociated from tumors excised at 2 h evoked higher tumor cell accumulation of DOX in samples treated with HFn-DOX compared to DOX (Figure 3C). Combining these results suggested that HFn-DOX were efficiently captured by tumor cells, while DOX was confined in blood vessels of the tumor to a much larger extent.

Impact of LDNM monotherapy on breast cancer management

Eight-week old Balb/C female mice were implanted with 4T1-L cells at day 0. Tumor-bearing mice were randomly divided into three experimental groups at day 5 and treated with placebo, DOX, pl-DOX or HFn-DOX under our LDNM setting: drug administration (1.24 mg DOX kg^{-1}) was performed at day 5, 9, 13 and 17. The progression of tumor volume was monitored *in vivo* before each individual drug injection by bioluminescence imaging. Images suggested that HFn-DOX could decrease tumor growth and metastatic spread (Figure 4A and Supplementary Table S1). Indeed, while DOX displayed a tumor progression similar to the control along the experimental window (Figure 4B), HFn-DOX could suppress the tumor growth as long as the drug was administered (day 17) and exhibited a prolonged effect up to the experimental endpoint (day 21). An even better effect was achieved with pl-DOX, which was indeed able to arrest the tumor development. Immunohistochemical analysis of tumor sections showed that the apoptotic effect

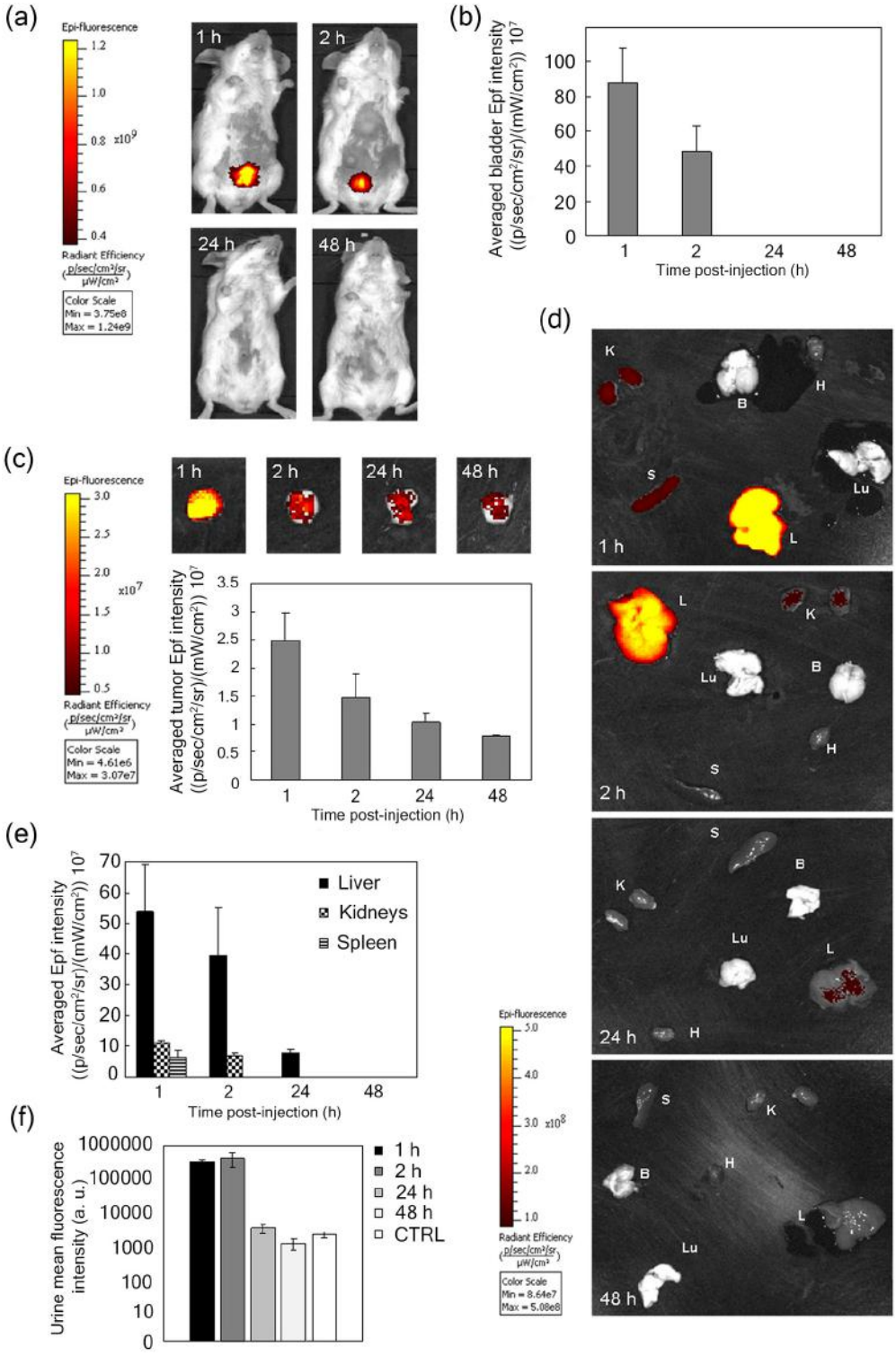

Figure 2: *In vivo* targeting and distribution of void HFn nanocarrier. a. Epifluorescence (Epf) images of mice bearing 4T1-L tumors acquired 1, 2, 24 and 48 h after intravenous (i.v.) injection into the tail vein of 5 μg kg^{-1} AF660-HFn and **b.** averaged Epf intensity of the bladder region of interest (ROI). **c.** Epf of isolated 4T1 tumors and averaged Epf intensity of tumor ROI acquired 1, 2, 24 and 48 h after exposure to HFn. **d.** Epf of isolated spleen (S), kidneys (K), liver (L), brain (B), heart (H), lungs (Lu), and **e.** averaged Epf intensity of the ROI obtained after 1, 2, 24 and 48 h exposure to HFn. **f.** Fluorescence intensity of urine collected 1, 2, 24 and 48 h after i.v. injection of AF660-HFn. The color scale in panels a, c and d indicates the averaged epifluorescence expressed as radiant efficiency [(p/sec/cm^2/sr)/(mW/cm^2)], where p/sec/cm^2/sr is the number of photons per second that leave a square centimeter of tissue and radiate into a solid angle of one steradian (sr). Values reported in panels b, c, e and f are mean ± SE of at least 4 different samples under each experimental condition.

of pl-DOX and HFn-DOX on BC cells was better than that of DOX (Figure 4C and Supplementary Figure S5), presumably due to the improved tumor accumulation of the drug. However, the absence of statistical significance in apoptosis between HFn-DOX and DOX treated samples advocated alternative factors in the stronger antitumor efficacy of HFn-DOX beyond mere cytotoxicity.

Impact of LDNM regimen on tumor angiogenesis and chemoresistance

In line with the observed discrepancy in the results from the DNA fragmentation assay (Figure 4C), we investigated the possible involvement of anti-angiogenic effect of HFn-DOX under the LDNM regimen. Vessel labeling with anti-CD31 antibody in BC histological

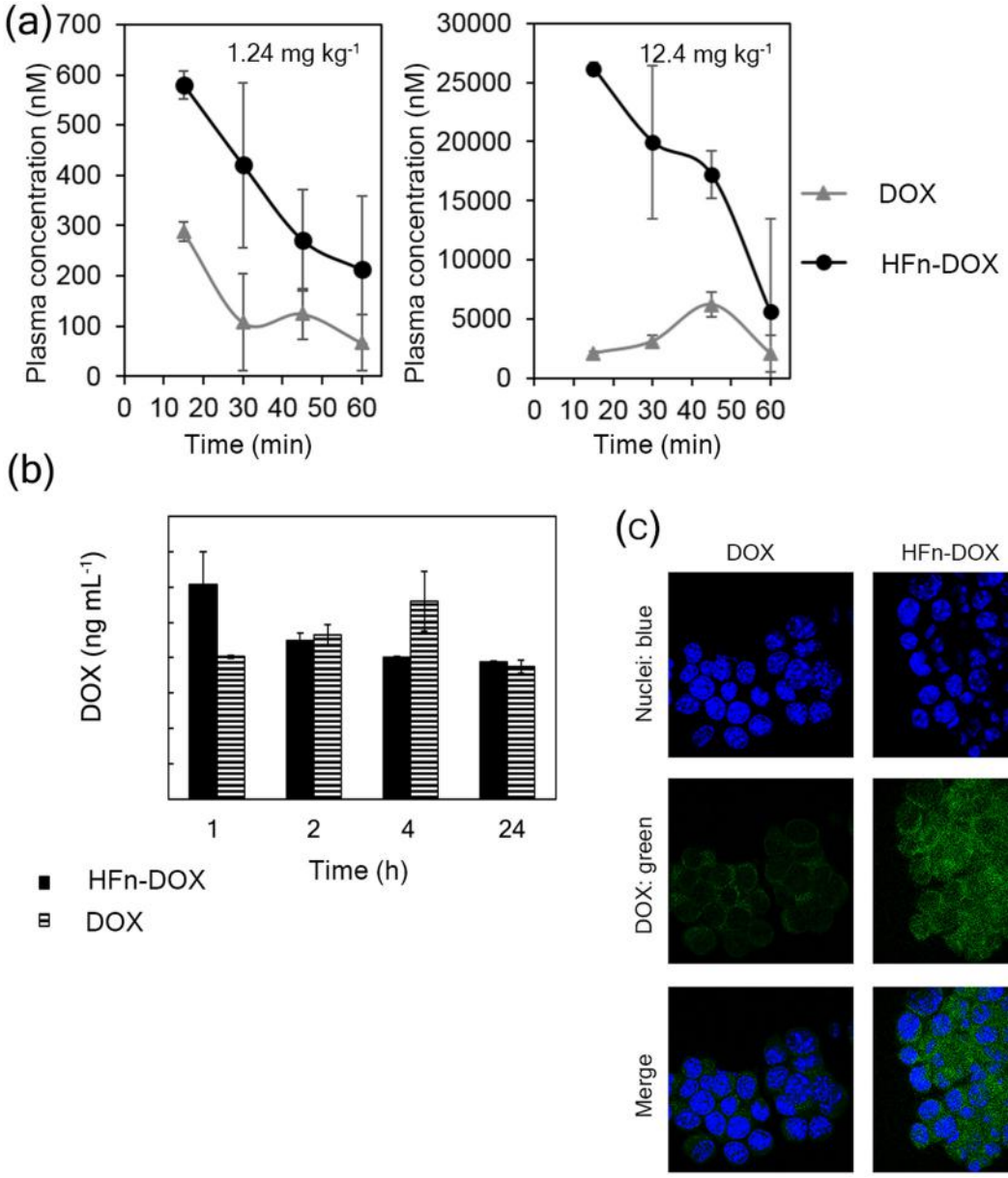

Figure 3: Bioavailability and tumor accumulation of HFn-DOX in comparison with free DOX. a. Bioavailability of DOX and HFn-DOX at different time points. Plasma concentration of DOX after i.v. injection of HFn-DOX (black circles) or DOX (gray triangles) at 1.24 mg kg^{-1} and 12.4 mg kg^{-1} in healthy mice. **b.** DOX accumulation at 4T1-L tumor in mice at different time points after administration of 1.24 mg kg^{-1} DOX as free molecule or HFn-DOX. Female Balb/C mice orthotopically implanted with 4T1-L murine mammary carcinoma cells were injected 6 days after implantation (time 0) with DOX or HFn-DOX. DOX levels in tumor have been determined 1, 2, 4, and 24 h after i.v. injection following acidified isopropanol extraction from tumor homogenates. Aliquots from six mice per each time point concentration have been extracted and analyzed by spectrofluorimeter. Reported values are means of 3 samples/group ± SE. *P* values are summarized in Table S5. **c.** Confocal microscopy images of 4T1-L cells dissociated from tumor harvested 2 h after i.v. injection of DOX and HFn-DOX. DOX signal is represented in green, while nuclei were stained with DAPI (blue). Scale bar: 10 μm.

slides revealed a remarkable decrease in the number of CD31-positive cells compared to DOX (Figure 5A and Supplementary Figure S6), suggesting a role of the HFn-DOX-promoted antiangiogenic effect on the inhibition of tumor progression and diffusion. Analogously, it is likely that the strong inhibition in tumor growth observed with pl-DOX (Figure 4B) was primarily due to anti-angiogenic activity (Figure 5A). 4T1-L BC cells have been described to develop drug resistance owing to induced overexpression of MDR-1 protein upon standard treatment with DOX [28]. Western blot performed on 4T1 cells treated for 72 h with 0.1 μM DOX corroborated DOX induction of MDR-1 expression *in vitro* (Supplementary Figure S7). We examined MDR-1 expression in tumor tissues dissected after LDNM treatment. Tumor sections from DOX and pl-DOX-treated mice displayed a three-fold and five-fold increase in MDR-1-positive cells, respectively, compared to animals treated with placebo and HFn-DOX treated animals (Figure 5B and Supplementary Figure S8). As expected, both DOX and pl-DOX induced an obvious overexpression of MDR-1 in tumor cell membranes, which was particularly pronounced in the proximity of the tumor endothelium [34]. In contrast, MDR-1 expression was undetectable in tumor cell membranes after HFn-DOX treatment and was found only to a limited extent in tumor vessels after HFn-DOX

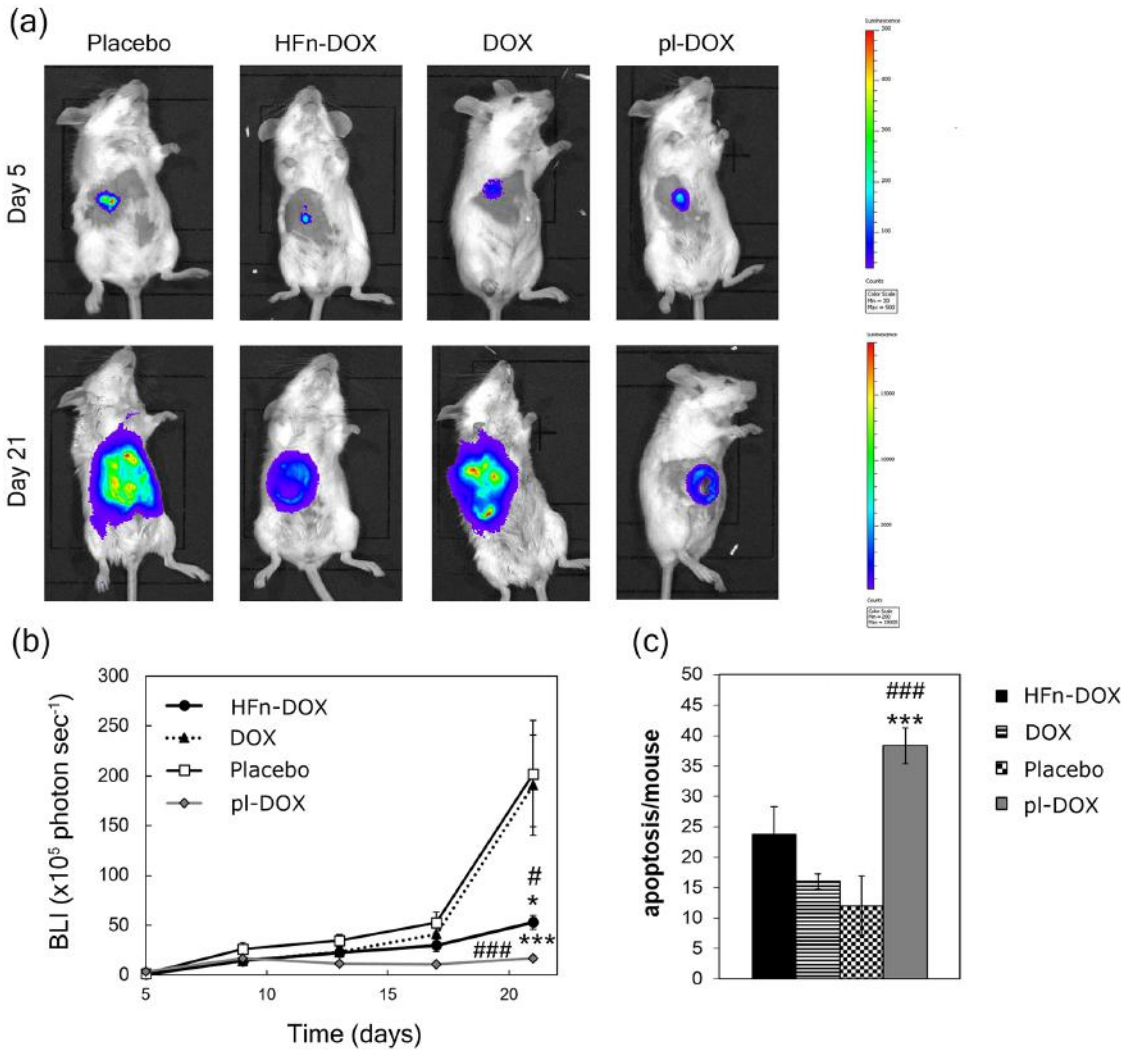

Figure 4: Efficacy of LDNM treatment with HFn-DOX. a. DOX and HFn-DOX *in vivo* efficacy. Bioluminescence imaging of female Balb/C mice (n = 12/group) orthotopically implanted (day 0) with 4T1-L murine mammary carcinoma cells were treated with placebo or with 1.24 mg kg^{-1} of DOX, pl-DOX or HFn-DOX. Drug injections were performed into the tail vein at day 5, 9, 13 and 17. Mice were sacrificed at day 21. **b.** Quantification of tumor volume. Tumor volume was quantified by measuring the bioluminescence intensity signal of 4T1-L cells 5 min after intraperitoneal injection of luciferin. Dots represent the normalized mean value of BLI tumor signal ± SE. Statistical significance *vs*. placebo #P<0.05 ###P<0.005; *vs*. DOX *P<0.05 ***P<0.005. **c.** Quantification of apoptosis in tumor tissue upon treatment with HFn-DOX. Tumors excised at day 21 (n = 6/group) were fixed with formalin and embedded in paraffin. Histological slides were processed to label DNA fragments of apoptotic cells. Reported values are the mean of apoptotic cells number/field/sample ± SE. The count was performed on 10 fields/sample. Magnification 20×. Statistical significance *vs*. placebo ###P<0.005; *vs*. DOX ***P<0.005.

treatment, at the same level of the placebo. This result is relevant in view of a protracted metronomic treatment preventing the onset of chemoresistance, and it is even more surprising considering that pl-DOX is commonly used in patients previously treated with anthracyclines and therefore affected by potentially chemoresistant cancers.

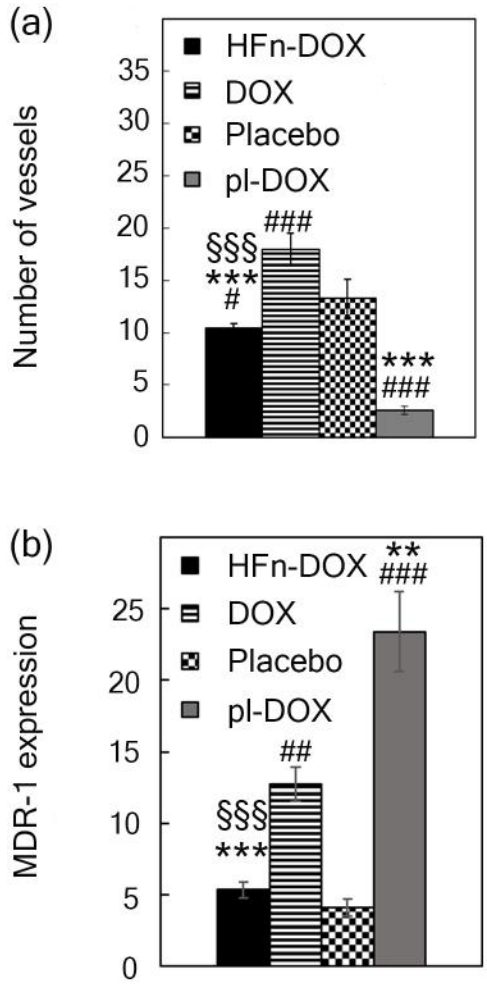

Figure 5: Impact of LDNM regimen on tumor angiogenesis and chemoresistance. a. Quantification of angiogenesis in tumor tissue upon treatment with HFn-DOX. Tumors excised at day 21 (n = 5/group) were fixed with formalin and embedded in paraffin. Immunohistochemistry of histological slides were processed to label CD31+ cells. Reported values are mean of vessel number counted in 10 fields/sample ± SE. Magnification 40×. Statistical significance *vs.* placebo #*P*<0.005 ###*P*<0.00005; *vs.* DOX ***P<0.00005; *vs.* pl-DOX §§§*P*<0.0005. **b.** Quantification of MDR-1-expression. Excised tumors (n = 5/group) were processed for immunohistochemistry of MDR-1 antigen. The percentage of image area positive for MDR-1 expression was quantified using ImagePro Plus Software. Reported values are the mean of the percentage of MDR-1 positive signal counted in 5 fields/sample ± SE. Statistical significance *vs.* Placebo ##*P*<0.0005 ###*P*<0.00005; *vs.* DOX **P<0.005 ***P<0.0005; *vs.* pl-DOX §§§*P*<0.0005.

HFn-DOX suppresses DOX cardiotoxicity and systemic dysfunction under a LDNM therapeutic setting

Cardiotoxicity represents a life-threatening unresolved issue associated to DOX chemotherapy under clinically relevant settings [35]. To evaluate the incidence of LDNM monotherapy on cardiotoxicity, we followed a multiparametric approach [36]. First, histological slides of heart tissues were treated with FITC-conjugated wheat germ agglutinin (FITC-WGA), a cell membrane label, and imaged by fluorescence microscopy (Supplementary Figure S9). Cardiomyocyte cross-sections from mice treated with HFn-DOX, pl-DOX, DOX or non-treated were measured at day 21. Images showed a significant increase of cardiomyocyte area in DOX and pl-DOX samples suggesting a strong cellular damage response compared to HFn-DOX samples (Figure 6A). Detailed ultrastructural analysis of cardiac cells in DOX and pl-DOX treated samples revealed an increased number of mitochondria compared to HFn-DOX (Figure 6B and Supplementary Figure S10). In addition, changes in mitochondria morphology, including larger surface area and cristae depletion, typical effects of DOX-induced cardiomyopathy [36], were clearly evident in DOX and pl-DOX treated samples but not in HFn-DOX samples (Figure 6C-6E). Therefore, the absence of obvious alterations in mitochondria number and morphology in heart samples from mice treated with HFn-DOX strongly supports the lack of cardiotoxicity in LDNM HFn-DOX treatment, even compared to pl-DOX, which is currently considered the most safe anthracycline therapy in terms of cardiotoxicity.

To further investigate if the ultrastructural alterations were associated to mitochondrial dysfunction, mitochondria isolated from heart tissue of DOX, pl-DOX or HFn-DOX treated mice were analyzed in detail. The membrane potential decreased by 30% in DOX and pl-DOX samples compared to HFn-DOX (Figure 6F). As mitochondrial impairment was expected to generate reactive oxygen species (ROS) [37], we quantified the level of the ROS quencher glutathione (GSH) in heart tissue [38]. Figure 6G displays the lower amount of reduced GSH in DOX and pl-DOX-treated mice in comparison to HFn-DOX, confirming mitochondrial dysfunction induced by treatment with free and liposomal DOX only.

Finally, we assessed the systemic toxicity of HFn-DOX by histopathological examination of liver, kidneys, lung, spleen, heart, gut and brain isolated at day 21. No histological lesions were found in all organs (Supplementary Figure S11). Liver and kidney functionalities were also determined to further evaluate the toxicity profile of HFn-DOX treatment. Serum levels of aspartate transaminase (AST) and alanine transaminase (ALT) (Supplementary Table S2), and urea and creatinine

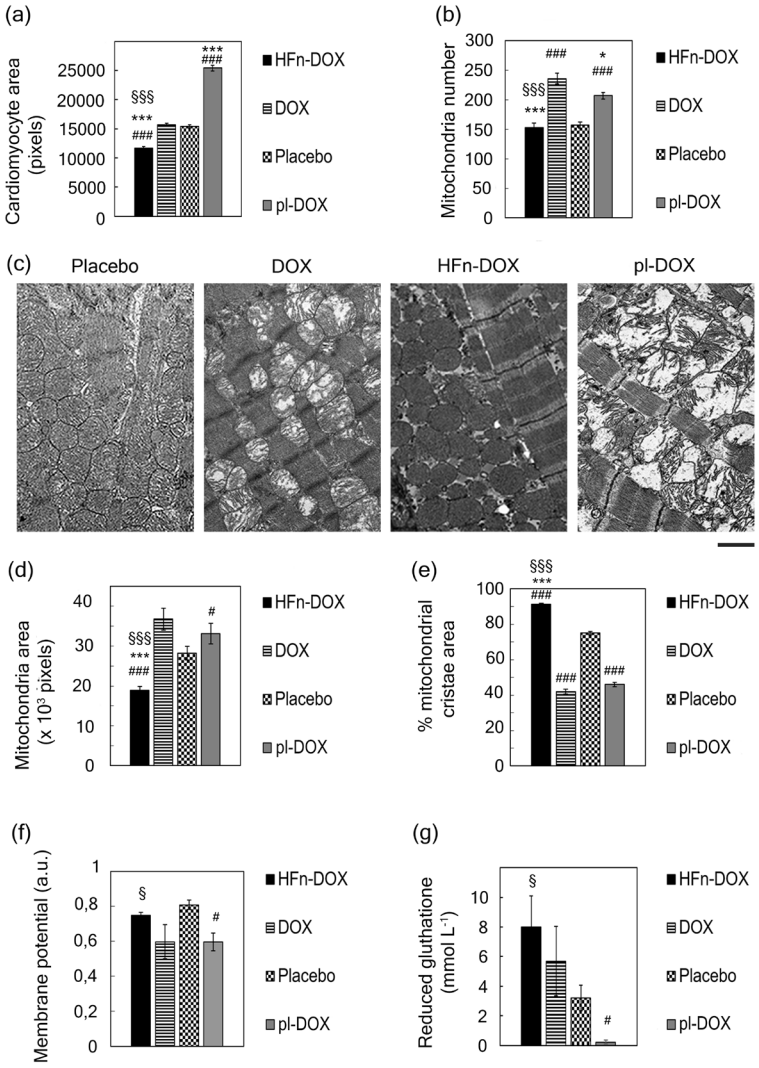

Figure 6: Examination of cardiotoxicity of HFn-DOX, pl-DOX and DOX. a. Nanodelivery protects cardiomyocytes from DOX-induced hypertrophy. Hearts excised at day 21 (n = 3/group) from mice treated with placebo or with 1.24 mg kg^{-1} of DOX, pl-DOX or HFn-DOX were fixed with formalin and embedded in paraffin. Histological slides of cardiac sections stained with FITC-WGA were analyzed with ImageJ software to measure cross-section area of cardiomyocytes. Quantification was performed on at least 5 images/group, reporting the mean value of cross-section area of 250 cells/group± SE. Statistical significance *vs.* Placebo ###*P*<0.00005; *vs.* DOX ***P<0.00005; *vs.* pl-DOX §§§P<0.00005. **b.** Nanodelivery protects against DOX-induced mitochondrial toxicity. Hearts excised at day 21 (n = 3/group) from mice treated with placebo or with 1.24 mg kg^{-1} of DOX, pl-DOX or HFn-DOX were fixed with glutaraldehyde and embedded in epoxy-resin. TEM images of ultrathin heart sections of cardiac tissues acquired at 4200 magnifications were analyzed with ImageJ to measure the number of mitochondria in heart tissue. Quantification was performed on at least 9 images/group, reporting the mean mitochondria number/image ± SE. Statistical significance *vs.* Placebo ###*P*<0.00005; *vs.* DOX ***P<0.00005 *P<0.005; *vs.* pl-DOX §§§P<0.00005. **c.** Representative images of hearts excised at day 21 (n = 3/group) from mice treated with placebo or with 1.24 mg kg^{-1} of DOX, pl-DOX or HFn-DOX. TEM images of ultrathin heart sections of cardiac tissues have been acquired at 11500 magnifications. **d.** Nanodelivery reduces the mitochondrial size growth due to DOX treatment. Quantification of TEM images (ImageJ) of ultrathin heart sections acquired at 11500 magnifications. Quantification was performed on at least 10 images/group, measuring at least 100 mitochondria/sample. Values represent the mean mitochondrial area ± SE. Statistical significance *vs.* Placebo ###*P*<0.00005 #*P*<0.05; *vs.* DOX ***P<0.00005; *vs.* pl-DOX §§§P<0.00005. **e.** Nano delivery limits the damage of mitochondrial cristae from DOX. Quantification of TEM images (Image J) of ultrathin heart sections acquired at 11500 magnifications. Quantification was performed on at least 10 images/group, measuring at least 100 mitochondria/sample. Values represent the percentage of mitochondrial area occupied by cristae ± SE. Statistical significance *vs.* Placebo ###*P*<0.00005; *vs.* DOX ***P<0.00005; *vs.* pl-DOX §§§P<0.00005 **f.** HFn-DOX does not affect mitochondrial membrane potential. Mitochondrial membrane potential was measured by staining-isolated mitochondria from mouse heart tissue dissected at day 21 (n = 3/group) from mice treated with placebo or with 1.24 mg kg^{-1} of DOX, pl-DOX or HFn-DOX. Statistical significance *vs.* Placebo #*P*<0.05; *vs.* pl-DOX §P<0.05. **g.** HFn-DOX does not decrease the concentration of reduced GSH. The extent of reduced GSH was measured in lysates of hearts excised at day 21 (n = 3/group) from mice treated with placebo or with 1.24 mg kg^{-1} of DOX, pl-DOX or HFn-DOX. Values represent the mean GSH concentration in heart extracts± SE. Statistical significance *vs.* Placebo #*P*<0.05; *vs.* pl-DOX §P<0.05.

(Supplementary Table S3), were monitored as markers of liver and kidney condition, respectively. Our results showed that AST/ALT and urea/creatinine ratios in HFn-DOX treated mice were comparable to the control and in the range of reference, confirming the overall nanodrug safety.

DISCUSSION

In the present study a highly aggressive metastatic BC model based on murine 4T1 cells was established. This allowed us to simulate the dramatic clinical picture of advanced BC patients and to evaluate the impact of DOX nanoformulation under LDM monotherapy in compromised subjects, as DOX remains a mainstay therapy in various solid tumors. Our results suggest that DOX monotherapy does not affect tumor progression significantly: although the expected cytotoxicity was confirmed *in vitro*, this did not translate into substantial antitumor activity *in vivo* in an advanced-stage BC model, whereas off-target tissue accumulation and myocardial damage largely occurred. This result is reminiscent of the frustrating clinical condition in which chemotherapy fails to overcome BC progression and combination therapies become necessary to control the disease. Therefore, the potential of LDM DOX to overcome the limitations of dose-dense regimens in advanced-stage tumors remains questionable, since DOX requires high doses to gain a proper drug concentration at cancer deposits [39–40]. In contrast, the results of our study demonstrate that our LDNM strategy, which combines LDM administration of DOX with HFn-delivery resulted in a targeted effect of DOX on 4T1 cancer cells together with a sustained antiangiogenic activity in the tumor microenvironment. Indeed, HFn-DOX exhibited potent antitumor activity when administered at frequent doses as low as 1.24 mg kg^{-1} *in vivo* compared to free DOX and placebo. Such a strongly improved activity correlates with the pharmacokinetic profile of LDNM DOX, as emerged from a recent biodistribution study [41]. Indeed, while DOX displayed reduced bioavailability, high levels of HFn-DOX were recovered in plasma during the first few hours post-injection that were attributable to a lower sequestration by off-target organs [41]. HFn-DOX could accumulate in the tumor site exploiting the EPR effect [42] or by endothelial wall transcytosis promoted by TfR-1 recognition [43] and it is internalized in tumor cells by receptor-mediated endocytosis [44]. HFn-mediated target selectivity conferred earlier intra-tumor activity to the drug, lower off-target accumulation with fast liver metabolism and rapid clearance of circulating excess drug by renal excretion, suggesting optimal therapeutic index in future clinical translation [41, 44]. Beyond its favorable bioavailability and target selectivity, a plausible explanation for enhanced antitumor activity of LDNM HFn-DOX resides in HFn propensity to behave like a Trojan horse, imparting DOX with drastically enhanced nuclear penetration even in resistant cancer cells [25, 45]. Such HFn property can greatly improve current strategies of LDM chemotherapy, due to sustained nuclear release of a DNA-damaging drug. Indeed, our *in vitro* experiments showed that HFn-mediated delivery allowed a 15.2-fold increase of DOX nuclear concentration within 3 h as compared to the drug alone.

Even drug resistance significantly impacts on BC management, accounting for a relevant proportion of patients in which anthracycline therapy fails to persistently eradicate the tumor [46]. MDR-1 protein is one of the most active multidrug resistance mediators in BC and it is gradually overexpressed under DOX chemotherapy regimens [28]. Negligible MDR-1 induction in tumor cells *in vivo* after LDNM DOX administration suggested that the multidrug resistance machinery of BC cells did not "sense" the cytotoxic agent in HFn-DOX. Otherwise, the dramatic increase of MDR-1 expression observed in samples from mice treated with DOX and even with pl-DOX, suggested that LDNM administration associated with cell nuclear targeting could circumvent DOX resistance dependent by MDR-1.

The general assumption that LDM therapy is essentially due to inhibition of angiogenesis, rather than directly killing residual cancer cells [8], should be reconsidered in the framework of LDNM regimen, in which a key role of targeted action could be reappraised. Combining our data from angiogenesis inhibition with the results from tumor progression (i.e BC growth curves and DNA fragmentation assay) we concluded that targeted action of HFn-DOX on BC cells and antiangiogenic effect of LDNM regimen could play a synergistic role in the increased antitumor efficacy of HFn-DOX compared to DOX alone.

Importantly, LDNM chemotherapy exhibited a safe toxicity profile, as proven by apparent lack of systemic side effects. This is expected to have great clinical impact because cardiotoxicity and general side effects lead to major restriction in the clinical use of anthracyclines. HFn-DOX was less cardiotoxic compared to DOX and even to pl-DOX, although the latter has been associated with improved cardiac safety in various clinical studies. Nevertheless, myocardial alterations provoked by pl-DOX (Figure 6) are not surprising. Indeed, a certain degree of myocardial damage has been previously demonstrated in endomyocardial biopsies of patients treated with pl-DOX, and ultrastructural damage of pl-DOX has not been explored [38, 47]. Moreover, although pl-DOX is less cardiotoxic, it does not significantly reduce relevant cardiac events, and a clinician's preference for pl-DOX over conventional DOX to avoid clinically significant cardiac events is not justified in patients without concurrent cardiac disorders that were not previously subjected to anthracycline exposure [48]. Therefore, the general confidence on low cardiotoxicity

of pl-DOX should be reconsidered in the light of these considerations. Otherwise, LDNM treatment with HFn-DOX didn't display anthracycline-related cardiotoxicity, even in comparison with pl-DOX, and it is therefore a promising option for anthracycline therapeutic regimens in cardiosensitive subjects.

We acknowledge a potential limitation relating to immunogenicity in clinical translation of HFn-DOX [49]. Although it is difficult to predict the long-term effect of prolonged treatments in humans, we have collected preliminary data suggesting negligible immunogenicity of HFn in animals. Another limitation of the study is the experimental timespan limited to three weeks. However, based on our findings we could postulate that after 21 days the metronomic treatment by HFn-DOX would lead to further reduction of cancer deposits, as expected by the excellent cytotoxicity showed by HFn-DOX *in vitro*. Moreover, the fact that MDR-1 expression remained stable over time upon treatment with HFn-DOX suggests avoidance of chemoresistance, thus a sustained anticancer activity even after 21 days is expected. About cardiotoxicity, our findings suggest that substantially no myocardial damage is present after treatment with HFn-DOX, and we should expect the same lack in cardiotoxicity even after experimental timespan.

In summary, this study provides robust evidence that LDNM monotherapy with HFn-DOX is expected to remodel the therapeutic outcome of advanced metastatic BC compared to the drug alone and also to improve anthracycline therapies based on liposomal DOX, with a redefinition of the central role of DOX for solid malignancies under the new perspective of metronomic treatments. Further investigations are necessary to thoroughly elucidate the individual contributions of targeted therapy and neoangiogenesis inhibition in the strong enhancement of the antitumor efficacy of HFn-DOX. On the horizon after this study is the possibility of countless developments, one of which is a reappraisal of current clinical settings by combining low toxic LDNM regimens with administration of established antiangiogenic agents.

MATERIALS AND METHODS

Cell cultures and *in vitro* studies

Murine Bioware-Ultra 4T1-Luc2 cell line (4T1-L), used as model of BC cells, have been purchased in 2011 from Perkin Elmer, confirmed by IMPACT I PCR profiling by the source, and have been passaged for fewer than 6 months. 4T1-L were cultured in RPMI 1640 medium supplemented with 10% foetal bovine serum, 2 mM l-glutamine, penicillin (50 UI mL^{-1}) and streptomycin (50 mg mL^{-1}) at 37 °C in humidified atmosphere containing 5% CO_2 and sub-cultured prior to confluence using trypsin/EDTA. 4T1 cells, were used for *in vitro* tests and orthotopically implanted at passages lower than 4 in female Balb/C mice to obtain the BC animal model.

Details of HFn-DOX production, cell binding, proliferation, death and DNA damage assays, intracellular localization by confocal laser scanning microscopy, are provided in the Supplementary Materials and Methods.

Study design

The hypothesis was that HFn-DOX would exhibit higher antitumor efficacy and would induce minimal or negligible side effects compared to free drug and pl-DOX (Caelyx) in mice bearing strongly invasive and metastatic BC. HFn-DOX dose was set at 1.24 mg kg^{-1} DOX, about 1/7 of the average MTD dosage administered in 4T1 murine BC [26]. This tumor model was selected for its aggressiveness and spontaneous tendency to spread to multiple metastatic sites after orthotopic injection of luciferase-tagged cells. The endpoint of the *in vivo* experiments was defined at 21 days to appreciate the parametric differences in tumor growth, resistance onset and cardiotoxicity in living animals, while allowing us to operate in compliance with the National and European legislations that regulate animal experiments. The number of animals for each biodistribution, bioavailability, therapy and cardiotoxicity experiment was calculated with a power of at least 80 ± 5 %. Mice were randomized by primary tumor size before initiation of treatments. Dye-labeled HFn was first injected in tumor-bearing mice by tail vein, then targeting and biodistribution were assessed by live fluorescence imaging, while drug bioavailability was evaluated in healthy animals. Rodents were administered intravenously with placebo, DOX, pl-DOX or HFn-DOX at day 5, 9, 13 and 17, and monitored for 21 days during which tumor growth was followed by measurement of bioluminescence signal intensity (BLI) of 4T1-L cells after intraperitoneal injection of luciferin. BLI analyses were undertaken under standardized conditions to gain a quantitative estimation of live BC cells. Intermediate BLI values and mouse weights were determined before each administration. Collected BLI data were normalized to the mean tumor size calculated for all mice within each group at each time point. Animals were euthanized at day 21 to analyze resected tissues with the aim of determining the antitumor efficacy, anti-angiogenic activity and cardiotoxicity of DOX, pl-DOX and or HFn-DOX. Histopathology and immunohistochemistry were analyzed from blinded samples. Outliers were not excluded. All experiments were conducted under an approved protocol of the Italian Ministry of Health. Animals were cared for according to the guidelines of the Italian Ministry of Health (see the Supplementary Materials and Methods).

In vivo experiments

Details of the preparation of orthotopic 4T1 model, tumor cell injection, tumor imaging, targeting and

biodistribution, plasma half-life, drug accumulation at the tumor of DOX and HFn-DOX and antitumor *in vivo* efficacy of DOX, pl-DOX or HFn-DOX are provided in Supplementary Materials and Methods.

Ex vivo analyses

Excised tumors were analyzed by fluorescence imaging and by confocal microscopy of cryosections to establish the HFn cellular targeting *in vivo*, immunofluorescence of dissociated tumor to assess DOX accumulation, immunohistochemistry to determine the CD31 and MDR-1 expression in endothelial and tumor cells, respectively, and Tumor TACS In Situ Apoptosis Detection kit to determine cellular apoptosis. Excised organs were analyzed by fluorescence imaging to establish the HFn biodistribution in non-target organs. Histopathology was performed on samples from liver, kidneys, spleen, heart, brain, gut and lung tissues. Kidney and liver functionality was assessed before and after the treatment. The size of cardiomyocytes extracted from resected heart tissues was measured after wheat germ agglutinin (WGA) fluorescence labeling. Isolated mitochondria from heart tissue samples were investigated by membrane potential and ultrastructural analysis of transmission electron micrographs; the extent of ROS in heart was assessed by glutathione assay. Details are reported in Supplementary Materials and Methods.

Statistical analysis

Statistical analyses were conducted using two-tailed Student's *t*-test. All plots show mean values ± SE. All tests assumed normal distribution and the statistical significance threshold was set at $P < 0.05$

Ethics statements

Investigation has been conducted in accordance with the ethical standards and according to the Declaration of Helsinki and according to national and international guidelines and has been approved by the authors' institutional review board.

ACKNOWLEDGMENTS

We thank R. Allevi (University of Milano) for TEM images. We acknowledge the "Centro di Microscopia Elettronica per le Nanotecnologie applicate alla Medicina" at University of Milano for imaging facility.

CONFLICTS OF INTEREST

No potential conflicts of interest were disclosed.

GRANT SUPPORT

The research was supported by the Fondazione Regionale per la Ricerca Biomedica (NANODRUG platform project to D.P. and F.C.), the Fondazione Umano Progresso (to D.P.) and the Regione Lombardia and Fondazione Cariplo (grant n° 2016-0919 to S.M.). FRRB supported M.B., M.T. and M.A.R. with Research Fellowships, S.M. and L.F. were supported by the NanoMeDia project (Regione Lombardia to F.C. and D.P.).

Author contributions

Conception and design: D. Prosperi, S. Mazzucchelli, F. Corsi.

Development of methodology: M. Bellini, M. A. Rizzuto, S. Mazzucchelli, M. Truffi, L. Fiandra, M. Nebuloni.

Acquisition of data (provided cells, acquired and managed animals, provided facilities, etc.): S. Mazzucchelli, L. Fiandra, L. Sorrentino, M. Truffi, M. Nebuloni, E. Longhi.

Analysis and interpretation of data (e.g., statistical analysis, biostatistics, computation analysis): L. Fiandra, S. Mazzucchelli, M. Nebuloni, F. Corsi, D. Prosperi.

Writing, review, and/or revision of the manuscript: S. Mazzucchelli, F. Corsi, D. Prosperi. All authors edited the manuscript.

Administrative, technical, or material support (i.e., reporting or organizing data): S. Mazzucchelli, L. Fiandra, M. Nebuloni.

Study supervision: F. Corsi, D. Prosperi.

REFERENCES

1. Kareva I, Waxman DJ, Klement GL. Metronomic chemotherapy: an attractive alternative to maximum tolerated dose therapy that can activate anti-tumor immunity and minimize therapeutic resistance. Cancer Lett. 2015; 358:100-6.
2. Loven D, Hasnis E, Bertolini F, Shaked Y. Low-dose metronomic chemotherapy: from past experience to new paradigms in the treatment of cancer. Drug Discov Today. 2013; 18:193-201.
3. Kaur H, Budd T. Metronomic therapy for breast cancer. Curr Oncol Rep. 2004; 6:49-52.
4. Cao Y, Langer R. Optimizing the delivery of cancer drugs that block angiogenesis. Sci Transl Med. 2010; 2:15ps3.
5. Nars MS, Kaneno R. Immunomodulatory effects of low dose chemotherapy and perspectives of its combination with immunotherapy. Int. J. Cancer 2013; 132:2471-2478.
6. Veronesi U, Stafyla V, Luini A, Veronesi P. Breast cancer: from "maximum tolerable" to "minimum effective" treatment. Front Oncol. 2012; 2:1-5.

7. Pasquier E, Kavallaris M, Andre N. Metronomic chemotherapy: new rationale for new directions. Nat Rev Clin Oncol. 2010; 7:455-465.
8. Kerbel RS, Kamen BA. The anti-angiogenic basis of metronomic chemotherapy. Nat Rev Cancer. 2004; 4:423-436.
9. Andre N, Carre M, Pasquier E. Metronomics: towards personalized chemotherapy? Nat Rev Clin Oncol. 2014; 11:413-431.
10. Kerbel RS, Grothey A. Gastrointestinal cancer rationale for metronomic chemotherapy in phase III trials. Nat Rev Clin Oncol. 2015; 12:313-314.
11. Hanahan D, Bergers G, Bergsland E. Less is more, regularly: metronomic dosing of cytotoxic drugs can target tumor angiogenesis in mice. J Clin Invest. 2000; 105:1045-1047.
12. Morris PG, Hudis CA. Optimizing dose-dense regimens for early-stage breast cancer. Nat Rev Clin Oncol. 2010; 7:678-679.
13. Kerbel RS. Antiangiogenic therapy: a universal chemosensitization strategy for cancer? Science. 2006; 312:1171-1174.
14. Kerbel RS. Improving conventional or low dose metronomic chemotherapy with targeted antiangiogenic drugs. Cancer Res Treat. 2007; 39:150-159.
15. Lien K, Georgsdottir S, Sivanathan L, Chan K, Emmenegger U. Low-dose metronomic chemotherapy: a systematic literature analysis. Eur J Cancer. 2013; 49:3387-3395.
16. Cruz-Munoz W, Di Desidero T, Man S, Xu P, Jaramillo ML, Hashimoto K, Collins C, Banville M, O'Connor-McCourt MD, Kerbel RS. Analysis of acquired resistance to metronomic oral topotecan chemotherapy plus pazopanib after prolonged preclinical potent responsiveness in advanced ovarian cancer. Angiogenesis. 2014; 7:661-673.
17. Ng SSW, Sparreboom A, Shaked Y, Lee C, Man S, Desai N, Soon-Shiong P, Figg WD, Kerbel RS. Influence of formulation vehicle on metronomic taxane chemotherapy: albumin-bound versus cremophor EL-based paclitaxel. Clin Cancer Res. 2006; 12:4331-4338.
18. Riganti C, Gazzano E, Gulino GR, Volante M, Ghigo D, Kopecka J. Two repeated low doses of doxorubicin are more effective than a single high dose against tumors overexpressing P-glycoprotein. Cancer Lett. 2015; 360:219-226.
19. Lotrionte M, Biondi-Zoccai G, Abbate A, Lanzetta G, D'Ascenzo F, Malavasi V, Peruzzi M, Frati G, Palazzoni, G. Review and meta-analysis of incidence and clinical predictors of anthracycline cardiotoxicity. Am J Cardiol. 2013; 112:1980-1984.
20. Octavia Y, Tocchetti CG, Gabrielson KL, Janssens S, Crijns HJ, Moens, AL. Doxorubicin-induced cardiomyopathy: from molecular mechanisms to therapeutic strategies. J Mol Cell Cardiol. 2012; 52:1213-1225.
21. Rivera E. Current status of liposomal anthracycline therapy in metastatic breast cancer. Clinical Breast Cancer. 2003; 4:S76-S83.
22. Xing M, Yan F, Yu S, Shen P. Efficacy and cardiotoxicity of liposomal doxorubicin-based chemotherapy in advanced breast cancer: a meta-analysis of then randomized controlled trials. PLoS ONE. 2015; 10:e0133569.
23. Corsi F, Mazzucchelli S. The potential of protein-based nanocages for imaging and drug delivery. Ther Deliv. 2016; 7:149-151.
24. Fan K, Cao C, Pan Y, Lu D, Yang D, Feng J, Song L, Liang M, Yan X. Magnetoferritin nanoparticles for targeting and visualizing tumour tissues. Nat Nanotechnol. 2012; 7:459-464.
25. Bellini M, Mazzucchelli S, Galbiati E, Sommaruga S, Fiandra L, Truff, M, Rizzuto MA, Colombo M, Tortora P, Corsi F, Prosperi D. Protein nanocages for self-triggered nuclear delivery of DNA-targeted chemotherapeutics in cancer cells. J Controlled Rel. 2014; 196:184-196.
26. Zhang L, Li L, Di Penta A, Carmona U, Yang F, Schöps R, Brandsch M, Zugaza JL, Knez M. H-Chain Ferritin: A Natural Nuclei Targeting and Bioactive Delivery Nanovector. Adv. Healthcare Mat. 2015; 4:1305-1310.
27. Liang M, Fan K, Zhou M, Duan D, Zheng J, Yang D, Feng J, Yan X. H-ferritin-nanocaged doxorubicin nanoparticles specifically target and kill tumors with a single-dose injection. Proc Natl Acad Sci USA. 2014; 111:14900-14905.
28. Bao L, Haque A, Jackson K, Hazari S, Moroz K, Jetly R, Dash S. Increased expression of P-glycoprotein is associated with doxorubicin chemoresistance in the metastatic 4T1 breast cancer model. Am J Pathol. 2011; 178:838-852.
29. Pulaski BA, Ostrand-Rosenberg S. Mouse 4T1 breast tumor model. Curr Protoc Immunol. 2001; Ch. 20:Unit 20.2. doi:10.1002/0471142735.im2002s39.
30. Aslakson CJ, Miller FR. Selective events in the metastatic process defined by analysis of the sequential dissemination of subpopulations of a mouse mammary tumor. Cancer Res. 1992; 52:1399-1405.
31. Fiandra L, Mazzucchelli S, De Palma C, Colombo M, Allevi R, Sommaruga S, Clementi E, Bellini M, Prosperi D, Corsi F. Assessing the *in vivo* targeting efficiency of multifunctional nanoconstructs bearing antibody-derived ligands. ACS Nano. 2013; 7:6092-6102.
32. Mayer LD, Dougherty G, Harasym TO, Bally MB. The role of tumor-associated macrophages in the delivery of liposomal doxorubicin to solid murine fibrosarcoma tumors. J Pharmacol Exp Ther. 1997; 280:1406-1414.
33. Laginha KM, Berwoert S, Charrois GJR, Allen TM. Determination of doxorubicin levels in whole tumor and tumor nuclei in murine breast cancer tumors. Clin Cancer Res. 2005; 11:6944-6949.
34. Guo Z, Zhu J, Zhao L, Jin X. Expression and clinical significance of multidrug resistance proteins in brain tumors. J Exp Clin Cancer Res. 2010; 29:122-127.

35. Khiati S, Dalla Rosa I, Sourbier C, Ma X, Rao VA, Neckers LM, Zhang H, Pommier Y. Mitochondrial topoisomerase I (Top1mt) is a novel limiting factor of doxorubicin cardiotoxicity. Clin Cancer Res. 2014; 20:4873-4881.

36. Tsusui H, Kinugawa S, Matsushima S. Oxidative stress and heart failure. Am Physiol Heart Circ Physiol. 2011; 301:H2181-2190.

37. Mari M, Morales A, Colell A, Garcia-Ruiz C, Fernandez-Checa J C. Mitochondrial glutathione, a key survival antioxidant. Antiox Redox Signal. 2009; 11:2685-2700.

38. Berry G, Billingham M, Alderman E, Richardson P, Torti F, Lum B, Patek A, Martin FJ. The use of cardiac biopsy to demonstrate reduced cardiotoxicity in AIDS Kaposi's sarcoma patients treated with pegylated liposomal doxorubicin. Ann Oncol. 1998; 9:711-716.

39. Todorova VK, Kaufmann Y, Klimberg VS. Increased efficacy and reduced cardiotoxicity of metronomic treatment with cyclophosphamide in rat breast cancer. Anticancer Res. 2011; 31:215-20.

40. Mainetti LE, Rico MJ, Fernández-Zenobi MV, Perroud HA, Roggero EA, Rozados VR, Scharovsky OG. Therapeutic efficacy of metronomic chemotherapy with cyclophosphamide and doxorubicin on murine mammary adenocarcinomas. Ann Oncol. 2013; 24:2310-2316.

41. Mazzucchelli S, Ravelli A, Gigli F, Minoli M, Corsi F, Ciuffreda P, Ottria R. LC-MS/MS method development for quantification of doxorubicin and its metabolite 13-hydroxy doxorubicin in mouse biological matrices: application to a pharmaco-delivery study. Biomed Chromatogr. 2016; doi: 10.1002/bmc.3863.

42. Fisher J, Devraj K, Ingram J, Slagle-Webb B, Madhankumar AB, Liu X, Klinger M, Simpson IA, Connor JR. Ferritin: a novel mechanism for delivery of iron to the brain and other organs. Am J Physiol Cell Physiol. 2007; 293:C641-C649.

43. Li L, Fang CJ, Ryan JC, Niemi EC, Lebrón JA, Björkman PJ, Arase H, Torti FM, Torti SV, Nakamura MC, Seaman WE. Binding and uptake of H-ferritin are mediated by human transferrin receptor-1. Proc Natl Acad Sci USA. 2010; 107:3505-3510.

44. Sengupta S, Eavarone D, Capila I, Zhao G, Watson N, Kiziltepe T, Sasisekharan R. Temporal targeting of tumour cells and neovasculature with a nanoscale delivery system. Nature. 2005; 436:568-572.

45. Alkhateeb AA, Connor JR. Nuclear ferritin: a new role for ferritin in cell biology. Biochim Biophys Acta. 2010; 1800:793-797.

46. Wood KC. Mapping the pathways of resistance to targeted therapies. Cancer Res. 2015; 75:4247-4251.

47. Gabizon AA, Lyass O, Berry GJ, Wildgust M. Cardiac safety of pegylated liposomal doxorubicin (Doxil/) demonstrated by endomyocardial biopsy in patients with advanced malignancies. Cancer Invest. 2004; 22:663-669.

48. Yamaguchi N, Fujii T, Aoi S, Kozuch PS, Hortobagyi GN, Blum RH. Comparison of cardiac events associated with liposomal doxorubicin, epirubicin and doxorubicin in breast cancer: a Bayesian network meta-analysis. Eur J Cancer. 2015; 51:2314-20.

49. Truffi M, Fiandra L, Sorrentino L, Monieri M, Corsi F, Mazzucchelli S. Ferritin nanocages: A biological platform for drug delivery, imaging and theranostics in cancer. Pharmacol Res. 2016; 107:57-65.

Delivering Colloidal Nanoparticles to Mammalian Cells: A Nano–Bio Interface Perspective

*Paolo Verderio, Svetlana Avvakumova, Giulia Alessio, Michela Bellini, Miriam Colombo, Elisabetta Galbiati, Serena Mazzucchelli, Jesus Peñaranda Avila, Benedetta Santini, and Davide Prosperi**

Understanding the behavior of multifunctional colloidal nanoparticles capable of biomolecular targeting remains a fascinating challenge in materials science with dramatic implications in view of a possible clinical translation. In several circumstances, assumptions on structure–activity relationships have failed in determining the expected responses of these complex systems in a biological environment. The present Review depicts the most recent advances about colloidal nanoparticles designed for use as tools for cellular nanobiotechnology, in particular, for the preferential transport through different target compartments, including cell membrane, cytoplasm, mitochondria, and nucleus. Besides the conventional entry mechanisms based on crossing the cellular membrane, an insight into modern physical approaches to quantitatively deliver nanomaterials inside cells, such as microinjection and electroporation, is provided. Recent hypotheses on how the nanoparticle structure and functionalization may affect the interactions at the nano–bio interface, which in turn mediate the nanoparticle internalization routes, are highlighted. In addition, some hurdles when this small interface faces the physiological environment and how this phenomenon can turn into different unexpected responses, are discussed. Finally, possible future developments oriented to synergistically tailor biological and chemical properties of nanoconjugates to improve the control over nanoparticle transport, which could open new scenarios in the field of nanomedicine, are addressed.

1. Introduction

1.1. Understanding Nanoparticle Properties at the Cellular Level

In the last decade, colloidal nanoparticles have been established as an emerging tool for the study of biological processes with an increasing number of possible applications in biotechnology and medicine.[1–3] Depending on their constitutional materials, nanoparticles have different chemical–physical properties such as high electron density and strong optical absorption (e.g., gold nanoparticles, AuNPs), magnetic moment (e.g., iron oxide nanoparticles, IONPs), and photoluminescence (e.g., semiconductor quantum dots, QDs). The complex interactions between nanoparticles and the cellular environment have been thoroughly examined, such that the knowledge of these relationships remains of fundamental attractiveness. This is the reason why the scientific community involved in nanomaterials evolution has raised numerous questions in order to understand the dynamic forces and the molecular components that shape these interactions. At the moment, several research groups are focusing on the creation of properly "designed" nanoparticles, as an essential prerequisite for each individual nano-biomedical and nano-biotechnological application. With a general impression of the biological interfaces that nanoparticles meet when interacting with living cells (i.e., membrane, cytoplasm, nucleus, and internal organelles), researchers have now the possibility to define how these interactions remodel the fundamental forces that govern the behavior of colloidal nanoparticles in a complex biological system. In addition, other works highlight the importance of correlating nanoparticle fluid dynamics to their physicochemical features, which adds a basic but, at the same time, capital information to predict potential toxicological risks of such materials. Such correlations would help us to construct new materials and thus find the optimal mechanism of intracellular delivery of different nanoparticle platforms, evaluating and reducing their toxicity to the minimum level.[4,5]

These basic issues, which can be collected in a unique concept that can be referred to as nano–bio interface, give rise to a very intricate system to investigate, as the nano–bio interface consists in a plethora of dynamic components. Most available

P. Verderio, Dr. S. Avvakumova, M. Bellini, Dr. M. Colombo, E. Galbiati, J. P. Avila, B. Santini, Dr. D. Prosperi
Dipartimento di Biotecnologie e Bioscienze
Università di Milano-Bicocca
piazza della Scienza 2, 20126 Milano, Italy
E-mail: davide.prosperi@unimib.it

DOI: 10.1002/adhm.201300602

Dr. S. Avvakumova, G. Alessio, Dr. S. Mazzucchelli
Dipartimento di Scienze Biomediche e Cliniche "Luigi Sacco"
Università di Milano
Ospedale L. Sacco, via G. B. Grassi 74, 20157 Milano, Italy
Dr. D. Prosperi
Laboratory of Nanomedicine and Clinical Biophotonics
Fondazione Don Carlo Gnocchi ONLUS
Via Capecelatro 66, 20148 Milan, Italy

studies correlate these interactions with surface properties of nanomaterials, including size, shape, and curvature, roughness, porosity, and crystallinity.[6–8] Other works deal with the properties of the solid–liquid interface originated when nanoparticles are suspended in the surrounding medium, including for instance the effective surface charge,[9,10] the state of aggregation and the stability of the suspension over time and at different cellular pH values. Moreover, the solid–liquid contact zone with biological substrates might be influenced by the nature of surface ligands and chemical functionalization of nanoparticles.[11,12] In particular, the contact with hydrophobic or charged regions of cells determines the nanoparticle preferential pathway of interaction with the cellular external environment and, later on, the formation of stable or transient complexes with their binding molecules and the route of internalization and metabolism of nanoparticles.[13]

Another nanoscale engagement with biological processes is the identification of the biomolecular "protein corona" that provides the biological identity of nanomaterials.[14] To better understand this concept, we should try to envision that when nanoparticles, which have higher free energy than the corresponding bulk materials, are suspended in a biological fluid, they are rapidly coated by a selected group of biomolecules to form a molecular corona essentially consisting in a layer of adsorbed proteins that represent the main biomolecular components of that fluid. Is this protein corona what the external biological environment actually "sees" when interacting with a suspended nanoparticle. As will be discussed below, this process leads to the formation of a near-monolayer of biomolecules, usually termed "hard" corona, which tightly, yet reversibly, binds to the nanoparticle surface. In addition, an exchangeable layer of biomolecules is formed as an outer shell over the hard corona; this process is more dynamic and reversible and this is the reason why it is called "soft" corona.[15,16] Interestingly, from several specific analyses, it has been observed that only few molecules available in biological medium are found in the hard corona and they hardly correspond to the most abundant proteins in plasma. It is worth emphasizing that the protein corona is not only relevant in passive cellular adhesion and internalization (passive targeting), but is also relevant when antibodies or target molecules are immobilized on the nanoparticle surface with the aim of achieving a targeting action directed toward a selected molecular receptor (active targeting). In these cases, the corona may affect these specific interactions much more thoroughly than expected.[17] For this reason, the surface modification with "bioinvisible" polymeric moieties (e.g., pegylation) is often required to reduce the formation of nonspecific bindings of biomolecules,[18] thus making more relevant the role played by the active targeting component.

1.2. Designing the Nanoparticle "Framework": A Progressive Evolution

Outcomes from studies of nano–bio interface have largely influenced nanomaterials design for biomedical applications. To date, three generations of nanoparticles can be recognized, which have been engineered to this purpose (**Figure 1**). The first generation is represented by nanomaterials functionalized through basic surface chemistries to assess biocompatibility, enhance cellular uptake, and reduce toxicity. The second generation is focused on nanomaterials with optimized surface boundaries that improve stability and targeting in biological systems.[19–23] These studies were characterized by two important

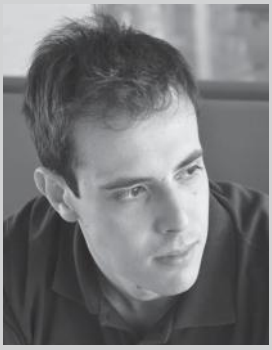

Paolo Verderio obtained his Master degree in 2009 in Industrial and Management Chemistry at University of Milano. Next, he worked as a research fellow at the Hosp. Luigi Sacco until 2011 focusing on iron oxide nanoparticles as contrast agents for early breast cancer diagnosis. He started the Ph.D. in Chemical Science at the University of Milano–Bicocca in 2011 where he is currently working. His scientific interests are based on synthesis and biofunctionalization of inorganic and organic nanoparticles for drug delivery applications.

Dr. Svetlana Avvakumova is a post-doc researcher in Department of Biomedical and Clinical Sciences at University of Milan. She graduated from Colloidal Chemistry at University of St. Petersburg in 2007. Prior to joining Dr. Prosperi's group, she obtained her Ph.D. degree in Chemistry at University of Milan in 2013. Her research interests have been focused on design and development of multifunctional nanoparticles for efficient targeting and drug delivery-based therapy of different tumors.

Dr. Davide Prosperi studied Chemistry at University of Milano, where he obtained his Master degree in 1998. He earned his Ph.D. degree at the same University in 2002. Subsequently, he was a Researcher in the Nanobiotechnology Unit at the ISTM-CNR until 2008. Next, he moved to his present position as an Assistant Professor of Biochemistry and Nanobiotechnology at the University of Milano-Bicocca, where he leads the NanoBioLab. His scientific interests concern the synthesis and biological investigation of colloidal and biomimetic nanoparticles for biomedical applications.

DOI: 10.1002/adhm.201300602

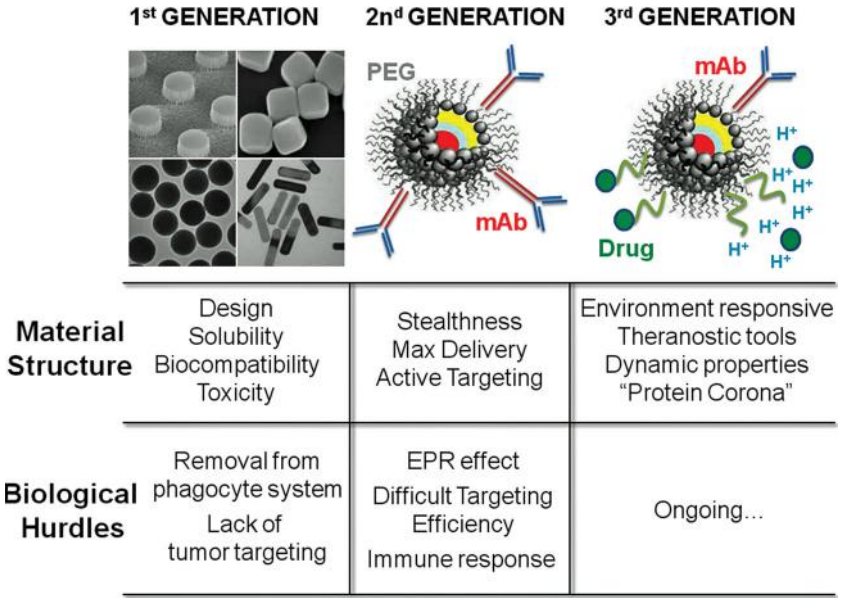

Figure 1. The evolution of nanomaterials and their biological challenges.

tasks: "stealthiness" and active targeting. The aim of developing "stealth" nanoparticles is to maximize blood circulation half-life to enhance the continuous delivery of nanoparticles into the target tissue via a leaky vasculature, exploiting the so-called tumor "enhanced permeability and retention" (EPR) effect. To gain this goal, chemistry has been evolved by adding an amphiphilic polymer coating capable of minimizing nonspecific interactions, such as polyethylene glycol (PEG), to the nanoparticle surface. In this context, the overall PEG chain length and its density on the surface strongly affect the nanoparticle stability over time.[18] In addition, the main advantage of having a ligand bound to a nanoparticle, as opposed to the free molecule in solution, is that the nanoparticle surface creates a region of highly concentrated ligands, which is generally associated to an increase in the avidity for the membrane receptor resulting in clustering effects at the cell surface.[24]

The third generation of nanomaterials, defined "environment-responsive," is in continuous evolution. These dynamic nanoparticles take advantage of a combination of physical, chemical, and biological properties, either deriving from intrinsic features or arising from the interaction of the nanoparticles with a specific environment they are in contact with, in order to maximize their effect into targeted subcellular compartments.[25,26] Cellular delivery based on these more sophisticated nanomaterials remains a great challenge in the design of effective nanodrugs, while an understanding of how cells traffic their constituents to the appropriate place inside or outside the cell could provide valuable information to improve the targeting efficiency and to reduce the toxicity of the system.

Based on the above considerations, in this review we wish to provide a general overlook on the interaction processes at the nano–bio interface that mediate cellular internalization routes of nanoparticles and on their relevant outcomes. Next, we will describe recent advances in developing strategies for nanoparticle sub-cellular targeting and delivery. Finally, we aim to shed a light on the future developments and long-term implications of these findings. This overview would enable researchers to restructure the assembly of composite nanovectors that is expected to afford the highest possible specific efficiency in targeted delivery of drugs and diagnostic agents.

2. Interactions of Nanoparticles with Mammalian Cells

2.1. Delivery Through the Cellular Membrane

At the cellular level, there are several biological barriers that nanoparticles must face to reach their destination: cell membrane is the first. Indeed, the hydrophobic nature of plasma membrane lipid bilayer prevents the diffusion of polar complexes larger than 1 kDa.[27] Conveniently, nanoparticles are on the same size order of large proteins and of typical cellular and extracellular components, so that they can efficiently penetrate living cells by exploiting the ordinary cellular endocytic mechanisms.

Although small and positively charged nanoparticles can enter cells by passive diffusion through the plasma membrane,[28] most of them are internalized by active processes, which could be subdivided into two broad categories: phagocytosis (or "cell eating") and pinocytosis (or "cell drinking"). Phagocytosis is conducted by specialized cells, including macrophages, monocytes, and neutrophils, whereas pinocytosis is more general and may occur in all cell types by at least four basic mechanisms: macropinocytosis, clathrin-mediated endocytosis (CME), caveolae-mediated endocytosis, and clathrin- and caveolae-independent endocytosis. Clathrin is a coat-protein exploited by the cell to assist the formation of endocitic vesicles to safely transport selected molecules within and between the cells, whereas caveolae are caveolin-1-enriched invaginations of the plasma membrane that form a 50–100 nm subdomain of lipid rafts. All of these processes have been already reviewed in detail (**Figure 2**).[29,30]

Obviously, the pathway of entry is a crucial factor in orienting the subcellular trafficking and thereby the fate of a nanomaterial.[31] Different inhibitors capable of interfering with the nanoparticle uptake can be used to study which pathways are preferentially chosen by the cell to internalize a certain nanoparticle. Example of such inhibitors include sucrose, which alters clathrin-mediated endocytosis, chlorpromazine, which disrupts the clathrin-coated pits, nystatin, which inhibits lipid-raft-dependent endocytosis, and dynasor, which interferes with dynamin-mediated pathways.[32,33]

In recent years, great efforts have been spent to clarify the mechanisms behind cell–nanoparticle interactions. In order to try to elucidate the transport pathway of nanoparticles in epithelial cells, He et al. studied endocytosis, exocytosis,

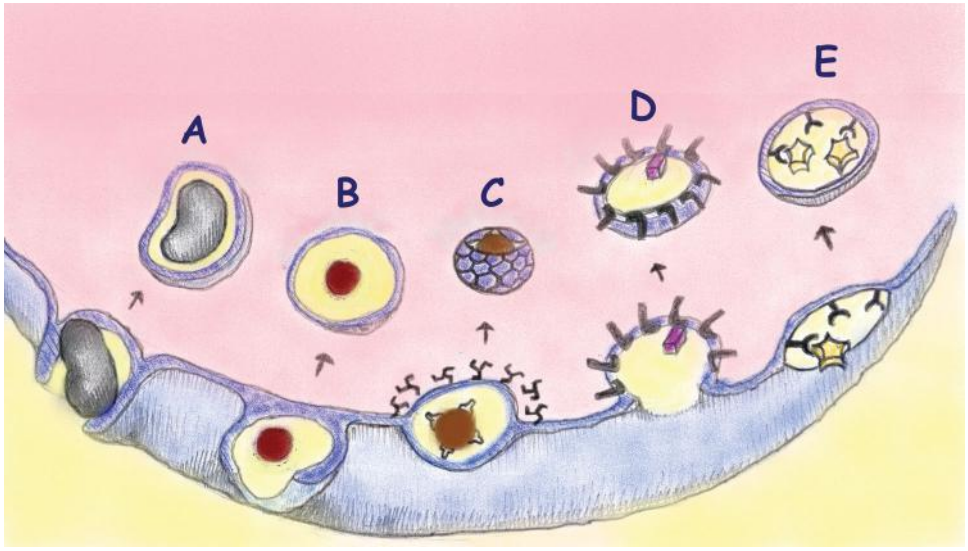

Figure 2. Cellular internalization models: A) phagocytosis; B) macropinocytosis; C) clathrin-mediated endocytosis; D) caveolae-mediated endocytosis; E) clathrin-independent and caveolin-independent endocytosis.

and transcytosis processes using MDCK epithelial cells and unmodified poly(lactide-*co*-glycolide) (PLGA) nanoparticles. By means of various endocytosis inhibitors, the authors demonstrated that nanoparticles could be endocytosed via multiple pathways involving both lipid raft and clathrin mechanisms, but not macropinocytosis.[33] Binding and uptake of the same PLGA nanoparticles in Caco-2 cells proved to be either energy-dependent or independent and nanoparticles underwent multiple pathways including clathrin-mediated uptake, lipid raft/caveolae-mediated endocytosis, and macropinocytosis, thus displaying nonspecific endocytosis routes.[34]

However, the use of targeting functionalities introduced in the nanoconstruct usually affects the internalization route. In a recent study, Huang et al. described the interaction between tumor cells and selenium (Se) nanoparticles functionalized with transferrin (Tf) as a targeting ligand. Tf significantly enhanced the cellular uptake of drug-loaded Se nanoparticles through clathrin-mediated and dynamin-dependent lipid-raft-mediated endocytosis in cancer cells over-expressing Tf receptors, concomitantly increasing their selectivity toward cancer cells compared with normal cells.[32]

In accordance with the cellular equilibrium principles, as any type of molecules, nanoparticles can enter and distribute within cells by energy-dependent pathways.[35–37] At the interface between nanomaterials and biological systems, nanoparticle uptake depends from several factors related to the nanoparticle properties, including size, shape, surface charge, and coating. Actually, size is a hot topic because a common predominant point of view about what dimension promotes cellular uptake is missing. However, it should be discussed that some types of nanoparticles that, due to their size, can cross the membrane in a receptor-mediated way under normal conditions, in a biological environment can be subjected to destabilizing forces and be endocytosed by the cells as aggregates.[38,39] The effect of shape on cellular uptake is principally due to two different causes: 1) the specific functional groups protruding from the nanoparticle with directionalities that are affected by the surface geometry and 2) different surface geometries often lead to dissimilar uptake profiles, which may be due to the orientation of the nanoparticle at the cellular interface.[40] The resulting variety of endocytic pathways can induce in turn different options to process the nanoparticles by the cell, usually dependent on the cell type and phenotype. For example, rod shape causes a lower uptake compared to spherical nanoparticles because the nanoparticle wrapping by the membrane requires a far longer process in the case of elongated shape.[41] Finally, surface coating has a significant impact on nanomaterials translocation into cells especially in terms of charge. Verma et al. propose a model in which nanoparticles coated with amphiphilic molecules in an ordered ribbon-like alternating arrangement should be able to penetrate the cell membrane, whereas nanoparticles bearing molecules presented in a random arrangement are taken up by the endocytosis pathway.[42] In a simplified model, due to the negative charge of phospholipids bilayer, nanoparticles with a surface charge of the same sign of the membrane basically present no contact, nanoparticles with a neutral surface show a minimal interaction with cells, while strong interaction is achieved using positively charged nanoparticles.[43] However, further complexity originates from the patchiness and heterogeneity of the cell membrane,[44] which is a 6-nm-thick soft interface consisting of a lipid bilayer incorporating variable distributions of proteins, lipids, and glycosylated architectures often containing portions on the extracellular side exploited by the cell to communicate with the external environment.[30] Several cell features can affect the nanoparticle process of uptake. One such feature is the cell-type: uptake differences between polarized and non-polarized cells were recovered, caused by the respective different endocytic properties of their apical and basolateral side. In fact, while in non-polarized cells nanoparticles are mainly internalized via macropinocitosis, in polarized cells,

DOI: 10.1002/adhm.201300602

the same nanoparticles can be incorporated both by macropinocytosis and clathrin-mediated endocytosis.[42,45] Nanoparticle entry is also dependent on the contingent state of the cell. For example, cells can be closely packed in a compact barrier rather than isolated or fluctuating in a medium. Also relevant is how old are cells and in which phase of the cell cycle they are,[46] because, in each phase, protein and lipid expression can change significantly resulting in a dramatic alteration of the membrane structure and thus of nanoparticle interaction.

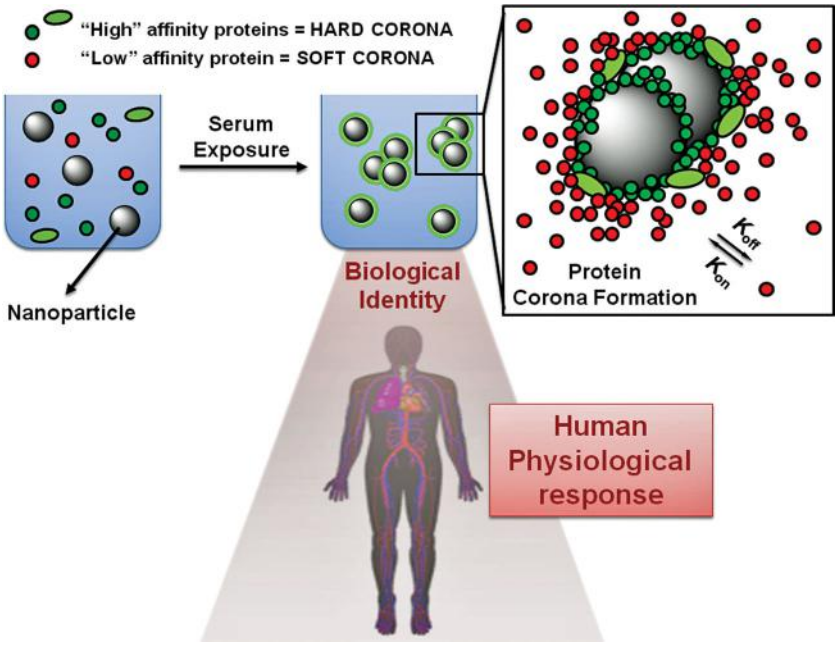

Figure 3. The formation of a protein corona occurs when a nanomaterial is soaked into a physiological environment. Biomolecules with high affinity (green) and low affinity (red) form a thin layer of molecules on the nanomaterial surface, which can be tightly bound ("hard" corona) and/or reversibly adsorbed ("soft" corona), or both. The formation of the protein corona is one of the key factors managing the cellular response in terms of uptake, accumulation, and elimination.

2.2. Influence of Protein Adsorption on the Biological Identity of Nanomaterials

The above arguments suggest that the interaction between nanomaterials and cells is of fundamental importance to understand and predict the fate of a composite hybrid nanoconstruct in a biological system. We mentioned that physicochemical properties of nanoparticles, as well as surface chemistry and functionalization, play a pivotal role in determining the modification of the physiology of interacting cells.[28] Indeed, they can affect uptake (amount, ratio and mechanism), transportation (accumulation, localization and exclusion), and cytotoxicity (necrosis, apoptosis and reduced cell proliferation). This section is dedicated to discuss how the biological identity of a nanoparticle determines the physiological response, including signaling, kinetics, transport and accumulation.[47]

As soon as a nanomaterial is introduced into a biological environment, proteins and other molecules from that media rapidly adsorb on its surface forming a biomolecular layer, essentially consisting of proteins.[15,16] This phenomenon, mostly referred to as "protein corona," alters the size and interfacial composition of that nanomaterial, giving it a biological identity that is distinct from its originally intended structure (**Figure 3**).

The structure of the protein corona is described by five parameters: i) thickness and density, ii) identity and quantity, iii) arrangement, orientation, iv) conformation, and v) affinity. Altogether, these parameters define the interaction of a nanomaterial within a specific biological environment. The thickness and density of the corona determine the overall size of the nanomaterial while the identity and number of adsorbed proteins affects the array of possible biological interactions according to their binding strengths. The orientation determines the accessibility of potential binding and/or catalytic domains, while protein conformation influences the activity of a protein and its interaction with other molecules. Finally, protein affinity to the nanomaterial surface regulates whether it adsorbs, remains bound, or dissociates during biophysical interactions or translocation to a new biological compartment.

The mechanism of protein absorption is mostly regulated by changes in Gibbs free energy:

$$\Delta G_{ads} = \Delta H_{ads} - T\Delta G_{ads} \leq 0 \quad (1)$$

where ΔG_{ads}, ΔH_{ads}, and ΔS_{ads} are free energy, enthalpy, and entropy, respectively, during adsorption, and T is the temperature. There are a number of interactions that contribute to favorable changes in enthalpy ($\Delta H_{ads} < 0$), or entropy ($\Delta S_{ads} > 0$), including the formation of covalent and noncovalent bonds, rearrangement of interfacial water molecules, or conformational changes in either the protein or the nanomaterial surface.

Protein adsorption does not necessarily involve direct interaction with the colloid surface, but may occur instead via protein–protein interactions, which could be either specific (complementary amino acid sequences) or nonspecific (conformational changes that expose charged or hydrophobic domains in a protein that interacts with other proteins). This highlights the fact that biological impact might be driven both by the composition of the biomolecular corona and by distortions conferred to the conformation of the proteins following adsorption on the nanoparticles. One example where the mechanism has been disclosed involves nanoparticle-induced protein unfolding leading to initiation of the nuclear factor-κB (NF-κB) pathway and inflammation.[48]

Several recent works suggest that adsorbed proteins are not uniformly bound to the nanoparticle surface and the strength of the interaction is dependent on the protein affinity toward that material.[49,50] Specifically, molecules adsorbed with high affinity form the "hard" corona, consisting of tightly bound

proteins that do not easily desorb, while molecules adsorbed with low affinity assemble the "soft" corona, consisting of loosely bound proteins. The general hypothesis defines that the hard corona binds directly with the nanoparticle surface, whereas the soft corona interacts preferentially with the hard corona via weak protein–protein interactions. Moreover, the corona probably consists of multiple layers: since most of plasma proteins have very small hydrodynamic size (range 3–15 nm), the average corona usually detected on nanoparticles is too thick to be accounted for by a single layer of adsorbed proteins.[15,51]

At present, we can understand the complex role of the protein corona at the cellular level and we have means to investigate its possible outcomes when using nanomaterials in vivo. As a result, it has been suggested that the biological identity of a nanoparticle actually determines its interactions with biomolecules and biological barriers in a physiological environment. For example, there is a strong positive correlation between the plasma protein binding capacity of a nanomaterial and the rate at which it is taken up by cells in vitro.[52] As a consequence, in vivo, nanoparticles that readily capture plasma proteins tend to interact strongly with tissue-resident macrophages of the reticuloendothelial system (RES), leading to a rapid blood clearance,[49] whereas, in vitro, are often associated with cellular toxicity to some extent.[53] In addition, a set of plasma proteins called *opsonins* promotes the phagocytosis of nanomaterials by macrophages. Adsorption of the major plasma opsonin IgG enhances the recognition and uptake of a number of nanoparticles by macrophages both in vitro and in vivo. In a recent work, it has been demonstrated that the interaction of adsorbed IgGs with CD64 (a high affinity IgG-Fc receptor) initiates the phagocytosis of carboxyl- and amino-functionalized polystyrene nanoparticles by human macrophages.[54]

In certain cases, adsorbed plasma proteins do not act exclusively as opsonins. Cell uptake can occur in the absence of plasma proteins: this process, often referred to as "serum-independent uptake," presumably results from direct recognition of the nanoparticle surface by cell-membrane receptors. Serum-independent cell uptake is typically observed in vitro using serum-free cell cultures. For instance, knocking down the expression of scavenger receptor A in RAW 264.7 cells significantly lowers the uptake of anionic silica nanoparticles.[55]

In a recent study,[53] the protein corona of lipid nanoparticles was investigated and the most enriched constituents were identified to be apolipoproteins (Apo A-I, Apo C–II, Apo D, and Apo E).[56] As the total apolipoprotein content is relevant, nanoparticles with protein corona exhibit a propensity to target PC3 prostate carcinoma cell line that expresses high levels of scavenger receptor class B type 1 receptor, which mediates the bidirectional lipid transfer between low-density lipoproteins, high-density lipoproteins, and cells, thus enhancing the total amount of nanoparticles inside the cell. By contrast, the presence of serum can dramatically reduce the efficiency of cell uptake. For instance, uptake of oxidized silicon microparticles by human umbelical vein endothelial cells (HUVEC) in serum is remarkably lower than in a serum-free medium.[57] A possible strategy to overcome the effect of serum protein adsorption on cellular uptake, in this case, may reside in introducing targeting ligands onto the nanoparticle surface. These molecules enhance the specific cellular uptake concomitantly reducing nonspecific binding of proteins from the environment. However, in the presence of a biological *milieu*, it is likely that the interface they form with their biological target is much more complex than predicted, which may roughly explain the partial lack of success that sometimes occurs in targeting strategies.[17]

Despite much progress has been made toward a comprehensive knowledge of biomolecular corona, several key problems still remain that need to be addressed. The macroscopic composition of molecules that form the hard corona could be investigated with a combination of complementary techniques, including: i) dynamic light scattering (DLS), differential centrifuge sedimentation (DCS), and size exclusion chromatography (SEC) to assess the shell thickness; ii) colorimetric assays to argue the protein density; iii) poly(acrilamide) gel electrophoresis (PAGE), liquid chromatography/mass spectroscopy (LC/MS) to determine the protein identity; iv) circular dichroism (CD) and computational simulations to predict the average protein conformation; v) surface plasmon resonance (SPR) and isothermal titration calorimetry (ITC) to quantify the affinity toward specific receptors. However, to fully understand the complex relationships between the properties of the corona and the biology of nanoparticles, more detailed information on the composition, structural organization, and dynamics of these phenomena is needed.[58] A key challenge in the next future will be to determine the structure of the hard–soft corona interface in detail, for which researchers will require more sophisticated technologies and methods than those used at present in the field. All of these approaches could support the efforts to correlate and even predict aspects of the biological interactions of new materials, which are by now hidden behind a small layer of proteins.

2.3. Electroporation

Electroporation is a physical technique based on an electrical pulse for the active internalization of intrinsically charged extracellular materials into the cell cytosol through a temporary permeabilization of plasma membrane (**Figure 4**). This method

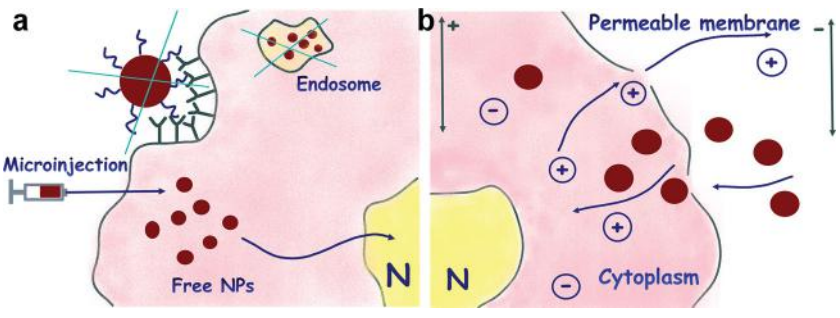

Figure 4. Physical methods to deliver colloidal nanoparticles inside cells: A) microinjection; B) electroporation.

Adv. Healthcare Mater. **2014**,
DOI: 10.1002/adhm.201300602

is commonly used to transfect cells with nucleic acids, proteins, and peptides,[59] and it has been adopted also for the controlled incorporation of different kinds of nanoparticles.[60] The nanoparticles used for this approach should have appropriate size, because of the small pores generated, and good dispersion and stability in cell culture media to prevent the formation of aggregates.

Electroporation allows for a specific delivery in adherent and non-adherent cells and it is highly reproducible compared to other passive-targeting techniques, but it suffers from inability to tailor a specific cell type. In addition, it is not amenable for in vivo targeting and is used only in in vitro experiments with cells. Nanoparticles that are not able to cross the cell membrane can be internalized into the cellular cytosol with electroporation in a controlled and highly reproducible manner, which enables sensing and imaging of cell parameters. In a recent example, electroporation was exploited for the fast delivery of silver nanoparticles (AgNPs) into living cells for use as an intracellular signal amplification device for surface-enhanced Raman spectroscopy (SERS).[61,62] Unfortunately, as well as other active delivery approaches, the cell physical manipulation is highly invasive and often results in compromising the cellular viability.[63] Pack et al. showed that the diffusion and brightness of standard silica nanoparticles in solution were not affected by the electrical discharge necessary for electroporation and investigated their distribution in cell compartments after passive uptake following electroporation.[64]

Electroporation is recommended for tagging cells or bacteria with nanoparticles when much higher loading efficiency is requested than it can be achieved by standard incubation. A typical example is the case in which high concentrations of incorporated nanoparticles as signal emitters are required to track labeled cells in vivo.[65–67] Exploiting photoluminescent or magnetic properties of QDs and IONPs, respectively, it is possible to monitor the fate of transplanted cells, their targeting to solid tumors and to localize metastases. In addition, magnetic nanoparticles can be further utilized as mediators to modulate the cell membrane electroporation induced by an applied current, for cell tracking under various imaging modalities, and for facilitated drug delivery.[68] The optimal condition to obtain a suitable level of poration efficiency maintaining good cell viability should be carefully adjusted depending on cell types and nanoparticle size. Moreover, Lee et al. investigated the effect of nanoparticle polarity on gene transfection in HeLa cells: this study suggested that anionic nanoparticles were more efficient as genetic material transporters compared to the cationic ones.[69]

2.4. Microinjection

Microinjection is an alternative physical technique that allows nanoparticles to be injected directly inside the cytoplasm of the cells, without any residence time in the culturing medium. This novel approach avoids any possible effect related to receptor-mediated endocytosis. The interaction between cells and bare nanoparticles is straightforward and their access is consistent (Figure 4). In this way, the overall cellular response is not affected by the presence of proteins bound to the nanoparticles prior to the uptake. It is possible to deliver very small sample volumes using a fine-tipped glass micro-capillary, thus guiding the cellular targeting with a fluorescent microscope. Microinjection enables nanoparticle delivery to the interior of the cell in a monodisperse form and it is the only technique that allows the target cell to be directly visualized first. On the other hand, it requires each cell to be individually selected, manipulated, and then injected. Thus, not all cells in a field of view will be successfully microinjected due to physical constraints, so it requires a well-trained operator. Moreover, microinjection is a very efficient technique but is also very expensive.

In a first seminal work, Dubertret et al. used QDs to revolutionize biological imaging: they injected into *Xenopus* embryos these fluorescent nanocrystals coated with a phospholipid block-copolymer to follow different evolutionary stages in embryogenesis.[70] With this study, they demonstrated that QDs microinjected into cells allow fluorescence-based in vitro and in vivo studies. Candeloro et al. microinjected Ag and Fe_3O_4 nanoparticles inside Hela cells.[71] The aim of this work was to investigate the cytotoxic effects due to the interaction of nanoparticles with cells and the authors observed that microinjection allows that the effects observed were only due to the nanoparticles themselves and not to the solvents or the technique used. In fact, they put in evidence a different behavior of the cells treated with nanoparticles in comparison with the control cells. This is supposed to be generated by an emerging oxidative stress due to the nanoparticles. Derfus et al. also used microinjection as a means of introducing QDs into the cytoplasm.[72] The authors used this technique to see a subcellular localization of QDs. QDs were endowed with an inert coating of PEG: in one case, a nuclear localization signal (NLS) peptide was added, in another case, a mitochondria localization sequence (MLS) peptide was used in place of NLS. The use of peptide localization sequences and PEG coating combined with microinjection allowed the delivery and subcellular localization of QDs in living cells. Medintz et al. used cellular microinjection of QD-fluorescent protein assemblies as an alternative strategy for intracellular delivery that could bypass the endocytic pathway.[73] QDs functionalized with two different peptides were injected directly into COS-1 cells and this study demonstrated that cellular uptake is favored by the presence of cell-penetrating peptides within the QD–protein conjugates. Muro et al. investigated the intracellular stability and targeting of QDs that present three different surface chemistries using microinjection, electroporation, and pinocytosis to deliver them into the cytoplasm.[74] In particular, QDs endowed with different surface chemistries were injected into *Xenopus laevis* embryos and their behavior was observed for a prolonged time. The authors concluded that the QD intracellular aggregation behavior is strongly dependent on the surface chemistry in all the delivery methods they used.

3. Delivering Nanoparticles to Selected Cellular Compartments

3.1. Targeting the Cellular Membrane

The interaction between nanobioconjugates and the cellular membrane starts with the particle adhesion to a cell-surface

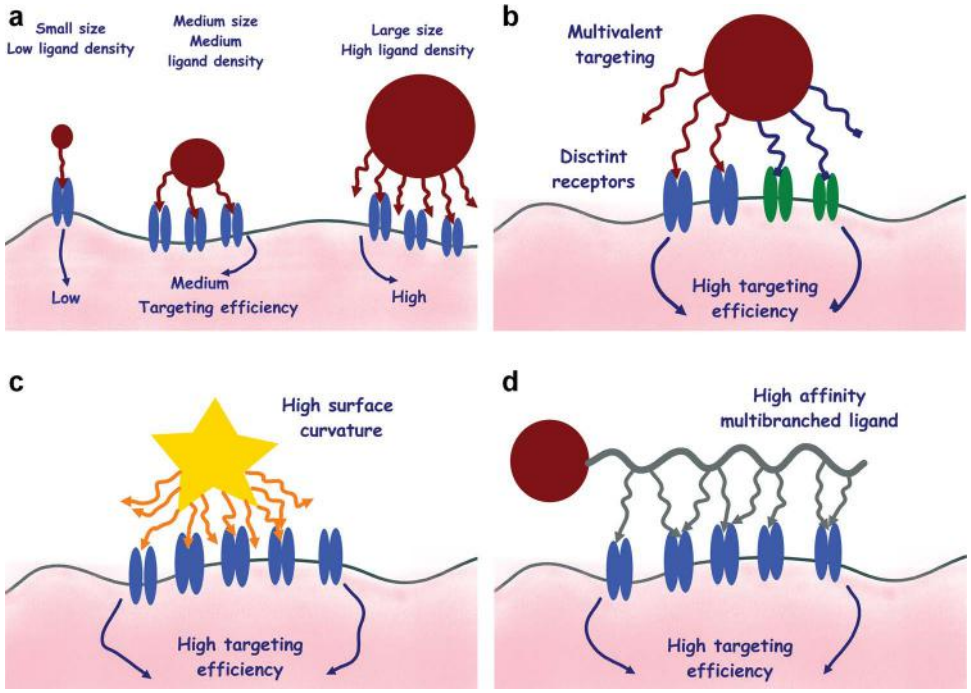

Figure 5. Properties of nanoparticles in correspondence of the cellular membrane: A) size-effect; B) multivalency effect; C) surface curvature effect; D) multibranched affinity ligand.

lipid bilayer or with a recognition event between a biomolecule exposed from the nanoparticle surface and a target receptors or a specific protein on the cell. Nanoparticle contact and membrane wrapping are dependent on different factors, such as the nanoparticle size and shape, the density and distribution of ligands on the nanoparticle surface. It has been established that particle adherence requires specific or nonspecific binding interactions to overcome the resistive forces that hinder particle uptake.[30] On the other hand, the "wrapping time" by membrane is determined by the particle size and shape, rate of receptor diffusion and elasticity of the cell membrane (**Figure 5**).[30]

One of the most commonly used approaches to target the cellular membrane is based on the bio-recognition between a receptor and antibody-bound nanoparticles.[20,75–77] Importantly, the nanoconjugation was shown to affect both the mechanism of internalization and distribution inside the cell and the rate of endocytosis in a cell line characterized by a differential expression of a receptor.[78] For example, it was found that gold nanoparticles conjugated with cetuximab were able to promote faster endocytosis of epidermal growth factor receptor (EGFR) compared to unconjugated antibody, due to enhanced clustering of EGFR induced by nanoconjugation. Moreover, it should be noticed that ligand tailoring on the nanoparticle surface by conjugating different amounts of antibody did not affect significantly the endocytosis pattern.[79] Interestingly, the combination of two different antibodies, that is, farletuzumab and cetuximab, conjugated to AuNPs, drastically improved targeting efficiency of cancer cells expressing both folate receptor α and EGFR via dual targeting.[79] To further understand the potential of nanoconjugation in improving the targeting efficiency of specific molecular scaffolds, the selective targeting by using nanoparticles engaging two distinct receptors expressed in the same cell, namely androgen receptor and a novel G-protein coupled receptor, was shown to facilitate cell death in treatment-resistant cancer at nanomolar nanoparticle concentrations. Anti-androgen AuNPs were found to bind androgen receptor with 5 to 11 times higher affinity compared with free anti-androgen antibody and to bind androgen receptor with affinity superior to endogenous androgens, providing opportunities for further increased treatment efficacy via drug co-conjugation.[80] Kim et al. have developed a nanoprobe for multimodal simultaneous targeting of three different proteins: nucleolin, integrin $\alpha_v\beta_3$, and tenascin-C. The nanoprobe, consisting of a cobalt ferrite core coated with a silica shell containing Rhodamine B isothiocyanate, was conjugated with AS1411 and TTA1 aptamers, as well as RGD peptide. Five different cancer cell lines, including C6 (brain tumor), NPA (thyroid papillary cancer), DU145 (prostate cancer), HeLa (cervical cancer), and A549 (non-small lung carcinoma), and two normal cell lines, including CHO (Chinese hamster ovary cell) and L132 (epithelial lung cell), were tested. Compared with the single cancer probe, the multitarget nanoprobe showed dramatically enhanced cancer targeting efficiency in all five cancer cell lines, whereas none of the multitarget conjugates demonstrated detectable fluorescence intensity in the normal healthy cells, and there was no significant difference in fluorescence when compared with single target probes, demonstrating the specificity of each of the multi-target conjugates. These findings demonstrate that the multi-target cancer probe with additional aptamers or other novel sets of cancer probes can be used to diagnose a variety of cancers as a master probe.[80]

DOI: 10.1002/adhm.201300602

The presence of a targeting ligand is not always necessary for cellular labeling, as it was shown by Yan and co-workers. Having screened 474 clinical specimens from patients with nine types of cancer, the researchers established that magnetoferritin (M-HFn) nanoparticles generated by encapsulating IONPs inside a HFn shell were able to target transferrin receptor 1 (TfR1) without any additional recognition ligands on their surface, with high sensitivity (98%) and specificity (95%).[81]

An interesting alternative strategy for cell membrane targeting was proposed by Stephan et al., in which liposome-like nanoparticles were directly bound to the plasma membrane of T cells, taking advantage from the fact that most cells have high levels of reduced thiol groups on their surfaces. The particles with a drug-loaded core and a phospholipid surface layer with exposed thiol-reactive maleimide headgroups were incubated with the cells to allow maleimide-thiol coupling, followed by in situ conjugation to thiol-terminated polyethylene glycol to quench residual reactive groups of the particles. The authors found that such a targeting did not induce toxicity or affect intrinsic cell functions. The particles followed the characteristic in vivo migration patterns of their cellular vehicles, endowing their carrier cells with substantially enhanced function using low drug doses that, by contrast, exhibited no effect when administered by traditional systemic routes.[82]

Another kind of molecules able to interact with the cellular membrane via cationic groups, bringing about direct cellular entry due to so-called "proton sponge effect," is such polymers as polyethyleneimine (PEI) and polyamidoamine.[83,84] A careful control of the cationic density created by the polymers should be due in this case, as these interactions may compromise the cell membrane integrity, potentially leading to hole formation, membrane thinning or erosion and, thereby, cytotoxicity.[85] Nel et al. have found that the cytotoxicity can be significantly reduced or even prevented by using shorter length polymers for nanoparticle fabrication.[85] By contrast, conjugation of PEI with a targeting molecule such as folic acid allowed for the efficient receptor targeting and cellular uptake of nanoparticles into specific cancer cells.[86]

Hydrophobicity and roughness also have a great influence on the interaction of nanoparticles with cellular membrane. Nanoparticles that are more hydrophobic than the surface membrane are more readily engulfed than their less-hydrophobic counterparts. Moreover, the number of contact sites between membrane and particle surface play an important role in nanoparticle wrapping. Therefore, such parameters as radius of curvature and ligand density influence the particle–membrane interaction.[87–89] Chan et al. thoroughly studied the efficiency of ErbB2 tyrosine kinase receptor targeting and cellular uptake efficiency using AuNPs and AgNPs, in 2–100 nm range, conjugated with Herceptin (Her).[88] The authors found the internalization of Her–GNPs to be highly dependent on size, with the most efficient uptake occurring within the 25–50 nm size range. Due to their inability to promote multivalent binding, smaller nanoparticles dissociate from the receptors before being engulfed by the membrane owing to a low-binding avidity. In contrast, extremely large nanoparticles possess a much higher antibody density on the particle surface, which, in turn, requires the involvement of more distant receptors causing a reduction of membrane wrapping necessary for nanoparticle internalization.[88] On the other hand, Johnson and co-workers have found a dependence of cellular uptake into $EGFR^+$ A431 cancer cells on surface tailoring of nanoparticles, where the number of Clone 225 antibodies bound to gold coated iron oxide nanoroses was varied from 1 to 74, corresponding to either submonolayer or multilayer coverage. The nanoroses conjugated with 54 antibodies were found to show the most efficient cellular uptake (about 7000 nanoparticles per cell), compared to a much lower cellular uptake of spherical AuNPs, conjugated by the same protocol. The small overall hydrodynamic diameter, the high antibody density on the surface, and the orientation of the antibodies with respect to each other which is influenced by high local surface curvature do bring about, in turn, to the high cell uptake by antibody conjugated nanoroses.[87]

Finally, the structure of targeting molecules and their valence also greatly contribute to the effectiveness of cellular targeting. In contrast to using low-affinity ligands for nanoparticle conjugation, the use of multivalent ligands can lead to enhanced affinities, engaging numerous receptors simultaneously to provide enhanced interactions. For example, Brown et al. have found how to improve the affinity of nanoparticles to a lung cancer cell line using liposomes conjugated with a H2009.1 tetrameric peptide: nanoparticles displaying this multivalent tetrameric peptide exhibited 5–10-fold higher delivery efficiency compared to liposomes displaying the lower affinity monomeric H2009.1 peptide, even when the same number of peptide subunits are displayed on the liposome.[90]

3.2. Cytosolic Delivery

Nowadays, the identification of more effective strategies for a low toxic drug administration remains the main challenge in pharmacology and clinical practice.[91] Therefore, increasing efforts are made to design and synthesize nanostructures able to efficiently deliver drugs to target tissues and to penetrate into the cellular environment.[92] Before entering the cell, a nanoparticle has to cross the cell membrane. As mentioned previously, there are different strategies to overcome cell membrane barrier in order to deliver nanoparticles directly inside the cytoplasm avoiding the classical endocytotic pathway, including microinjection and electroporation. An additional approach exploits a passive diffusion through the phospholipid bilayer, which is usually achieved using cell-penetrating peptides (CPPs).[93] CPPs present a great variety in terms of amino acid composition and 3D structure, with examples of cationic, anionic, and neutral sequences showing variable degrees of hydrophobicity and polarity. Over a hundred CPPs have been discovered so far, mostly bearing a net positive charge. Several peptides act as CPPs, including the transactivator of transcription (TAT peptide), an 11-amino-acid peptide of the HIV-1 TAT protein (YGRKKRRQRRR), the transcription factor from Antennapedia, and the VP22 protein from Herpes Simplex Virus 90. It was demonstrated that the amino acidic regions responsible for penetration in the cellular environment are either amphipathic sequences or arginine-containing stretches of 30 amino acids.[93] On the other hand, the peptide secondary structure is of crucial importance for cell-penetration. Peptides conformation

can significantly change depending on whether they are free in solution, near the membrane interface, inside the membrane, or bound to a vehicle, thus affecting the mode of uptake. Finally, the heterogeneity of the cell membrane, including lipid composition, density, and dynamics, depends on different factors, such as the cell type, the specific region of the membrane, and a variety of signaling pathways. This results in different levels and modes of uptake depending on the conditions of each individual experiment.[94]

Endocytosis and direct translocation through the cellular membrane are the major mechanisms used by CPPs to gain entry into the cell. Endocytosis pathway has been reported above, therefore, we will stress here the non-endocytic (i.e., energy independent) pathway. This may include different mechanisms that have been described, including inverted micelle formation, pore formation, the carpet-like model, and the membrane thinning model. The first stage in all of these mechanisms includes an interaction of the positively charged CPP with negatively charged components of membrane (heparan sulfate and phospholipid bilayer), which occurs involving stable or transient destabilization of the membrane associated with folding of the peptide on the lipid membrane. The interaction between hydrophobic residues, such as tryptophan, and the hydrophobic part of the membrane was shown to take part in the "inverted micelle" mechanism. The translocation via pore formation is explained by two alternative models: 1) the barrel stave model, possible for helical CPPs, suggesting a formation of a barrel by which hydrophobic residues are close to the lipid chains, and hydrophilic residues form the central pore; 2) the toroidal model, suggesting the lipids bending in a way to ensure CPP proximity to the headgroup: in this way, both CPP and lipids form a pore. Finally, in the carpet-like model and in the membrane thinning model, interactions between negatively charged phospholipid and cationic CPPs result in a carpeting and thinning of the membrane, respectively, facilitating the peptide translocation. Whatever the mechanism actually involved, one should take in mind that the translocation of the CPP is achieved when CPP concentration is above a certain concentration threshold.[95]

Gold nanospheres conjugated with 17-amino acid α-helix peptides (P-GNS) show a different cell-penetrability upon changing just one amino acid in the peptide sequence. Moreover, the cytotoxic activity of an anti-cancer drug doxorubicin (DOX) conjugated to the P-GNS may strongly depend on the peptide sequence and penetrating capability.[96] Pegylated PLGA nanoparticles modified with poly(arginine) enantiomers were found to exhibit significantly increased cellular uptake and transportation of insulin, thus improving the intestinal absorption of that protein.[97] Nanoparticles unable to cross the cellular membrane are internalized by endocytosis mechanisms but remain entrapped inside the endosomal–lysosomal compartments, the main intracellular barrier that nanoparticles have to overcome to diffuse into the cytosol.[98] However, it is widely accepted that an endocytosis process is involved in internalization of CPPs and CPP-conjugates, including CPP-nanoparticle conjugates, probably due to their large dimensions. Although the detailed mechanism of entry has not been fully elucidated, it is recognized that is dependent on CPP sequence, cell-type, size, shape, and charge of cargo moieties.[92] Despite continuous improvements in direct membrane translocation of CPPs and their cargoes, endosomal entrapment remains a major limitation to CPP-mediated cytoplasmic delivery.[92] An important step forward in the cytosolic delivery of CPP-functionalized nanoparticles has been done by Delehanty and co-workers, who have developed a peptide sequence (JB829-JB826) that stimulates the initial endocytosis of peptide-QDs and then causes the QDs release to the cytosol within 48 h.[99,100]

In the following, we describe a few strategies that have been explored to enhance nanoparticle endosomal escape. The first approach is based on a mechanism involving the formation of a cationic ion pair, which was originally proposed by Xu et al. to facilitate endosomal escape of nucleic acids.[101] Endosome was destabilized by ion pair formation between cationic lipids and anionic lipids within the endosome membrane.[102] Liposomes are the main example of nanoparticles able to escape from endosomes by this mechanism.[103] However, pegylation, adopted to improve the systemic delivery, inhibited ion-pair formation.[104] Thus, liposome-polycation-DNA (LPD) nanoparticles coated with a sheddable PEG were developed. PEG was arranged in the brush mode on the nanoparticle surface to protect the nanoparticle from the reticulo-endothelial system (RES) for an initial period of time and to favor the penetration into the tumor by EPR effect. After tumor penetration, nanoparticles were internalized by a ligand-induced endocytosis process, the shedding of PEG from LPD nanoparticles occurred by exposing the positive charges of the nanoparticles and allowing the charge–charge interaction with the endosomal membrane, which resulted in membrane fusion and endosomal escape.[105,106]

Successful escape of nanoparticles from endosome and release of the payload into the cytoplasm is usually obtained by the so-called "proton-sponge" effect (**Figure 6**).[98] pH-buffering agents are widely exploited to promote cargo release, due to the acidic nature of endosomal-lysosomal vesicles. Macromolecules with low pK_a amine groups, such as poly(ethyleneimine) (PEI), chitosan, poly(L-lysine) (PLL), poly(allylamine), poly(amidoamine) (PAMAM), dendrimers, and some cationic lipids, promote a proton-sponge effect under acidic conditions.[107–109] Nanoparticles forming complexes with these macromolecules are internalized by the cell, then endosome buffering leads to the vesicle lysis, releasing the nanoparticles into the cytosol. For example, charge-reversal copolymers could shift their charge between positive and negative in a pH-dependent fashion.[107,108,110] Charge conversion can occur at the endosome or lysosome stages (pH 5.6), next these copolymers facilitate the endosomal escape of nanoparticles enhancing the proton-sponge aptitude.

This nanoparticle escape mechanism has been reported in a recent work, in which PEG- and PEI-functionalized zinc(II) phthalocyanine (ZnPc)-loaded mesoporous silica nanoparticles (MSNs) exhibited a high escape efficiency from the lysosomes to the cytosol due to the proton-sponge effect of PEI.[111] However, the mechanism of the proton-sponge effect as been questioned, as it has been demonstrated that there are no changes in lysosomal pH after PEI accumulation even in the presence of endosomal escape.[112] Whatever the real mechanism that determines the endosomal escape after treatment with PEI or other similar macromolecules, this kind of strategy has a low

DOI: 10.1002/adhm.201300602

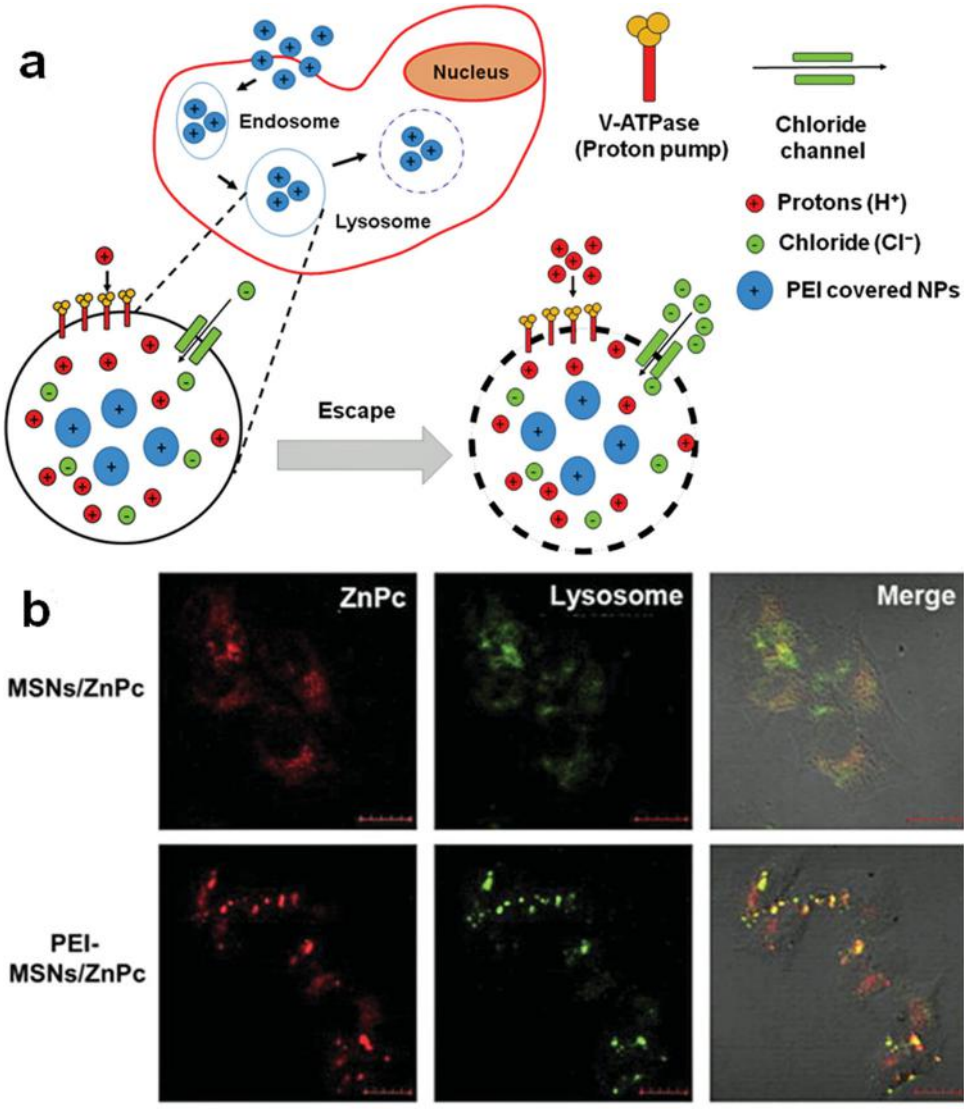

Figure 6. The "proton-sponge effect". A) Cationic particles bind with high affinity to lipid groups on the plasma membrane and are endocytosed. Once these nanoparticles enter into a lysosomal compartment, the unsaturated amino groups are capable of sequestering protons that are supplied by the v-ATPase (proton pump). This process keeps the pump functioning and leads to the retention of one Cl^- ion and one water molecule per proton. Subsequent lysosomal swelling and rupture leads to nanoparticle release in the cytoplasm. B) Estimation of the lysosome disruption capability of MSNs/ZnPc, PEIeMSNs/ZnPc, by confocal microscopy. Representative confocal images showing colocalization of MSNs/ZnPc and PEIeMSNs/ZnPc (red) with late endosomes/lysosomes (green) after 24 h of exposition to nanoparticles. Scale Bar, 10 μm. Reproduced with permission.[111] Copyright 2012, Elsevier Ltd.

efficiency in comparison with viral alternatives. This is probably due to the fact that an insufficient amount of nanocarrier actually accumulates in each endosome, thus preventing the achievement of the necessary buffering capacity in vivo. Moreover, cationic nanomaterials are usually associated to high toxicity and immunogenicity, which limit their clinical implementation.[106] One promising approach to bypass these problems resides in the development of "synthetic viruses." These structures are consist of elements that mimic the delivery functions of viral particles and surface domains that prevent undesired biological interactions and enable specific cell receptor binding.[113]

An alternative strategy to overcome endosomal accumulation takes advantage of the use of membrane-destabilizing macromolecules. These compounds mimic the action of viral hemagglutinin, which is a pH-sensitive and membrane-destabilizing protein that helps viral vectors to disrupt the endosome and enter the cytoplasm.[114] Hemagglutinin acts by shifting from an ionized and hydrophilic conformation to a hydrophobic and membrane-active conformation in response to the environment changes from neutral to acidic, and this results in destabilization of the endosomal wall. Several peptides and polymers that simulate the function of hemagglutinin were synthesized. The incorporation of membrane-destabilizing peptides is another

strategy to utilize the low pH environment of endosomes-lysosomes.[114] Among membrane destabilizing peptides, GALA (glutamic acid-alanine-leucine-alanine), a pH-sensitive fusogenic peptide, is the most studied. A multifunctional envelope nanodevice functionalized with GALA and an 8-arginine tail was developed, which led to an endosomal release of siRNA resulting in an efficient knockdown.[115] Krpetic et al. reported on the intracellular trafficking of gold nanoparticles functionalized with Tat-peptide, showing their ability to overcome intracellular boundaries: unusually, the particles were initially found in the cytosol, in the nucleus and in mitochondria, and later within densely filled vesicles, from which they could be released again via an endosomal escape mechanism by penetration of the vesicle membrane followed by membrane rapture.[116,117]

In addition to the ability to escape from endosomes, the ideal nanocarrier should be capable of releasing the drug into the cytoplasm. The design of polymeric micelles able to respond to the changes of intracellular environment has represented a promising strategy. To this purpose, an effective approach has been to incorporate cleavable links into the polymer structure, either to cause a structural change of the delivery systems, or to direct conjugate drug molecules, which could be released upon cleavage of the links.[118]

Intelligent macromolecules or nanoparticles for drug delivery have been developed using acetal bond, that is the most widely used among pH-sensitive bonds due to its rapid degradation in endosomes.[119–123] Nanoparticles containing acetal bonds are supposed to be degraded in endosomes, thus releasing their cargo. Hydrolysis of acetal bond is a hydrogen-consuming reaction, which also promotes cargo escape from endosome by increasing endosomal osmotic pressure. Endosomal escape of nanoparticles could be also achieved by stimulating membrane lysis through a hydrophobic modification of cationic polymers.[124,125] Finally, membrane penetration can be promoted by means of a phage-mimetic carrier that takes advantage of the presentation of the scavenger receptor class B type I, a natural membrane channel that mediates the intracellular delivery of hydrophobic molecules,[126] or exploiting isolated naturally produced exosomes for siRNA delivery into the cytosol.[127]

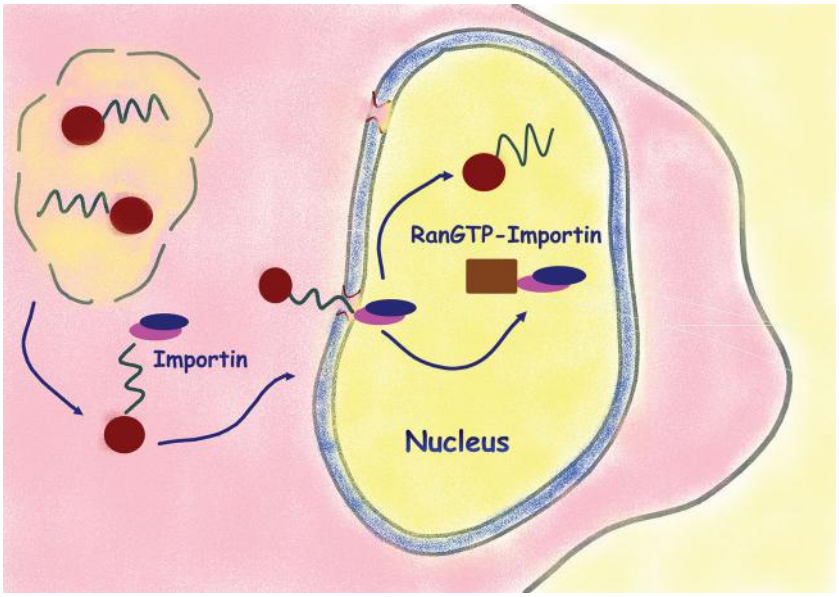

Figure 7. Nuclear preferential transport pathway. Nanoparticles with specific NLS peptide bind to an importin in order to achieve preferential transport inside the cell nucleus.

3.3. Nuclear Preferential Transport

The nucleus is surrounded by a double membrane called nuclear envelope (NE). The communication between the nucleus and the cytoplasm is mediated by the nuclear pore complexes (NPCs). NPCs are specialized channels that allow passive diffusion of ions and small molecules (<40 kDa). Whereas the nucleus-cytoplasmic traffic of large molecules (>40 kDa) is regulated by specific nuclear import and export systems,[128–132] the transport of these macromolecules requires a signal- and energy-dependent mechanism. The active transport is basically mediated by a specific molecule, usually referred to as the nuclear localization signal (NLS), which comprises a basic amino acid-rich short sequence. The energy-dependent step is mediated by a heterodimer of proteins called importin α (Imp-α) and importin β (Imp-β). Imp-α binds the NLS sequence, while Imp-β is responsible for the increase in the affinity of Imp-α toward the NLS and mediates the transfer of the cargo-Imp-α complex across the NPC. After passing through an NPC, the cargo of Imp-α is released inside the nucleus upon binding of the monomeric guanine nucleotide RAs related nuclease protein Ran-GTP to Imp-β (**Figure 7**). Once the dissociation of Imp-β and its cargo protein has occurred, Imp-β is recycled and sent back to the cytoplasm bound to Ran-GTP. The conversion of Ran-GTP to Ran-GDP releases the Imp-β protein that, in this form, is able to bind new cargoes. Ran-GDP is indeed transported into the nucleus by its own specific nuclear transporter in order to replenish its nuclear concentration.[133]

These NLSs are divided in classical NLSs and non-classical sequences. Classical NLSs consist of one or two sequences of arginine and lysine: the most frequent classical monopartite NLS (PKKKRKV^{132}) has been found in the SV40 large tumor antigen (T-ag), while an example of bipartite NLS consisting of two sequences of basic amino acids separated by a spacer of 10–12 residues (KRPAATKKAGQAKKKK^{170}) was isolated from the Xenopus nucleoplasmin.

It has been shown that not only NLS peptide is used for nuclear transport, but also the HIV TAT peptide is able to transport cargoes across both the plasma membrane and the nuclear membrane. TAT peptide-mediated nuclear transport has different import properties if compared to NLS. Cardarelli et al. demonstrated that the dominant mechanism in live cells is the passive diffusion, whereas Truant et al. demonstrated that Imp-α is both necessary and sufficient for the nuclear translocation of TAT in the absence of Imp-β in vitro.[131,132]

Adv. Healthcare Mater. **2014**,
DOI: 10.1002/adhm.201300602

Table 1. Nuclear localization signals (NLSs) for nuclear transport and types of nanoparticles involved.

Nanoparticle type	Origin of peptide	Peptide sequence	Refs.
Polymeric micelles and iron oxide	Monopartite	PKKKRKV	142-149
Polymeric micelles and iron oxide	Nucleoplasmin NLS	KRPAATKKAGQAKKKK	129,150
CdSe/ZnS QDs, Gold	SV40 large T NLS	CGGGPKKKRKVGG	138-142
Liposomes, Gold, QDs	SV40 NLS	PKKKRRV	140,151
Silica, Silver, CdSe/ZnS QDs	TAT peptide	YGRKKRRQRRR	132,137,141

The different classes of NLSs have been attached to different cargoes with the aim to enhance the nuclear transport and delivery: some examples are summarized in table (**Table 1**).

Also the cell cycle plays an important role in nuclear targeting. In non-dividing cells, vehicles must enter the nucleus through the NPCs. By contrast, in dividing cells, the majority of vehicles are supposed to enter the nucleus during mitosis. In a seminal study on the dependence of the efficiency of the delivery vehicle from the cell cycle, the highest level of transfection was obtained with cells that started in the G2 phase.[134] However, more recently, it has been demonstrated that NLS sequence is necessary for nuclear proteins/nanoparticles retention after mitosis.[135]

In order to enter the nucleus, nanoparticles have to cross the NPC and, for this reason, nanoparticles and vehicles must have specific requirements, including small size, cationic charge, proper shape, and surface functionalization.[136] Moreover, they should be able to bind specific receptors on the plasma membrane, escape endosomal and lysosomal digestion, and help importins to cross the nuclear pore complex and to limit toxicity.

Nuclear targeting is exploited mainly for imaging (in diagnostic) and drug/gene delivery (in therapy). Nanoparticles can be effectively imaged by several techniques, including, for instance, surface-enhanced Raman scattering (SERS) spectroscopy, magnetic resonance imaging (MRI), and fluorescence. The use and the choice of one of these techniques depend on the variety of materials and on their physical and chemical skills. Gold and silver nanomaterials have unique optical properties, including the localized surface plasmon resonance (LSPR), which are leveraged in SERS. We can find examples of AuNPs and AgNPs functionalized with NLS or TAT for nuclear targeting and visualization/detection in single living cell.[137–139] The AuNP LSPR adsorption is size-dependent: when nanoparticles are smaller than 3 nm, they lose their LSPR character, but they acquire photoluminescence properties. These kinds of nanoclusters are called gold quantum dots (GQDs), which might be very useful in cellular imaging. For example, by taking advantage of a combination of small size and intense emission, GQDs were functionalized with SV40 NLS and used for nuclear targeting and intracellular imaging.[140] More in general, the brightness and the photostability of QDs, allow tracing the trajectories of individual QDs in living cells, using both confocal and internal reflection microscopes.[141] The biofunctionalization of IONPs can be used to enhance the tissue contrast in MRI. For example, Xu et al. functionalized Fe_3O_4 SPIO with NLS to attempt nucleus targeting.[142]

The second fundamental application of nuclear targeting is to produce nanoparticles/carriers for nuclear drug delivery. This function is very important because a large number of drugs exert the main cytotoxic action at the nucleus. Yu et al. have produced glycol chitosan micelles for doxorubicin nuclear delivery,[129] whereas Misra et al. developed doxorubicin-loaded PLGA nanoparticles for this purpose.[143] A poly(2-(pyridin-2-yldisulfanyl)ethyl acrylate (PDS) delivery system, a novel redox stimulus-responsive nanoparticle system conjugated with RGD peptide, was designed to enhance the nuclear drug delivery of doxorubicin.[144]

It is also possible to combine two or more applications in the same construct to create a multifunctional nanoparticle. Liu et al. developed multifunctional nanoparticles that targeted cell nuclei, delivering the drug and at the same time detecting cell nucleus by a dual imaging modality including MRI and fluorescence.[145]

Finally, the literature reports several examples of different nanoparticles that have been used for studying nuclear mechanisms of targeting and uptake, with special focus on the effect of nanoparticle morpho-structural characteristics, including charge and size, on nuclear uptake,[126] but also for investigating the cytotoxicity caused by the chemical nature of nanoparticles. For instance, Austin and co-workers revealed the difference between AuNPs and AgNPs for nuclear targeting during cell cycle.[139,146]

3.4. Mitochondrial Targeting

Mitochondria can be considered the powerhouse of the cell because they act as the site for the production of high-energy compounds (e.g., ATP), which are the vital energy source for several cellular processes. Mitochondria play important roles in a variety of vital cellular processes, most of which are related to cell disease. For this reason, targeting of this organelle may present a few important benefits.[27] The relationship between mitochondrial DNA (mtDNA) mutations and human myopathies indicates that the delivery of nucleic acids plays a vital role that will be analyzed. Another important reason for targeting the mitochondria arises from its ability to propagate reactive oxygen species and oxidative stress signaling,[152] which is one of the main causes of cellular toxicity.

In order to attempt the identification of mitochondria-specific targeting is necessary to stand out the main compartments in which they are divided, that is, the outer mitochondrial membrane (OMM), the inner membrane space (IMS), the inner mitochondrial membrane (IMM), and the mitochondrial matrix. There are several strategies for the targeting of mitochondria.[153] In a first example, the electrochemical potential maintained across the IMM is exploited for the confined delivery using some molecules, also referred to as delocalized lipophilic cations (DLCs), that are particularly effective in crossing the hydrophobic membrane layers and, hence, that preferentially accumulate in mitochondria. Studies on dibenzylammonium cation in isolated mitochondria and on the

fluorescent dye rhodamine in cultured cells suggest that DLCs actively accumulate in mitochondria in a potential-dependent manner. Indeed, DLCs, including the commercial Mitotracker, tetraphenylphosphonium (TPP), and 5,5′-6,6′-tetrachloro-1,1′,3,3′-tetra-ethylbenzimidazolcarbocyanine iodide (JC-1), are commonly used as mitochondria-specific dyes for staining and studying mitochondrial physiology.[153] Another strategy, used to selectively target mitochondria, takes advantage of the mitochondrial protein import machinery, which is naturally utilized by cells for the delivery of nuclear-encoded mitochondrial proteins. These proteins are directed to the mitochondria post-translationally through cleavable *N*-terminal peptide sequences. Mitochondrial targeting sequences (MTSs) are basically 20–40 amino acids in length with structural motifs recognized by the mitochondrial import machinery. When an MTS is recognized by a specific receptor on the outer membrane, the attached protein is transported into the IMS by threading through the pore of the outer mitochondrial membrane. Once entered the matrix, the MTS is cleaved in one or two proteolytic steps by mitochondrial processing peptidases, and, with the help of matrix-localized chaperones, such as mhsp70, the protein refolds into its mature form.[153] This approach has been used successfully with a variety of molecules like proteins, nucleic acids, and endonucleases. The use of vesicle-based transporter for the mitochondrial targeting has also shown good efficiency in transporting large or impermeable cargoes, such as drug molecules. This strategy is based on the use of surface-bound cationic peptides to deliver a liposome-based carrier for macromolecular delivery to the mitochondria.[154]

Various tailoring nanocarriers for the intracellular transport of biological cargoes, including DNA, proteins, and drug molecules have been actively investigated.[155] To target the acidic endosomal/lysosomal compartments, nanovectors with pH-cleavable linkers were reported to improve payload bioavailability. In 2011, Zhou et al. reported a set of tunable, pH-activatable micellar (pHAM) nanoparticles based on the supramolecular self-assembly of ionizable block copolymer micelles.[156] Despite these significant advances, specific transport and activation of nanoparticles in different organelles during endocytosis in living cells is not well documented.

From a medical point of view, targeting of mitochondria using engineered nanovectors is gaining interest in chemotherapy, as mitochondria are key regulators of cell death and their functions are often altered in neoplasia. For this reason, the development of mitochondria-targeted drugs represents a promising approach for eradicating chemotherapy-refractory cancer cells.[156] Promising strategies are based on electrostatic interactions between the engineered nanoparticles and the mitochondrial membrane, which has a membrane potential in the 130–150 mV range that is lower than other membranes in the cell and can be exploited by grafting cationic species, such as triphenylphosphonium (TPP) cations, to the surface of the nanocarrier.[153] In particular, cationic TPP has been applied in various studies for mitochondrial targeting of antioxidants with the aim of protecting them from oxidative damage.[157] Peptide ligands provide an alternative method for targeting mitochondria. For instance, Yamamoto and co-workers made an approach by conjugating a peptide-based mitochondrial targeting sequence to QDs.[157] The sequence was attached to n-trioctylphosphine oxide-capped QDs in a multi-step process by a thiol-exchange method. In order to generate carboxyl-QDs, a 3-mercaptopropanoic acid was used and then coupled with a cysteine to get free sulfhydryl groups on the surface of QDs. The amino group of the mitochondrial targeting sequence Mito-8 (NH_2-MSVLTPLLLRGLTGSARRLPVPRAKIHWLC-COOH) was then attached using sulfo-SMCC. Results showed that QD520-Mito8 exhibited a strong mitochondrial localization in living cells compared to QDs modified with a control peptide, which was assessed by mitochondrial staining using confocal microscopy.[157]

Another interesting application of nanoparticles for mitochondrial targeting has been recently explored by Chou et al., who have demonstrated the induction of cell death by physical trapping of mitochondria using bacterial-derived magnetic nanoparticles (BMPs) labeled with cytochrome c (Cyt c)-specific binding aptamers, combined with an applied external static magnetic field.[155] Cyt-C has an important role in the life-supporting function of ATP synthesis. In this way, the authors demonstrated that the method might be useful for targeted cell therapy, with the advantage of conferring remote control over subcellular elements by means of a magnetic field.

Finally, Chamberlain et al. reported the targeting of doxorubicin into mitochondria using mitochondria-penetrating peptides (MPPs) formed by cationic sequences that can deliver cargoes into the mitochondrial matrix (**Figure 8**).[158] Doxorubicin, an inhibitor of DNA topoisomerase II (TopoII), is used in the treatment of a wide range of cancers, and its principal mechanism of action is the generation of TopoII-mediated lesions in nuclear DNA leading to cell apoptosis.[158] A mitochondrially targeted version of doxorubicin (mtDox) was synthesized by coupling the primary amine of the sugar motif to a succinic anhydride conjugated to the N-terminus of the MPP. This compound was shown to maintain the ability to inhibit TopoII and to induce damage to mtDNA selectively. At the same time, the potency of mtDox is somewhat diminished compared with the parent drug in sensitive cells, which may indicate that TopoII is not as essential in mitochondria as in the nucleus. For that reason, mtDox may also find application in the study of the enzyme mtTopoII.

In another work, mitochondria-targeted nanoparticles based on PLGA-*b*-PEG and a lipophilic triphenyl phosphonium (TPP) cation were used for the delivery of a therapeutic payload, specifically, a zinc phthalocyanine photosensitizer.[159] The action of these nanoparticles upon light activation inside the mitochondria was shown to produce reactive oxygen species (ROS), which caused cell death via apoptosis and necrosis. The authors demonstrated that tumor antigens generated from the treatment of breast cancer cells with theses nanoparticles activate dendritic cells (DCs) upon light stimulation to produce high levels of interferon-gamma (IFN-γ). The advantages of this activation process are: 1) activated DCs can be produced in bulk quantities, 2) ex vivo culture conditions can be carefully controlled, and 3) DC quality can be controlled before the cells are administered to the patient. These results open the possibility of using mitochondria-targeted nanoparticles, light-activated cancer cell supernatants as possible vaccines and the approach has the potential to be readily transferred to the clinical practice.

Adv. Healthcare Mater. **2014**,
DOI: 10.1002/adhm.201300602

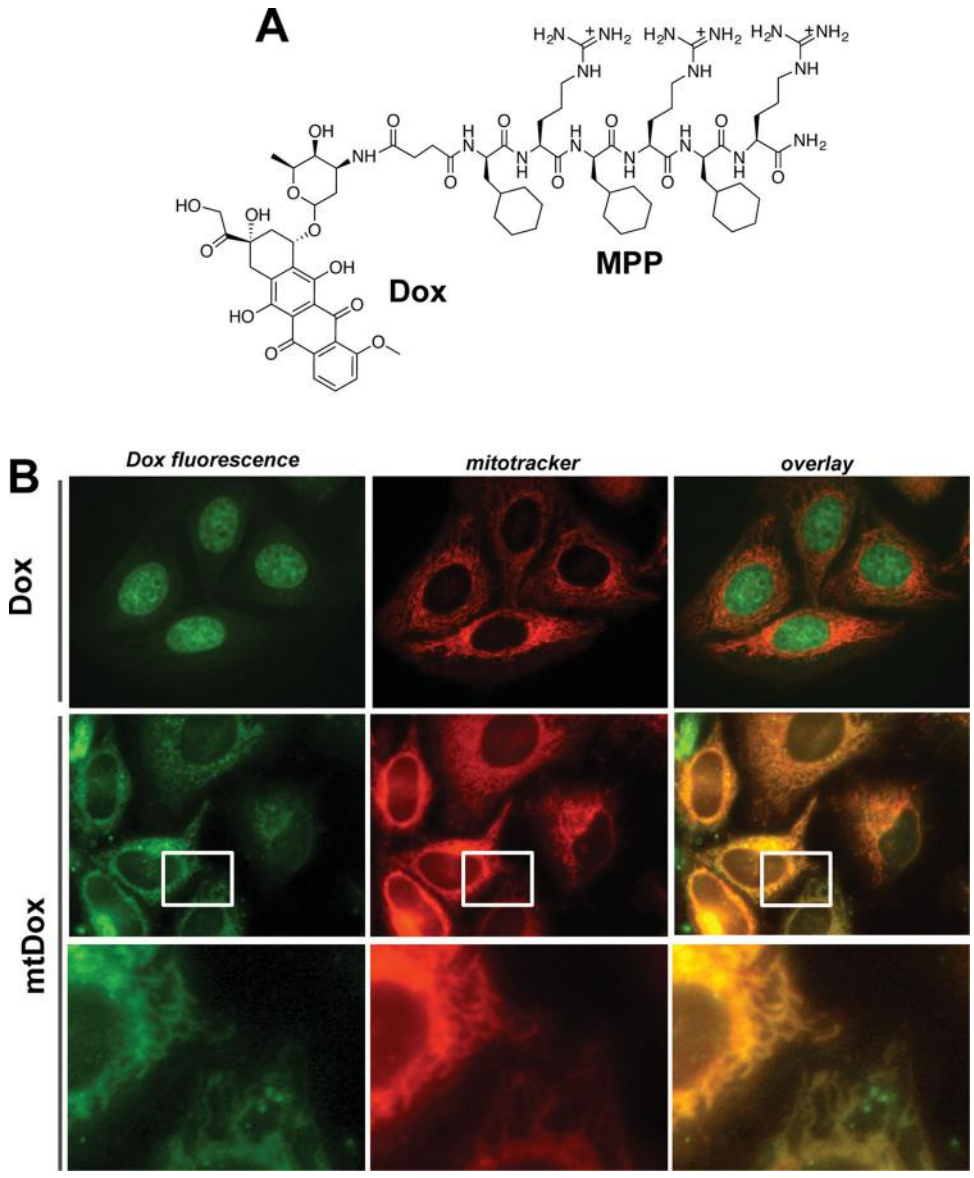

Figure 8. Mitochondial targeting by mitochondria-penetrating peptides. A) Structure of doxorubicin (Dox) conjugated to a mitochondria-penetrating peptide (MPP) (mtDox conjugate). B) Subcellular localization of mtDox. Top row: Dox (green channel) demonstrates strong nuclear staining as monitored using its intrinsic fluorescence and no colocalization with Mitotracker 633 (red channel) as shown in overlay image (right). Middle row: mtDox (red channel) shows a high level of mitochondrial accumulation with a staining pattern that matches Mitotracker 633 (green channel). The high degree of colocalization can be visualized in the bottom row close-up images. Reproduced with permission.[158] Copyright 2013, ACS American Chemical Society.

4. Perspectives: Future Developments in Nanoparticle Delivery

In the last decade, a lot of research work has been devoted to the development of nanoconjugates able to penetrate the cells both for drug delivery application and intracellular targeting. Although nanotechnology combined with bioscience has been developing rapidly with new bioconjugation approaches to be discovered, the guided nanoparticle delivery inside the cell remains a challenging task.[160–163] Recently, a new modern approach, so-called Halo Tag technology, has been designed to provide new options for rapid, site-specific labeling of proteins in living cells and in vitro, and based on the efficient formation of a covalent bond between the Halo Tag protein and synthetic ligands (**Figure 9**a).[164–166] Besides being used in biology for protein expression studies, this technology has been gaining a lot of interest in nanobiotechnology as well. At the moment, there are only few examples reporting the Halo tag use in nanoparticle studies. In a recent research from our group, Halo tag was used as nanoparticle capture module, taking advantage of a new covalent bond formation by site-specific reaction with a chloro-alkane linker immobilized on the surface of an

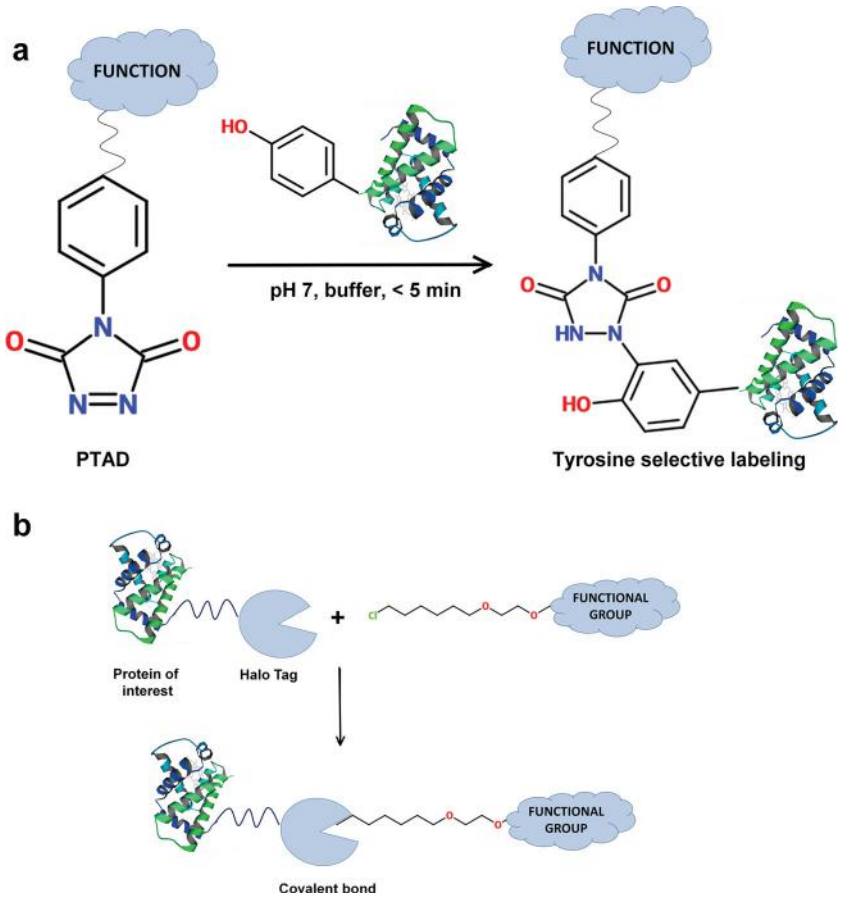

Figure 9. Orientation controlled site-specific labeling of proteins via a) Halo tag covalent bond formation, and b) tyrosine selective conjugation.

IONP. Expressing Halo Tag in fusion with a small peptide of 11 amino acids (U11) with a high affinity for urokinase plasminogen activator receptor (uPAR), we were able to successfully label cancer cells in an orientation-controlled manner.[23] Similarly, Ting and co-workers used Halo tag-conjugated QDs for labeling of specific membrane proteins in living cells. In this case, the protein of interest was genetically fused to a 13 amino acid recognition sequence and subsequently conjugated with 10-bromodecanoic acid for site-specific attachment of a lipoic acid ligase enzyme.[167] Another useful, highly efficient, and chemoselective strategy for the conjugation of small molecules, peptides, and entire proteins involves the tyrosine "click" reaction of 4-phenyl-3H-1,2,4-triazoline-3,5(4H)-diones (PTAD) derivatives (Figure 9b). While tyrosine residues are commonly found in proteins, surface accessible tyrosines only seldom occur and provide attractive opportunities for minimal labeling. The reaction is selective for the phenolic side chain of tyrosine and occurs in buffered aqueous media over a broad pH range without the requirement of added heavy metals or other reagents, resulting in a C–N linkage, which is significantly more stabile to extreme pH, high temperatures, and in human serum for extended periods of time in comparison with the more popular maleimide-based methods.[168]

Beyond their use as tumor targeting platforms, nanoparticles are attracting much interest as potential cancer vaccines. Recently, several reviews describing some recent advances in nanoscale systems designed for cancer immunotherapy, as well as the potential for these systems to translate into clinical cancer vaccines, have been reported.[169,170] For instance, Cameron et al. have used small AuNPs decorated with Tn-antigen (truncated core 1 mucin-type) glycans in a "multicopy-multivalent" manner, giving rise to a nanoparticle with a surface that mimics much more closely the surface of cancer cells. Immunological studies successfully proved that these nanoparticles were able to generate strong and long-lasting production of antibodies that were selective to the Tn-antigen glycan and cross-reactive toward mucin proteins displaying Tn, thus demonstrating the possibility to use glycosylated AuNPs as an anticancer vaccine even in the absence of a typical vaccine protein component.[169,170] In another example, Barchi et al. have used AuNPs coated with both the tumor-associated glycopeptides antigens containing the cell surface mucin MUC4 with Thomsen Friedenreich (TF) antigen attached at different sites and a 28-residue peptide from the complement-derived protein C3d to act as a B-cell activating "molecular adjuvant." As a result, the authors obtained nanoparticles that could act both as immunogens and immune system stimulants, showing statistically significant antibody response in mice to each glycopeptide antigen.[171,172] Finally, it was also found elsewhere that nanoparticle shape and size greatly influence the immune response both in vivo and in vitro.[173] In conclusion, although several advantages in subcellular targeting by nanoconjugates have been observed, many challenges still need to be overcome to increase the targeting efficiency and reduce the overall cytotoxicity. For this reason, an ad hoc design of nanoconjugates, including studies on their morphological properties and choice of the proper targeting ligands, is needed to drive the uptake efficiency and pathway of entry. These studies are expected to take advantage of modern simulation methods, which could provide researcher with new predictive tools for the de novo design of more efficient, high-affinity molecular nanoconjugates.[174,175] Moreover, the combination of targeting and therapeutic functions to create an "ideal" theranostic nanoplatform for tumor treatment will be of great utility in the purpose to improve tumor treatment efficiency on earlier stages.

5. Conclusions and Outlooks

In the present review, we have provided the most recent advances and challenges on the use of nanoparticles designed ad hoc for cellular nanobiotechnology. In particular, we have pointed out different strategies for delivering nanoparticles through the targeting of different cellular compartments such

DOI: 10.1002/adhm.201300602

as cellular membrane, cytoplasm, nucleus, and mitochondria, which are intended to meet the medical needs emerging by the modern challenges in the diagnosis and therapy of highly threatening human diseases.

Besides the well-documented internalization mechanisms based on the crossing of cellular membrane, we have described also the physical approaches that have been used to deliver nanoparticles inside the cellular matrix. A few examples using advanced techniques, such as microinjection and electroporation, have been illustrated. However, at present, incubation remains by far the preferred strategy to investigate the biological interactions between nanoparticles and cells reproducing the ordinary living conditions avoiding invasive destabilization of the cellular environment. From this rapid overview, it appears how the nanoparticle nature and functionalization could affect the interaction at the nano-bio interface, which, in turn, mediates nanoparticle internalization routes. In addition, we have discussed some hurdles occurring when this small interface faces the physiological environment and how this phenomenon can turn into different unexpected responses. Eventually, we have concluded with a picture of future perspectives on new possible improvements and developments, which could open new directions towards potential applications in nanomedicine.

Once fully mapped, the relationships between synthetic nanoparticle chemistry, molecular recognition, and cellular biology will converge and could enable researchers to predict the physiological response of colloidal nanoparticles. These concepts will also help the researchers to design "ideal" and rational conjugate nanosystems, which could be used as nanovector to ensure the efficient and selective delivery of a specific agent to a specific cellular compartment, with the aim of an in vitro screening of its efficacy and possible toxicity, prior to an in vivo validation. Disclosing these relationships will require an extensive research and we would expect that also new experimental techniques and strategies will be the major driving forces directing the progress in the future of nanomedicine.

Acknowledgements

P.V. and S.A. contributed equally to this work. This work was supported by Fondazione Regionale per la Ricerca Biomedica (FRRB), NanoMeDia Project (A. O. "L. Sacco" and Regione Lombardia), the "NanoBioSense" Project (Sardegna-Lombardia), and Cariplo Foundation ("The MULAN program", Project N° 2011–2096). S.A. and G.A. acknowledge a research fellowship from "Fondazione Romeo ed Enrica Invernizzi" and CMENA.

Received: October 31, 2013
Revised: December 5, 2013
Published online:

[1] S. Dufort, L. Sancey, J. L. Coll, *Adv. Drug. Delivery Rev.* **2012**, *64*, 179.
[2] J. B. Haun, N. K. Devaraj, S. A. Hilderbrand, H. Lee, R. Weissleder, *Nat. Nanotechnol.* **2010**, *5*, 660.
[3] K. Prapainop, D. P. Witter, P. A. Wentworth, *J. Am. Chem. Soc.* **2012**, *134*, 4100.
[4] G. L. Pilar, D. J. De Aberasturi, V. Wulf, B. Pelaz, P. Del Pino, Y. Zhao, J. M. De La Fuente, I. R. De Larramendi, T. Rojo, X. J. Liang, W. J. Parak, *Acc. Chem. Soc.* **2013**, *6*, 743.
[5] C. Luccardini, A. Yakovlev, S. Gaillard, M. van't Hoff, A. P. Alberola, J. M. Mallet, W. J. Parak, A. Feltz, M. Oheim, *J. Biomed. Biotechnol.* **2007**, *7*, 68973.
[6] A. Albanese, P. S. Tang, W. C. W. Chan, *Annu. Rev. Biomed. Eng.* **2012**, *14*, 1.
[7] W. K. Oh, S. Kim, O. Kwon, J. Jang, *J. Nanosci. Nanotechnol.* **2011**, *11*, 4254.
[8] L. Florez, C. Herrmann, J. M. Cramer, C. P. Hauser, K. Koynov, K. Landfester, D. Crespy, V. Mailänder, *Small* **2012**, *8*, 2222.
[9] D. Hünh, K. Kantner, C. Geidel, S. Brandhold, I. De Cock, S. J. H. Soenen, P. R. Gil, J. M. Montenegro, K. Braekmans, K. Müllen, G. U. Nienhaus, M. Klapper, W. J. Parak, *ACS Nano* **2013**, *7*, 3253.
[10] C. Sweigher, R. Hartmann, F. Zhang, W. J. Parak, T. H. Kissel, *J. Nanobiotechnol.* **2012**, *10*, 10.
[11] K. E. Sapsford, W. R. Algar, L. Berti, K. B. Gemmill, B. J. Casey, E. Oh, M. H. Steward, I. L. Medintz, *Chem. Rev.* **2013**, *113*, 1904.
[12] S. Fraga, H. Faria, M. E. Soares, J. A. Duarte, J. P. Soares, M. L. Bastos, H. Carmo, *J. Appl. Toxicol.* **2013**, *33*, 1111.
[13] W. J. Stark, *Angew. Chem. Int. Ed.* **2011**, *50*, 1242.
[14] M. P. Monopoli, C. Åberg, A. Salvati, K. A. Dawson, *Nat. Nanotechnol.* **2012**, *7*, 779.
[15] M. P. Monopoli, D. Walczyk, A. Campbell, G. Elia, I. Lynch, F. Baldelli Bombelli, K. A. Dawson, *J. Am. Chem. Soc.* **2011**, *133*, 2525.
[16] A. Lesniak, F. Fenaroli, M. P. Monopoli, C. Åberg, K. A. Dawson, A. Salvati, *ACS Nano* **2012**, *6*, 5845.
[17] A. Salvati, A. S. Pitek, M. P. Monopoli, K. Prapainop, F. Baldelli Bombelli, D. R. Hristov, P. M. Kelly, C. Åberg, E. Mahon, K. A. Dawson, *Nat. Nanotechnol.* **2013**, *8*, 137.
[18] J. V. Jokerst, T. Lobovkina, R. N. Zare, S. S. Gambhir, *Nanomedicine* **2011**, *6*, 715.
[19] E. Occhipinti, P. Verderio, A. Natalello, E. Galbiati, M. Colombo, S. Mazzucchelli, A. Salvadè, P. Tortora, S. M. Doglia, D. Prosperi, *Nanoscale* **2011**, *3*, 387.
[20] F. Corsi, L. Fiandra, C. De Palma, M. Colombo, S. Mazzucchelli, P. Verderio, R. Allevi, A. Tosoni, M. Nebuloni, E. Clementi, D. Prosperi, *ACS Nano* **2011**, *8*, 6383.
[21] M. Colombo, S. Sommaruga, S. Mazzucchelli, L. Polito, P. Verderio, P. Galeffi, F. Corsi, P. Tortora, D. Prosperi, *Angew. Chem. Int. Ed.* **2012**, *51*, 496.
[22] F. Danhier, F. Ansorena, J. M. Silva, R. Coco, A. Le Breton, V. Preat, *J. Controlled Release* **2012**, *161*, 505.
[23] S. Mazzucchelli, M. Colombo, P. Verderio, E. Rozek, F. Andreata, P. Tortora, F. Corsi, D. Prosperi, *Angew. Chem. Int. Ed.* **2013**, *52*, 3121.
[24] S. Mazzucchelli, P. Verderio, S. Sommaruga, M. Colombo, A. Salvadè, F. Corsi, P. Galeffi, P. Tortora, D. Prosperi, *Bioconjugate Chem.* **2011**, *22*, 2296.
[25] S. Huang, K. Shao, Y. Kuang, Y. Liu, J. Li, S. An, Y. Guo, H. Ma, X. He, C. Jiang, *Biomaterials* **2013**, *34*, 5294.
[26] P. Kocbek, S. Kralj, M. E. Kreft, J. Kristl, *Eur. J. Pharm. Sci.* **2013**, *50*, 130.
[27] R. A. Petros, J. M. De Simone, *Nat. Rev. Drug Discovery* **2010**, *9*, 615.
[28] L. Treuel, X. Jiang, G. U. Nienhaus, *J. R. Soc. Interface* **2013**, *10*, 20120939.
[29] S. D. Conner, S. L. Schmid, *Nature* **2003**, *422*, 37.
[30] A. E. Nel, L. Mädler, D. Velegol, D. Xia, E. M. V. Hoek, P. Somasundaran, F. Klaessig, V. Castranova, M. Thompson, *Nat. Mater.* **2009**, *8*, 543.
[31] J. V. Georgieva, D. Kalicharan, P. O. Couraud, I. A. Romero, B. Weksler, D. Hoekstra, I. S. Zuhorn, *Mol. Ther.* **2011**, *19*, 318.

[32] Y. Huang, L. He, W. Liu, C. Fan, W. Zheng, Y. S. Wong, T. Chen, *Biomaterials* **2013**, *34*, 7106.
[33] B. He, Z. Jia, W. Du, C. Yu, Y. Fan, W. Dai, L. Yuan, H. Zhang, X. Wang, J. Wang, X. Zhang, Q. Zhang, *Biomaterials* **2013**, *34*, 4309.
[34] B. He, P. Lin, Z. Jia, W. Du, W. Qu, L. Yuan, W. Dai, H. Zhang, X. Wang, J. Wang, X. Zhang, Q. Zhang, *Biomaterials* **2013**, *34*, 6082.
[35] V. E. Kagan, J. Shi, W. Feng, A. A. Shvedova, B. J. Fadeel, *Occup. Environ. Med.* **2010**, *52*, 943.
[36] G. Oberdörster, *J. Intern. Med.* **2010**, *267*, 89.
[37] A. Salvati, C. Åberg, T. Dos Santos, J. Varela, P. Pinto, I. Lynch, K. A. Dawson, *Nanomedicine* **2011**, *7*, 818.
[38] S. J. H. Soenen, U. Himmelreich, N. Nuytten, T. R. Pisanic, A. Ferrari, M. De Cuyper, *Small* **2010**, *6*, 2136.
[39] D. A. Heller, R. Sharma, M. S. Strano, *ACS Nano* **2009**, *3*, 149.
[40] H. Herd, N. Daum, A. T. Jones, H. Huwer, H. Ghandehari, C. M. Lehr, *ACS Nano* **2013**, *7*, 1961.
[41] E. C. Cho, L. Au, Q. Zhang, Y. Xia, *Small* **2010**, *6*, 517.
[42] A. Verma, O. Uzun, Y. Hu, Y. Hu, H. S. Han, N. Watson, S. Chen, D. J. Irvine, F. Stellacci, *Nat. Mater.* **2008**, *7*, 588.
[43] A. Verma, F. Stellacci, *Small* **2010**, *6*, 12.
[44] T. Hamada, M. Morita, M. Miyakawa, R. Sugimoto, A. Hatanaka, M. C. Vestergaard, M. Takagi, *J. Am. Chem. Soc.* **2012**, *134*, 13990.
[45] T. Fujiwara, H. Akita, H. Harashima, *Int. J. Pharm.* **2010**, *386*, 122.
[46] J. A. Kim, C. Åberg, A. Salvati, K. A. Dawson, *Nat. Nanotech.* **2011**, *7*, 62.
[47] M. Rahman, in Springer Series in Biophysics, Springer–Verlag Berlin, Heidelberg, Germany **2013**, Vol. *15*, p. 21.
[48] Z. J. Deng, M. Liang, M. Monteiro, I. Toth, R. F. Minchin, *Nat. Nanotechnol.* **2011**, *6*, 39.
[49] W. Liu, J. Rose, S. Plantevin, M. Auffan, J. Bottero, C. Vidaud, *Nanoscale* **2013**, *5*, 1658.
[50] D. Dell'Orco, M. Lundqvist, C. Oslakovic, T. Cedervall, S. Linse, *PLoS ONE* **2010**, *5*, e10949.
[51] M. A. Dobrovolskaia, A. K. Patri, J. W. Zheng, J. D. Clogston, N. Ayub, P. Aggarwal, B. W. Neun, Hall, S. B. McNeil, *Nanomedicine* **2009**, *5*, 106.
[52] M. S. Ehrember, E. Freidman, J. N. Finkelstein, G. Oberdoster, J. L. McGrath, *Biomaterials* **2009**, *30*, 603.
[53] M. J. D. Clift, S. Bhattacharjee, D. M. Brown, V. Stone, *Toxicol. Lett.* **2010**, *198*, 358.
[54] O. Lunov, T. Syrovets, C. Loos, J. Beil, M. Delacher, K. Tron, G. U. Nienhaus, A. Musyanovych, V. Mailander, K. Landefester, T. Simmet, *ACS Nano* **2011**, *5*, 1657.
[55] G. A. Orr, W. B. Chrisler, K. J. Cassens, R. Tan, V. J. Tarasevich, L. M. Markillie, R. C. Zangar, B. D. Thrall, *Nanotoxicology* **2011**, *5*, 296.
[56] A. L. Barràn-Berdòn, D. Pozzi, G. Caracciolo, A. L. Capriotti, G. Caruso, C. Cavaliere, A. Riccioli, S. Palchetti, A. Laganà, *Langmuir* **2013**, *29*, 6485.
[57] R. E. Serda, J. H. Go, R. C. Bhavane, X. Liu, C. Chiappini, P. Decuzzi, M. Ferrari, *Biomaterials* **2009**, *30*, 2440.
[58] P. Sandin, L. W. Fitzpatrick, J. C. Simpons, K. A. Dawson, *ACS Nano* **2012**, *6*, 1513.
[59] J. A. Stolwijk, C. Hartmann, D. Balani, S. Albermann, C. S. Keese, I. Giaever, J. Wegener, *Biosens. Bioelectron.* **2011**, *26*, 4720.
[60] J. B. Delehanty, H. Mattoussi, I. L. Medintz, *Anal. Bioanal. Chem.* **2009**, *393*, 1091.
[61] X. D. Wang, J. A. Stolwijk, T. Lang, M. Sperber, R. J. Meier, J. Wegener, O. S. Wolfbeis, *J. Am. Chem. Soc.* **2012**, *134*, 17011.
[62] J. Lin, R. Chen, S. Feng, Y. Li, Z. Huang, S. Xie, Y. Yu, M. Cheng, H. Zeng, *Biosens. Bioelectron.* **2009**, *25*, 388.
[63] J. B. Delehanty, C. E. Bradburne, K. Boeneman, K. Susumu, D. Farrell, B. C. Mei, J. B. Blanco-Canosa, G. Dawson, P. E. Dawson, H. Mattoussi, I. L. Medintz, *Integr. Biol.* **2010**, *2*, 265.
[64] C. G. Pack, M. R. Song, E. L. Tae, M. Hiroshima, K. H. Byun, J. S. Kim, Y. Sako, *J. Controlled Release* **2012**, *163*, 315.
[65] Y. Liu, M. Zhou, D. Luo, L. Wang, Y. Hong, Y. Yang, V. Y. Sha, *Biochem. Biophys. Res. Commun.* **2012**, *425*, 769.
[66] T. Kim, E. Momin, J. Choi, K. Yuan, H. Zaidi, J. Kim, M. Park, N. Lee, M. T. McMahon, A. Quinones-Hinojosa, J. W. Bulte, T. Hyeon, A. A. Gilad, *J. Am. Chem. Soc.* **2011**, *133*, 2955.
[67] J. S. Yoo, H. B. Kim, N. Won, J. Bang, S. Kim, S. Ahn, B. C. Lee, K. S. Soh, *Mol. Imaging Biol.* **2011**, *13*, 471.
[68] Y. C. Liu, P. C. Wu, D. B. Shieh, S. N. Wu, *Int. J. Nanomed.* **2012**, *7*, 1687.
[69] J. A. Kim, W. G. Lee, *Nanoscale* **2011**, *3*, 1526.
[70] B. Dubertret, P. Skourides, D. J. Norris, V. Noireaux, A. H. Brivanlou, A. Libchaber, *Science* **2002**, *298*, 1759.
[71] A. Candeloro, L. Tirinato, N. Malara, A. Fregola, E. Casals, V. Puntes, G. Perozziello, F. Gentile, M. L. Coluccio, G. Das, C. Liberale, F. De Angelis, E. Di Fabrizio, *Analyst* **2011**, *136*, 4402.
[72] A. M. Derfus, W. C. W. Chan, S. N. Bhatia, *Adv. Mater.* **2004**, *16*, 961.
[73] I. L. Medintz, T. Pons, J. B. Delehanty, K. Susumu, F. M. Brunel, P. E. Dawson, H. Mattoussi, *Bioconjugate Chem.* **2008**, *19*, 1785.
[74] E. Muro, T. Fragola, N. Pons, N. Lequeux, A. Ioannou, P. Skouridies, B. Dubertret, *Small* **2012**, *8*, 1029.
[75] F. M. Kievit, Z. R. Stephen, O. Veiseh, H. Arami, T. Wang, V. P. Lai, J. O. Park, R. G. Ellenbogen, M. L. Disis, M. Zhang, *ACS Nano* **2012**, *6*, 2591.
[76] P. A. McCarron, W. M. Marouf, D. J. Quinn, F. Fay, R. E. Burden, S. A. Olwill, C. J. Scott, *Bioconjugate Chem.* **2008**, *19*, 1561.
[77] L. W. Chan, Y. N. Wang, L. Y. Lin, M. P. Upton, J. H. Hwang, S. H. Pun, *Bioconjugate Chem.* **2013**, *67*, 167.
[78] S. Bhattacharyya, R. Bhattacharya, S. Curley, M. A. McNiven, P. Mukherjee, *Proc. Nat. Am. Soc.* **2010**, *107*, 14541.
[79] S. Bhattacharyya, J. A. Khan, G. L. Curran, J. D. Robertson, R. Bhattacharya, P. Mukherjee, *Adv. Mater.* **2011**, *23*, 5034.
[80] H. Y. Ko, K. J. Choi, C. H. Lee, S. Kim, *Biomaterials* **2011**, *32*, 1130.
[81] K. Fan, C. Cao, Y. Pan, D. Lu, D. Yang, J. Feng, L. Song, M. Liang, X. Yan, *Nat. Nanotechnol.* **2012**, *7*, 459.
[82] M. T. Stephan, J. J. Moon, S. H. Um, A. Bershteyn, D. J. Irvine, *Nat. Med.* **2010**, *16*, 1035.
[83] F. N. Al-Deen, J. Ho, C. Selomulya, C. Ma, R. Coppel, *Langmuir* **2011**, *27*, 3703.
[84] C. Xu, D. Yang, L. Mei, B. Lu, L. Chen, Q. Li, H. Zhu, T. Wang, *ACS Appl. Mater. Interfaces* **2013**, *5*, 2715.
[85] T. Xia, M. Kovochich, M. Liong, H. Meng, S. Kabehie, S. George, J. I. Zink, A. E. Nel, *ACS Nano* **2009**, *3*, 3273.
[86] H. Yoo, S. K. Moon, T. Hwang, Y. S. Kim, H. J. Kim, S. W. Choi, J. K. Kim, *Langmuir* **2013**, *29*, 5962.
[87] L. L. Ma, J. O. Tam, B. W. Willsey, D. Rigdon, R. Ramesh, K. Sokolov, K. P. Johnston, *Langmuir* **2011**, *27*, 7681.
[88] W. Jiang, B. Y. S. Kim, J. T. Rutka, W. C. W. Chan, *Nat. Nanotechnol.* **2008**, *3*, 145.
[89] Y. W. Huang, H. Liu, X. Xiong, Y. Chen, W. Tan, *J. Am. Chem. Soc.* **2009**, *131*, 17328.
[90] B. P. Gray, S. Li, K. C. Brown, *Bioconjugate Chem.* **2013**, *24*, 85.
[91] M. Youns, J. D. Hoheisel, T. Efferth, *Curr. Drug Targets* **2011**, *12*, 357.
[92] J. G. Huang, T. Leshuk, F. X. Gu, *Nanotoday* **2011**, *6*, 478.
[93] L. Rajendran, H. J. Knölker, K. Simons, *Nat. Rev. Drug Discovery* **2010**, *9*, 29.
[94] F. Milletti, *Drug Discovery Today* **2012**, *17*, 850.

[95] F. Madani, S. Lindberg, U. Langel, S. Futaki, A. Graslund, *J. Biophys.* **2011**, 414729.
[96] H. Park, H. Tsutsumi, H. Mihara, *Biomaterials* **2013**, *34*, 4872.
[97] X. Liu, C. Liu, W. Zhang, C. Xie, G. Wei, W. Lu, *Int. J. Pharm.* **2013**, *448*, 159.
[98] S. Guo, L. Huang, *J. Nanomater.* **2011**, 742895
[99] J. B. Delehanty, J. B. Blanco-Canosa, C. E. Bradbourne, K. Susumu, M. H. Stewart, D. E. Prasuhn, P. E. Dawson, I. L. Mednitz, *Chem. Commun.* **2013**, *49*, 7878.
[100] K. Boheneman, J. B. Delehanty,, J. B. Blanco-Canosa, K. Susumu, M. H. Stewart, E. Oh, A. L. Huston, G. Dawson, S. Ingale, R. Walters, M. Domowicz, J. R. Deschamps, W. R. Algar, S. DiMaggio, J. Manono, C. M. Spillmann, D. Thompson, T. L. Jennings, P. E. Dawson, I. L. Mednitz, *ACS Nano* **2013**, *7*, 3778.
[101] Y. Xu, F. C. Szoka, *Biochemistry* **1996**, *37*, 5616.
[102] I. M. Hafez, N. Maurer, P. R. Cullis, *Gene Ther.* **2001**, *8*, 1188.
[103] S. D. Li, L. Huang, *Biochim. Biophys. Acta* **2009**, *1788*, 2259.
[104] S. D. Li, L. Huang, *J. Controlled Release* **2010**, *145*, 178.
[105] H. Hatakeyama, H. Akita, H. Harashima, *Adv. Drug Delivery Rev.* **2011**, *63*, 152.
[106] Z. Rehman, I. S. Zuhom, D. Hoekstra, *J. Controlled Release* **2013**, *166*, 46.
[107] R. R. Sawant, S. K. Sriraman, G. Navarro, S. Biswas, R. A. Dalvi, V. P. Torchilin, *Biomaterials* **2012**, *33*, 3942.
[108] F. Pittella, M. Zhang, Y. Lee, H. J. Kim, T. Tockary, K. Osada, T. Ishii, K. Miyata, N. NIshiyama, K. Kataoka, *Biomaterials* **2011**, *32*, 3106.
[109] H. C. Kang, H. J. Kang, Y. K. Bae, *Biomaterials* **2011**, *32*, 1193.
[110] X. Liu, J. Zhang, D. M. Lynn, *Soft Matter* **2008**, *4*, 1688.
[111] J. Tu, T. Wang, W. Shi, G. Wu, X. Tian, Y. Wang, D. Ge, L. Ren, *Biomaterials* **2012**, *33*, 7903.
[112] R. V. Benjaminsen, M. A. Mattebjerg, J. R. Henriksen, S. M. Moghimi, T. L. Andresen, *Mol. Ther.* **2013**, *1*, 149.
[113] E. Wagner, *Acc. Chem. Soc.* **2012**, *45*, 1005.
[114] I. Nakase, S. Kobayashi, S. Futaki, *Peptide Sci.* **2010**, *94*, 763.
[115] N. Toriyabe, Y. Haiashi, H. Harashima, *Biomaterials* **2013**, *34*, 1337.
[116] Z. Krpetic, S. Saleemi, I. A. Prior, V. See, R. Qureshi, M. Brust, *ACS Nano* **2011**, *5*, 5195.
[117] P. Nativo, I. A. Prior, M. Brust, *ACS Nano* **2008**, *2*, 1639.
[118] H. Wei, R. X. Zhuo, X. Z. Zhang, *Prog. Polym. Sci.* **2013**, *3*, 503.
[119] M. S. Shim, Y. J. Kwon, *Biomaterials* **2010**, *31*, 3404.
[120] M. S. Shim, C. S. Kim, Y. C. Ahn, Z. Chen, Y. J. Kwon, *J. Am. Chem. Soc.* **2010**, *132*, 8316.
[121] M. S. Shim, Y. J. Kwon, *Biomaterials* **2011**, *32*, 4009.
[122] S. C. Semple, A. Akinc, J. Chen, A. P. Sandhu, B. L. Mui, C. K. Cho, D. W. Sah, D. Stebbing, E. J. Crosley, E. Yaworski, I. M. Hafez, J. R. Dorkin, J. Qin, K. Lam, K. G. Rajeev, K. F. Wong, L. B. Jeffs, L. Nechev, M. L. Eisenhardt, M. Jayaraman, M. Kazem, M. A. Maier, M. Srinivasulu, M. J. Weinstein, Q. Chen, R. Alvarez, S. A. Barros, S. De, S. K. Klimuk, T. Borland, V. Kosovrasti, W. L. Cantley, Y. K. Tam, M. Manoharan, M. A. Ciufolini, M. A. Tracy, A. de Fougerolles, I. MacLachlan, P. M. Cullis, T. D. Madden, M. J. Hope, *Nat. Biotechnol.* **2010**, *28*, 172.
[123] M. S. Shim, Y. J. Kwon, *Bioconjugate Chem.* **2009**, *20*, 488.
[124] S. Guo, Y. Huang, T. Wei, W. Zhang, W. Wang, D. Lin, H. Zhang, A. Kumar, Q. Du, J. Xing, L. Deng, Z. Liang, P. C. Wang, L. Dong, X. J. Liang, *Biomaterials* **2011**, *32*, 879.
[125] A. Dehshahri, R. K. Oskuee, W. T. Shier, A. Hatefi, M. Ramezani, *Biomaterials* **2009**, *30*, 4187.
[126] Z. Zhang, W. Coa, H. Jin, J. F. Lovell, M. Yang, L. Ding, J. Chen, I. Corbin, Q. Luo, G. Zheng, *Angew. Chem. Int. Ed.* **2009**, *48*, 9171.
[127] J. G. van der Boorn, M. Schlee, C. Coch, G. Hartmann, *Nat. Biotechnol.* **2011**, *29*, 325.
[128] D. Drescher, J. Kneipp, *Chem. Soc. Rev.* **2012**, *41*, 5780.
[129] Y. Yu, X. Xie, M. Zheng, L. Yu, L. Zhang, J. Zhao, D. Jiang, X. Che, *Int. J. Nanomed.* **2012**, *7*, 5079.
[130] P. L. Mallet, F. Bachand, *Traffic* **2013**, *14*, 282.
[131] F. Cardarelli, M. Serresi, A. Albanese, R. Bizzarri, F. Beltram, *J. Biol. Chem.* **2011**, *286*, 12292.
[132] L. Pan, J. Liu, Q. He, L. Wang, J. Shi, *Biomaterials* **2013**, *34*, 2719.
[133] M. Nagai, Y. Yoneda, *Biochim. Biophys. Acta.* **2013**, *1830*, 2813.
[134] S. Brunner, T. Sauer, S. Carotta, M. Cotten, M. Saltik, E. Wagner, *Gene Ther.* **2000**, *7*, 401.
[135] J. D. Larsen, N. L. Ross, M. O. Sullivan, *J. Gene Med.* **2012**, *14*, 580.
[136] I. Ojea-Jiménez, L. García-Fernández, L. Lorenzo, V. F. Puntes, *ACS Nano* **2012**, *6*, 7692.
[137] M. K. Gragas, J. P. Scaffidi, B. Lauly, T. Vo-Dinh, *App. Spect.* **2010**, *64*, 858.
[138] W. Xie, L. Wang, Y. Zhang, L. Su, A. Shen, J. Tan, J. Hu, *Bioconjugate Chem.* **2009**, *20*, 768.
[139] L. A. Austin, B. Kang, C. W. Yen, M. A. El-Sayed, *J. Am. Chem. Soc.* **2011**, *133*, 17594.
[140] S. Y. Lin, N. T. Chen, S. P. Sum, L. Lo, C. S. Yang, *Chem. Commun.* **2008**, *21*, 4762.
[141] C. W. Kuo, D. Y. Chueh, N. Singh, F. C. Chien, P. Chen, *Bioconjugate Chem.* **2011**, *22*, 1073.
[142] C. Xu, J. Xie, N. Kohler, E. G. Walsh, Y. E. Chinand, S. Sun, *Chem. Asian. J.* **2008**, *3*, 548.
[143] R. Misra, S. K. Sahoo, *Eur. J. Pharm. Sci.* **2010**, *39*, 152.
[144] R. Bahadur, B. Thapa, P. Xu, *Mol. Pharm.* **2012**, *9*, 2719.
[145] J. N. Liu, W. Bu, L. M. Pan, S. Zhang, F. Chen, L. Zhou, K. L. Zhao, W. Peng, J. Shi, *Biomaterials* **2012**, *33*, 7282.
[146] L. A. Austin, B. Kang, C. W. Yen, M. A. El-Sayed, *Bioconjugate Chem.* **2011**, *22*, 2324.
[147] L. Yong-Yong, D. Hai-Qing, C. Xiao-Jun, R. Tian-Bin, *Mater. Sci. Eng. C. Mater. Biol. Appl.* **2013**, *33*, 2698.
[148] R. Tian-Bin, X. Wen-Juan, D. Hai-Qing, L. Yong-Yong, *Polymer* **2011**, *52*, 3580.
[149] L. Yong-Yong, H. Shou-Hu, X. Wang, W. Hui-Yuan, L. Xiao-Hua, L. Cao, C. Si-Xue, Z. Xian-Zheng, Z. Ren-Xi, *J. Mater. Chem.* **2011**, *21*, 3100.
[150] L. C. Knight, J. E. Romano, B. Krynska, S. Faro, F. B. Mohamed, J. J. Gordon, *Mol. Biomark. Diagn.* **2010**, *1*, 1.
[151] D. Kurihara, M. Akita, A. Kudo, T. Masuda, S. Futaki, H. Harashima, *Biol. Pharm. Bull.* **2009**, *3*, 1303.
[152] D. M. Hockenbery, *Environ. Mol. Mutagen.* **2010**, *51*, 486.
[153] L. F. Yousif, K. M. Stewart, S. O. Kelley, *ChemBioChem* **2009**, *10*, 1939.
[154] Y. Yamada, H. Harashima, *Adv. Drug Delivery Rev.* **2008**, *60*, 1439.
[155] J. Choi, J. Shin, J. Lee, M. Cha, *Chem. Commun.* **2012**, *48*, 7474.
[156] K. Zhou, Y. Wang, X. Huang, K. Luby-Phelphs, B. D. Sumer, J. Gao, *Angew. Chem. Int. Ed.* **2012**, *123*, 6233.
[157] M. Breunig, S. Bauer, A. Goepferich, *Eur. J. Pharm. Biopharm.* **2008**, *68*, 112.
[158] G. Chamberlain, D. Tulumello, S. Kelley, *ACS Chem. Biol.* **2013**, *8*, 1389.
[159] S. Marrache, S. Tundup, D. Harn, S. Dhar, *ACS Nano* **2013**, *7*, 7392.
[160] M. Colombo, S. Mazzucchelli, V. Collico, S. Avvakumova, L. Pandolfi, F. Corsi, F. Porta, D. Prosperi, *Angew. Chem. Int. Ed.* **2012**, *10*, 9272.
[161] S. Mazzucchelli, S. Sommaruga, M. O'Donnell, P. Galeffi, P. Tortora, D. Prosperi, M. Colombo, *Biomater. Sci.* **2013**, *1*, 728.
[162] M. Colombo, S. Mazzucchelli, J. M. Montenegro, E. Galbiati, F. Corsi, W. J. Parak, D. Prosperi, *Small* **2012**, *21*, 1492.

[163] S. Mazzucchelli, M. Colombo, C. De Palma, A. Salvadé, P. Verderio, M. D. Coghi, E. Clementi, P. Tortora, F. Corsi, D. Prosperi, *ACS Nano* **2010**, *4*, 5693.
[164] G. V. Los, L. P. Encell, M. G. McDougall, D. D. Hartzell, N. Karassina, C. Zimprich, M. G. Wood, R. Learish, R. Friedman Ohana, M. Uhr, D. Simpson, J. Mendez, K. Zimmermann, P. Otto, G. Vidugiris, Zhu, A. Darzins, D. H. Klaubert, R. F. Bulleit, K. V. Wood, *ACS Chem. Biol.* **2008**, *3*, 373.
[165] S. N. Peterson, K. Kwon, *Current. Chem. Genomics* **2012**, *6*, 8.
[166] T. K. Neklesa, H. S. Tae, A. R. Schneekloth, M. J. Stulberg, *Nat. Chem.* **2011**, *7*, 538.
[167] D. S. Liu, W. S. Phipps, K. H. Loh, M. Howarth, A. Y. Ting, *ACS Nano* **2012**, *6*, 11080.
[168] H. Ban, M. Nagano, J. Gavrilyuk, W. Hakamata, T. Inokuma, C. F. Barbas, *Bioconjugate Chem.* **2013**, *24*, 520.
[169] J. M. Silva, M. Videira, R. Gaspar, V. Prèat, H. F. Florindo, *J. Controlled Release* **2013**, *168*, 179.
[170] Y. Krishnamachari, S. M. Geary, C. D. Lemke, A. K. Salem, *Pharm. Res.* **2011**, *28*, 215.
[171] A. L. Parry, N. A. Clemson, J. Ellis, S. R. Bernhard, B. G. Davis, N. R. Cameron, *J. Am. Chem. Soc.* **2013**, *135*, 9362.
[172] R. P. Brinãs, A. Sundgren, P. Sahoo, S. Morey, K. Rittenhouse-Olson, G. E. Wilding, W. Deng, J. J. Barchi, *Bioconjugate Chem.* **2012**, *23*, 1513.
[173] K. Nikura, T. Matsunaga, T. Suzuki, S. Kobayashi, H. Yamaguchi, Y. Orba, A. Kawaguchi, H. Hasegawa, K. Kajino, T. Ninomiya, K. Ijiro, H. Sawa, *ACS Nano* **2013**, *7*, 3926.
[174] F. Ding, S. Radic, R. Chen, P. Y. Chen, N. K. Geitner, J. M. Brown, P. C. Ke, *Nanoscale* **2013**, *5*, 9162.
[175] Jie Feng, J. M. Slocik, M. Sarikaya, R. R. Naik, B. L. Farmer, H. Heinz, *Small* **2012**, *8*, 1049.

Adv. Healthcare Mater. **2014**,
DOI: 10.1002/adhm.201300602